

OPTICAL FIBRE, NEW DEVELOPMENTS

OPTICAL FIBRE, NEW DEVELOPMENTS

Edited by
CHRISTOPHE LETHIEN

In-Tech
intechweb.org

Published by In-Teh

In-Teh

Olajnica 19/2, 32000 Vukovar, Croatia

Abstracting and non-profit use of the material is permitted with credit to the source. Statements and opinions expressed in the chapters are those of the individual contributors and not necessarily those of the editors or publisher. No responsibility is accepted for the accuracy of information contained in the published articles. Publisher assumes no responsibility liability for any damage or injury to persons or property arising out of the use of any materials, instructions, methods or ideas contained inside. After this work has been published by the In-Teh, authors have the right to republish it, in whole or part, in any publication of which they are an author or editor, and the make other personal use of the work.

© 2009 In-teh

www.intechweb.org

Additional copies can be obtained from:

publication@intechweb.org

First published December 2009

Printed in India

Technical Editor: Melita Horvat

Optical Fibre, New Developments,

Edited by Christophe Lethien

p. cm.

ISBN 978-953-7619-50-3

Preface

The optical fibre technology is one of the hot topics developed at the beginning of the 21st century and could do many services for application dealing with lighting, sensing and communicating systems. Many improvements have been carried out since 30 years to reduce the fibre attenuation and to improve the fibre performance. Nowadays, new applications have been developed over the scientific community and this book titled "Optical Fibre, New Developments" fits into this paradigm. It summarizes the current status of know-how in optical fibre applications and represents a further source of information dealing with two main topics:

- the development of fibre optics sensors,
- the application of optical fibre for telecommunication systems.

Over 24 chapters, this book reports specific information for industrial production and for the research community about the optical fibre potentialities for telecommunication and sensing. It gives an overview of the existing systems and the main credit of this book should go to all the contributors who have summarized the contemporary knowledge in the field of the optical fibre technology.

This book could be divided into two parts. The first part covers the applications of fibre based distributed sensors network or local sensor developments for:

- Temperature sensing (fictive temperature measurement of bulk silica glass and silica based optical fibres),
- Strain sensing,
- Chemical sensing (detection of hydrogen leaks, chemical species detection using advanced nanostructured material (carbon nanotubes, tin oxide particles)...),
- Electric field sensing in electric power industry, high intensity electric field environments and high intensity telecommunications signal,
- Structural health monitoring,
- Structures monitoring using distributed sensors network (bridges, building...)
- Corrosion measurement using multipoint distributed corrosion sensor based on an optical fibre and the optical time domain reflectometry technique,
- Turbidimetry based on optical fibre sensor for environmental measurement in urban or industrial waste water.

The second part of the book titled "Optical Fibre, New Developments" deals with the new developments realized in the field of optical fibre communication in particular:

- The use of optical fibre delay lines for phase array radar system and microwave signal processing as well as for wavelength selective switching,
- The theoretical modelling of all optical Impulse Radio Ultra Wideband generation without optical filter,
- The potential of graded index glass and polymer multimode fibre used in low cost 10Gbps small office/home office baseband network and Radio over Fibre systems,
- The development of 60-GHz millimetre wave over fibre system based on two innovative solutions using polymer multimode fibre,
- The use of graded index plastic optical fibre for broadband access networks up to 40Gbps combined with the special design of the light injection setup,
- The development of all optical logic gates based on non linear optical loop mirror
- The theoretical modelling and experimental demonstration of fibre based optical parametric amplifier using novel highly non linear fibres (photonic crystal fibres),
- The Orthogonal Frequency Division Multiplexing Ultra Wideband radiofrequency (RF) signal transmission over glass multimode fibre by optical means using either parallel RF/serial optics or parallel RF/parallel optics topologies,
- The combined use of back propagation technique with dispersion managed transmission to extend the linear behaviour of optical fibre.
- The development of high speed, high power and high responsivity photodiode for Radio over Fibre systems

A specific chapter finding applications in the field of biomedical and material processing (power scaling in fibre laser) using large mode area microstructured fibres is also developed.

This book is so address to engineers or researchers who want to improve their knowledge of optical fibre technologies in sensing and communicating systems.

I thank you my family for its patience and its support during the writing.

December 2009,

Christophe Lethien

Book editor

Associate professor for University of Lille 1 - Institute of Electronics,
Microelectronics and Nanotechnologies CNRS UMR 8520 (France)

Contents

Preface	V
1. Fabrication of sensitive fibre-optic gas sensors based on nano-assembled thin films	001
Sergiy Korposh and Seung-Woo Lee	
2. Optical fibres in aeronautics, robotics and civil engineering	017
Giuseppe De Maria, Aldo Minardo, Ciro Natale, Salvatore Pirozzi and Luigi Zeni	
3. Optical Fibre Sensor System for Multipoint Corrosion Detection	035
Joaquim F. Martins-Filho and Eduardo Fontana	
4. Fiber Sensor Applications in Dynamic Monitoring of Structures, Boundary Intrusion, Submarine and Optical Ground Wire Fibers	045
Xiaoyi Bao, Jesse Leeson, Jeff Snoddy and Liang Chen	
5. Near-Field Opto-Chemical Sensors	069
Antonietta Buosciolo, Marco Consales, Marco Pisco, Michele Giordano and Andrea Cusano	
6. Electric field sensing schemes using low-coherence light and LiNbO ₃ electrooptical retarders	101
Celso Gutiérrez-Martínez	
7. Fictive temperature measurements in silica-based optical fibers and its application to Rayleigh loss reduction	125
Matthieu Lancry, Elise Régnier and Bertrand Poumellec	
8. Optical Fibres Turbidimetres	161
Miguel A. Pérez and Rocío Muñoz	
9. Distributed Optical Fibre Sensors for Structural Health Monitoring: Upcoming Challenges	177
Vincent Lanticq, Renaud Gabet, Frédéric Taillade and Sylvie Delepine-Lesoille	
10. Finding hydrogen leaks by means of the fiber Bragg gratings technology	201
Marc Debliquy, Driss Lahem, Christophe Caucheteur, Patrice Megret	
11. Fiber Optic Chemical Sensors based on Single-Walled Carbon Nanotubes: Perspectives and Challenges	227
Marco Consales, Antonello Cutolo, Michele Penza, Patrizia Aversa, Michele Giordano and Andrea Cusano	

12. Low Cost Multi-fiber Model Distributed Optical Fiber Sensor Chuanong Wang	259
13. Potentialities of multimode fibres as transmission support for multiservice applications: from the wired small office/home office network to the hybrid radio over fibre concept Christophe Lethien, Christophe Loyez, Jean-Pierre Vilcot and Paul Alain Rolland	283
14. An overview of radio over fibre systems for 60-GHz wireless local area networks and alternative solutions based on polymer multimode fibres Christophe Loyez, Christophe Lethien, Jean-Pierre Vilcot and Nathalie Rolland	321
15. Application of Graded-Index Plastic Optical Fiber in broadband access networks Jianjun Yu	333
16. High-Speed, High-Power, and High Responsivity Photodiode for Radio-Over-Fiber (ROF) Communication J.-W. Shi, F.-M. Kuo and Y.-S. Wu	367
17. Ultrawideband-over-fiber technologies with directly-modulated semiconductor lasers V́ctor Torres-Company, Kamau Prince, Xianbin Yu, Timothy Braidwood Gibbon and Idelfonso Tafur Monroy	397
18. All Optical Generation and Processing of IR UWB Signals Y. Ben Ezra, B.I. Lembrikov, M. Ran and M. Haridim	415
19. High Spectral Efficiency Optical Transmission of OFDM Ultra-wideband Signals beyond 40 Gb/s B.I. Lembrikov, Y. Ben Ezra, M. Ran and M. Haridim	435
20. Nonlinear Impairment Compensation using Backpropagation Ezra Ip and Joseph M. Kahn	457
21. Fiber Optical Parametric Amplifier as Optical Signal Processor Shunsuke Ono	485
22. Fibre Based Schemes for Ultrafast Subsystems: Nonlinear Optical Loop Mirrors Traditional Design and Novel Applications Antonella Bogoni, Francesco Fresi, Paolo Ghelfi, Emma Lazzeri, Luca Poti and Mirco Scaffardi	505
23. Digitally Fast Programmable Optical Signal Processing Devices Xinwan LI, Zehua HONG, Shuguang LI and Jianping CHEN	529
24. All Glass Micro-structured Optical Fibres Liang Dong	555

Fabrication of sensitive fibre-optic gas sensors based on nano-assembled thin films

Sergiy Korposh and Seung-Woo Lee
The University of Kitakyushu
Japan

1. Introduction

Optical techniques offer powerful tools for the characterisation of chemical and biological systems. The variety of different designs and measurement schemes of fibre-optic sensors provides the potential to create very sensitive and selective measurement techniques for the purpose of environmental monitoring.

Different approaches exist for creation of fibre-optic sensors (FOS), which generally can be classified into two groups depending on the sensing mechanism: intrinsic and extrinsic fibre-optic sensors (Grattan & Meggitt, 1999). Intrinsic FOS allows to implement different measurements designs within an optical fibre based on the gratings (Bragg Gratings and long period gratings, LPG) written into the fibre core in which the changes in the reflected light due to changes in the grating period is measured to detect the effect caused by an external stimulus (Vohra et al., 1999; Schroeder et al., 1999). Interferometric sensors can be made that use some external effect to cause a change in the optical path way or a phase difference in the interferometer caused by some external effect. All traditional interferometers such as Michelson, Mach Zehnder (Bucholtz et al., 1989; Dandridge, 1991; Yuan & Yang, 2005), Fizeau, Sagnac (Russell & Dakin, 1999) and Fabry Perot (Rao et al., 2000; Cibula & Donlagic, 2004; Lin et al., 2004) used for measuring of both chemical and physical parameters can be constructed utilizing optical fibres. The other type of intrinsic fibre-optic sensors is based on the evanescent wave absorption effect (Leung et al., 2006).

The advantages of the fibre-optic sensors allow to create measurements systems with the high sensitivity and selectivity, providing an excellent tool for the environmental monitoring. In general, sensitive elements are needed for efficient fibre-optic sensing, which amplify the chemical interaction of analytes and convert it into a measurable optical response as signal. Current research in the field of optical fibre sensors is focusing on the creation and development of new sensitive elements which can expand an application area and increase the number and range of the analytes that can be measured by fibre-optic sensors.

Generally there are some requirements to the sensitive elements of fibre-optic sensors and they should be:

- transparent in the appropriate spectral range;
- change their optical properties under the influence of the specific chemical species;

- fast in response and have wide dynamic range;
- reversible;
- selective;
- easy to immobilize onto glass/quartz/ plastic fibre;
- easily and cheaply manufactured.

Employing different sensitive elements deposited onto the side of single-mode (Monzón-Hernández & Villatoro, 2006) and multimode (Rajan et al., 2005) optical fibres allows the creation of an FOS with high sensitivity and selectivity.

For instance a pH fibre-optic sensor coated with porous silica film was prepared by the sol-gel procedure to measure the pH of the solution with sensors sensitivity up to 0.66 dB/pH for the pH range of 7–10.5 (Rayss & Sudolski, 2002). Using a sol-gel film doped with a dye (e.g. coumarin, brilliant green, rhodamine 6G, and rhodamine B) (Beltrán-Pérez et al., 2006; Gupta & Sharma, 1997; Gupta & Sharma, 1998) the dynamic range of the pH measurement can be increased to cover pH values from 2 up to 12. The sensor sensitivity was increased by decreasing the probe light wavelength, with the highest sensitivity being achieved at 400 nm (Beltrán-Pérez et al., 2006).

A sensor element doped with polypyrrole was used as a sensitive element for nerve agent detection; using a 1,5 naphthalene disulphonic acid (NDSA) -doped polypyrrole coating produced by the *in situ* deposition technique a sensitivity of up to 26 ppm with a response time of a few seconds was achieved. Utilizing different deposition techniques and using different doping materials has produced fibre-optic sensors with different sensitivities and performances (Bansal & El-Sherif, 2005).

The transparency of an optical fibre depends on the fibre material and the wavelength of the probe light. Thus different fibres are appropriate for different spectral ranges; for the near infrared spectra (NIR) the chalcogenide (Lucas et al., 2006; Walsh et al., 1995), for Mid-IR the silver halide (Le Coq et al., 2002; Beyer et al., 2003), and for the UV-Vis quartz (Abdelghani et al., 1997) or plastic optical fibres (Ogita, et al., 2000) can be selected.

Chalcogenide glass fibres were used to perform remote infrared analysis of non-polar organic species in aqueous solution. This technique permits the observation of disruption induced in living mammalian cells by at least two different types of toxins and it is possible to distinguish between the effect of a genotoxic agent (which damages nucleic acids) and a cytotoxic agent (which damages other cellular components) based on the cell's response to IR light (Lucas et al., 2006).

For the detection of chemical species with very low concentration in water, chalcogenide fibres which had special chemical treatment were applied for evanescent wave absorption spectroscopy (Le Coq et al., 2002). The concentration of chloroform and ethanol in water were measured using the variations of their absorbance in the infrared spectral range of 8.6–10 μm (Figure 1). The lower limit of detection for ethanol in water was approximately 0.5%, when the length of the sensing zone (removed cladding) was 3 cm (Le Coq et al., 2002).

A fibre-optic sensor consisting of a silver halide ($\text{AgBr}_x\text{Cl}_{1-x}$) optical fibre coated with polyisobutylene (PIB) or Teflon was developed for the *in situ* monitoring of pesticides and chlorinated hydrocarbons in water for the spectral range of 8.5–12 μm (Beyer et al., 2003). The sensitivity of this FOS was in the region of 100 ppb and it could be enhanced by increasing the interaction of the evanescent field with the investigated medium.

A mid-IR grating spectrometer operating in the wavelength range of 8–12.5 μm was developed for the detection of chlorinated hydrocarbons with a detection limit of 900 ppb

for tetrachloroethylene. The sensor was based on the detection of the characteristic absorption of chlorinated hydrocarbons in the polymer membrane coated onto the sensor silver halide fibre and the effects of the samples on the evanescent field of the guided light (Walsh et al., 1995).

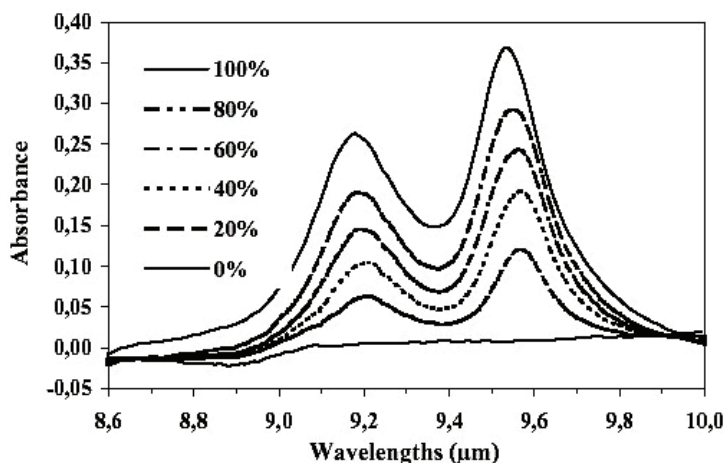


Fig. 1. Absorbance spectrum of the different concentration of ethanol in water measured in the infrared spectral range of 8.6–10 μm (Le Coq et al., 2002)

The most suitable fibres in the visual spectral range for the creation of intrinsic FOS based on the generation of an evanescent wave are the plastic cladded silica fibres (PCS); because the plastic cladding can be easily removed by mechanical stripping or by means of chemical etching. This FOS coated with an appropriate sensitive material could be used for the detection of chemical parameters and species (Kawahara et al., 1983; Sharma & Gupta, 2005; Ronot et al., 1994).

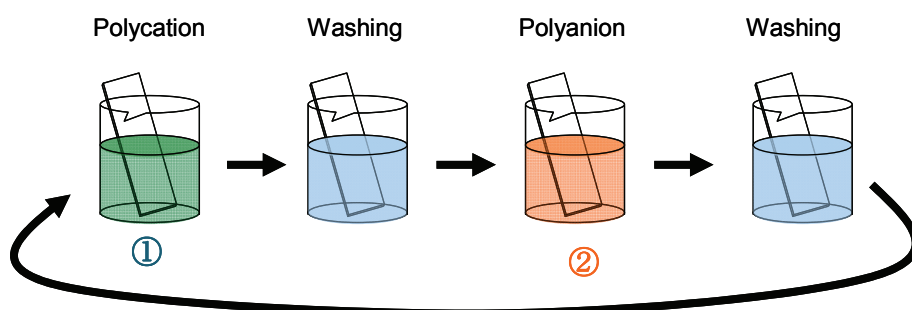


Fig. 2. Schematic illustration of the layer-by-layer (LbL) method

In the deposition of a sensitive coating onto the optical fibre it is crucial to provide the sensor with stable parameters and prevent the functional material from leaching or desorbing from the optical fibre. Different immobilization procedures based on the covalent

and noncovalent bond could be used for the deposition of the sensitive element onto the optical fibre. The Langmuir-Blodgett (LB) technique has been employed for the coating of the fibre-optic with aim of developing long period grating fibre sensor (James & Tatam, 2006). This deposition technique allows to control material at nanolevel and is based on the transferring of the orientated monolayers onto the solid substrate. Alternative approach is the electrostatic layer-by-layer (LbL) method that has been useful for the preparation of molecularly assembled films with the good adhesion properties to the quartz surfaces, Figure 1 (Iler, 1966; Ichinose et al., 1996). One of the advantageous of this method over LB process is that wide class of materials can be deposited on the different types of surfaces. This deposition technique is still expanding its potential because of its versatility for fabrication of ordered multilayers with well controlled thickness and the possibility to use both inorganic and organic materials (Lee et al., 1998).

Porphyrin compounds can be used as a sensitive element for optical sensors because their optical properties (absorbance and fluorescence features) depends on the environmental conditions in which molecule is present (Takagi et al., 2006). Porphyrins are tetrapyrrolic pigments that widely occur in nature and play an important role in many biological systems (Kadish et al., 2000). The optical spectrum of the solid state porphyrin is modified as compared to that of porphyrin in solution, due to the presence of strong π - π interactions (Schick et al., 1989). Interactions with other chemical species can produce further optical spectral changes, thus creating the possibility that they can be applied to optical sensor systems. The high extinction coefficient ($> 200,000 \text{ cm}^{-1}/\text{M}$) makes porphyrin especially attractive for the creation of optical sensors.

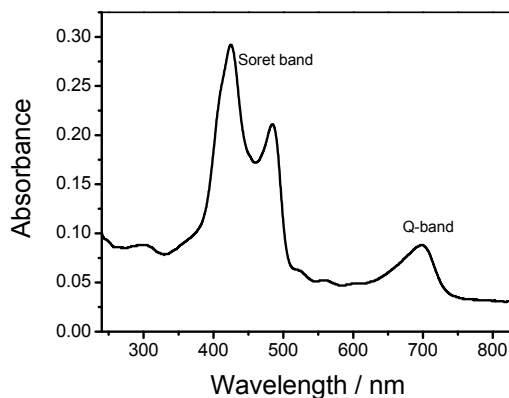


Fig. 3. Absorbance spectrum of a *J*-aggregated porphyrin film deposited onto a quartz substrate (Korposh et al., 2006)

For example, Fig. 3 shows a typical absorbance spectrum of tetrakis-(4-sulfophenyl)porphine (TSPP) in an alternate film with a cationic polymer, which consists of two Soret bands (425 and 484 nm) and one pronounced Q-band (700 nm). Exposure of the porphyrin compound to chemical analytes leads to the alternation of the *J*-aggregation

which in turn changes the absorbance spectrum and this phenomenon can be used for the optical sensor development (Korposh et al., 2006).

Moreover, the optical properties of the porphyrin compound can be controlled by metallation of its core which in turn will lead to a higher sensitivity and wider class of chemical compounds that could be measured, Fig. 4 (Rakow & Suslik, 2000). Exposure of a metalloporphyrin sensor array to chemical species leads to the different colour change which can be used for the fibre-optic sensor development.

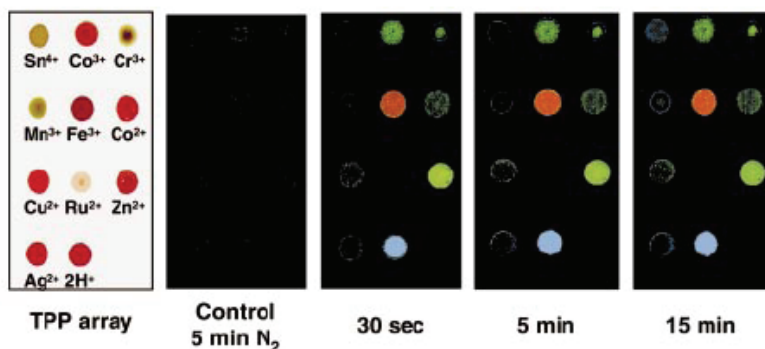


Fig. 4. Colour change profiles of a metalloporphyrin sensor array as a function of exposure time to *n*-butylamine vapour (Rakow & Suslik, 2000)

In this chapter, we would like to describe the use of the LbL method for the deposition of a porphyrin thin film onto a multimode silica core/plastic clad optical fibre with the aim of developing an evanescent wave fibre optic gas sensor. A short section of the plastic cladding was replaced with a functional coating of alternate poly(diallyldimethylammonium chloride) (PDDA) and TSPP layers. The measurement principle of the device is based on the ammonia-induced optical change in the transmission spectrum of the coated optical fibre. As light travels along the core of the optical fibre, a small portion of energy penetrates the cladding in the form of an *evanescent wave*, the intensity of which decays exponentially with the distance from the interface between the cladding and the surrounding environment. The penetration depth (d_p) of the evanescent wave is described by (Grattan & Meggitt, 1999):

$$d_p = \frac{\lambda}{2\pi(n_{eff}^2 - n_c^2)^{1/2}}, \quad (1)$$

where λ is the wavelength of light in free space, n_c is the refractive index of the cladding and n_{eff} is the effective refractive index of the mode guided by the optical fibre. The deposition of a functional coating layer onto the optical fibre leads to the chemically induced modulation in the transmission spectrum and provides quantitative and qualitative information on the chemical species under examination. The employment of the proposed fibre optic sensor based on the intrinsic evanescent wave has an additional advantage to offer cheap and compact devices, due to combination of light emitting diode (LED) and photodetector components. Moreover, the sensitivity of the device can be improved by varying the length of the sensing area and the process for film deposition will be less time-consuming.

2. Evanescent wave fibre-optic sensor

2.1 Sensor fabrication

Tetrakis-(4-sulfophenyl)porphine (TSPP) and poly(diallyldimethylammonium chloride) (PDDA, Mw: 200000–350000, 20 wt% in H₂O) were purchased from Tokyo Kasei, Japan (Figure 2). Deionized pure water (18.3 M Ω ·cm) was obtained by reverse osmosis followed by ion exchange and filtration (Nanopure Diamond, Barnstead, Japan). An HCS200 multimode silica core/plastic cladding optical fibre (OF) with core and cladding diameters of 200 μ m and 400 μ m, respectively, was purchased from Ocean Optics (USA). Standard ammonia gas of 100 ppm in dry air was purchased in a cylinder from Japan Air Gases Corp. All of these chemicals were of analytical grade and used without further purification.

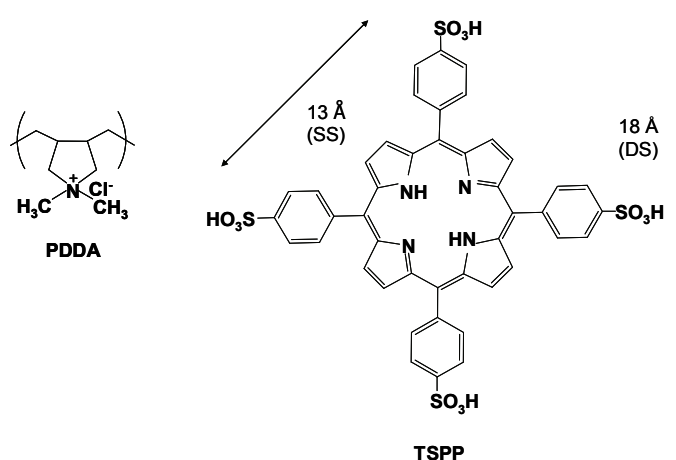


Fig. 5. Structural models of the polycation (PDDA) and porphyrin (TSPP) compounds used in this study (Agira et al., 1997): SS, side length of square; DS, diagonal length of square

The electrostatic layer-by-layer adsorption method was employed for the deposition of a porphyrin thin film onto a multimode optical fibre (OF). A schematic illustration of this method using PDDA and TSPP is shown in Fig. 6a. A multimode optical fibre from which the plastic cladding has been removed over an area 1 cm in length was rinsed in ethanol and distilled water prior to film deposition. The plastic cladding could be easily burned off from the fibre using a burner flame (temperature < 500 °C, the property of the silica core is not changed within the temperature range). One end of the optical fibre was connected to a deuterium-halogen light source (DH-2000-Ball, Mikropack), the other end was connected to a spectrometer (S1024DW, Ocean Optics). The stripped section of the optical fibre was fixed within a special deposition cell for film preparation, as shown in Fig. 6b.

Before assembly, the previously stripped section of the optical fibre was cleaned with concentrated sulfuric acid (96%), rinsed several times with deionized water, and treated with 1 wt% ethanolic KOH (ethanol/water = 3:2, v/v) for about 10 min with sonication in order to functionalize the surface of the silica core with a OH group. The fibre core was then rinsed with deionized water, and dried by flushing with dry nitrogen gas. The film is denoted (PDDA⁺/TSPP)_x, where x = 5 and indicates the number of adsorption cycles. The

film was prepared by the alternate deposition of PDDA (5 mg mL⁻¹ in water) and TSPP (1 mM in water) (where one cycle is considered to be a combined PDDA⁺/TSPP⁻ bilayer) by introducing a coating solution (150 μL) into the deposition cell with intermediate processes of water washing and drying by flushing with nitrogen gas being undertaken between the application of layers. In every case, the outermost surface of the alternate film was TSPP.

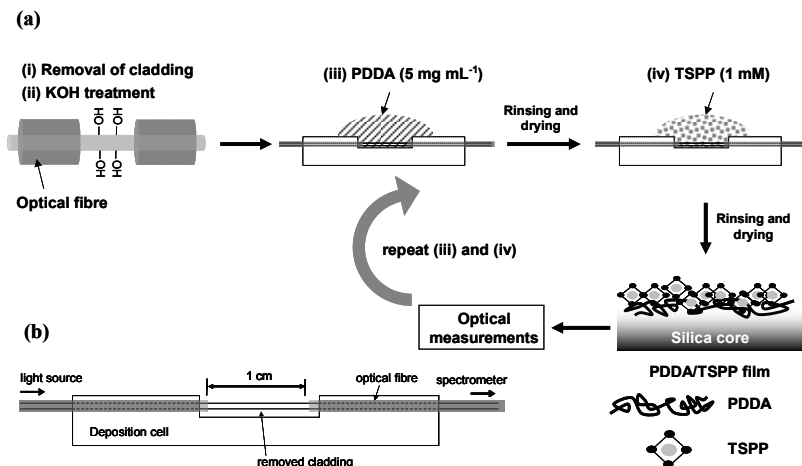


Fig. 6. (a) Schematic illustration of the layer-by-layer adsorption of TSPP and PDDA on a multimode optical fibre and (b) deposition cell used for coating the optical fibre

The assembly process was monitored using an S1024DW spectrometer (Ocean Optics). The absorbance was determined by taking the logarithm of the ratio of the transmission spectrum of the coated fibre, $T(\lambda)$, to the transmission spectrum measured prior to film deposition $T_0(\lambda)$,

$$A(\lambda) = -\log \frac{T(\lambda)}{T_0(\lambda)} \quad (2)$$

The assembly process was characterised and the thickness of the film was measured using a quartz crystal microbalance technique, as described in our previous work (Korposh et al., 2006).

2.2 Optical measurements

The desired gas concentrations were produced using a two-arm flow system, as shown in Fig. 7a. Dry compressed air and ammonia gas of 100 ppm passed through two flowmeters, and the two flows were recombined with a final analyte concentration (volume fraction) c in the measurement chamber being calculated using,

$$c = \frac{L_1 \cdot z}{L_1(1+z) + L_2} \quad (3)$$

where z is the mole fraction of ammonia, and L_1 and L_2 are the flow rates of dry air and ammonia gas, respectively. L (where $L = L_1 + L_2$) was kept constant at 1 L min⁻¹ and ammonia concentration was adjusted by varying L_1 and L_2 . A specially designed sensor

chamber made of Teflon (Fig. 7b) was used in order to estimate the ammonia response. The optical fibre coated with the functional film was inserted inside the chamber and connected to the light source and spectrometer, as shown in Fig. 7b.

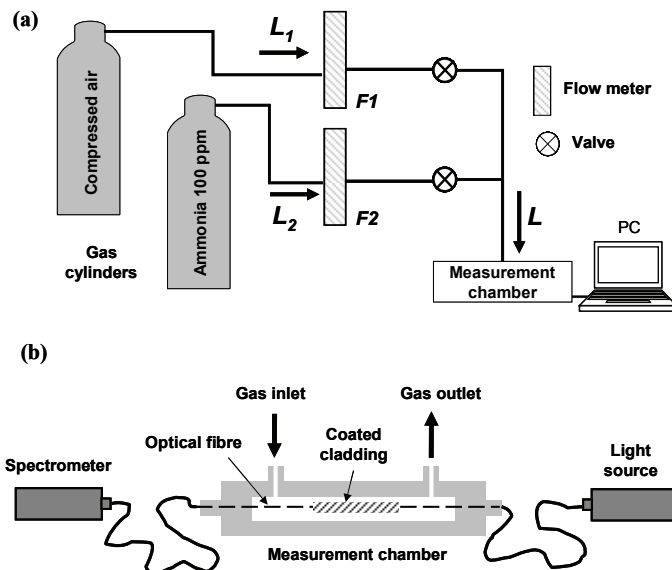


Fig. 7. (a) Apparatus of a two-arm flow gas generation system: F1 and F2 are flowmeters; L_i represents the concentration of the gases in the different arms of the system. (b) Schematic illustration of the measurement setup: light source, Ocean optics light source emitting light in the range of wavelengths from 200 to 1100 nm; spectrometer, Ocean Optics S1024DW spectrometer

The sensor response at a given analyte concentration was measured every second by recording the transmission spectrum of the film deposited on the optical fibre. The difference spectrum was plotted by subtracting a spectrum measured at a given analyte concentration from the spectrum recorded in the presence of dry air. The baseline spectrum of each experiment was recorded by passing dry air through the measurement chamber until the signal measured at wavelengths of 350, 470 and 706 nm reached equilibrium. The dynamic sensor response was also measured at the same wavelengths.

The optical fibre sensor response (SR) was calculated using

$$SR = 100 (I_0 - I) / I_0 , \quad (4)$$

where I_0 and I describe the light intensities of the PDDA⁺/TSPP⁻ film in the absence and presence of the analyte gas, respectively, measured at a given wavelength.

3. Results and Discussion

3.1 Optical spectra of PDDA⁺/TSPP⁻ alternate layers

The assembly of the PDDA and TSPP layers after each deposition cycle was measured by monitoring the optical change in the transmission spectra of the optical fibre. Fig. 8 shows the evolution of the transmission spectrum of the optical fibre during the deposition of a five-cycle PDDA⁺/TSPP⁻ thin film.

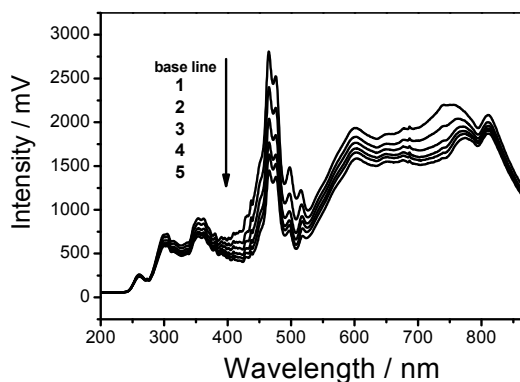


Fig. 8. Evolution of the transmission spectra (data as measured) as a multilayer film of PDDA⁺/TSPP⁻ that was deposited onto a 200 μm core diameter multimode optical fibre with a stripped silica core of 1 cm

The absorbance spectra were derived from the transmission spectra using eq. (2), Figure 9a. The largest absorbance due to the deposition of the (PDDA⁺/TSPP⁻) bilayer was observed at a wavelength of 420 nm, which corresponds to the Soret band. The absorbance increased in proportion to the number of adsorption cycles (Fig. 9a). The absorbance spectra of the (PDDA⁺/TSPP⁻) film are characterized by a double peak in the Soret band occurring at 420 and 480 nm, and by a pronounced peak of the Q band at 706 nm. These spectral characteristics suggest that TSPP molecules exist in the *J*-aggregate state, in which the absorbance maxima of the Soret and Q bands are red-shifted compared with those in the monomeric state (Agira et al., 1997; Gregory van Patten et al., 2000; Snitka et al., 2005). The aggregation state of TSPP and hence its spectral features are controlled by the protonation/deprotonation of the porphyrin pyrrole ring (Agira et al., 1997). Fig. 9b shows the absorbance change monitored at two Soret bands (420 and 480 nm) and at the Q band (706 nm) versus the number of adsorption cycles.

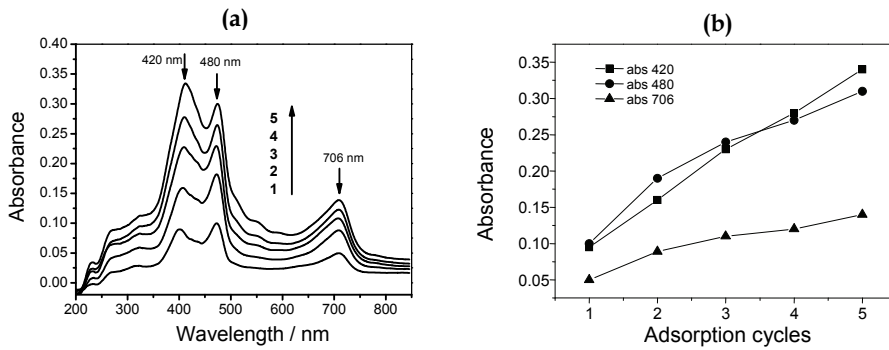


Fig. 9. Evolution of the spectrum as a multilayer film of PDDA⁺/TSPP⁻ that was deposited onto a 200 μm core diameter multimode optical fibre with a stripped silica core of 1 cm: (a) absorbance spectra (derived from the transmission spectra using eq. (2)); (b) absorbance change due to film deposition monitored at wavelengths of 420 nm (squares), 480 nm (circles), and 706 nm (triangles).

3.2 Optical response to ammonia

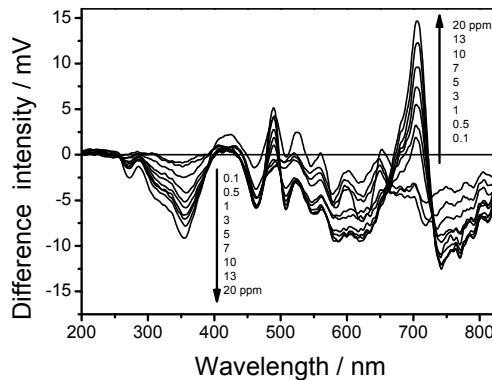


Fig. 10. Optical transmission difference spectra of the optical fibre consisting of a five-cycle PDDA⁺/TSPP⁻ alternate film for ammonia concentrations ranging from 0–20 ppm.

Ammonia-induced optical changes in the transmission spectrum of the (PDDA⁺/TSPP⁻)₅ film are shown in Fig. 10. As ammonia concentration increased from 0 to 20 ppm, the intensity change occurs at several wavelengths; at 706 nm, intensity increases, whereas at 350 and 470 nm it decreases. Upon exposure of the (PDDA⁺/TSPP⁻)₅ film to ammonia, the largest intensity change was observed at 706 nm. The interaction between ammonia and TSPP molecules leads to the deprotonation from the pyrrole ring and hence affects the interaction between TSPP molecules. Similarly, the largest change in absorbance is observed

at 706 nm (Q band), which is attributed to the aggregation structure of TSPP (Gregory van Patten et al., 2000).

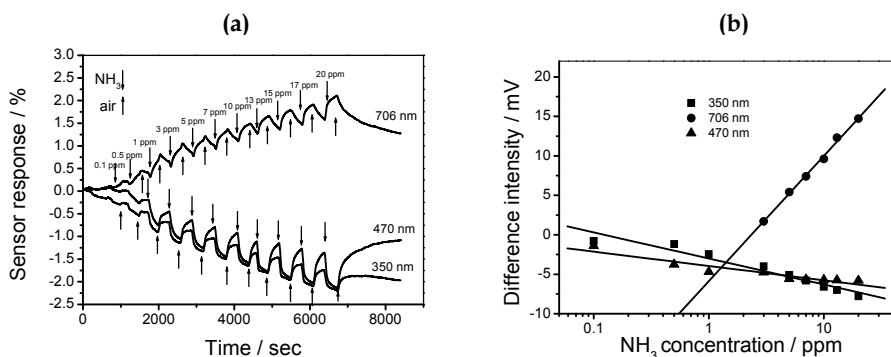


Fig. 11. (a) Dynamic response of the optical fibre consisting of a five-cycle PDDA⁺/TSPP-alternate film for ammonia concentrations ranging from 0–20 ppm at 350, 470, and 706 nm. (b) Calibration curves at 350 nm (squares), 470 nm (rhombuses), and 706 nm (circles). Lines show the linear fitting and are used only as guidance to an eye.

The dynamic sensor response of the (PDDA⁺/TSPP)₅ film to ammonia was monitored at 350, 470 and 706 nm (Fig. 11a). As can be seen from the result, the sensor response is fully reversible for low ammonia concentrations (up to 1 ppm). However, at higher concentrations the recovery time of the sensor response takes a longer time to return to the base line. The base line may be recovered when flushed with air for sufficient time, as shown in Fig. 11a. Alternatively, the sensor response can be regenerated by rinsing for a few seconds in distilled water (Korposh et al., 2006). The calibration curve at each wavelength was plotted from the recorded spectra at given ammonia concentrations. The sensor shows linear responses at all wavelengths for a wide concentration range from 0.1 to 20 ppm and the highest sensitivity was observed at 706 nm (Fig. 11b).

Table 1 shows a summary of the sensor parameters, including sensitivity, response and recovery times and limit of detection (*LOD*) measured at different wavelengths. The response and recovery times (*t*₉₀) of the sensor to increasing ammonia concentration were within 1.6–2.5 min and 1.8–3.2 min, respectively (see Fig 11a). The sensitivity of the sensor depends on the wavelength and has different directions; for 350 and 470 nm, it is negative, and for 706 nm it is positive. The highest sensitivity was measured at 706 nm, corresponding to the optical change of the Q band of TSPP.

The current sensor system has a limit of detection (*LOD*) on the ppm order ranging from 0.9 to 2.6 ppm. The limit of detection was defined according to $LOD=3\sigma/m$, where $\sigma \approx 0.31$ is the standard deviation, and m is the slope ($\Delta I/\Delta c$) of the calibration curve, where c is the ammonia concentration and I is the measured intensity (mV) (Swartz & Krull, 1997). The presence of different features in the optical spectrum after exposing the PDDA⁺/TSPP- film to ammonia offers the ability to create a low-cost fibre optic sensor by selecting a LED and a photodiode with parameters that will coincide with the wavelength at which the largest ammonia-induced changes were observed (706 nm). Difference spectra derived from Fig. 8

were obtained by subtracting a spectrum measured in ammonia atmosphere from a spectrum measured in air.

wavelength / nm	^a Sensitivity / slope	^b Response time / min	^b Recovery time / min	Linear range / ppm	^c LOD / ppm
350	-0.50 ± 0.08	2.0	1.8	0.1-20	1.90
470	-0.35 ± 0.06	2.5	2.4	0.1-20	2.65
706	0.98 ± 0.07	1.6	3.2	0.1-20	0.90

^a Slope calculated from the calibration curve (Fig. 11b).

^b Response and recovery times determined as the interval needed for the signal to achieve 90% of their saturated condition when measured of an NH₃ concentration of 10 ppm.

^c LOD: limit of detection.

Table 1. Summary of the sensors parameters (sensitivity, response and recovery times, and limit of detection) for the five-cycle PDDA⁺/TSPP⁻ film.

3.3 Sensing mechanism

Porphyrin compounds can be used as sensitive elements for optical sensors because their optical properties (absorbance and fluorescence features) depend on the environmental conditions in which chemicals are present (Takagi et al., 2006). Generally, the change of porphyrin absorption spectra is induced by (i) solvent effects, (ii) redox reactions, (iii) the protonation or metallation of core nitrogen atoms, (iv) π - π electron interaction, (v) electronic changes due to structural changes such as flattening or distortion, or (vi) interactions between porphyrins (aggregation) (Takagi et al., 2006). The alternation of the spectral features observed when the (PDDA⁺/TSPP⁻)₅ film was exposed to ammonia (Fig. 10 suggests the following mechanisms of the interaction between TSPP and ammonia gas:

- (i) Interaction between ammonia and porphyrin compounds leads to the deprotonation of the TSPP pyrrole ring and the formation of ammonium ions, as shown in Fig. 12. This deprotonation leads to the disruption of *J*-aggregation and is mainly accompanied by spectral changes occurring at 470 and 706 nm (Agira et al., 1997; Gregory van Patten et al., 2000; Takagi et al., 2006);
- (ii) We can speculate that a decrease in the transmittance noted at 350 nm may be attributed to the distortion of the aggregation structure due to the adsorption of ammonia (Takagi et al., 2006);

The above mentioned sensing mechanisms are mainly based on the dissociation of *J*-aggregated TSPP molecules and the original structure of the PDDA⁺/TSPP⁻ film can be recovered by protonation from ammonium ions. The future challenge is to test the selectivity of the proposed device. Preliminary results obtained by exposing the fibre optic sensor coated with the five-cycle PDDA⁺/TSPP⁻ film to some of volatile organic compounds (VOCs) revealed a higher selectivity towards amine compounds (data not shown).

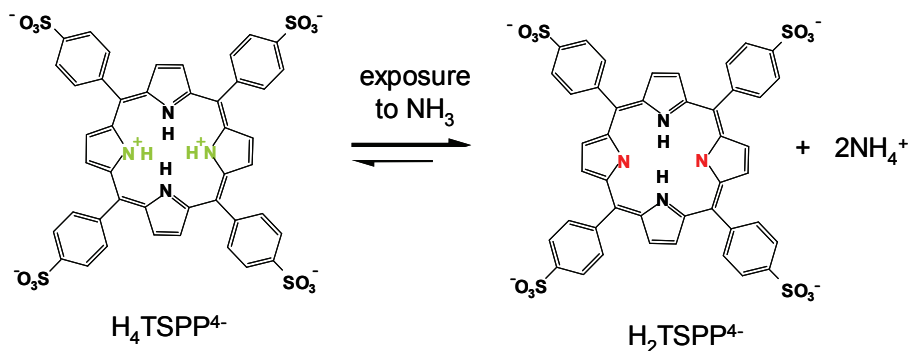


Fig. 12. Schematic representation of the interaction between ammonia and TSPP compounds in the PDDA⁺/TSPP⁻ film.

4. Conclusion

In conclusions, fibre optic sensors combined with the chemically reactive element provide a wide range of possibilities for the development of the cheap, sensitive and highly selective sensor systems. As an example, a fibre optic ammonia sensor based on a PDDA⁺/TSPP⁻ alternate thin film deposited on the core of a multimode optical fibre using a layer-by-layer approach is demonstrated. The intensity of the light propagating through the optical fibre decreases proportionally with the increase in the thickness of the TSPP layers deposited over the optical fibre. The exposure of the five-cycle PDDA⁺/TSPP⁻ film to ammonia induces changes in the absorption spectrum via the deprotonation of TSPP, which could be observed in the transmission spectrum of the coated optical fibre. The highest sensitivity (0.98 mV ppm⁻¹) was observed when measured at 706 nm, which corresponds to the Q band of the porphyrin compound; for low-cost-sensor development it is possible to use a simple LED-photodiode system operating at around 700 nm. The sensor showed a linear sensitivity to the presence of ammonia with a limit of detection of 0.9 ppm in the concentration range of 0.1–20 ppm and sensor response and recovery times were less than 4 min. The demonstrated sensor offers an opportunity for the detection of different chemicals by coating an optical fibre with an appropriate sensitive material. Further work is needed to optimize sensor performance and to study the effect of coating thickness, relative humidity and presence of the other chemical compounds on sensor parameters.

5. References

- Abdelghani, A.; Chovelon, J. M.; Jaffrezic-Renault, N.; Lacroix, M.; Gagnaire, H.; Veillas, C.; Berkova, B.; Chomat, M. & Matejec, V. (1997). Optical fibre sensor coated with porous silica layers for gas and chemical vapour detection. *Sensors and Actuators B: Chemical*, Vol. 44, No. 1-3, p. 495–498, ISSN 0925-4005
- Ariga, K.; Lvov, Y. & Kunitake, T. (1997). Assembling alternate dye-polyion molecular films by electrostatic layer-by-layer adsorption. *Journal of American Chemical Society*, Vol. 119, No. 9, p. 2224–2231, ISSN 0002-7863
- Bansal, L. & El-Sherif, M. (2005). Intrinsic optical-fibre sensor for nerve agent sensing. *IEEE Sensors Journal*, Vol. 5, No. 4, p. 648–655, ISSN 1530-437X

- Beltrán-Pérez, G.; López-Huerta, F.; Muñoz-Aguirre, S.; Castillo-Mixcóatl, J.; Palomino-Merino, R.; Lozada-Morales, R. & Portillo-Moreno, O. (2006). Fabrication and characterization of an optical fibre pH sensor using sol-gel deposited TiO₂ film doped with organic dyes. *Sensors and Actuators B: Chemical*, Vol. 120, No. 1, p. 74–78, ISSN 0925-4005
- Beyer, T.; Hahn, P.; Hartwig, S.; Konz, W.; Scharring, S.; Katzir, A.; Steiner, H.; Jakusch, M.; Kraft, M. & Mizaikoff, B. (2003). Mini spectrometer with silver halide sensor fibre for in situ detection of chlorinated hydrocarbons. *Sensors and Actuators B: Chemical*, Vol. 90, No. 1-3, p. 319–323, ISSN 0925-4005
- Bucholtz, F.; Dagenais, D. M. & Koo, K. P. (1989). High frequency fibre-optic magnetometer with 70 fT per square root hertz resolution. *Electronics Letters*, Vol. 25, No. 25, p. 1719–1721, ISSN 0013-5194
- Cibula, E. & Donagic, D. (2004). All-fibre Fabry-Perot strain sensor. *Proceedings of 2nd European Workshop on OFS*, pp. 180–183, ISBN 9780819454348, Spain, June 2004, SPIE
- Dandridge, A. (1991). Fibre optic sensors based on the Mach-Zehnder and Michelson interferometers, In: *Fiber Optic Sensors: An Introduction for Engineers and Scientists*, edited by E. Udd. New York: Wiley
- Grattan, K.T.V. & Meggitt, B.T. (1999). *Chemical and environmental sensing*, Dordrecht, Boston : Kluwer
- Gregory van Patten, P.; Shreve, A.P. & Donohoe, R.J. (2000). Structural and photophysical properties of a water-soluble porphyrin associated with polycations in solutions and electrostatically-assembled ultrathin films. *Journal of Physical Chemistry:B*, Vol. 104, No. 25, p. 5986–5992, ISSN 1089-5647
- Gupta, B. D. & Sharma, D. K. (1997). Evanescent wave absorption based fibre optic pH sensor prepared by dye doped sol-gel immobilization technique. *Optical Communications*, Vol. 140, No. 1-3, p. 32–35, ISSN 0030-4018
- Gupta, B. D. & Sharma, S. (1998). A long-range fibre optic pH sensor prepared by dye doped sol-gel immobilization technique. *Optical Communications*, Vol. 154, No. 5-6, p. 282–284, ISSN 0030-4018
- Ichinose, I.; Fujiyoshi, K.; Mizuki, S.; Lvov, Yu. & Kunitake, T. (1996). Layer-by-layer assembly of aqueous bilayer membranes on charged surfaces. *Chemical Letters*, Vol. 25, No. 4, p. 257-258, ISSN 1348-0715
- Iler, R. K. (1966). Multilayers of Colloidal Particles. *Journal of Colloid Interface Science*, Vol. 21, No. 6, p. 569-594, ISSN 0021-9797
- James, S. W. & Tatam R. P. (2006). Fibre optic sensors with nano-structured coatings. *Journal of Optics A: Pure and Applied Optics*, Vol. 8, No. 7, p. S430-S444, ISSN 1741-3567
- Kadish, K. M.; Smith, K. M. & Guillard R. (2000). *The Porphyrin Handbook*, Academic Press, ISBN 0123932009, San-Diego
- Kawahara, F. K.; Fuitem, R. A.; Silvus, H. S.; Newman, F. M. & Frazar, J. H. (1983). Development of a novel method for monitoring oils in water. *Analytical Chimia Acta*, Vol. 151, p. 315–327, ISSN 0003-2670
- Korposh, S. O.; Takahara, N.; Ramsden, J. J.; Lee, S-W. & Kunitake, T. (2006). Nano-assembled thin film gas sensors. I. Ammonia detection by a porphyrin-based multilayer film. *Journal of Biological and Physical Chemistry*, Vol. 6, No. 3, p. 125–133, ISSN 1512-0856

- Le Coq, D.; Michel, K.; Keirss, J.; Boussard- Plédel, C.; Fonteneau, G.; Bureau, B.; Le Quéré, J.-M.; Sire, O. & Lucas, J. (2002). Infrared glass fibres for in-situ sensing, chemical and biochemical reactions. *Comptes Rendus Chimie*, Vol. 5, No. 12, p. 907-913, ISSN 1631 - 0748
- Lee, S.-W.; Ichinose, I. & Kunitake, T. (1998). Molecular Imprinting of Azobenzene Carboxylic Acid on a TiO₂ Ultrathin Film by the Surface Sol-Gel Process. *Langmuir*, Vol. 14, No. 10, p. 2857-2863 ISSN 0743-7463
- Leung, A.; Rijal, K.; Shankar, P. M. & Mutharasan, R. (2006). Effects of geometry on transmission and sensing potential of tapered fibre sensors. *Biosensors and Bioelectronics*, Vol. 21, No. 12, p. 2202-2209, ISSN 0956-5663
- Lin, C.-J.; Tseng, Y.-T.; Lin, S.-C.; Yang, C.-S. & Tseng, F.-G. (2004). A novel in-vitro and in-situ immunoassay biosensor based on fibre-optic Fabry-Perot interferometry, *Proceedings of 2nd European Workshop on Optical Fibre Sensors*, pp. 304-307, ISBN 9780819454348, Spain, June 2004, SPIE
- Lucas, P.; Solis, M. A.; Le Coq, D.; Juncker, C.; Riley, M. R.; Collier, J.; Boesewetter, D. E.; Boussard-Plédel, C. & Bureau, B. (2006). Infrared biosensors using hydrophobic chalcogenide fibres sensitized with live cells. *Sensors and Actuators B: Chemical*, Vol. 119, No. 2, p. 355-362, ISSN 0925-4005
- Monzón-Hernández, D. & Villatoro, J. (2006). High-resolution refractive index sensing by means of a multiple-peak surface plasmon resonance optical fibre sensor. *Sensors and Actuators B: Chemical*, Vol. 115, No. 1, p. 227-231, ISSN 0925-4005
- Ogita, M.; Nagai, Y.; Mehta, M. A. & Fujinami, T. (2000). Application of the adsorption effect of optical fibres for the determination of critical micelle concentration. *Sensors and Actuators B: Chemical*, Vol. 64, No. 1-3, p. 147-151, ISSN 0925-4005
- Rajan; Chand, S. & Gupta, B. D. (2005). Fabrication and characterization of a surface plasmon resonance based fibre-optic sensor for bittering component—Naringin. *Sensors and Actuators B: Chemical*, Vol. 115, No. 1, p. 344-348, ISSN 0925-4005
- Rakow, N.A. & Suslick, K. S. (2000). A colorimetric sensor array for odour visualization. *Letters to Nature*, Vol. 406, 710-713, ISSN 0028-0836
- Rao, Y. J.; Cooper, M. R.; Jackson, D. A.; Pannell, C. N. and Reekie, L. (2000). High resolution static strain measurement using an in-fibre-Bragg-grating-based Fabry Perot sensor. *Proceedings of 14th International Conference on Optical Fibre Sensors*, pp. 284-287, October 2000, Italy, SPIE
- Rayss, J. & Sudolski, G. (2002). Ion adsorption in the porous sol-gel silica layer in the fibre optic pH sensor. *Sensors and Actuators B: Chemical*, Vol. 87, No. 3, p. 397-405, ISSN 0925-4005
- Ronot, C.; Gagnalre, H.; Goure, J. P.; Jaffrezic-Renault, N. & Plchery, T. (1994). Optimization and performance of a specifically coated intrinsic optical-fibre sensor for the detection of alkane compounds. *Sensors and Actuators B: Chemical*, Vol. 42, No. 1-3, p. 529-534
- Russell, S. J. & Dakin, J. P. (1999). Location of time-varying strain disturbances over a 40 km fibre section, using a dual-Sagnac interferometer with a single source and detector. *Proceedings of 13th International Conference on Optical Fibre Sensors*, pp. 580-584, ISBN 9780819432285, Korea, April 1999, SPIE

- Schick, G.A.; Schreiman, I.C.; Wagner, R.W.; Lindsey, J.S. & Bocian, D.F. (1989). Spectroscopic characterization of porphyrin monolayer assemblies. *Journal of American Chemical Society*, Vol. 111, No. 4, p. 1344-1350, ISSN 1520-5126
- Schroeder, R. J.; Yamate, T. & Udd, E. (1999). High pressure and temperature sensing for the oil industry using fiber Bragg gratings written onto side hole single mode fiber. *Proceedings of 13th International Conference on Optical Fibre Sensors*, pp. 42-45, ISBN 9780819432285, Korea, April 1999, SPIE
- Sharma, A. K. & Gupta, B. D. (2005). Fibre optic sensor based on surface plasmon resonance with nanoparticle films. *Photonics and Nanostructures - Fundamentals and Applications*, Vol. 3, No. 1, p. 30-37, ISSN 1569-4410
- Snitka, V.; Rackaitis, M. & Rodaite, R. (2005). Assemblies of TPPS₄ porphyrin investigated by TEM, SPM and UV-vis spectroscopy. *Sensors and Actuators B: Chemical*, Vol. 109, No. 1, p. 159-166, ISSN 0925-4005
- Swartz, M. E. & Krull, I. S. (1997). *Analytical Method Development and Validation*, Marcel Dekker, Inc. NY, USA
- Takagi, S.; Eguchi, M.; Tryk, D. A. & Inoue, H. (2006). Porphyrin photochemistry in inorganic/organic hybrid materials: Clays, layered semiconductors, nanotubes, and mesoporous materials, *J. Photochem. Photob. C: Photochem. Rev.*, Vol. 7, No. 2-3, p. 104-126, ISSN 1389-5567
- Vohra, S. T.; Todd, M. D.; Johnson, G. A.; Chang, C. C. & Danver, B. A. (1999). Fibre Bragg grating sensor system for civil structure monitoring: applications and field tests, *Proceedings of 13th International Conference on Optical Fibre Sensors*, pp. 32-37, ISBN 9780819432285, Korea, April 1999, SPIE
- Walsh, J. E.; MacCraith, B. D.; Meaney, M.; Vos, J. G.; Regan, F.; Lancia, A. & Artiushenko, S. (1995). Midinfrared fiber sensor for the in-situ detection of chlorinated hydrocarbons. *Proceedings of Chemical, Biochemical, and Environmental Fiber Sensors VII*, pp. 233-237, ISBN: 9780819418661, Munich, June 1995, SPIE
- Yuan, L., & Yang, J. (2005). Two-loop based low-coherence multiplexing fibre optic sensors network with Michelson optical path demodulator, *Proceedings of 17th International Conference on Optical Fibre Sensors*, pp. 595-598, ISBN 9780819458551, Bruges, May 2005, SPIE

Optical fibres in aeronautics, robotics and civil engineering

Giuseppe De Maria, Aldo Minardo, Ciro Natale,
Salvatore Pirozzi and Luigi Zeni

*Dipartimento di Ingegneria dell'Informazione, Seconda Università degli Studi di Napoli
Aversa (CE), 81031, Italy*

1. Introduction

Glass optical fibres are made from fused silica, are about the diameter of a human hair, and transmit light over large distances with very little loss. They can also be made to be sensitive to their state and environment and are therefore well suited as sensors. Optical fibres sensors (OFSs) have been the subject of a remarkable interest in the last 30 years, since they present some distinct advantages over other technologies (Culshaw & Dakin, 1997). The principal single attractive feature of optical-fibre sensors is undoubtedly their ability to function without any interaction with electromagnetic fields. This opens applications in the electrical power industry and assists very significantly where long transmission distances of relatively weak signals are an essential part of the sensing process. The lack of electrical connections has other, broader implications. Optical sensors have major advantages when conductive fluids, such as blood or sea water, are involved. Also, the need for intrinsic safety (for example, in monitoring the presence of explosives gases or in assessing petrochemical plants) is often paramount. The optical fibre is also remarkably strong, elastic, and durable, and has found its place as an instrumentation medium for addressing smart structures, where the sensors must tolerate the environment to which the structure is subjected and therefore to be immune to large physical strain excursions, substantial temperature excursions, and often a chemically corrosive operating environment.

Fibre optic sensor technology has been a major user of technology associated with the optoelectronic and fibre optic communications industry. Many of the components associated with these industries were often developed for fibre optic sensor applications. Fibre optic sensor technology, in turn, has often been driven by the development and subsequent mass production of components to support these industries. As component prices have fallen and quality improvements have been made, the ability of fibre optic sensors to displace traditional sensors for rotation, acceleration, electric and magnetic field measurement, temperature, pressure, acoustics, vibration, linear and angular position, strain, humidity, viscosity, chemical measurements, and a host of other sensor applications has been enhanced (Udd, 2002).

In the early days of fibre optic sensor technology, most commercially successful fibre optic sensors were squarely targeted at markets where existing sensor technology was marginal

or in many cases nonexistent. The inherent advantages of fibre optic sensors were heavily used to offset their major disadvantages of high cost and end-user unfamiliarity. The situation is changing. Laser diodes that cost \$3000 in 1979 with lifetimes measured in hours now sell for a few dollars in small quantities, have reliability of tens of thousands of hours, and are widely used in compact disc players, laser printers, laser pointers, and bar code readers. Single-mode optical fibre that cost \$20/m in 1979 now costs less than \$0.10/m, with vastly improved optical and mechanical properties. Integrated optical devices that were not available in usable form at that time are now commonly used to support production models of fibre optic gyros. Also, they could drop in price dramatically in the future while offering ever more sophisticated optical circuits. As these trends continue, the opportunities for fibre optic sensor designers to product competitive products will increase and the technology can be expected to assume an ever more prominent position in the sensor marketplace.

In the following sections we will review the main fields in which we successfully adopted optical fibre sensor technology. In particular, we will focus on the use of distributed fibre sensors for structural health monitoring; then we will describe an application of fibre-optics Bragg grating technology in the field of aeronautic engineering. Finally, an optical fibre-based tactile sensor for robotic applications will be described. The selection of these applications has been made to clearly show how the same base device, i.e. the optical fibre, can be successfully used to address sensing problems at very different scales, from large structures down to micro-scale devices.

2. Application in civil engineering

The safety assessment of ordinary structures is usually based on the experimental testing of displacements or strains under the design loads, by taking into consideration measures related to a selected discrete number of points. For many engineering works of strategic significance like bridges, pipes, rising buildings, dams and tunnels, safety should be continuously assessed during their complete life-time. It is worth to note that the response of these structures, which for their nature could be damaged by severe load conditions, has to be monitored along the whole construction. When compared with traditional electrical strain gauges used for strain monitoring of large structures, OFSs have several distinguishing advantages, including:

1. A much better invulnerability to electromagnetic interference, including storms, and the potential capability of surviving in harsh environments;
2. A much less intrusive size (typically 125 μm in diameter—the ideal size for embedding into composites without introducing any significant perturbation to the characteristics of the structure);
3. Greater resistance to corrosion when used in open structures, such as bridges and dams;
4. A higher temperature capacity with a widely selectable range;
5. A longer lifetime, which could probably be used throughout the working lifetime of the structure (e.g., >25 years) as optical fibres are reliable for long-term operation without degradation in performance.

Besides the above mentioned advantages, fibre optics technology offers the unique possibility to perform the experimental reading of strains over the structure in a fully distributed manner. This feature is accomplished by the so-called distributed optical fibre

sensors, by which not only can the magnitude of a physical parameter or measurand be monitored, but also its variation along the length of the fibre can be measured. Distributed sensors are especially appropriate when there is no a priori information allowing a spatial delimitation of the sensing region. The experimental procedure consists of durable devices set on the structure at an early stage of the building process that is particularly able to detect the onset of damages or defects during the whole life-time of the structure (Measures 2002). Truly distributed sensing techniques are commonly based on some kind of light scattering mechanism occurring inside the fibre. Spatial resolution is typically achieved by using the optical time domain reflectometry (OTDR) (Barnosky & Jensen 1976), in which optical pulses are launched into an optical fibre and the variations in backscattering intensity caused by measurand is detected as a function of time.

While OTDR is a quite simple and established technique, it does not allow strain sensing. The latter can be achieved by exploiting the phenomenon of Brillouin scattering. In Brillouin effect an optical pump wave is scattered by acoustic waves leading to Stokes (a longer wavelength than that of the pump) or anti-Stokes (a shorter wavelength than that of the pump) components (see Fig. 1).

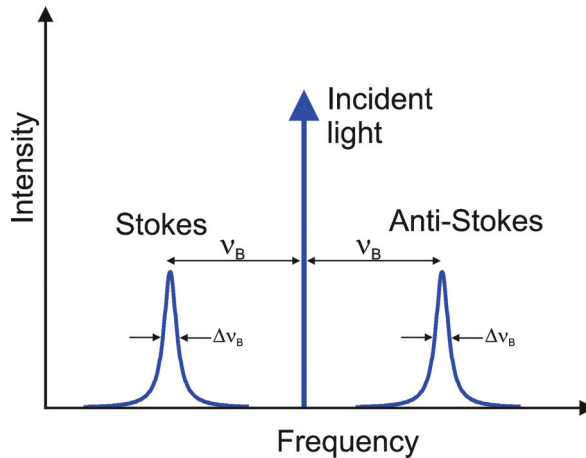


Fig. 1. The Brillouin spectrum.

Essentially, scattering occurs as a result of a Bragg-type reflection from moving diffraction gratings created from the refractive-index variations caused by acoustic waves propagating axially in the fibre material. These acoustic waves can be generated spontaneously by thermal excitation and, when this is the case, the resulting scattering effect on optical waves is known as *spontaneous Brillouin scattering*. However, as the optical pump power is increased the wave scattered backwards from an acoustic wave will increase in amplitude and will interfere significantly with the forward-travelling pump wave. An optical beat signal arises within the fibre, which generates a pressure wave having the same frequency as the optical beat signal, via the phenomenon of electrostriction; this pump-induced index grating scatters the pump light through Bragg diffraction. Scattered light is down-shifted or up-shifted in frequency because of the Doppler shift associated with a grating moving at the acoustic velocity V_A . This positive feedback, backscattering process is known as the

stimulated Brillouin scattering (SBS). It leads to much larger backscattering at the Stokes frequency than in the spontaneous case. Brillouin effect leads to a Stokes and anti-Stokes frequency shift in the optical fibre which is given by (Agrawal 2001):

$$v_B = \pm \frac{2nV_A}{\lambda} \quad (1)$$

where n is effective refractive index of the guided mode, V_A is the acoustic velocity and λ is the free-space pumping wavelength. For silica fibre at a pumping wavelength of $1.55 \mu\text{m}$ we have $v_B \approx 10.8 \text{ GHz}$. As Brillouin frequency shift depends on both the optical refractive index and the acoustic wave velocity, it changes whenever these quantities change in response to local environmental variations and can be used to deduce the temperature and strain along the fibre. Several experiments have demonstrated an excellent linearity of the Brillouin frequency shift with respect to both fibre strain and temperature, for a wide range of these quantities. At a pump wavelength of $1.32 \mu\text{m}$, a typical temperature coefficient of $1.36 \text{ MHz}/^\circ\text{C}$ and strain coefficient of $594.1 \text{ MHz}/\%$ are reported (Niklès et al., 1997).

As an example of application of distributed sensors in the field of structural health monitoring (SHM), we report the results of strain measurements carried out along an 8-meters-long "I" steel beam subjected to load (Bernini et al., 2006a). In particular, the measurements were carried out by using a transportable prototype able to carry out SBS distributed sensing in the time-domain. Two tests were performed: the first one refers to the integral beam, while the second one was performed after the intentional formation of a defect localized over a 10cm-long portion of the beam. The results, shown in Figs. 2 and 3, demonstrated the capability of the sensor to identify both position and amount of damage.

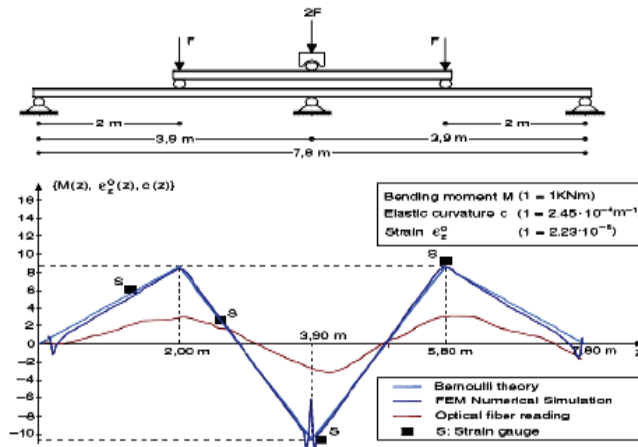


Fig. 2. Strain profile measured along the integral beam and comparison with the theoretical profile.

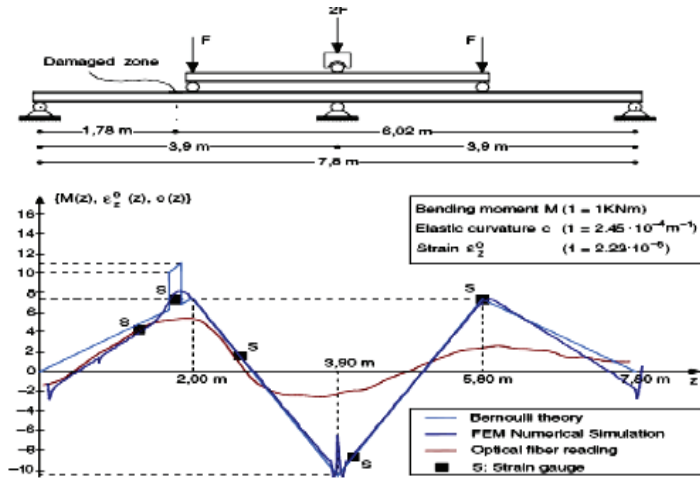


Fig. 3. Strain profile measured along the beam with a defect and comparison with the theoretical profile.

Distributed strain measurements can be carried out also by using a detection scheme operating in the frequency-domain (Garus et al., 1996). In this case, the pump beam intensity is sinusoidally-modulated, and the corresponding modulation induced on the cw probe beam intensity is coherently measured in magnitude and phase. Synchronous detection offered by frequency-domain schemes allows for spatial resolution and accuracy typically higher than time-domain approaches (Bernini et al., 2002). As an example, we report strain measurements carried out along a 4m-long, L-shaped aluminium beam subjected to a 2kg-load at the beam middle section (Bernini et al. 2006b).

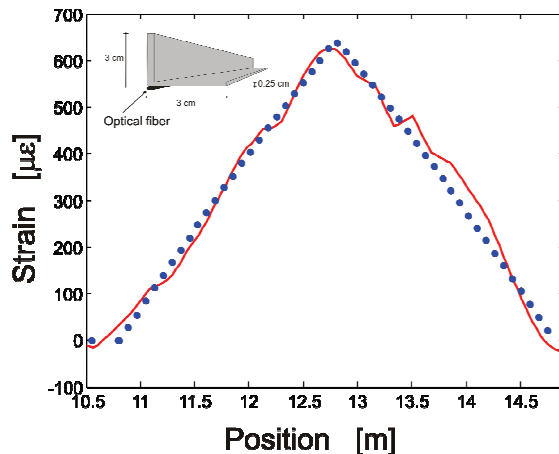


Fig. 4. Strain profile measured along the integral beam (solid red line), and comparison with the theoretical profile (circles). The inset shows the optical fibre position with respect to the loaded beam.

The comparison between the measurement and the strain profile calculated by a finite-elements method (FEM), shown in Fig. 4, demonstrates the high level of accuracy offered by frequency-domain SBS approaches.

Another interesting application of fibre-optic distributed sensor, consists in the monitoring of pipelines. In particular, it has been demonstrated that by measuring the strain profile along three longitudinal directions of a pipe, it is possible to identify the position and the vectorial amount of pipe dislocation (Bernini et al., 2008). Such a technique can be applied, both directly for pipeline integrity monitoring, both in the geotechnical field for the monitoring of deformation of the soil surrounding the pipe itself. Experimental tests were performed by using a frequency-domain SBS-based sensor. In particular, a 1.5m-long polyethylene (PE) pipe was used, along which strains were read by attaching an optical fibre running along three longitudinal directions angularly spaced of 120° . As an example, we show in Figure 5 the measurements carried out after displacing a 25cm-long section of the pipe of 20cm along the $-x$ direction.

An appealing aspect of such measurements is the possibility to reconstruct, section by section, the spatial deformation of the pipe. Actually, by making simple calculations based on the Bernoulli theory, pipe dislocation along the x - and y - directions can be deduced at each pipe section. A 3D reconstruction of the deformed pipe, obtained by opportune processing of the data shown in Fig. 5, is reported in Fig. 6, along with the ideal reconstruction obtained by using the numerically calculated deformations.

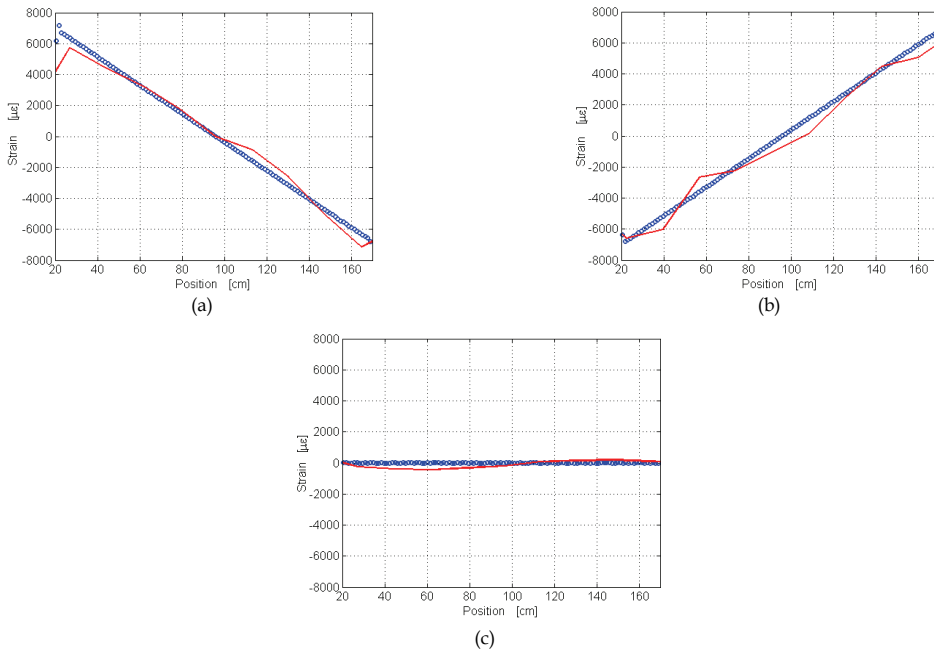


Fig. 5. Experimental (solid red line) and numerically calculated (circles) strain profiles along fibre A (a), fibre B (b) and fibre C (c), for a 20-cm displacement of the pipeline along the negative x -direction.

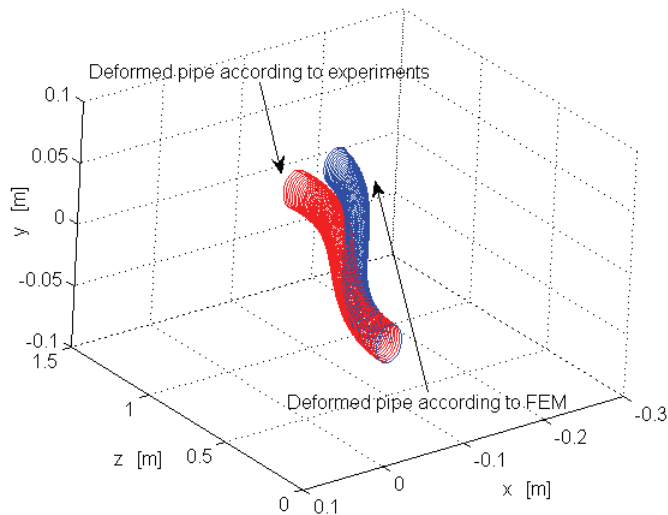


Fig. 6. 3D representation of the deformed pipe, estimated according to the experimental strains (leftmost red pipe) and the FEM numerically calculated strains (rightmost blue pipe).

3. Application in aeronautics

Many research projects worldwide tackled the problem of noise and vibration reduction in aeronautic structures for improvement of both cabin comfort and of structural health. Among these, the European project MESEMA had the main objective of designing and implementing an active noise control system on a full-scale test rig consisting of a segment of a civil aircraft fuselage. The problem addressed was the reduction of cabin noise in a broad frequency band, ranging from 100 Hz to 500 Hz. The active control was realized by using actuators based on a proven and patented concept, the magnetostrictive auxiliary mass damper, which was optimally designed for this application (May et al. 2006).

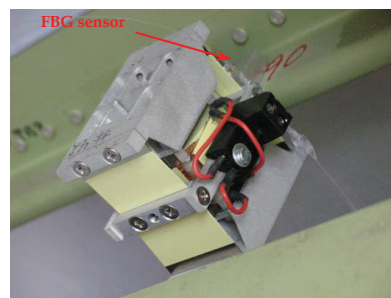
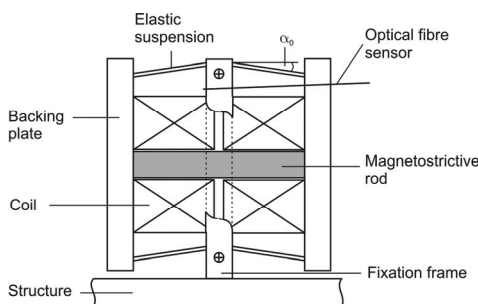


Fig. 7. Actuator with integrated optical sensor: schematic and actual installation on the aeronautic structure.

Unfortunately, the dynamic behaviour of this device was affected by two sources of nonlinearity. The first one due to the elastic suspension kinematics used for displacement

amplification; the second one due to the hysteretic behaviour of the magnetostrictive material. In order to overcome the limitation and negative effects of these nonlinearities within the main control system, the actuator was equipped with an optical sensor based on a Fibre Bragg Grating (FBG) used for low-level actuator control to measure the displacement of the inertial mass, so as to estimate the state of the mechanical system.

The possibility to use an FBG as strain sensor is related to the changes in its optical reflection spectrum produced by an applied strain (Kersey et al. 1997). In particular, the centre wavelength of the FBG reflection spectrum is linearly dependent on strain, so that the latter can be retrieved on a wavelength-encoding basis. In case of static strain measurements, FBG interrogation is typically performed by using a wideband optical source, such as an LED, while monitoring the portion of the source spectrum reflected by the grating. By doing so, the centre wavelength of the reflected spectrum provides a direct measurement of the applied strain. Such an approach typically involves the use of an optical spectrum analyzer in order to acquire the reflection spectrum, so that it is inherently slow and not suitable for dynamic measurements. For our dynamic measurements, we choose to adopt a narrowband demodulation approach, capable of detecting strain changes up to the kHz range. Apart from the possibility to detect fast strain changes, the narrowband demodulation technique presents other advantages, such as high signal-to-noise ratio, low cost, and ease of use (Zhao & Liao 2004). The principle of operation of the narrowband technique can be understood by looking at the optical set-up connected to the FBG, and schematically illustrated in Fig. 8. Light emitted by a distributed feedback (DFB) diode laser is sent to a Y-coupler, which directs laser light to the FBG. Light reflected from the FBG is then re-directed to a high-speed photodiode (PD). Assuming that the laser frequency is within the linear range of the FBG reflection slope, the strain signal will produce a change in the reflected optical power, which is measured by the photodetector. In other words, using a narrowband laser at a fixed wavelength permits to convert any FBG spectrum wavelength modulation induced by the strain signal, into an intensity signal, which is finally converted into an electrical signal by the photodiode. In our measuring set-up, the electrical output from the photodiode was sent to a conditioning electronics, which basically comprises a bandpass filter used to eliminate the dc component and the high-frequency noise.

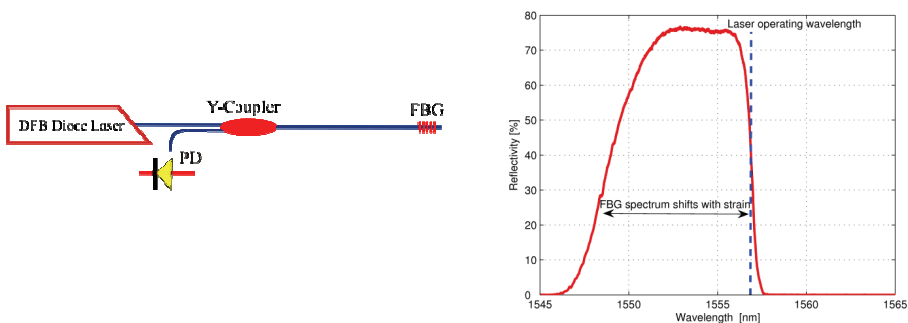


Fig. 8. FBG interrogation scheme (left) and reflectivity spectrum of the grating (right).

Figure 8 shows the reflectivity spectrum of the FBG used in our experiments, as measured at room temperature and with no applied strain. It can be seen that the spectrum has a quasi-

flat top from 1552 nm to 1556 nm, with a peak reflectivity greater than 75%. The leading edge of the FBG reflection curve extends from 1547.28 nm to 1550.95 nm (measured from 10% to 90% of maximum reflectivity), whereas the trailing edge extends from 1556.37 nm to 1557.24 nm. The trailing edge of the FBG reflection curve allowed for about 72 GHz linear slope width, and it was chosen as the operating range due to the higher linearity exhibited by the FBG reflectivity in this spectral portion. In order to keep a linear relationship between the reflected optical power and the strain signal, the DFB laser emitting wavelength must lie within the trailing edge of the FBG reflectivity spectrum (see Fig. 8). Moreover, assuming a typical FBG curve shift of 1 nm for an applied strain of $1000 \mu\epsilon$ ((Kersey et al. 1997), the strain level must be kept lower than $870 \mu\epsilon$ in order to avoid sensor output saturation.

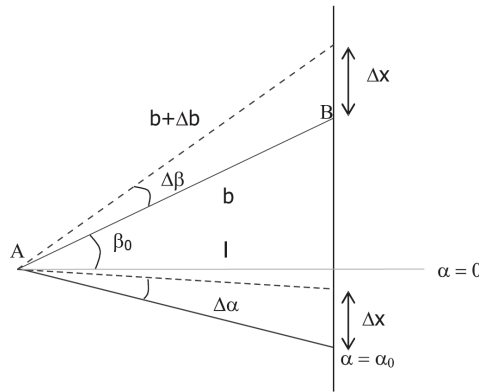


Fig. 9. Sketch of sensor mounting setup.

Before attaching the FBG to the magnetostrictive actuator, the portion of fibre jacket corresponding to the grating position was removed, so as to avoid strain transfer loss from actuator to FBG. The FBG was then pre-stressed and glued to the actuator by epoxy resin. Pre-stressing of the FBG was necessary in order to avoid buckling of the fibre in which the sensor is written. Mounting of the FBG was carried out, such that the output of the optical sensor is a measurement of one of the state variables of the system, $\alpha(t)$. A sketch of the mounting set-up is shown in Fig. 9. As the output provided by the FBG is proportional to the strain of the fibre segment between the two bonding points A and B, the relationship between the strain and the angular displacement has to be determined. Such a relationship can be obtained by means of geometrical considerations. Referring to Fig. 9, let us start by considering that, under real experimental conditions, the displacement Δx of the moving mass is much smaller than the lever arm length l , hence $\Delta x \approx l\Delta\alpha$. Moreover, Δx is also much smaller than the fibre segment b , so that we can also assume $\Delta\beta \approx 0$. Under this approximation, the displacement Δx is nearly equal to Δb . As the optical sensor provides an output proportional to the strain $\Delta b/b$, we can finally write:

$$\epsilon \equiv \frac{\Delta b}{b} \approx \frac{l}{b} \Delta\alpha \quad (2)$$

Hence, under the small signal hypothesis, the quantity measured by the FBG is directly proportional to the angle variation $\Delta\alpha = \alpha - \alpha_0$. After bonding the FBG, the DFB laser emitting

wavelength was temperature-tuned in order to guarantee a linear response of the sensor, over the whole range of actuator displacements. Calibration of the FBG was carried out by aid of an accelerometer mounted to the moving mass, so as to measure the acceleration along the vertical axis. The sensor sensitivity was estimated by comparing the measured frequency response functions from the excitation signal to the second time derivative of the FBG output signal, and from the excitation signal to the accelerometer output signal, respectively. Results are shown in Fig. 10. Based on the calibration constant of the accelerometer, we estimated an FBG sensitivity of about $37.6 \text{ mV}/\mu\text{m}$.

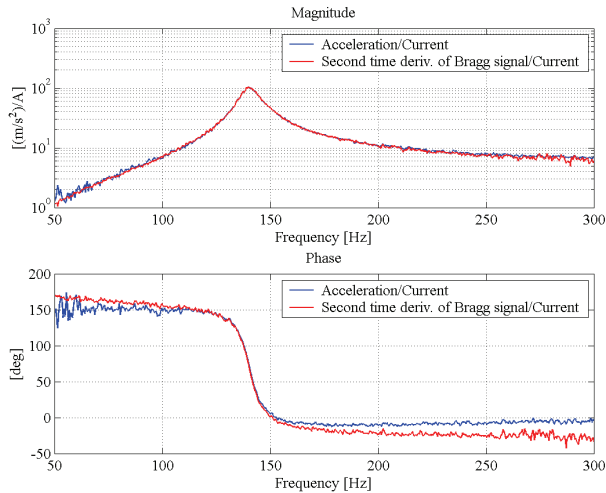


Fig. 10. Bragg calibration result: accelerometer (blue), Bragg second time derivative (red).

As mentioned before, the actuator nonlinearity causes a dependence of the structural frequency response on the amplitude of the driving current. This nonlinearity affects the satisfaction of the force requirements and makes the actuator difficult to implement in the noise control system. Therefore, a feedback controller exploiting the FBG measurement has been designed to reduce alterations of the structural response due to variations of the input current level. The control scheme is reported in Fig. 11 and the details of the design procedure can be found in (Cavallo et al. 2009). The control law basically tries to impose a desired dynamic behaviour to the actuator as specified in the reference model, which is linear time-invariant system with a fixed resonant frequency, so that the actual resonant frequency does not depend on the current level any more.

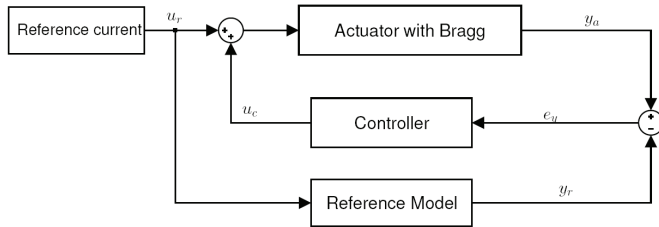


Fig. 11. Actuator feedback control scheme.

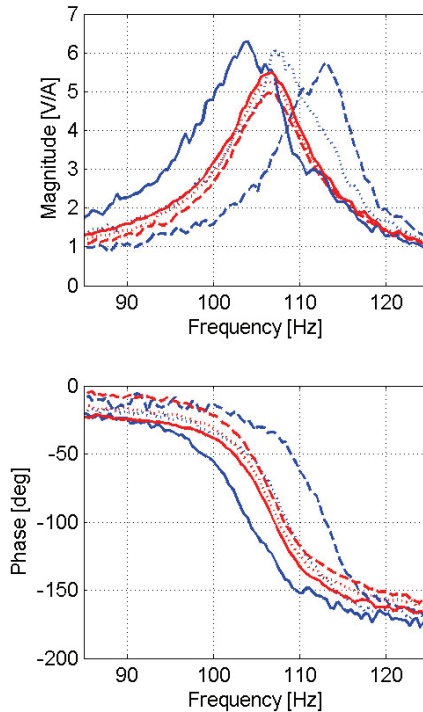


Fig. 12. Actuator behaviour at different current levels: control off (blue), control on (red).

Fig. 12 reports the experimental results obtained applying this control scheme. The blue lines represent the actuator frequency response function measured at three different input currents without the feedback control. In the same figure, it is possible to see the positive effects on the actuator behaviour of the feedback control exploiting the sensor measurement. In fact, the red lines represent the same FRFs measured with the control loop activated, and they all exhibit the same resonant frequency, resulting in a phase shift almost insensitive to the input current amplitude. Of course such a characteristic is mandatory when the actuator resonance is exploited to actively control the vibrations of a flexible structure subject to a disturbance force field in a frequency range containing the actuator resonant frequency itself.

4. Application in robotics

The number of application domains of robotic systems is rapidly growing and in particular the service robotics is becoming the most popular. In such application field a high degree of autonomy is required for the robot and thus a large number of exteroceptive sensors appear necessary. When multifingered robotic hands are considered, the requirement of minimally invasiveness for the sensory system is of major importance due to the limited space available in a mechanical structure with several degrees of freedom. In a robotic hand, different exteroceptive sensors are required to ensure stable grasping and manipulation of objects. Among these, sensing of both contact point and contact force appears mandatory for any control algorithm which intends to achieve such goals. Even though many different technologies have been explored and tested to build tactile sensors, like piezo-resistive (Liu et al., 1993), capacitive (Morimura et al., 2000), piezoelectric (Krishna & Rajanna, 2002), magneto-resistive (Tanie, 1986), optoelectronic approaches demonstrated their potential since the beginning of tactile sensors development (Maekawa et al., 1993). Also, on the market optoelectronic tactile sensors can be found that measure distributed tactile information, but such tactile information is generally limited to pressure force, and spatial resolution is coarse, a few millimetres order. Generally, a commercial sensor accurately responds to a load of 0.25 N or more up to 2 N, but such a range can be too narrow for manipulation tasks. More recently, a number of different optical approaches have been pursued, among which the solution based on an LEDs matrix has been presented in (Rossiter & Mukai, 2005) and the solution based on a CCD camera is reported in (Ohka et al., 2006).

Among optical approaches, those based on the use of optical fibres appear particularly suitable for pressure sensing, thanks to the low size and minimum invasivity of fibres themselves. Since the advent of fibre optics, it has been recognized that optical fibres can be used as effective pressure (and tactile) sensors. One of the earliest demonstrations of such a capability relied on the pressure-induced displacement of a diaphragm placed close to the tip of an optical fibre (Cook & Hamm, 1979). The fibre was operated in reflection mode, so that changes in reflected intensity can be used as a measure of the pressure applied on the diaphragm. In case of tactile sensing, such an approach presents the disadvantage of requiring a complex micromachining at the tip of the fibre. Another possible approach is based on the intensity loss resulting from pressure-induced bending of the fibre (Fields et al., 1980). However, in this case the response of the sensor is highly nonlinear due to the exponential dependence of the bending loss on the radius of curvature of the fibre. More complex examples can be found based on interferometric approaches, where the changes in the optical phase are used as transducer mechanism to sense the pressure (Saran et al., 2006, Wang et al., 2001, Yuan et al., 2005). Interferometric sensors exhibit high sensitivity, but also present some disadvantages, such as low tolerance to external disturbances, and periodicity in their response.

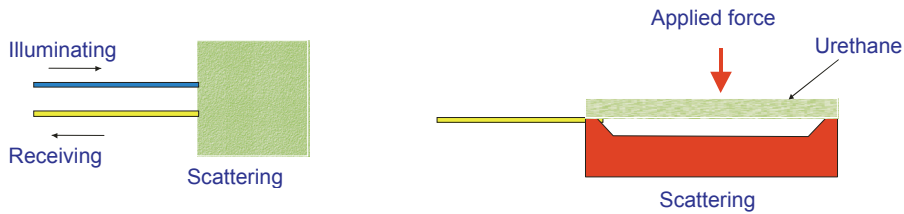


Fig. 13. Sketch of the single sensing element (taxel).

Recently, we proposed a solution based on the scattering of the light illuminating the surface of urethane foam (De Maria et al., 2008). The configuration makes use of a couple of emitter/receiver fibres placed at the edge of a micromachined well covered by the foam. The distance between the two fibres can be chosen in order to ensure a desired sensitivity of the sensing element. As a demonstration of the effectiveness of the proposed configuration, we present the results of two sensors, in which the relative distance between the two fibres was properly selected in order to fit the range of pressures to be detected. Top and lateral schematic views of a single taxel are shown in Fig. 13. The sensor works as follows: the light emitted by the illuminating fibre is scattered by the internal surface of the urethane foam and a fraction of its power is collected by the receiving fibre, depending on the applied pressure. In particular, when one applies a pressure on the external surface of the urethane foam, the distance between the tip of the collecting fibre and the internal surface of the foam is reduced, and this will result in an increased fraction of power collected by the receiving fibre. The use of a scattering surface, such as that of the urethane foam employed for the realization of the prototypes, is justified by the fact the multiple scattering permits to smooth (average-out) local variation of light intensity within the cavity, and thus reduce the sensitivity of the collected power on micro-displacements of the illuminating and/or receiving fibre. As the power collected by the receiving fibre is a function of the pressure applied on the foam surface, it can be used as a measure of the applied force. Obviously, the collected light is also a function of the relative distance between the illuminating and the receiving fibres. In our experiments, such a distance was kept constant and was not a function of the applied force. However, we can exploit such dependence, by choosing an opportune distance giving rise to a desired sensitivity of the sensor on the applied pressure. Generally speaking, a smaller distance will result in a higher sensitivity, so that smaller pressures can be measured.

On the other hand, a higher sensitivity implies a reduced dynamic range, i.e. the sensor response will saturate at lower pressure levels. Hence, a trade-off must be found between sensitivity and dynamic range.

One advantage of the proposed technique is that it can be easily extended to a number of taxels, so as to acquire a pressure distribution. Figure 14 shows a possible configuration of a matrix of taxels to realize a complete tactile sensor able to detect both contact point and contact force applied on a finite area.

Two different taxels have been produced with the same well and two different distances between the emitting/receiving fibres, i.e. 10 μm and 200 μm . The micromachined well size is 5x5 mm². The optical source was a superluminescent LED operating at a central wavelength of 1550nm, and having an output optical power of 3mW. The output pigtail of

the source was connected to the illuminating fibre, whereas the receiving fibre was connected to an InGaAs photodiode, whose output signal was fed to an oscilloscope having an input impedance of $1\text{ M}\Omega$. Both illuminating and receiving fibres were SMF-28, single-mode optical fibres. The two prototypes have been calibrated with a load cell mounted as shown in Fig. 15. The results corresponding to the calibration of the first prototype are reported in Fig. 16 (left), where the output voltage, proportional to the optical power collected by the receiving fibre, is plotted against the load applied to the sensor. As expected, the sensitivity is very high but with a limited dynamic range. Moreover, to test the repeatability of the measurements, different sets of measurements have been collected and two of them are reported in the figure.

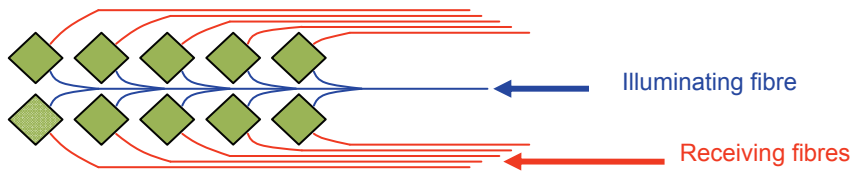


Fig. 14. Schematic diagram of a 10-taxel tactile sensor.

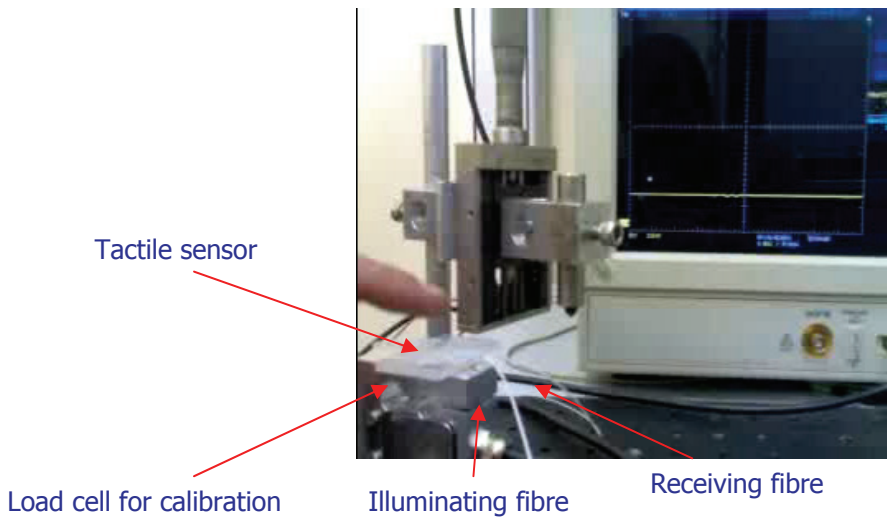


Fig. 15. Experimental set-up for the fibre-optics based taxel.

The second prototype, as expected, had a lower sensitivity but wider dynamic range, as shown by the calibration curve of Fig. 16 (right). In both cases, the sensitivity is certainly better than the typical values of commercial optical tactile sensors.

5. Conclusions

In this chapter, a number of experimental demonstrations on the use of the optical fibre sensor technology have been reported. It has been shown that different application fields can take advantage of the peculiar characteristics of optical fibre sensors. In particular, distributed fibre sensors have great potentiality in the field of structural health monitoring, as they permit to perform continuous measurements of the quantity of interest. On the other hand, fibre Bragg grating technology offers high sensitivity and accuracy, and in general it benefits from the immunity to electromagnetic interference, in common with other fibre-optic sensors. Finally, the small size and minimally invasiveness of optical fibres have been demonstrated to be useful in robotic applications, where the use of fibre-optics may lead to efficient exteroceptive sensing systems.

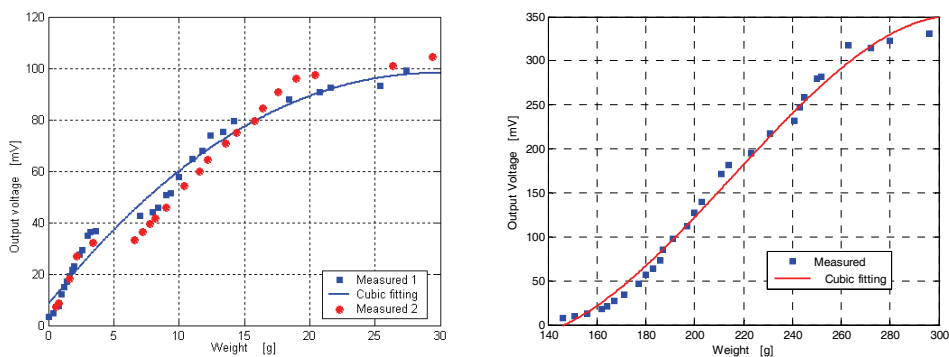


Fig. 16. Calibration curves of the first prototype with 10 μm distance between the fibres (left) and of the second prototype with 200 μm distance between the fibres (right).

6. References

- Agrawal, G.P. (2001). *Nonlinear Fibre Optics*. Academic Press, San Diego.
- Barnoski, J.K. & Jensen, S.M. (1976). Fibre waveguides: A novel technique for investigating attenuation characteristics. *Appl. Opt.* Vol. 15, No. 9, 2112-2115.
- Bernini, R.; Crocco, L.; Minardo, A.; Soldovieri, F. & Zeni, L. (2002). Frequency-domain approach to distributed fibre-optic Brillouin sensing. *Opt. Lett.* Vol. 27, No. 5, 288-290.
- Bernini, R.; Fraldi, M.; Minardo, A.; Minatolo, V.; Carannante, F.; Nunziante, L. & Zeni, L. (2006a). Identification of defects and strain error estimation for bending steel beams using time domain Brillouin distributed fibre sensors. *Smart Materials and Structures* Vol. 2, 612-622.
- Bernini, R.; Minardo, A. & Zeni, L. (2006b). An accurate high resolution technique for distributed sensing based on frequency domain Brillouin scattering. *IEEE Photonics Technology Letters* Vol. 18, No. 1, 280-282.

- Bernini, R.; Minardo, A. & Zeni, L. (2008). Vectorial dislocation monitoring of pipelines by use of Brillouin-based fibre-optics sensors. *Smart Materials and Structures*. Vol. 17, 015006.
- Cavallo, A.; May, C.; Minardo, A.; Natale, C.; Pagliarulo, P. & Pirozzi, P. (2009). Modelling and control of a smart auxiliary mass damper equipped with a Bragg grating for active vibration control, *Sensors and Actuators A*, in press.
- Cook, R.O. & Hamm, C.W. (1979). Fibre optic lever displacement transducer. *Appl. Opt.* Vol. 18, No. 19, 3230-3241.
- Culshaw, B. & Dakin, J. 1997. *Optical Fibre sensors Vol. 4*. Artech House Publishers, 0890069409.
- De Maria, G.; Minardo, A.; Natale, C.; Pirozzi, S. & Zeni, L. (2008). Optoelectronic Tactile Sensor Based on Micromachined Scattering Wells. *FIRST MEDITERRANEAN PHOTONICS CONFERENCE*, European Optical Society Topical Meeting, 25-28 June 2008, Ischia, Italy.
- Fields, J.N.; Asawa, C.K.; Ramer, O.G. & Barnowski, M.K. (1980). Fibre Optic Pressure Sensor. *J. Acoust. Soc. Am.*, Vol. 67, 816-818.
- Garus, D.; Krebber, K.; Schliep, F. & Gogolla, T. (1996). Distributed sensing technique based on Brillouin optical-fibre frequency-domain analysis. *Opt. Lett.*, Vol. 21, No. 17, 1402-1404.
- Kersey, A. D.; Davis, M. A.; Patrick, H. J.; LeBlanc, M.; Poo, K. P.; Askins, A.G.; Putnam, M. A. & Friebele, E. J. (1997). Fibre grating sensors, *Journal of Lightw. Technol.*, vol. 15, no. 8, pp. 1442-1462.
- Krishna, G.M. & Rajanna, K. (2002). Tactile sensor based on piezoelectric resonance. *Proc. of 2002 IEEE Conference on Sensor*, pp. 1643- 1647.
- Liu, L.; Zheng, X. & Li, Z. (1993). An array tactile sensor with piezoresistive with single crystal silicon diaphragm. *Sensors and Actuators-A32*, 193-196.
- Maekawa, H.; Tanie, K. & Komoriya, K. (1993). A finger-shaped tactile sensor using an optical waveguide. *Proc. of 1993 IEEE International Conference on Systems, Man and Cybernetics*, pp. 403-408.
- Measures, R.M. (2002). *Structural monitoring with fibre optic technology*. Academic press, San Diego.
- Morimura, H.; Shigematsu, S. & Machinda, K. (2000). A novel sensor cell architecture and sensing circuit scheme for capacitive fingerprint sensors. *IEEE Journal of Solid State Circuits*, Vol, 35, 724-731.
- May, C.; Pagliarulo, P. & Janocha, H. (2006). Optimisation of a magnetostrictive auxiliary mass damper. *Proc. 10th International Conference on New Actuators ACTUATOR2006*, Bremen, Germany, pp. 344-348.
- Nikles, M.; Thevenaz, L. & Robert, P.A. 1997. Brillouin gain spectrum characterization in single-mode optical fibres. *J. Lightw. Technol.*, Vol. 15, No. 10, 1842 - 1851.
- Ohka, M.; Kobayashi, H.; Takata, J. & Mitsuya, Y. (2006). Sensing Precision of an Optical Three-axis Tactile Sensor for a Robotic Finger. *Proc. Of the 15th IEEE International Symposium on Robot and Human Interactive Communication*, pp. 214-219.
- Rossiter, J. & Mukai, T. (2005). A novel tactile sensor using a matrix of LEDs operating in both photoemitter and photodetector modes. *Proc. of 2005 IEEE Conference on Sensor*, pp. 994-997.

- Saran, A.; Abeysinghe, D.C. & Boyd, J.T. (2006). Microelectromechanical system pressure sensor integrated onto optical fibre by anodic bonding. *Appl. Opt.*, Vol. 45, 1737-1742.
- Tanie, K. (1986). Advances in tactile sensors for robotics. *Proc. of the 6th Sensor Symposium Japan*, pp. 63-68.
- Udd. E. (2002). Overview of fibre optic sensors, In: *Fibre Optic Sensors*. Francis T. S. Yu; Shizhuo Yin, pp. 1-40, Routledge, 978-0-203-90946-1, USA.
- Wang, A.; Xiao, H.; Wang, J.; Wang, Z.; Zhao, W. & May, R.G. (2001). Self-calibrated interferometric-based-optical fibre sensors. *J. Lightw. Technol.*, Vol. 19, No. 10, 1495-1501.
- Yuan, S.; Ansari, F.; Liu, X. & Zhao, Y. (2005). Optical fibre based dynamic pressure sensor for WIM sensor. *Sens. and Actuat. A*, Vol. 120, No. 1, 53-58.
- Zhao, Y. & Liao, Y. (2004) "Discrimination methods and demodulation techniques for fibre Bragg grating sensors", *Opt. Lasers Eng.*, vol. 41, pp. 1-18.

Optical Fibre Sensor System for Multipoint Corrosion Detection

Joaquim F. Martins-Filho and Eduardo Fontana
*Department of Electronics and Systems, Federal University of Pernambuco
Brazil*

1. Introduction

Over the past thirty years there has been intense research and development on optical fibre sensors for many applications, basically because of their advantages over other technologies, such as immunity to electromagnetic interference, lightweight, small size, high sensitivity, large bandwidth, and ease in signal light transmission. The applications include sensing temperature, strain, pressure, current/voltage, chemical/gas, displacement, and biological processes among others. To accomplish those, different optical technologies have been employed such as fibre grating, interferometry, light scattering and reflectometry, Faraday rotation, luminescence and others. A review on fibre sensors can be found in (Lee, 2003).

Corrosion and its effects have a profound impact on the infrastructure and equipment of countries worldwide. This impact is manifested in significant maintenance, repair, and replacement efforts; reduced access, availability and production; poor performance; high environmental risks; and unsafe conditions associated with facilities and equipment. There have been some efforts from different countries to estimate the cost of corrosion and the results indicate that it can reach 2 to 5% of the gross national product. For example, corrosion damage represented an estimated cost of US\$ 276 billions in the United States of America in 2002 (Thompson et al., 2005). Therefore, corrosion monitoring is an important aspect of modern infrastructure in industry sectors such as mining, aircraft, shipping, oilfields, as well as in military and civil facilities.

Optical fibre-based corrosion sensors have been investigated in recent years mainly because of the advantages obtained by the use of optical fibres, as already pointed out. A short review of the technologies employed in the fibre-based corrosion sensors can be found in (Wade et al., 2008). The reported applications include corrosion monitoring in aircrafts (Benounis & Jaffrezic-Renault, 2004), in the concrete of roadways and bridges (Fuhr & Huston, 1998) and in oilfields.

2. Corrosion Monitoring in Deepwater Oilfield Pipelines

In the oil industry, to which we focus the sensing approach described in this chapter, a very challenging problem is that related to surveillance and maintenance of deepwater oilfield pipelines, given the harsh environment to be monitored and the long distances involved.

These structures are subject to corrosion and sand-induced erosion in a high pressure, high temperature environment. Moreover, the long distances (kilometres) between the corrosion points and the monitoring location make the commercially available instruments not appropriate for monitoring these pipelines. Costly, regularly scheduled, preventive maintenance is then required (Staveley, 2004; Yin et al., 2000). Electronic and electromagnetic-based corrosion sensors (Yin et al., 2000; Vaskivsky et al., 2001; Andrade Lima et al., 2001) are also not suitable in these conditions. Fibre optic based corrosion sensors are ideal for this application. However, the sensing approaches reported in the literature are either single point (Qiao et al., 2006; Wade et al., 2008) or use a stripped cladding fibre structure that requires a high precision mechanical positioning system with moving parts for light detection, which compromises the robustness of the sensor system (Benounis et al., 2003; Benounis & Jaffrezic-Renault, 2004; Saying et al., 2006; Cardenas-Valencia et al., 2007). An optical fibre PH sensor has been recently developed for the indirect evaluation of the corrosion process in petroleum wells (Da Silva Jr. et al., 2007). It employs a fibre Bragg grating mechanically coupled to a PH-sensitive hydrogel, which changes its volume according to the PH of the medium. Thus, the change in PH is translated into a mechanical strain on the Bragg grating, which can be interrogated by standard optical methods. Although it can easily be multiplexed for multipoint measurements, this technique is limited to the evaluation of the chemical corrosion due to acid attack inside the well, disregarding the combined effects of other important sources of corrosion, such as mechanical (erosion), chemical, thermic and biological (microorganisms). The oil industry can also make use of the time domain reflectometry (TDR) technique to evaluate the corrosion process inside pipelines and oil wells (Kohl, 2000). The proposed scheme involves the deployment of a metallic cable inside and along the pipeline or well. The conductor is exposed to the fluid at selected locations such that it should be susceptible to the same corrosive processes as the pipeline. A signal generator launches a pulsed electrical signal to the conductor cable and an electronic receiver measures the reflected pulses intensity and delay. The reflections come from the locations where the exposed cable was affected by the corrosion process, which changes its original impedance. This TDR technique has also been applied to the monitoring of corrosion in steel cables of bridges (Liu et al., 2002). Although this technique has the advantage of being multipoint or even distributed, it is limited in reach. For practical purposes the maximum distance covered by the sensor is about 2 km. This is suitable for standard wells, but not for deep oilfields, especially those from the recently discovered presalt regions in Brazil, which are over 6 km deep.

3. A Multipoint Fibre Optic Corrosion Sensor

We have recently presented for the first time the concept and first experimental results of a fibre-optic-based corrosion sensor using the optical time domain reflectometry (OTDR) technique as the interrogation method (Martins-Filho et al., 2007; Martins-Filho et al., 2008). Our proposed sensor system is multipoint, self-referenced, has no moving parts and can detect the corrosion rate several kilometres away from the OTDR equipment. These features make it very suitable to the problem of corrosion monitoring of deepwater pipelines in the oil industry. It should be pointed out, however, that the approach is not limited to this specific application and can be employed to address a number of single or multipoint corrosion detection problems in other industrial sectors.

In this chapter we present a detailed description of the sensor system, further experimental results and theoretical calculations for the measurement of the corrosion rate of aluminium films in controlled laboratory conditions and also for the evaluation of the maximum number of sensor heads the system supports.

3.1 Sensor Setup

Our proposed sensor system consists of several sensor heads connected to a commercial OTDR equipment by a single-mode optical fibre and fibre couplers. Figure 1 shows the corrosion sensor setup. The OTDR is connected to a 2 km long single mode optical fibre. Directional couplers can split the optical signal such that a small fraction (3 to 9%) is directed to the sensing heads. The OTDR operates at 1.55 μm , with a pulsewidth of 10 ns, which corresponds to a spatial resolution of 2 m. The OTDR is set to measure 50000 points for the total distance of 5 km (one point every 10 cm). The optical fibres and couplers are standard telecommunication devices. The sensor heads have 100 nm of aluminium deposited on cleaved fibre facets by a standard thermal evaporation process and they are numbered from 1 to 11 in Fig. 1.

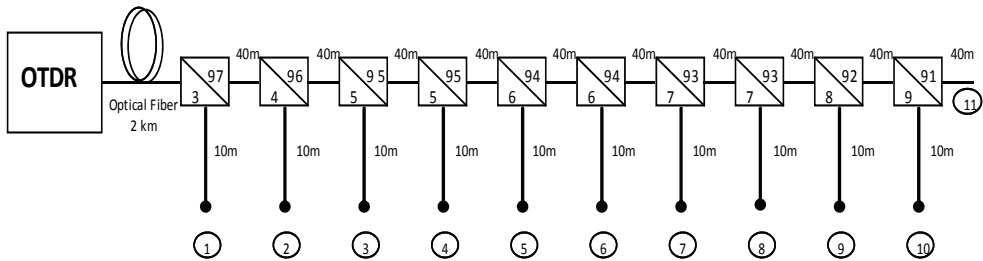


Fig. 1. Schematic diagram of the corrosion sensor. Sensor heads are numbered. Fibre lengths and split ratios are shown.

3.2 Results

For laboratory measurements the corrosion action was simulated by controlled etching of the Aluminium film on the sensor head. We used 25 H_3PO_4 : 1 HNO_3 : 5 CH_3COOH as the Al-etcher. The expected corrosion rate of Al from this etcher is 50 nm/min. Figure 2-a shows the OTDR trace where each peak, numbered from 1 to 11, indicates the reflection from the corresponding sensing head. The head number 6 is immersed in the Al-etcher. As the aluminium is being removed from the fibre facet the reflected light measured in the OTDR decreases, as shown in Fig. 2-b.

In Fig. 3 we plot the ratio of peak (point A) to valley (point B) of the reflected light shown in Fig. 2-b as a function of the aluminium corrosion time. Figure 3 shows that up to 60 seconds of corrosion there is no significant change in the OTDR measured reflected light, since the aluminium is still too thick. Further up from this point the reflection drops to a minimum and then stabilizes at a constant level. The constant level means that the corrosion process on the fibre facet has ended. We obtain the corrosion rate by taking the deposited metal thickness and the time taken to reach the constant level, as show in Fig. 3.

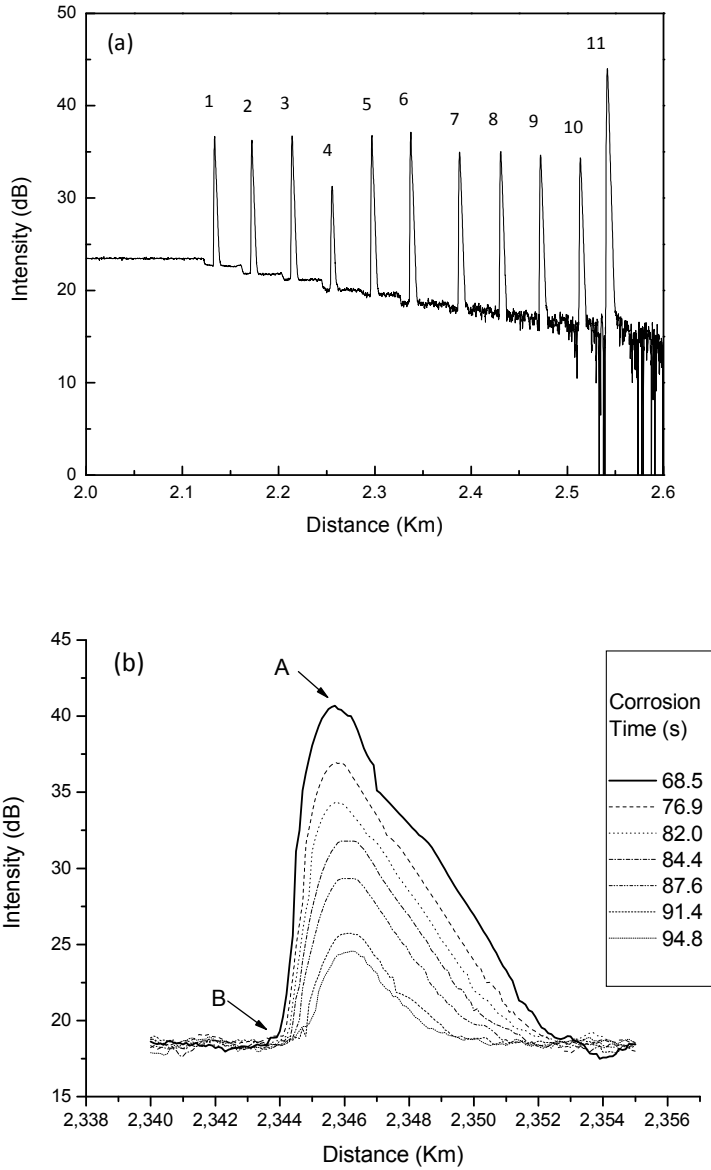


Fig. 2. (a) OTDR trace, corresponding to the intensity of the reflected light as a function of distance along the fibre. Sensor head numbers are shown. (b) OTDR traces for sensor head number 6, for several corrosion times.

The measured corrosion rate was 47.5 nm/min, which is very close to the expected value (50 nm/min). Other measurements performed using different sensor heads showed similar results. It is important to note that since the corrosion rate is obtained from the ratio of peak (point A) to valley (point B) of the OTDR trace as a function of time, this measurement is self-referenced, because the ratio is immune, to a certain extent, to small optical power fluctuations that may occur due to changes in the OTDR signal power, optical fibre and fibre coupler loss variations along the sensor system.

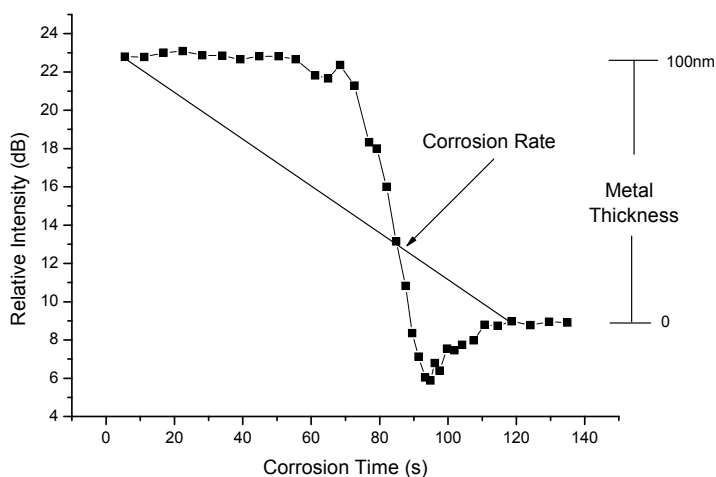


Fig. 3. Relative intensity obtained from Fig. 2-b, as a function of the corrosion time. Metal thickness and corrosion rate are shown.

Figure 3 also shows a valley in the relative reflected intensity just before the constant level used for corrosion determination. Although this feature does not seem to be important for the determination of the corrosion rate, we verified if it would be an artifact due to the pulsed OTDR operation in the multipoint (multireflection) setup scheme shown in Fig.1, by performing measurements in the single head setup shown in Fig. 4. This new setup uses a CW laser source and an optical power meter, instead of the OTDR. The laser light at 1.55 μm from the CW laser with fibre pigtail is coupled to an optical isolator and then to a 50% coupler and to a 79/21 coupler. The output of this coupler has another optical isolator in one end and a sensor head in the other end. The sensor head used here is similar to those used in the multipoint setup of Fig. 1. The light reflected from the sensor head reaches the optical power meter through the optical couplers. The two isolators avoid unwanted reflections to reach the power meter and the laser source, which could cause interference effects and instabilities. For corrosion measurements we used the same Aluminium etcher as described before. Figure 5 shows the optical power as a function of the corrosion time obtained from the single head setup of Fig. 4. This result also exhibits the valley observed in the multipoint setup that uses the OTDR (Fig. 3), indicating that this feature is not a measurement artifact. Also, Fig. 5 confirms the corrosion rate obtained from Fig. 3, since the constant level starts at about 120 seconds of corrosion.

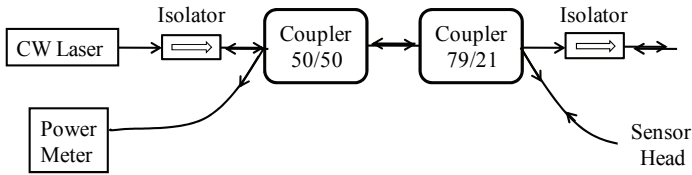


Fig. 4. Schematic diagram of the single head setup.

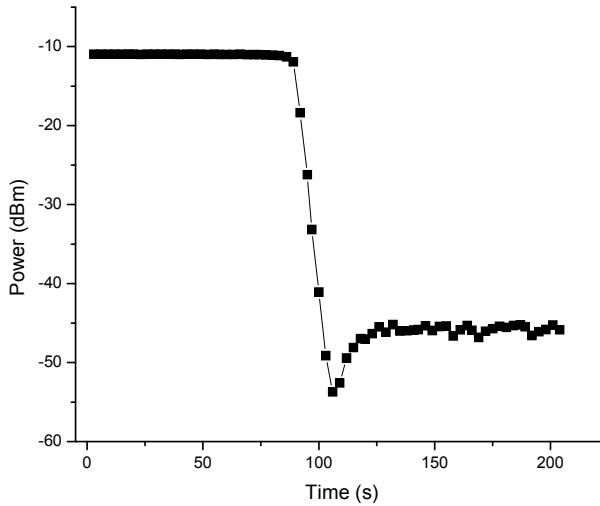


Fig. 5. Reflected optical power from a single head setup as a function of the corrosion time.

We also used the Fresnel reflection formulation (Fontana & Pantell, 1988) for a silica-Al-liquid single layer structure, as shown in Fig. 6, to study the reflection properties of the sensing head. Neglecting the small beam divergence of the guided mode, the reflectance is given by

$$R = \left| \frac{r_{12} + r_{23} \exp(-j2k_0 \sqrt{\epsilon_2} d)}{1 + r_{12} r_{23} \exp(-j2k_0 \sqrt{\epsilon_2} d)} \right|^2, \quad (1)$$

where

$$r_{i,i+1} = \frac{\sqrt{\epsilon_{i+1}} - \sqrt{\epsilon_i}}{\sqrt{\epsilon_{i+1}} + \sqrt{\epsilon_i}} \quad (2)$$

is the normal incidence reflectivity at the interface between media i and $i+1$ ($i = 1, 2$), $k_0 = 2\pi/\lambda$, ϵ_i is the relative electrical permittivity of medium i ($i = 1, 2, 3$) and d is the metal film thickness.

We assumed that the etching solution had a refractive index close to that of pure water, for the sake of simplicity. Optical parameters for silica (Malitson, 1965), pure water (Schiebener et al., 1990) and Al (Lide, 2004) at $\lambda = 1.55 \mu\text{m}$ were used in the calculations.

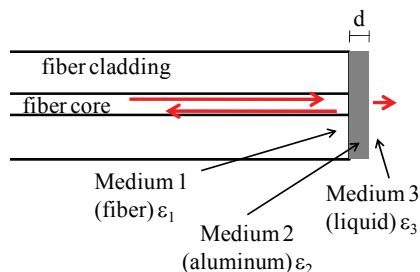


Fig. 6. Schematic diagram of the sensing head showing the Aluminium film of thickness d on the fibre facet.

Figure 7 shows a theoretical simulation as well as the experimental data for the reflectance at the metalized fibre facet as a function of the metal film thickness. The experimental data were obtained from Fig. 5. The theoretical result showed no evidence of a minimum reflectance with the strong depth observed experimentally at an estimated Al film thickness of 15 nm. In fact, the theoretical prediction yields almost 100% reflectance at this thickness value, as can be noticed in Fig. 7. The difference between theoretical and experimental results indicates that the valley observed in the experimental results is not due to any interference effect that could occur in the fibre-metal-liquid interfaces.

Due to the resonant nature of the reflectance minima shown in Figs. 3 and 5, it is very likely that they occur due to roughness induced, resonant coupling to surface plasmons (Fontana & Pantell, 1988) at the metal-liquid interface as a thin and rough layer of metal may result during the etching process. The coupling is thickness dependent and the strength depends on the average size of irregularities on the surface (Fontana & Pantell, 1988). Given that the dispersion relation of surface plasmons is very near that of photons in this spectral region, surface roughness could provide the required small increase in momentum for efficient coupling to the surface plasmon oscillation. A more elaborated calculation will be performed in future work taking into account the change in dispersion relation of surface plasmons due to roughness (Fontana & Pantell, 1988), to account for this effect.

It is worth noticing from Fig. 7 that the reflectance predicted theoretically with no metal film was 26.7 dB lower than that at maximum thickness, a result that differs significantly from the drop of ~ 14 dB observed experimentally in Fig. 3 and ~ 35 dB in Fig. 7. This is probably due to the residual clusters left on the fibre facet that form an absorbing, non-homogeneous interface that changes the reflectance relative to that predicted theoretically for a single glass-liquid interface. In fact we observed from a direct inspection with an optical microscope that some clusters of material still remained on the fibre facet, which were no longer affected by the Al-etcher. As can be seen from Figs. 3 and 7, the resonant features in the experimental results are similar, although the minima occur at different time points. There is, however, a significant difference from 14 to 35 dB in the final reflectance drop obtained from the data of Figs. 3 and 7, respectively, which may be due to the distinct procedures used to carry out the experiments. For the data shown in Fig. 3, obtained with

the OTDR, since the equipment is somewhat slow to execute several measurements to average them in time, the head was placed in the etcher for a given time and then in water for OTDR reading and averaging for each data point. For the case of Fig. 7, we used the single head setup of Fig. 4, and we attempted to avoid artifacts introduced by the use of alternate solutions and employed an optical power meter for fast data reading and averaging, and thus the sensor head could remain immersed in the etcher during the entire measurement. These distinct procedures may lead to different residual clustering in the fibre facets, which can be the cause of the difference in the results of Figs. 3 and 7. It will be further investigated in the future.

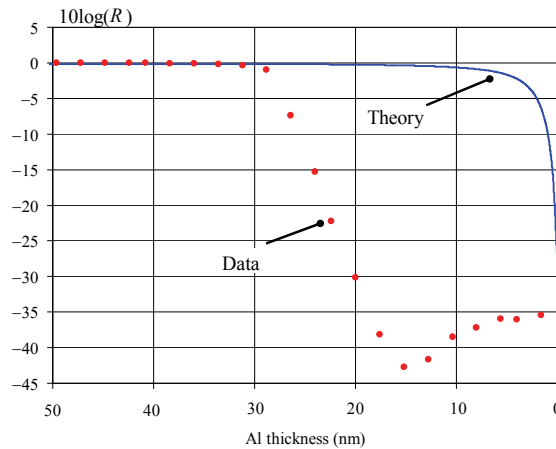


Fig. 7. Theoretical (line) and experimental data (dots) for the reflectance as a function of the Aluminium film thickness.

We also evaluated experimentally the maximum number of sensor heads our sensor system can support, and we found that it depends on the dynamic range of the OTDR. For the OTDR pulsewidth used to obtain the results shown here (10 ns) its dynamic range is about 7 dB. Since each coupler has an insertion loss of about 0.7 dB, we can have up to 10 sensor heads in this configuration. This can be verified from Fig. 2-a. One can see that as the number of heads increases along the fibre length the OTDR trace becomes noisier. This noisy trace should have impact on the accuracy of the measured corrosion rate for the heads located further away from the OTDR. On the other hand, for 500 ns pulsewidth the OTDR dynamic range is 20.4 dB, which allows the use of up to 30 sensing heads. In this case the OTDR spatial resolution is about 100 m. Therefore, the minimum separation between consecutive sensor heads should be of about 200 m. In this configuration the sensor system would cover a total length of 6 km, with a sensor head every 200 meters.

4. Conclusions

We proposed and demonstrated experimentally an optical fibre sensor for the corrosion process in metal (Aluminium) using the optical time domain reflectometry technique. We

presented experimental results for the measurement of the corrosion rate of aluminium films in controlled laboratory conditions. The obtained corrosion rate matched the expected rate of the etcher used. We also evaluated experimentally the maximum number of sensor heads the system supports. It depends on the OTDR dynamic range and it has implications on the distance between consecutive sensor heads.

Our proposed sensor system is multipoint, self-referenced, has no moving parts (all-fibre) and can detect the corrosion rate for each head several kilometres away from the OTDR, thus making the system ideal for “in-the-field” monitoring of corrosion and erosion. This system may have applications in harsh environments such as in deepwater oil wells and gas flowlines (including from the presalt region), for the evaluation of the corrosion and erosion processes in the inner wall of the casing pipes. In this case, different materials can be deposited on the fibre facet to better match the pipe materials under corrosion/erosion. This system may enable inferred condition-based maintenance without production interruption, decreasing the cost of oil production, and substantially reducing the risk of environmental disasters due to the failure of unmonitored flowlines.

Our experimental results also revealed a feature that may indicate the occurrence of the surface plasmon effect at the metal-liquid interface. It could be due to the roughness coupling to surface plasmons at the metal-liquid interface as a thin and rough layer of metal may result during the etching process. Although we believe at this point that this effect is not vital for the operation of the proposed sensor, nor to the measurement of the corrosion rate, it will be investigated in future work.

5. References

- Andrade Lima, E. & Bruno, A. C. (2001). Improving the Detection of Flaws in Steel Pipes Using SQUID Planar Gradiometers. *IEEE Transactions on Applied Superconductivity*, Vol. 11, No. 1, Mar 2001, 1299-1302, ISSN 1051-8223.
- Benounis, M.; Jaffrezic-Renault, N.; Stremstoerfer, G. & Kherrat, R. (2003). Elaboration and standardization of an optical fibre corrosion sensor based on an electroless deposit of copper. *Sensors and Actuators B*, Vol. 90, 2003, 90-97, ISSN 0925-4005.
- Benounis, M. & Jaffrezic-Renault, N. (2004). Elaboration of an optical fibre corrosion sensor for aircraft applications. *Sensors and Actuators B*, Vol. 100, March 2004, 1-8, ISSN 0925-4005
- Cardenas-Valencia, A. M.; Byrne, R. H.; Calves, M.; Langebrake, L.; Fries, D. P. & Steimle, E. T. (2007). Development of stripped-cladding optical fiber sensors for continuous monitoring II: Referencing method for spectral sensing of environmental corrosion. *Sensors and Actuators B*, Vol. 122, 2007, 410-418, ISSN 0925-4005
- Da Silva Jr., M. F.; D'almeida, A. R.; Ribeiro, F. P.; Valente, L. C. G.; Braga, A. M. B. & Triques, A. L. C. (2007). Optical Fiber PH Sensor, US Patent no. 7251384, granted in July 2007, available in <http://www.freepatentsonline.com/7251384.html>
- Fontana, E. & Pantell, R. H. (1988). Characterization of multilayer rough surfaces by use of surface-plasmon spectroscopy. *Physical Review B*, Vol. 37, No. 7, 1988, 3164-3182, ISSN 0163-1829.
- Fuhr, P. L. & Huston, D. R. (1998). Corrosion detection in reinforced concrete roadways and bridges via embedded fiber optic sensors, *Smart Materials and Structures*, Vol. 7, 1998, pp. 217-228, ISSN 0964-1726.

- Kohl, K. T., (2000). System and method for monitoring corrosion in oilfield wells and pipelines utilizing time-domain-reflectometry, US Patent no. 6114857, granted in September 2000, available in <http://www.freepatentsonline.com/6114857.html>
- Lee, B. (2003). Review of the present status of optical fiber sensors. *Optical Fiber Technology*, Vol. 9, 2003, pp. 57-79, ISSN 1068-5200.
- Lide, D. R. (2004). *Handbook of Chemistry and Physics*, 85th Edition, CRC Press, ISBN 0-8493-0485-7, USA, 2004, pp. 12-133 - 12-156.
- Liu, W.; Hunsperger, R. G.; Chajes, M. J.; Folliard, K. J. & Kunz, E. (2002). Corrosion Detection of Steel Cables using Time Domain Reflectometry. *Journal of Materials in Civil Engineering*, Vol. 14, No. 3, May/June 2002, pp. 217-223, ISSN 0899-1561.
- Malitson, I. H. (1965). Interspecimen comparison of the refractive index of fused silica. *Journal of the Optical Society of America*, Vol. 55, No. 10, 1965, 1205-1209.
- Martins-Filho, J. F.; Fontana, E.; Guimaraes, J.; Pizzato, D. F. & Souza Coelho, I. J. (2007). Fiber-optic-based Corrosion Sensor using OTDR, *Proceedings of the 6th Annual IEEE Conference on Sensors*, pp. 1172-1174, Atlanta, USA, 2007.
- Martins-Filho, J. F.; Fontana, E.; Guimaraes, J. & Souza Coelho, I. J. (2008). Multipoint fiber-optic-based corrosion sensor, *Proceedings of the 19th International Conference on Optical Fibre Sensors*, pp. 70043P-1-70043P-4, Perth - Australia, 2008.
- Qiao, G.; Zhou, Z. & Ou, J. (2006). Thin Fe-C Alloy Solid Film Based Fiber Optic Corrosion Sensor, *Proceedings of the 1st IEEE International Conference on Nano/Micro Engineered and Molecular Systems*, pp. 541-544, Zhuhai, China, January 2006, IEEE.
- Staveley, C. (2004). Applications of Optical Fibre Sensors to Structural Health Monitoring, Optimisation and Life-cycle Cost Control for Oil and Gas Infrastructures, *Business Briefing: Exploration & Production: The Oil & Gas Review 2004*. 72-76 Available: <http://www.touchoilandgas.com/applications-optical-fibre-sensors-a231-1.htm>
- Saying, D.; Yanbiao, L.; Qian, T.; Yanan, L.; Zhigang, Q. & Song Shizhe, S. (2006). Optical and electrochemical measurements for optical fibre corrosion sensing techniques. *Corrosion Science*, Vol. 48, 2006, 1746-1756, ISSN 0010-938X.
- Schiebener, P.; Straub, J.; Levelt Sengers, J.M.H. & Gallagher, J.S. (1990). Refractive Index of Water and Steam as Function of Wavelength, Temperature and Density. *Journal of the Physical and Chemical Reference Data*, Vol. 19, 1990, 677-717, ISSN 0047-2689.
- Thompson, N.; Yunovich, M. & Dunmire, D. J. (2005). Corrosion costs and maintenance strategies – a civil/industrial and government partnership, *Materials Performance*, Vol. 44, No. 9, September 2005, pp. 16-20.
- Vaskivsky, V.P.; Kempa, Ya.M.; Koba, S.I.; Klymonchuk, R.V.; Lyashchyk, O.B.; Naumets, N.A.; Rybak, Ya.N. & Tsukornuk, G.V. (2001). Microwave pipe corrosion detector, *Proceedings of 11th International Conference on Microwave and Telecommunication Technology*, pp. 660 - 661, Ukraine, 2001
- Wade, S.A.; Wallbrink, C.D.; McAdam, G.; Galea, S.; Hinton, B.R.W. & Jones, R. (2008). A fibre optic corrosion fuse sensor using stressed metal-coated optical fibres, *Sensors and Actuators B*, Vol. 131, No. 2, January 2008, pp. 602-608, ISSN 0925-4005.
- Yin, J.; Lu, M. & Piñeda de Gyvez, J. (2000). Full-Signature Real-Time Corrosion Detection of Underground Casing Pipes. *IEEE Transactions on Instrumentation and Measurement*, Vol. 49, No. 1, February 2000, 120-128, ISSN 0018-9456.

Fiber Sensor Applications in Dynamic Monitoring of Structures, Boundary Intrusion, Submarine and Optical Ground Wire Fibers

Xiaoyi Bao, Jesse Leeson, Jeff Snoddy and Liang Chen
University of Ottawa, (Physics Department)
Canada

1. Introduction

The pressure of reducing cost in industrial sectors has pushed the development of monitoring techniques for civil structures, transportation departments, manufacturing processes and security related applications. For the applications of civil engineering monitoring, we refer to bridges, tunnels, highways, railways, dams, pipelines, seaports and airports, which are associated to our daily lives. To assure them operating in good condition requires static and dynamic monitoring of strains and vibrations, which provides insight of the structural condition similar to monitoring human health. By identifying the abnormal vibration patterns via the frequency range and amplitude, or the strain magnitude and distribution, structural engineers can access the condition of civil structures. This may act as a warning sign for potential problems and to trigger the repairing process to prevent potential disaster and to protect our citizens. All useful monitoring tools should be able to find critical events via unusual frequency ranges and strain readings, which are stored as record for a specific structure for the purpose of determining the repairing time and scopes. Another front of important application is fiber cable monitoring, such as aerial, submarine and optical ground wire (OPGW) around high voltage power lines. The motivation of monitoring submarine and aerial fibers is to identify the fast polarization changes, as the polarization effect induces pulse broadening in dynamic fashion due to environmental effects, such as temperature and wind, and hence errors in the high speed communication system at rates higher than 10 GB/s. This monitoring process also produces an additional benefit: as the rotation of the polarization state is also proportional to the surrounding magnetic field via the Faraday effect. This means one can explore the high electrical current phenomena via polarization effect to identify local high magnetic fields, if the measurement is distributed, so that we can protect the power system.

The application to water wave and current measurement is driven by the advantage of fiber sensors with large coverage in environments such as seaports, rivers and waterways. Marine biologists use sound to identify marine mammals. Geophysicists record deep-sea seismic events from resulting pressure waves. The measured acoustic frequency varies for each application, with seismicity monitored at $O(5\text{ Hz})$, marine mammals at $O(50\text{ Hz})$ and ship passage at $O(100\text{ Hz})$. This frequency range is similar to the concrete bridge monitoring

requirement with much larger coverage than the bridges due to the size of the waves in water.

Although the above applications are very different, they are all related to the measurement of birefringence change in optical fibers. When the fiber is disturbed locally by stress, temperature or acoustic wave, the local birefringence will change. This change can be measured in the form of a polarized light change in transmission using direct detection or phase change by interferometers, and Rayleigh scattering or Brillouin gain for its dependence on the polarization state change.

2. Birefringence and Polarization Effects

When a monochromatic plane-wave (linear polarized beam) with a wavelength λ is launched in optical fibers, the electrical field can be described as

$$\vec{E}(\vec{r}) = E_x(z)\vec{i} \exp(-j\omega t) + E_y(z)\vec{j} \exp(-j\omega t) \quad (1)$$

where E_x and E_y are the electrical fields projection in the x and y directions at position z, $E_x(z) = E_{x0} \exp[j(\beta_x z + \delta_x)]$ and $E_y(z) = E_{y0} \exp[j(\beta_y z + \delta_y)]$, and $\beta_x = n_x k$ and $\beta_y = n_y k$ are the propagation constants, for the case of homogeneous and isotropic medium, $n_x = n_y = n_z$ and $k = 2\pi/\lambda$ which is the free space propagation constant, $\omega = 2\pi\nu$ is the angular frequency. The light is propagating in z-direction. The state of polarization (SOP) refers to the electrical field behavior at a particular point in space. δ_x and δ_y are the initial phases at $z=0$ for the electrical field which are associated to the initial polarization state, and E_{x0} and E_{y0} are the initial amplitude of the electrical field at $z=0$. As fiber is a birefringent medium, the index of refraction of n_x and n_y are different ($n_x \neq n_y$) which gives different propagation velocities, which makes the polarization state changes along the fiber. To a good approximation, the fundamental fiber mode is linearly polarized in the x or y direction depending on whether E_x or E_y dominates. In this case, a single mode fiber (SMF) is not a truly single mode; it in fact supports two modes of orthogonal polarizations. The two orthogonally polarized modes of a single mode fiber are degenerate ($n_x \approx n_y$) under ideal condition.

A strictly monochromatic plane of electromagnetic light means an infinitely long wave train which is completely polarized with zero spectral width, which is highly coherent. Any real physical source has a finite spectral width, for a laser with narrow linewidth $\Delta\nu$ ($\Delta\nu \ll \nu_0$), ν_0 is central frequency of the light source, we can call it quasi-monochromatic waves. A quasi-monochromatic signal can be the superposition of a large number of randomly timed statistically independent pulses with the same central frequency, which is partially polarized light.

There are three time scales to consider in the partially polarized quasi-monochromatic light for the fluctuations of the amplitude and phase of the electric field (Brosseau, 1998) $\tau_1 \equiv 1/\nu_0$ ($\sim 10^{-15}$ s), the period of quasi-monochromatic light, which is the time duration for the wave to go through a complete cycle; 2) $\tau_2 \equiv 1/\Delta\nu$ ($\sim 10^{-9} - 10^{-4}$ s), the time of coherence, which provides a measure of the time interval over which a field acts like a monochromatic wave; and 3) $\tau_3 \equiv t_{\text{det}}$ ($\sim 10^{-3}$ s), which is the response time of the detector. When $\tau > \tau_2$, the amplitude and phase of the electric field are considered as random functions of time, such as natural light; $\tau < \tau_2$, we can take the amplitude and phase as constants, partially

polarized light exhibiting both intensity and phase fluctuations. If $\tau \ll \tau_2$, the electric field can be treated as polarized light and it can be described as an ellipse whose size, eccentricity and orientation are randomly changed in time and its orthogonal components are mutually correlated. For a light source of well-stabilized laser, the coherence time τ_2 can be as small as 10^{-4} s, equivalent to a linewidth of ~ 10 kHz, such as the external-cavity-laser (ECL). For a He-Ne laser, the linewidth is 1.5 GHz, which corresponds to $\tau_2 = 10^{-9}$ s.

The polarization state of the output electrical field in optical fiber depends on the orientation of the electrical field relative to the refractive index axes of the birefringent medium, such as optical fiber. It can be described by the Jones matrix (Measures, 2001)

$$\vec{E}(z, t) = \text{Re} \begin{bmatrix} E_{x0}(z, t) \exp[j(\beta_x z - \omega t + \delta_x)] \\ E_{y0}(z, t) \exp[j(\beta_y z - \omega t + \delta_y)] \end{bmatrix} \quad (2)$$

If we take phase as $\phi(z, t) = \beta_x z - \omega t + \delta_x$ and differential phase as $\delta(z) = (\beta_y - \beta_x)z + \delta_y - \delta_x = (n_y - n_x)kz + \delta_y - \delta_x$, then Eq. (2) can be re-written as

$$\vec{E}(z, t) = \begin{bmatrix} E_{x0} \cos \phi(z, t) \\ E_{y0} \cos[\phi(z, t) + \delta(z)] \end{bmatrix} \quad (3)$$

For homogeneous and isotropic medium, such as glass, $\delta(z) = \delta = \delta_y - \delta_x$. The polarization angle is defined as $\theta(z, t) = \arctan(\text{Re}[E_y(z, t)/E_x(z, t)])$. Using Eq. (3) we have

$$\theta(z, t) = \arctan \left(\frac{E_{y0} \cos[\phi(z, t) + \delta(z)]}{E_{x0} \cos \phi(z, t)} \right) \quad (4)$$

To determine the state of polarization (SOP) we introduce $\gamma = E_{y0}/E_{x0}$, and then we can write

$$\tan(\theta(z, t)) = \gamma [\cos \delta(z) - \sin \delta(z) \tan(\phi(z, t))] \quad (5)$$

When the fiber is subjected to a local disturbance, such as stress or temperature, it leads to the change of modal birefringence $\delta n = |n_x - n_y|$, so the SOP will change accordingly following the Eq. (4) of $\theta(z, t)$.

For a linear polarized light at the input end of the fiber, this means $\delta(0) = \delta_y - \delta_x = m\pi$ and $\tan \theta(0) = \gamma \cos(m\pi) = (-1)^m \gamma$. At the output end of the fiber, the polarization state varies due to environmental effects, which induces modulation to the SOP so that $\beta_x(z) \neq \beta_y(z)$. Hence $\delta(z)$ varies with position which causes the output intensity to change with the time and position following the disturbance. Based on this principle we can detect fast changes in aerial (Waddy et al., 2005) and submarine fibers (Zhang et al., 2006) due to the wind, sun radiation and wave changes, as well as the electrical current changes in optical ground wire (OPGW) (Leeson et al., 2009) for the purpose of polarization mode dispersion (Chen et al., 2007) compensation in transmission direction. To get the spatial information, we can use the backscattering light, such as Rayleigh and Brillouin scattering light. By sending a pulsed light to optical fiber, we can detect the disturbance location via optical time domain reflectometry (OTDR) (Barnoski & Jensen, 1976).

3. Rayleigh and Brillouin Scattering in Fibers

Scattering in general arises from microscopic or macroscopic variations in density, composition or structure of a material through which light is passing. In a glass fiber, the random ordering of molecules and the presence of dopants cause localized variations in density (and therefore refractive index) that are small compared to the wavelengths of light that are used. These give rise to Rayleigh scattering which causes attenuation of the forward-propagating signal (and creation of a backward-propagating wave) that is proportional to λ^{-4} . Rayleigh scattering is a linear scattering process in that the scattered power is simply proportional to the incident power. Also, no energy is transferred to the glass in Rayleigh scattering; therefore there is no change in frequency of the scattered light.

In an homogeneous and isotropic dielectric medium such as glass, the response of the medium to an electric field (\vec{E}) is described by the polarisation vector (\vec{P}_s) defined as

$$\vec{P}_s = \epsilon_0 \chi \vec{E} \quad (6)$$

where ϵ_0 is the vacuum dielectric constant and χ is the medium susceptibility. The scattering is induced by fluctuations $\Delta\epsilon$ of the medium dielectric constant ϵ . These fluctuations can then cause a small polarisation change $\delta\vec{P}_s$ such that the displacement vector \vec{D}_s of the scattered field can be expressed as a linear combination of the scattered (\vec{E}_s) and the input field (\vec{E}_p) (Landau & Lifchitz, 1969)

$$\vec{D}_s = \epsilon_0 \epsilon \vec{E}_s + \Delta\epsilon \vec{E}_p = \epsilon_0 \epsilon \vec{E}_s + \delta\vec{P}_s \quad (7)$$

The spatial (x, y, z) and temporal (t) dependence of the scattered wave must then be described by the perturbed wave equation

$$\nabla^2 \vec{E}_s - \left(\frac{n}{c_0}\right)^2 \frac{\partial^2 \vec{E}_s}{\partial t^2} = \mu_0 \frac{\partial^2 \delta\vec{P}_s}{\partial t^2} \quad (8)$$

where μ_0 is the magnetic permeability of vacuum, c_0 is the velocity of light in vacuum and n is the refractive index of the medium.

Rigorously, $\Delta\epsilon$ is a tensor even for an isotropic medium, which can be separated into three components: a scalar scattering, a symmetric scattering and an anti-symmetric scattering (Landau & Lifchitz, 1969; Boyd, 2003). Fluctuations of pressure, temperature, entropy and density, i.e. all thermodynamic fluctuations, are the origin of scalar scattering, and hence, at the origin of Brillouin and Rayleigh scattering. Mathematically, scalar scattering is given by the trace of the fluctuation tensor $\Delta\epsilon$. The variation of $\Delta\epsilon$ is induced by the thermodynamic quantities ρ and T (Boyd, 2003)

$$\Delta\epsilon = \left(\frac{\partial\epsilon}{\partial\rho}\right)_T \Delta\rho + \left(\frac{\partial\epsilon}{\partial T}\right)_\rho \Delta T \quad (9)$$

The second term can be neglected because density fluctuations affect the dielectric constant significantly more than temperature fluctuations (the error of not taking that term into account is 2%). We now expand the density fluctuations in terms of pressure (p) and entropy (s) fluctuations

$$\Delta\rho = \left(\frac{\partial\rho}{\partial p}\right)_s \Delta p + \left(\frac{\partial\rho}{\partial s}\right)_p \Delta s \quad (10)$$

The first term corresponds to adiabatic density fluctuations associated to acoustic waves, which is the origin of Brillouin scattering. The second term is an isobaric density fluctuation (which is entropy or temperature fluctuations) and leads to Rayleigh scattering associated to a diffusion process. If we neglect the entropy fluctuations the dielectric constant fluctuation via density can be expressed as

$$\Delta\varepsilon = \left(\frac{\partial\varepsilon}{\partial\rho} \right)_T \left(\frac{\partial\rho}{\partial p} \right)_s \Delta p = \frac{\gamma_e}{\rho_0} \left(\frac{\partial\rho}{\partial p} \right)_s \Delta p, \quad (11)$$

where the electrostrictive constant γ_e , is defined (Boyd, 2003) as

$$\gamma_e = \rho_0 \left(\frac{\partial\varepsilon}{\partial\rho} \right)_T \quad (12)$$

ρ_0 is the average density of the material.

If we assume that the sound wave propagates along the fibre optical axis, then the density fluctuation propagates according to (Boyd, 2003)

$$\frac{\partial^2 \Delta\rho}{\partial t^2} - \Gamma' \frac{\partial^2}{\partial z^2} \left(\frac{\partial \Delta\rho}{\partial t} \right) - V_A^2 \frac{\partial^2 \Delta\rho}{\partial z^2} = 0 \quad (13)$$

where Γ' is the damping parameter and V_A the velocity of the acoustic wave.

Brillouin scattering is a relatively narrow-band process with a natural linewidth of roughly 30 MHz in standard single-mode fiber in the spontaneous regime. The frequency relationships among several different scattering processes are shown in Fig. 1 (not to scale), in particular the Brillouin Stokes and anti-Stokes components are separated from the Rayleigh peak by the Brillouin frequency ν_B .

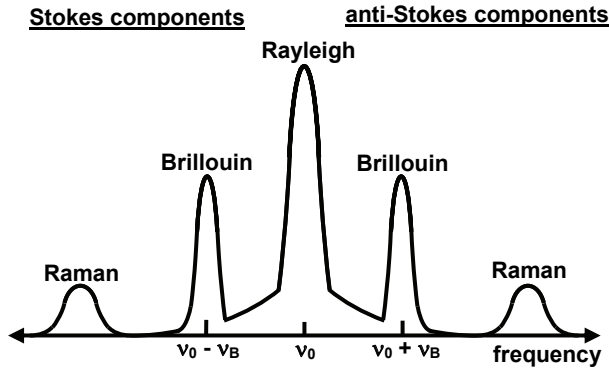


Fig. 1. Spontaneous scattering components (Snoody, 2008).

4. Birefringence Effect in Submarine Fiber and Optical Ground Wire (OPGW)

With the development of higher speed communication system (> 10 GB/s), polarization mode dispersion (PMD) and polarization dependent loss (PDL) become additional limitations and a major source of concern for the system's performance (Huttner et al., 2000; Gordon & Kogelnik, 2000). It is important to measure the fastest PMD change, so that PMD compensation can follow the changes in real time.

The field test about the time evolution of polarization effects has been studied mostly in buried and aerial fibers. Previous experiments showed that in buried fibers, SOP drift is relatively slow, on the order of hours or days, and PMD fluctuation is due to temperature (Karlsson et al., 2000; Cameron et al., 1998; Allen et al., 2003); while in aerial fibers, SOP drift is relatively fast, on the order of microseconds in winter (Waddy et al., 2001), and PMD fluctuation is due to temperature, wind or even power line current variations since aerial fibers are often cabled together with power lines (Wuttke et al., 2003). Although, another type of fiber, submarine fiber, is widely used in global telecommunication networks, so far, very little work on polarization effects in it has been conducted, as submarine fibers are usually installed at remote areas, which are hard to get access to.

In May 2005, we had an opportunity to conduct a field test on three pairs of submarine fibers under Caribbean Sea, collaborated with Caribbean Crossing. One pair of fiber was measured ~ 26 hours with a fast PMD technique sampling at 15 s intervals. SOP information has usually been utilized to investigate the time evolution of polarization effects, which sets upper limit for PMD compensation in the high speed communications.

Since a fast polarization measurement was desired, the state-of-the-art polarization analyzer Adaptif A2000 was used for the test. Because we are interested in how fast the SOP and DGD decorrelate in submarine fibers (Zhang et al., 2006) we focused on the ACF (autocorrelation function) in the first few minutes. Fig. 2(a) describes the normalized ACF of SOP, PSP, DGD and cross correlation function (CCF) of SOP and PSP. There is some correlation between SOP and PSP within SOPs decorrelation time. Obviously, SOP decays faster than PSP and DGD. In Fig. 2(b) the decorrelation time was found to be 3 min for this combined submarine/buried fiber. The experimental ACF has a quick drop at the second point, which means the fastest change in this submarine fiber is less than 15 s. Fig. 2(c) compares the ACF of SOP during the day and night. The fitting parameter is chosen to be 1.1 and 5 min, respectively. As we expected, ACF in the day has a faster decay, which means the cable is in a relative static environment during the night. Similar to the wind effects on aerial fibers, the tension induced by ocean waves/currents may affect the signals in submarine fibers. Some segments may not touch the seabed but suspend over the trough, which is a normal situation for submarine fibers. It is natural to think the sun and moon are the main causes of the different current activities. The unevenness in ocean temperature, water density and salinity are the direct causes for currents. In the daytime, the solar radiation can strengthen these perturbations and hence, produce stronger currents. This may explain the different SOP drift times between the day and the night.

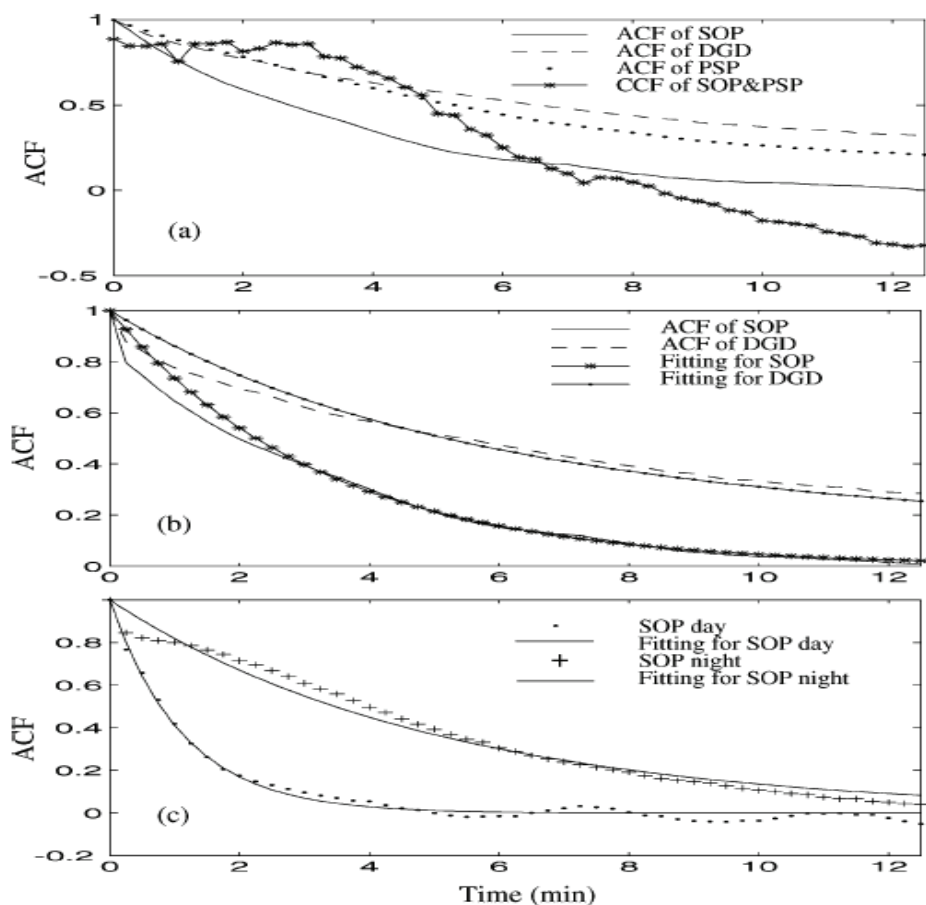


Fig. 2. (a) Small-scale view of experimental ACF of SOP, DGD, PSP, and CCF of SOP and PSP. (b) Comparison of theoretical and experimental ACF of SOP and DGD. (c) Comparison of experimental ACF of SOP during the day (11:00 A.M. to 18:00) and the night (23:00 to 6:00 A.M. the next morning) with corresponding curve fittings. From Zhang et al. (2006).

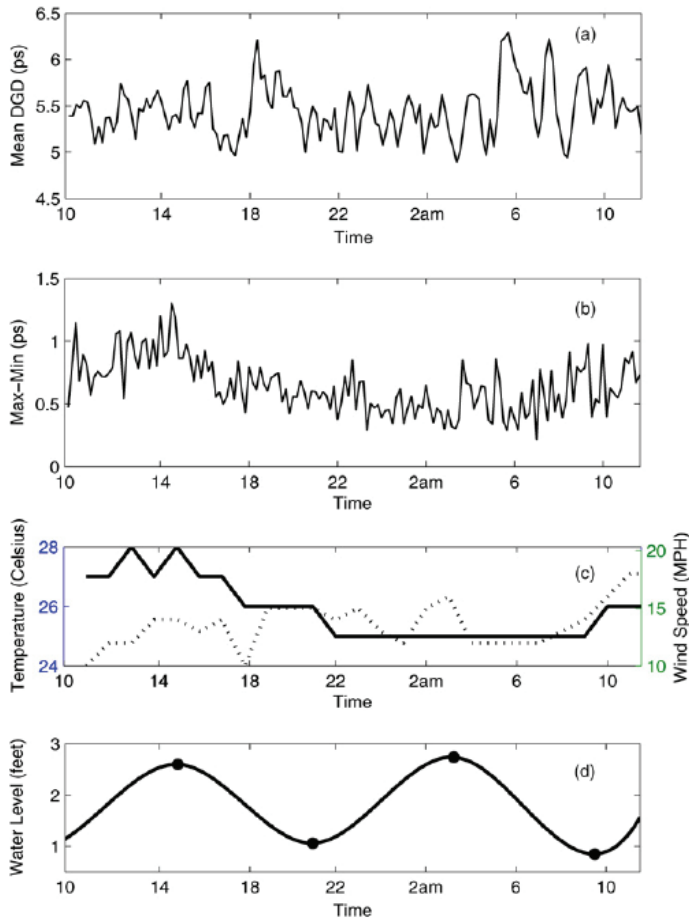


Fig. 3. (a) Time evolution of DGD averaged over both wavelength and 10 min time, (b) wavelength-averaged DGD fluctuation in every 10 min of fiber A, (c) temperature (solid line) and wind (dotted line) data during measurement period, (d) tide (vertical water level) information. From Zhang et al. (2007).

The time evolution of DGD averaged over wavelength at each 10 min interval is shown in Fig. 3(a). The PMD (mean DGD) over 26 h was calculated to be 5.45 ps. It was found in (Gisin et al., 1996) that with mean PMD $\langle \Delta\tau \rangle$ over wavelength range $\Delta\omega$, the uncertainty is $\Delta\tau \times 0.9 / \sqrt{\Delta\tau \times \Delta\omega}$. Using this relation, the uncertainty of the measurement was 0.27 ps. In order to investigate the PMD fluctuation within every 10 min, Fig. 3(b) shows the difference between maximum and minimum PMD value (mean DGD). The fluctuation is relatively large during the day and relatively small during the night, then it increases again in the following morning. We may conclude sun radiation is correlated to PMD fluctuation in submarine fibers. Fig. 3(d) shows the water level of the sea during the measurement period at one end of FUT. Two PMD peaks are observed in Fig. 3(a) at 18:20 in the first day and 6:00

am the next morning. They have some correlation to the large downward changes in tide level.

The time evolution of PMD is of greater interest to system designers. Tide is the periodic rise and fall of a body of water resulting from gravitational interactions between the Sun, Moon and Earth. It is the observed recurrence of high and low water along the seashore – usually, but not always, twice daily. Current associated with tide, is the horizontal flow of water. It floods in which makes the tide rise and ebbs out which makes the tide falls. As described in Fig. 3(d), the testing place has a semidiurnal tide, which means there are two high tides and two low tides in one day. The current may flow quickly when a high tide recedes. One high tide appeared at 15:00 and the subsequent low tide arrived at 21:00, so the current with maximum speed was around 18:00. Similarly the current flows quickly at about 6:15 next morning. Since the tidal/current effect has particular direction, at the moment of maximum current, submarine fiber should have the maximum induced tension or displacement if any, which corresponds to the large absolute PMD value. Therefore, around those two time moments, PMD reached two peak values as shown in Fig. 3(a). Since the distance between the two ends of fiber is about 80 km, it is conceivable that tide times at the two ends are different. And the fluctuation of PMD magnitude is a combined tidal effect on the cable over the entire length. Therefore, there are some smaller peaks following the main peaks in Fig. 3(a).

OPGWs are a common type of aerial fiber installed worldwide on high voltage power lines. An OPGW cable provides ground wire protection for important electrical current carrying power lines and a high capacity communication network. Due to the proximity of the OPGW to the electrical current there is magnetic field exposure to optical fiber in OPGW. The component of magnetic field in the propagation direction of the light signal induces circular birefringence by way of the first order Faraday effect, the resulting SOP dynamics are unique from typical aerial fiber (Leeson et al., 2009). The OPGW network provides new difficulties for PMD compensation designers because polarization changes can reach 300 Hz due to harmonic magnetic fields. On the other hand, the magnetic field exposure may allow high magnetic field detection providing SHM from ice buildup on ground wires and power lines, a major problem during the winter in many areas where high voltage power lines are deployed.

In August 2007, we conducted a field test on two different fibers installed within an OPGW. The measurement was ~ 60 hours. The SOP changes were monitored simultaneously on both fibers using two Agilent 8509 polarization analyzers at a sampling rate of 1 KHz. A major difficulty in the development of a polarization monitoring technique for SHM of the OPGW network is the presence of time varying birefringence from temperature changes, wind (Aeolian vibrations/cable swings) and solar radiation. The drift of polarization entering a magnetic field section de-correlates the linear relation between magnetic field and the SOP changes. A Faraday Rotating Mirror (FRM) should be installed to observe the nature of the magnetic field induced birefringence, as it minimizes static and quasi-static reciprocal birefringence. For this reason, we monitored two fibers, one fibers transmission and another with an FRM installed, Fig. 4 shows the power spectrum up to 330Hz calculated for a one min daytime period for both fibers. In Fig. 4(a), on this time scale for the transmission signal, we observe a peak at < 1 Hz, a large spectral base up to ~100 Hz and a 60 Hz peak with 120 Hz and 180 Hz harmonics. The < 1 Hz peak is correlated to OPGW cable swings as discussed in (Wuttke et al., 2003). The 0 Hz to ~100 Hz spectral base matches

the OPGW the natural Aeolian frequency of 10 - 80 Hz for a wind speed range of 3.6 to 25.2 km/h (Krispin et al., 2007). Because we observe very similar frequencies to the reported natural Aeolian frequencies, and the wind is 17 km/h during this period, these modulations are most likely due to this environmental effect. The 60 Hz peak exists because the electrical current carried by the high voltage lines is 60 Hz and is modulating the SOP by the Faraday effect; the harmonic peaks exist due to nonlinear voltage/electrical current properties of electrical devices that result in harmonic magnetic fields each modulating the SOP. In Fig. 4(b) we see the effect the FRM has on improving our observation of the nature of the magnetic field induced SOP changes. We observe the same 60 Hz peak resulting from the 60 Hz electrical current and now harmonic peaks up to 300 Hz. 300 Hz is the fastest polarization modulation reported in OPGW/aerial fiber, this sets the requirement for PMD compensation on the OPGW network.

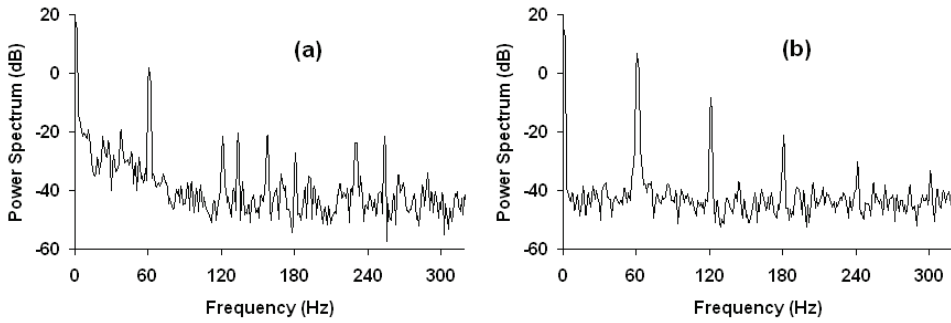


Fig 4. Power spectrum up to 330Hz calculated for a one minute daytime period (a) for transmission and (b) with an FRM installed. From Leeson et al. (2009)

We calculated for the OPGW fiber with the FRM installed the maximum arc length that is mapped out over a given time interval on the Poincare's sphere in radians, for PMD compensation information. The fast 60 Hz polarization changes are maximized for a time interval of 8 ms, for our sampling rate of 1 KHz. To observe the decorrelation over the entire measurement time we used the ACF of the SOP and defined t_{half} , which describes the time at which the SOP has de-correlated 50 % (Waddy et al., 2005). The change in the way the SOP de-correlates for 10 min intervals ($T = 600$ s) can then be observed using:

$$\text{ACF50\%}(t_{\text{half}}) = \frac{T - t_{\text{half}}}{T} \quad (14)$$

Where at the maximum value of $\text{ACF50\%} = 1$ there is the fastest SOP change possible. Fig. 5(a) shows data representing the fast surrounding SOP modulating phenomena, i.e. the wind speed and the electrical current carried by the neighboring conductors and Fig. 5(b) shows the maximum arc length in radians for one min periods and the ACF50%. We see a correlation between the maximum arc length and the electrical current during the nighttime periods we could not observe without the FRM installed. The minimizing of temperature fluctuation and wind induced linear birefringence allows us to observe the magnetic fields contribution to polarization changes. As the FRM is not ideal, we still observe linear birefringence effects during the daytime period. During the daytime fast variations in the arc length appear. These variations must be caused by sun radiation induced temperature

gradients between the cable core and cable surface, because the variations show no apparent correlation to any other environmental factors. The ACF50% shows that SOP drift is correlated to electrical current during most of the acquisition time. The SOP Autocorrelation function is shown to de-correlate as electrical current increases despite the presence of the solar gradient effect during the day. It is therefore possible that electrical current may induce detrimental errors in high speed communication systems (> 10 Gb/s). While we have shown that the FRM is required for accurately detecting the electrical current, to provide location information a distributed Polarization-OTDR (POTDR) may be required with the FRM to locate and diagnose a disturbance.

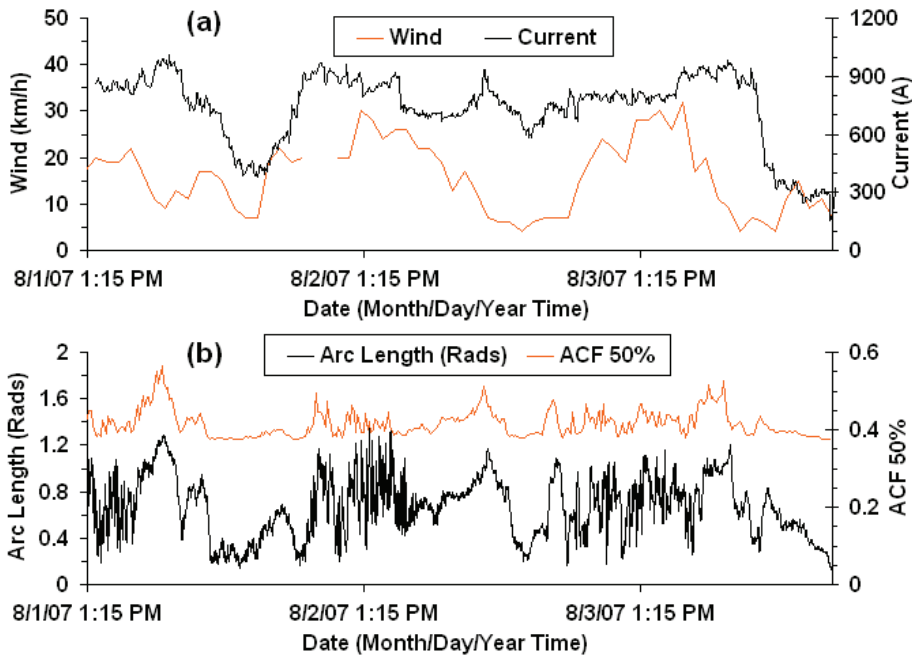


Fig. 5. (a) Wind and electrical current data plotted in an OPGW with a FRM installed and (b) calculated maximum arc length plotted with ACF 50%. From Leeson et al. (2009)

5. Distributed Fiber Vibration Sensor Based on Polarization Dependence in Stimulated Brillouin Scattering

5.1 The polarization dependence of the Brillouin gain

The distributed Brillouin sensor is an optical fiber based sensor that relies on the effect known as Brillouin scattering in order to measure the temperature and strain in a distributed fashion. The system monitors the interaction of two counter-propagating light waves within a sensing fiber by the pump and the probe waves. The Brillouin interaction results in power being transferred from the pump wave into the probe wave, and the efficiency of this process depends on several factors including the beat frequency between the pump and probe lasers, and the polarization states of these waves. The interaction is

optimized if the beat between the lasers matches the Brillouin frequency (probe wave at the Stokes frequency), which is a material property of the optical fiber, and if the polarization states are the same for pump and probe waves. The Brillouin frequency shift is linearly dependent on the temperature and strain of the fiber, allowing the system to measure both of these properties. The Brillouin frequency can be measured by sweeping the beat frequency of the pump and probe lasers over a range and measuring the loss of the pump wave (or gain of the probe wave) at each frequency to construct the Brillouin spectrum at each location in the sensing fiber. Spatial information is acquired by matching the time of flight of the pulse to a location in the fiber, a process known as Brillouin optical time domain analysis (BOTDA).

The vibration sensor based on stimulated Brillouin scattering is shown in Fig. 6. The probe wave gets amplified by the Brillouin interaction with the pump and it is this signal that is directed to the detection arm and measured (alternatively, the loss of the pump wave can be detected in the Brillouin loss technique). For optimal sensitivity, the pump and probe laser frequencies must be locked to the Brillouin frequency corresponding to the static strain of the optical fiber under test. At the fixed Brillouin frequency, one can measure the birefringence change induced modulation to the Brillouin gain spectrum as illustrated in Fig. 7.

There are two physical mechanisms that make it possible to detect vibrations of an optical fiber via the stimulated Brillouin scattering. One mechanism is the fact that as the fiber is undergoing vibration, there will be strain introduced along the fiber. The strain in the fiber will cause the Brillouin frequency of single mode fiber to shift by roughly $0.05 \text{ MHz}/\mu\epsilon$. This kind of measurement requires a polarization scrambler for each scanned Brillouin frequency.

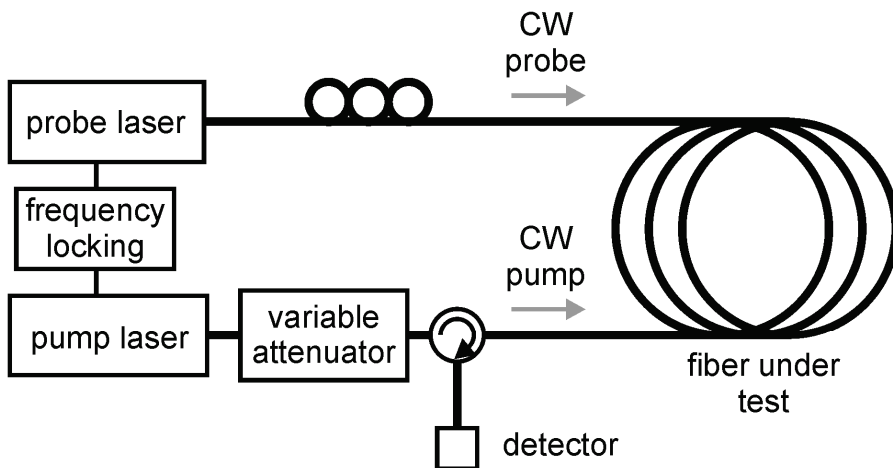


Fig. 6. Brillouin vibration sensor setup

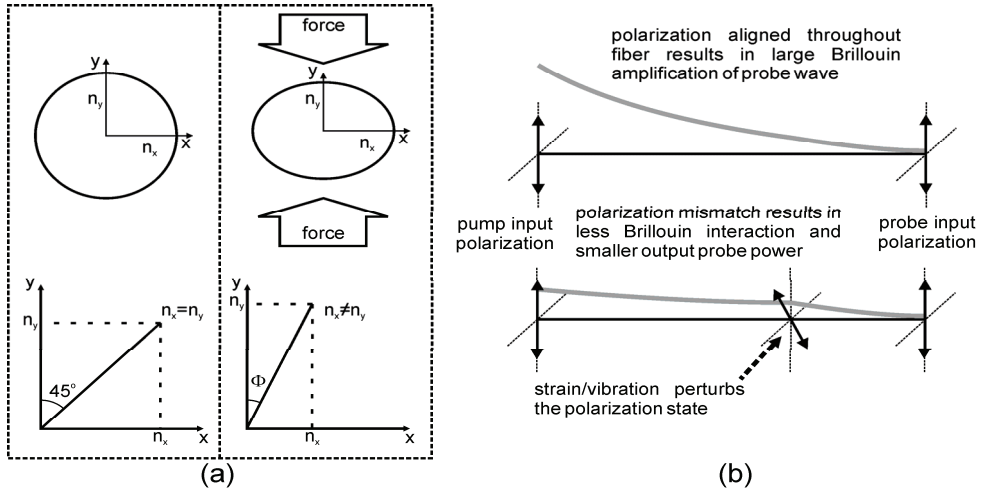


Fig. 7. (a) Local birefringence change caused by force on optical fiber. (b) Sensing mechanism based on perturbation of the polarization states – the growth in the probe wave traveling from right to left is represented by the thick black line. From Snoodly (2008).

If the pump and probe polarization states are aligned for an unstrained loose fiber, the Brillouin interaction will be large throughout the entire fiber (the polarization states drift only gradually in the time scale of minutes as explained in section 4). When the fiber is disturbed, the Brillouin interaction will not be optimal and the detected probe power exiting the fiber will be reduced as depicted in Fig. 7(b).

To show the vibration induced birefringence change and the associated Brillouin gain change, the fiber under test was a 15 m length of standard single mode fiber wrapped around a piezo fiber stretcher vibrating at 100 Hz. The results in Fig. 8(a) show that the sensitivity of the system was improved by an order of magnitude due to the Brillouin amplification when the pump wave was turned on.

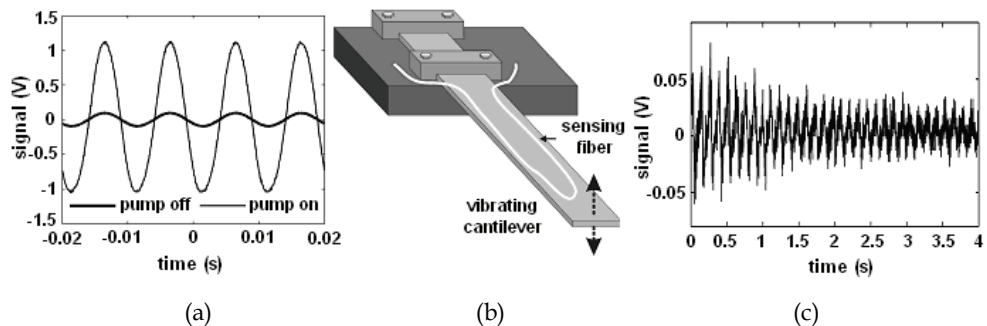


Fig. 8. (a) Effect of introducing pump wave – system sensitivity increases by an order of magnitude; (b) Experimental setup for vibrating cantilever; and (c) Experimental results for vibrating cantilever.

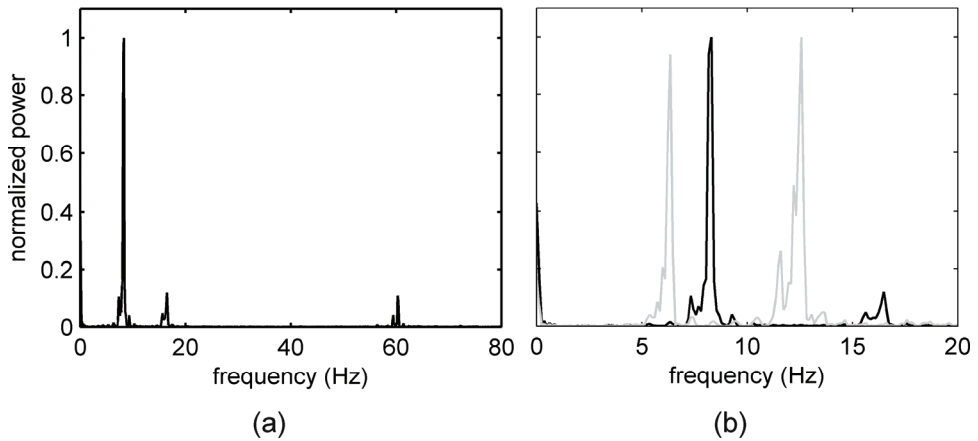


Fig. 9. (a) Power spectrum of vibrating cantilever; (b) Effect of damaging cantilever (grey)

The following experiment was done to detect the frequency of a vibrating steel cantilever. A section of fiber was bonded to the surface of a steel cantilever of which roughly 0.5 m was allowed to oscillate (Fig. 8(b)). The oscillations of the steel strip were clearly observed as well as the damping behavior of the vibration as seen in Fig. 8(c). Damage to structures can be detected by changes in vibration behavior, both amplitude and frequency, and so it is imperative to measure the frequency characteristics of the vibrating structure. The Fourier transform of the data of Fig. 8(c) was taken and the resulting power spectrum is shown in Fig. 9. The main vibration frequency of 8.5 Hz is clearly evident as well as smaller contributions at other frequencies including a peak at 60 Hz which is due to electrical mains noise and should be filtered out.

To test the system's capability to measure damage to a structure, the steel cantilever was damaged by adding a C-clamp to the beam and monitored. By observing the changes in the frequency spectrum, it is possible to see that the vibration characteristics of the cantilever have been modified, indicating structural damage. In Fig. 9(b), it can be seen that when damage was introduced the vibration frequencies shift lower and the relative power of the secondary peak has grown significantly.

5.2 Distributed vibration sensor based on birefringence of the Brillouin gain

To add distributed sensor ability we used 20 ns pulses equivalent to 2 m spatial resolution from a light source. With the pulsed probe wave, the Brillouin interaction only occurs at a particular fiber location when the pulse is present at that location. An 80 cm section of a 120 m fiber was bonded to a 40 cm steel cantilever which was allowed to vibrate. Fig. 10 shows the performance of the vibration sensor zoomed in on the fiber location which is vibrating. The data shown is the Brillouin loss signal which has been processed by subtracting the waveform for the stationary cantilever to reveal only the changes in the Brillouin signal as the cantilever vibrates. During the vibration the birefringence of the optical fiber is altered which perturbs the states of polarization of the pump and probe waves in that section of fiber. Since the strength of the Brillouin interaction depends on the alignment of the pump and probe SOP, this perturbation alters the strength of the Brillouin loss detected at the

vibrating location. The spatial resolution of the sensor is shown to be 2 m in Fig. 10(a), as expected for a 20 ns pulse. The small section of vibrating fiber is clearly visible against the background signal of the otherwise stationary fiber. Fig. 10(b) shows the vibration response of the steel cantilever as measured by the sensor at a single fiber position corresponding to the peak of the vibration response from Fig. 10(a) for 1 s at a sampling rate of over 100 Hz with each waveform consisting of 50 averages. The frequency of vibration of the cantilever is found to be 13 Hz.

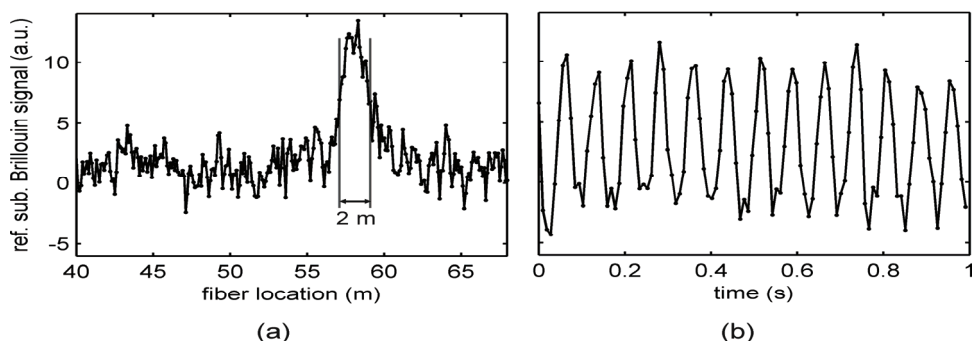


Fig. 10. (a) Spatial resolution of vibration sensor. (b) Vibration response of steel cantilever.

The distributed impact waves due to highway traffic on concrete slabs reinforced with fiber reinforced polymer (FRP) bars are monitored in real time using stimulated Brillouin scattering (Bao et al., 2008). The impact wave is caused by the traffic passing on the highway pavement at high speed (> 100 km/h), which induced pressure on the concrete slabs, and in turn created a local birefringence change, leading to variation of the local state of polarization change (SOP). The pump and probe waves of the stimulated Brillouin scattering 'see' the SOP change and react with a decrease of the Brillouin gain or loss signal relative to the input SOP of the pump and probe waves. The frequency difference between the pump and probe waves are locked at the static-strain-related Brillouin frequency. Optical fiber was embedded throughout the concrete pavement continuously reinforced with FRP bars in highway to detect impact waves caused by cars and trucks passing on these pavements at a sampling rate of 10 kHz. A spatial resolution of 2 m was used over a sensing length of 300 m. The maximum measured frequency was 15 Hz.

6. Measurement of the Vibration and Acoustic Wave in Structures

As explained in section 2, in single mode fiber the random imperfections during the manufacturing process breaks the circular symmetry of the fiber core, causing two orthogonally polarized components of light to travel with different velocities. The birefringence in fiber varies with many physical parameters such as: strain, temperature, pressure wave, ultrasonic fields, etc., leading to changes in the phase shift between two polarization eigenmodes. Thus, the output state of polarization (SOP) changes at the fiber end. By monitoring the power change of polarized light in the time and frequency domain, one can detect the impact wave as well as the vibration frequency in real time. This method has been used to characterize a PZT for its frequency response and phase delay (Zhang &

Bao, 2008a). The experimental setup is shown in Fig. 11. To test its impact wave response, a cantilever beam was designed with a piece of spring steel with dimension $320 \times 40 \times 0.9$ mm ($L \times W \times H$), and one end was clamped on a stage. Its shape was designed to be an isosceles trapezoid, which experiences a uniform strength impact wave along the beam. The bare fiber (SMF-28) was taped by clear lightweight scotch tape on the beam with a total length of 60 cm. Impact wave was induced by the tip of a bent nose pliers at the fixed end. A slight tapping on the cantilever beam is applied to minimize the overall oscillations.

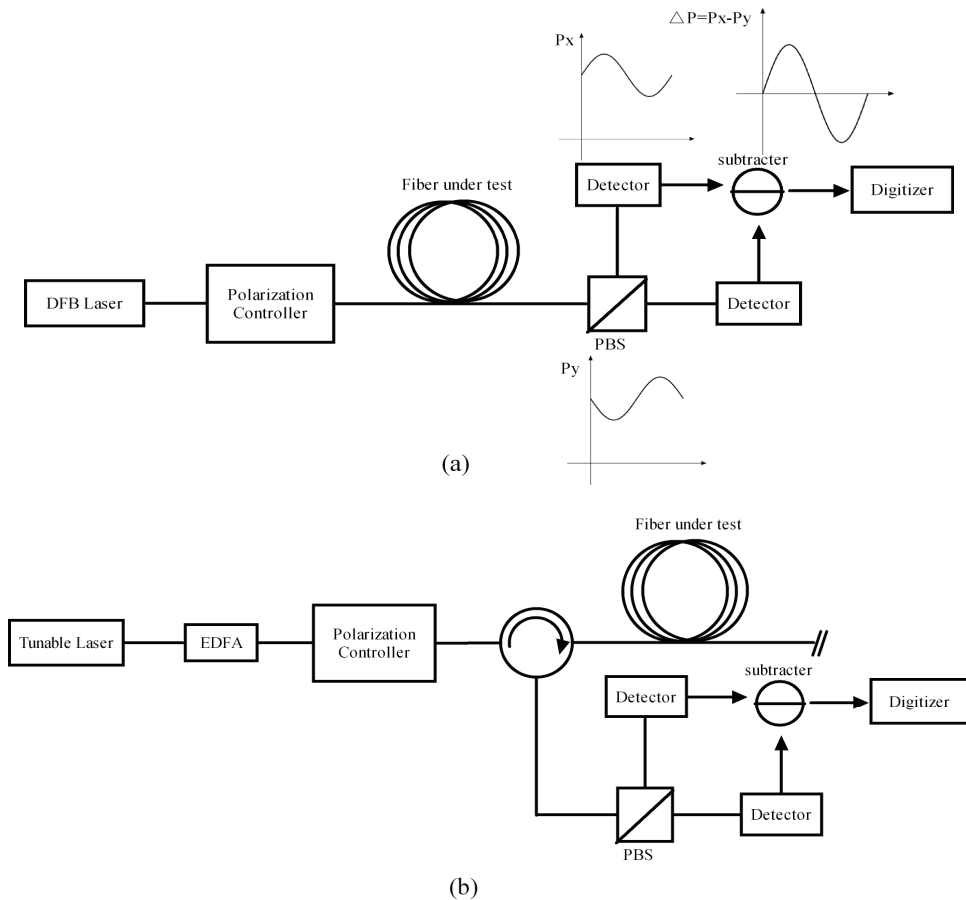


Fig. 11. Experimental setup of optical fiber diversity vibration/acoustic sensor for the transmission and Rayleigh backscattering.

Fig. 12(a) shows the response of the optical fiber sensor and an accelerometer after a single hit, both of which have clear damped trends in time domain. The result is obtained with no averaging or filtering (Zhang, 2008a). After the first 0.2 s, the accelerometer decays

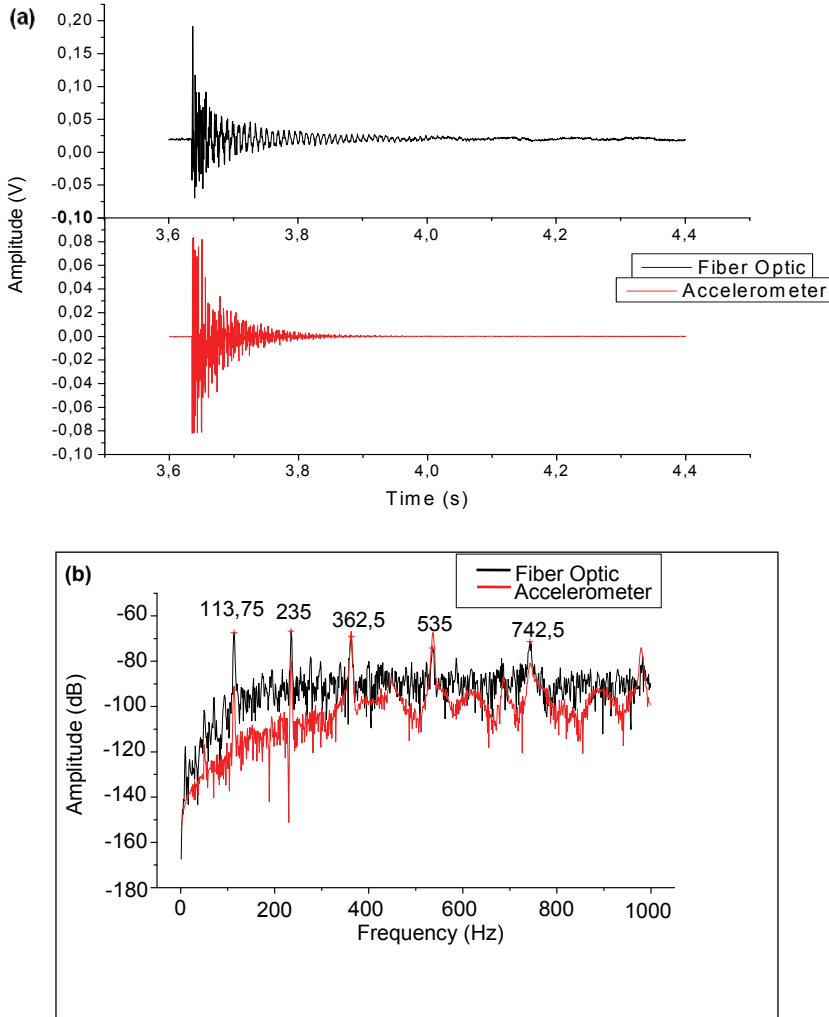


Fig. 12. Impact detection of a cantilever beam with the optical fiber sensor (black) and the accelerometer (red): (a) time trace; (b) normalized power spectrum (Zhang et al., 2008a)

to zero. While the optical fiber sensor still shows some small oscillations due to its long length coverage over the entire beam. In order to compare their frequency components, fast Fourier transforms are computed and the power spectrums are depicted in Fig. 12(b). All five main peaks appear at the same frequencies: 113.75 Hz, 235 Hz, 362.5 Hz, 535 Hz and 742.5 Hz, respectively, which represent different excited modes within the cantilever beam because of the strength of the initial hit. We also notice the tendency that the power spectrum amplitude of the accelerometer is lower than that of the fiber sensor. This is caused by a lower sensitivity of the accelerometer in the low frequency range. The

accelerator is designed to detect higher frequency components above a few hundred Hz. For low frequency vibration/acoustic measurements, velocity or displacement transducers work more efficiently than accelerometers. Apparently, the fiber sensor has the ability to detect wider frequency ranges to accurately measure the dynamic properties of structures under impact waves in real time.

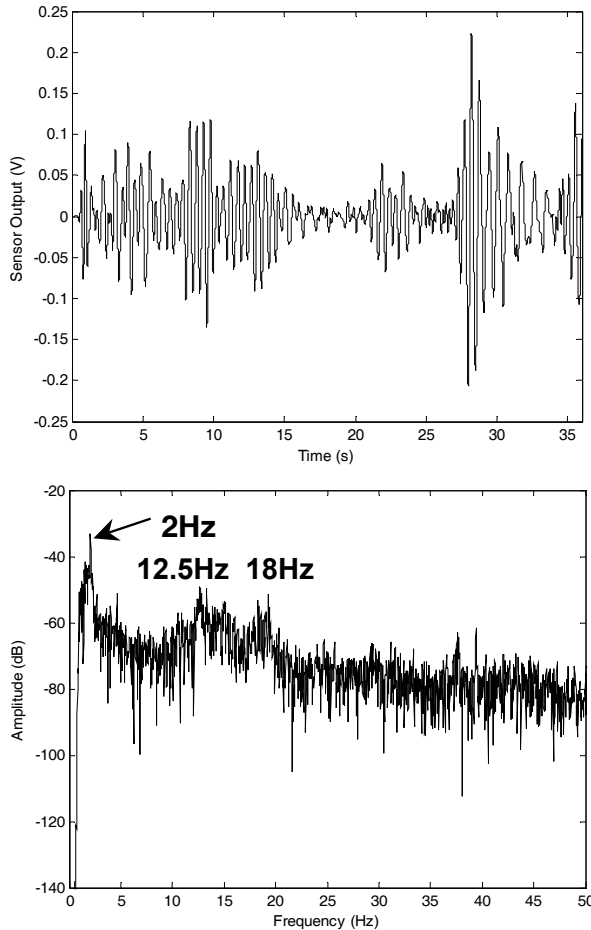


Fig. 13. Field test of traffic impact monitoring with 5 cars or trucks passing: (a) Time trace of the signal around 2 Hz, after 1 Hz-5 Hz bandpass filter; (b) Power spectrum up to 50 Hz of the raw data after 1 Hz highpass filter.

The dynamic data was collected when cars and trucks were passing on the concrete slabs reinforced by FRP bars, hence the birefringence of the optical fiber attached to them would be affected. The sampling rate of our sensor was set to be 1 kHz as the frequencies of interest should be fairly low. A bandpass filter (1 Hz - 5 Hz) was applied on one set of the raw data to retrieve the signal around 2 Hz as plotted in Fig. 13(a) within 36 seconds. During this time

period, five cars and trucks passing on the two slabs were observed visually. Each vehicle represents one oscillation profile. In the first 15 seconds, it seems two or more impact events overlapping each other, as the damping time of the slab is much longer than the spacing time between cars. The maximum amplitude is at the 28th second, corresponding to a loaded truck passing by, and the damping time is for 6 seconds till the next impact event occurs. The weight of the car may be identified by its damping time; if the calibration of the car weight and decay time is characterized. Fig. 13(b) represents a typical power spectrum of the testing signal from 50 m sensing with the main frequency components below 20 Hz. This matches the previous research on dynamic testing of highway bridge using traffic loads (Bao et al., 2008). The first peak locates at 2 Hz, about 18 dB higher than the second peak at 12.5 Hz, and the third peak at 18 Hz. These three frequencies should correspond to the natural frequencies of the whole test slabs' structure. Apparently the frequency and damping time of the concrete slab can be determined by the proposed method.

7. Water wave frequency detection

Underwater acoustic sensing is an area in which fiber optic sensors have great advantages due to the possibility of multiplexing and distributed techniques existing in fiber communication and fiber sensor systems. Using the state of polarization (SOP) change in optical fiber under water one can measure the power spectrum of the oscillatory water currents due to water movement (Zhang et al., 2008b).

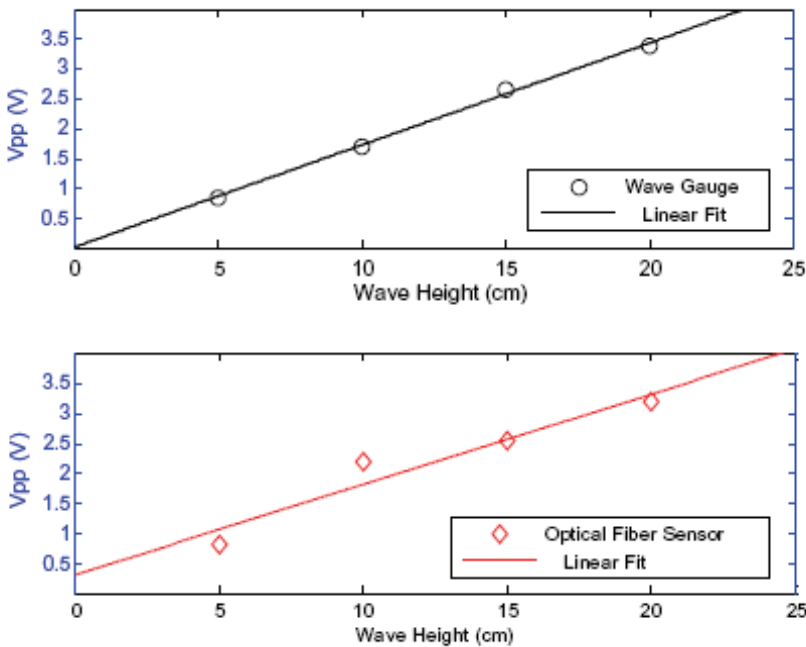


Fig. 14. Linearity of the (a) wave gauge and (b) optical fiber sensor.

In the experiment, the fiber has been laid across a section of wave flume, which is essentially a long water channel equipped with a wave generator at one end and a wave absorbing device at the other end; hence the fiber serves as a point sensor acting as a wave gauge. The fiber sensor is capable of detecting water wave frequencies accurately for all types of wave generated by the flume. With the optimum sag of fiber, the output response of the optical fiber sensor is linear within $0.7 \text{ m} \pm 0.2 \text{ m}$ wave level. Fig. 14 is the wave measurement by the wave gauge and fiber sensor.

The sensor monitors the polarization state change induced intensity variation of the light when the sensing fiber is affected by the presence of the water wave. As a result, the sensing fiber should be fully submerged in the water and be able to be moved physically by the water wave for the frequency range of 1-10 Hz, although the vibration sensor can have a KHz response signal. The sensor is capable of providing accurate frequency distributions for both regular waves and irregular waves, confirmed by a conventional wave gauge.

8. Spectral analysis of POTDR for intrusion sensing

Up to now, distributed optical fiber sensors have been mainly studied for static measurements, i.e. no time-varying or slowly time-varying signals, such as, static strain or temperature. Dynamic measurements using the above techniques are difficult to achieve because of the large number of waveforms required to average out the polarization effect induced signal fluctuation or because of the large range of frequency scans that are needed in order to obtain a reasonable signal to noise ratio (SNR) and spatial resolution over a kilometer fiber length.

A frequency modulated source to realize distributed Brillouin sensor based on correlation of pump and probe in fiber is demonstrated for vibration measurement (Hotate & Ong, 2003]. However, each time only one sensing point is chosen by the correlation peak of pump and probe light, it is particularly suitable for material processing over a short fiber distance while it is not essentially a fully distributed sensor which should provide information for every point along the fiber under test simultaneously. A truly distributed vibration sensor has been demonstrated recently based on the spectrum density of POTDR system (Zhang & Bao, 2008b). This new sensor can detect a vibration frequency of 5 KHz over 1 km sensing length with 10 m spatial resolution.

POTDR was developed as the first fully distributed optical fiber measurement for static physical parameters in the earlier 80's (Rogers, 1981) and then adopted as a diagnostic tool in optical communication systems to identify high polarization mode dispersion (PMD) fiber sections (Gisin et al., 1999). In conventional POTDR, the SOP is measured with 4 polarization controllers so that the rotation angle of SOP can be measured in every location to recover the PMD or strain, this process takes minutes, as a result, it can only be used for static measurement. To realize dynamic measurement with ms time scale, only one polarizer is sufficient to identify dynamic events, through which the birefringence change along the fiber could be detected; the setup is shown in Fig. 15. Moreover, with a novel fast Fourier transform (FFT) spectrum analysis, multiple simultaneous events with different vibration frequencies or even with the same frequencies are able to be accurately located. The spectral density function of location change is equivalent to many variable narrowband filters with bandwidth of $< 1\text{Hz}$ to improve the SNR of multiple events detection, which allows the disturbance to be detected simultaneously at any location along the sensing fiber.

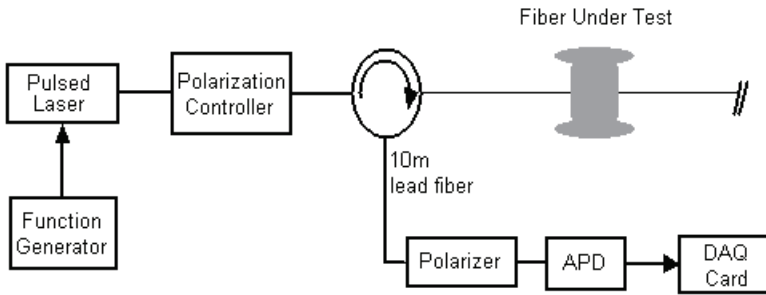


Fig. 15. Experimental setup of POTDR system

Data processing for the POTDR is done using four steps: in step (1) a large number of POTDR curves are acquired, step (2) at a particular position the time domain plot can be acquired from multiple POTDR curves, step (3) the FFT can be performed at that position using the time domain information and step (4) by performing steps (2) and (3) at all points along the fiber the magnitude of a certain frequency can be plotted as a function of distance. The post-signal processing is shown in Fig. 16. Step (1) to (3), is employed here by taking an average every 100 POTDR curves in step (2). Considering a 10 kHz repetition rate of the pulsed light, the effective sampling rate becomes 100 Hz, which has set the limitation for impact wave detection. Fig. 17(a) plots the FFT spectrum of 1.5 seconds time domain data at 550 m with a peak at 22 Hz when the PZT is driven by 5 V_{pp}, 22 Hz square wave. Benefited to its high sensitivity, this POTDR system makes it possible to measure higher frequency disturbance without any averaging in step (2). Hence, the maximum detectable frequency is 5 kHz using a 10 kHz sampling rate. In Fig. 17(b) when the driven frequency of the piezo is set to 4234 Hz, this peak frequency is clearly shown in the FFT spectrum at 550 m.

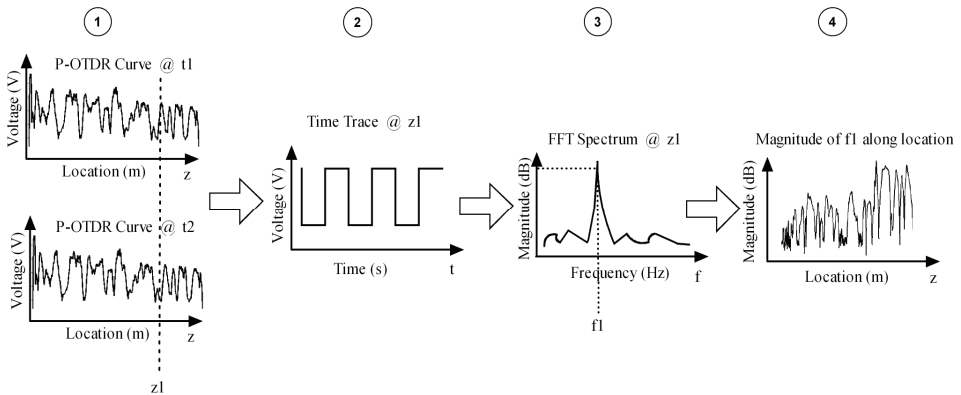


Fig. 16. The data processing of the spectrum density of POTDR

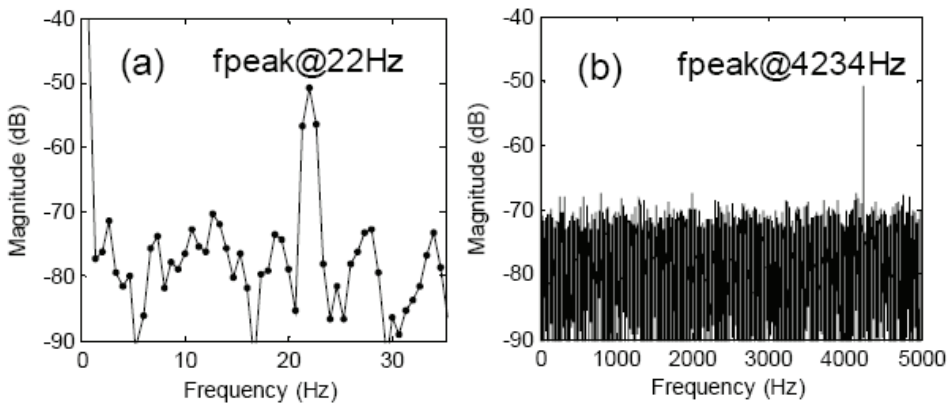


Fig. 17. Piezo fiber stretcher driven by 5 Vpp square wave, FFT spectrum of time trace signal at 550 m of (a) 22 Hz driven signal; (b) 4234 Hz driven signal

The present sensing uses post-signal processing, with the introduction of a micro-processor there would be a significant reduction of the signal processing time without going through computer for digitization and programming timing, which makes the current system response in the ms time frame, as the FFT signal processing and averaging can be conducted by electronic circuits directly. This new technology could in a cost-effective manner provide intrusion sensing for perimeter security at various places or structure health monitoring for large structures, such as bridges, highway pavements, pipeline leakage, etc. with low fault rate due to the multiple frequency components discrimination at < 1 Hz narrow band.

9. Conclusion

Monitoring of health is not a new idea and it is literally practiced by physicians using a knowledge base, tools, methods, and systems for diagnosis and then prognosis of one's state of health. Some of these tools were specifically developed for the practice of medicine and in a similar fashion this occurred in the current chapters.

The ability to accurately and efficiently monitor the long-term performance of engineering structures is an extremely valuable one. The potential benefits of structural monitoring includes reducing lifetime maintenance costs, improved safety and the ability to confidently use more efficient designs and advanced materials.

Today, a new and interdisciplinary area of structural health monitoring is likewise needed in order to address the structural, economic, and safety needs of the 21st century society and beyond. As with other industries, civil engineering must also undergo such a catharsis for a similar industry development.

In this Chapter we focused on fiber sensors using birefringence properties which have the fastest response to dynamic changes, using this idea combined with nonlinear effects we have demonstrated point and distributed sensors for dynamic monitoring in structures, communication fibers and security applications.

10. References

- Allen, C.; Kondamuri, P.; Richards, D. & Hague, D. (2003). Measured temporal and spectral PMD characteristics and their implications for network-level mitigation approaches. *J. Lightwave Technol.*, Vol. 21, No. 1, (January 2003) 79–86, doi:10.1109/JLT.2003.808634
- Bao, X.; W. Li, W.; Zhang, C.; Eisa, M.; El-Gamal S. & Benmokrane, B. (2008). Monitoring the distributed impact wave on concrete slab due to the traffics based on polarization dependence on the stimulated Brillouin scattering. *Smart Mater. Structures*, Vol. 17, No. 1, (November 2008) 1-5, doi:10.1016/j.engstruct.2004.05.018
- Barnoski, J. K. & Jensen, S. M. (1976). Fiber waveguides: A novel technique for investigation attenuation characteristics. *Appl. Opt.*, Vol. 15, No. 9, (Sept. 1976) 2112-2115
- Boyd, R. W. (2003). *Nonlinear Optics, Second Edition*, Academic Press, ISBN: 0-12-121682-9, San Diego
- Brosseau, C. (1998). *Fundamentals of Polarized Light: A Statistical Optical Approach*, Wiley Inter-Science, ISBN: 978-0-471-14302-4, New York
- Cameron, J.; Chen, L.; Bao, X. & Stears, J. (1998). Time evolution of polarization mode dispersion in optical fibers. *Photon. Technol. Lett.*, Vol. 10, No. 9, (September 1998) 1265–1267, ISSN: 1041-1135
- Chen, L.; Zhang, Z. & Bao, X. (2007). Combined PMD-PDL effects on BERs in simplified optical systems: an analytical approach. *Opt. Express*, Vol. 15, No. 5, (March 2007) 2106-2119, doi:10.1364/OE.15.002106
- Gisin, N.; Gisin, B.; der Weid, J. P. V. & Passy, R. (1996). How accurately can one measure a Statistical Quantity like Polarization-Mode Dispersion?. *Photon. Technol. Lett.*, Vol. 8, No. 12, (December 1996) 1671–1673, ISSN: 1041-1135
- Gordon, J. P. & Kogelnik, H. (2000). PMD fundamentals: polarization mode dispersion in optical fibers. *Proc. Nat. Acad. Sci.*, Vol. 97, No. 9, (April 2000) 4541-4550, PMID: 10781059
- Hotate, K. & Ong, S. L. (2003). Distributed dynamic strain measurement using a correlation-based Brillouin sensing system. *IEEE Photon. Technol. Lett.*, Vol. 15, No. 2, (February 2003) 272–274, ISSN: 1041-1135
- Huttner, B.; Gisin, B. & Gisin, N. (1999). Distributed PMD measurement with a polarization-OTDR in optical fibers. *J. Lightwave Technol.* Vol. 17, No. 10, (October 1999) 1843-1848, ISSN: 0733-8724
- Huttner, B.; Geiser, C. & Gisin, N. (2000). Polarization-induced distortion in optical fiber networks with polarization-mode dispersion and polarization-dependent losses. *IEEE J. Select. Topics Quantum Electron.*, Vol. 6, No. 2, (March/April 2000) 317-329, ISSN: 1077-260X
- Karlsson, M.; Brentel, J. & Andrekson, P. (2000). Long-term measurement of PMD and polarization drift in installed fibers. *J. Lightw. Technol.*, Vol. 18, No. 7, (July 2000) 941-951, ISSN: 0733-8724
- Krispin, H.; Fuchs, S. & Hagedorn, P. (2007). Optimization of the efficiency of aeolian vibration dampers, *Proceeding of Power Engineering Society Conference and Exposition in Africa*, South Africa, pp 1-3, ISBN: 978-1-4244-1477-2, July 2007, IEEE PowerAfrica '07, Johannesburg

- Landau, L. & Lifchitz, E. M. (1981). *Electrodynamics of Continuous Media* (J. B. Sykes & J. S. Bell, Trans.), Pergamon Press, ISBN: 0080091059, Oxford (Original work published 1969)
- Leeson, J; Bao X.; Côté, A. (2009). Polarization Dynamics in Optical Ground Wire (OPGW) Network. *Appl. Opt.*, Vol. 48, No. 14, (May 2009) 2214-2219, doi:10.1364/AO.48.002214
- Measures, R. M. (2001). *Structural Monitoring with Fibre Optics Technology*, Academic Press, ISBN: 0-12-487430-4, London
- Rogers, A. J. (1981). Polarization-optical time domain reflectometry: A technique for the measurement of field distributions. *Appl. Opt.*, Vol. 20, No. 6, (March 1981) 1060-1074, ISSN: 0003-6935
- Snoody, J. (2008). *Study on Brillouin Scattering in Optical Fibers with Emphasis on Sensing*. Unpublished master's thesis, University of Ottawa, Ottawa, Canada
- Waddy, D.; Lu, P.; Chen, L. & Bao, X. (2001). Fast state of polarization changes in aerial fiber under different climatic conditions. *Photon. Technol. Lett.*, Vol. 13, No. 9, (September 2001) 1035-1037, ISSN: 1041-1135
- Waddy, D. S.; Chen, L. & Bao, X. (2005). Polarization effects in aerial fibers. *Opt. Fiber Technol.*, Vol. 11, No. 1, (October 2005) 1-19, doi:10.1016/j.yofte.2004.07.002
- Wuttke, J.; Krummrich, P. & Rosch, J. (2003). Polarization oscillations in aerial fiber caused by wind and power-line current. *Photon. Technol. Lett.*, Vol. 15, No. 6, (June 2003) 882-884, ISSN: 1041-1135
- Zhang, Z.; Bao, X.; Yu, Q. & Chen, L. (2006). Fast states of polarization and PMD drift in submarine fibres. *Photon. Technol. Lett.*, Vol. 18, No. 9, (May 2006) 1034-1036, ISSN: 1041-1135
- Zhang, Z.; Bao, X.; Yu, Q. & Chen, L. (2007). Time evolution of PMD due to the tides and sun radiation on submarine fibers. *Opt. Fiber Technol.*, Vol. 13, No. 1, (January 2007) 62-66, doi:10.1016/j.yofte.2006.07.003
- Zhang, Z & Bao, X. (2008a). Continuous and damped vibration detection based on fiber diversity detection sensor by rayleigh backscattering. *J. Lightwave Technol.*, Vol. 26, No. 7, (April 2008) 852-838, ISSN: 0733-8724
- Zhang, Z. & Bao, X. (2008b). Distributed optical fiber vibration sensor based on spectrum analysis of polarization-OTDR system. *Opt. Express*, Vol. 16, No. 14, (July 2008) 10240-10247, doi:10.1364/OE.16.010240
- Zhang, Z.; LeBlanc, S.; Bao X. (2008a). Concrete pavement vibration monitoring due to the car passing using optical fiber sensor, *Proceedings of the 19th International Conference on Optical Fibre Sensors (OFS-19)*, pp.1-5, ISBN: 9780819472045, Australia, June 2008, SPIE, Perth
- Zhang Z.; Bao X.; Rennie C. D.; Nistor I. & Cornett A. (2008b). Water wave frequency detection by optical fiber sensor. *Opt. Communication*, Vol. 281, No. 24, (December 2008) 6011-6015, ISSN: 0030-4018

Near-Field Opto-Chemical Sensors

Antonietta Buosciolo¹, Marco Consales², Marco Pisco²,
Michele Giordano¹ and Andrea Cusano²

¹*National Research Council, Institute for Composite and Biomedical Materials
Napoli, Italy*

²*University of Sannio, Optoelectronic Division, Engineering Department,
Benevento, Italy*

1. Introduction

Nanotechnology and nanoscale materials are a new and exciting field of research. The inherently small size and unusual optical, magnetic, catalytic, and mechanical properties of nanoparticles not found in bulk materials permit the development of novel devices and applications previously unavailable. One of the earliest applications of nanotechnology that has been realized is the development of improved chemical and biological sensors. Remarkable progress has been made in the last years in the development of optical nanosensors and their utilization in life science applications.

This new technology demonstrates the breadth of analytical science and the impact that will be made in the coming years by implementing novel sensing principles as well as new measurement techniques where currently none are available.

What is exciting in sensor research and development today? This is a tough question. There are many significant innovations and inventions being made daily. Micro and nanotechnology, novel materials and smaller, smarter and more effective systems will play an important role in the future of sensors.

With the increasing interest in and practical use of nanotechnology, the application of nanosensors to different types of molecular measurements is expanding rapidly. Further development of delivery techniques and new sensing strategies to enable quantification of an increased number of analytes are required to facilitate the desired uptake of nanosensor technology by researchers in the biological and life sciences.

To fulfil the promise of ubiquitous sensor systems providing situational awareness at low cost, there must be a demonstrated benefit that is only gained through further miniaturization. For example, new nanowire-based materials that have unique sensing properties can provide higher sensitivity, greater selectivity and possibly improved stability at a lower cost and such improvements are necessary to the sensor future.

Nano-sensors can improve the world through diagnostics in medical applications; they can lead to improved health, safety and security for people; and improved environmental monitoring. The seed technologies are now being developed for a long-term vision that

includes intelligent systems that are self-monitoring, self-correcting and repairing, and self-modifying or morphing not unlike sentient beings.

On this line of argument, in last years, our interdisciplinary group has been involved in research activities focused on the development of novel opto-chemical nano-sensors employing near-field effects to enhance the overall performance of the final device.

In this chapter, thus, we report recent findings on new class of opto-chemical sensors whose excellent sensing performance are related to an enhancement effect of the optical near-field induced by semiconductive structures of tin dioxide (SnO_2) when their spatial dimensions are comparable to the employed radiation wavelength (λ).

The main objective is to investigate the possibility to concentrate the electro-magnetic field in precise localized spots, by means of metal oxide micro and nano-sized structures, to increase light matter interaction and provide innovative and valuable sensing mechanisms for next generation of fiber optic chemical and biological nano-sized sensors (Pisco et al., 2006; Buosciolo et al., 2006).

Due to the strong interdisciplinary nature of the problem, research activities have been carried out following an integrated approach where all the aspects (material selection, integration techniques and transducer development), have been simultaneously addressed and optimized.

Taking this line, interest was focused on issues like investigation of the surface morphology and of the near-field optical properties in relation to suitable processing and post-processing conditions; correlation of the surface layer morphology and the emerging near-field intensity distribution with the sensing performance [Consales et al., 2006b; Cusano et al., 2006]. We found that sensitive layers with very rough morphologies inducing a significant perturbation of the optical near-field, exhibited surprisingly sensing performance for both water chemicals monitoring and against chemical pollutants in air environment, at room temperature (Cusano et al., 2006; Buosciolo et al., 2008b).

Similar effects of light manipulation have been observed, in recent years, only in noble metal nanostructures explained in terms of localized surface plasmons and in subwavelength hole arrays in both metal films and non metallic systems; in a recent convincing theoretical model (Lezec & Thio, 2004) relative to the last case, the transmission of light is modulated not by coupling to surface plasmons, but by interference of diffracted evanescent waves generated by subwavelength periodic features at the surface, leading to transmission enhancement as well as suppression.

In light of this argument, it is clear that the manipulation of light through semiconductive micro and nano sized structures opens new frontiers not only in sensing applications but have also vast potential to be applied in many fields ranging from high performance nanometer-scale photonic devices up to in-fiber micro systems.

Here, we review the technological steps carried out by our group for the demonstration of a novel sensing mechanism arising from near-field effects in confined domains constituted by particle layers of tin dioxide with size approaching the optical wavelength. To this aim, we have structured the present chapter as follows: sections 2 and 3 are focused on the properties and characteristics of tin dioxide as sensing layer for chemical transducers with particular emphasis on the state of the art on chemical sensors based on this type of semiconductor. Section 4 deals with the principle of operation of the proposed reflectometric opto-chemical sensors and with the electrostatic-spray pyrolysis method as valuable tool to deposit particle layers of tin dioxide on optical fiber substrates at wavelength scale. Section 5

reports the morphological and optical characterization of the so produced superstrates carried out by atomic force and scanning near-field optical microscopy, very useful to clearly outline the effects of processing parameters on particles size and distribution as wells on the optical near-field emerging from the overlays. Finally, in section 6 we present the sensing performances of fiber optic chemo-sensors incorporating tin dioxide particle layers in both air and liquid environments discussing the dependence of the sensing properties on film morphology and optical near-field.

2. Tin dioxide as sensing material

Metal oxides are widely used as sensitive materials for electrical gas sensors in environmental, security and industrial applications. The idea of using semiconductors as gas sensitive devices leads back to 1952 when Brattain and Bardeen first reported gas sensitive effects on germanium (Brattain & Bardeen, 1952). Later, Seiyama et al. found gas sensing effect on metal oxides (Seiyama et al., 1962).

The principle of operation of such class of sensors relies upon a change of electrical conductivity of the semiconductor material as a consequence of the gas adsorption.

Even if many chemo-physical coupled phenomena, such as surface and bulk chemical reactions and mass and energy diffusion, are involved in the operation of the semiconductor solid state conductivity sensors (Lundstrom, 1996), in general, the sensing principle is dominated by the variation of the electronic properties of wide-band-gap semiconductors such as SnO₂ and ZnO due to the gases adsorption that modifies the intrinsic electronic defect formation (Szklański, 1989). The gas sensitivity of semiconductor materials is underlain by reversible effects resulting from chemisorption of molecules, formation of space charge areas, and variation of the concentration of the charge carriers in the subsurface layer.

Although the general principle of the detection mechanism is appreciated, the size of the change of electric conductivity (sensor signal) is largely determined by the structural type of the semiconductor, the nature and concentration of surface reactive centers, and the real structure of the material: the size, structure, and degree of agglomeration of crystallites, specific surface area, and pore geometry (Rumyantseva et al., 2008).

In principle, any semiconducting oxide can be exploited as a sensor by monitoring changes of its resistance during interaction with the detected gas molecules at an operating temperature typically above 200 °C. Because tin oxide (SnO₂) offers high sensitivity at conveniently low operating temperatures, attention has been concentrated on this material although lately many studies extended also to other oxides.

In fact, several commercial devices based on SnO₂ for detecting low concentration of both flammable, i.e. CH₄ and H₂, and toxic; i.e. CO, H₂S and NO_x, gases, are available. SnO₂ sensors can be referred to as the best-understood prototype of oxide based gas sensors. Nevertheless, highly specific and sensitive SnO₂ sensors are not yet available. It is well known that sensor selectivity can be fine-tuned over a wide range by varying the SnO₂ crystal structure and morphology, dopants, contact geometries, operation temperature or mode of operation, etc. The electric conductivity of oxide semiconductors is extremely sensitive to the composition of the surface, which reversibly varies as a consequence of surface reactions involving chemisorbed oxygen (O₂⁻, O₂²⁻, O⁻) and the gas mixture components, proceeding at 100–500°C. (Rumyantseva et al., 2008; Barsan, et al., 1999).

Moreover, tin oxide is sensitive to both oxidizing gases, such as ozone, O_3 , and NO_2 , and reducing species, such as CO and CH_4 (Becker, 2001). In particular, in the case of oxidizing gases the raising in conductivity upon gas-solid interaction is due to the injection into the conductivity band of electrons produced by the surface reaction between the gas and the chemically active species, O_{ads}^- of tin oxide, as an example $CO + O_{ads}^- \rightarrow CO_2 + e^-$; while, in the case of reducing gases, the reactions consume the conduction electrons increasing the tin oxide resistivity, as an example $NO_2 + e^- \rightarrow NO + O_{ads}^-$.

In conclusions, the advantages offered by wide-band-gap semiconductor oxides as sensing materials include their stability in air, relative inexpensiveness, and easy preparation in the ultradispersed state (Rumyantseva et al., 2008). Three main drawbacks characterize such class of sensors materials: the relatively high operative temperature, the poor selectivity due to unspecificity of the contribution made by the gas phase molecules to the total electric response and the long term drift (Sberveglieri, 1995).

3. State of the art on SnO_2 based sensors

The first great production and utilization of tin dioxide based gas sensors started in Japan from a patent (Taguchi, 1962) deposited by Naoyoshi Taguchi in the far 1962. His work was completed in the years 1968-69 when he established mass production and started selling the Taguchi Gas Sensor (TGS) and founded the "Figaro Engineering Inc." currently a world leader company in gas sensors production. The first TGS was a ceramic thick film sensor using tin-dioxide powder as sensitive element. The rapid success and the grown in the production of the TGSs in the years following the first TGS realization is attributed not only to the exhibited performances but also to the large diffusion in that years in Japan of bottled gas and the consequent numerous accidental gas explosions (Ihokura & Watson, 1994), leading to the need of security gas sensors.

After almost fifty years since the first TGS realization, many and many technological advancements in the sensing field strongly widened the classes of available sensors both commercially and in the scientific community. Many of them are still based on tin dioxide as sensitive material.

The first generation of sensors based on tin dioxide as sensitive material was manufactured by ceramic thick film technology. In ceramic thick film sensors, the tin dioxide is most commonly sintered onto a substrate, usually of alumina (Ihokura, 1981). In operation, this substrate is heated by an electrically energized filament and the resistance of the active material, which is very high in fresh air, falls as the concentration of (combustible) contaminant gas rises (Watson, 1984).

Since thick film sensors' performance depend on percolation path of electrons through intergranular regions, by varying small details in the preparation process, each sensor differed slightly in its initial characteristics. Therefore the materials fabrication processes have been improved towards thin film technology, that offers higher reproducibility and long term stability.

In order to enhance the performances and the selectivity of these sensors, several approaches have been pursued.

An approach consists in the careful choice of the working temperature of the sensor that is able to enhance the sensitivity to certain gases by comparison with others (Fort et al., 2002). Since the optimum oxidation temperatures are different from gas to gas, operating the

transducer at two different temperatures leads to the enhancement of the sensor selectivity (Heilig et al., 1999).

A large number of additives in SnO₂, such as In, Cd, Bi₂O₃ and noble metals (i.e. palladium or platinum) either in thick or in thin films based sensors have been investigated to improve the selectivity and to enhance the response of the tin-dioxide gas sensors (Yamazoe, 1983). These dopants are added to improve sensor sensitivity to a particular gas, to minimize cross sensitivity to other gases and to reduce temperature of operation. Palladium inclusions, for example, leads to a lowering of the sensor resistance, a speeding up of transient behavior and modifies the selectivity characteristics of the sensor by changing the rates of the redox reactions (Watson et al., 1993; Cirera et al., 2001). The doping of SnO₂ with Pt reduces in particular the optimum operating temperature for sensing CO gas. On the other hand, the doping of SnO₂ with trivalent additive favors the detection of oxidant gases. By suitably selecting the dopant the temperature of device operation can be tailored for a specific application (Erann et al., 2004; Ivanov et al., 2004). Other additives such as gold, rhodium, ruthenium and indium have more significant effects on selectivity, as do several metal oxides including those of lanthanum and copper.

A widely employed approach to enhance the sensor selectivity concerns exploiting different measurement techniques and/or data processing algorithms. Of course, these approaches are not limited to tin-oxide based sensors. Nonetheless, interesting results have been achieved also with tin oxide by measuring the transducer conductivity variations during chemical transients obtained with abrupt changes in target molecules concentration. In fact in this case the reaction kinetics can be exploited to differentiate among different compounds (Schweizer-Berberich et al., 2000; Llobet et al., 1997; Ngo et al., 2006).

More generally, the realization of an array of sensors with different features and the employment of pattern recognition techniques demonstrated to be a suitable strategy to discriminate among different target molecules (Gardner et al., 1992; Hong et al., 2000; Lee et al., 2001; Delpha et al., 2004).

The effect of grain size on the sensitivities of SnO₂ films has been also investigated since 1991, when Yamazoe (Yamazoe, 1991) showed that reduction of crystallite size caused a huge improvement in conductometric sensor performance. In fact, in a low grain size metal oxide almost all the carriers are trapped in surface states and only a few thermal activated carriers are available for conduction. In this configuration the transition from activated to strongly not activated carrier density, produced by target gases species, has a great effect on sensor conductance. The challenge thus became to prepare stable materials with small crystallite size. This process has been assisted by the recent progress in nanotechnology, thank to which fine control over the crystallinity, morphology, composition and doping level of these sensing materials could be obtained.

An important step forward has been achieved by the successful preparation of stable single crystal quasi-one-dimensional semiconducting oxides nanostructures (the so-called nanobelts, nanowires or nanoribbons) (Pan et al., 2001; Comini et al., 2002).

This was followed by the publication of some fundamental demonstrations (Cui et al., 2001; Law et al., 2002; Arnold et al., 2003; Li et al., 2003) of detecting a variety of chemicals and bio-agents using semiconducting 1-D oxides. Since then, this area has been experiencing significant growth in the past six years and it is not yet clear whether it will reach saturation soon (Comini, 2008; Chen et al., 2008).

In particular, SnO₂ nanowires and nanobelts have been widely reported in a number of reports as conductometric chemical sensors, both in normal resistor or in Field Effect Transistor (FET) configurations (Maffeis et al., 2002; Panchapakesan et al., 2006; Helwig et al., 2007). The first SnO₂ nanobelt chemical sensor was realized in 2002 and employed for the detection of CO, NO₂, and ethanol (Comini et al., 2002). It relied on simple DC-resistive measurements and was made by dispersing SnO₂ nanobelts atop platinum interdigitated electrodes, prefabricated on an alumina substrate. In 2005, the possibility to integrate tin oxide nanobelts with micro-machined substrate has been proved by Yu et al. (Yu et al., 2005), that reported on a single-SnO₂-nanobelt sensor integrated with microheaters to sense dimethyl methylphosphonate (DMMP), a nerve agent stimulant. Recently, Wan et al. (Wan et al., 2008) proposed a high-performance ethanol sensor based on branched SnO₂/Sb-doped SnO₂ nanowire films.

Chemical sensors based on metal oxide 1-D structure configured in FET devices have also been extensively studied. For example, Law et al. (Law et al., 2002) published a contribution on the room temperature NO₂ sensing properties of a FET sensor based on a single crystalline tin oxide nanowire. They made use of UV light, that has proven to be effective also with thin films (Comini et al., 2001), to improve adsorption and desorption process. Zhang et al. (Zhang et al., 2004) also presented some experiments on SnO₂ single nanowire sensor in a FET structure in pure nitrogen, nitrogen-oxygen and nitrogen-oxygen-CO atmospheres.

Enhanced performances have also been demonstrated in the last years with 1-D SnO₂ nanostructure-based conductometric sensors with Pd (Kolmakov et al., 2005), Ag (Chen & Moskovits, 2007), Ni (Sysoev et al., 2006) and Au (Qian et al., 2006) nanoparticles decorated on the surface of nanowires and nanobelts.

The main disadvantage of conductometric sensors is their need for a high working temperature, which leads to power wastage. Recently, some contribution on new (and yet not well explored) optical detection methods have also been proposed for the realization of tin oxide chemical sensors. They are based on the measurements of optical response of SnO₂-based materials to environmental changes, instead of the electrical ones. In particular, some contributions have been reported on the quenching in the visible photoluminescence (PL) of tin oxide nanostructures due to the introduction of NO₂, NH₃, and CO in dry and humid synthetic air and normal ambient pressure conditions (Faglia et al., 2005; Baratto et al., 2005; Setaro et al., 2008).

Also, in the last few years, SnO₂ was exploited as sensitive wavelength-scale particle layers for the realization of a new concept near-field fiber optic chemical sensors able to work at room temperature, either in air or water environments (Cusano et al., 2006; Buosciolo et al., 2008b). The electrostatic spray pyrolysis was exploited to transfer SnO₂ thin films composed of grains with wavelength and subwavelength dimensions atop the termination of standard optical fibers (Pisco et al., 2006). This layer morphology demonstrated to be very promising for optical sensing because it is able to significantly modify the optical near-field profile emerging from the film surface. As matter of fact, local enhancements of the evanescent wave contribute occurs leading to a strong sensitivity to surface effects induced as consequence of analyte molecule interactions (Cusano et al., 2007).

4. Tin dioxide opto-chemical nano-sensors

4.1 Principle of operation

For the realization of the proposed near-field opto-chemical sensors, the reflectometric configuration has been exploited (Pisco et al., 2006). It is essentially based on a modified extrinsic Fabry-Perot (FP) interferometer which, as schematically represented in Fig. 1, uses a microstructured tin dioxide sensitive film deposited at the distal end of a properly cut and prepared optical fiber.

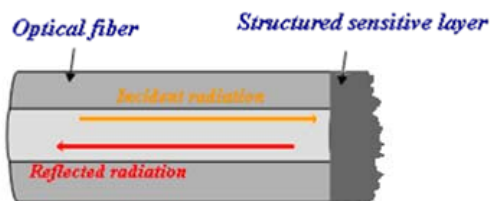


Fig. 1. Schematic view of the reflectometric configuration.

In line of principle, the key point of this configuration is the dependence of the reflectance at the fiber/sensitive layer interface on the optical and geometric properties of the sensitive materials. In particular, the interaction with target analyte molecules promote changes in the chemo-optic features of the active layers surface, basically its dielectric constant. In this case in fact, contrarily to what happen for the standard FP configurations (Pisco et al., 2006), the interaction of the field with the chemicals present within the atmosphere occurs not in the volume of the layer but mainly on its surface by means of the evanescent part of the field, promoting a significant improvement of the fiber optic sensor performance. The chemo-optic variations induced by the surface-chemicals interaction lead to changes in the film reflectance and thus in the intensity of the optical signal reflected at the fiber/film interface. As we will see in the section 6.1, this optical intensity modulation is simply detectable by means of single-wavelength reflectance measurements.

4.2 Integration of sensing layers with standard optical fibers

Many sensitive materials and transducing techniques are today available to develop opto-chemical sensors, but it's necessary to find the suitable deposition technique, depending on the nature of the material and the transducing substrate, in order to control the morphological and geometrical features of the sensitive layer. This governance is, in fact, essential to fully benefit of the materials properties and to be able to mathematically schematize the sensor for a reasonable design of its performances. Hence, the challenge in this field is not just relating to the chemical tailoring of the material properties, but also the integration of the material with the sensing platform. At the same time simple and low cost fabrication procedure and equipment are mandatory for a fast and cost-effective evolution of the devices from laboratories to market.

In the following, a brief introduction to the Electrostatic Spray Pyrolysis (ESP) technique and a description of its optimization and customization for the deposition of the selected sensitive material onto the fiber substrates are presented.

Moreover, the possibility to obtain thin films at nano and micro scale and to tailor the sensitive layers features by properly changing the ESP deposition parameters will also be reported.

4.3 Electrostatic Spray Pyrolysis (ESP) deposition technique

The spray pyrolysis technique has been, during the last three decades, one of the major techniques to deposit a wide variety of materials in thin film form (Perednis & Gauckler, 2005). Unlike many other film deposition techniques, spray pyrolysis represents a very simple and relatively cost effective processing method (especially with regard to equipment costs). It offers an extremely easy technique for preparing films of any composition and it does not require high quality substrates or chemicals. The method has been employed for the deposition of dense films, porous films, and for powder production. Even multilayered films can be easily prepared using this versatile technique.

Thin metal oxide and chalcogenide film deposited by spray pyrolysis and different atomization techniques were reviewed for example by Patil (Patil, 1999).

ESP is a spray deposition technique in which the precursor solutions are electro sprayed toward substrates from the end of a highly biased metal capillary (typically 5–25 kV).

In fact, this methodology is based on the phenomenon of electrolyte (usually ethanol or water solutions of metal chlorides) polarization on charged droplets by an electrostatic field, applied between a vessel provided with a metal capillary and a heated substrate. The polarized droplets separate one from each other by means of repulsive forces and they are carried by electrostatic field along its force lines (Higashiyama et al., 1999). The moving droplets form a cone in the space, called Taylor's cone. The substrate coverage by droplets is quasi uniform in terms of amount of drops per square unit. When droplets of solution reach the heated substrate (the substrate temperature is usually in the range 300–450°C), chemical reaction of metal chloride with solution water vapor, stimulated by the temperature, takes place with formation of the oxide film (Matsui et al., 2003):



Thereby, metal oxide layer grows due to the thermal transformation of metal chloride to metal oxide as a consequence of the interaction with water vapor.

It's evident from this brief description that ESP involves many processes occurring either simultaneously or sequentially. The most important of these are aerosol generation and transport, solvent evaporation, droplet impact with consecutive spreading, and precursor decomposition. The deposition temperature is involved in all mentioned processes, except in the aerosol generation. Consequently, the substrate surface temperature is the main parameter that determines the electrical properties of the layers, like resistivity and charge carrier mobility, and structural properties like crystalline size and surface morphology.

For instance, for SnO₂ samples deposited at higher temperatures, low resistivity and higher roughness were observed, whereas for films deposited at temperatures less than 340°C high resistivity, lower crystalline size and less ratio of polycrystalline phase were found (Patil et al., 2003). A more recent work of Ghimbeu et al. (Ghimbeu et al., 2007), report on the influences of deposition temperature on the surface morphology of SnO₂ and Cu-doped SnO₂ thin films. Dense films with a smooth surface characterized by several cracks were deposited at low temperature such as 150°C; denser films comprised of large particle of about 1 μm, which are agglomerates of small particles, were obtained at 250°C; while films

prepared at 350 and 400°C showed a porous structure and a surface roughness that increase with increasing temperature.

The precursor solution is the second important process variable. Solvent, type of salt, concentration of salt, additives and sprayed volume influence the physical and chemical properties of the precursor solution. Therefore, structure and properties of a deposited film can be tailored also by changing the precursor solution.

For example, porous SnO₂ and SnO₂-Mn₂O₃ films were prepared using the ESP deposition technique and employed in Taguchi type hydrogen sensors (Gourari et al., 1998; Gourari et al., 1999). The grain size of the porous films ranged from 1 to 10 μm. It was observed that the grain size increases with a higher concentration of the precursor in the ethanol solvent.

Thin SnO₂ films for gas sensors were also prepared by spray pyrolysis using an inorganic as well as an organic precursor solution (Pink et al., 1980). Smooth but not very uniform films were obtained using a solution of (NH₄)₂SnCl₆ in water. On the other hand, very uniform but relatively rough films were deposited using a solution of (CH₃COO)₂SnCl₂ in ethylacetate. Suitable electric properties were measured for films obtained from the organic solution. The sensitivity and rise time were found to depend on the deposition temperature and the type of precursor solution used. The best results were achieved by spraying an organic precursor solution onto a substrate at about 300°C.

The first attempts to prepare SnO₂ layers using the ESP were carried out by Gourari et al. (Gourari et al., 1998) and Zaouk et al. (Zaouk et al., 2000). Although conductive substrates were conventionally used in ESP, Zaouk et al. (Zaouk et al., 2000) revealed the availability of ESP for the insulator substrate. They investigated the electrical and optical properties of the fluorine doped SnO₂ layers sprayed on Corning 7059 substrates.

4.4 Customization and optimization of ESP deposition technique

The ESP technique was used for the first time for the deposition of a tin dioxide layer upon the distal end of standard silica optical fibers (SOFs) by the authors in the 2005 (Pisco et., 2005). To this purpose, an optimization and customization of the standard ESP method was used. For the SnO₂ particle layers deposition, single mode optical fibers were prepared by stripping the protective coating a few centimeters from the fiber-end. The bare fiber were washed in chloroform in order to remove any coating residuals. Then the fiber-end were properly cut, by using a precision cleaver, in order to obtain a planar cross-section, where the SnO₂ films were deposited. A schematic view of the experimental set-up used for the sensors fabrication is shown in Fig. 2.

It consists of a high voltage source (FUG, 0-30kV), two syringes connected with a flexible pipe for the solution handling, a needle with an external diameter of 0.5 mm, connected with a high voltage source (17 ± 0.1 kV) in order to create a high electric field between the needle itself and a grounded metal substrate where the fiber-end is located. The necessary temperature has been reached by means of a resistive heater, in contact with the substrate, constituted by two stainless steel plates of a few square centimeters and by a nichrome wire connected with a 300W voltage source. The heater was supplied with a chromium-nickel thermocouple connected with a multimeter for the temperature monitoring. The distance between the needle and the optical fiber-end was about 30 mm.

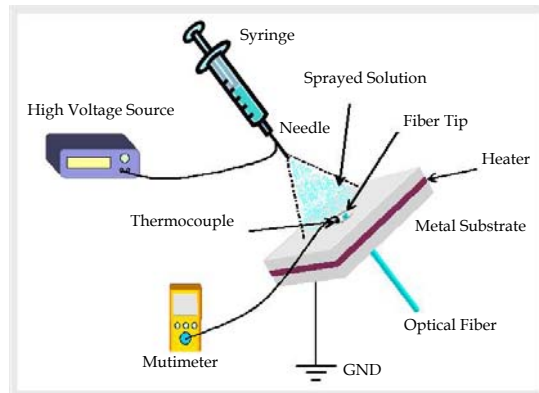
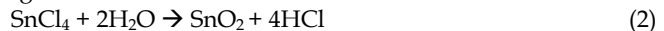


Fig. 2. Schematic view of the experimental set-up used for the deposition of the sensitive layer onto the optical fibers.

The deposition was performed at a constant temperature of 320 ± 5 °C. Liquid flow has been regulated by means of an air pump connected with the first syringe. Tin dioxide films are grown according to the following reaction:



The SnO_2 layers fabrication was performed by means of a constant volume, 5 ml, of an ethanol solution of $\text{SnCl}_4 \cdot 5\text{H}_2\text{O}$ at two different concentrations: 0.01 and 0.001 mol/l.

During the deposition, it is also possible the formation of amorphous SnO phase. Thermal treatment is one of the ways to transform SnO_x to SnO_2 and clean the films surface from the other dopants like water or alcohol present in the initial solution (Ramamoorthy et al., 2003). For this reason, after the deposition procedure, the prepared samples were annealed at 500 ± 5 °C for 1 hour. The temperature was increased from room temperature to 500 °C with a constant rate of 5 °C/min and, after the annealing procedure, the temperature was decreased with the same rate down to the room temperature.

5. Characterization of the surface morphology and of the transmitted optical field in near proximity of the overlays

As described in the previous section 4.1, the principle of operation of the proposed sensors relies on the dependence of the reflected power at the fiber end on the optical and geometric properties of the layer itself. The interaction of the analyte molecules with the sensitive overlay leads to changes in its complex dielectric function and, in turn, in the amount of reflected power. So it's clear that the heart of a chemical sensor is the sensitive layer and for this reason a strong effort was devoted to investigate the properties of the deposited SnO_2 films in terms of the surface morphology and the optical behaviors by means of scanning probe microscopy.

In the present section, we first introduce something about the above mentioned characterization technique and the employed experimental apparatus; then we report on the influence of surface features on the transmitted optical field in near proximity of the

overlays; finally we describe how, by acting on the deposition parameters and on thermal annealing, it is possible to obtain layers able to manipulate light at sub wavelength level. In particular, we will show that: the near-field collected in presence of SnO₂ layers with a smooth topography and a surface roughness of the order of tens of nanometers, has the typical Gaussian shape of the fundamental mode propagating through the single-mode optical fiber; in presence of layers characterized by several SnO₂ grains, with mean spatial dimensions greater than about 500 nm, the near-field profile results to be significantly modified in correspondence of them; finally, layers characterized by the presence of isolated microstructures, with dimensions comparable to radiation wavelength, reveal high capability of near-field enhancement combined with a strong increasing of the evanescent wave content.

5.1 Scanning probe microscopy

Atomic force microscopy (AFM) and scanning near-field optical microscopy (SNOM) analyses were performed on the deposited SnO₂ films, before employing them in sensing applications; as we will see in the following, neither any damage was produced nor any treatment was necessary in order to perform this kind of analysis.

The invention of scanning tunneling microscopy in 1981 began a revolution in microscopy, which has led to a whole new family of microscopies (Meyer et al., 2003), known collectively as scanning probe microscopy (SPM), among them AFM and SNOM. SPMs do not use lenses to produce the magnified image; instead, a local probe is scanned over the surface of the specimen and measures some physical property associated with the surface. This local probe is fabricated from a material appropriate for the measurement of the particular surface property. The scanning process is simply mechanical, but with extremely high precision and without producing any damage of the specimen. Moreover, SPM is capable of imaging all kind of specimen (including soft materials and biomolecular systems) at sub-molecular resolution, without the need for staining or coating, in a range of environments including gas and liquid, so offering major advantages over other forms of microscopy.

In Fig. 3 it is reported the AFM-SNOM system employed for the surface morphology and optical properties characterization; in fact, it is capable of simultaneous SNOM and normal force AFM imaging using the same probe (Buosciolo et al., 2006).

The super-resolution of SNOM is achieved via a sub-wavelength aperture placed in the near-field of the sample: a tapered optical fiber coated with 150 nm of a metal. Measurements were carried out in collection mode using a Cr/Al-coated fiber with 200 nm aperture diameter and illuminating the fiber under investigation with a superluminescent diode (central wavelength $\lambda_1=1310$ nm, $\lambda_2=1550$ nm). The tip was maintained in the near-field of the sample surface using optically detected normal force feedback. This was accomplished by oscillating the tip and detecting the scattered light from a laser focused onto the end of the tip. As the tip approaches the surface, the signal decreases and a feedback circuit can be used to maintain a constant tip-sample distance while scanning the sample under the tip. During the imaging scan, the probe collects the light coming out of the sample exactly at the end face. In this way, the optical intensity distribution from the fiber end face is mapped into a SNOM image and an independent AFM normal force image is recorded simultaneously by the feedback signal that produces a three-dimensional image of the SnO₂ film surface.

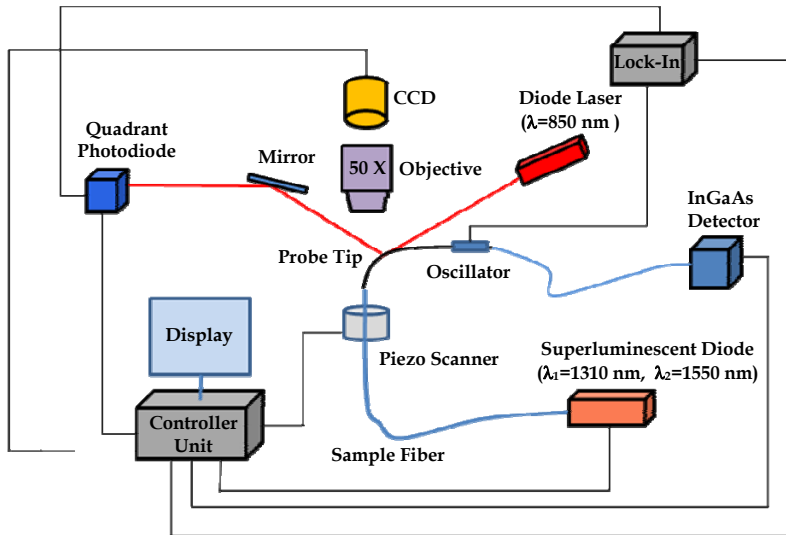


Fig. 3. Scanning probe system: simultaneous atomic force (AFM) and scanning near-field optical microscopy (SNOM).

The resolution of SNOM images is limited by the aperture size of the probe (200 nm); as regards the AFM characterization, in the x and y directions, the resolution is limited by the effective dimension of the terminal part of the probe (aperture diameter plus the metallization layer), while in the z direction is only limited by external vibrations.

All images were obtained in air using tapping mode operation and in a region approximately centered onto the fiber core. Moreover, image acquisition times were between 30 and 40 min for images with pixel resolution of 256x256.

Images were processed by WSxM free software downloadable at <http://www.nanotec.es>. In particular, topographic images were flattened, off-line, using zero-or-first order polynomial fits to account for z offsets and sample tilt.

5.2 Influence of surface layer morphology on the near-field intensity distribution

AFM and SNOM measurements allow to obtain quantitative information on the surface structures of the sensitive coatings and the knowledge of the relationship between the layer morphology and the optical near-field collected in the close proximity of the fabricated probes (Consales et al. 2006).

As an example, in Fig.4 (a) is reported the typical bi-dimensional (2D) image of a SnO₂ layer (sample A) deposited upon the distal end of the optical fiber, by ESP technique using a solution volume of 5 ml of ethanol solution of SnCl₄·5H₂O with a concentration of 0.01 mol/l. The image refers to a (12x12) μm² area, approximately centered on the optical fiber core, indicated with the green circle.

The most important measurement of surface roughness can be given with a statistical parameter: the root mean square (RMS) roughness that is the standard deviation of the height values within a given area. Figure 4 (a) reveals that the deposited layer is very smooth with a RMS roughness of about 27.98 nm. In addition, Fig. 4 (b) shows that the

shape of the electromagnetic field collected in the close proximity of the film surface is not influenced by the presence of such SnO₂ layer, as demonstrated by the fact that it assumes the typical Gaussian profile of the field emerging from the cleaved end of a single mode optical fiber.

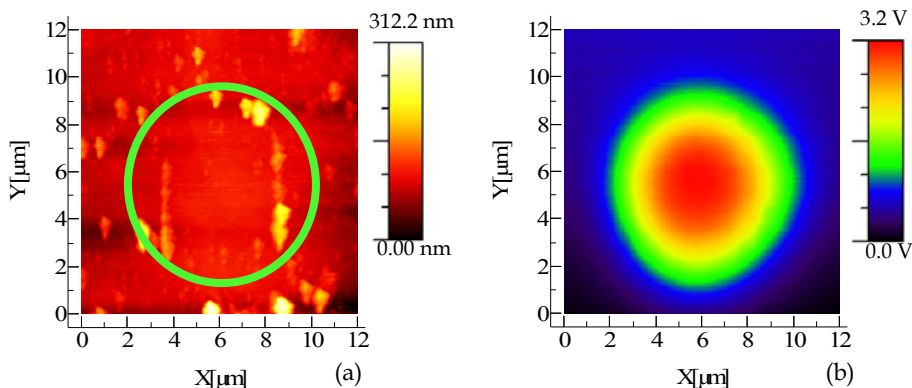


Fig. 4. Topographic image of the sample A (a) and optical near-field simultaneously collected by the SNOM probe in the same region (12×12) μm² (b).

Different morphologies of the SnO₂ particles layers can be obtained by changing the parameters of the ESP deposition process, such as the concentration and the volume of the ethanol solution of SnCl₄·5H₂O, the alignment of the optical fiber end under the needle from which the precursor solution is sprayed or the substrate temperature during the deposition. As matter of the fact, Fig. 5 (a) shows the 2D image of another tin dioxide particles layer, sample B, fabricated by means of the same deposition parameters (5 ml of ethanol solution of SnCl₄·5H₂O with a concentration of 0.01 mol/l) except for the fact that it was differently aligned under the syringe needle.

It can be observed that a very different morphology and, as a consequence, optical near-field profile, have been obtained. In this case, in fact, the sensitive layer exhibits an highly rough surface characterized by the presence of a number of tin dioxide grains which cause an increase of the RMS roughness up to 136.65 nm. By an analysis of the heights and sizes distributions of the grains, a mean height of approximately 400 nm and mean lateral (x, y) dimension of approximately 465 nm were estimated.

Fig. 5 (b) reveals that, in this case, the optical profile of the emergent near-field is significantly influenced by such overlay morphology. As matter of fact, the Gaussian shape of the near-field collected in the close proximity of the layer surface, appears modified in correspondence of the SnO₂ grains with dimensions comparable with the light wavelength. In fact, relatively to the core region only, the biggest grains able to produce a perturbation of the field have a mean height of about 700 nm and a mean width of about 550 nm.

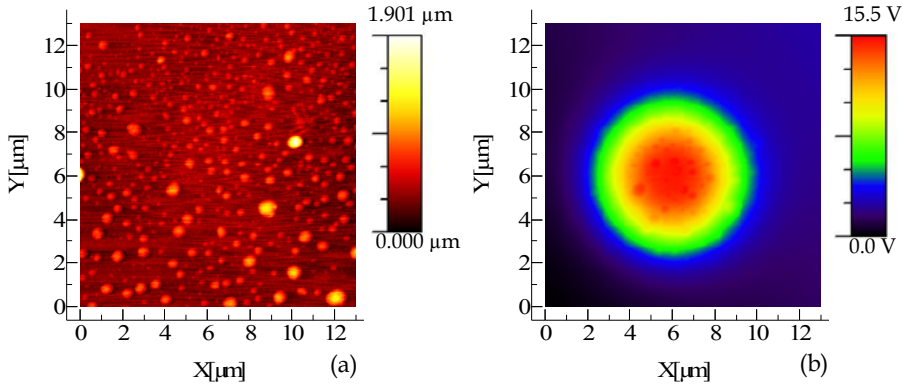


Fig. 5. Topographic image of the sample B (a) and optical near-field simultaneously collected by the SNOM probe in the same region (13×13) μm^2 (b).

It was demonstrated that this effect can be attributed to the high refractive index of the SnO_2 grains (approximately 1.967 for $\lambda = 1550$ nm) which try to guide the light but, the lateral dimensions and the grains spacing (mean grains spacing is about $1 \mu\text{m}$) are too small to allow a correct light localization due to the significant overlap of the evanescent field. This interpretation was confirmed by additional experiments focused on the investigation of the particle layer effects in the case of larger and isolated grains (Cusano et al., 2007).

In fact, the near field enhancement effect was observed for the first time by the authors in 2007 (Cusano et al., 2007) in the case of SnO_2 grains whose spatial dimensions approach the radiation wavelength.

Here, we report the case of the sample C obtained in the same deposition condition of sample A, but using a different concentration of ethanol solution of $\text{SnCl}_4 \cdot 5\text{H}_2\text{O}$ equal to 0.001 mol/l . As it is possible to note from the 2D representation of sample C topography reported in Fig. 6 (a), the isolated microstructure has approximately the shape of an half ellipsoid, with dimensions $x \approx y \approx 1.4 \mu\text{m}$ and $z \approx 1.0 \mu\text{m}$, on a flat SnO_2 substrate. It is evident from Fig. 6 (b) that the optical near-field is strongly enhanced in correspondence of the such grain. The local intensity enhancement, calculated as the ratio between the maximum measured intensity and the corresponding intensity of the unperturbed field is about 1.8. (Cusano et al., 2007).

In order to demonstrate that the field enhancement is observable only in the near-field range, the emergent field at a constant sample-probe distance of approximately $2 \mu\text{m}$, was also recorded, as reported in Fig. 7 (a).

For a sample-tip distance comparable to the optical wavelength, the field profile is not able to completely maintain information about the film morphology, even if a significant distortion of the beam shape is still clearly observable in Fig. 7 (a). By increasing the sample-tip distance, up to few times the wavelength the collected optical field profile assumes the Gaussian shape, as expected in far field imaging.

Moreover, it was possible to construct a map of the radiation intensity coupled into the standard optical fiber coated with the SnO_2 overlay simply by coupling the cantilevered

optical probe to the superluminescent diode and the fiber sample to the InGaAs detector (named reverse configuration, compared to the forward one reported in Fig. 3).

It was found that the profile of the radiation intensity coupled to the sample fiber using the reverse configuration, reported in Fig. 7 (b), is very similar to that one transmitted through the optical fiber coating and collected in the forward configuration (Fig. 6 (b)). In this case the local intensity enhancement is about 1.5 calculated using the same procedure reported above in the text.

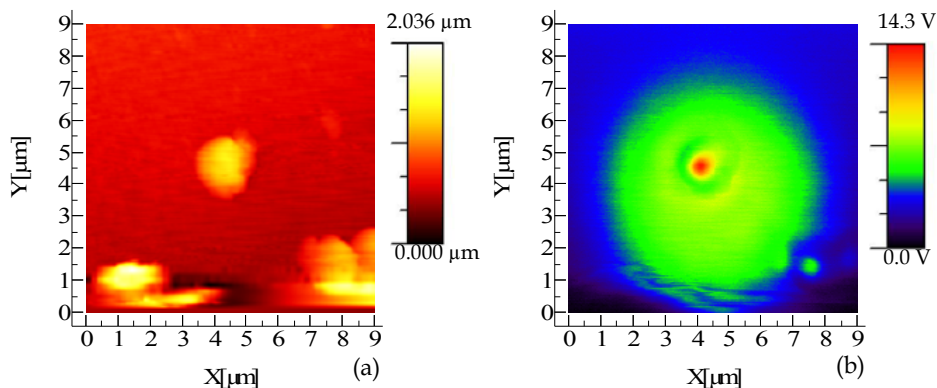


Fig. 6. Topographic image of the sample C (a) and optical near-field simultaneously collected by the SNOM probe in the same region ($9 \times 9 \mu\text{m}^2$) (b).

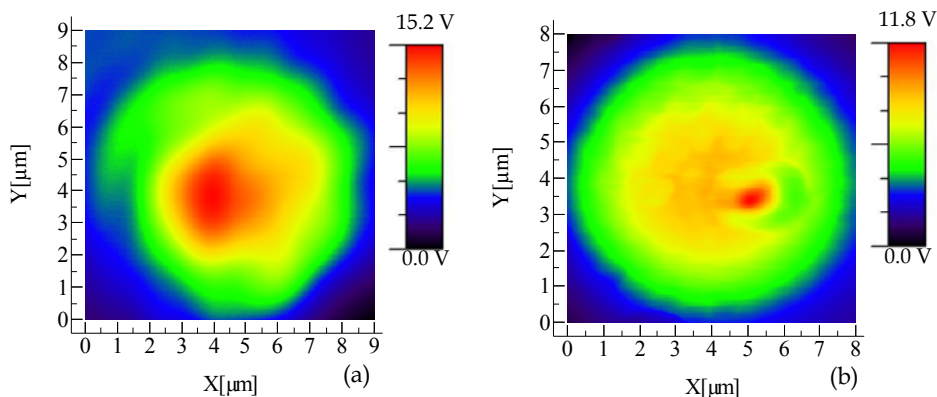


Fig. 7. Emergent field collected from the sample C at constant sample-tip distance of about $2 \mu\text{m}$ (a) and radiation intensity coupled into the standard optical fiber when it was illuminated by the SNOM probe (b).

In light of these experimental results, the authors were able to give an effective explanation of the observed phenomenon: the radiation impinging at the base of the grain, coming from the layer of the same material, continues to propagate inside of it (confined by the high

refractive index contrast between the oxide and the air and by the geometry of the grain), and near the grain surface a significant part of the propagative field becomes evanescent. Moreover, since the structure dimensions are comparable to the radiation wavelength (as revealed from AFM measurements) it is possible to state that the local field enhancement is not due to truly evanescent field. In fact, the reverse profile is very similar to that one obtained in forward configuration indicating a strong reciprocity not compatible with a structure able to convert at its ends (due to diffraction limit) all the propagating contribute in the evanescent counterpart.

In other words, the particular microstructures found on the core of the fibers showed a high capability of locally enhance the optical near-field. The observed phenomenon lead to foresee the possibility to develop a new concept of SnO₂-transducer based on a surface localized interaction of the optical near-field with chemicals, named by the authors near-field opto-chemical sensors.

In this framework, we demonstrated the capability of the developed near-field opto-chemical sensors to detect very low concentrations of toluene and xylene in air environment and also of ammonia molecules in water, at room temperature.

In particular, a comparison between the sensing performance of SnO₂-based sensors characterized by almost flat (unable to influence the near-field) and peculiar rough surfaces (able to perturb the near-field) will be reported to demonstrate that sensitive layers able to strongly enhance the optical near-field have the best sensing characteristics, either in terms of sensitivity and responses dynamics (Cusano et al., 2006; Consales et al., 2007a; Buosciolo et al., 2008b).

5.3 Effect of the processing parameters

As mentioned in the section 4.3, it was shown in literature that the concentration of the sprayed solution plays an important role in the film surface morphology. Since the overlay topography determines the near-field properties, the effect of such process variable and the influence of post processing thermal treatment on the overlay morphology were investigated by the authors; the obtained results were collected in some recent reports (Consales et al., 2006b; Buosciolo et al., 2008a; Buosciolo et al., 2008b).

To this aim, two groups of samples were fabricated by using different solution concentration: 0.001 mol/l and 0.01 mol/l.

Here, for the sake of simplicity, the description relative to only two samples belonging to the mentioned groups is reported. The full description of the two groups of samples can be found in the cited article (Buosciolo et al., 2008b).

In Fig. 8 (a) and (c) the typical 2D height images of two SnO₂ layers (sample D, sample E) prepared by using a solution volume of 5 ml of ethanol solution of SnCl₄·5H₂O with a concentration of 0.001 mol/l, are reported.

Figures 8 (b) and (d) demonstrate that the most pronounced modification of the typical Gaussian profile, emerging from standard single mode optical fibers, occurs in correspondence of the sample D. In fact, the structures dimensions approach the optical wavelength (1550 nm) and the structures spacing is large enough to make possible an effective light localization in the high refractive index SnO₂ grains (Cusano et al., 2007).

In Fig. 9 (a) and (c) the typical 2D height images of two SnO₂ layers (sample F, sample G) prepared by using a solution volume of 5 ml of ethanol solution of SnCl₄·5H₂O with a concentration of 0.01 mol/l, are reported.

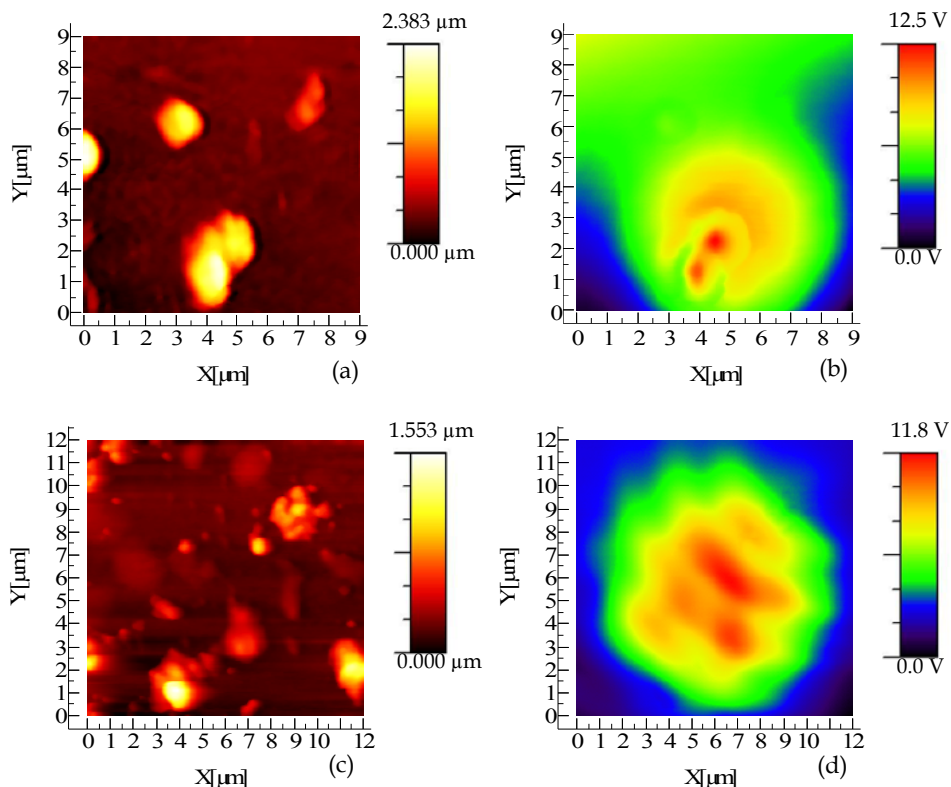


Fig. 8. AFM topographic images (a), (c) and near-field intensity simultaneously collected by the NSOM probe (b), (d) on the sample D and E respectively, prepared using a solution concentration of 0.001 mol/l, before annealing process.

Sample F topography (see Fig. 9 (a)) is characterized by the presence of several grains, but with no regular shape. The major part of them have lateral dimensions smaller than 500 nm and a mean height of the order of 150 nm, while few others have mean lateral dimensions of the order of 1 μm and a mean height of 300 nm. There is only one microstructure whose characteristic dimensions are $a \approx 1430$ nm, $b \approx 1900$ nm and $h \approx 450$ nm.

Sample G topography (see Fig. 9 (c)) presents several structures of rectangular shape whose lateral dimensions a and b vary in the following range: $a \in (2.3 \div 3.4)$ μm , $b \in (3.4 \div 4.8)$ μm , while the average height is about 4.0 μm .

Figures 9 (b) and (d) demonstrate that the most pronounced modification of the near-field profile occurs in correspondence of the sample G.

The conclusion is that increasing the metal chloride concentration it is possible to obtain a more structured surface morphology able to significantly influence the optical near-field.

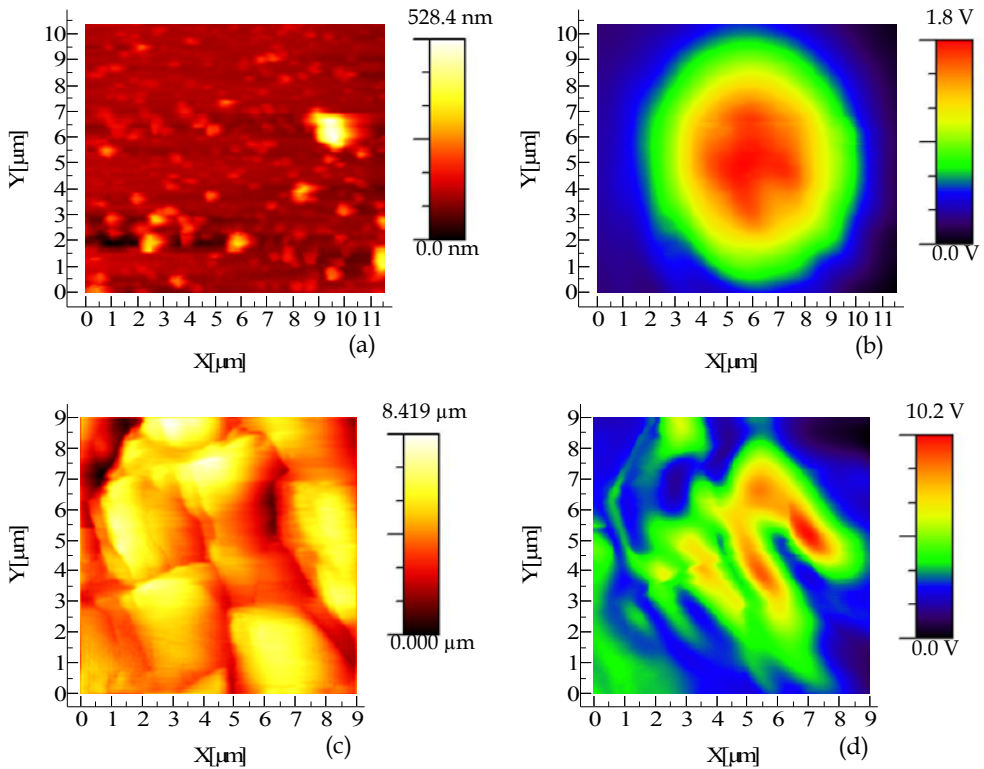


Fig. 9. AFM topographic images (a), (c) and near-field intensity simultaneously collected by the NSOM probe (b), (d) on the sample F and G respectively, prepared using a solution concentration of 0.01 mol/l, before annealing process.

5.4 Effect of the post-processing thermal annealing

In the same work (Buosciolo et al., 2008b), the effect of post processing thermal annealing on surface morphology was also investigated. As matter of fact, two groups of sensors were fabricated by using two different solution concentrations and were characterized before and after the annealing process.

As said in the section 4.4, after the deposition procedure and after the morphological and optical characterization, the prepared samples have been annealed at $500 \pm 5^\circ\text{C}$ for 1 hour in order to transform SnO_x to SnO_2 and to clean the films surface from the other dopants, like water or alcohol present in the initial solution. Successively, we were able to compare the sample topography before and after the annealing process since, collecting the emerging near-field from the sample fiber, the accurate definition of the fiber core was possible.

Here we report, for example, the effect of thermal annealing on sample F and G.

After the thermal treatment sample F topography (see Fig. 10 (a)) is characterized by the presence of several microstructures well separated from each other, whose dimensions are much larger compared to the mean structures dimensions of the SnO₂ grain present on the sample surface before annealing. The structures characteristic mean dimensions are: $a=1.136 \mu\text{m}$, $b= 1.347 \mu\text{m}$ and $h= 114 \text{ nm}$. As described before, the presence of such microstructures strongly modify the collected near-field intensity, as it possible to see in Fig. 10 (b).

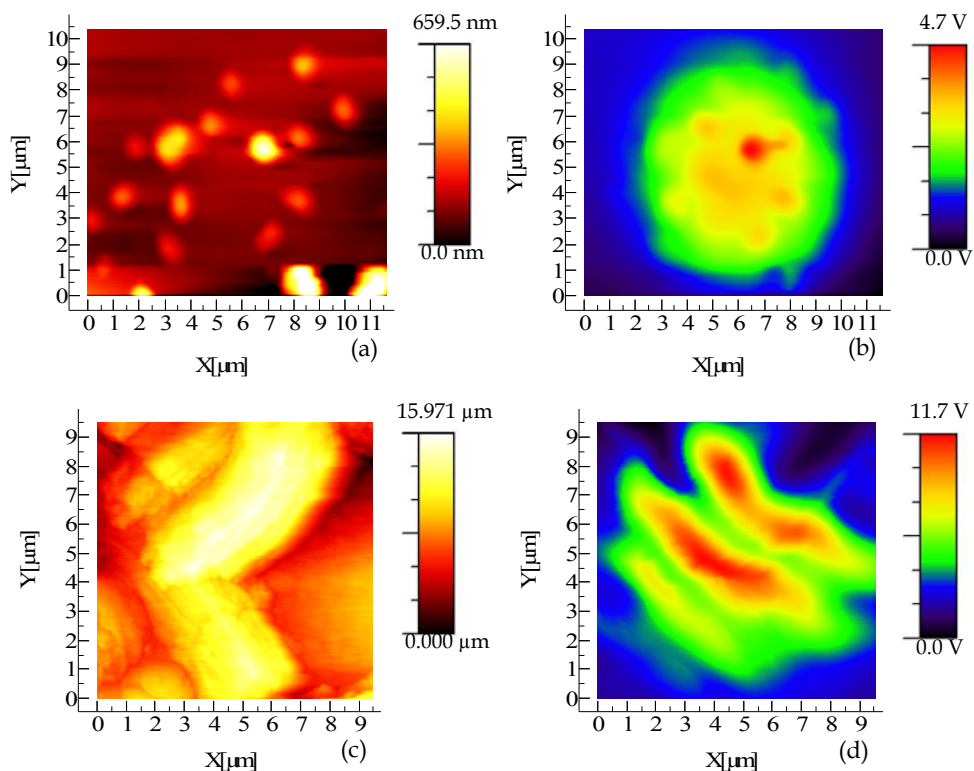


Fig. 10. AFM topographic images (a), (c) and near-field intensity simultaneously collected by the NSOM probe (b), (d) on the sample F and G respectively, after the thermal annealing process.

In fact, the structures spacing is large enough to make it possible an effective light localization in the high refractive index grains. In particular, the prominent effect takes place in correspondence of the central one whose lateral dimension match very well with λ : $a=1.437 \mu\text{m}$, $b=1.542 \mu\text{m}$, while the height is $h=250 \text{ nm}$. We also analyzed the distribution of the heights in the two images reported in Fig. 9 (a) and 10 (a). It was found: an average surface height of 134 nm and a RMS roughness of 48 nm before annealing; while an average surface height of 231 nm and a RMS roughness of 54 nm after annealing. In this case the RMS roughness before and after the annealing is of the same order of magnitude.

In Fig. 10 (c) we report the AFM image of the sample G topography and in 10 (d) the near-field intensity distribution simultaneously collected, after the annealing process. As observable, the surface morphology mainly consists of two elongated structures with mean lateral dimensions $(3.6 \times 4.1) \mu\text{m}$, $(3.3 \times 8.3) \mu\text{m}$ and average height about $8.0 \mu\text{m}$ and $13.5 \mu\text{m}$ respectively. Moreover, it can be seen that the structures are formed by aggregating grains with mean lateral dimensions less than $1 \mu\text{m}$. From Fig. 10 (d), the strong modifications of the emergent near-field profile induced by the aforementioned morphology can be clearly appreciated. Also in this case we report the analysis of the distribution of the heights in the two images reported in Fig. 9 (c) and 10 (c). It was found: an average surface height of $4.431 \mu\text{m}$ and a RMS roughness of $1.313 \mu\text{m}$ before annealing; while an average surface height of $8.847 \mu\text{m}$ and a RMS roughness of $3.487 \mu\text{m}$ after annealing. In this case the RMS roughness after the annealing became almost three times higher.

As matter of fact, experimental results prove that thermal annealing could be usefully used to increase the crystalline degree of the deposited overlay and mainly to tailor the morphology of the final structure. However, results also show a strong dependence of the effects of the thermal annealing on the initial distribution and size of the particle layers obtained after the deposition stage. This means that the effectiveness of thermal annealing as post processing tool can be really exploited if a controlled particle layer distribution is obtained at the deposition time.

6. Environmental monitoring application

In this section, the experimental results demonstrating the high capability of the proposed near-field opto-chemical sensors to be exploited for a wide range of environmental monitoring applications are presented.

In particular, a comparison of the output signal variations of SnO_2 -based sensors characterized by unperturbed and highly perturbed near-field distributions are reported to demonstrate that the near-field enhancement effect is a key parameter in the optimization of the sensing performances.

The room temperature sensing performances were tested in air, against toluene and xylene vapors, and in water environment against aqueous ammonia.

6.1 Interrogation scheme

The optoelectronic architecture exploited for the interrogation of the proposed near-field fiber optic sensors is schematized in Fig. 11. It enables the continuous and real time monitoring of fiber-film reflectance changes occurring as a consequence of analyte interaction with the sensitive tin oxide overlays. It is simple to implement and requires just few widespread commercial and low-cost optoelectronic components while preserving excellent performances.

The sensitive layer was lighted by a pigtailed Superluminescent Light Emitting Diode (SLED) operating in one of the two main telecommunication wavelengths (1310 and 1550 nm). A source controller was used to keep the SLED at a constant temperature and feed it with an input current, which allowed the source to emit an optical power of few mW. This power was split by a 2×2 in-fiber directional coupler, providing the necessary connections between light source, sensing interface and two InGaAs photodiodes. The first photodiode is for the measurement of the reflected signal:

$$V_{signal} = k_1 \cdot Z_1 \cdot P_{source} \cdot R_{Film} \quad (3)$$

where P_{source} is the power emitted by the source, k_1 is a constant which takes account of the power losses due to the coupling factor of the 2x2 directional coupler and the photodiode responsivity, Z_1 represents a gain factor introduced by the first photoreceiver device, and R_{Film} is the fiber/film interface reflectance.

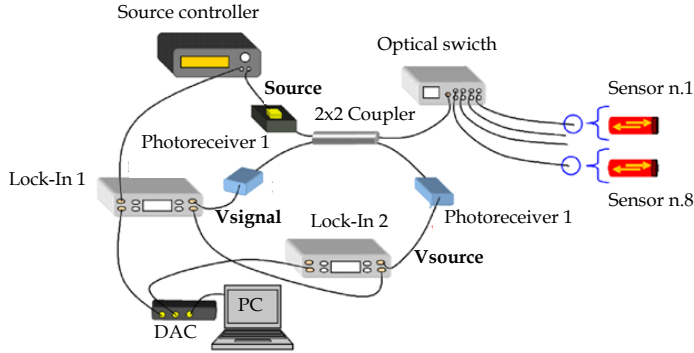


Fig. 11. Schematic illustration of the typical interrogation scheme.

The second arm of the 2x2 coupler was used to provide a valid intensity monitoring channel for the compensation of the sensor response. As matter of fact, the second photodiode provides a voltage signal directly related to the optical power levels within the optical chain according to:

$$V_{source} = k_2 \cdot Z_2 \cdot P_{source} \quad (4)$$

where k_2 ($k_2 \neq k_1$) takes into account the losses coming from the connection between source, 2x2 coupler and photodiode and Z_2 ($Z_2 \neq Z_1$) is a gain factor introduced by the second photoreceiver device. The intensity compensation was obtained by considering the ratio between the voltage signals at the two photo-receivers according to:

$$I = \frac{V_{signal}}{V_{source}} = \frac{k_1 \cdot P_{source} \cdot Z_1 \cdot R_{Film}}{k_2 \cdot Z_2 \cdot P_{source}} = \alpha \cdot R_{Film} \quad (5)$$

$$\alpha = \frac{k_1 \cdot Z_1}{k_2 \cdot Z_2} \quad (6)$$

where α defined by equation (6), takes into account all the set-up parameters. As evident, the normalized response of the sensor is only sensitive to the change in the reflectance induced by chemical sorption within the sensing overlay and not to the fluctuations of the optical power levels along the whole measurement chain. In the followings, the relative change of the sensor output $\Delta I/I_0$ has been considered (where I_0 is the output signal in the reference or initial condition), which, in turn, corresponds to the relative reflectance change occurring at the fiber-sensitive layer interface ($\Delta R/R_0$).

Synchronous detection was typically implemented to enhance the system performances, by amplitude modulating the light source at 500 Hz and retrieving the photodetector voltages by using a dual channel lock-in amplifier. In addition, a Time Division Multiplexing (TDM)

approach was typically exploited to perform the quasi-simultaneous interrogation of up to eight optical probes by means of a multi-channel fiber optic switch. Finally, the optical data were stored in a notebook controlling the sensing process in LabView software by a NI-DAQ card (Penza et al., 2004; Penza et al., 2005; Consales et al., 2007).

6.2 Detection of volatile organic compounds (VOCs) in air

In this section, the experimental results on the sensing capability in air environment of two previously characterized SnO₂-based probes (respectively sample E and sample G) are reported and compared (Buosciolo et al., 2008b). As observed in the previous sections, the two selected probes were characterized by very dissimilar overlay topographies and by different optical near-field behaviors reported in Fig. 8 (c), 8 (d), 10 (c) and 10 (d) respectively. This enabled a comprehension of the influence of the sensitive layer features on the chemical sensing performance.

The experimental measurements were conducted by adopting the experimental setup reported in Fig. 12. It was used to test the two selected sensors towards ppm concentrations of toluene and xylene vapors, at room temperature. In particular the two transducers were located in a properly designed test chamber characterized by a volume of approximately 1500 ml (Consales et al., 2006 a). The vapors of the analyte under testing were generated by the bubbling method and carried inside the chamber by dry air gas. Dry air was also chosen as reference gas. The total flow rate per exposure was held constant at 2000 ml/min, and controlled by a mass flow-meter driven by a controller-unit communicating with a PC via standard RS-485 serial bus. A thermo-hygrometer was also inserted inside the chamber in order to continuously monitor temperature and humidity variations of the test ambient.

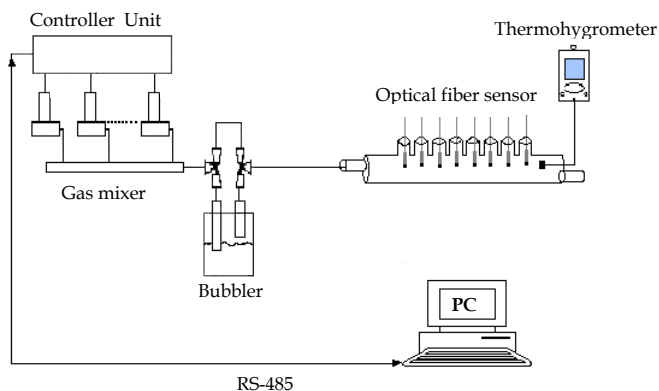


Fig. 12. Schematic representation of the experimental set-up exploited for chemical detection measurements in air, at room temperature.

In Fig. 13, we report the output signal variations (ΔI) demonstrated by the two near-field opto-chemical sensors E and G during the exposure to different pulses of xylene and toluene vapors at room temperature.

The analytes concentration ranged from 25 to 44 ppm and 40 to 83 ppm, respectively. The results revealed that significant variations of the overlay reflectance and thus of the sensors output ΔI occur as a consequence of the analyte molecules interaction with the SnO₂ particle

layer, demonstrating the surprising capability of the tested metal oxide based transducers of detecting few tens of ppm of the chosen chemicals at room temperature. This effect is especially evident for sample G which, as previously described, turned out to be characterized by the most pronounced modification of the optical near-field transmitted through the fiber coating. As matter of fact the signal changes in the case of the probe G are approximately of two orders of magnitude higher than the ones obtained for the counterpart sensor E.

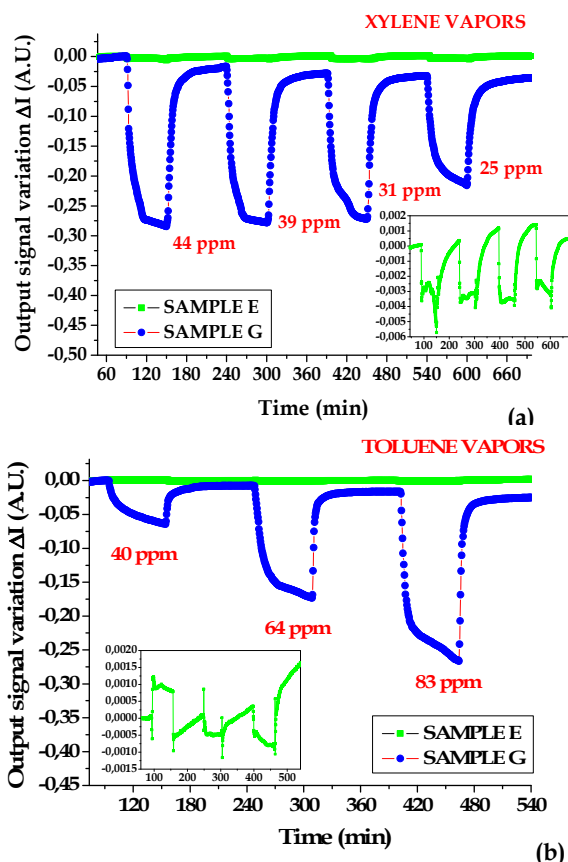


Fig. 13. Output signal variations (ΔI) occurred to the near-field opto-chemical sensors E and G upon the exposure to different concentration pulses of xylene (a) and toluene (b) vapors at room temperature. The insets report the responses of sensor E.

Very dissimilar response dynamics were also observed for the two sensors, with the sample E characterized by a faster response. This could be attributed to a different interaction with the selected chemical. Sample E also revealed to be less reliable than sample G, as demonstrated by the opposite in sign responses it exhibited upon the exposure to different toluene pulses (see inset in Fig. 13 (b)). In particular, with regards sample G, excellent sensitivities (calculated as output signal variation upon concentration unit) of $6.6 \cdot 10^{-3} \text{ ppm}^{-1}$

and $3.0 \cdot 10^{-3}$ ppm⁻¹ for xylene and toluene vapors, respectively, that lead to sub-ppm limits of detection, good and fast reversibility features as well as response times of approximately 25 and 35 minutes, respectively were obtained.

The excellent sensing capabilities of sensors G with respect to sample E can be explained by the fact that, optical probes coated by sensitive overlays with very rough morphologies are characterized by enhanced detection performance with respect to those based on almost flat SnO₂ overlays. As matter of fact, when the SnO₂ overlay surface exhibits microstructures able to strongly perturb the emergent optical field profile producing its local enhancement, the interaction of the field with the analyte occurs mainly on its surface by means of the evanescent part of the field. This is able to improve the performance of fiber optic sensors based on metal oxides since they rely mainly on surface interactions.

In conclusion, by properly tailoring the deposition parameters, different morphologies of the tin dioxide coatings can be obtained in order to suite the particular application. This particular feature allowed by the ESP method, together with the possibility to tailor the sensitivity and dynamics characteristics of the SnO₂-based SOF probes could be very useful in chemical sensing applications. In fact, the correlation between data collected from sensors coated by layers of the same materials exhibiting highly dissimilar characteristics could enhance the features extraction from a hybrid system by means of pattern recognition methods. Consequentially, this could allow to overcome the typical low-selectivity of the exploited sensitive materials towards a given chemical specie.

6.3 Detection of ammonia molecules in water

In this section, the experimental results on the sensing capability in water environment of two previously characterized SnO₂-based probes (respectively sample A and sample B) are reported and compared (Cusano et al., 2006; Consales et al., 2006b). As observed in the previous sections, the two selected probes were characterized by very dissimilar overlay topographies and by different optical near-field behaviors reported in Fig. 4 (a), 4 (b), 5(a) and 5 (b), respectively.

To this aim, the optoelectronic transducers in the reflectometric configuration have been inserted in a Pyrex beaker containing pure water, as reported in Fig. 14 (Pisco et al., 2005; Pisco et al., 2006).

The presence within the test ambient of ammonia molecules was promoted by its injection inside the beaker. The volume of an aqueous solution of ammonia was chosen, each time, in order to obtain the desired analyte concentration. In addition, after each ammonia exposure, the capabilities of the proposed SOF sensors to recover the initial steady state level were tested by restoring the initial condition of pure water. To this aim, pure water was continuously injected in the test chamber, while the contaminated water, previously present in it, contemporarily stilled out.

The two near-field opto-chemical sensors A and B were exposed to different concentration of ammonia in water ranging from 1 ppm to 12 ppm. In Fig. 15 are reported the results obtained from several testing performed on the probe sample A over a time interval of 1 month (Cusano et al., 2006).

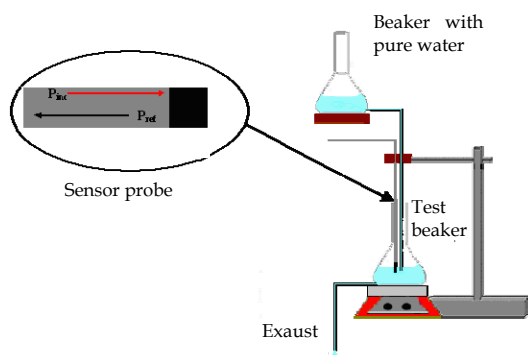


Fig. 14. Schematic view of the experimental set-up exploited for the in water chemical detection measurements.

In particular, Fig. 15 reveals that very different behaviors in the sensor response occur in the same test conditions. The change direction and amplitude as well as the response dynamics are strongly dissimilar during the testing carried out in different days using the same testing features. On the contrary, the results obtained by exposing the probe sample B to ammonia with repeated concentrations of 1 ppm and 5 ppm (reported in Fig. 16 (a)) were highly satisfactory.

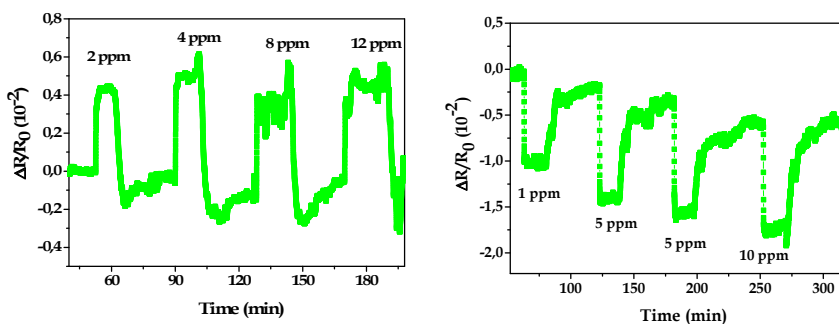


Fig. 15. Optical responses obtained with the probe sample A from several ammonia adsorption testing in water at room temperature.

In fact a good sensitivity was obtained (the resolution of the sensor was estimated to be approximately 80 ppb), together with fast response and recovery times (response time of 5 and 7 min and recovery times of 12 and 15 min were calculated for 1 and 5 ppm, respectively) as well as a good repeatability of the sensor response, as demonstrated by a repeatability error lower than the sensor resolution. The slight drift which can be observed on the steady state level of the sensor response is due to the thermal changes ΔT (also reported in Fig. 16 (a)) occurred inside the test chamber, since it is not perfectly thermostated.

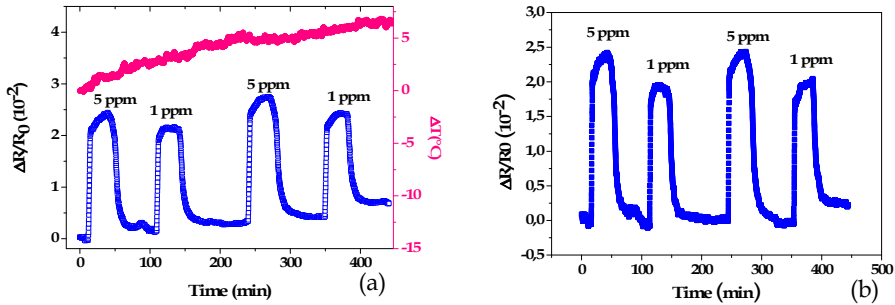


Fig. 16. Optical response obtained with the probe Sensor B in correspondence of four injections of ammonia, with repeated concentrations of 1ppm and 5ppm, and temperature changes ΔT occurred during the same testing (a), and sensor response after the temperature compensation procedure (b).

However this drift was been easily compensated by a proper compensation procedures employing an optical Fiber Bragg Grating temperature sensor, which was inserted inside the chamber or even integrated within the sensing fibers (Cusano et al., 2004). This is evident from the results shown in Fig. 16 (b), the response of the probe sample B after the compensation procedure has been reported, and shows that the drift previously observable on the signal baseline is totally compensated. In addition the probe sample B, differently from what happened with the probe sample A, demonstrated to be sufficiently reliable, since its stability in water was observed over the whole testing period of five weeks.

All the results obtained from the experimental measurements confirm the surprising potentiality of the proposed ammonia sensor and its feasibility to be used for water quality monitoring applications. Moreover, similarly to what happens for the detection in air, also in the case of water monitoring the SnO_2 layers topography and hence the near-field profile, strongly influences the sensor response, allowing to appropriately tailor the film features in order to obtain the best performances.

7. Conclusion

In conclusion, in this work, we demonstrated a novel technological platform for opto-chemical sensing employing particle layers of tin dioxide at wavelength scale with performances enhanced by the near-fields effects due to the confined domains of the layer. For the integration of the chemo sensitive layer onto fiber optic substrates, the ESP deposition technique has been selected providing a good balance between easily implementation and particle size and distribution control by acting on the processing parameters. In order to understand the influence of the film morphology on the optical field emerging from the film, AFM-SNOM characterization has been carried out revealing that layers with surface features of the order of the radiation wavelength demonstrated their capability to generate and to modify the optical near-field emerging from the overlay. From this phenomenon arise the excellent sensing performances of the SnO_2 -based transducers, as most of the interaction between the sensing coatings and analyte molecules

occurs on the layer surface by means of the evanescent wave, strongly enhanced by near-field effects. Also, we showed how by acting on the deposition parameters and by using post processing stages (such as thermal annealing), it is possible to modify the morphology of the sensitive overlay in terms of grain size, spacing and distribution.

It is important to note that significant margins exist for the improvements of this class of sensors especially after completing the investigation on the influence of process and post process variables (electric field, concentration, volume, deposition time, substrate deposition temperature) on the overlay morphology.

Also, an important step should be devoted to the identification of the correspondence morphology-near-field effects and its consequences on the sensing performance of the final device. Finally, it is important to remark that high sensitivity opto-chemical sensors employable in both air and aqueous environments with sub-ppm resolution have been demonstrated by using a simple and low cost fabrication method, also usable with other multifunction materials.

8. References

- Ansary, S. G.; Gosavi, S. W.; Gangal, S. A.; Karekar, R. N.; Aiyer, R. C. (1997). Characterization of SnO₂-based H₂ gas sensors fabricated by different deposition techniques. *Journal of Materials Science: Materials in Electronics*. Vol. 8, No. 1, (1997), 23–27.
- Arnold, M. S.; Avouris, P.; Pan, Z. W.; Wang, Z. L. (2003). Field-effect transistors based on single semiconducting oxide nanobelts. *Journal of Physical Chemistry B*, Vol. 107, (2003), 659-663.
- Baratto, C.; Comini, E.; Faglia, G.; Sberveglieri, G.; Zha, M.; Zappettini, A. (2005). *Sensors and Actuators B*, Vol. 109 (2005) 2–6.
- Barsan, N.; Schweizer-Berberich, M.; Gopel, W. (1999). Fundamental and practical aspects in the design of nanoscaled SnO₂ gas sensors: a status report. *Fresenius' Journal of Analytical Chemistry*, Vol. 365, (1999), 287–304.
- Becker, T.; Ahlers, S.; Bosh-v.Braunmuhl, C.; Muller, G., Kiesewetter, O. (2001). Gas sensing properties of thin- and thick-film tin-oxide materials. *Sensors and Actuators B*, Vol. 77, (2001), 55-61.
- Brattain, W.H.; Bardeen, J. (1952). Surface properties of germanium. *Bell System Technical Journal*, Vol. 32 (1952) 1.
- Buosciolo, A.; Consales, M.; Pisco, M.; Cusano A.; Giordano, M. (2008 b). Fiber Optic Near-Field Chemical Sensors Based on Wavelength Scale Tin Dioxide Particle Layers. *Journal of Lightwave Technology*, Vol. 26, No. 20, (October 2008), 3468-3475.
- Buosciolo, A.; Consales, M.; Pisco, M.; Cusano, A.; Giordano, M. (2008 a). Near-Field Fiber Optic Chemo Sensors. *Proceedings of the First Mediterranean Photonics Conference*, pp. 302-304, Ischia, Italy, June 2008.
- Buosciolo, A.; Pilla, P.; Consales, M.; Pisco, M.; Cutolo, A.; Giordano, M.; Cusano, A. (2006). Near Field Behaviour of SnO₂ Particle-layers Deposited on Optical Fibers: New Perspectives for Sensing Applications. *Technical Digest of 18th International Optical Fiber Sensors Conference*, Paper TuE77, Cancun, Mexico, October 2006.

- Chen, X. H. and Moskovits, M. (2007). Observing catalysis through the agency of the participating electrons: Surface-chemistry-induced current changes in a tin oxide nanowire decorated with silver. *Nano Letters*, Vol. 7, (2007), 807-812.
- Chen, P.; Shen, G.; Zhou, C. (2008). Chemical Sensors and Electronic Noses Based on 1-D Metal Oxide Nanostructures. *IEEE Transactions on Nanotechnology*, Vol. 7, No.6, (2008), 668-682.
- Cirera, A.; Cabot, A.; Cornet, A.; Morante, J.R. (2001). CO CH₄ selectivity enhancement by in situ Pd-catalysed microwave SnO₂ nanoparticles for gas detectors using active filter. *Sensors and Actuators B*, Vol. 78, (2001), 151- 160.
- Comini, E.; Faglia, G.; Sberveglieri, G.; Pan, Z. W.; Wang, Z. L. (2002). Stable and highly sensitive gas sensors based on semiconducting oxide nanobelts. *Applied Physics Letters*, Vol. 81, (2002), 1869-1871.
- Comini, E. (2008). Metal oxide nano-crystal for gas sensing. *Analytica Acta*, Vol. 568, (2008), 28-40.
- Comini, E.; Faglia, G.; Sberveglieri G. UV light activation of tin oxide thin films for NO₂ sensing at low temperatures. *Sensors and Actuators B*, Vol. 78, No. 1-3, (August 2001), 73-77.
- Consales, M.; Campopiano, S.; Cutolo, A.; Penza, M.; Aversa, P.; Cassano, G.; Giordano, M.; Cusano, A. (2006 a). Carbon nanotubes thin films fiber optic and acoustic VOCs sensors: Performances analysis. *Sensors and Actuators B*, Vol. 118, No. 1-2, (October 2006), 232-242.
- Consales, M.; Cutolo, A.; Penza, M.; Aversa, P.; Cassano, G.; Giordano, M.; Cusano, A. (2007 b). Carbon Nanotubes Coated Acoustic and Optical VOCs Sensors: Towards the Tailoring of the Sensing Performances. *IEEE Transactions on Nanotechnology*, Vol. 6, No. 6, (November 2007), 601-612.
- Consales, M.; Pisco, M.; Buosciolo, A.; Viter, R.; Smyntyna, V.; Cutolo, A.; Giordano M.; Cusano, A. (2007 a). High Sensitivity Near-Field Opto-Chemical Sensors Based on SnO₂ Particles Layers. *Proceedings of the Third European Workshop on Optical Fibre Sensors*, Vol. 6619, pp. 66191G1-G4, Naples, Italy, July 2007.
- Consales, M.; Pisco, M.; Pilla, P.; Cusano, A.; Buosciolo, A.; Giordano, M.; Viter, R.; Smyntyna, V. (2006 b). Influence of Layers Morphology on the Sensitivity of SnO₂-Based Optical Fiber Sensors. *Proceedings of 5th IEEE Conference on Sensors*, pp. 581-584, Daegu, Korea, October 2006.
- Cui, Y.; Wei, Q. Q.; Park, H. K.; Lieber, C. M. (2001). Nanowire Nanosensors for Highly Sensitive and Selective Detection of Biological and Chemical Species. *Science*, Vol. 293, (2001), 1289-1292.
- Cusano, A.; Consales, M.; Pisco, M.; Pilla, P.; Cutolo, A.; Buosciolo, A.; Viter, R.; Smyntyna V.; Giordano, M. (2006). Opto-chemical sensor for water monitoring based on SnO₂ particle layer deposited onto optical fibers by the electrospray pyrolysis method. *Applied Physics Letters*, Vol. 89, (September 2006), 111103 1-3.
- Cusano, A.; Pilla, P.; Consales, M.; Pisco, M.; Cutolo, A.; Buosciolo A.; Giordano, M. (2007). Near field behavior of SnO₂ particle-layer deposited on standard optical fiber by electrostatic spray pyrolysis method. *Optics Express*, Vol. 15, No. 8, (April 2007), 5136-5146.

- Cusano, A.; Persiano, G.V.; Russo, M.; Giordano, M. (2004). Novel optoelectronic sensing system for thin polymer films glass transition investigation. *IEEE Sensors Journal*, Vol. 4, No. 6, (December 2004), 837- 844
- Delpha, C.; Lumbreras, M.; Siadat, M. (2004). Discrimination and identification of a refrigerant gas in a humidity controlled atmosphere containing or not carbon dioxide: application to the electronic nose. *Sensors and Actuators B*, Vol. 98, (2004), 46-53.
- Eranna, G.; Joshi, B. C.; Runthala, D. P.; Gupta, R. P. (2004). Oxide Materials for Development of Integrated Gas Sensors - A Comprehensive Review. *Critical Reviews in Solid State and Materials Sciences*, Vol. 29, No. 3, (2004), 111-188.
- Faglia, G.; Baratto, C.; Sberveglieri, G.; Zha, M.; Zappettini, A. (2005). Adsorption effects of NO₂ at ppm level on visible photoluminescence response of SnO₂ nanobelts. *Applied Physics Letters*, Vol. 86, (2005), 011923.
- Fort, A.; Gregorkiewitz, M.; Machetti, N.; Rocchi, S.; Serrano, B.; Tondi, L.; Ulivieri, N.; Vignoli, V.; Faglia G.; Comini E. (2002). Selectivity enhancement of SnO₂ sensors by means of operating temperature modulation. *Thin Solid Films*, Vol. 418, No. 1, (October 2002), 2-8.
- Gardner, J.W.; Hines, E.L.; Tang, H.C. (1992). Detection of vapours and odours from a multisensor array using pattern-recognition techniques. Part II. Artificial neural networks, *Sensors and Actuators B*, Vol. 9, (1992), 9-15.
- Ghimbeu, C.M.; Van Landschoot, R.C.; Schoonman, J.; and Lumbreras, M. (2007) Preparation and characterization of SnO₂ and Cu-doped SnO₂ thin films using electrostatic spray deposition (ESD). *Journal of the European Ceramic Society*, Vol. 27, No. 1, (2007), 207-213.
- Gourari, H.; Lumbreras, M.; Landschoot, R.V. ; Schoonman, J. (1998). Elaboration and characterization of SnO₂-Mn₂O₃ thin layers prepared by electrostatic spray deposition. *Sensors and Actuators B*, Vol. 47, (April 1998), 189-193.
- Gourari, H.; Lumbreras, M.; Landschoot, R.V. ; Schoonman, J. (1999). Electrode nature effects on stannic oxide type layers prepared by electrostatic spray deposition. *Sensors and Actuators B*, 58 Vol. 1-3, (September 1999) 365-369.
- Heilig, A.; Barsan, N.; Weimar, U.; Gopel, W. (1999). Selectivity enhancement of SnO₂ gas sensors: simultaneous monitoring of resistances and temperatures. *Sensors and Actuators B*, Vol. 58, (1999), 302-309.
- Helwig, A.; Muller, G.; Sberveglieri, G.; Faglia, G. (2007). Gas response times of nano-scale SnO₂ gas sensors as determined by the moving gas outlet technique. *Sensors and Actuators B*, Vol. 126, (2007), 174-180.
- Higashiyama, Y.; Tanaka, S.; Sugimoto, T.; Asano, K.; (1999). Size distribution of the charged droplets in an axisymmetric shower. *Journal of Electrostatics*, Vol. 47, (1999), 183-195.
- Hong, H.K.; Kwon, C.H.; Kim, S.R.; Yun, D.H.; Lee, K.; Sung, Y.K. (2000). Portable electronic nose system with gas sensor array and artificial neural network. *Sensors and Actuators B*, Vol. 66, (2000), 49-52.
- Ihokura, K. (1981). Tin oxide gas sensor for deoxydising gases. *New Matter. New Processes in Electrochemical Technology*, Vol. 143 (1981).
- Ihokura, K.; Watson, J. (1994). *The stannic oxide gas sensor: principles and applications*. CRC Press, Boca Raton, ISBN 0849326044 (1994).

- Ivanov, P.; Llobet, E.; Vilanova, X.; Brezmes, J.; Hubalek, J.; Correig, X. (2004). Development of high sensitivity ethanol gas sensors based on Pt-doped SnO₂ surfaces. *Sensors and Actuators B*, Vol. 99, (2004), 201–206.
- Kolmakov, A.; Klenov, D. O.; Lilach, Y.; Stemmer, S.; Moskovits, M. (2005). Enhanced gas sensing by individual SnO₂ nanowires and nanobelts functionalized with Pd catalyst particles. *Nano Letters*, Vol. 5, (2005), 667–673.
- Law, M.; Kind, H.; Messer, B.; Kim, F.; Yang, P. D. (2002). Photochemical sensing of NO₂ with SnO₂ nanoribbon nanosensors at room temperature. *Angewandte Chemie-International Edition*, Vol. 41, (2002), 2405–2408.
- Lee, D.S.; Jung, J.K.; Lim, J.W.; Huh, J.S.; Lee, D.D. (2001). Recognition of volatile organic compounds using SnO₂ sensor array and pattern recognition analysis. *Sensors and Actuators B*, Vol. 77, (2001), 228–236.
- Lezec, H. J.; Thio, T. (2004). Diffracted evanescent wave model for enhanced and suppressed optical transmission through subwavelength hole arrays. *Optics Express*, Vol. 12, (2004), 3629–3651.
- Li, C.; Zhang, D. H.; Liu, X. L.; Han, S.; Tang, T.; Han, J.; Zhou, C. W. (2003). In₂O₃ nanowires as chemical sensors. *Applied Physics Letters*, Vol. 82, (2003), 1613–1615.
- Llobet, E.; Brezmes, J.; Vilanova, X.; Sueiras, J.E.; Correig, X. (1997). Qualitative and quantitative analysis of volatile organic compounds using transient and steady-state responses of a thick-film oxide gas sensor array. *Sensors Actuators B*, Vol. 41 (1997) 13–21.
- Lundstrom, I. (1996). Approaches and mechanisms to solid state based sensing. *Sensors and Actuators B*, Vol. 35–36, (1996), 11–19.
- Maffeis, T. G. G.; Owen, G. T.; Penny, M.W.; Starke, T. K. H.; Clark, S. A.; Ferkel, H.; Wilks, S. P. (2002). Nano-crystalline SnO₂ gas sensor response to O₂ and CH₄ at elevated temperature investigated by XPS. *Surface Science*, Vol. 520, (2002), 29–34.
- Matsui, Y.; Mitsuhashi, M.; Goto, Y. (2003). Early stage of tin oxide film growth in chemical vapor deposition. *Surface and Coatings Technology*, Vol. 169, (2003), 549–552.
- Matsushima, Y.; Nemoto, Y.; Yamazaki, T.; Maeda, K.; Suzuki, T. (2003). Fabrication of SnO₂ particle-layer on the glass substrate using electrospray pyrolysis method and the gas sensitivity for H₂. *Sensors and Actuators B*, Vol. 96, (May 2003) 133–138.
- Meyer, E.; Hug, H. J.; Bennewitz R. (2003). *Scanning probe microscopy: the lab on a tip*. Springer, ISBN 3540431802. Berlin.
- Ngo, K.A.; Lauque, P.; Aguir, K.(2006). Identification of toxic gases using steady state and transient responses of gas sensor array. *Sensor Materials*, Vol. 18 (2006) 251–260.
- Pan, Z.W.; Dai Z.R.; Wang, Z.L. (2001). Nanobelts of semiconducting oxides. *Science*, Vol. 291, (2001), 1947–1949.
- Panchapakesan, B.; Cavicchi, R.; Semancik, S.; DeVoe, D. L. (2006). Sensitivity, selectivity and stability of tin oxide nanostructures on large area arrays of microhotplates. *Nanotechnology*, Vol. 17, (2006), 415–425.
- Patil, P. S. (1999). Versatility of chemical spray pyrolysis technique. *Materials Chemistry and Physics*, Vol. 59, (February 1999), 185–198.
- Patil, P. S.; Kawar, R. K.; Seth, T.; Amalnerkar D. P.; Chigare, P.S. (2003). Effect of substrate temperature on structural, electrical and optical properties of sprayed tin dioxide (SnO₂) thin films. *Ceramics International*, Vol.20, No. 7, (2003), 725–734.

- Penza, M.; Cassano, G.; Aversa, P.; Antolini, F.; Cusano, A.; Cutolo, A.; Giordano, M.; Nicolais, L. (2004). Alcohol detection using carbon nanotubes acoustic and optical sensors. *Applied Physics Letters*, Vol. 85, No. 12, (September 2004), 2379 1-3.
- Penza, M.; Cassano, G.; Aversa, P.; Antolini, F.; Cusano, Consales, M.; Giordano, M.; Nicolais, L. (2005). Carbon nanotubes-coated multi-transducing sensors for VOCs detection. *Sensors and Actuators B*, Vol. 111-112, (November 2005), 171-180.
- Perednis D.; Gauckler L. J. (2005). Thin film deposition using spray pyrolysis. *Journal of Electroceramics*, Vol. 14, (2005), 103-111.
- Pink, H.; Treitinger, L.; Vité, L. (1980). Preparation of Fast Detecting SnO₂ Gas Sensors. *Japanese Journal of Applied Physics*, Vol. 19, (1980), 513-517.
- Pisco, M.; Consales, M.; Campopiano, S.; Viter, R.; Smyntyna, V.; Giordano M.; Cusano A. (2006). A novel opto-chemical sensor based on SnO₂ sensitive thin film for ppm ammonia detection in liquid environment. *Journal of Lightwave Technology*, Vol. 24, N. 12, (December 2006), 5000-5007.
- Pisco, M.; Consales, M.; Viter, R.; Smyntyna, V.; Campopiano, S.; Giordano, M.; Cusano, A.; Cutolo, A. (2005). Novel SnO₂ based optical sensor for detecting low ammonia concentration in water at room temperatures. *Semiconductor Physics, Quantum Electronics & Optoelectronics*, Vol. 8, No. 1, (2005) 95-99.
- Qian, L. H.; Wang, K.; Li, Y.; Fang, H. T.; Lu, Q. H.; Ma X. L. (2006). CO sensor based on Au-decorated SnO₂ nanobelt. *Materials Chemistry and Physics*, Vol. 100, (2006), 82-84.
- Ramamoorthy, R.; Kennedy, M. K.; Nienhaus, H.; Lorke, A.; Kruis, F. E.; Fissan, H. (2003). Surface oxidation of monodisperse SnO_x nanoparticles. *Sensors and Actuators B*, Vol. 88, (2003) 281-285.
- Rumyantseva, M. N.; Kovalenko, V. V.; Gaskova, A. M.; Pagnier, T. (2008). Metal-Oxide Based Nanocomposites as Materials for Gas Sensors. *Russian Journal of General Chemistry*, Vol. 78, No. 5, (2008), 1081-1092.
- Sberveglieri, G. (1995). Recent developments in semiconducting thin-film gas sensors. *Sensors and Actuators B*, Vol. 23, (1995) 103-109.
- Schweizer-Berberich, M.; Zdralek, M.; Weimar, U.; Gopel, W.; Vidal, T.; Martinez, D.; Peyre-Lavigne, A.; (2000). Pulsed mode of operation and artificial neural networks evaluation for improving the CO selectivity of SnO₂ gas sensors. *Sensors and Actuators B*, Vol. 65, (2000), 91-93.
- Seiyama, T.; Kato, A.; Fujushi, K.; Nagatani, M. (1962). A new detector for gaseous components using semiconductive thin films. *Analytical Chemistry*, Vol. 34, (1962), 1502f.
- Setaro, A.; Bismuto A.; Lettieri S.; Maddalena P.; Comini E.; Bianchi S.; Baratto C.; Sberveglieri G. (2008). Optical sensing of NO₂ in tin oxide nanowires at sub-ppm level. *Sensors and Actuators B*, Vol. 130, (2008), 391-395.
- Sysoev, V. V.; Button, B. K.; Wepsoec, K.; Dmitriev, S.; Kolmakov, A. (2006). Toward the nanoscopic "electronic nose": Hydrogen vs. carbon monoxide discrimination with an array of individual metal oxide nano- and mesowire sensors. *Nano Letters*, Vol. 6, (2006), 1584-1588.
- Szklarski, Z. (1989). Thin oxide films as gas sensors. *Thin Solid Films*, Vol. 174, (1989), 269-275.
- Taguchi, N. (1962). Japanese Patent, S45-38200, (1962).

- Wan, Q.; Huang, J.; Xie, Z.; Wang, T.; Dattoli, E. N.; Lu, W. (2008). Branched SnO₂ nanowires on metallic nanowire backbones for ethanol sensors application. *Applied Physics Letters*, Vol. 92, (2008), 102101-102103.
- Watson, J. (1984). The tin oxide gas sensor and its applications. *Sensors and Actuators B*, Vol. 5, (1984), 29-42.
- Watson, J.; Ihokura K.; Colest, G.S.V. (1993). The tin dioxide gas sensor. *Measurement Science and Technology*, Vol. 4, (1993), 711-719.
- Yamazoe, N.; Kurokawa, Y.; Seiyama T. (1983). Effects of additives on semiconductor gas sensors. *Sensors and Actuators B*, Vol. 4, 283-289.
- Yamazoe, N. (1991). New approaches for improving semiconductor gas sensors. *Sensors and Actuators B*, Vol. 5, (1991), 7-19.
- Yu, C.; Hao, Q.; Saha S.; Shi, L.; Kong, X.; Wang, Z. L. (2005). Integration of metal oxide nanobelts with microsystems for nerve agent detection. *Applied Physics Letters*, Vol. 86, (2005), 063101-063103.
- Zaouk, D.; Zaatar, Y.; Khoury, A.; Llinares, C.; Charles, J.-P.; Bechara, J. (2000). Electrical and optical properties of pyrolytically electrostatic sprayed fluorine-doped tin-oxide: dependence on substrate-temperature and substrate-nozzle distance. *Journal of Applied Physics*, Vol. 87, No. 10, (May 2000) 7539-7543.
- Zhang, Y.; Kolmakov, A.; Chretien, S.; Metiu H.; Moskovitz, M. (2004). Control of Catalytic Reactions at the Surface of a Metal Oxide Nanowire by Manipulating Electron Density Inside It. *Nano Letters*, Vol. 4, No. 3, (2004), 403-407.

Electric field sensing schemes using low-coherence light and LiNbO_3 electrooptical retarders

Celso Gutiérrez-Martínez

*Instituto Nacional de Astrofísica, Óptica y Electrónica (INAOE)
México*

1. Introduction

Electric fields sensing and measurement of high and low intensity fields coming either from natural phenomena, or from human activities is an important subject as it impacts the daily activities in industrial and commercial environments around the world. Static and dynamic electric fields are produced by different sources including electric power equipment, power generation and distribution facilities, high voltage transmission lines, telecommunication equipments, electromagnetic interference, human medical signals, etc. The detection and measurement of electric fields are important tasks as they are related to safety of equipments and personnel and even health of people.

More common electric field meters use conductive electrodes linked by cables to the measuring electronics and very often such arrangements distort the unknown field. Different techniques and apparatus for the measurement of either extremely high or extremely low electric fields are reported in the technical literature (Johnston et al, 1986; Kirkham, 2006).

Using optical techniques are very promising and are being explored, aiming to minimize distortion and interference on electric field measurements. Optical techniques use light to sense electric fields taking advantage of their interaction in electro-optic crystals. Additionally, as the optical techniques disturb minimally the electric fields and are inherently immune to electromagnetic interference, a wide variety of electric field sensing schemes using electro-optic devices have been tested up to date. Most of such schemes use the Pockels effect either in bulk or in integrated optics Lithium Niobate (LiNbO_3) devices. Polarization and Mach-Zehnder interferometers are being used as electric field sensors.

Sensor devices either using electrodes or electrode-less can be studied and integrated on sensing schemes. Using electrodes on the sensing devices gives a high sensitivity but the main disadvantage is that the electrodes may disturb the measured electric field. Such schemes are very well adapted to measure low intensity electric fields (mV/m to hundreds V/m) as found in telecommunication systems and electronic apparatus (Meier et al, 1994; Rao et al, 1999; Yim et al, 1998; Lee et al, 2006). Electrode-less sensors disturbs minimally the measured field but the sensitivity is relatively low and such devices are better adapted to

the measurement of high intensity fields ranging from some kV/m to hundreds of kV/m (4 to 2000 kV/m), as found in natural lightning strikes, high power electrical facilities and high voltage transmission lines (Johnston et al, 1986; Kirkham, 2006).

In an electric field sensing scheme based on the electro-optic interaction between light, the electric field modulates the intensity of an optical beam passing through an electro-optic bulk crystal or optical waveguide. The modulated light can be transmitted through optical fiber channels or even over free space optical links.

Optical intensity modulators can be implemented by two-wave interferometers such as polarization or Mach-Zehnder. Mach-Zehnder modulators have been widely studied and reported as electric field sensors based on intensity modulation of light (Meier et al, 1994; Rao et al, 1999; Yim et al, 1998; Lee et al, 2006; Hidaka and Fujita, 1982; Naghski et al, 1994; Cecelja et al, 2001).

In an alternative approach, electric fields can be sensed by schemes associating low-coherence optical sources and electro-optical polarization interferometers, which in this case, introduce optical delays. The sensed electric field modulates an optical delay, instead of the optical intensity. The modulation of optical delays is well known as optical coherence modulation (Delisle & Cielo, 1975; Brooks and Wentworth, 1985; Chu & Dickey, 1991; Bock & W. Urbanczyk, 2000).

In coherence modulation of light, electric fields are imprinted on light as a sequence of optical delays, provided they are greater than the coherence time of the optical source. Coherence modulation of light uses electro-optic retarders and practical realizations are based on lithium niobate (LiNbO₃) electro-optic technology (Porte & Goedgebuer, 1992; Gutiérrez-Martínez et al, 1995). A sensing scheme can be implemented using fiber optics components and electrode-less LiNbO₃ electro-optic retarders. The demodulation of the sensed electric field is realized directly by scanning Michelson interferometry or by a fiber or integrated optics two-wave interferometer, when sensor and demodulator are matched at the same optical delays.

Electric field sensing implementation using coherence modulation of light is described in this chapter. Experiments of sensing high intensity and wide band electric fields, using electrode-less optically matched electro-optical retarders are described. Electric field detection using such a technique has been previously reported describing the detection of 60 Hz electric fields (Rodríguez-Asomoza & Gutiérrez-Martínez, 2001; Gutiérrez-Martínez et al, 2002; Gutiérrez-Martínez & Santos-Aguilar, 2004). Wider band, up to 20 kHz has been also was successfully tested by detecting high intensity electric fields, ranging from 20 to 350 kVpp/m [22-23](C. Gutiérrez-Martínez et al, 2007; Gutiérrez-Martínez & Santos-Aguilar, 2008).

A very attractive feature of coherence modulation is that it allows serial or parallel multiplexing of optical delays (Goedgebuer et al, 1987; Goedgebuer & Hamel, 1987; Gutiérrez-Martínez et al, 1997.) and, from this fact, multi-point sensing arrays can be proposed. Serial coherence multiplexing can be a promising technique in fibred schemes for distributed sensing arrays as several optical delays can be cascaded over a single optical channel.

2. Coherence modulation operating principle

To recall the operating principle, the block diagram of an integrated optics electric field sensor system, based on coherence modulation of light, is shown in figure 1. The system includes a low-coherence optical source, an electro-optic sensor (optical retarder), an optical fiber channel and a receiver module, which is implemented by a second optical retarder (either integrated optics or a fiber passive interferometer) as coherence demodulator, and a photo-detector.

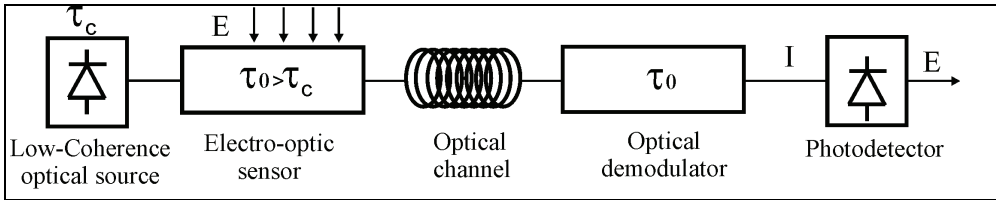


Fig. 1. Electric field sensor system using coherence modulation of light

According to the block diagram, light coming from a low-coherence optical source is injected into the electro-optic sensor, which introduces an optical delay τ_0 , greater than the source coherence time τ_c . In this model, when low-coherence light $s(t)$ is delayed, the light at the output of the optical retarder is given as (Gutiérrez-Martínez, 1994)

$$s_o(t) = \frac{1}{2}s(t) + \frac{1}{2}s(t - \tau_0) \quad (1)$$

The detected optical intensity at the output of the demodulator is now

$$\begin{aligned} I_m &= \langle s_o^*(t)s_o(t - \tau_0) \rangle = \frac{1}{4}|s(t)|^2 + \frac{1}{4}|s(t - \tau_0)|^2 + \frac{1}{4}\{\langle s(t - \tau_0)s^*(t) \rangle + \langle s^*(t - \tau_0)s(t) \rangle\} \\ &= \frac{1}{2}P_0 + \frac{1}{2}\text{Re}\{G(\tau_0)\} \end{aligned}$$

P_0 is the average optical power from the source and $G(\tau_0)$ is the autocorrelation function.

The transmitted optical intensity for the normalized real part of $G(\tau_0)$ is given as

$$I_m = \frac{P_0}{2} \left\{ 1 + |g(\tau_0)| \cos\left(2\pi \frac{1}{\lambda_0} v \tau_0\right) \right\} \quad (2)$$

λ_0 is the center optical wavelength and v is the light propagation velocity.

From expression (2), one finds that optical interference will exist on depending on the superposition of two delayed waves, in the range of the optical coherence, e.g. when the optical delay is shorter than the coherence time or equivalently, when the optical path-difference (OPD), is shorter than the coherence length. As the optical delay is longer than the coherence time, the optical interference disappears and the optical intensity becomes $\frac{P_0}{2}$,

figure 2.

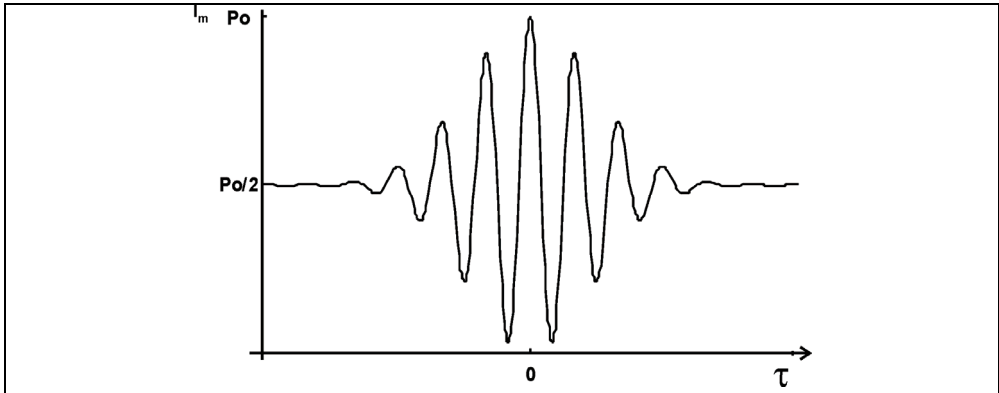


Fig. 2. Transmitted optical intensity from an optical retarder.

An optical delay can be dynamically modulated by an information signal thus becoming an optical information carrier. The modulated signal is centered on a static optical delay (or optical path-difference) and the modulation process is optimal when the static delay is longer than the coherence time.

As shown in figure 1, the demodulation process can be achieved using the same operating principle; e. g. by introducing a second optical delay or optical path-difference (OPD), which is matched to the same value on the first retarder (modulator). Such a situation allows that the two delayed waves interfere mutually. When detecting the optical interference, a photodetector delivers an average optical power.

The optical signal from the electrooptic sensor can be expressed as

$$s_o(t) = \frac{1}{2}s(t - \frac{\tau_0}{2}) + \frac{1}{2}s(t + \frac{\tau_0}{2}) \quad (3)$$

If the optical demodulator introduces a second delay τ_d ; its output optical signal $s_d(t)$ is

$$s_d(t) = \frac{1}{2}s_o(t - \frac{\tau_d}{2}) + \frac{1}{2}s_o(t + \frac{\tau_d}{2}) \quad (4)$$

The detected optical intensity at the output of the demodulator is now

$$\begin{aligned} I_d &= \langle s_d^*(t)s_d(t) \rangle \\ &= \left\langle \left[\frac{1}{2}s_o^*(t - \frac{\tau_d}{2}) + \frac{1}{2}s_o^*(t + \frac{\tau_d}{2}) \right] \left[\frac{1}{2}s_o(t - \frac{\tau_d}{2}) + \frac{1}{2}s_o(t + \frac{\tau_d}{2}) \right] \right\rangle \\ &= \frac{P_0}{4} + \frac{P_0}{4}g(\tau_0) + \frac{P_0}{4}g(\tau_d) + \frac{P_0}{8}g(\tau_d - \tau_0) + \frac{P_0}{8}g(\tau_d + \tau_0) \end{aligned} \quad (5)$$

The detected optical intensity can be expressed in terms of the optical path-differences $d = v\tau_d$, $d_{m0} = v\tau_0$; v is the light propagation speed and as $g(\tau_0) \approx 0$, such an intensity becomes

$$I_d(d) = \frac{1}{4}P_0 + \frac{P_0}{4}g(d) + \frac{P_0}{8}g(d - d_{m0}) + \frac{P_0}{8}g(d + d_{m0}) \quad (6)$$

Eq. 6 represents the autocorrelation function of the delayed light, showing the fringe pattern at the output of the optical demodulator when the optical path difference is scanned between $-d_{m0}$ through $+d_{m0}$, as depicted in figure 3.

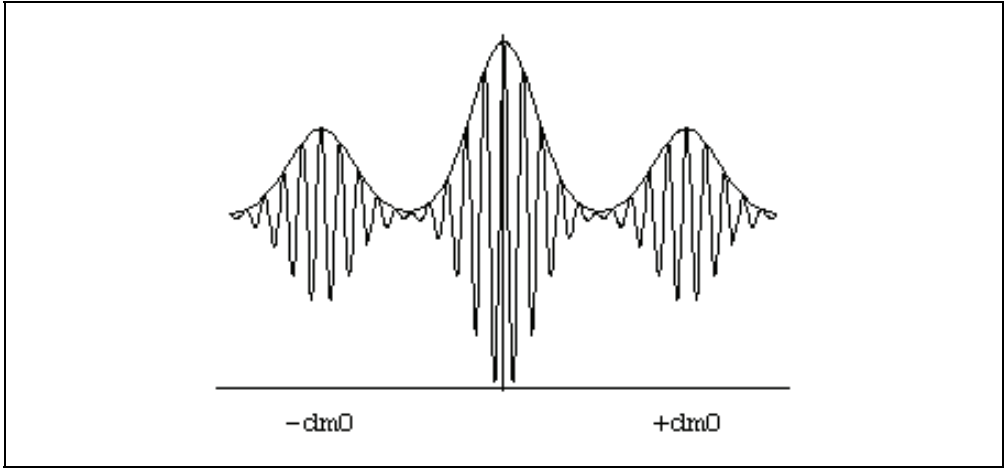


Fig. 3. Autocorrelation of the detected light at the output of the optical demodulator

Based on the previously described operating principle, an information signal can be transmitted using the optical path-difference $d_m = d_{m0} + \Delta d(t)$, as a modulated carrier. To recuperate the information, the optical demodulator will be tuned to $d \cong d_{m0}$.

$$I_d(d \cong d_{m0}) = \frac{1}{4}P_0 + \frac{P_0}{4}g(d_{m0}) + \frac{P_0}{8}g(d_{m0} - d_{m0}) + \frac{P_0}{8}g(d_{m0} + d_{m0})$$

Finally, as $d_{m0} \gg l_c$, the detected optical intensity at the output of the coherence demodulator is

$$I_d(d \cong d_{m0}) = \frac{1}{4}P_0 + \frac{P_0}{8}g(d_{m0} - d_{m0} - \Delta d(t)) \quad (7)$$

An electric signal $E(t)$ can modulate the optical path-difference and, at the demodulator, the electric field can be detected as an intensity variation on the autocorrelation of the received light. The variation is the strongest when the optical path-differences on the modulator and the demodulator are perfectly matched.

The modulated optical path-difference is

$$d_m = d_{m0} + KE(t) \quad (8)$$

d_{m0} is the static optical path-difference, $KE(t)$ is the dynamic variation by the electric field and K is the modulator sensitivity. The electric field is recuperated by matching the static path-differences at d_{m0} .

$$I_d = \frac{P_0}{4} + \frac{P_0}{8}g(d_{m0} - d_{m0} + KE(t))$$

If $KE(t) \ll d_{m0}$, then from eq. 2, $g(d_{m0} - d_{m0} + KE(t)) = |g(0)|\cos(2\pi \frac{1}{\lambda_0} KE(t))$ and as $|g(0)| = 1$,

$$I_d = \frac{P_0}{4} + \frac{P_0}{8}\cos(2\pi \frac{1}{\lambda_0} KE(t)) \quad (9)$$

The dynamic variation on the detected optical intensity is depicted by figure 4.

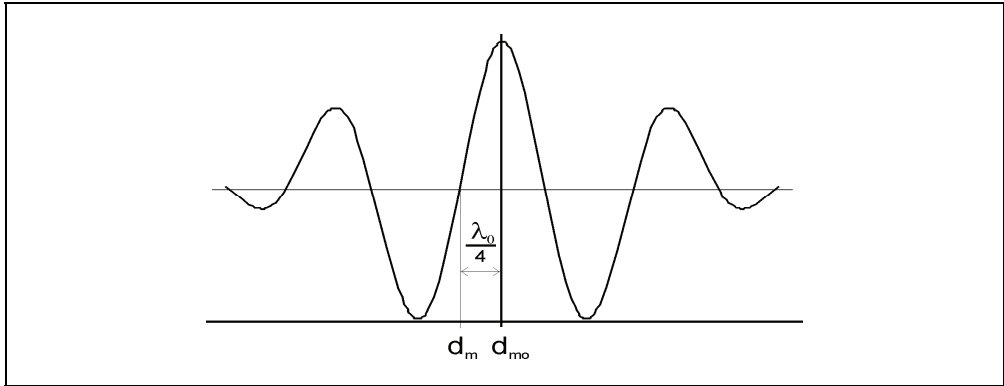


Fig. 4. Intensity variation at the output of the matched optical demodulator

As shown in figure 4, a linear detection of the modulating electric field can be achieved by shifting the static optical path-difference to

$$d_m = d_{m0} - \frac{\lambda_0}{4} + KE(t) \quad (10)$$

Eq. 10 can be substituted in Eq. 9, giving

$$I_d = \frac{P_0}{4} + \frac{P_0}{8} \cos\left(\frac{2\pi}{\lambda_0} KE(t) - \frac{\lambda_0}{4}\right) \quad (11)$$

Or, equivalently

$$I_d = \frac{P_0}{4} \left[1 + \frac{1}{2} \sin\left(2\pi \frac{1}{\lambda_0} KE(t)\right) \right] \quad (12)$$

The range between the maximum and minimum of I_d determines the half-wave voltage

$$E_\pi = \frac{\lambda_0}{2K}$$

Eq. 12, becomes then

$$I_d = \frac{P_0}{4} \left[1 + \frac{1}{2} \sin\left(\frac{\pi}{E_\pi} E(t)\right) \right] \quad (13)$$

Now when $E(t) \ll E_\pi$

$$I_d = \frac{P_0}{4} \left[1 + \frac{1}{2} \frac{\pi}{E_\pi} E(t) \right] \quad (14)$$

When $E(t)$ is small, the detected optical intensity is linear around $d_{m0} \pm \frac{\lambda_0}{4}$.

The generation of optical delays can be achieved by means of two-wave interferometers such as Michelson, Mach-Zehnder and polarization (Gutiérrez-Martínez, 1994).

The Michelson interferometer, consists of two mirrors, which are illuminated by a split optical beam coming from the same optical source. The mirrors are placed at distances

d_1 and d_2 from the beam splitter. If v is the light propagation velocity, the optical delay is $\tau = \frac{2(d_2 - d_1)}{v}$.

The Mach-Zehnder interferometer consists of two mirrors and two optical splitters. Light follows two separate identical paths. One path is modified by an optical slab of thickness e and refractive index n_e , thus introducing an optical delay $\tau = \frac{2(n_e - 1)e}{v}$.

The polarization interferometer consists of a birefringent optical waveguide, exhibiting ordinary n_o and extraordinary n_e refractive index and length L . The optical waveguide is located between optical polarizers. The introduced optical delay is given as

$$\tau = \frac{(n_o - n_e)L}{v}.$$

In the remainder of this chapter, polarization interferometers are the main studied devices. Such devices can be easily implemented either by birefringent optical waveguides or polarization maintaining optical fibers (PMF), although autocorrelation of light and measurement of optical path-differences are easily realized by scanning Michelson interferometry.

3. Coherence modulation based on LiNbO₃ electrooptic crystals and waveguides.

In coherence modulated schemes, light emitting diodes (LED), superluminescent diodes (SLD) and multi-longitudinal laser diodes (MLLD), are well adapted as those devices provide low coherence light. The optical delays are easily generated by lithium niobate (LiNbO₃) electro-optic waveguides, acting as polarization interferometers. Such devices generate static optical delays (or equivalently, optical path-differences, OPD's), which can be modulated by an electric field. The optical retarders often used are Z-cut Y-propagating LiNbO₃ birefringent optical waveguides, which introduce optical delays as 45° polarized light is projected in orthogonal propagating modes TE and TM (Rodríguez-Asomoza & Gutiérrez-Martínez, 2001). Such modes travel in the waveguide at different velocities, as determined by the ordinary and extraordinary refractive index difference $(n_o - n_e)_g = 0.083$ at $\lambda_0 = 1310$ nm. An optical waveguide acting as an optical retarder (coherence modulator) is depicted in figure 5.

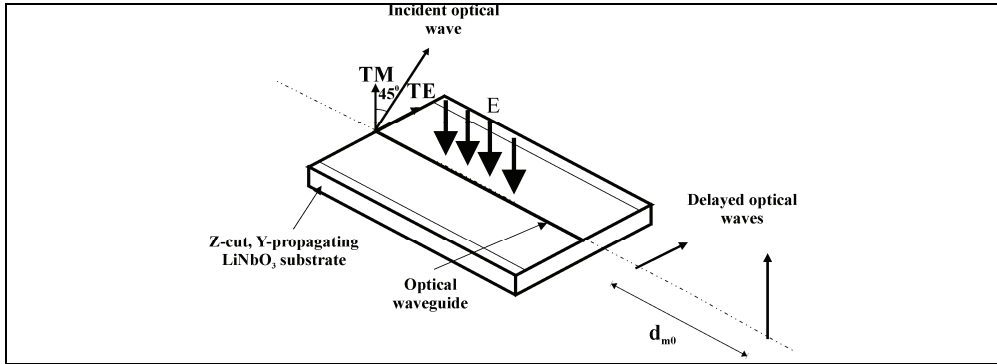


Fig. 5. An integrated optics LiNbO₃ optical retarder

In agreement to the theoretical principles in the previous section, the optical delay between the orthogonal waves TE and TM is given as

$$\tau_0 = \frac{(n_o - n_e)_g L}{v}$$

L is optical waveguide length and v is the light propagation velocity in the waveguide. The corresponding static OPD is then

$$d_{m0} = \tau_0 v = (n_o - n_e)_g L \quad (15)$$

When an electric field $E_z(t)$ is sensed by the coherence modulator, it induces a dynamic variation $\Delta d(t)$ on the optical path-difference. On a z-cut LiNbO₃ birefringent waveguide, the electric field is oriented on the Z-axis of the crystal, taking advantage of the linear electro-optic coefficients r_{13} and r_{33} . The time-varying optical path-difference is then given as

$$d_m(t) = d_{m0} + \Delta d(t) \quad (16)$$

From expression (14), $\Delta d(t) = \frac{\lambda_0}{2} \frac{E_z(t)}{E_\pi}$, E_π is the half-wave electric field given as

$$E_\pi = \lambda_0 / \left(r_{33} n_e^3 \Gamma_{TM} - r_{13} n_o^3 \Gamma_{TE} \right) L \quad (17)$$

According to expression (17), L represents the interaction length between the electric field and the optical wave, r_{13} and r_{33} are the electro-optic coefficients, Γ_{TE} and Γ_{TM} are the electric-optical overlapping coefficients and λ_0 is the center wavelength of the optical source. The half-wave electric field depends mainly on the length of the electro-optics sensor. A basic sensing scheme based on matched optical path-differences and coherence modulation of light is shown in figure 6.

In this scheme, the electric field sensor is an optical waveguide on an LiNbO₃ electrooptic crystal. The sensed electric field is imprinted in the optical path-difference given by eq. (16). The optical signal is transmitted through the optical channel. The coherence demodulator is a two-wave interferometer which will introduce a second optical path-difference. The modulating electric field will be recuperated when the path-differences are optically matched. The coherence demodulator can be implemented either by a second optical

waveguide or by a fiber passive interferometer. This last device is easily implemented by segments of polarization-maintaining fiber (PMF).

At the output of the optical demodulator, in agreement to expression 6, optical interference exists when the optical path-differences are matched.

$$I_r(d_{m0}) = \frac{P_0}{4} + \frac{P_0}{8} g(d_{m0})$$

And from expression 13, the optical intensity is given as

$$I_r(t) = \frac{P_0}{4} + \frac{P_0}{8} \text{sen}\left(\pi \frac{E_z(t)}{E_\pi}\right)$$

Additionally, if $E_z(t) \ll E_\pi$, from eq. 14, the measured optical power is

$$Pr(t) = \frac{P_0}{4} \left(1 + \frac{\pi E_z(t)}{2 E_\pi}\right) \quad (18)$$

This last expression represents an intensity modulation and the electric field is then detected as a linear variation of the received optical power.

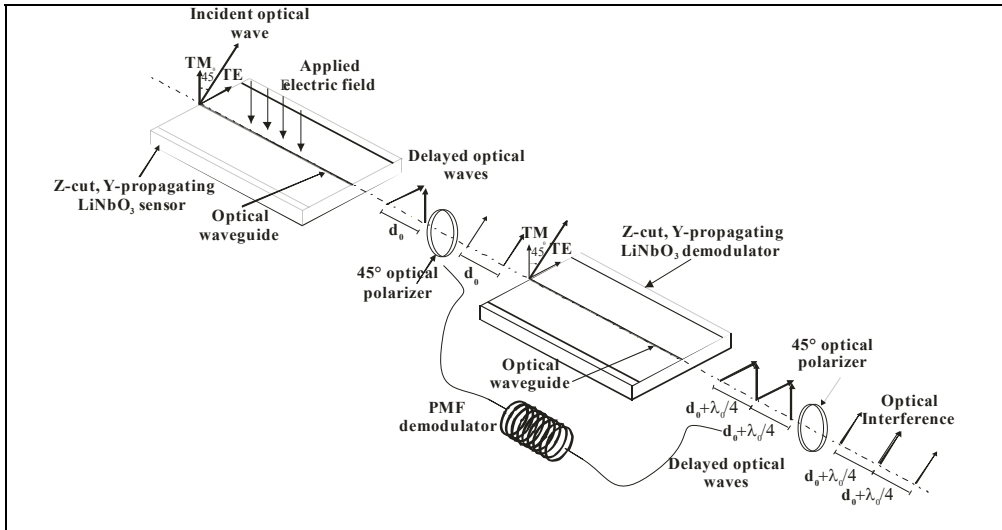


Fig. 6. Optical matching in an electric field sensing scheme.

4. Electrooptic sensors characterization

4.1 Optical Transfer Function and half-wave electric field

The optical transfer function of an LiNbO₃ sensor relates the optical output power and the sensed electric field. The transfer function is determined by sensing DC electric fields, which modulate the light traveling through the sensing optical waveguide, as shown in figure 7.

When the optical waveguide is used as a dielectric sensor, no electrodes are associated to the crystal and the electric field is present in the dielectric environment surrounding it (most commonly air $\epsilon_r = 1$).

The uniform electric field E_1 , in the air, finds a boundary condition and hence a discontinuity on the surface of the electro-optic sensor. The discontinuity is determined by the crystal permittivity, $\epsilon_r = 35$ (Gutiérrez-Martínez & Santos-Aguilar, 2008). As the electric field is perpendicular to the crystal surface and considering the boundary conditions, the optical waveguide senses a uniform electric field E_2 , given as (Ulaby, 2000).

$$E_2 = \frac{\epsilon_{r1}}{\epsilon_{r2}} E_1 \tag{19}$$

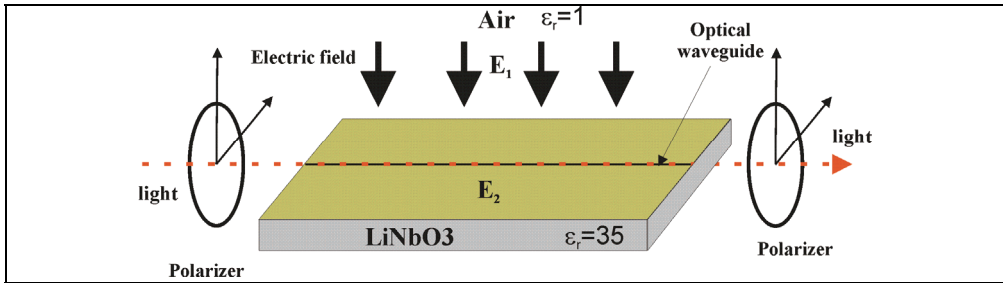


Fig. 7. Polarization interferometer as electric field sensor

After sensing-detection, the electro-optic transfer function given by eqs. 18 and 19, becomes

$$Pr(t) = \frac{P_0}{4} \left(1 + \frac{\pi E_2}{2 E_\pi} \right) \tag{20}$$

From eq. 17, the half-wave electric fields (E_π), for $L=10, 30$ and 60 mm LiNbO₃ electrooptic sensors, at $\lambda_0=1310$ nm, are = 430, 144 and 72 kVpp/m, respectively.

The optical transfer function for a 36 mm LiNbO₃ sensor has been calculated and measured at the output of the coherence demodulator for a DC electric field ranging between 0-330 kVpp/m. The optical transfer function is shown in figure 8.

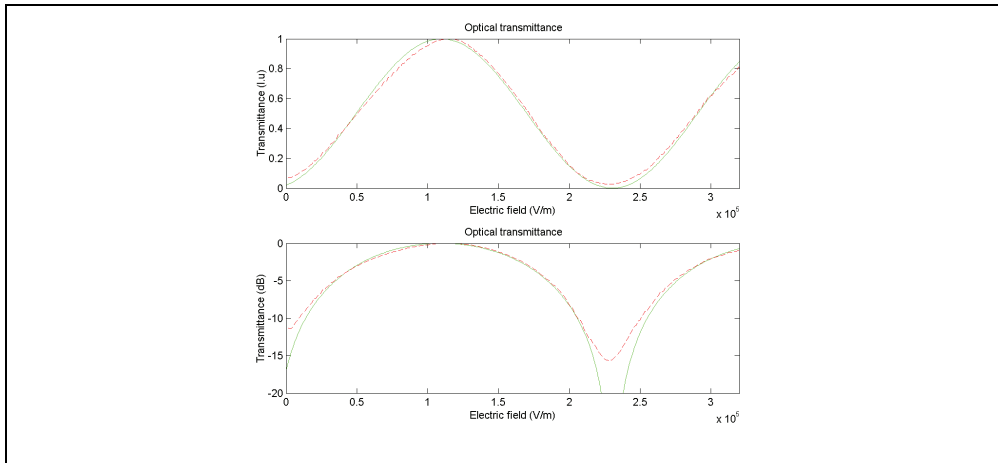


Fig. 8. Theoretical and measured optical transfer function of a 36 mm electrooptic sensor

In this figure, the upper graph shows a continuous curve corresponding to linear-scale measurement; the theoretical optical transfer is shown in dashed lines. The lower graph shows the transfer function in logarithmic scale. The measured half-wave electric field is of about 112 kVpp/m, in good agreement to the theoretical 120 kVpp/m, given by eq. 17. On the linear-scale, the optical transfer function shows a sinusoidal shape in agreement to eq. 13 and the regions of linear response can be identified. A first linear region is around 50 KV/m; a second one is at around 175 kVpp/m and so on. Linear sensing of electric fields can be considered, depending on the field intensity ranges.

4.2 Optical correlation and path-differences

To implement a coherence modulation electric field sensing system, the static optical path-differences of coherence modulators and demodulators, must be firstly determined. A straightforward way to measure the optical autocorrelation and optical path-differences is by using a Scanning Michelson Interferometer (SMI) (Gutiérrez-Martínez et al, 2000), figure 9(a).

The measurement set-up is based on a super-luminescent diode (SLD) exhibiting a coherence length of about 60 μm . The electric field sensor is an LiNbO₃ coherence modulator. The SMI measures the autocorrelation of the transmitted light. The light is photodetected, amplified and the output voltage, corresponding to the received optical intensity, is digitized for further data processing. Figure 9(b) shows the auto-correlation fringe pattern of a coherence electrooptic sensor exhibiting a static optical-path-difference $d_0 = 1.57$ mm, corresponding to a physical length of 19 mm. The SMI can itself, be useful to detect a sensed electric field when adjusting it to the sensor optical path-difference.

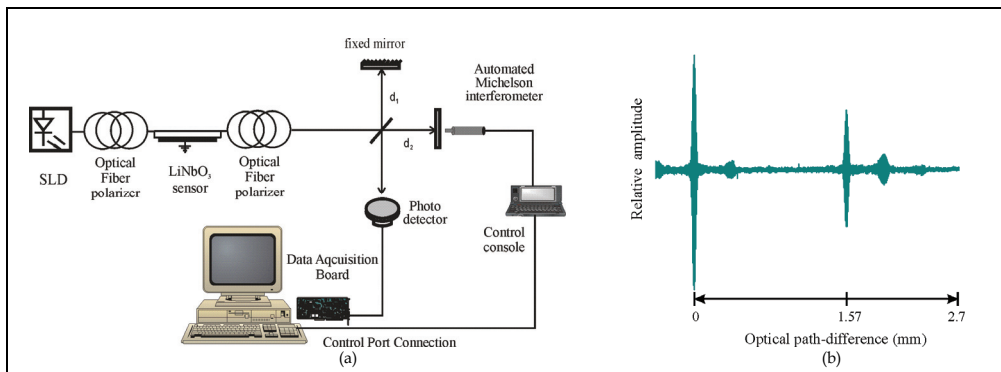


Fig. 9. Measurement of optical autocorrelation and path-differences.

5. Implementing experimental electric field sensing schemes

In the frame of this chapter, the implementation of an experimental electric field sensing scheme is described in this section, figure 10.

The experimental system includes a super-luminescent diode (SLD), emitting at $\lambda_0 = 1310$ nm, with a coherence length of about 60 μm and an average emitted power of 500 μWatts . The electric field sensor is a fiber pigtailed Z-cut Y-propagating LiNbO₃ integrated optics

coherence modulator, which introduces a static OPD d_{m0} . The optical demodulator has been implemented in two ways:

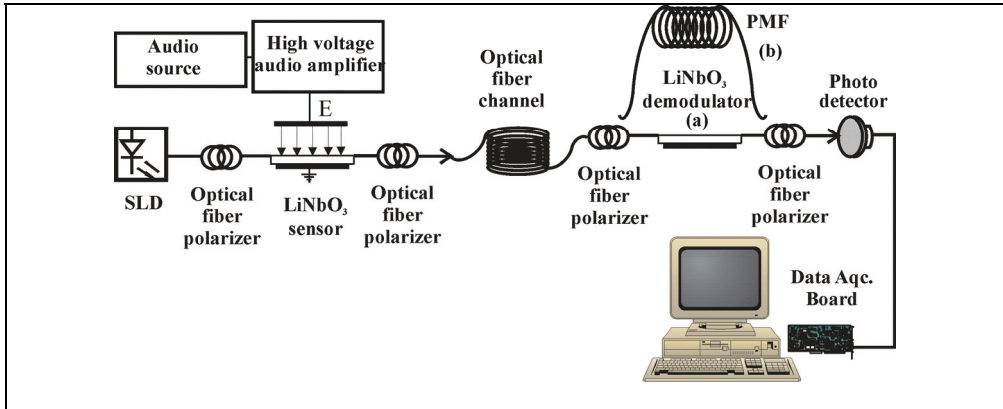


Fig. 10. Experimental electric field sensing system.

1. A pigtailed electro-optic birefringent optical waveguide, acting as a two-wave interferometer, matched to the sensor's OPD, insert (a) in figure 10.
2. An all fiber two-wave interferometer, implemented using polarization maintaining optical fiber (PMF), also matched to the electro-optic sensor, insert (b) in figure 10.

The 45° optical fiber polarizers ensure the propagation of TE and TM optical modes on the electro-optic birefringent waveguides, thus introducing OPD's.

A 700 m-optical fiber channel completes the experimental set-up.

To implement the electric field sensing system, the static optical path-differences of the coherence sensor and the optical demodulators were measured.

In a first case, two identical 13 mm-length birefringent optical waveguides were used. As it can be observed on figure 11(a), the electro-optic crystals exhibit identical static optical-path-differences around $d_{m0} = 1$ mm. The figure shows the overlapping of the OPD's on the sensor and demodulator crystals, when both devices are cascaded and the transmitted light is measured by a scanning Michelson Interferometer. Figure 11(b) corresponds to a second case, when an LiNbO₃ sensor (13.2 mm-length), is matched to a PMF two-wave interferometer. The fiber interferometer has been implemented using 3.45 m of 3M FS-CG-6121 PMF. In this second case, the optical path-difference is of about $d_{m0} = 1.1$ mm and the crystal and fiber demodulator are also well matched. A main advantage, when using a PMF demodulator, is that the photodetected signal is stronger, thus ensuring a higher signal to noise ratio. To achieve a linear detection of the optical signal, the demodulators (electrooptic crystal and PMF) were designed to introduce an OPD ($d_{m0} \pm \frac{\lambda_0}{4}$); however, ($\frac{\lambda_0}{4} = 325$ nm) is a very small length and it is difficult to define it accurately when constructing and polishing the crystal or fiber optical faces.

After setting-up the two electro-optic sensor schemes, figures 11(a) and 11(b) show the measured matched OPD's. As it can be observed, the electro-optic sensors exhibit static optical-path-differences around $d_{m0} = 1$ and 1.1 mm, respectively. A zoom of the

interference fringes around 1 mm gives a more accurate measurement, thus confirming that interference exists only in the range of the coherence length of the optical source and ensuring the demodulation of the sensed electric field. This represents an unequal feature of the implemented sensing schemes.

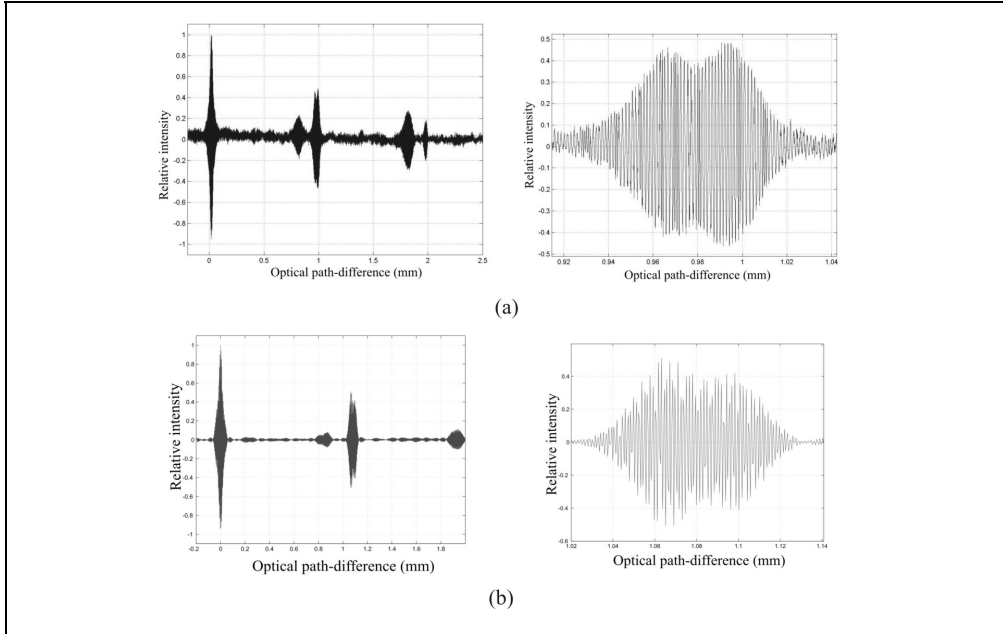


Fig. 11. Matched optical path differences: (a) LiNbO₃ electro-optic sensor and LiNbO₃ optical demodulator; (b) LiNbO₃ electro-optic sensor and PMF two-wave interferometer demodulator.

5.1 A wideband sensing scheme

To test the sensing scheme, a first experiment consisted in applying sinusoidal electric fields to the coherence electro-optic sensor, in a frequency band up to 20 kHz. The modulated light was then transmitted through the 700 m optical fiber channel. At the receiver, light was measured by the electro-optic coherence demodulator, already tuned around the static optical path-difference of 1 mm. The frequency response of the sensing scheme was limited by the bandwidth of a wide-area photodetector to 20 kHz. Such a response was measured resulting flat in the frequency range as depicted on figure 12(a). The electric field was generated by a signal generator and then amplified to a high voltage, which was applied to two parallel plates, not in contact with the electro-optic sensor, in order to generate a uniform electric field. A sinusoidal AC electric field, ranging between 10 and 350 kV_{pp}/m was measured. The field sensing-detection process shows a good linearity in the range of 10-350 kV_{pp}/m, as shown in figure 12(b).

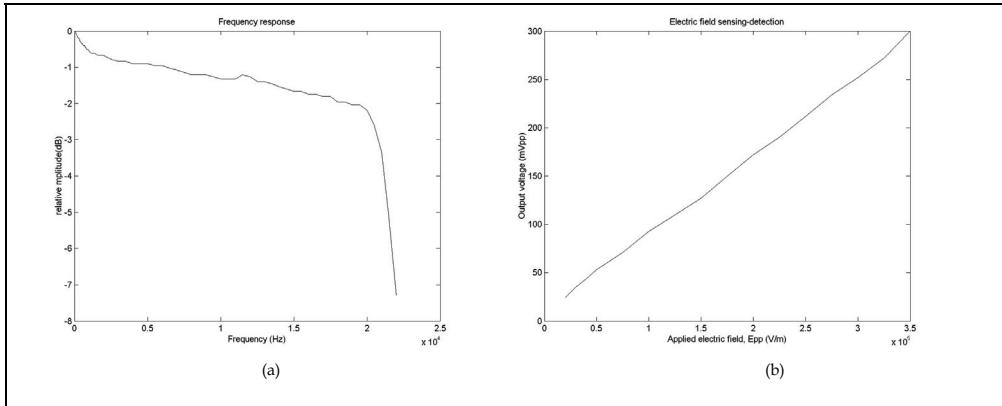


Fig. 12. Frequency response of the electric field sensing scheme.

To illustrate the operation of the experimental set-up, high-intensity electric fields of different frequencies were measured. Figure 13 illustrates the input and output waveforms for electric fields of 200 kVpp/m and 100 Hz and 20 kHz respectively. In figure 13, the input signal corresponds to a 200 kVpp/m electric field and the output signal level is of 200 mVpp. The noise level is of about 2mVpp. The signal to noise ratio (SNR) of the recuperated signal corresponding to a 200 kVpp/m was better than 30 dB.

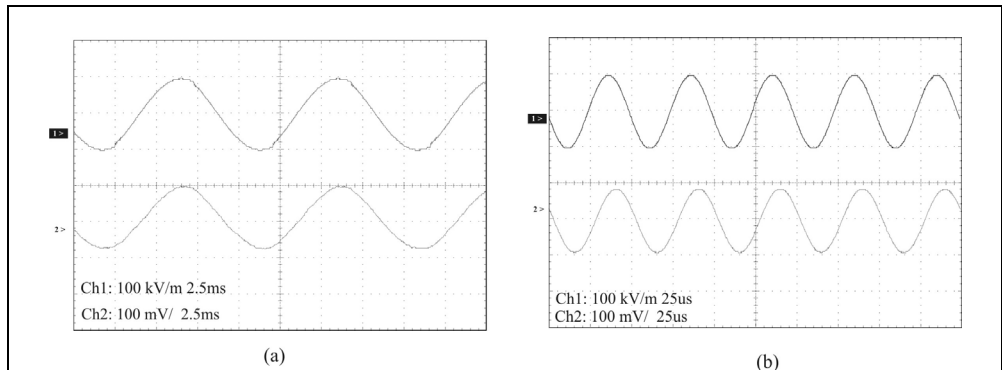


Fig. 13. Detected electric fields: (a) 100 Hz, 200 kVpp/m; (b) 20 KHz, 200 kVpp/m.

The minimum detected electric field was determined experimentally by decreasing the intensity of the sensed electric field. As given by expression 17, the half-wave electric field depends on the length of the electrooptic sensor. A longer sensor will be more sensitive and the minimum detected field will be lower. Figure 14 depicts measurements for two crystal lengths; figure 14(a) shows the minimum detected signal for a 13 mm length sensor when an 18 kVpp/m electric field is sensed. For comparison, 14(b) shows the recuperated signal for the same applied electric field when using a 36 mm sensor. These measurements indicate that for same sensed electric field, the sensitivity of the shorter sensor is significantly lower

than for the longer one; this is concluded by comparing the recuperated amplitude in both cases (14 mVpp and 60 mVpp, respectively), which corresponds to a ratio of about 13 dB.

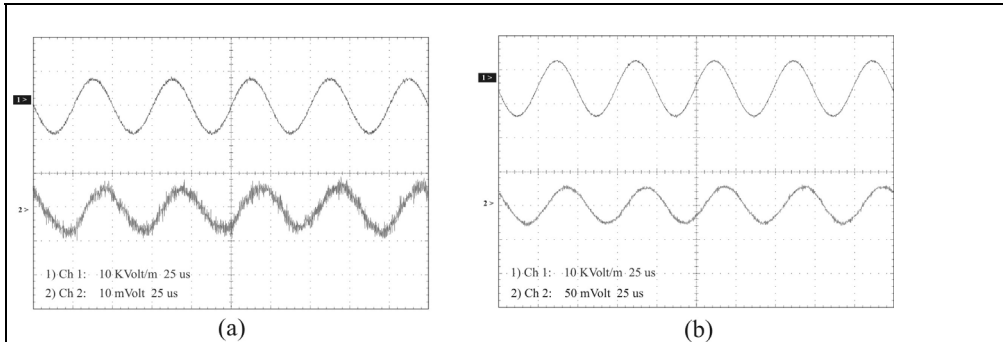


Fig. 14. Comparative sensitivities for two different lengths crystal sensors: (a) 13 mm; (b) 36 mm

5.2 Coherence multiplexed electric field sensing schemes

To explore novel applications of electro-optic sensors and coherence modulation of light, in this section an experimental coherence-multiplexed electric field sensing system using LiNbO₃ electro-optic coherence is described. A serial coherence multiplexed architecture seems attractive as the scheme uses only one optical source and the multi-channel optical signal is transmitted through a single optical fiber. Such a simple scheme can be proposed for a distributed electric field sensing array. A serial coherence multiplexed sensing array is shown in figure 15.

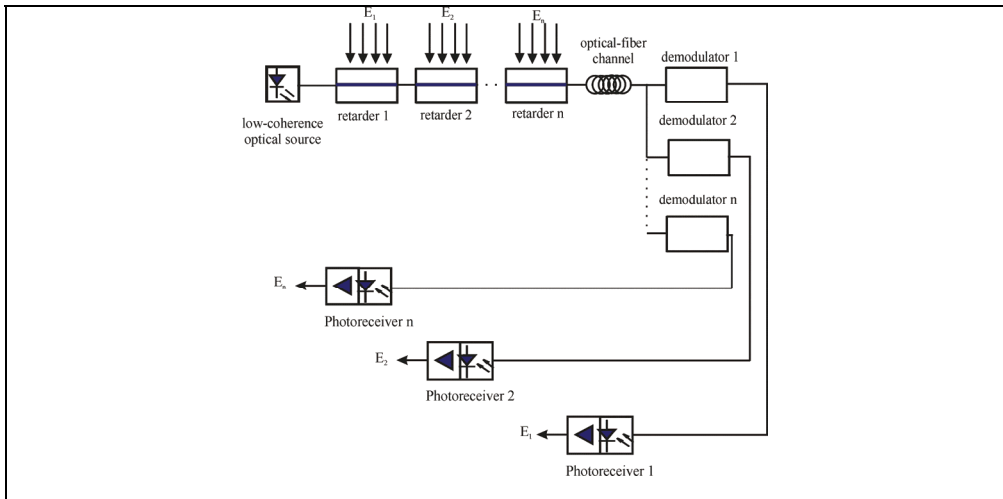


Fig. 15. Serial coherence multiplexed sensing array

The coherence modulated system described here represents an alternative to the classic

optical intensity measurement techniques and is additionally attractive as it can be used to implement serial coherence multiplexed sensor arrays, using only one optical source and a single optical channel.

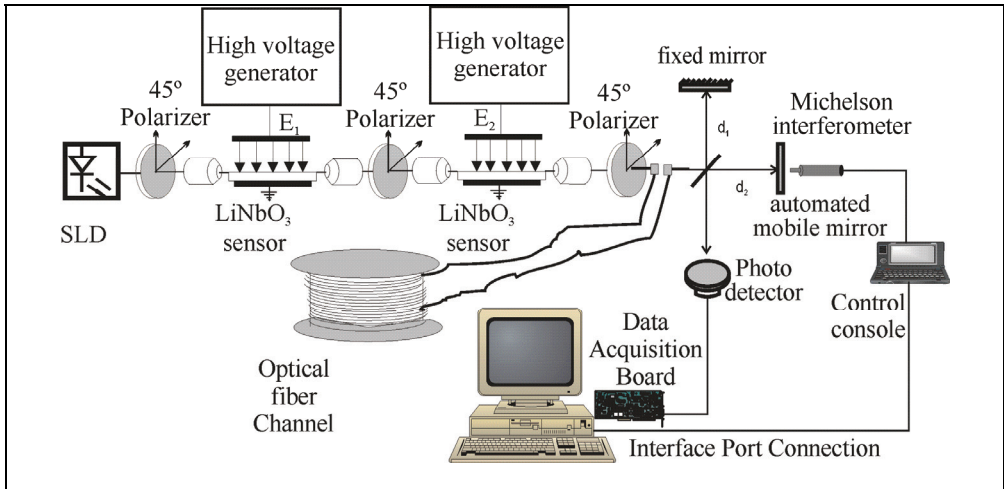


Fig. 16. Experimental two-channel coherence multiplexed electric field sensing scheme.

On the sensing side, light coming from the low-coherence optical source is injected into the first optical sensor, which introduces a first OPD. As explained before in this chapter, OPD's are generated by LiNbO₃ electro-optic sensors. The output of the first sensor becomes the input of the second one. At the output of the second stage, light exhibits two successive OPD's, that are modulated by two different electric fields.

For a two-channel transmission scheme (Goedgebuer et al, 1987; Gutiérrez-Martínez et al, 2002), from expression 1, the optical signal at the output of the first sensor introducing an optical delay τ_{01} , is given as

$$S_{m1}(t) = \frac{1}{2} s\left(t - \frac{\tau_{01}}{2}\right) + \frac{1}{2} s\left(t + \frac{\tau_{01}}{2}\right) \quad (21)$$

$s(t)$ is the low coherence optical signal coming from the SLD.

The optical signal given by expression 21, is the input to the second sensor, which introduces a second optical delay τ_{02}

$$S_{m2}(t) = \frac{1}{4} \left\{ s\left(t - \frac{\tau_{01}}{2} - \frac{\tau_{02}}{2}\right) + s\left(t - \frac{\tau_{01}}{2} + \frac{\tau_{02}}{2}\right) + s\left(t + \frac{\tau_{01}}{2} - \frac{\tau_{02}}{2}\right) + s\left(t + \frac{\tau_{01}}{2} + \frac{\tau_{02}}{2}\right) \right\} \quad (22)$$

At the output of the coherence demodulator (the Michelson interferometer), which introduces an optical delay τ , the received optical signal is

$$S_r(t) = \frac{1}{4} \left[S_{m2}\left(t - \frac{\tau}{2}\right) + S_{m2}\left(t + \frac{\tau}{2}\right) \right]$$

The corresponding detected optical intensities at the output of each channel are respectively

$$I_{r1, r2} = \langle S_{r1, r2}^*(t) S_{r1, r2}(t) \rangle$$

Finally, after some cumbersome mathematics, the detected optical intensities I_{r1} or I_{r2} , at the output of each channel, in terms of OPD's, are given as

$$I_{r1,r2}(d) = \frac{I_0}{16} \left[1 + g(d) + \frac{1}{2}g(d \pm d_{m01}) + \frac{1}{2}g(d \pm d_{m02}) + \frac{1}{4}g(d \pm (d_{m02} - d_{m01})) + \frac{1}{4}g(d \pm (d_{m02} + d_{m01})) \right] \quad (23)$$

I_0 is the average power of the optical source, d_{m01} and d_{m02} are the static OPD's for channels 1 and 2, $g(\bullet)$ is the normalized auto-correlation of the received optical field and $I_{r1,2}(d)$ are the received optical intensities at the output of the corresponding channels 1 or 2. Expression 23 represents a group of fringe patterns $g(d)$, located along the OPD axis. It can be observed that fringe patterns are located around zero, $\pm d_{m01}$, $\pm d_{m02}$, etc. As the optical path-differences d_{m01} and d_{m02} are greater than the coherence length l_c of the optical source, no interference occurs between the optical delays and a serial coherence-multiplexing process has been achieved. At the receiver, when the coherence demodulator is matched to each electrooptic sensor, only $g(d \pm d_{m01})$ or $g(d \pm d_{m02})$, will remain.

For implementing the two channel sensing scheme, the static optical path-differences of the coherence sensors were firstly measured. Figure 17(a) shows the auto-correlation fringe patterns of the cascaded coherence modulators. According to the LiNbO₃ crystal lengths, the introduced OPD's are of $d_{m01} = 1.53$ mm and $d_{m02} = 2.34$ mm. These OPD's are modulated by the sensed electric fields. The electric fields can be detected at the receiver by adjusting the Michelson interferometer at OPD's $d_1 = (d_{m01} - \frac{\lambda_0}{4})$ and $d_2 = (d_{m02} - \frac{\lambda_0}{4})$. For a dynamic test of the sensing scheme, steady 60-Hz sinusoidal electric fields were generated and applied to the electro-optic sensors. The modulated light was transmitted through the 700 m optical fiber channel. The received light was then measured by the Michelson interferometer when adjusted in the linear region around the static optical path-differences.

The applied field was varied in the range 100-250 kVpp/m and in all cases, linear detection was achieved. Figure 17(b), illustrates the form of a 250 kVpp/m applied electric field and it also shows the detected voltages, which correspond to the detected electric field on each sensor channel. No cross-talk was observed between the two channels, as ensured by the continuous spectrum and low-coherence SLD optical source.

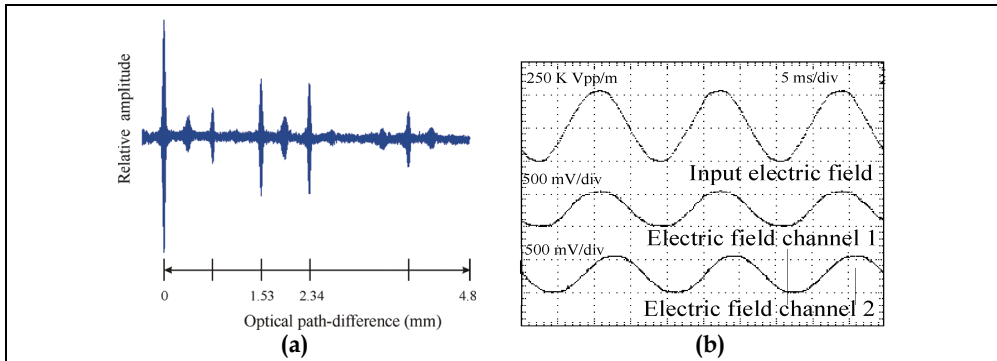


Fig. 17. Experimental two-channel coherence multiplexed electric field sensing scheme.

6. Wide-Band Electric Field Sensing

The frequency response of the studied electric field sensing schemes, is determined by the modulation sensitivity of the LiNbO₃ sensor, which depends on its high relative permittivity $\epsilon_r = \sqrt{\epsilon_{13}\epsilon_{33}} = 35$, $\epsilon_{13} = 44$ and $\epsilon_{33} = 28$. As it has been well established on theoretical and experimental work (Kaminow & Liu, 1963; Rigrod & Kaminow, 1963; Nash & Smith, 1968; Chen, 1978), the frequency response will depend on the nature of the interaction between the electric and optical fields. If the electric field is applied via lumped electrodes, by using parallel plates, the frequency response is a trade-off of the optical-electrical interaction length, in this case the crystal length L , as given by

$$f_m \cdot L = \frac{c}{\pi \sqrt{1 + \frac{\sqrt{\epsilon_{13}\epsilon_{33}}}{2}}} \quad (24)$$

Such a response is equivalent to around 2.2 GHz-cm.

Sensing high frequency electric fields is an important issue, as a lot of human activities are related to the generation, transmission and use of electromagnetic energy. In electric power facilities, telecommunications, medicine, etc., electric fields are present and under particular circumstances they can become harmful for equipments, facilities, operators and users. High frequency electric fields are attracting attention as their effects on security and health are no yet well known.

Research in progress aims to sense multi-MHz electric fields using coherence electrooptic sensors. In the previous section of this chapter, 20 KHz electric field sensing has been described. However, sensing schemes for high intensity fields in frequencies up to 10 MHz, are being studied. In a recent experiment, a dynamic 0-1 MHz signal has been generated by a video high voltage amplifier, producing an electric field adapted to the sensing range in the linear regions of the previously described schemes. The experimental set-up has already been tested for signals up to some hundreds of KHz. Measurements of 50 and 100 KHz electric fields are shown in figures 18 (a) and (b). The upper signal in each figure corresponds to the input signal to the wide band amplifier. The lower curve corresponds to the sensed electric field at the output of an available 100 KHz-bandwidth photoreceiver.

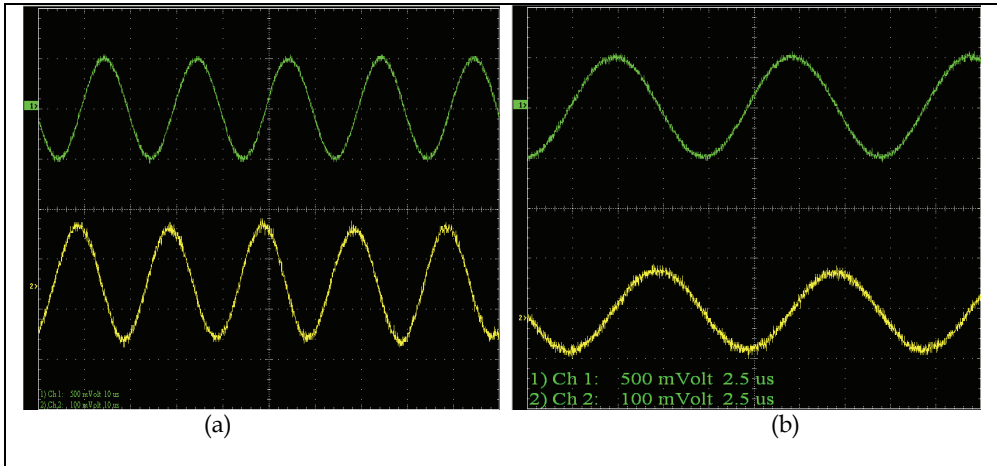


Fig. 18. Sensing wide-band electric fields (a) 50 KHz; (b) 100 KHz.

The electric field range in these first results is of about 50 kVpp/m. Work is in progress for optimizing high-sensitivity photoreceivers for detecting video signals in the range of some tenths of MHz.

7. SNR performance

An important parameter for evaluating the electric field sensing system performance is the signal to noise ratio (SNR), which determines the minimum detectable electric field. The SNR is limited by noise (spontaneous beat, thermal and shot) at the photodetection process (Derickson, 1998; Killen, 1991; Hall, 1973).

At the receiver, the instantaneous photodetected current is of the form

$$I(t) = RP_r(1 + m \cos \omega mt) \quad (25)$$

$R = \frac{\eta q}{h\nu}$ is the optical responsivity ($\eta = 0.7$) is the quantum efficiency, q is the charge unit, h is the Planck constant and ν is the optical frequency; P_r is the received optical power and m is the modulation index ($m = \frac{\pi E_{z0}}{2E\pi}$).

The total photodetected current can be expressed as

$$I = I_{dc} + I_p(t) \quad (26)$$

$I_{dc} = RP_r$ is the average photocurrent and $I_p(t)$ is the signal current with mean square value $\langle I_p^2 \rangle = \frac{1}{2} m^2 R^2 P_r^2$.

The overall SNR is then given as

$$SNR = \frac{\langle I_p^2 \rangle}{RIN \bullet R^2 P_r^2 B + 2qI_{dc}B + \frac{4kTB}{Re}} \quad (27)$$

In this expression, $RIN \bullet R^2 P_r^2 B$ corresponds to the beat noise power, $2qI_{dc}B$ is the shot noise power and $\frac{4kTB}{Re}$ is the thermal noise power. RIN is the relative intensity noise of the optical source, k is the Boltzmann constant, T is the absolute temperature, B is the electrical bandwidth and Re is the equivalent load resistance of the photodetector.

To evaluate the SNR, the three main noises are considered. The beat noise, related to RIN, comes from the incoherent optical source whereas the shot and thermal noise are associated to the photodetection process (Derickson 1998; Killen, 1991; Andonovic & Uttamchandani, 1989; Baney et al, 1994; Baney & Sorin, 1995; Obarski & Hale, 1999).

In our experimental sensing schemes, the noise sources are related to the characteristics of the optical source, the photodetector and the associated electronic amplifier. The optical source is a broadband SLD, emitting a gaussian spectrum centered at $\lambda_0 = 1310$ nm and spectral width $\Delta\lambda = 60$ nm. The received average optical power is of about $0.5 \mu\text{W}$ and the electrical bandwidth on the photoreceiver is $B = 20$ KHz. After the theoretical basis, such a gaussian optical source will exhibit a maximum $RIN = \frac{0.66}{\Delta\nu}$. $\Delta\nu = \frac{c\Delta\lambda}{\lambda_0^2}$ being the optical

bandwidth. For the SLD the RIN is of about -132 dB/Hz. This corresponds to a spontaneous beat noise power of about -188 dBm. A similar calculation, regarding the shot noise power, gives -176 dBm.

When supposing that our system is only shot noise limited, the signal to noise ratio is

$$SNR = \frac{\eta m^2 P_r}{2h\nu B}$$

The minimum detectable external electric field is obtained when $SNR = 1$.

$$E_{z \min} = \varepsilon r \frac{4}{\pi} \sqrt{\frac{2h\nu B}{\eta P_r}} E_\pi \text{ (Vpp/m)} \quad (28)$$

From this expression, for an LiNbO_3 sensor crystal of 13 mm in length and permittivity $\varepsilon r = 35$, the minimum detected external electric field, in agreement to expression 19, is of about 2 kVpp/m. For a crystal of 35 mm and the same optical parameters, the minimum detected field is of 0.7 kVpp/m. This theoretical calculation shows that sensitivity on the electrooptic sensors, depends strongly on the crystal dimensions. The longer crystals will present lower half-wave electric fields and hence higher sensitivities. In practical applications, the longest crystals are of around 75 mm (3 inches), limited by the size of LiNbO_3 commercial wafers.

8. Conclusion

Optical coherence modulation of light using LiNbO_3 electrooptical retarders and low coherence optical sources for electric field sensing schemes have been described in this chapter. The described principles were applied in experimental fiber and integrated optics

coherence-modulated optical schemes for sensing audio frequency electric fields. The detection of high-intensity electric fields, ranging from 10 to 350 kVpp/m and 0 to 20 kHz respectively, based on matched optical retarders, has been successfully tested in our laboratory. Work is in progress to achieve larger bandwidths, e.g., in the Megahertz range. In this kind of sensing schemes, the bandwidth is only limited by the light transit time on the electro-optic sensor. LiNbO₃ electro-optic devices are inherently very wide-band, responding potentially from DC to several GHz. The relative high-intensity operating range of our experimental scheme is determined by the use of short electro-optic crystals as the half wave electric field is high. As demonstrated in the experimental results, longer crystals allow lower half-wave fields and hence the measurement of lower intensity electric fields.

Sensing electric fields based on coherence modulation is a relatively novel approach and several aspects need to be investigated before becoming a real technical alternative for practical applications. It is very well known that fiber polarizers and the electro-optic birefringent sensors are sensitive to environmental variations. In particular, these elements are sensitive to temperature changes that affect their performances and potential long term drift can be observed on the sensor and demodulator operating points. In our experimental set-up no drift has been observed even if the system has been operating for several hours a day. However this drift may exist as it is inherent on the devices we used in our experimental work. To overcome the potential temperature dependence on the electro-optic crystals, polarization-independent electro-optic devices are being studied. Such devices much less are polarization sensitive and can be promising to implement more performant electric field sensing schemes. Work in such a direction is in progress in our laboratory.

The described sensing schemes represent potential applications of wide-band coherence-modulated sensors in more complex schemes, involving optical multiplexing to give distributed arrays of sensors, based on matched electro-optic sensors and demodulators, in fiber optics architectures. A fiber serial coherence multiplexing, in a simple array implementation could be useful for detecting and analyzing multi-point electric fields in the electric power industry, in high-intensity electric-fields environments, for high intensity telecommunication signals, etc.

9. References

- Johnston, A. R.; Kirkham, H. & Eng B. T. (1986). Dc electric field meter with fiber optic readout. *Rev Sci. Instrum*, vol. 57, No. 11, (November 1986)(2746-2753).
- Kirkham, H. (2006). Measuring Electric Fields from Power Lines: Part 1. *IEEE Instrumentation and Measurement Magazine*, Vol. 9, No. 3, (June 2006)(54-56).
- Kirkham, H. (2006). Measurement of Electric Fields Generated from Alternating Current. *IEEE Instrumentation and Measurement Magazine*, Vol. 9, No. 5, (October 2006)(58-61).
- Kirkham, H. (2006). Dust Devil and Dust Fountains: The measurement Challenges. *IEEE Instrumentation and Measurement Magazine*, Vol. 9, No. 6, (December 2006)(48-52).
- Harland, C. J. ; Clark, T. D. & Prance, R. J. (2002). Remote detection of human electroencephalograms using ultrahigh input impedance electric potential sensors. *Applied Physisc Letters*, Vol. 81, No. 17, (21 october 2002)(3284-3286).

- Meier, T.; Kostrzewa, C.; Petermann, K. & Schuppert, K. B. (1994). Integrated Optical E-Field Probes with Segmented Electrodes. *IEEE Journal of Lightwave Technology*, Vol. 12, No. 8, (August 1994) (1497-1503).
- Rao, Y. J.; Gnewuch, H.; Pannell, C. N. & Jackson, D. A. (1999). Electro-optic electric field sensor based on periodically poled LiNbO₃. *Electronics Letters*, Vol. 35, No. 7, (1st April 1999)(596-597).
- Yim, Y-S.; Shin, S-Y.; Shay, W-T & Lee, Ch-T. (1998). Lithium niobate integrated-optic voltage sensor with variable sensing ranges. *Optics communications*, Vol. 152, (1 July 1998)(225-228).
- Lee, T-H.; Hwang, F-T.; Shay, W-T & Lee, Ch-T. (2006). Electromagnetic Field Sensor Using Mach-Zehnder Waveguide Modulator. *Microwave and Optical Technology Letters*, Vol. 48, No. 9, (9 September 2006)(1897-1899).
- Hidaka, K. & Fujita, H. (1982). A new method of electric field measurement in corona discharge using Pockels device. *Journal of Applied Physics*, Vol. 53, No. 9, (September 1982)(5999-6003).
- Naghski, D. H. ; Boyd, J. T.; Jackson, H.; E. Sriram, S.; Kingsley, S. A. & Latess, J.(1994). An integrated Photonic Mach-Zehnder Interferometer with No-Electrodes for Sensing Electric Fields, *IEEE Journal of Lightwave Technology*. Vol. 12, No. 6, (June 1994)(1092-1097).
- Cecelja, F.; Bordovsky, M. & Balachandran, W. (2001). Lithium Niobate Sensor for Measurement of DC Electric Fields. *IEEE Transactions on Instrumentation and Measurement*, Vol. 50, No. 2, (April 2001)(465-469).
- Delisle, C. & Cielo, P. (1975). Application de la modulation spectrale à la transmission de l'information", *Can. J. Phys.*, 53, (1975)(1047-1053).
- Brooks, J. L. & Wentworth, R. H. (1985). Coherence multiplexing for fiber-optic interferometric sensors. *IEEE J. Lightwave Technology*, vol. LT-3, (May 1985)(1062-1072).
- Chu, K. W. & Dickey, F. M. (1991). Optical coherence multiplexing for interprocessor communications. *Opt. Eng.*, vol. 30, no. 3, (March 1991)(337-344).
- Bock, W. J. & Urbanczyk, W. (2000). Coherence multiplexing of fiber-optic pressure and temperature sensors based on highly birefringent fibers. *IEEE Trans. On Instrumentation and Measurement*, vol. 49, no. 2, (April 2000)(392-397).
- Porte, H. & Goedgebuer, J. P. (1992). An LiNbO₃ Integrated Coherence Modulator. *J. Lightwave Technology*, vol.10. No.6, (June 1992).
- Gutiérrez-Martínez, C.; Porte, H. & Goedgebuer, J. P. (1995). Microwave Integrated Optics LiNbO₃ Coherence Modulator for High-Speed Optical Communications. *Microwave Opt. Technol. Lett.*, vol. 10, no. 1, (Sep. 1995)(62-66).
- Rodríguez-Asomoza, J. & Gutiérrez-Martínez, C. (2001). Electric Field Sensing System Using a Ti: LiNbO₃ Optical Coherence Modulator", *Proceedings of IEEE-International Measurement Technology Conference (IMTC01)*, pp. 1075-1078, May 2001, Budapest, Hungary.
- Gutiérrez-Martínez, C.; Trinidad-Garcia, G. & Rodríguez-Asomoza, J. (2002). Electric Field Sensing System Using Coherence Modulation of Light. *IEEE Transactions on Instrumentation and Measurement*, Vol. 51, No. 5, (October 2002)(985-989).
- Gutiérrez-Martínez, C. & Santos-Aguilar, J. (2004). Wide-band Electric Field Sensing System Using Coherence Modulation of Light", *Proceedings of IEEE-International*

- Measurement Technology Conference (IMTC 2004)*, pp. 1882-1885, May 2004, Como, Italy.
- Gutiérrez-Martínez, C.; Santos-Aguilar, J. & Ochoa-Valiente, R. (2007). An All-Fibre and Integrated Optics Electric Field Sensing Scheme Using Matched Optical Delays and Coherence Modulation of Light. *Measurement Science and Technology*, IOP Publishing, Vol. 18, No. 10, (October 2007)(3223-3229).
- Gutiérrez-Martínez, C. & Santos-Aguilar, J. (2008). Electric Field Sensing Scheme Based on Matched LiNbO₃ Electro-Optic Retarders. *IEEE Transactions on Instrumentation and Measurement*, Vol. 57, No. 7, (July 2008)(13625-1368).
- Goedgebuer, J. P.; Porte, H. & Hamel, A. (1987). Electrooptic Modulation of Multilongitudinal Mode Lasers Diodes: Demonstration at 850 nm with simultaneous Data Transmission by Coherence multiplexing. *IEEE J. Quantum Electron*, Vol. QE-23. No. 7, (July 1987)(1135-1144).
- Goedgebuer, J. P. & Hamel, A. (1987). Coherence multiplexing using a parallel array of electrooptic modulators and multimode semiconductor lasers. *IEEE J. Quantum Electron*, Vol. QE-23. No. 12, (1987)(2224-2237).
- Gutiérrez-Martínez, C.; Porte, H. & Goedgebuer, J. P. (1997). A Microwave coherence-multiplexed optical transmission system on Ti:LiNbO₃ integrated optics Technology. *Microwave and optical technology letters*, Vol. 14. No.1, (1997).
- Gutiérrez-Martínez, C. (1994). Multiplexage par Modulation de Cohérence en Optique Intégrée sur Niobate de Lithium (LiNbO₃); Etude et Réalisation de Modulateurs Rapides de Cohérence. *PhD. Thesis*. 1994. U de Franche-Comté, Besançon, France.
- Ulaby, F. T. (2000). Chapter 4. In: *Fundamentals of Applied Electromagnetics*, , Prentice Hall.
- Gutiérrez-Martínez, C.; Sánchez-Rinza, B.; Rodríguez-Asomoza J. & Pedraza-Contreras, J. J. (2000). Automated measurement of optical coherence lengths and optical delays for applications in coherence modulated optical transmissions. *IEEE Trans. On Instrumentation and Measurement*, vol. 49, no. 1, (February 2000)(32-36).
- Kaminow, I. P. & Liu, J. (1963). Propagation characteristics of partially loaded two-conductor transmission line for broadband light modulators. *Proceedings of the IEEE*, (January 1963)(132-135).
- Rigrod, W. W. & Kaminow, I. P. (1963). Wide-band microwave light modulation. *Proceedings of the IEEE*, (January 1963)(137-140).
- Nash, F. R. & Smith, P. W. (1968). Broadband optical coupling modulation. *IEEE Journal of Quantum Electronics*, (January 1968)(26-34).
- Chen, F-S. (1978). Modulators for optical communications. *Proceedings of the IEEE*, Vol. 58. No.10, (October 1978)(1440-1457).
- Derickson, D. (editor). (1998). Hewlett-Packard professional books: *Fiber optic test and measurement*, pp (246-283). Prentice Hall PTR. Upper Saddle River, NJ.
- Killen, H. B. (1991). *Fiber optics communications*, pp (43-68). Prentice Hall PTR. Englewood Cliffs, NJ.
- Hall, C. (1973). Questions and answers about noise in electronics, pp (17-68). Howard W. Sams & Co. Indianapolis, Indiana.
- Andonovic, I. & Uttamchandani, D. (1989). *Principles of modern optical systems*, pp (109-120). Artech House. Norwood, Mass.

- Baney, D. M.; Sorin, W. V. & Newton, S. A. (1994). High-frequency photodiode characterization using a filtered intensity noise technique. *IEEE Photonics Technology Letters*, Vol. 6, No. 10, (October 1994)(1258-1260).
- Baney D. M. & W. V. Sorin, W. V. (1995). Broadband frequency characterization of optical receivers using intensity noise. *Hewlett-Packard Journal*, Vol. 46, (February 1995)(6-12).
- Obarski G. E. & Hale, P. D. (1999). How to measure relative intensity noise in lasers. *Laser Focus World*, (May 1999)(273-277).

Fictive temperature measurements in silica-based optical fibers and its application to Rayleigh loss reduction

Matthieu Lancry¹, Elise Régnier² and Bertrand Poumellec¹

(1) *Institut de Chimie Moléculaire et des Matériaux d'Orsay, Laboratoire de Physico-chimie de l'Etat Solide, UMR CNRS-UPS 8182, Université Paris Sud 11, Bâtiment 410, 91405 Orsay, France*

(2) *Draka Communications, Centre Data 4, Route de Nozay, 91460 Marcoussis, France*

1. Introduction

For many applications, silica is the preferred material, providing excellent physical and chemical properties such as optical transparency from IR to UV range, a low thermal expansion coefficient, and a high resistance to laser induced damage. Silica-based glasses thus provide the backbone for many of today's rapidly expanding photonics applications across fields such as optical telecommunications, electronics, sensor technologies, medical applications, and materials processing.

Thus, numerous elaboration methods are used to produce v-silica-based devices. For example, the technique of vapor phase deposition i.e. Axial Deposition (VAD), Outside Vapor Deposition (OVD), Modified Chemical Vapor Deposition (MCVD), Plasma Enhanced Chemical Vapor Deposition (PECVD) is common in the fabrication of most standard telecommunication silica-based fibers or planar waveguides (Miller and Chynoweth 1979). Furthermore, other processes including sol-gel synthesis (Simmons-Potter, Potter Jr et al. 1996) or conventional melting of raw materials are routinely used to manufacture optical fibers. As a result of this large variety of elaboration processes, all the SiO₂-based glasses are different in terms of chemical composition and structural disorder (Hosono, Ikuta et al. 2001). One way to characterize the glass structural disorder is to determine the fictive temperature T_f .

As described in section 2, it is well known that the fictive temperature is linked to various glass properties such as density (Bruckner 1970; Agarwal and Tomozawa 1997), mechanical fatigue resistance (Bruckner 1970; Agarwal and Tomozawa 1997) or Rayleigh scattering loss (Saito, Kakiuchida et al. 1998). From optical fiber manufacturing point of view, monitoring the fictive temperature is thus a quick and reliable way to optimize the manufacturing process in order to reduce the Rayleigh scattering loss which is the major source of loss in telecommunication optical fibers. For a single mode telecommunication fiber, this corresponds to 90% loss at 1310nm and 80% at 1550nm (e.g. 0.16dB/km for a total of 0.19dB/km).

As recently reported in several papers (Agarwal, Davis et al. 1995; Champagnon, Chemarin et al. 1998; Le Parc 2002; Helander 2004; Koike, Ryu et al. 2005), the fictive temperature T_f of silica based glasses can be determined easily and in a reliable manner by Fourier Transform Infra-Red spectroscopy (FTIR) or Raman scattering spectroscopy. In these methods, scientists use an empirical relation that exists between the wavenumber, width or intensity of silica structural bands and the fictive temperature. Section 3 provides an overview of these methods.

However, one problem is that the features of the silica bands (position, intensity and width) vary not only with T_f but also with the elaboration process and the material composition (Agarwal and Tomozawa 1995; Kim, Tomozawa et al. 2001; Lancry, Flammer et al. 2007; Lancry, Flammer et al. 2007). This is an issue as the chemical composition of a fiber is not constant throughout its cross section but varies for designing the desired refractive index profile for a targeted application e.g. Single Mode Fiber (SMF), Multi-Mode Fiber (MMF), Pure Silica Core Fiber (PSCF), Dispersion Compensating Fiber (DCF), Dispersion Shifted Fiber (DSF). Thus, calibration curves between T_f and the IR band peak characteristics (position, intensity, width) are needed for each material composition (F, P, Ge...). In section 4, we will present an overview of all calibration curves found in the literature together with the method to realize such calibration curves.

An other important parameter that has to be taken into account is that, in general, a glass sample can exhibit different fictive temperatures at its surface and in bulk. This situation can occur, for example, when a glass is rapidly cooled from the liquid state, as it is done in fiber production. In this case, a higher T_f is expected at the fiber surface than in the bulk due to a faster cooling rate at the surface (Peng, Agarwal et al. 1997; Lancry, Flammer et al. 2007). One objective of section 5 is to examine this phenomenon in conventional optical fibers.

Minimizing the optical losses in fibers is a recurrent target for fiber manufacturers. In literature, two approaches have been proposed to reduce Rayleigh scattering loss in silica-based fibers via a reduction of T_f . Indeed, we can optimize the core and/or cladding chemical compositions (Kakiuchida, Sekiya et al. ; Tajima, Ohashi et al. 1992; Lines 1994; Saito and Ikushima 1998; Saito, Kakiuchida et al. 1998; Tsujikawa, Tajima et al. 2000; Kakiuchida, Saito et al. 2002; Saito and Ikushima 2002; Kakiuchida, Saito et al. 2003; Saito, Yamaguchi et al. 2004), or optimize the thermal conditions of the fiber drawing (Todoroki and Sakaguchi 1997; Sakaguchi and Todoroki 1998; Sakaguchi 2000; Tsujikawa, Tajima et al. 2000; Tsujikawa, Tajima et al. 2005). These two approaches are discussed in section 6.

This paper will thus give an overview of methods to measure the fictive temperature in silica-based optical fibers. We will first recall what is T_f in section 2. We will see that both Raman and IR spectroscopies can be used (Section 3). We will also show in section 4 that measuring T_f in optical fibers requires taking many corrections into account. Section 5 will thus give some examples of T_f profiles measured in optical fibers manufactured in different conditions. Finally, section 6 will present two approaches to reduce Rayleigh scattering loss in silica-based fibers via a reduction of T_f .

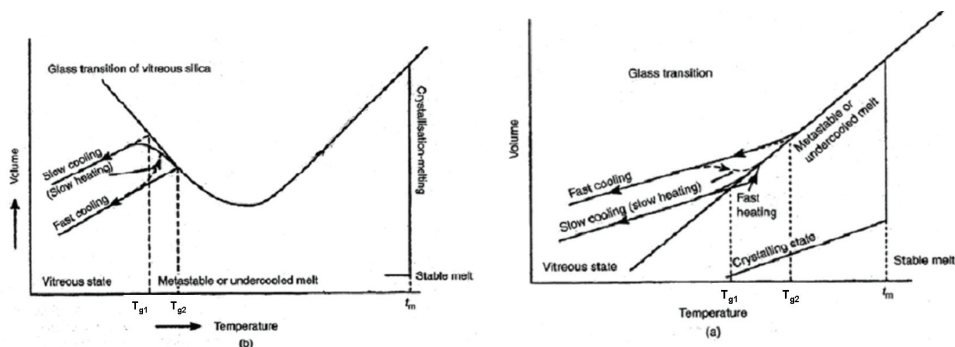


Fig. 1. Schematic diagram of specific volume-temperature relations for a) a normal glass and b) silica glass in the anomalous region (Bruckner 1970).

2. What is the fictive temperature T_f ?

2.1 Definition

Glass is not merely a super-cooled liquid. The volume-temperature diagram shown in Fig. 1a illustrates this distinction. When a liquid is cooled, it crystallizes at or slightly below the melting point. If there are not enough crystal nuclei or if the viscosity is too high to allow sufficient crystallization rates, under-cooling of the liquid can occur. However, in the case of a glass, the viscosity of the liquid rapidly increases with decreasing temperature, and atomic rearrangement slows down more than would be typical for the super-cooled liquid. These observations result in the deviation from the metastable equilibrium curve as it can be seen in Fig. 1a. This change in slope is characteristic of a glass. The cooling rate determines the knee position when the deviation (from the extrapolated liquid curve) begins to occur. Slower cooling, for instance, results in a smaller deviation from the extrapolated liquid curve. Figure 1 shows that the point of intersection of the two slopes defines a transformation point i.e. glass-transition temperature (T_g), which depends on the cooling rate. Practical limitation on cooling rate defines the transformation range [T_{g1} - T_{g2}] in which the cooling rate can affect the structure-sensitive properties such as density or refractive index. The structure, which is frozen-in during the glass transformation, persists at all lower temperatures. Thus, a glass has a configurational temperature or fictive temperature that may differ from its T_g . **The fictive temperature is the temperature at which the glass structure is frozen. It describes thus the structure of a glass and is related to the cooling rate. A fast-quenched glass will have a higher fictive temperature than a slowly cooled glass.**

	Increase in fictive temperature
Density	↑ ($T < 1773\text{ K}$); ↓ ($T > 1773\text{ K}$) [Bruckner 1970; Fraser 1968; Shackelford, Masaryk et al. 1970; Zarzycki 1982; Hong 2003]
Refractive index	↑ [Bruckner 1970]
Viscosity	↓ [Hetherington 1964; Hong 2003]
Thermal expansion α	↑ [Bruckner 1970]
Etch rate	↑ [Agarwal 1997]
Water diffusion	↓ [Roberts 1966]
Compressibility	↓ [Fraser 1968]
Shear modulus	↓ [Fraser 1968]
Young's modulus	↑ [Fraser 1968]
Rayleigh scattering	↑ [Pirmow, Candau et al. 1968; Pirmow, Candau et al. 1968; Lines 1984; Sakaguchi and Todoroki 1998; Kakiuchida, Saito et al. 2003; Tsujikawa, Tajima et al. 2005; Le Parc 2002, Champagnon 2000]

Table 1. Qualitative behavior of the effect of fictive temperature increase on silica glass structure and properties ($1273\text{ K} < T < 1873\text{ K}$). Adapted from Ref. (Agarwal and Tomozawa 1997).

2.2 Qualitative link between fictive temperature and properties of silica glass

Given a well defined chemical composition, silica glass can have different structures and properties depending upon its thermal history (Bruckner 1970; Agarwal, Davis et al. 1995). This is attributed to different fictive temperatures. Thus, the fictive temperature allows learning about glass properties such as density, refractive index, hardness, mechanical strength and chemical durability. In this section, the changes in various properties of silica glasses induced by thermal or mechanical processes reported in the literature are compared. These observations are summarized in Table 1 (adapted from (Agarwal and Tomozawa 1997)). The structural changes induced by modification of fictive temperature are considered in the anomalous region. This anomalous region is the range of fictive temperatures from 1273 K to 1773 K , where the density of silica glass increases with increasing fictive temperature (Fraser 1968; Bruckner 1970; Shackelford, MASARYK et al. 1970; Zarzycki 1982). This is the opposite to what happens in the other glasses. This is illustrated in Fig. 1b. In addition, Fig. 2 shows the density according to T_f for such silica glasses.

As it can be seen in Table 1, a glass with a higher fictive temperature has larger light scattering loss, larger mechanical fatigue resistance, lower viscosity and larger HF etching rate. Concerning the fiber drawing parameters, fictive temperature of fiber core and inner cladding is higher for fibers processed with a faster cooling rate, which generally corresponds to higher drawing speed or lower tension force.

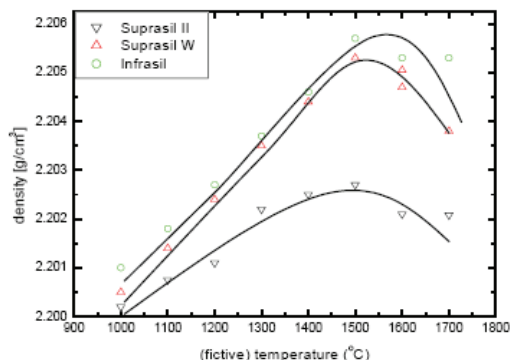


Fig. 2. Densities of various silica glasses as a function of fictive temperature (Bruckner 1971) in the anomalous region.

As this paper is dedicated to fictive temperature in optical fibers, in the following we briefly discuss the **relationship that is well known between Rayleigh scattering and fictive temperature** to estimate the intrinsic loss of silica-based fibers (Saito, Kakiuchida et al. 1998). The Rayleigh scattering coefficient R (dB/km/ μm^4) is expressed as the sum of two contributions R_p and R_c which are the Rayleigh scattering coefficients resulting from density fluctuations and concentration fluctuations, respectively. R_c is assumed to be independent on T_f (Martinez and Angell 2002) as it is mainly governed by dopant concentration fluctuations (e.g. polarizability differences between dopants and host material) arising from the elaboration process (e.g. higher concentration fluctuations in VAD process when compared to MCVD process (Dalle)) and the thermodynamics.

$$R_p = \frac{8}{3} \pi^3 n^8 p^2 k_B \beta_T T_f \quad (1)$$

R_p is expressed as Eq. (1), where n is the refractive index, p the average photo-elastic coefficient, T_f the fictive temperature, and β_T the isothermal compressibility for a given fictive temperature. This equation highlights the strong impact of n and T_f on the Rayleigh scattering. Equation (1) indicates that R_p is proportional to T_f (Pinnow, Candau et al. 1968; Pinnow, Candau et al. 1968; Lines 1984). This is indeed confirmed by experimental results that show that the Rayleigh scattering coefficient has a linear relationship with T_f in pure silica glasses and in fibers which have only density fluctuations (only R_p) (Sakaguchi and Todoroki 1998; Kakiuchida, Saito et al. 2003). Usually, for low dopant concentrations (case of most SMFs used in telecommunications), Rayleigh scattering is mainly caused by frozen-in density fluctuations. Figure 3 shows the relationship between the R (sum of $R_p + R_c$) value and T_f . The solid and dotted lines express the dependency in the cases of pure silica and slightly GeO_2 -doped (typ. 5w %) silica glasses, respectively. In addition, the Rayleigh losses depend strongly on the wavelength (λ^{-4} dependence), that's why telecommunication transmission windows are in the NIR (Near-Infra-Red) range around the minimum attenuation window.

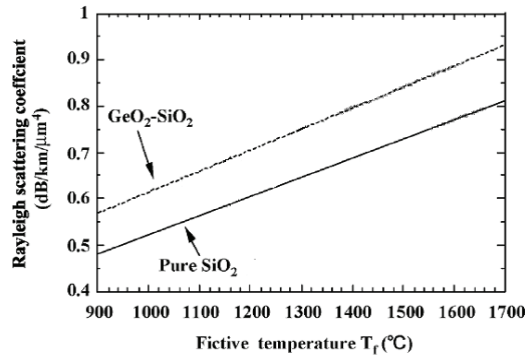


Fig. 3. Relationship between the Rayleigh scattering coefficient and T_f . Extracted from Ref. (Tsujikawa, Tajima et al. 2005).

3. Methods to determine the fictive temperature of silica glasses

3.1 Overview of methods to measure T_f

In principle, fictive temperature of a glass can be determined by measuring any glass properties. In practice, Differential Scanning Calorimetric analysis is a popular method to measure fictive temperature of vitreous materials. However this method cannot be used for silica glasses (and thus optical fibers) since they show a negligible change in specific heat around the glass transition region.

Recently, several authors have reported two methods based on IR absorption (or reflection) and Raman scattering to determine the fictive temperature of silica glass. In these methods, one uses an empirical relation between T_f and the intensity I , wavenumber σ or bandwidth $\Delta\sigma$ of silica vibrational structural bands. These correlations are summarized in Table 2 together with the interpretation and the corresponding references. Using these correlations, it is possible to determine the fictive temperature of different types of silica glasses providing that a calibration was previously established.

Method	Observations	References
Raman 440 cm^{-1} band	$T_f \uparrow \Rightarrow \sigma \uparrow$ $\Delta\sigma \downarrow$	Le Parc 2002; Galeener 83
Raman D_1 (485 cm^{-1}) band D_2 (600 cm^{-1}) band	$T_f \uparrow \Rightarrow I \uparrow$	Le Parc 2002; Bates 1974; Stolen 1976; Mikkelsen 1980
Raman 800 cm^{-1} band	$T_f \uparrow \Rightarrow \sigma \uparrow$	Le Parc 2002; Galeener 1983
Raman 1060/1200 cm^{-1} band	$T_f \uparrow \Rightarrow \sigma \downarrow$	Le Parc 2002; Galeener 1983
FTIR, Reflectance 1120 cm^{-1}	$T_f \uparrow \Rightarrow \sigma \downarrow$ $\Delta\sigma \uparrow$	Le Parc 2002; Kim 2001; Agarwal 1995; Kim 2001; Peng 1997; Hong 2003; Helander 2004
FTIR, Transmission 2260 cm^{-1}	$T_f \uparrow \Rightarrow \sigma \downarrow$	Le Parc 2002; Kim 2001; Hong 2003

Table 2. Relations between fictive temperature and IR absorption and Raman scattering bands' characteristics in pure silica.

On the one hand, Raman scattering method is well adapted to realize T_f cross-section profile in optical fibers and especially in SMF as it provides a good spatial resolution ($\sim 1\mu\text{m}$) (Martinet, Martinez et al. 2008). On the other hand, it has been shown that the IR absorption band located near 1120 cm^{-1} , and which corresponds to the fundamental asymmetric stretching vibration of the Si–O–Si structure, is the most sensitive to structural changes and thus to the T_f changes. This IR vibrational structural band is therefore related to the Si–O–Si bond angle (Bell, Bird et al. 1968; Galeener 1979). In addition, the determination of the peak position is much reliable using FTIR technique. Thus, in the following, the asymmetric bond-stretching vibration observed near 1120 cm^{-1} in the IR reflection spectra is monitored to determine the fictive temperature for several types of silica glasses or optical fibers. As reported in the literature, this method remains well adapted to realize T_f cross-section profiles in optical fibers (Peng, Agarwal et al. 1997; Kim and Tomozawa 2001; Kim, Tomozawa et al. 2001; Hong 2003) as the spatial resolution can be as small as 10 microns. At the opposite, IR transmission measurements are less precise (lower slope of the calibration curve between the peak position and the fictive temperature) and require to prepare very thin samples (thinner than $50\ \mu\text{m}$).

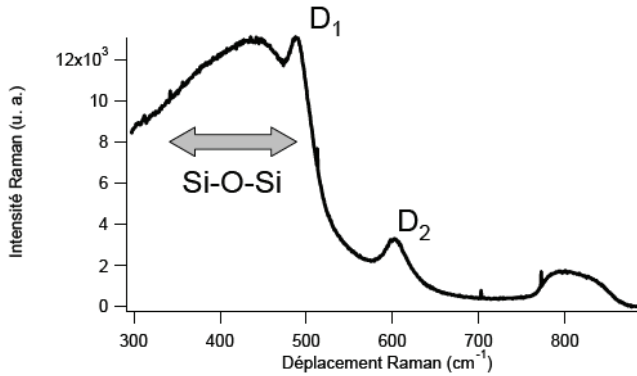


Fig. 4. Typical Raman scattering spectrum of a pure silica glass. Le parc, R. (2002)

An example of the resulting reflectance spectrum is shown in Fig. 5. This spectrum was recorded in a pure silica glass. Typically, there is a predominant IR band at 1120 cm^{-1} accompanied by a shoulder at 1200 cm^{-1} . This shoulder is due to the component which is parallel to the direction of the light propagation (the longitudinal optical, LO mode) while the main band at 1122 cm^{-1} is caused by the transversal optical (TO) mode (Bell, Bird et al. 1968; Galeener 1979).

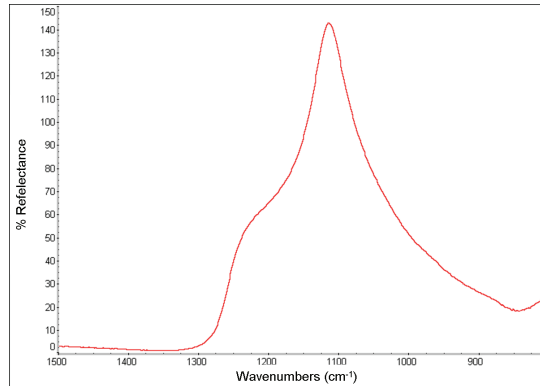


Fig. 5. Typical IR reflection spectrum of pure silica glass collected using Nexus FTIR micro-spectrometer with a maximum reflection angle of 37° .

3.2 Sample preparation, the three investigated methods

Three different methods can be used to determine the fictive temperature of SMF's (Single Mode Fiber) or MMF (Multi-Mode Fiber) cores.

3.2.1 Cleaved fiber and standard FTIR reflection measurements

The fiber was simply cleaved and then mounted vertically in epoxy resin at 90 ± 1 degrees off the horizontal direction using a V-groove metal support. Then, the mounted fiber was etched for 30s in 10% HF-10% H_2SO_4 solution to remove surface water and to reveal boundaries of the core, inner cladding and outer cladding. Figure 6 displays an optical microscope photograph of a SMF made by MCVD process. Thanks to etching we can clearly see the different parts of the fiber such as core, inner-cladding and outer-cladding. Another possibility to reveal core-cladding area will be to observe the samples between cross-polarized. Indeed, due to the chemical composition profile, relative changes in thermal expansion coefficient result in a stress and thus birefringence is radially symmetric (Bachmann, Hermann et al. 1987).

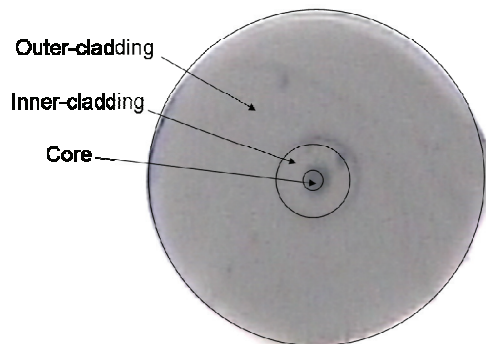


Fig. 6. Optical microscope photograph of SMF after 30 s etching in 10% HF-10% H_2SO_4 solution.

Standard FTIR: Finally, IR reflection spectra were recorded by means of FTIR spectrometer. The spatial resolution can be reduced down to $20\ \mu\text{m} \times 20\ \mu\text{m}$. Therefore this technique is well adapted to MMF measurements where the average core diameter is at least 50 microns wide. However in SMF, this results in an average value of T_i including both core and cladding. Since the beam probe size is much larger than the SMF core, it is thus necessary to perform “strong” correction, due to the cladding’s impact. This degrades strongly the reproducibility of our measurements.

FTIR with FPA type detector: On the other hand, the FTIR reflection spectra can be recorded by means of a FTIR Spotlight 300 Perkin Elmer equipped with the new technology of FPA (Focal Plane Array) detector. The instrument provides 6:1 imaging on a MCT (Mercury Cadmium Telluride) detector, resulting in a nominal resolution of $8\ \mu\text{m} \times 8\ \mu\text{m}$. Using this technique, we are thus able to measure SMF’s core only. However, the alignment of the probe beam on the fiber core is quite difficult since the core and pixel size are roughly similar. This can result in less reliable measurements.

Treatment	Time	Diluents
Mounting in epoxy resin	3h	
Polishing with SiC 600	few min	Water
Polishing with SiC 1200	10 min	Water
Polishing with $6\ \mu\text{m}$ diamond slurry	10 min	Oil
Polishing with $1\ \mu\text{m}$ diamond slurry	10 min	Oil
Polishing with $0.25\ \mu\text{m}$ diamond slurry	15 min	Oil
10%HF-10% H_2SO_4 etching	30s	Water

Table 3. Samples treatments before FTIR reflection experiments: mounting, polishing and etching.

3.2.2 Blaze polished fiber and FTIR

Instead of trying to reduce the beam probe size, as shown in the previous section, in the following, the fiber is cleaved and then polished at very small angle (typ. a few degrees), in order to increase the fiber core surface area. In this view, the fibers are mounted in epoxy resin a few degrees off the horizontal direction using a thin taper plastic as a holder. This is illustrated in Fig. 7a. Next, the mounted fibers are polished horizontally to reach optical quality ($\lambda/50$). The samples are polished with a series of 600 and 1200 grid silicon carbide and then using $6\ \mu\text{m}$, $1\ \mu\text{m}$ and $0.25\ \mu\text{m}$ diamond polishing powder in oil. The typical parameters are reported in Table 3. The polishing machine was configured to 100rpm. Notice that the polishing step is very important since surface roughness strongly impacts both the IR peak intensity and its position when measured in reflectance configuration. This is illustrated in Fig. 8 where the peak is shown for various surface roughnesses. Typically the peak shift (towards smaller wavenumbers) can be as high as $4\ \text{cm}^{-1}$ when average surface roughness (RMS) increases from 0.055 to 0.27 microns (Hong 2003).

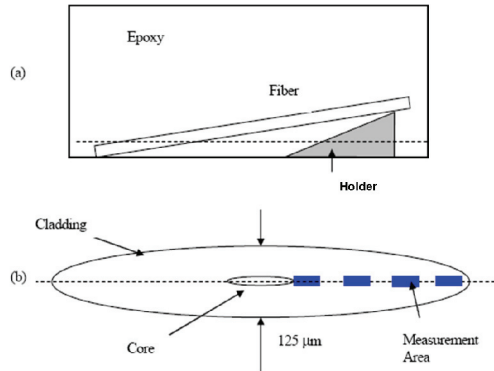


Fig. 7. Schematic diagram for the procedure to create an elongated cross-section of an optical fiber (Hong 2003). a) Mounting of the fiber in epoxy resin at an oblique angle using a thin tapered base. b) Cross-section of the fiber after polishing up to the dotted line indicated in Fig. a.

The polished fibers were subsequently etched for 30 s in 10% HF-10% H₂SO₄ solution to reveal boundaries of the core, inner-cladding and outer-cladding. Finally, the FTIR reflection spectra were recorded by means of standard FTIR spectrometer as shown in Fig. 7b. Spectra have been recorded in the 800 cm⁻¹ to 2000 cm⁻¹ spectral range with a spectral resolution of 4 cm⁻¹ and by averaging 512 scans. The mask size was close to 8 μm x 100 μm resulting in a probe area corresponding to the SMF core only.

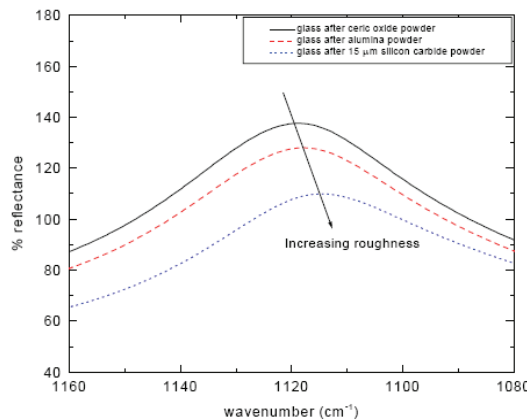


Fig. 8. Shifts in peak positions and intensity of the 1120 cm⁻¹ band in IR reflection for GeO₂ doped silica glasses with different surface roughness (Hong 2003).

3.3 Experimental setup

FTIR reflectance spectra were recorded by means of either a Nexus FTIR Spectrometer (Nicolet) or a FTIR Spotlight 300 (Perkin Elmer) equipped with the new technology FPA

(Focal Plan Array) MCT (Mercury Cadmium Telluride) detector. This last instrument provides 6:1 imaging on MCT detector, resulting in nominal resolution of $8 \mu\text{m}$. Visible images are recorded under white light LED illumination and are collected via a charge couple device CCD camera to give pictures of arbitrary size and aspect ratio. The desired regions for the IR images are selected from visual images. Typically, we need a few minutes only to perform a mapping of 1 mm^2 area. The spectra have been recorded in the 800 cm^{-1} to 2000 cm^{-1} spectral range using a spectral resolution of 4 cm^{-1} . The spectra were obtained by averaging only 32 scans (because the signal to noise ratio remains quite high using this technique). When using a standard FTIR spectrometer, spectra have been recorded in the 800 cm^{-1} to 2000 cm^{-1} spectral range with a spectral resolution of 4 cm^{-1} and by averaging 512 scans. In a general manner, the mask size can be reduced down to $20 \mu\text{m} \times 20 \mu\text{m}$.

Notice that the specular reflection data were collected at a fixed angle of incidence. Indeed, as shown in Fig. 9, a variation in the angle of incidence changes the IR reflection band positions (Almeida 1992; Hong 2003). Thus, the use of the same angle of incidence (i.e. 37° in our experiments) is needed for a reliable determination of fictive temperature.

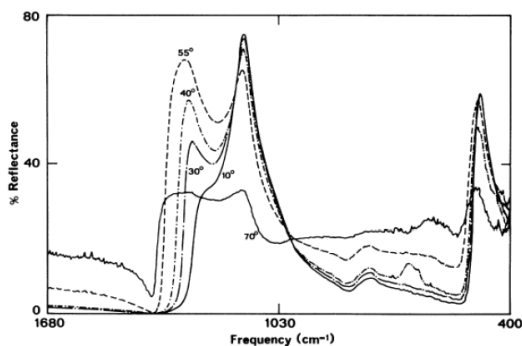


Fig. 9. Specular reflectivity spectra of vitreous silica at different angles of incidence (Almeida 1992).

3.4 Data treatment

An example of the resulting reflectance spectra is shown in Fig. 5. Typically, there is a predominant IR band at 1120 cm^{-1} accompanied by a shoulder at 1200 cm^{-1} . However, one cannot simply choose the wavenumber associated to the largest intensity of an IR band data and call it the peak position because spectral data points are only collected every 2 or 4 cm^{-1} . Indeed, lower spectral resolution results in a much higher noise in the peak determination and thus less precise fictive temperature determination. Hence, the IR peak position was determined by performing a least square polynomial fit and then calculating the minimum of the second derivative using OMNIC@Nicolet or any other fitting software. This is illustrated in Fig. 10. However, one has to be careful because firstly, the sensitivity to noise increases with increasing polynomial degree. Secondly, the choice of the discrete data points used for the fit is very crucial. For instance, if the spectral window width chosen for the fit is too large, shifting the data one step towards higher or lower wavenumber can change the peak position as much as 0.3 cm^{-1} . As the peak position shifts in wavenumber according to the probing area, it is also necessary to change data points for the fit (we cannot keep a fixed

spectral window). Thus, we choose to fix the set of 25 data points around the maximum peak position. Indeed, some interference from a shoulder around 1200 cm^{-1} might occur for larger range. Finally, by changing the set of data or the window width and recalculating the peak position, the stability of the fit is verified. Using this treatment and optimized experimental conditions, we are then able to determine the peak wavenumber with a precision around 0.1 cm^{-1} .

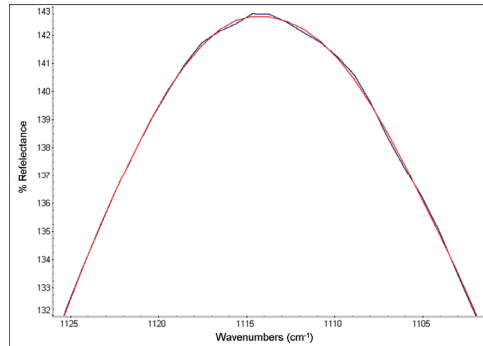


Fig. 10. Illustration of the spectral fitting process. Blue curve is a guide for eye while red curve is for the fit curve.

3.5 Typical results

To summarize, three different methods have been presented to follow the fictive temperature within either MMF or SMF core. In all cases, the 'bond-stretching' vibration mode observed near 1120 cm^{-1} in the FTIR reflection spectra was considered to determine the fictive temperature of the fiber core. Table 4 summarizes the main parameters for each case: type of sample (MMF or SMF, core or cladding), method, spent time (sample preparation + five measurements), spatial resolution, repeatability on T_f measurements (relative error) and number of scans.

For MMF core, there are no peculiar problems due to the large core size (at least 50 microns). We can simply cleave the fiber and probe the core using a standard micro-spectrometer. Typically, the relative error on T_f is lower than $\pm 20^\circ\text{C}$. In the case of SMF core, this is slightly more complex due to the small core size i.e. around 8 microns in diameter. From our results, the blaze polished fiber method is the most precise, straight and reliable method, at the expense of a larger time spent.

Specimen	Method	Spent time	Spatial resolution	T_f relative error	Scan times
MMF core	Cleaved	1 hour	$30\ \mu\text{m} \times 30\ \mu\text{m}$	$\pm 20^\circ\text{C}$	512
SMF core	Cleaved	1 hour	$20\ \mu\text{m} \times 20\ \mu\text{m}$	$\pm 30^\circ\text{C}$	512
SMF core	Cleaved + FPA	1 hour	$8\ \mu\text{m} \times 8\ \mu\text{m}$	$\pm 40^\circ\text{C}$	32
SMF core	Blaze polished	6 hours	$8\ \mu\text{m} \times 100\ \mu\text{m}$	$\pm 20^\circ\text{C}$	512
SMF inner-cladding	Blaze polished	6 hours	$20\ \mu\text{m} \times 100\ \mu\text{m}$	$\pm 20^\circ\text{C}$	512
SMF outer-cladding	Blaze polished	6 hours	$40\ \mu\text{m} \times 100\ \mu\text{m}$	$\pm 20^\circ\text{C}$	512

Table 4. Comparison between methods used to estimate the fictive temperature in SMF core.

4. Determination of calibration curves between the IR peak wavenumber and the fictive temperature T_f in silica-based optical fibers

Currently, the main dopants involved in optical telecommunications are, on the one hand, germanium and phosphorus to increase the refractive index, and on the other hand, fluorine to lower the index. The impact of these elements is not limited to a simple variation of refractive index. By doping silica, viscosity, chemical diffusion, absorption, non-linear index etc ... are modified.

Germanium is now the most widely used dopant in silica-based glasses. Indeed, GeO_2 is common for increasing the refractive index of silica (Kao 1983). It is usually found in concentrations ranging from 1 to 30 w%. Up to now, GeO_2 remains also the most prominent dopant to obtain highly photosensitive silica glass to UV light, allowing thus the writing of optical components such as fiber Bragg gratings (Othonos 1997).

Fluorine-doped silica glasses occurs in a variety of technological applications (Gonnet, Nouchi et al. 2007; Matthijsse, Gooijer et al. 2007; Regnier, Kuyt et al. 2008), due mainly to the beneficial changes in optical and physical properties that results from the addition of small quantities of fluorine to pure amorphous silica. Notice that in contrast to Ge and P, which are network formers, fluorine is a network modifier. For optical fiber technology, fluorine is one of only two dopants that decreases the refractive index of silica, the other being boron (Kao 1983). This has resulted in the widespread application of fluorine doping of silica to control the refractive index profile of optical fibers (Kao 1983; Matthijsse, Gooijer et al. 2007). Small contents of F (<1 wt%) have also been introduced to reduce the additional imperfection loss by allowing viscosity-matching. Note that this viscosity-matching technique can also be used with dopants like GeO_2 or P_2O_5 (Kao 1983).

The presence of P_2O_5 reduces strongly the glass viscosity. In optical fiber manufacturing, this allows a relatively low deposition temperature. However, this also leads to a strong increase of the thermal expansion coefficient (and thus a mismatch between P-doped and P-free parts). In addition, the presence of large amounts of P_2O_5 in the core or the cladding can lead to an attenuation increase at long wavelengths (Regnier, Poumellec et al. 2005). Therefore phosphorus is rarely used at high content, and it is then rarely used alone as dopant in silica. That is why many studies on phosphorus have been made in Ge or F co-doped silica glasses (Irven, Harrison et al. 1981). F-P co-doped cladding allows bringing the cladding viscosity closer to that of the core and therefore decreases excess loss. This allows stress reduction at the core-cladding interface and thus reduction in defects and imperfections at the interfaces.

4.1 Literature survey of the calibration curves in silica-based glasses

The radial variation of T_f in optical fiber cross section has been studied recently with some divergent results (Peng, Agarwal et al. 1997; Wissuchek, Ponader et al. 1999; Kim and Tomozawa 2001; Kim, Tomozawa et al. 2001; Helander 2004). One problem is that the reflection peak position varies not only with T_f but also with the material composition (Tajima, Ohashi et al. 1992; Lines 1994; Saito and Ikushima 1998; Saito, Kakiuchida et al. 1998; Tsujikawa, Tajima et al. 2000; Saito and Ikushima 2002; Saito, Yamaguchi et al. 2004). This is an issue as an optical fiber has different compositions in the core and in the cladding surrounding the core. Thus, calibration curves between T_f and the IR band peak position

must be determined for each material composition and especially for Ge, P and F-doped silica.

We have thus reported in Table 5, most of the calibration curves reported in the scientific literature for various silica-based glasses. We have also displayed the experimental temperature range and the corresponding references. The equations displayed in Table 5 are in the form: $\sigma_{1120} = A - B \cdot T_f$, where σ (cm^{-1}) is the peak wavenumber (or spectral position) of the Si-O-Si asymmetric stretching band measured in reflectance and T_f (K) is the fictive temperature of the silica glass.

Materials	Calibration equation $\sigma_{1120} = A - B \cdot T_f$	Experimental temperature range (K)	Reference
Doped silica			
Ge-doped preform core			
3.6 w%	1130.494 - 0.00709. T_f	1150-1500	Hong 2003 Hong 2004
4.7 w %	1129.325 - 0.00678. T_f		
5.7 w%	1128.412 - 0.00681. T_f		
6.3 w %	1127.855 - 0.00687. T_f		
5 w% Ge-doped bulk	1128.3197 - 0.00673. T_f	1150-1500	
5.3 w% Ge-doped bulk	1128.0034 - 0.00569. T_f	1150-1500	
F-doped Inner cladding	1131.088 - 0.00583. T_f	1150-1600	Kim 2001
Pure silica			
Silica bulk glasses (e.g. infrasil, suprasil 2, suprasil W2, ...)	1132.01 - 0.00686. T_f	1150-1500	Hong 2003 Agarwal 1995
Silica bulk glass	1131 - 0.0069. T_f	1350-1750	Le Parc 2002
CVD silica bulk cladding	1131.500 - 0.00742. T_f	1250-1550	Hong 2003 Tomozawa 2005
CVD silica fiber outer-cladding	1132.501 - 0.00669. T_f	1150-1600	Kim 2001 Hong 2003

Table 5. Calibration curves (between T_f and 1120cm^{-1} peak wavenumber measured in reflection) reported in the scientific literature for various silica glasses and optical fibers.

It is worth noticing that no significant difference was found between the different kinds of pure silica glasses i.e. Infrasil, Suprasil 2, Suprasil W2. In contrast, doped silica exhibit strongly different calibration curves, especially for the A coefficient. Unfortunately, the fictive temperature of highly Ge-doped glasses (> 6.7 w % in GeO_2) cannot be estimated reliably due to the lack of calibration curves (Kim, Tomozawa et al. 2001; Hong 2003; Hong, Ryu et al. 2004). Thus, we determine in next section a complete set of calibration curves for germanosilicate glasses for Ge from 1w% to 30w%. Using these curves, we will be able to determine the T_f of Ge-doped glasses whatever the Ge-content may be (between 1 and 30 wt%).

4.2 Determination of calibration curves in Ge-doped silica

4.2.1 Samples preparation and treatments

The specific case of strongly Ge-doped silica has never been reported to our knowledge because it is impossible to cut a highly Ge-doped preform rod into slices without breaking it because of the high level of stress. We have thus circumvented this tricky point by using a graded index preform and by reducing the preform diameter by a factor of 100. A graded index preform with a Ge-doping level up to 30w% was thus stretched into "capillaries"; which are in fact full rods corresponding to the initial preform composition but with a smaller diameter. This allows cutting the capillaries into slices while keeping the spatial resolution to perform many calibration curves for various Ge contents in the same sample. The capillaries were then cut to the desired length to realize the calibration standards. In order to achieve different uniform fictive temperatures in the calibration standards, the samples were held at various temperatures for long time periods, long enough (up to a few 100s hours) to ensure full structural relaxation of the whole preform diameter (i.e. outer-cladding, tube and core). The typical temperatures selected were between 1223 K and 1523 K with an uncertainty around ± 2 K (furnace uncertainty). Previous data on bulk silica glass (Sakaguchi and Todoroki 1999; Kim, Tomozawa et al. 2001; Hong 2003) were used to determine appropriate heat treatment times needed to obtain a complete structural relaxation at each heat-treatment temperature. Typical heat-time of bulk silica glasses are shown in Table 6. After heating treatment, these samples were rapidly (< 1 s) quenched in water to fix the uniform fictive temperature at the heating temperature (since the relaxation times have been estimated to be a few 100's at these temperatures (Sakaguchi and Todoroki 1999)). Then, the capillaries were polished with a series of 600 and 1200 grid silicon carbide and then to an optically smooth finish with $6\mu\text{m}$, $1\mu\text{m}$ and $0.25\mu\text{m}$ diamond polishing powder in oil. The polishing machine was configured to 100rpm. Finally, the IR reflection spectra were measured as a function of the radial position (and thus the Ge content) within capillaries.

Temperature	Ge-doped Core	F-doped inner cladding	Pure silica outer cladding
1223K	134h	8h	
1273K	32h	3h	200h
1323K	29h	2h	120h
1373K	8h	1h	66h
1423K	5h	1h	45h
1473K	2h	1h	15h
1523K	1h	1h	3h
1573K			1h

Table 6. Heating treatment conditions of optical fiber capillaries.

4.2.2 Examples of IR reflection spectra in Ge-doped silica

An example of the resulting reflectance spectra is shown in Fig. 11. These spectra were recorded at various locations corresponding to various Ge content of a GI-MMF capillary. We have shown four spectra corresponding to silica outer-cladding (i.e. natural undoped silica), and 5 w%, 15 w% and 25 w% Ge-doped cores. Typically, there is a predominant IR

band at 1120 cm^{-1} accompanied by a shoulder at 1200 cm^{-1} . We can see that the higher is the Ge concentration the lower the wavenumber of TO mode related peak.

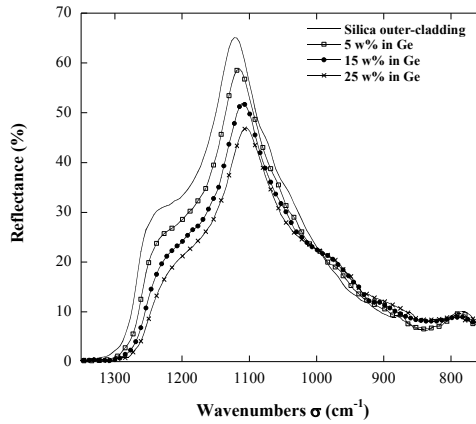


Fig. 11. Typical reflectance spectra corresponding to various location and thus Ge content for the GI-MMF capillary.

4.2.3 2D distribution of the IR peak wavenumber in GI-MMF capillaries annealed at various temperature

Figure 12 displays the 2D distribution of the peak wavenumber σ related to the Si-O-Si asymmetric stretching band recorded in reflection. The circle (black solid line) corresponds to the core part within the capillary. In this figure, the darker the color, the higher the peak wavenumber σ (in cm^{-1}). These results indicate that the concentric distribution of σ is quite constant for a fixed radial position r (constant along a circle) whereas it changes strongly according to the radial position r . In the following, we will extract the radial profiles from these data.

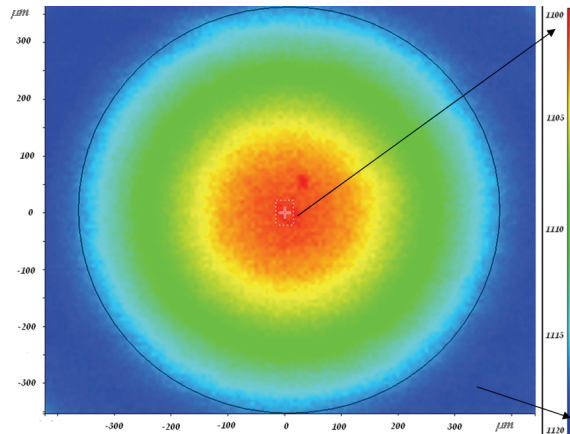


Fig. 12. 2D distribution of the reflectance peak wavenumber σ in the core of the MMF capillaries cross section

4.2.4 Determination of calibration curves: influence of the Ge concentration

In this part, we will extract the data obtained above in order to determine calibration curves between the fictive temperature and the IR reflection peak wavenumber σ for Ge concentrations up to 30 w %. Firstly, we have assumed that the drawing around 2300 K of the preform into rods did not change the germanium concentration profile since it has been shown that it did not change significantly the refractive index profile [20] when compared to our spatial resolution. We have thus converted the radial position r into Ge concentration in the GI-MMF rods using the well-known GI-MMF concentration profile in preform. Now, we are able to follow the evolution of the peak wavenumber according to the fictive temperature T_f (also called the calibration curves or master curves) for various Ge contents.

Figure 13 displays several of these calibration curves for pure silica glass and for various GeO_2 contents from 5 w % to 30w%. In this figure, the symbols are for experimental data while the full lines correspond to best fits of the data using a linear law. The least square regression analysis reveals the following relationship between fictive temperature and IR peak position: $\sigma(\text{Ge}, T_f) = A(\text{Ge}) - B(\text{Ge}) \times T_f$, where the coefficients A and B could depend on the Ge content. Based on those calibration curves, the fictive temperatures of Ge-doped (up to 30 w %) optical fibers can be estimated once the composition of the core is known.

In the following, we will investigate more precisely the effect of the Ge content on the calibration curves parameters: i.e. the ordinate at the origin (coefficient A in cm^{-1}) and the slope B (in $\text{cm}^{-1} \text{K}^{-1}$). We have thus extracted these values from the above linear regressions for various Ge concentrations up to 30 w %. Figures 14 and 15 display the evolution of these two parameters according to the Ge concentration together with the error bars. As it can be seen, the coefficient A follows a linear relationship with the Ge content (*up to 30 w %*): $A = (1129.8 \pm 0.1) - (0.469 \pm 0.004) \times [\text{Ge}]$. In contrast, the slope B appears to gradually decrease with increasing Ge content. However, this decrease is not significant enough when compared to our measurements uncertainty. In the following, we will thus assume that the slope B is independent on $[\text{Ge}]$: $B = 0.0102 \pm 0.0002$.

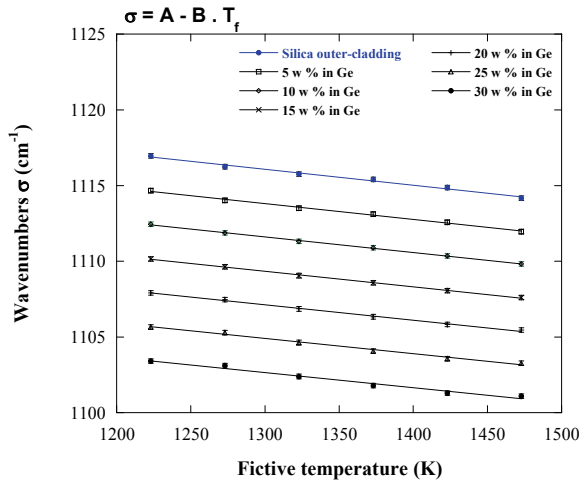


Fig. 13. The relationship between IR peak wavenumber and the fictive temperature for Ge-doped bulk silica for various Ge concentrations.

Our results are in good agreement in terms of both slope and peak position evolutions according to the Ge content when compared to those already published by Hong et al. (Hong 2003; Hong, Ryu et al. 2004) (from 3.6 w % to 6.7 w % in Ge). However, there exists a small discrepancy in the absolute values of A and B coefficients. Indeed, one can find in the literature various data (Agarwal, Davis et al. 1995; Kim, Tomozawa et al. 2001; Le Parc 2002; Hong 2003; Hong, Ryu et al. 2004) in which the slope B changes from 0.0065 to 0.0075 and A from 1131 cm⁻¹ to 1132.5 cm⁻¹. There are two main explanations (not exclusive) for A variations. Firstly, a change in the maximum angle of incidence of the IR beam probe (28° for Hong measurements and 37° in our experiments) changes the IR reflection band wavenumber (Almeida 1992). Secondly, due to the significant influence of the surface roughness on the peak position (Hong 2003), the difference in the HF etching time or HF etching rate (due to the different dopant concentration) can lead to changes in the peak position.

Next the difference on the B coefficient could be due to the large difference into elaboration process: MCVD in Hong experiments, PCVD in this study. Indeed, this leads to different kind (and/or level) of "impurities" (e.g. Na, Cl, Al) or small compositional variations such as the presence of F or P. Furthermore, it is well known that a few 100's ppm (or even less) of such impurities can change A and B coefficients significantly (Tajima, Ohashi et al. 1992; Lines 1994; Saito and Ikushima 1998; Kim, Tomozawa et al. 2001).

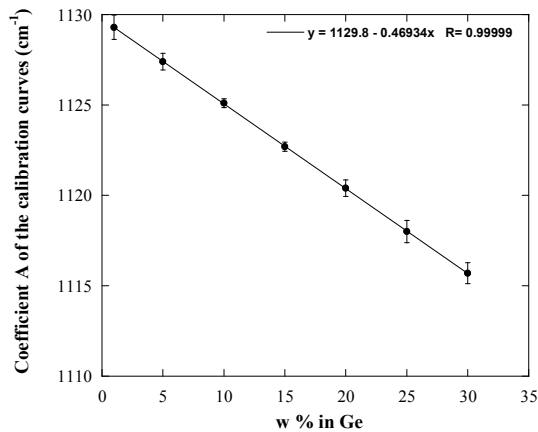


Fig. 14. Relationship between the ordinate at the origin A of the calibration curves for various Ge concentrations.

From above results, we have determined the relation (2) to estimate the fictive temperature profile from the IR peak wavenumber σ . In this relation, [Ge] is the germanium content in w % in the range between 1 and 30 w %. This allows us to estimate the fictive temperature (in K) for any radial position r providing that the Ge concentration [Ge] is known.

$$T_f(r) = \frac{A(\text{Ge}) - \sigma(r)}{B} = \frac{1129.8 - 0.469 \cdot [\text{Ge}](r) - \sigma(r)}{0.0102} \quad (2)$$

Using the above reported uncertainties, we have estimated an absolute uncertainty in the fictive temperature around 4 %. This estimate is mainly due to the slope B uncertainty. In

contrast, the relative error (from one sample to another) which is independent on the calibration curves is around 1 %.

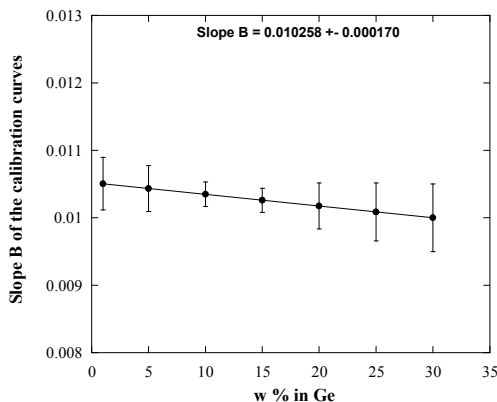


Fig. 15. Relationship between the slope B of the calibration curves for various Ge concentrations.

5. Application 1: measurements of fictive temperature distribution in multimode optical fibers

In general, a glass sample can exhibit a different fictive temperature T_f at its surface and in bulk. This situation can occur, for example, when a glass is rapidly cooled from the liquid as it is done in fiber production. In this case, a higher T_f is expected on the fiber surface than in the bulk due to a faster cooling rate at the surface (Peng, Agarwal et al. 1997; Lancry, Flammer et al. 2007; Martinet, Martinez et al. 2008). One objective of the present section is to examine this occurrence in graded index multimode optical fibers (GI-MMF) and the difficulty is that the composition changes with the radius position.

5.1 Samples

Prototype graded index multimode fiber (GI-MMF) labeled P1 was realized in typical drawing conditions (i.e. drawing speed and tension) for these experiments by Draka Communications using PCVD process. Fiber has silica outer cladding with a diameter of 125 μm and a GeO_2 -doped core with a diameter of 50 μm . The typical refractive index profile follows a parabolic law within the core. The maximum Ge concentration of the investigated fibers is 15.00 ± 0.05 w%. The outer-cladding was made with pure silica. Next, the fiber was cleaved and mounted in epoxy resin at 90 ± 1 degrees using a V-groove metal support. The mounted fiber was then etched for 30s in 10% HF-10% H_2SO_4 solution to remove surface water and to reveal boundaries of the core, inner cladding and outer cladding. Finally, IR reflection spectra were recorded by means of the Spotlight 300 FTIR spectrometer.

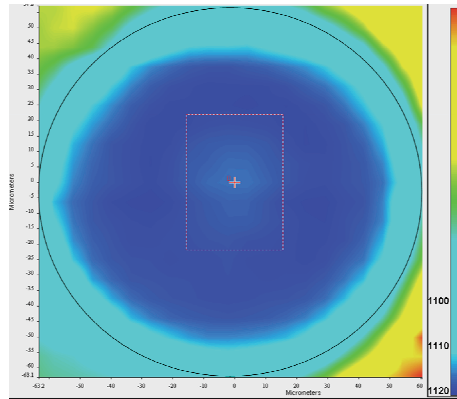


Fig. 16. 2D distribution of the reflectance peak wavenumbers σ for the GI-MMF fiber cross section.

5.2 Measurements of σ distribution in multimode optical fibers

Figure 16 displays the 2D distribution of the peak wavenumbers related to the Si-O-Si asymmetric stretching band in reflection. As it can be seen, we have added two concentric circles (solid lines) on this picture corresponding to the core and the fiber outer-diameter. Darker is the color, higher the peak wavenumber σ . These results indicate that the concentric distribution of σ is quite constant for a fixed radial position r (constant along a circle) whereas it changes according to radius value. For going further in our analysis, we extract the radial profiles from these data in the following. Figure 17 shows the evolution of σ as a function of radial position for P1 multimode optical fiber. Firstly, the peak wavenumber radial distribution is not uniform across the core. More precisely, one can observe a nearly parabolic profile within the core. This is presumably due to the effect of the Ge-doped core, the wavenumber increases from the center of the core towards the tube. Secondly, the values of σ shift towards higher wavenumber near the fiber edges (fiber surface).

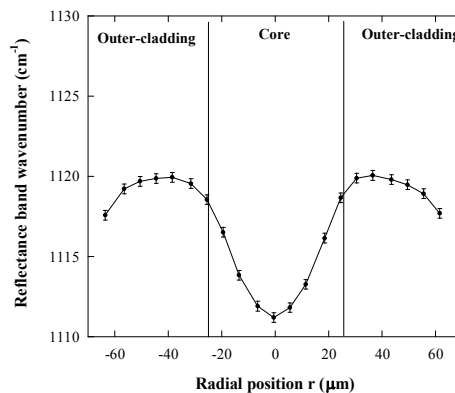


Fig. 17. Radial profile of the reflectance peak wavenumber σ for MMF cross section. Fiber was MMF made by PCVD process.

5.3 Determination of fictive temperature radial profile in MMF

As explained in the introduction, it is well known that the reflection peak position varies not only with T_f but also with the material composition (e.g. core/cladding). As in the case of MMF, the Ge concentration [Ge] in the core is not constant but follows a parabolic law, we need to use our calibration curves between T_f and σ for various Ge content in order to correct the peak wavenumber radial profile for determining the T_f profile. Therefore, we have calculated the Germanium concentration radial profile in the MMF's for converting the profile $\sigma = f(r)$ into fictive temperature profile using the relation (1). Figure 18 shows the estimated fictive temperature distribution on the cross section of the P1 optical fiber. Those data correspond to the IR peak wavenumber σ shown in Fig. 17. The absolute error bars in fictive temperature have been estimated from those in wavenumbers and calibration curves (see section 4). The T_f along the entire cross-section for the P1 fiber varied with radial position. Firstly, the estimated fictive temperatures at the near-surface region are $\approx 200^\circ\text{C}$ higher than inside presumably due to the faster cooling. Secondly, there is an increase ($\approx 150^\circ\text{C}$) of the fictive temperature from the core-cladding interface towards the center of the core (higher Ge content) which is likely due to the constrained cooling of the fiber core.

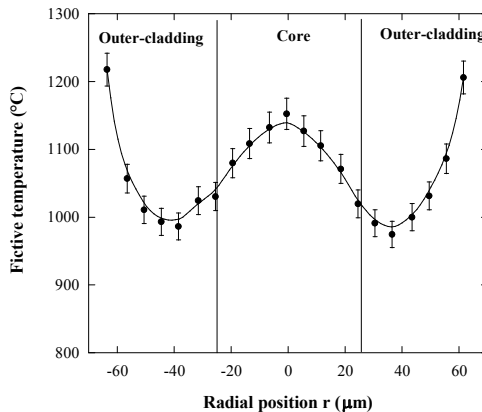


Fig. 18. Estimated fictive temperature as a function of the radial position for P1 fiber. The solid line is a guide for eyes. Fiber was MMF made by PCVD process.

5.4 Discussion

The absolute error in fictive temperature has been estimated from those in wavenumbers and due to the calibration (i.e. the calibration coefficients A and B in Equation 2). Using the above reported uncertainties, we have estimated an absolute uncertainty around 4 % in the fictive temperature which is mainly due to uncertainty on the slope B. The absolute error on the fictive temperature is thus around 40°C . Furthermore, the relative error which is independent of the calibration curves is around $\pm 20^\circ\text{C}$.

Now, let us discuss the reliability of the fictive temperature profile shape. In the GI-MMF, the pure silica outer-cladding had the highest viscosity while the Ge-doped core had the lowest viscosity. Typically when cooled at a constant rate, a glass with higher viscosity is expected to acquire a higher fictive temperature. Therefore, the core is expected to have 1/ a non uniform T_f due to the Ge profile (lower T_f for higher Ge content) and 2/ a lower fictive

temperature than the outer-cladding. However, in our measurements, the fictive temperature of the core is higher in the center (higher Ge content) and even higher than in the interior (e.g. from -50 to -25 μm) of the outer-cladding. This is puzzling. This can be due to the stress distribution as discussed in the next paragraph.

A problem that we could meet is the impact of the way to establish the calibration curves. Indeed we need a uniform T_f across sample cross-section but because of the different properties (e.g. viscosity) at different location of the sample; it is possible that samples would not have a perfectly uniform fictive temperature even after an extended heat-treatment and quenching. Normally the best way to have uniform T_f within our samples should be to cut the glass sample into small pieces with nearly uniform composition and use them to obtain the calibration curves. However, such a study has never been reported because 1/ it is impossible to cut a highly Ge-doped preform rod into slices without breaking it due to the high level of stress, and 2/ this procedure is time and preforms consuming. But heating the fiber, drawn from the same perform, during a long time enough at a temperature T and next using our calibration curves yields a completely uniform T_f profile around T . This gives some confidence in our calibration curves.

Next, two main hypotheses (not exclusive) can be put forward to explain such observation. One explanation is the influence of the stress distribution on our \square measurements resulting in incorrect calibration curves since the stresses are different in the capillaries preform (used for calibration) and in fibers (used for measurements).

As it is well known, the IR reflection band of silica structural band near 1120cm^{-1} , which corresponds to the IR absorption band or Raman band at 1050cm^{-1} , shifts towards higher wavenumber under tensile stress and to lower wavenumber under compressive stress (Tomozawa, Lee et al. 1998; Tomozawa, Hong et al. 2004). However, the opposite trend has also been observed earlier for silica fibers, this artifact was caused by a surface corrosion layer (Tomozawa, Lee et al. 1998). Therefore, we have etched our samples just before FTIR experiments to remove this layer.

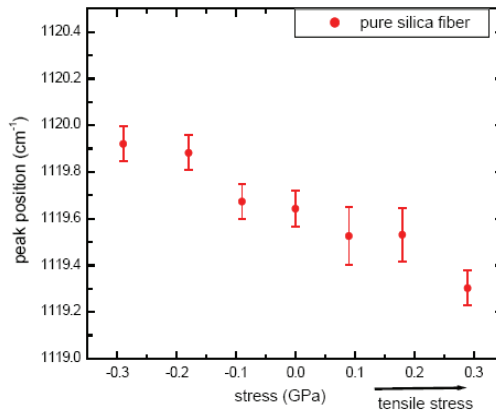


Fig. 19. Evolution of the 1120 cm^{-1} peak position according to the stress in pure silica core fiber (PSCF) (Hong 2003). Fiber was SMF made by MCVD process.

For example, MCVD GeO₂-doped core/SiO₂ cladding fiber was found to have an axial compressive stress in the inner cladding while tensile stress in the core, tube and outer-cladding (Limberger 2002). Furthermore, the higher the Ge-content, the higher the tensile stress in the core (Limberger 2002). Notice that this tensile stress would shift the peak to lower wavenumbers (Devine 1993; Tomozawa, Lee et al. 1998; Tomozawa, Hong et al. 2004), which is opposite to the observed trend.

Typically, the stress values recorded in optical fibers are around ± 100 MPa within the core (depending on the drawing tension and chemical composition) and less than 20 MPa in the tube or in the outer-cladding. Thus, the maximum compressive or tensile stress within the core of optical fibers is estimated to be in the range of -50 MPa and +100 MPa respectively in the axial direction.

The effect of residual stress on the IR peak wavenumber has been also investigated by Hong et al (Hong 2003). This is illustrated in Fig. 19 for a pure silica core fiber (PSCF). It is shown that the maximum elastic stress-induced shift of the 1120cm⁻¹ band (or the equivalent one in Raman) was around 0.6 cm⁻¹/GPa (Tomozawa, Lee et al. 1998; Tomozawa, Hong et al. 2004). Thus, a -100 MPa uniaxial compressive stress is estimated to produce a peak shift < 0.1 cm⁻¹, which is much smaller than the observed peak shift attributed to the fictive temperature change. On the other hand, this value corresponds to our experimental error. **Therefore, the effect of the residual stress commonly found in optical fibers on the IR peak wavenumber is expected to have no measurable influence on our measurements.**

Another possibility is an inelastic strain within MMF cross section i.e. glass deformations that are not accompanied by the generation of stress. The inelastic strain is caused by the large temperature changes during fiber-drawing that freeze-in the relaxation contribution of the elastic properties (i.e. compressibility and shear compliance). It was reported that these inelastic contributions are frozen to their respective values at the glass fictive temperature (Dürr 2005). The inelastic strains mainly occur in the fiber region of highest viscosity which is, in general, the fiber cladding. It is possible that inelastic strain within outer-cladding does not allow the structural relaxation of the fiber core. **Thus, when the core changes from the supercooled liquid to the glass state, it is constrained by the cladding and cannot change its volume freely. This might produce a higher fictive temperature state in the core when compared with unconstrained cooling.**

This is in agreement with Ref. (Kim and Tomozawa 2001) where some “anomalies” were observed. Indeed, the Ge-doped silica glass used for the core had a higher viscosity, when compared to F-doped inner-cladding. When the fibers are produced at a given cooling rate, the glass with higher viscosity should have a higher T_f. Therefore, the Ge-doped core T_f was expected to exceed that of the F-doped inner cladding but we observe the opposite situation. Kim et al. (Kim and Tomozawa 2001; Kim, Tomozawa et al. 2001) suggested that when the inner cladding changes from a supercooled liquid to a glass state, the inner cladding is constrained by two rigid glasses (Ge-doped core and pure silica outer-cladding) on both sides, and then this could produce a higher T_f.

T_f vs densification effect:

In general, the fictive temperature increase is accompanied by small densification of glass structures. This volume change can be estimated from T_f changes. In this view, we will use the known relationship between fictive temperature and specific volume (density) for silica glass (Bruckner 1971) as shown in Fig. 20. The obtained relationship, below 1400°C, between

volume and T_f for type III silica glass is $V \text{ (cm}^3/\text{g)} = 0.4556 - 1.0937 \cdot 10^{-6} \cdot T_f \text{ (}^\circ\text{C)}$, with $R^2 = 0.99$. This implies that for a 100°C T_f increases, this corresponds to roughly 10^{-4} relative volume change. On the other hand we can also deduce the impact of this small densification effect on the refractive index profile. Indeed, Arndt and Stoffler [27] have reported that the refractive index of silica glasses (at a constant OH content) increases with density for type III silica glass. Next, Hong et al. (Hong 2003) have extracted these data and drawn a regression line which is $n = 1.8528 - 0.8683 \cdot V \text{ (cm}^3/\text{g)}$ with $R^2 = 0.96$. Finally, the expected increase of refractive index (either at the fiber edges or in the fiber core) due to this densification effect was of the order of 10^{-4} .

On the other hand, it should be pointed out that the densification and refractive index changes estimated within the fiber core would be the maximum values to be expected from T_f changes. Indeed, the densification estimated would be realized only if the sample material can change its volume freely upon the T_f change. In the present sample, the Ge-doped fiber core cannot change its volume freely, constrained by the surrounding cladding. Therefore, the full densification expected by the fictive temperature increase may not occur. Furthermore, the impact of this densification effect (if occurs) on the fiber index profile remains quite negligible since it corresponds to less than 1% of the core/cladding index difference.

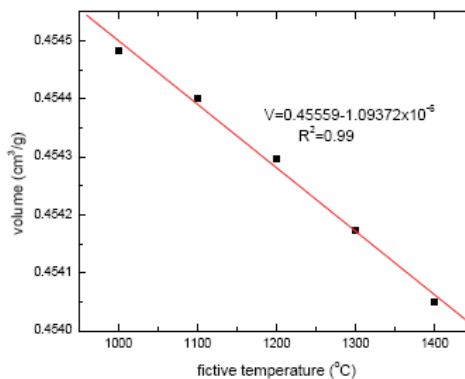


Fig. 20. Relationship between fictive temperature and specific volume (density) for bulk silica glass (Bruckner 1971; Hong 2003).

6. Applications 2: How to reduce T_f and thus Rayleigh scattering loss

Figure 21 shows the relationship between the Rayleigh scattering coefficient R and T_f . The solid and dotted lines show the relationships of pure and GeO_2 -doped silica glass, respectively. The four circles and shaded areas represent the results for preforms and optical fibers, respectively. As shown in Fig. 21, the rapid cooling (without specific optimization) during the drawing process results in fiber T_f , which is at least 400°C higher than that measured in bulk samples. Thus, by lowering T_f , there is still a large possibility of reducing the Rayleigh scattering loss in optical fibers. These results strongly suggest that we should use the Rayleigh scattering coefficient of glass preforms to estimate the “intrinsic loss” or “minimum loss”. With this definition, the intrinsic loss of each fiber is independent of its

drawing condition. Therefore, we will be able to consider the intrinsic loss as a practical target for loss reduction.

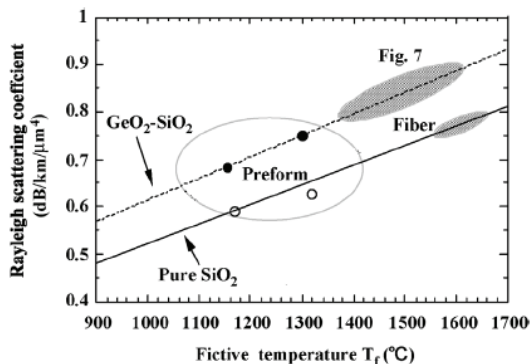


Fig. 21. Relationship between the R value and T_f . The four circles and shaded areas represent the results for preforms and optical fibers, respectively. Extracted from Ref. (Tsujikawa, Tajima et al. 2005).

In the literature, two main approaches have been practiced to reduce R via a reduction of T_f , namely one can optimize the core and/or cladding chemical compositions (Tajima, Ohashi et al. 1992; Lines 1994; Saito and Ikushima 1998; Saito, Kakiuchida et al. 1998; Tsujikawa, Tajima et al. 2000; Saito and Ikushima 2002; Saito, Yamaguchi et al. 2004), or optimize the thermal conditions of the fiber drawing (Todoroki and Sakaguchi 1997; Sakaguchi and Todoroki 1998; Sakaguchi 2000; Tsujikawa, Tajima et al. 2000; Tsujikawa, Tajima et al. 2005) against T_f . Physically, using these methods, the idea is to play with the structural relaxation time (e.g. τ becomes shorter). This should result in lower T_f and thus lower Rayleigh scattering coefficient R_p due to density fluctuations.

6.1 Optimization of the thermal conditions used for the fiber drawing

One possibility to reduce T_f as much as possible is to accelerate the structural relaxation by optimizing the fiber drawing process. In ref. (Hong 2003), Hong et al. study the influence of the drawing parameters (drawing tension, drawing speed) on the fictive temperature. The fiber composition was similar to commercial optical fibers (i.e. the core is 5.7 wt% of GeO_2). The fibers were produced under different process conditions such as cooling rates, drawing speed and tension force. Fiber samples were prepared following the blaze polished method, and the IR peak wavenumbers were then measured as a function of the fiber radius, as described in section III.B. Based on the calibration curves obtained in section IV, the fictive temperatures of fibers can be estimated.

6.1.1 Influence of drawing speed

(Hong 2003) has measured the fictive temperatures of three SMFs (made by MCVD) drawn at different speeds (between 400 m/min and 1000 m/min) and a constant tension force (30g). IR measurements were monitored on the fiber cross-section. The changes of fictive temperature are shown in Figure 22.

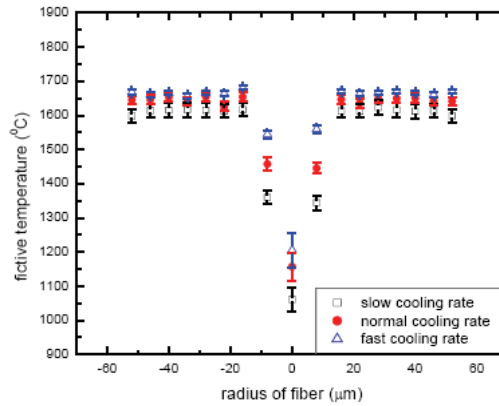


Fig. 22. T_f profile for 3 MCVD SMFs made with different drawing speeds. Extracted from Ref. (Hong 2003).

These measurements clearly show that the fictive temperature of the outer cladding is larger than that of the inner cladding, which is even larger than that of the core. The fictive temperatures of core, inner cladding and outer cladding at low drawing speed (drawing speed around 400m/min) are around $\sim 1150^\circ\text{C}$, $\sim 1450^\circ\text{C}$ and $\sim 1650^\circ\text{C}$, respectively. The fictive temperatures of both the core and the inner-cladding were higher at a higher drawing speed, while the fictive temperature of the outer-cladding was slightly higher at a higher drawing speed. The obtained fictive temperature changes are consistent with what was expected: as drawing speed increases, the cooling rate increases, yielding higher fictive temperatures.

6.1.2 Influence of drawing tension

The fictive temperatures of optical fibers made under different tension forces were also estimated. Holding the drawing speeds constant (400 m/min), two different drawing tensions were tested (30 g and 120g) (Hong 2003). Figure 23 shows the changes of fictive temperature with different tension forces. As tensile forces increased, the fictive temperatures decreased in both the core and the inner cladding. The T_f of the core decreases from 1280°C down to 1220°C (high tension). This leads to an increase of the Rayleigh density fluctuation coefficient i.e. $\Delta R_p \approx +5\text{-}10\%$.

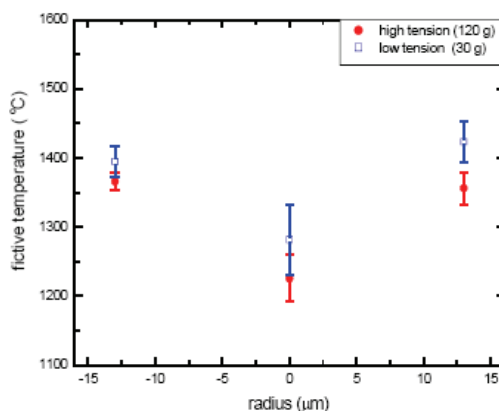


Fig. 23. The fictive temperature changes of MCVD SMF drawn with different tensions as a function of the fiber radius. Extracted from Ref. (Hong 2003).

6.1.3 Influence of drawing temperature

Figure 24 shows the relationship between the R value of various optical fibers and their drawing temperature T_d . The lowest R value, 0.66 for P_2O_5 -doped silica core fiber, results from the low T_f value, because P_2O_5 doping effectively reduces the glass viscosity. On the other hand, the R value of the GeO_2 -doped silica core fiber decreased linearly as the T_d value decreased. This proves that the R value of optical fibers can be controlled via T_f by adjusting the drawing temperature and speed (Tajima 1998; Tsujikawa, Tajima et al. 2000; Tsujikawa, Tajima et al. 2005) i.e. by drawing them slowly at a lower temperature. However, since relaxation time τ increases exponentially with decreasing T_d , the cooling should become exponentially slower for decreasing T_f , which makes it difficult to reduce optical loss. In addition, this usually results in higher stress level (Limberger 2002). The optimum thermal conditions have already been analyzed theoretically and reported in Refs (Sakaguchi and Todoroki 1999; Sakaguchi 2000; Saito, Yamaguchi et al. 2003).

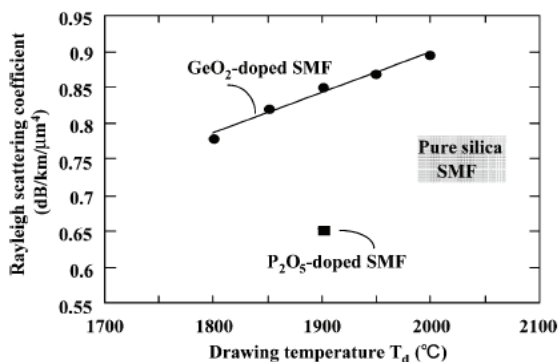


Fig. 24. Relationship between the R value of the test fibers and their drawing temperature T_d . Fibers were SMF made by VAD process. Extracted from Ref. (Tsujikawa, Tajima et al. 2005)

Figure 25 shows the intrinsic losses (multiphonon absorption and Rayleigh scattering) of silica-based fibers re-evaluated by using the R value of the preforms shown in Fig. 21. The theoretical loss of GeO₂-doped silica glass, which corresponds to conventional SMF, is 0.130 dB/km at 1.55 μm. The values for pure and slightly P₂O₅-doped silica glasses are 0.115 and 0.095 dB/km, respectively. These values are 0.03–0.05 dB/km lower than the lowest experimental value of 0.1484 dB/km for pure silica core SMF (Nagayama, Kakui et al. 2002). Knowing that the multiphonon absorption results in 0.01 to 0.02 dB/km at 1.55 μm. Thus, there is still a large possibility of reducing the Rayleigh scattering loss in such optical fibers (0.01 to 0.04 dB/km).

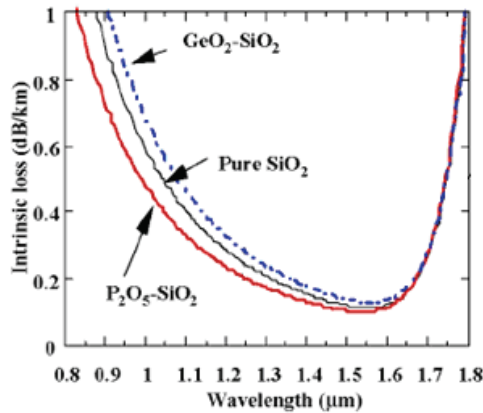


Fig. 25. Intrinsic losses of silica-based fibers re-evaluated by using the R values measured in preforms. Extracted from Ref. (TsujiKawa, Tajima et al. 2005).

6.1.4 Playing with the cooling profile: effect of optimized drawing conditions

Figure 26 shows the relative change in fictive temperature distribution on the cross section of the “reference” (not optimized drawing conditions) MMF together with that of P2 fiber (drawn in optimized conditions). The absolute error bars in fictive temperature have been estimated from those in wavenumbers and calibration curves. T_f along the entire cross-section for the “reference” P1 fiber varies with the radial position and was everywhere higher than that measured in the optimized P2 fiber. Firstly, the estimated fictive temperatures of the P1 fiber at the near-surface region are $\approx 200^\circ\text{C}$ higher than in the internal part of the outer cladding of the fiber. This is presumably due to a faster cooling rate at the fiber surface. Secondly, there is an increase ($\approx 150^\circ\text{C}$) of the fictive temperature from the tube towards the center of the core. In contrast, for the optimized P2 fiber, the fictive temperatures were relatively constant within the whole optical fiber cross section. From our calculation, this approach can lead up to a 15% loss reduction at 850nm in such MMF.

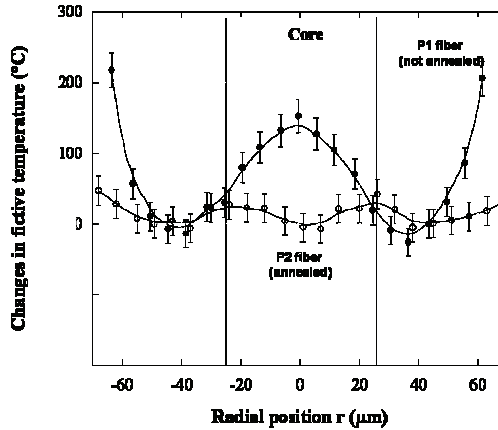


Fig. 26. Relative change in MMF fictive temperature as a function of the radial position for P1 (not optimized drawing conditions) and P2 (optimized drawing conditions) fibers. The solid lines are guides for eyes. Fibers were MMF made by PCVD process.

6.1.5 Playing with the cooling profile: Annealing furnace

Another possibility is to favor the structural relaxation during the fiber drawing process. To do that, annealing furnaces can be mounted on the drawing towers. The temperature of the furnace can be kept constant at an annealing temperature T_a , or it follows a gradient profile (Kakiuchida, Sekiya et al. ; Sakaguchi 2000; Tsujikawa, Tajima et al. 2005; Lancry, Flammer et al. 2007; Martinet, Martinez et al. 2008). *T_a profile, t_a (annealing time) and L (furnace length) should be optimized to minimize T_f by taking into account the thermal history (initial T_f).*

Figure 27 shows an example of the impact of the thermal cooling profile on the Rayleigh scattering level. In this case, the annealing furnace is 3m long and the drawing speed is either 600m/min ("normal" drawing speed) or 30m/min (slow drawing speed). The annealing furnace was set to 1400°C. Keeping the drawing speed relatively high (600m/min), it is possible to decrease the fictive temperature down to 1130°C, leading to a reduction of the Rayleigh scattering coefficient by 10% at least (Sakaguchi 2000). From a practical point of view, we can conclude that the annealing furnace allows to reduce efficiently T_f (and thus the Rayleigh scattering loss) within the fiber core.

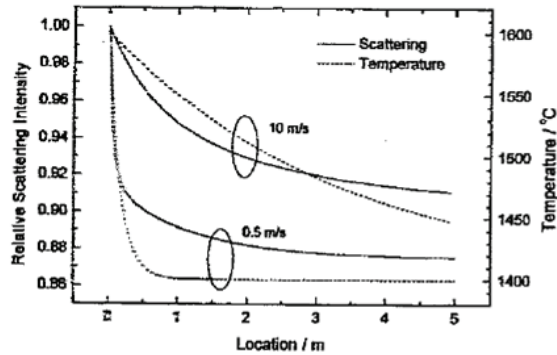


Fig. 27. Variations of the relative Rayleigh scattering loss and the fiber's temperature as a function of the length of the annealing furnace (set to 1400°C) mounted on the draw tower. Fibers were SMFs made by VAD process. Extracted from Ref. (Sakaguchi 2000).

To conclude this part, it is thus possible to optimize the cooling profile to minimize T_f by taking into account the thermal history. Furthermore, as the dopants can change the relaxation time, it follows that the chemical composition of both core and cladding has to be taken into account before performing the thermal optimization. This is the main objective of the next sub-section.

6.2 Optimizing the optical fiber chemical composition:

6.2.1 Playing with the core chemical composition

Instead of playing directly on the cooling profile, another possibility is to accelerate the relaxation time τ_{core} of the core for lowering T_f (and thus Rayleigh loss). Indeed, the relaxation time τ_{core} of the core can be shortened by an appropriate doping of the core and/or cladding (Kakiuchida, Sekiya et al. ; Tajima, Ohashi et al. 1992; Lines 1994; Saito and Ikushima 1998; Saito, Kakiuchida et al. 1998; Tsujikawa, Tajima et al. 2000; Kakiuchida, Saito et al. 2002; Saito and Ikushima 2002; Kakiuchida, Saito et al. 2003; Saito, Yamaguchi et al. 2004). Indeed, small compositional variations can have a huge impact on the glass viscosity and thermal expansion coefficient and thus on accessible drawing temperature, stress distribution (mainly due to thermal expansion coefficient mismatch) and thus in the resulting fictive temperature. This path has been extensively studied by Sumitomo and NTT to reduce the SMF fictive temperature efficiently. This implies the possibility of further reduction of the Rayleigh scattering by heat treatment for a shorter duration at lower temperature.

For example, it should be pointed out that F-doping (Kakiuchida, Saito et al. 2002; Saito and Ikushima 2002; Kakiuchida, Saito et al. 2003; Saito, Yamaguchi et al. 2004) or Cl-doping (Kakiuchida, Sekiya et al. ; Kakiuchida, Saito et al. 2003) of the core accelerates the reduction of the T_f in the core (with optimized thermal conditions). This is illustrated in Fig. 28 where the Rayleigh scattering coefficient is drawn according to the fictive temperature for various F content (Kakiuchida, Saito et al. 2002). It is shown that it is possible to achieve lower T_f but at the expense of higher Rayleigh scattering loss due to concentration fluctuations. Table 6 summarizes the most important results about this method.

Methods	Comments
Core	
Ge-doped 0 – 30 mol %	<ul style="list-style-type: none"> • ↑ Ge ⇒ lower viscosity ⇒ lower τ ⇒ lower T_f • ↑ Ge ⇒ lower Rayleigh loss sensibility to cooling conditions • ↑ Ge ⇒ concentration fluctuation ⇒ higher R_c (linear relationship)
P-doped 0 – 1 mol %	<ul style="list-style-type: none"> • ↑ P ⇒ lower viscosity ⇒ lower τ ⇒ lower T_f • Lower Rayleigh loss due to lower density fluctuation R_p • Concentration fluctuations R_c remain low because P concentration remains small
F-doped 0 – 7 mol %	<ul style="list-style-type: none"> • ↑ F ⇒ lower viscosity ⇒ lower τ ⇒ lower T_f • ↑ F ⇒ concentration fluctuation ⇒ higher R_c (linear relationship) • T_f and density fluctuation R_p independent of F content
Cl-doped 0 – 2 mol %	<ul style="list-style-type: none"> • Rayleigh loss (both R_c and R_p) independent of Cl content • Cl accelerates the structural relaxation of the core and T_f can thus be reduce by heat treatment for a shorter duration with higher Cl concentration
Cladding	
F-doped 0 – 4 mol %	<ul style="list-style-type: none"> • Lower T_f and Rayleigh loss in the fiber core • Slight increase of the R_c in the cladding • F accelerates the structural relaxation (smaller τ) (and thus volume change) <ol style="list-style-type: none"> 1) if $\tau_{cladd} > \tau_{core}$: Suppresses the structural relaxation in the core 2) if $\tau_{cladd} < \tau_{core}$: Accelerates the structural relaxation in the core
Na-doped < 100 ppm	<ul style="list-style-type: none"> • Na introduction in outer-cladding accelerates the structural relaxation of the core • Lower T_f and thus lower Rayleigh loss in the core • But higher Hydrogen sensitivity

Table 6. Optimizing the optical fiber chemical composition in order to decrease the Rayleigh scattering loss in silica-based optical fibers.

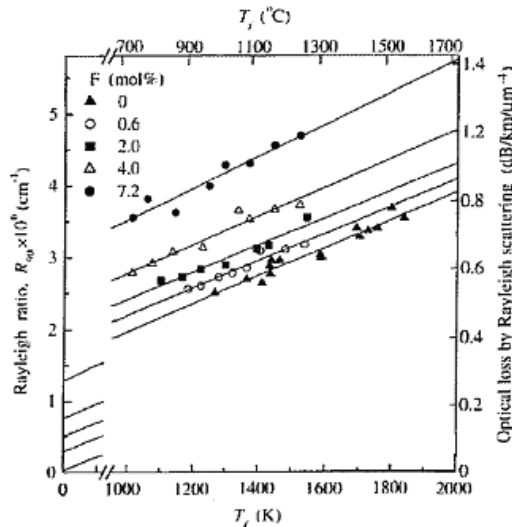


Fig. 28. Relationship between the Rayleigh scattering loss and the fictive temperature for F-doped silica core. The solid lines are linear fitting. Fibers were SMF made by VAD process. Extracted from Ref. (Kakiuchida, Saito et al. 2002).

6.2.2 Playing with the cladding chemical composition

However, a problem with core doping is that Rayleigh scattering due to concentration fluctuations (R_c) generally increases with increasing dopant concentration contrarily to the reduction of density fluctuation contribution R_p . To avoid this problem, small compositional variations (typ. below 1 w%) have been proposed and especially within the outer part (i.e. cladding, tube, outer-cladding). Indeed, it has been observed that τ_{core} is strongly affected by the structural relaxation of the cladding (Saito, Yamaguchi et al. 2004). *Basically, it has been suggested that when $\tau_{clad} > \tau_{core}$, the structural relaxation in the core is suppressed. Indeed, in this temperature range, the core is willing to increase its specific volume but cannot change its volume freely due to the cladding. The effective τ_{core} is thus larger than expected in unconstrained samples. At the opposite, if $\tau_{clad} < \tau_{core}$, the structural relaxation in the core becomes easier.* In the last case, the idea is to increase the structural relaxation time of the core by an appropriate doping of the outer-cladding. For example, it should be pointed out that F-doping (Saito, Yamaguchi et al. 2004; Gonnet, Nouchi et al. 2007) or Na-doping (see below) of the cladding favors the reduction of T_f in the core (with optimized thermal conditions) while the effect of Al should be the opposite.

A recent example has been developed at Draka Communications (Gonnet, Nouchi et al. 2007). The main idea was to introduce small compositional variations in the fiber outer-cladding. For example, the effect of doping MMF's outer-cladding with Na, K and F on the core T_f has been investigated. Such measurements are reported in Table 7. As it can be seen, the Na-doped MMF core has a T_f which is 100°C lower than the others. For going further in this direction, various Na contents were introduced within the outer-cladding. In the investigated range of Na content, the higher is the Na content in the outer-cladding, the lower is the T_f within the core. However, this method should not be pushed too far, as it has been shown that too large amounts of alkalines could lead to a larger H_2 -sensitivity of fibers (Ogai, Iino et al. 1987). If possible, it is thus important to avoid Na migration towards the fiber core by choosing appropriate drawing conditions.

Fiber label	P1	P2	P3	P4
Outer-cladding doping	Pristine	F	K	Na
ΔT_f (°C)	Ref	-50°C	-80°C	-100°C

Table 7. Changes in T_f for MMFs with different outer-cladding chemical compositions.

7. Conclusion

Infrared spectroscopy was demonstrated to be an efficient tool for determining the fictive temperatures of bulk silica glass and silica-based optical fibers. The calibration curves between IR wavenumbers and fictive temperature were obtained by monitoring the peak position of the fundamental structural band (asymmetric vibration band).

It has been shown that two approaches are efficient for reducing the Rayleigh scattering coefficient, namely optimization of the optical fiber core and/or cladding composition and optimization of the thermal conditions used for the fiber drawing (e.g. drawing temperature, drawing speed, drawing tension, cooling profile). A combination of these approaches is promising in terms of achieving further the loss reduction for silica-based optical fibers.

8. References

- Agarwal, A., K. Davis, et al. (1995). "A simple IR spectroscopic method for determining fictive temperature of silica glasses." *Journal of non-crystalline solids* **185**(1-2): 191-198.
- Agarwal, A. and M. Tomozawa (1995). "Determination of fictive temperature of soda-lime silicate glass." *Journal of the American Ceramic Society* **78**(3): 827-829.
- Agarwal, A. and M. Tomozawa (1997). "Correlation of silica glass properties with the infrared spectra." *J. Non-Cryst. Solids* **209**(1): 166-174.
- Almeida, R. (1992). "Detection of LO modes in glass by infrared reflection spectroscopy at oblique incidence." *Physical review. B, Condensed matter* **45**(1): 161.
- Bachmann, P., W. Hermann, et al. (1987). "Stress in optical waveguides. 2: Fibers." *Applied optics* **26**(7): 1175-1182.
- Bell, R., N. Bird, et al. (1968). "The vibrational spectra of vitreous silica, germania and beryllium fluoride." *Journal of Physics C Solid State Physics* **1**(2): 299-303.
- Bruckner, R. (1970). "Properties and structure of vitreous silica. I." *J. Non-Cryst. Solids* **5**(2): 123-175.
- Bruckner, R. (1971). "Metastable equilibrium density of hydroxyl-free synthetic vitreous silica." *J. Non-Cryst. Solids* **5**(4).
- Champagnon, B., C. Chemarin, et al. (1998). "Fictive temperature and medium range order in silicate glasses: a relationship between heat capacity and boson peak." *Philosophical Magazine Part B* **77**(2): 663-669.
- Dalle, C. Contribution à l'étude des mécanismes liés à la photosensibilité de type I et de type IIA des verres de silice par Spectroscopie Infrarouge et Microscopie Electronique en Transmission.
- Devine, R. (1993). "Ion implantation- and radiation-induced structural modifications in amorphous SiO₂?" *Journal of non-crystalline solids* **152**(1): 50-58.
- Dürr, F. (2005). Laser-induced stress changes in optical fibers, Ph. D. dissertation, Swiss Federal Inst. Technol.(EPFL), Lausanne, Switzerland.
- Fraser, D. (1968). "Factors influencing the acoustic properties of vitreous silica." *Journal of Applied Physics* **39**: 5868.
- Galeener, F. (1979). "Band limits and the vibrational spectra of tetrahedral glasses." *Physical Review B* **19**(8): 4292-4297.
- Gonnet, C., P. Nouchi, et al. (2007). Method for manufacturing an optical fiber preform, optical fiber preform and optical fiber, EP Patent 1,813,581.
- Helander, P. (2004). "Measurement of fictive temperature of silica glass optical fibers." *Journal of Materials Science* **39**(11): 3799-3800.
- Hong, J. (2003). FTIR investigation of amorphous silica fibers and nano-size particles Ph. D, dissertation Rensselaer Polytechnic Institute, Troy, NY.
- Hong, J., S. Ryu, et al. (2004). "Investigation of structural change caused by UV irradiation of hydrogen-loaded Ge-doped core fiber." *Journal of non-crystalline solids* **349**: 148-155.
- Hosono, H., Y. Ikuta, et al. (2001). "Physical disorder and optical properties in the vacuum ultraviolet region of amorphous SiO₂." *Physical review letters* **87**(17): 175501.
- Irven, J., A. Harrison, et al. (1981). "Long wavelength performance of optical fibres co-doped with fluorine." *Electronics Letters* **17**(1): 3-5.

- Kakiuchida, H., K. Saito, et al. (2003). Effects of halogen doping on structure of silica glass as a photonic material.
- Kakiuchida, H., K. Saito, et al. (2002). Rayleigh scattering in fluorine-doped silica glass.
- Kakiuchida, H., E. Sekiya, et al. "Effect of chlorine on Rayleigh scattering reduction in silica glass." *Jpn. J. Appl. Phys* **42**(12B pt 2).
- Kao, C. (1983). "Optical Fiber Systems: Technology, Design, and Application."
- Kim, D. and M. Tomozawa (2001). "Fictive temperature of silica glass optical fibers—re-examination." *Journal of non-crystalline solids* **286**(1-2): 132-138.
- Kim, D., M. Tomozawa, et al. (2001). "Fictive temperature measurement of single-mode optical-fiber core and cladding." *Journal of lightwave technology* **19**(8): 1155.
- Koike, A., S. Ryu, et al. (2005). "Adequacy test of the fictive temperatures of silica glasses determined by IR spectroscopy." *Journal of non-crystalline solids* **351**(52-54): 3797-3803.
- Lancry, M., I. Flammer, et al. (2007). "Fictive-Temperature Mapping in Highly Ge-Doped Multimode Optical Fibers." *Journal of lightwave technology* **25**(5): 1198-1205.
- Lancry, M., I. Flammer, et al. (2007). "Fictive temperature distribution in highly Ge-doped multimode optical fibers." *Journal of non-crystalline solids* **353**(5-7): 473-476.
- Le Parc, R. (2002). Diffusion de rayonnements et relaxation structurale dans les verres de silice et les préformes de fibres optiques Ph. D, dissertation Univ. Claude Bernard Lyon France.
- Limberger, H. (2002). POWAG'2002, White Nights' Summer School on Photosensitivity in Optical Waveguides and Glasses, St. Petersburg, Russia.
- Lines, M. (1984). "Scattering losses in optic fiber materials. I. A new parametrization." *Journal of Applied Physics* **55**: 4052.
- Lines, M. (1994). "Can the minimum attenuation of fused silica be significantly reduced by small compositional variations? I. Alkali metal dopants." *Journal of Non Crystalline Solids* **171**(3): 209-218.
- Martinet, C., V. Martinez, et al. (2008). "Radial distribution of the fictive temperature in pure silica optical fibers by micro-Raman spectroscopy." *Journal of Applied Physics* **103**: 083506.
- Martinez, L. and C. Angell (2002). "Chemical order lifetimes in liquids, and a second fictive temperature for glassformers." *Physica A: Statistical Mechanics and its Applications* **314**(1-4): 548-559.
- Matthijsse, P., F. Gooijer, et al. (2007). Fluorine-Doped Optical Fiber, Google Patents.
- Miller, S. and A. Chynoweth (1979). "Optical fiber telecommunications." New York: Academic Press, 1979, edited by Miller, Stewart E.; Chynoweth, Alan G.
- Nagayama, K., M. Kakui, et al. (2002). "Ultra-low-loss (0.1484 dB/km) pure silica core fibre and extension of transmission distance." *Electronics Letters* **38**(20): 1168-1169.
- Ogai, M., A. Iino, et al. (1987). "Behavior of alkali impurities and their adverse effect on germania-doped silica fibers." *Lightwave Technology, Journal of* **5**(9): 1214-1218.
- Othonos, A. (1997). "Fiber Bragg Gratings." *Review of scientific instruments* **68**: 4309.
- Peng, Y., A. Agarwal, et al. (1997). "Radial distribution of fictive temperatures in silica optical fibers." *J. Non-Cryst. Solids* **217**(2): 272-277.
- Pinnow, D., S. Candau, et al. (1968). "Brillouin scattering: viscoelastic measurements in liquids." *The Journal of the Acoustical Society of America* **43**: 131.
- Pinnow, D., S. Candau, et al. (1968). "Rayleigh Scattering: Orientational Relaxation in Liquids." *The Journal of chemical physics* **49**: 347.

- Regnier, E., G. Kuyt, et al. (2008). Radiation-resistant fluorine doped optical fiber, EP Patent 1,876,150.
- Regnier, E., B. Poumellec, et al. (2005). "Infrared optical properties of highly P doped silica fibres: a spectroscopic study." *Glass Technology* **46**(2): 99-102.
- Saito, K. and A. Ikushima (1998). "Structural relaxation enhanced by Cl ions in silica glass." *Applied Physics Letters* **73**: 1209.
- Saito, K. and A. Ikushima (2002). "Effects of fluorine on structure, structural relaxation, and absorption edge in silica glass." *Journal of Applied Physics* **91**: 4886.
- Saito, K., H. Kakiuchida, et al. (1998). "Light-scattering study of the glass transition in silica, with practical implications." *Journal of Applied Physics* **84**: 3107.
- Saito, K., M. Yamaguchi, et al. (2004). "Approach for reducing the Rayleigh scattering loss in optical fibers." *Journal of Applied Physics* **95**: 1733.
- Saito, K., M. Yamaguchi, et al. (2003). "Limit of the Rayleigh scattering loss in silica fiber." *Applied Physics Letters* **83**: 5175.
- Sakaguchi, S. (2000). "Relaxation of Rayleigh scattering in silica core optical fiber by heat treatment." *Electronics and Communications in Japan (Part II: Electronics)* **83**(12).
- Sakaguchi, S. and S. Todoroki (1998). "Rayleigh scattering of silica core optical fiber after heat treatment." *Applied optics* **37**: 7708-7711.
- Sakaguchi, S. and S. Todoroki (1999). "Viscosity of silica core optical fiber." *Journal of non-crystalline solids* **244**(2-3): 232-237.
- SHACKELFORD, J., J. MASARYK, et al. (1970). "Water Content, Fictive Temperature, and Density Relations for Fused Silica." *Journal of the American Ceramic Society* **53**(7): 417-417.
- Simmons-Potter, K., B. Potter Jr, et al. (1996). "Novel process for the production of large, stable photosensitivity in glass films." *Applied Physics Letters* **68**: 2011.
- Tajima, K. (1998). Low-loss optical fibers realized by reduction of Rayleighscattering loss.
- Tajima, K., M. Ohashi, et al. (1992). "Low Rayleigh scatteringP 2 O 5-F-SiO 2 glasses." *Lightwave Technology, Journal of* **10**(11): 1532-1535.
- Todoroki, S. and S. Sakaguchi (1997). "Rayleigh scattering and fictive temperature in VAD silica glass with heat treatment." *Nippon seramikku kyokai gakujutsu ronbunshi* **105**(5): 377-380.
- Tomozawa, M., J. Hong, et al. (2004). "IR investigation of the structure of silica glass fibers." *GLASS SCIENCE AND TECHNOLOGY-FRANKFURT AM MAIN-* **75**: 262-276.
- Tomozawa, M., Y. Lee, et al. (1998). "Effect of uniaxial stresses on silica glass structure investigated by IR spectroscopy." *J. Non-Cryst. Solids* **242**(2): 104-109.
- Tsujikawa, K., K. Tajima, et al. (2000). "Rayleigh scattering reduction method for silica-based optical fiber." *Journal of lightwave technology* **18**(11): 1528.
- Tsujikawa, K., K. Tajima, et al. (2005). "Intrinsic loss of optical fibers." *Optical Fiber Technology* **11**(4): 319-331.
- Wissuchek, D., C. Ponader, et al. (1999). Analysis of residual stress in optical fiber.
- Zarzycki, J. (1982). *Glass and the Vitreous State (Les Verres et l'Etat Vitreux)*, Masson, Paris.

Optical Fibres Turbidimetres

Miguel A. Pérez and Rocío Muñiz
University of Oviedo
(Spain)

1. Introduction

This chapter presents a new type of nephelometric turbidimeter capable of really functioning on-line, avoiding any type of sampling of the liquid to be measured and, as a result, not requiring valves, pumps or any other type of electromechanical device, which results in it lasting longer and reducing maintenance. In addition, it takes advantage of the possibility of light conduction via optical fibres to avoid the electrical parts coming into contact with or close proximity to the liquid; the use of optical fibres also avoids interference, improving the Signal-to-Noise ratio and offering remote measuring.

This type of turbidimeter is for general application in the literal sense and, amongst the range of uses measuring the turbidity of both urban and industrial waste and of water for human consumption could be mentioned; however, the application is presented for measuring turbidity in the wine industry during wine-making processes, which presents added problems such as colour interference and the high interval of recordable values, which can reach levels of almost nil to over 4000 NTUs.

The chapter discusses the various possibilities for measuring turbidity that could be used, analyzing their advantages and disadvantages. An experimentally verified alternative is suggested and is discussed in detail.

2. Turbidity measurement

2.1 Nephelometric turbidimetres

Turbidity is a parameter which quantifies the number of particles in suspension in a liquid and is of great interest in environmental monitoring (APHA-AWWA-WPOC; Harrison & Fish, 1999; ISO7027, 1990, US-EPA, 1999; Wilde & Gibs 1998) and, in several industrial sectors, such as food industry (Couto & Caldeira, 2002, 2003; OIV, 1994, 2000; Qi Xin et al., 2006). Turbidity is determined optically, illuminating the liquid to be measured with a light beam and observing the total of light scattered by the particles in suspension in that liquid: the greater the number of particles, i.e. greater turbidity, the greater the light dispersion (APHA-AWWA-WPOC; US-EPA, 1999; García et al., 2005; Mylavaganam & Jakobsen, 2001; Sadar; Honeywell). This process is usually carried out by using a light source and a sensor placed perpendicularly to the beam and so that the beam aperture angle and the angle at which the sensor is capable of reading the light do not interfere and, therefore, light does not reach the sensor directly from the emitter. The system is completed by a second light sensor

that reads the non-scattered light emitted and that crosses the liquid as shown in Fig. 1 (US-EPA, 1999; García et al., 2005).

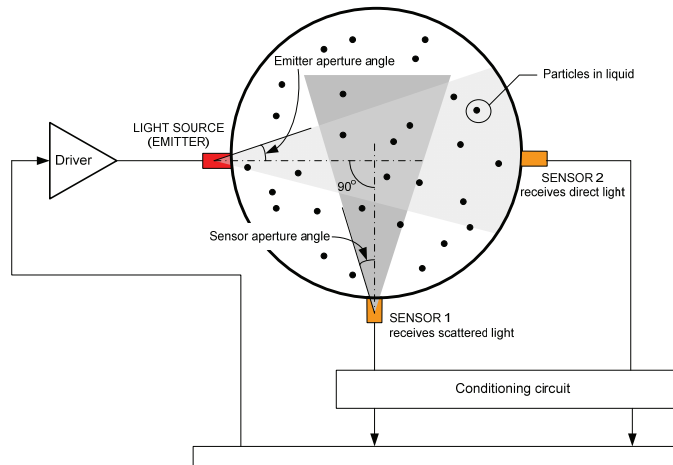


Fig. 1. Principle of operation of nephelometric turbidimeters: the light beam from emitter is scattered by particles in suspension: the scattered light - collected by sensor 1 - is proportional to the number of particles in suspension; light received by sensor 2 is used to correct any deviation of light emission level.

2.2 Operation problems in two-phases multi-beam turbidimetres

This basic system can be modified to improve its performance by adding a second emitter which alternates with the first one (García et al., 2006). In this case, each emitter is activated in a phase and the two sensors alternate the measurement of direct light and scattered light, eliminating the measurement uncertainty introduced by the differences between both subsystems; sensors and conditioning circuits (Fig. 2).

References can be found in the bibliography to other systems with a larger number of sensors to measure scattered light, situated at various angles - 60° , 120° or 135° - as shown in Fig. 3, in order to reduce final measurement uncertainty (APHA-AWWA-WPOC; US-EPA, 1999).

However, the latter systems with a high number of sensors are much more complex, and the presence of a larger number of devices reduces long-term reliability. The two-phase system in Fig. 2, though it may improve measurement by reducing uncertainty, presents other problems derived from the fact that both sensors must read a very intense signal - direct light - and a very weak one - scattered light, above all, at low turbidity levels - so a very high dynamic margin or two amplification circuits with very different gain are required, which would be commuted in each phase as we can see in Fig. 4 (García et al. 2005).

Whether using a system like that in Fig. 1 or either of those in Fig. 2, the scattered light depends on the quantity of light emitted, so a correct measurement must take into account the emission intensity to reduce any fluctuation in it, introducing uncertainty when measuring turbidity

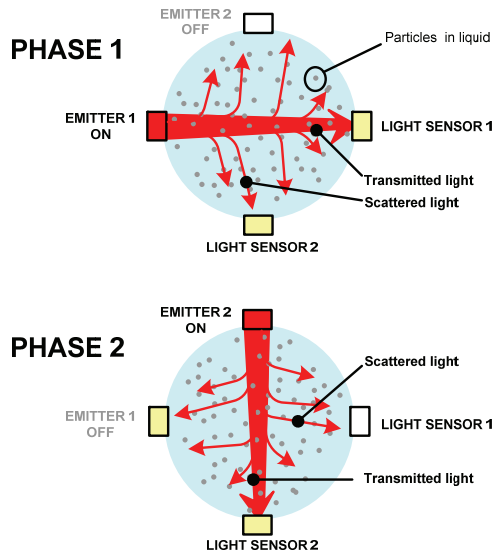


Fig. 2. Operation of four beam turbidimeter: light emission is alternated between emitters 1 and 2. During Phase 1, emitter 1 is on, sensor 1 receives the transmitted light, and sensor 2 receives scattered light; during Phase 2, the light emission is provided by emitter 2, transmitted light is received by light sensor 2, and scattered light, by light sensor 1.

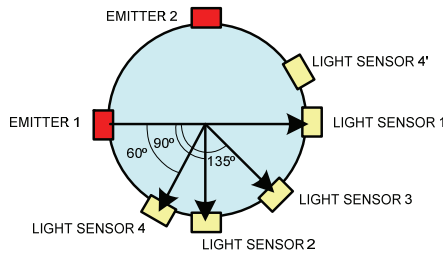


Fig. 3. Two-phases multi-beam turbidimeter.

This could be avoided by a ratiometric calculation which uses some magnitude dependent on emission light.

$$\text{Ratiometric value} = X(\text{turbidity, emission}) / Y(\text{emission}) \tag{1}$$

Unfortunately it is not easy to find that magnitude dependent only on the emission light since direct light read by the sensor depends on the turbidity so, if it is used in a ratiometric quotient, a non-linear and non-monotone expression will be obtained that produces equal values for different turbidity values, as shown in the experimental results in Fig. 5.

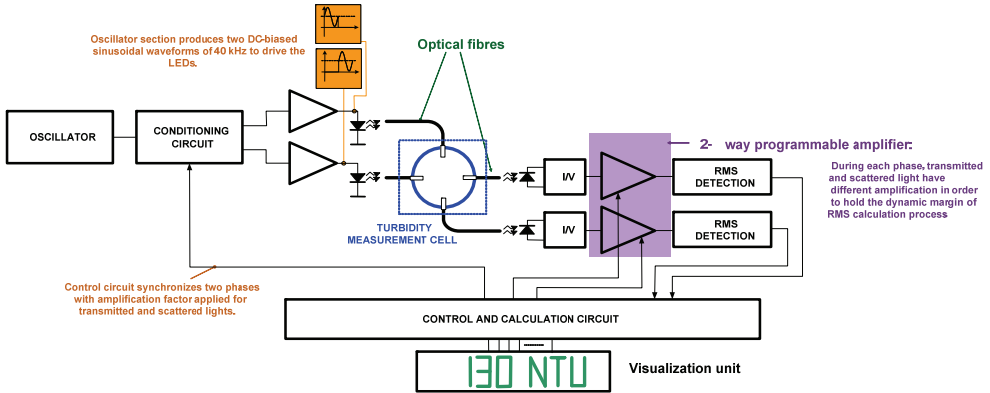


Fig. 4. Block diagram circuit for two-phases turbidimeter with optical fibres.

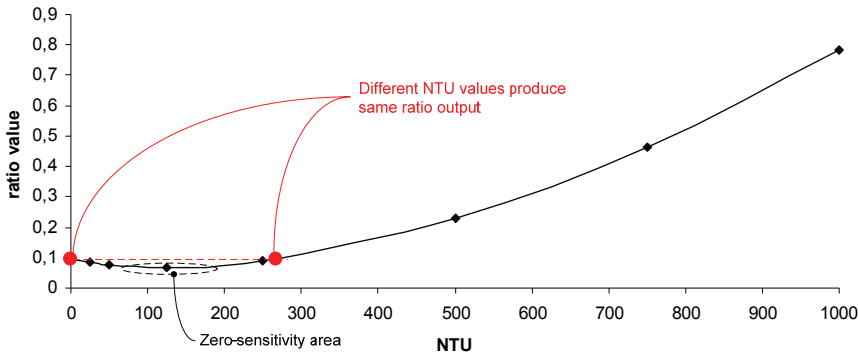


Fig. 5. The direct ratiometric measurement causes a no-defined problem due to the fact that different turbidity values produce the same output value. For example, a value is obtained with 260 NTU similar to that obtained with 0 NTU, which is completely unacceptable.

A calibration curve like the previous one would be unacceptable since it would produce uncertainty in the measurement by resolving the inverse problem and require more knowledge to help determine in which area of the curve the measurement is (Menke, 1989, Thikhonov & Arsenin, 1977). This problem shows in any configuration of the scattered light sensors and with any value of the distances between sensors, so the turbidimeters that compensate emission in this way have to work with two ranges or measurement zones and an intermediate area of zero sensitivity.

3. Application of optical fibres to turbidity measurement

3.1 Three-beams optical fiber turbidimeter

Commercial sensors that can work on-line function by some type of sample-taking system, like a peristaltic pump or similar which takes a fraction of liquid to the measuring cell and

then empties it (Sadar; Honeywell); in reality, they are not very different from the laboratory turbidimeters and only include some more devices that allow them to take the sample more or less automatically. As this process is not instantaneous, they cannot be classed as authentic on-line devices but rather an improvement in off-line laboratory equipment. In addition, the presence of electromechanical blocks, additional conductions, etc. increases maintenance and necessarily reduces reliability and useful life.

Here, we propose a system based on optical fibre that can be placed on the same line (conduction) on which turbidity is to be measured, without using any type of sample taking, so it is a truly on-line system which provides real-time turbidity information. In order to solve the previously described problems related to the shape of the calibration curve, the system uses a different technique which allows them to be eliminated, producing a monotone reading that increase with turbidity.

The idea on which the proposed technique is based is that of maintaining the quantity of light reaching sensor 2 in Fig. 1 constant, regardless of liquid turbidity. To do this, the value read by sensor 2 is feedback and the light emitted by the source is thus adjusted.

A regulator designed to guarantee the stability of the system and the best performance completes the system. As the objective is to obtain zero errors permanently, the most appropriate regulator for this case is a PI-type one. In this way the quantity of light received has not dependence on turbidity or any disturbance, amongst which the following can be mentioned:

- Ageing of the emission source.
- Warming-up processes of the emission source when starting up the system.
- General disturbances produced by the temperature.
- Disturbance caused by the liquid absorbing light, which can be a critical factor in coloured liquids, above all when working with sensitive wavelengths.

In this way the direct light is constant and its dispersion only depends on the quantity of particles in suspension in the liquid, that is, its turbidity, and can be read by the sensor placed at 90° to the beam.

To avoid light dispersion in the perpendicular to its path, the sensor must be placed at the shortest possible distance from the measurement area, but without it "directly seeing" the emission from the source. Fig. 6 shows this system. The proposed measuring system is a three-beam nephelometric turbidimeter similar in concept to that initially proposed in Fig. 1, but with a feedback of direct light in order to guarantee that it remains constant.

The turbidimeter proposed in Fig. 6 has been used to verify overall operation. The practical aspects of its construction follow.

3.2 Designing a prototype

This system can work with any type of light source, as feedback of the direct signal picked up by the sensor compensates for the possible disturbances that colour would introduce due to absorption phenomena. However, to reduce the effort of the regulator, infra-red light has been chosen as it has a large number of possible emitters and sensors, which simplifies its use. In this particular case the devices listed in Table 1 have been used as emitters and receptors.

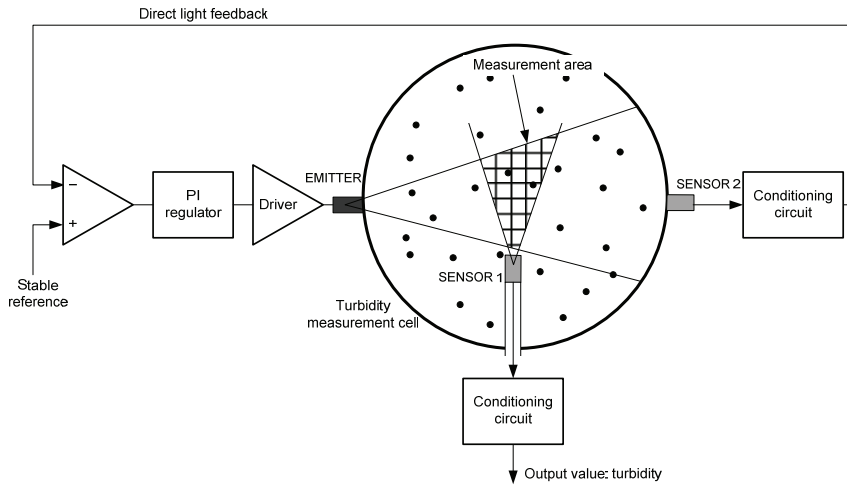


Fig. 6. Three-beam feedback turbidimeter. The sensor 1 conditioning circuit output contains the turbidity information.

Device	Spectral characteristics		
	Peak	Bandwidth	
LED L7758	850 nm	50 nm	$I_{max} = 100 \text{ mA}$
Photodiode AEPX65	820 nm	400 nm	Responsivity = 0.3 A/W

Table 1. Main characteristics of the devices used as light source and receptor.

The design of the sensor has no critical aspects except for guaranteeing its water tightness and preventing the beam of light emitted from interacting directly with the sensor placed at 90°. Fig. 7 proposes a possible design corresponding to a section of stainless steel pipe 32 mm in diameter with an 8 mm wall. The three optical fibres for transporting the light are made by SunOptics, 1 m long, multifilar and of a type of quartz- borosilicate - that means conduct is optimum in the spectrum area in which the emitters and receptors work. They are finished with an M8 stainless steel screw at one end - which is connected to the measuring cell - and SMA at the other.

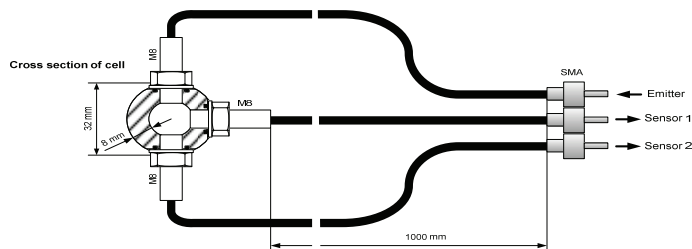


Fig. 7. Design of the turbidity measurement cell using optical fibres as light conductors.

Fig. 8 shows the measuring circuit and adds the LED excitation system, the conditioning circuits for the two receptor photodiodes and the feedback and regulator that allow the light level to be kept constant.

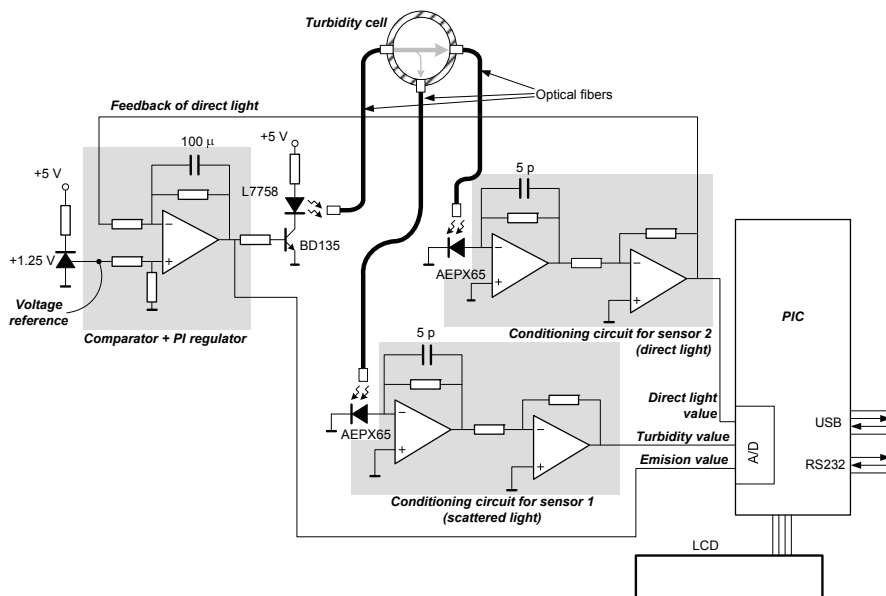


Fig. 8. Turbidimeter circuit. The calculation tasks, function test, display and distribution of the data are to be done by a PIC type low cost microcontroller.

Both the output providing information about the level of scattered light and direct light emission and reception are read by the A/D converter of a PIC-based microcontroller system for later processing, presentation and distribution of the reading obtained, thus completing the turbidimeter device. Although reading the direct light level is not necessary on the first approximation, as it is feedback and should not vary, that would only happen under ideal conditions with a perfect regulator. Under real conditions changes – though small – would occur, which could produce errors if ignored. In addition, permanent reading of those variables could be used to verify the correct functioning of the feedback loop, acting as a permanent test of the validity of the measurement obtained compared with failures of any kind or with a measurement range output.

3.3 Calibration curve

As the ratio between the turbidity and the scattered light measurement is not strictly linear and depends on the geometry of the sensor, the corresponding calibration curve was obtained using low uncertainty turbidity patterns from dilutions in ultra pure water of a certified 4000 NTU formacine ($C_2H_4N_2$) pattern from Dinko, code 1.9779.00, prepared from Baker reference materials, codes 1114, 3371 and 4218, following the specifications listed in (APHA-AWWA-WPOC). The patterns obtained by dilution are shown in Table 2 together with their uncertainty values.

NTU	0	50	100	150	200	250	300	400	500
Uncertainty(%)	-	.05	.11	.17	.24	.3	.35	.45	.58
NTU	750	1000	1200	1400	1600	1800	2000		
Uncertainty(%)	.77	1.0	1.2	1.4	1.7	1.9	2		

Table 2. Turbidity patterns obtained by diluting a certified 4000 NTU pattern.

Under these conditions the calibration curve was obtained by measuring the values provided by the two sensors after conditioning and amplifying; the excitation value of the light emitter was also read. The graphs in Figs. 9 to 11 show all the data obtained.

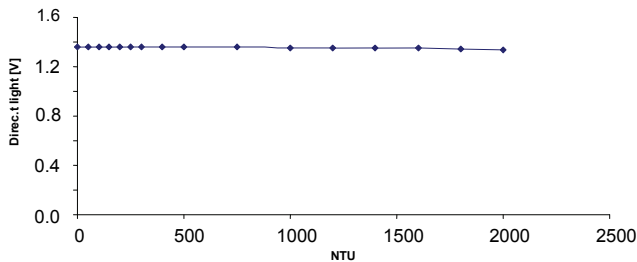


Fig. 9. Direct light as regards turbidity. Maximum variation is 1.5% over the turbidity span.

As can be seen, the direct light remains almost constant (Fig. 9) throughout the turbidity interval. This is due to the action of the regulator which conveniently raises the excitation applied to the LED (Fig. 10). The measured level of scattered light (Fig. 11) contains the turbidity information and, as can be seen, is increasingly monotone, as planned. However, although it presents quite a linear area for low turbidity, global conduct is not linear, and even, a polynomial adjustment returns a relatively high correlation coefficient, but which can be improved, as the next section shows.

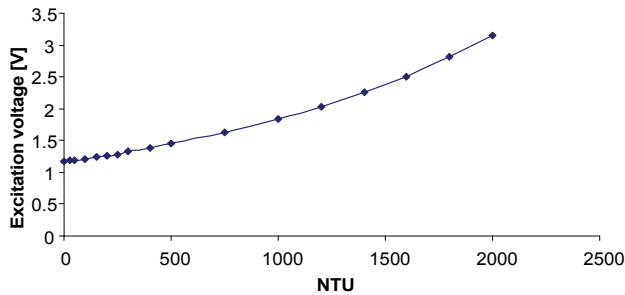


Fig. 10. Excitation signal from the emitter increasing with turbidity to maintain light constant in the direct light receptor.

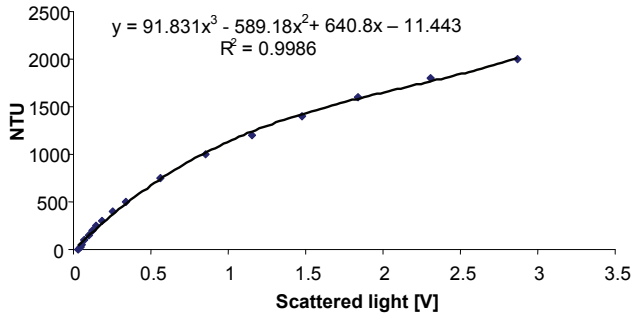


Fig. 11. Calibration curve using the signal received at the scattered light sensor to determine turbidity: the adjustment obtained is not excessively good, above all for low turbidity values.

This effect is due to the fact that the light is only guaranteed to be constant close to the receptor placed at 180° to the emission, but not in the central area, precisely the area where turbidity is measured. Fig. 12 explains this, showing the evolution in the light emission area in terms of turbidity.

To solve the problem a measurement can be made by obtaining a dimensionless ratiometric value (TRV) which eliminates the effect of the excitation light:

$$TRV = V_{scattered} / V_{excitation} \tag{2}$$

Obtaining this value of the measurement values gives the quasi-linear graph of Fig. 13, which the microcontroller will use to make the measurement. Table 3 shows the coefficients of three possible adjustments: linear and polynomial of orders 2 and 3, observing that the correlation coefficient is very high, above all in the last mentioned case.

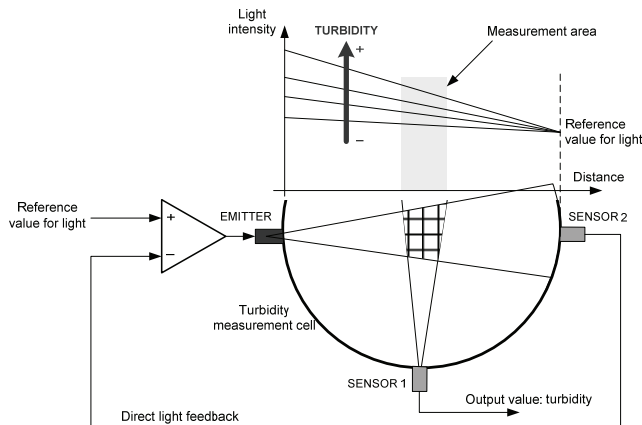


Fig. 12. The light illuminating the measurement area is not kept constant with the turbidity in spite of feedback.

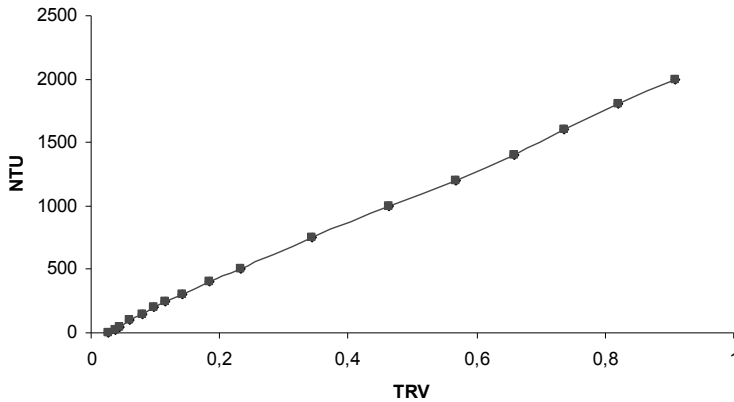


Fig. 13. Calibration curve obtained from the Turbidity Ratiometric Value (TRV). The appearance of the curve is much more linear than that of Fig. 11.

Function type	Coefficients	R^2
Linear	$2218.5 \cdot \text{TRV} - 30.378$	0.9992
2nd order	$-25.772 \cdot \text{TRV}^2 + 2240.6 \cdot \text{TRV} + 32.587$	0.9982
3rd order	$1035.9 \cdot \text{TRV}^3 + 1440.0 \cdot \text{TRV}^2 + 2735.7 \cdot \text{TRV} + 63.186$	0.9998

Table 3. Approximations obtained by least squares for the calibration curve of Fig. 13. A linear approximation produces acceptable behaviour, although that of the third order is somewhat better.

The complexity of the calculation software on passing from a linear approximation to a polynomial one is not significant, nor are the mathematical errors produced very different, so the most complex approximation that provides the highest veracity level has been chosen.

3.4 Experimental results

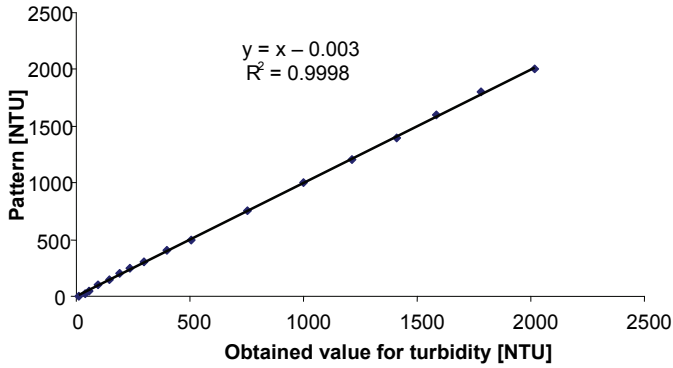
The system, designed as described in detail in the previous section, has been extensively checked, verifying that it works in the different measurement areas for which it was designed, using turbidity patterns obtained by dilution, as shown in Table 2. The results are shown in the graphs in Fig. 14, observing that there is an excellent ratio between the pattern value and that provided by the system (Fig. 14a) which is shown with a maximum error below 1% over the whole measuring range (Fig. 14b).

4. Application of optical fibre turbidimeters

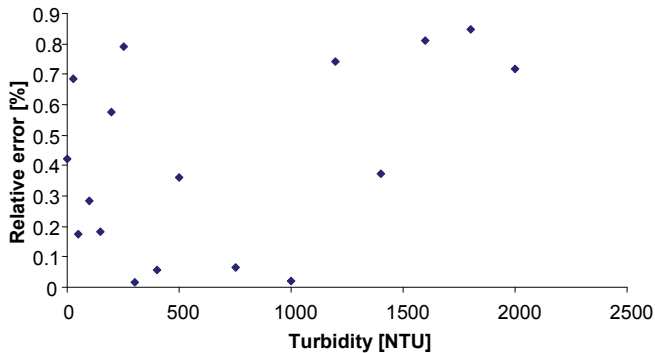
4.1 Environmental measurements

Environmental measurements in water includes a lot of parameters such as DO (Dissolved Oxygen), COD (Chemical Oxygen Demand), BOD (Biological Oxygen Demand),

contaminants concentration (heavy metals, tens active substances, pesticides...) and, of course turbidity as a indicator of the number of particles in suspension.



(a)



(b)

Fig. 14. (a) Turbidity obtained by the system vs. the pattern turbidity values; (b) relative error of the measuring system which does not exceed 1% in measurement span.

These measurements are carried out in monitoring process of continental water (rivers and lakes) and in sea water, and – of course – in drinkable water, disposal water and in the output of water treatment plants. In all these cases, water turbidity is one of most important parameter to define the quality and/or contamination level of each case.

Turbidity measurement in environmental applications is a special case because we must take into account some measurement conditions:

- A multi-position measurement is very usual to obtain a complete knowledge of contamination level in large volumes of water such as lakes or rivers.

- In most of cases, a remote measurement becomes necessary due to long distances between measurement point and processing unit.
- Turbidity measurement is carried out under external (ambient) light perturbations.

The use of optical fibres provides a good solution for the first and second conditions, but the third one needs an additional treatment.

The light levels used always in all previous Figures correspond to continuous (DC) values, so there is a certain risk of interference from exterior sources of light which could affect the measuring cell. This is a minor problem which occurs in few applications and which, in any case, could be solved without any great difficulty. However, if this interference becomes annoying, an AC signal, which could be filtered with a band pass filter, can be used, almost completely eliminating the external interference. The operation of the system must not vary as long as the frequency of the excitation signal is within the dynamic limits of the electronic system and of the emitters and receptors, which is not usually a very important limitation.

To verify it, a 10 kHz sinusoidal waveform on a bias level has been used as a reference signal for the system. Three experiments have been carried out under these conditions:

- Completely closed sensor without outside light affecting it.
- Sensor exposed to ambient fluorescent light with oscillations at 100 Hz.
- Sensor exposed to ambient light under indoor conditions plus a 60W incandescent light 0.3 m away from the sensor.

The values obtained are similar to those obtained continuously, due to the fact that the regulator acts correctly, compensating for the outside disturbance. The graph in Fig. 15 shows the results of this experiment with a much reduced effect from the outside disturbance. As we can see in Fig. 15, the three graphs obtained according to turbidity do not present important variations when the sensor does not receive any type of light, on being subjected to ambient illumination of fluorescent origin (100 Hz) or to close intense light.

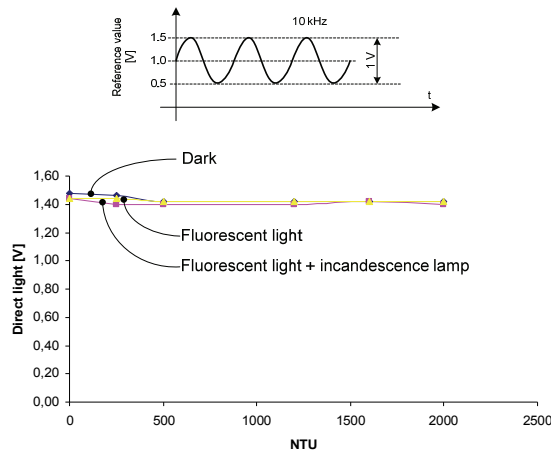


Fig. 15. Above, waveform used as a reference which consists of a 10 kHz sinusoidal, 0.5 V amplitude with a 1 V DC-bias. Below, amplitude of the signal received by the direct light sensor after amplification.

Therefore, whether working with continuous or alternating excitation the behaviour of the turbidimetre is very similar, choosing the latter if ambient light disturbances from outside are foreseeable.

4.2 Measurement of turbidity in food and related industries

Turbidity is an important parameter in food related industries because they use drinkable water. In those cases, turbidity measurement is quite similar to environmental cases, but in some special industries, the turbidity measurement process presents some problems.

In the particular case of the wine industry, turbidity is a basic control parameter during wine-making and of quality in the finished product. In addition, turbidity is related to the fermentation kinetic as it presents similar conduct to CO₂ release velocity (Colombre, Malherbe & Sablyrolles, 2005) which indicates the fermentation activity in the unfermented grape juice because it is linked to the growth of yeast and the increased production of fermentation gasses. Turbidity is usually very low for finished wine, in most cases below 1 or 2 NTUs but, during the wine-making processes, the values may exceed 2000 NTUs, a very wide measuring range. As an example, Fig. 16 shows the evolution of turbidity during a wine-making process in which these limits are exceeded.

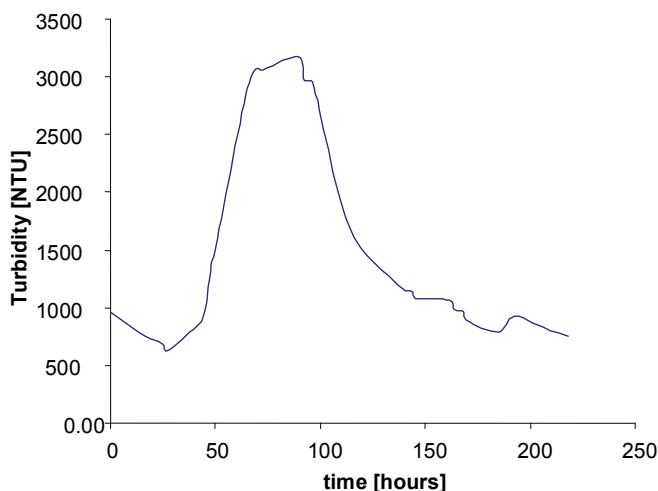


Fig. 16. Evolution of turbidity during a wine-making process lasting 10 days. This corresponds to a fermentation using tempranillo grapes

The application of the system to the wine industry for on-line measurement of turbidity during wine-making presents some disadvantages a priori:

- The presence of colour, which can produce light absorption phenomena.
- The presence of bubbles, which can modify measurements because they act by dispersing light, as do particles in suspension.

The first problem has little effect on measuring, since absorption in the infra-red area worked with is similar for different red, white and rosé wines, according to the tests carried out which appear in Table 4. The small differences recorded among finished wines made

from various grapes and with turbidity below 2 NTU, are compensated for without any difficulty by the regulation system to maintain the light level constant.

The problem of the gas bubbles is more complex to solve and presents difficulties for any type of turbidimeter which is used during wine-making, because fermentation produces a considerable amount of CO₂ and consequently of bubbles which cause light dispersion and an unreal rise in turbidity measurement values. In order to solve this problem, the measuring area can be pressurised by permanent derivation of the fluid without any major operation problems or losing sensor features as regards truly on-line measuring capacity. In the same way statistical treatment of the data eliminating the outliers solves the problem, providing real turbidity data.

Red wines

Zone	Grape type	Ageing in cask	IR absorption (in relation to ultra pure water)
Rioja	Tempranillo, Mazuelo	10 months	1%
Toro	Tinta de toro	3 months	1%
Somontano	Merlot, Cabernet Sauvignon	4 months	0.8%
Duero river	Tempranillo	-	0.9%
Navarre	Tempranillo	-	0.9%

Rosé wines

Navarre	Garnacha	-	0.2%
Catalonia	Tempranillo, Garnacha	-	0.2%
Rioja	Tempranillo	-	0.3%

White wines

Penedés	Chardonnay	20 days	negligible
Alicante	Muscat of Alexandria	-	negligible
Penedés	Parellada	-	negligible
Rueda	Verdejo	-	negligible

Table 4. Influence of the grape type on light absorption in the infra-red (AEPX 65 LED work area) in comparison with ultra pure water measured with an Ocean Optics VIS-NIR 2000 spectrophotometer. In all cases the absorption level is very low and is compensated by the feedback system without any significant effort.

5. Conclusions

A turbidity sensor is presented, based on a three-beam design including novelties such as the use of optical fibres for transporting the light and a feedback for the direct light - transmitted light - to guarantee constant excitation levels. The main advantages are that it works on-line without any type of sampling, its consequent low-cost and the elimination of safety and electrical risk limitations by avoiding the liquid coming into contact with or close to any voltage area.

In order to check whether it works in practice a low-cost specific prototype has been developed which works in the close infra-red and which presents optimum behaviour if a ratiometric value, the quotient between scattered and emitted light, is used as an output variable to represent turbidity. This produces a calibration curve with high linearity.

The developed prototype has been widely checked in experiments using certified patterns, obtaining excellent correlation between the real values and those provided by the equipment, the error remaining limited to below 1% throughout the measurement range. The effect of possible luminous type exterior disturbances has also been checked, and, if they exist, an elimination technique using biased sine type signals instead of DC signals has been proposed as a reference.

The use of turbidimeters based on the work principle described has an application in different fields, such as environmental measurements – urban or industrial waste water – or in industry itself as part of production processes. In this sense its application in measuring turbidity in wine-making processes, where it is significant, can be highlighted. In these cases the measurement range is very wide and colour can appear as an important measurement disturbance. For this case, behaviour with a large number of wines of varied origin and grape types has been checked, observing that the system is capable of compensating for the small variations in absorption that they cause in the infra-red, guaranteeing functioning truly independent of colour.

6. References

- APHA-AWWA-WPOC "Standards methods of Water Wastewater", APHA-AWWA-WPOC F, Ed. 16 and 17.
- Colombre, S., Malherbe, S., Sablryrolles J.M. (2005) "Modelling alcoholic fermentation in enological conditions: feasibility and interest", *Ann. J. Enol. Vitc.* 56:3
- Couto, L.M. & Caldeira, M.A. (2002) "Port-wine spectral monitoring" *Spectroscopy Europe* 14/5, pp. 22-27.
- Couto, L.M. & Caldeira, M.A. (2003) "Port wine spectronephelometry" *Optics and Laser* 25 Ed. Elsevier pp. 491-496.
- García, A. et al, (2005) "A New Design of Low-Cost Four-Beam Turbidimeter by Using Optical Fibers", *Proceedings of IEEE-IMTC'05, Canada.*
- Harrison D. & Fisch M., (1999) "Measurement, Instrumentation and sensors – Turbidity Measurement", CRC & IEEE Press.
- Honeywell, "Turbidity sensors", <http://content.honeywell.com>
- ISO 7027 (1990), Water quality, International Standard,
- Menke W. (1989) "Geophysical data analysis: discrete inverse theory", Academic Press, 1989.
- Mylvaganam S. & Jakobsen T., (2001) "Turbidity sensor for under water applications", Aanderaa Instruments Inc Press.
- OIV (2000) "Wine turbidity, Resolution OENO 4/2000".
- OIV, (1994) "Compendium of International Methods for Spirits, Alcohols and Aromatic Fractions in Beverages. Turbidity – Nephelometric Analysis Method".
- Qi Xin, Hou Zhi Ling, Tian Jian Long & Yu Zhu (2006) "The rapid determination of fat and protein content in fresh raw milk using the laser light scattering technology", *Optics and Lasers in Engineering*, 44, pp.858-869.

- Sadar M., "Turbidity Standards" Technical information series, Booklet No.12, <http://www.aquatrend.com/downloads/Lit/PDF/Whitepapers/7045.pdf>
- Thikhonov, A.N. & Arsenin V.Y. (1977) "Solutions of ill posed problems", Winston/Wiley, New York, 1977.
- United States Environmental Protection Agency. Office of water. (1999)"Guidance Manual for Compliance with the Interim Enhanced Surface Water Treatment Rule: Turbidity Provisions".
- Wilde F.D. & Gibs J. (1998) "Turbidity", U.S. Geological Survey TWRI Book 9, No. 4, chapter 6.7.

Distributed Optical Fibre Sensors for Structural Health Monitoring: Upcoming Challenges

Vincent Lanticq¹, Renaud Gabet²,
Frédéric Taillade³ and Sylvie Delepine-Lesoille⁴

¹*Electricité De France R&D*

²*Telecom-Paristech*

³*Laboratoire Central des Ponts et Chaussées*

⁴*Agence Nationale pour la gestion des Déchets RAdioactifs
France*

1. Introduction: SHM and optical fibre sensing

In the last mid-century, the new civil engineering structures have undergone a revolution in terms of complexity such as large dimensions (Millau Bridge in France, Rion-Antirion Bridge in Greece, Stonecutters Bridge in Hong Kong, Akashi Kaikyo Bridge in Japan, etc.). The authorities managing the old civil structures face the challenge of increasing lifetime of the structures meanwhile maintaining the transportation network limited cost with sparsely perturbations for the users.

In this context, a large sensor network placed inside or surface mounted on the structures is necessary to provide advanced warning of structural state, wear or damage of the structures. The measurement and monitoring often have an essential role in management. The information obtained is used to plan and design maintenance activities, increase the safety, verify hypothesis, etc. This new field of research and development techniques is named Structural Health Monitoring (SHM) (Ou & al., 2005). Typically, several hundred of strain or temperature gauges, accelerometers, etc. are installed in the civil structures. Electrical addressing through complex wiring harness is fine for laboratory use but *in situ* installations are costly and impractical. Indeed, the wires corrodes, the signals are perturbed by electromagnetic interferences which is physically bulky. To bypass these problems, the recent instrumentations are based on wireless sensor networks but they face the problem of storage and energy recovery. Another solution consists in using the Optical Fibre Sensor technology (Glisic & Inaudi, 2007).

Temperature and strain optical fibre sensor exists in various Forms: pressure, chemical (gas detection), radiation and even hygrometry may be sensed with commercially available sensors. As described with great details in (Lopez-Higuera, 2002), optical fiber sensors typically involve a light propagating beam which travels along an optical fibre waveguide. The light is then modulated in response to an external physical or chemical stimulus. The modulation induced can change the optic propagation delay, the optical path length, the spectral response, the amplitude transmission, the optical polarisation state or, through non

linear phenomenon, the optical frequency (wavelength). These changes are monitored after transmission through optical fibre. Optical fibre sensors (OFS) have certain advantages including immunity to electromagnetic interference, lightweight, small size, high sensitivity, large bandwidth, and ease in implementing multiplexed or distributed sensors. The serial multiplexed and distributed architectures are especially relevant for structural applications which usually need a lot of measurement points.

OFS can also be configured in point, point multiplexed, integrating or distributed formats as shown in figure 1. A lot of point-like optical fibre sensors based on Bragg gratings or small Fabry-Perot cavities (< 10cm) have been developed in the nineties, and their multiplexing is still an intensive research topic nowadays, mainly on the aim of cutting down the whole sensing system costs. Quasi-distributed sensors perform intrinsically integrated measurement into large Fabry-Perot cavities (> 20cm) induced by several inline partial mirrors in the fibre. The main advantage of this technique compared to point-like measurement is to avoid any Blind-zones (without sensitivity), as shows figure 1.

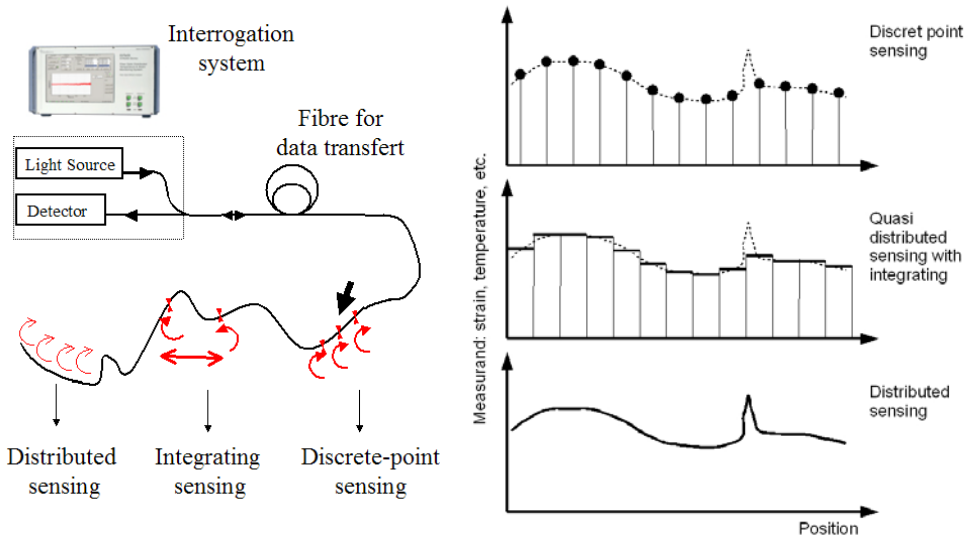


Fig. 1. Concepts of point, integrating and distributed sensing.

About ten years ago, distributed optical fibre sensing technologies appeared, constituting a breakthrough in sensor technology. A truly distributed measurement system for structural monitoring has the considerable advantage that the optical fibre itself can be used as the transduction mechanism without any further modifications to the optical fibre. In consequence, the meshing measurement is considerably improved. It depends on the physical phenomenon implemented and the optoelectronic interrogation unit used.

Those methods, based on elastic optical effect (Rayleigh) or inelastic optical effects (Raman, Brillouin) of the backscattered light, allow to measure temperature and strain into a long range zone (typically 20 km) with a relative small spatial resolution (typically 1 m), bringing consequently offer huge multiplexing possibilities. Now this technology has become quite

mature and suitable for industry, thanks to the creation of many companies providing distributed optical fibre sensing devices.

After a short introduction, the present chapter proposes an overview of the distributed sensing technologies in particular for the temperature and strain monitoring cases. The different technologies based on Optical Time Domain Reflectometry and on inelastic optical effect (Raman and Brillouin) are briefly described. The performances of these systems in term of localisation and spatial resolution of the measurement are discussed in section 3. Finally, the section 4 evokes the problem of the host material inclusion which plays an important role in the transfer mechanisms between the structure and the optical fibre sensor.

2. Distributed sensing for temperature and strain monitoring

The term distributed sensor designates the case in which the optical fibre itself becomes a sensor (Lopez-Higuera, 2002), as opposed to punctual sensors multiplexed in great number. It is thus no longer necessary to implement anticipated sensor positions since measurements are being performed all along the optical fibre hooked up to the reading device (as well as within the extension cables!). In addition, the processing and manipulations required to make Bragg gratings or mirrors delimiting the long-period strain sensors act to significantly weaken the optical fibre. On the other hand, for distributed OFS (D-OFS), the commercial optical fibre (G652 and others) is placed directly inside its mechanical protective coating, which would suggest a more robust instrumentation. Precautions to take while choosing this protective coating are addressed in section 4.

For the last three years, major improvements have occurred in optical fibre sensing area, in particular concerning distributed optical fibre temperature and strain sensing. As detailed in (Rogers, 1999), truly distributed measurements rely on Rayleigh, Raman or Brillouin scattering in optical fibres described in the following sections, paired with a localization process such as Optical Time Domain Reflectometry (OTDR described in this section), Optical Frequency Domain Reflectometry (OFDR, see section 3) or correlation probe-pump technique (section 3).

2.1 Distributed sensing fundamentals

a) Light backscattering

To understand how distributed sensors work, emphasis must be placed on the backscattering phenomenon taking place within optical fibres.

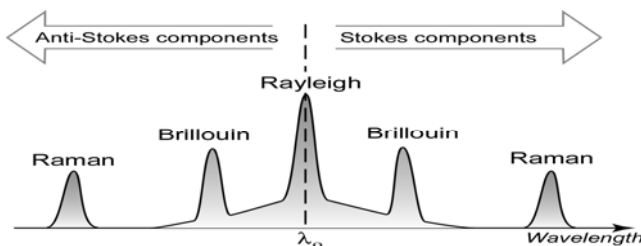


Fig. 2. Backscattering spectrum of a monochromatic wave within an optical fibre extracted from www.epfl.ch

As shown in Fig. 2, the light backscattered by an optical fibre segment without any defects or anormal characteristics is spectrally decomposed into three distinct peaks corresponding to three outstanding phenomena.

The first relates to Rayleigh scattering. The electromagnetic wave propagating in the fibre core interacts with the scattering centres, silica impurities and enhancing additives with dimensions well below the wavelength; these interactions give rise to a partial reflection in the vicinity of 10^{-7} m^{-1} , that can be detected and interpreted as described in the following (b). Raman scattering is an interaction between light and the corresponding coupling matter between a photon and the thermal vibration of silica molecules. As such, this phenomenon is highly dependent on temperature at the spectral level. The Brillouin effect originates from photon-phonon interaction; given its sensitivity to both fibre geometry and density, it depends on temperature and strain.

Temperature and/or strain distributed sensing systems based on these three backscattering phenomena are commercially available. They may take advantage of spontaneous or stimulated phenomenon, paired with a localisation process, the most common being OTDR.

b) Optical time domain reflectometry (OTDR)

Initially created to analyze losses inside optical telecommunication lines (Barnoski & Jensen, 1976), OTDR is categorized as an optical pulse-echo technique. As diagrammed in figure 3, this technique consists of injecting a laser pulse within an optical fibre and then measuring the backscattered intensity as a function of time: A period Δt corresponds to a pulse round-trip between the connector and a given point on the fibre located at distance d from the injection connector:

$$d = \frac{\Delta t}{2n_g} \quad (1)$$

where n_g means the group index. Range d_{max} of OTDR-based devices is limited only by roundtrip linear-loss which can come from material absorption or punctual damages. The width of measurement zones (each point of the trace is integration over this zone) is called spatial resolution and is linked with the temporal width of the pulse T_p by a similar relationship:

$$\delta z = \frac{T_p}{2n_g} \quad (2)$$

Spatial resolution is also the smallest distance to perform independent measurements.

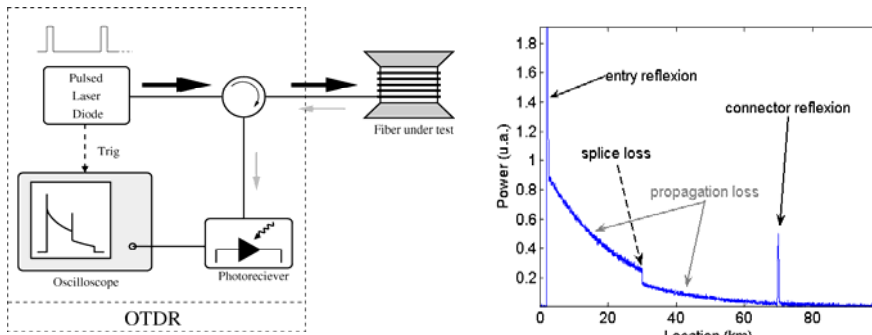


Fig. 3. OTDR (Optical Time Domain Reflectometry) operating principle, and typical trace.

OTDR instruments provide intensity variation measurements over distances in the tens of kilometres, with a spatial resolution at the meter scale. As illustrated in Fig. 3, by measuring intensity variations in the backscattered signal at the same wavelength as the injected wave, local optical fibre modifications may be detected: An abrupt return peak is interpreted as a mirror reflection (connector or damage on the fibre), and a sudden drop in intensity corresponds for example to shear loss.

2.2 Distributed sensing system families

a) Rayleigh backscattering based D-OFS systems

Light intensity variations cannot be precisely correlated with temperature nor deformations of the medium where the optical fibre has been embedded. Thus a simple OTDR be used as a measurement system for these parameters. To conduct the actual strain measurement, the value of the Rayleigh backscattering signal in optical fibres may be associated with optical fibres preliminarily fitted with punctual sensors, such as microbend sensors or another configuration that incorporates pre-calibrated losses (Wan & Leung, 2007) or Bragg gratings (LO et al., 2007) (Crunelle et al., 2009) in which cases the continuously-distributed aspect of the measurement would be lost.

Coherent OTDR showed recently great performances for temperature sensing by self-heterodyne detection, because of relatively long pulse duration, at time t , different wavelets backscattering from different locations of the fibre are simultaneously detected. If coherence time of the laser source is higher than the pulse duration, these wavelets can interfere, producing a slight beating signal around the classic OTDR trace. The frequency of the beating is strain and temperature dependent. A resolution about $0.01\text{ }^{\circ}\text{C}$ at 7 km distance with 1m spatial resolution has been performed by (Koyamada et al., 2009). A 10 s pulse is emitted from a coherent monochromatic laser source.

Another principle called OFDR uses Rayleigh scattering spectral properties (local complex reflectivity) to measure local optical path variations and deduce strain or temperature. It will be presented in great details in section 3 of this chapter.

b) Raman based D-OFS systems

Raman scattering originates from laser light photon interaction with thermal vibration of silica molecules (thermal phonons). It occurs into single-mode and multi-mode fibres. Fig. 4 sketches the well-known Stokes and Anti-Stokes process, occurring respectively if the virtual state of energy of a silica molecules is the fundamental or an excited state.

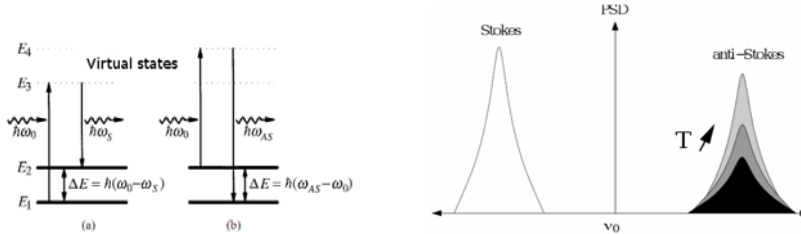


Fig. 4. Origin of Raman scattering (left) and sensitivity to temperature (right). “PSD” stands for power spectral density.

The anti-Stokes absorption mainly depends on temperature (Liu & Kim, 2003). Raman distributed optical fibre sensing systems are using OTDR pulsed technique previously described (in 2.1.b) to perform distributed intensity measurement of the anti-Stokes Backscattered light. This technique is called Raman-OTDR or R-OTDR. However, the anti-Stokes intensity evolution must be augmented with a reference measurement since optical fibre losses vary with time (increase with fibre aging, connector dirt or optical fibre curvatures etc.). Thus, Distributed Temperature Sensing (DTS) devices analyse the ratio between the Anti-Stokes and Stokes absorption line intensities (I_{RAS} and I_{RS}) using equation (3):

$$\frac{I_{RAS}}{I_{RS}} = \left[\frac{\lambda_S}{\lambda_{AS}} \right]^4 \exp\left(\frac{hc\Delta\nu}{kT}\right) \quad (3)$$

where λ_{AS} , λ_S are anti-Stokes and Stokes wavelengths, $\Delta\nu$ is their wave-number separation from the pump wavelength, h is Planck’s constant, c is the velocity of the light, k is Boltzmann’s constant, and T is the absolute temperature of the fibre core under measurement.

Nevertheless, Stokes intensity is a few times larger than anti-Stokes intensity and its bandwidth is usually much larger than the pump spectrum. What is more, few phenomena at the origin of optical fibre losses (bending losses especially in single-mode fibres, hydrogen darkening...) are wavelength-dependent and not modelled by formula (3). They may become highly sensitive as Stokes and anti-Stokes lines are separated by 80 nm at 1.55 μm . Recent developments combine various laser wavelengths (Lee et al., 2008). The optical fibre type is also a parameter to choose carefully while designing a Raman DTS: In multimode fibre the Raman scattering is bigger. For instance, (Farahani & Gogolla, 1999) shows that for a 15 km range, a graded-index multimode fibre is the optimum.

Several optoelectronic devices that conduct distributed temperature measurements using the Raman effect are available on the market and have already profoundly modified certain fields such as fire detection (Liu & Kim, 2003). The accuracy derived lies on the order of 0.1°C, 1 m of spatial resolution, over spans extending several tens of kilometres. As a case in point, the sensor Fibolaser from LIOS technologies company, commercialized by Siemens

(Glombitza, 2004) was installed on the Mont-Blanc Tunnel subsequently to the 1999 disaster. For distributed temperature measurements in civil engineering structures, EDF company (Electricité De France) has already implemented various field qualification of Raman scattering in multimode fibres. In the beginning of 2002 (Fry et al., 2004), although the optoelectronic instrument revealed some inabilities with field specificities, the sensing cable inserted inside 2 km of Oraison embankment (France) endured civil engineering construction works. Meanwhile optoelectronic instrument performances have been improved. 3km of Kembs embankment (France) were also instrumented with embedded sensors in 2006 (Hénault, 2006). Now, the focus is given in the way measurements may be interpreted with greater precision and less false alarm using statistics.

c) Brillouin based D-OFS systems

In optical fibres, Brillouin scattering takes origin from coupling between the optical mode and acoustic waves in the material (silica) produced by thermal excitation. Thanks to photoelasticity of the material, these acoustic waves create an index grating, moving at sound velocity in silica V_A . Thus, when an incident wave (so called pump wave) propagates in the fibre, a frequency-shifted optical wave (Stokes or anti-Stokes) is created, and propagates backward. To satisfy the coupling conditions, the frequency-shift (often pointed as the Brillouin frequency ν_B) is linked to optical and acoustic parameters by the following relationship:

$$\nu_B = \frac{2n_{eff}V_A}{\lambda_0} \quad (4)$$

where n_{eff} is the effective index of the optical mode *i.e.* the ratio between light speed in vacuum and in a medium, and λ_0 the operating wavelength.

Brillouin sensing consists in measuring the Brillouin frequency assuming it is proportional to temperature variations (ΔT) and strain ε :

$$\Delta \nu_B = C_T \Delta T + C_\varepsilon \varepsilon \quad (5)$$

where C_T and C_ε are characteristics of the fibre type (Standard single mode fibre) and the operating wavelength. At $\lambda_0 = 1550$ nm for standard fibres, typical values of these coefficients are $C_\varepsilon = 0.05$ MHz/ $\mu\varepsilon$ and $C_T = 1$ MHz/ $^\circ\text{C}$. Brillouin distributed sensing can be performed by two different means. One consist in the use of a pulsed laser source and the analysis of the spectrum coming from successively backscattered light. That gives plots of distributed Brillouin spectrum like on Fig. 5. This plot sketches measurements from a fibre we had previously coiled in a solid cylinder with 5 strain echelons of 0, 250, 500, 1000 and 200 $\mu\varepsilon$ (Lanticq et al., 2009a).

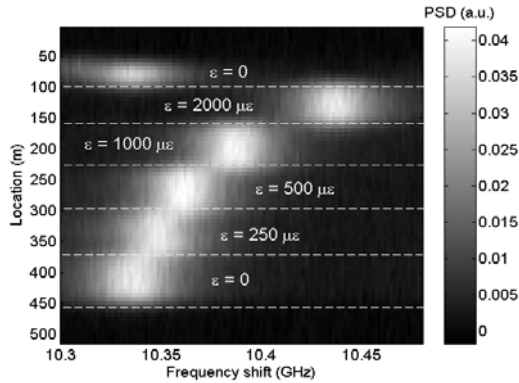


Fig. 5. Distributed Brillouin spectrum along a strained optical fibre.

Another is to use the non-linear effect called Stimulated Brillouin Scattering (SBS). It occurs when, simultaneously with the pump wave, a frequency-shifted wave –so called probe wave– is propagating backward. If the frequency shift between the two waves is close to the Brillouin frequency, then energy can be transferred from the pump to the probe wave. That can be interpreted as a gain spectrum for probe wave (Niklès et al., 1997). Distributed Brillouin spectrum can be recovered by use of a pulsed pump wave and a continuous probe wave, acquiring time traces for several frequency-shifts of the probe. The final trace of this method, called Brillouin Optical Time Domain Analysis (B-OTDA) is similar to B-OTDR one (see Fig. 5).

Various optoelectronic instruments using these techniques are commercially available and may be paired with many different sensing cables to provide either temperature or strain measurements as described in section 4.

In 2002, the first commercial system based on the Brillouin scattering was implemented; by 2007, the market had expanded to include at least five suppliers of Brillouin interrogation systems (Omnisens in Switzerland, Sensornet in England, OZ-Optics in Canada, Yokogawa and Neubrex in Japan). The accuracy derived lies on the order of 1°C , $20\ \mu\epsilon$ and 1 m of spatial resolution, over spans extending several tens of kilometres. The most widespread application is currently pipeline leak detection.

Nonetheless, three shortcomings are restricting this technology solely to the realm of research. First, the location of measurement performed by any distributed sensing technique is not perfectly known (uncertainty on index value). Second, using Brillouin sensing, spatial resolution is still fixed by pulse duration but it is limited by the phonon lifetime (Fellay et al., 1997). This latter parameter is in the order of 10 ns which corresponds to a 1 m spatial resolution. Finally, separating temperature from deformation influences requires the use of cables incorporating two optical fibres, one of which being mechanically isolated. Thus, research on the topic is extremely active, with respect to both the interrogation techniques for reaching centimeter-scale spatial resolutions (Imai et al., 2003) (Zou et al., 2005) and the choice of new optical fibres to enable discriminating thermal and mechanical influences (Lee & Chiang, 2001) (Zou & Bao, 2004).

3. Spatial issues of distributed measurement systems

We showed previously that new parameters were necessary to describe distributed OFS systems. We defined, with equation (1), the location of the performed measurement which value is evaluated in terms of time spent since the pulse entered the fibre, and spatial resolution (equation (2)). Improvement on knowledge of measurement location and decrease of the spatial resolution are still very challenging topics of research.

3.1 Spatial resolution

Brillouin devices offer sometimes lower spatial resolution than required by applications. In (Lanticq et al., 2009b) we showed an example of bad detection by such a device.

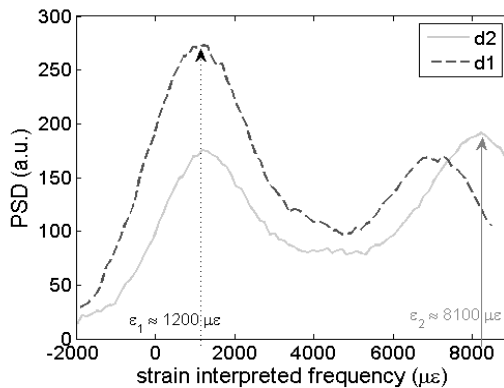


Fig. 6. Brillouin spectra obtained with a sensing system with insufficient spatial resolution

Indeed, as shows Fig. 6, if only one part of the sensing zone is highly strained 2 peaks appear on the spectrum trace. As devices are usually performing peak detection to estimate the Brillouin frequency from the spectrum, 2 cases can then occur:

1. Most power is on the peak corresponding to the high strain (grey curve), then detection is completed without any problem.
2. Most power is on the rest of the spectrum (dashed curve), then detection is missed.

As we mentioned before, the main cause of spatial resolution limitation is phonon lifetime. To get around this difficulty, it necessary to give up any time domain coding method. Thus we are going to deal with two of them: Frequency domain coding for Rayleigh reflectometry and correlation domain coding for pump-probe Brillouin measurement systems.

a) Frequency domain coding of Rayleigh reflectometry

OFDR (Optical Frequency Domain Reflectometry) systems use a tunable laser source and analyse the backscattered light in the spectral domain. Such a device uses ramp wavelength (frequency) modulation of the CW laser source. So at time t , the position from which comes the detected wavelet is frequency-domain coded. Similarly with OTDR, OFDR can provide local backscattered light intensity variation after FFT (Fast Fourier Transform) numerical process (see on left part of Fig. 7) of the detected signal. If the sensitivity of those instruments is so high that Rayleigh scattering uniformities in the fibre can be observed,

then a simple cross-correlation between two OFDR traces allows evaluating local strain all along the fibre.

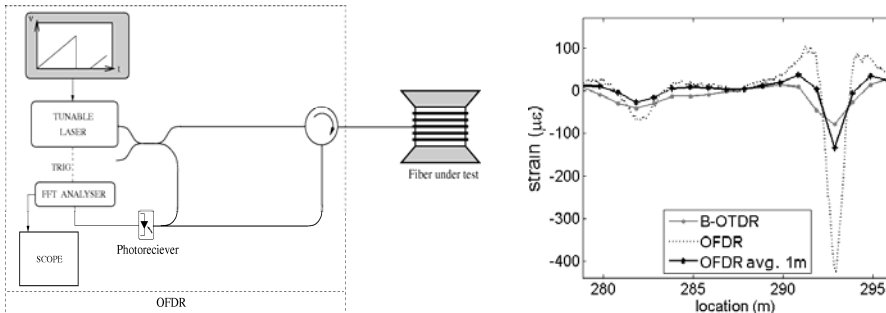


Fig. 7. (left) OFDR system block diagram, (right) strain traces obtained using both OFDR and B-OTDR simultaneously in the same cable; the black curve is drawn averaging OFDR measurements along each B-OTDR measurement zones.

As described in great details in (Glombitza et al. 2006), the OFDR spatial resolution δz is inversely proportional to the bandwidth of the tunable-laser frequency range:

$$\delta z = \frac{c}{2n_g(\Delta\nu)_{\max}} \quad (6)$$

Therefore, this parameter is only limited by $\Delta\nu$ which can reach very high values. On the other hand, measurement range usually decreases when frequency-range increases. Indeed, it is dependent on frequency resolution $\delta\nu$ by a similar relationship:

$$d_{\max} = \frac{c}{2n_g\delta\nu} \quad (7)$$

For example, the American firm Luna Technologies has been marketing since spring 2006 an OFDR based on optoelectronic device called OBR (Optical Backscatter Reflectometer), which constitutes the state of the art of such devices. It enables measuring optical fibre deformations (at homogeneous temperature) over 150 m with a millimetre-sized spatial resolution and a level of precision equal to a few micro-deformations.

This performance has been obtained by OFDR, in association with an advanced correlation method between the ongoing measurement and a reference state. Temperature change (ΔT) and strain (ϵ) are obtained by calculating local changes on optical path from the correlation function between last OFDR trace and a reference trace (Froggatt & Moore 1998). As shows right part of Fig. 7, we demonstrate in (Lanticq et al., 2009) that this device could be complementary of B-OTDR for short range detection of sub-meters straining events.

b) Correlation domain coding of Brillouin spectrum analysis

The frequency domain reflectometry technique has been adapted to Brillouin devices giving birth to Brillouin Optical Frequency Domain Analyser (Garus et al., 1996). Although they were very promising theoretically, these devices never showed performances much better than B-OTDA in terms of spatial resolution or range. To reach very better spatial resolutions

in Brillouin systems the best technical solution investigated is, to the best of our knowledge, correlation domain spectrum analysis.

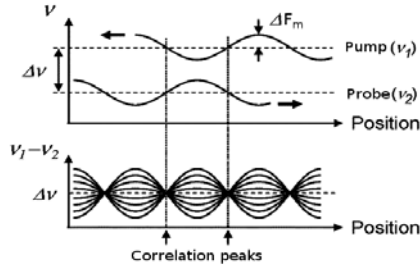


Fig. 8. Principle of correlation coding in B-OCDA systems (from (Hotate & Takemi ,2000)).

(Hotate & Takemi 2000) gives the outline of this method: Pump and probe (which frequency difference is $\Delta\nu$) injected in the fibre under test are created from the same frequency modulated CW wave. As they propagate in opposite directions, then actual frequency difference between the two waves is exactly $\Delta\nu$ only in finite number of location. This number can be reduce to 1, by using a chopped pump wave. If $\Delta\nu = \nu_B$ and if modulation depth ΔF_m is high enough, SBS occurs on only one very tight zone of the fibre. Location can be swept by tuning the modulation frequency f_m . Spatial resolution and range can be redefined with the following relationships:

$$\delta z = 1.52 \frac{c}{2\pi n_g \Delta F_m} \quad \text{if } f_m > \frac{\Delta \nu_B}{2} \quad \text{or} \quad \delta z = \frac{\Delta \nu_B}{f_m} \frac{c}{2\pi n_g \Delta F_m} \quad \text{if } f_m > \frac{\Delta \nu_B}{2} \quad (8)$$

$$d_{\max} = \frac{c}{2\pi n_g f_m} \quad (9)$$

where $\Delta \nu_B$ is the Brillouin linewidth which value is usually about 40 MHz. As this method uses continuous waves, spatial resolution is no more limited by phonon lifetime.

Indeed, this technique has led to highly resolved distributed measurements. For example, a spatial resolution as low as 2 mm has been reached by (Song et al., 2006). On the other hand range values, usually about several tens of meters, are far from reaching B-OTDR (or B-OTDA) ones. That is why, as Rayleigh OFDR, this technique remains complementary with OTDR-based methods.

3.2 Measurement localisation accuracy

As we mentioned at the beginning of this part, one of the major issue of distributed sensing is the uncertainty on the measurement locations. Indeed, as we showed in (Lanticq et al. 2009b), a lag could exist between measurement location estimated by different commercial devices. This is mainly due to group index value they are using during data processing. Indeed from (1), we can deduce this uncertainty $u(z)$ on location z from the one on the group index $u(n_g)$ and the distance z from the fibre entry:

$$\frac{u(z)}{z} = \frac{u(n_g)}{n_g} \quad (10)$$

assuming time spent from pulse entrance is perfectly known. In addition, the provided information is the curvilinear abscissa along an optical fibre coil, often partially embedded into structures to monitor, often in the km range. So uncertainty of location for the end used can be much higher if a sensor location map is not carefully drawn during installation.

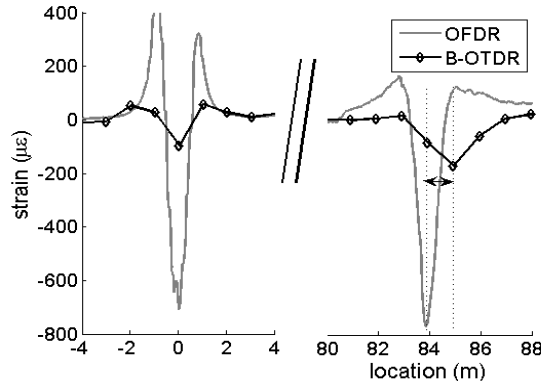


Fig. 9. position lag between two measurement systems interrogating the same sensor.

Fig. 9 highlights a lag of 1% between 2 different instrument traces, after only 85 m propagation into the fibre. This means that for distributed measurements along 20km (typical range of B-OTDR or R-OTDR), those technologies do not suit requirements. Indeed, for instance in the case of underground cavity detection, at 20 km distance the user should dig a 200m large zone to find the hole. Then a good solution for Brillouin devices is to include markers in the sensing line at several well known locations. (Honda et al., 2009) used spans of a different fibre (with a different Brillouin frequency shift) spliced to the sensing fibre (SMF) as absolute location markers. Highly strained or heated spans could be used as well. If it is possible those markers should be located out of the structure giving access to the fibre by the user. Then, high spatial resolution devices can be used on a short part of the sensing line previously identified as interesting (or risky) by the low spatial resolution apparatus.

4. Host material inclusion problems

4.1 Cable choice

The choice of the fibre and its coating is crucial in optical sensor applications, especially for Rayleigh or Brillouin scattering where multi-parameter sensitivity is to be handled. A sensitive optical fibre cable is made of:

- an optical fibre, namely 125 μm of silica (in few cases plastic optical fibres) in which the measurement is made, called the transducer,
- a material that surrounds the fibre, called primary coating, manufactured at the same time as the optical fibre in the drawling tower, usually made of polyimide or acrylate.

An external coating provides contact with the host material, concrete or soil for example. The sensor coating must ensure various functions. First it has to protect the fibre from all

kinds of aggression: Chemical (for instance concrete is alkaline, radiations in nuclear power plants), mechanical (concrete pouring and vibrating followed by aggregate sollicitation; introduction into ground, vibrating rollers passing) and thermal (temperature reaches 65°C during concrete pouring). As a result, the cable must be robust in order to resist to every stage of implementation as illustrated in Fig. 10. Second, it must ensure an optimal transfer of measured parameter changes from the host material to the sensitive optical fibre. This aspect is of utmost importance as it might strongly degrade the whole measurement system. It is highly dependent on the environment nature and should be targeted to reach optimal performance. So, the incorporation of OFS into civil engineering structures remains challenging. Third, it has to reduce stress concentration around the fibre and hence to minimise the obstrusivity, meanwhile preventing debonding of the sensor. Thanks to their size in the millimetre range, optical fibre sensors are known to be less invasive than traditional sensors. Yet, while designing an optical fibre sensing cable, the cable size should remain an important parameter adjusted to the host environment specificities.



Fig. 10. Sensor cable must be robust: example of concrete pouring . Extracted from (Dubois et al., 2007)

a) Orders of magnitudes of sensing cable influence

For point-like sensors, it has been reported (Caussignac et al., 2002), that commercially-available optical fibre extensometers embedded into concrete may underestimate strain by about 10%, shift correlated by finite element analysis with the shape and the Young's modulus of the sensor external coating.

For Raman distributed temperature sensing into single-mode fibres, sensor coating may even ruin measurements as described in (Dubois et al., 2009).

For Brillouin temperature-only monitoring, as pointed out in introduction, cross-sensitivity with strain may significantly shift the measurements. More precisely, Brillouin temperature sensitivity is modified by mechanical strain created inside the optical fibre by the thermal expansion of the specific coating (Kurashima et al, 1990). As depicted with great details in (Lanticq et al., 2008), (5) becomes (11) for an externally unstrained sensor:

$$\Delta \nu = (C_{T_{fiber}} + C_{\epsilon} \alpha_{sensor}) \Delta T = C' \Delta T \quad (11)$$

where $C_{T_{fiber}}$ and C_{ϵ} are the temperature and strain optical fiber sensitivity coefficients and α_{sensor} is the temperature expansion factor. If the sensor is completely bound up with the host material, one must take into account the expansion coefficient of the host material:

$$C''_T = C_T + C_{\epsilon} \alpha_{hostmaterial} \quad (12)$$

As $\alpha_{concrete} = 10 \times 10^{-6}/^{\circ}\text{C}$, $C_{T_{fiber}} = 0.92 \text{ MHz}/^{\circ}\text{C}$, then $C''_{T_{fiber}} = 1.42 \text{ MHz}/^{\circ}\text{C}$.

Error! Reference source not found. represents the recordings of temperature variations at the center of a 3m long concrete beam instrumented with optical fibre sensors collocated with reference temperature sensors. The Brillouin shift was measured with a commercially available Brillouin optical time-domain reflectometer (BOTDR) operating at $1.55\mu\text{m}$. Temperature variations during the 60th hours of concrete hardening were recorded. The dotted curve (no strain S1) represents the raw results, corresponding to equation (5). The black curve represents the temperature curve recorded by the reference sensor. Exothermic chemical reaction causes an increase in temperature until the 25th hour after the pouring of concrete, time of the highest temperatures measured by the sensor. We made a mistake in (Lanticq et al., 2008), claiming that until the 45th, the concrete is considered as a liquid and that the cable is not seen as connected to the structure. Actually, according to the concrete maturation theory, since the chemical reaction has started, the concrete become solid and its strength is quickly high enough to drag the sensor. Thus, taking into account the strain due to thermal expansion, the thermal coefficient of the sensor is C''_T , defined by equation (12), as soon as temperature starts to increase in the material (15h after pouring, in our case). Then, as shows figure 11, if all the Brillouin frequency variations are interpreted as thermally induced (see the raw Brillouin measurement curve), the temperature variation is clearly underestimated, compared to temperature measured by an electronic resistive sensor (solid curve).

This is due to mechanical strain in the beam perturbing Brillouin measurement: it is created in the early hours by the young age autogenous shrinkage of concrete. On figure 11, this additional compressive strain has been estimated by equation (5) using the measured Brillouin frequency and the electronic temperature sensor measurement. Fourier filtering of the mechanical strain (dashed curve) has been used in the aim of evaluating noise on Brillouin temperature measurement. Standard deviation between strain-compensated Brillouin temperature measurements (gray curve) and reference sensor measurements is 0.4°C . This is promising compared to results available in literature (Rajesh et al., 2006) (Wade et al., 2004), but one shall remember that all the data-processing described here wouldn't have been possible without additional reference measurements.

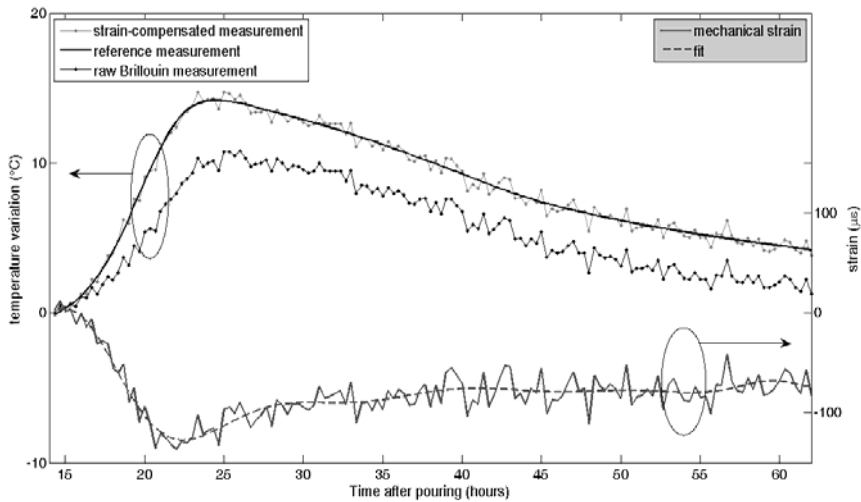


Fig. 11. Use of Brillouin measurements and reference temperature measurements to evaluate the mechanical strain.

For strain measurement, not only the coating must perform optimal strain field transfer from the host material to the optical fibre, but it must also be adjusted to the environment in terms of variation range. Concrete mechanical normal evolution range is smaller than silica that can handle few percent tensile loading. On the contrary, for ground applications (dikes and embankment monitoring), optical fibre use may be restrictive. Fig. 11 presents strain measurements performed by OBR instrument into a sensing cable embedded into an embankment where artificial cavities were created in order to simulate sinkhole formation (Lanticq et al., 2009b). When tensile loading exceeded 0.1% (referred to 'large strain') unexpected strain peaks seem to scramble the measurement. This phenomenon is even worse if strain increases anymore (huge strain $\sim 1\%$). The optical fibre locally disunited with the cable, involving very close (sub-millimetres) tensile and compressive strain zones. Unfortunately, this effect is irreversible, signifying that this cable is not robust enough for use under strain up to 0.1%.

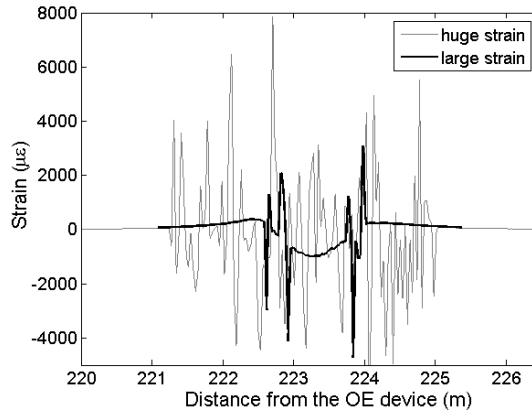


Fig. 11. Strong deformations measurements within an optical fibre embedded into an embankment where sinkhole formation were simulated.

b) Strain sensing optical fibre cable design

One major difficulty is the strain-field transfer from the host material to the embedded optical fibre. Literature reports ways to calculate a calibration factor linked with stiffness difference between a sensor and its host material under uniform loads (Ansari & Libo, 1998) and even with non-uniform strain distribution (Okabe et al., 2002). Moreover, besides materials, the shape of the sensors strongly influences the difference between the strains in the optical fibre and in the host material, and more generally, the sensor response. For point-like sensor a commonly-used I-shaped sensor body has been described and optimized (Winter et al., 2005) (Choquet et al., 2000). For distributed sensors, specific packaging are proposed by various distributors, as shown on Fig. 12, representing different types of Smartec extensometers.

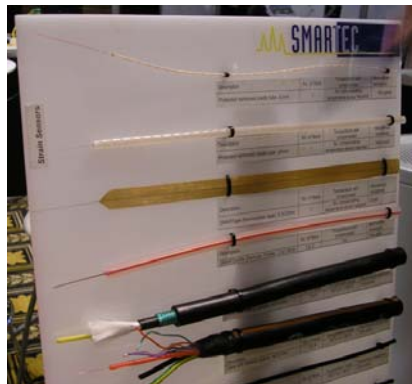


Fig. 12. Range of distributed strain sensors proposed by the Smartec company.

The first step is to list optical fibre sensor specifications: Presence of hydrogen, maximal temperature to be handled, durability (linked with structure), required sensitivity. Then a

sensor coating may be found within commercially available products. Corresponding publications (Inaudi & Glisic, 2006) (Dewynter et al., 2007) describing optical fibre sensor coating designs are to be read carefully. Then a qualification process should be realized, as described for dike monitoring by EDF in the previous paragraph. An example can be found in (Delépine-Lesoille et al., 2006) detailing the design and realization of a wave-like sensor specially developed to embed optical fibre extensometers into concrete. As shown on Fig. 13, finite-element analysis performed with thermal and mechanical models enabled optimizing materials and shapes. It resulted in a composite materials with appropriate stiffness, a braid made of glass fibres impregnated with epoxy on top of polyimide primary coating. The realization process has then been defined to reach great accordance with the theoretical design. Temperatures during epoxy reticulations, type of glass to remain compatible with concrete, as well as geometric result were considered. The method for bringing the fibre into the braid was also a challenge so as to ensure that the fibre does not suffer from microbendings (and related losses). Laboratory and field evaluations were carried out. Finally, this coating has been validated with different sensing principles, from point-like sensors (temperature Bragg grating sensors), to long base extensometers (Delépine-Lesoille et al., 2006) to Brillouin sensing chain (Lanticq et al., 2008), the sensitive part also being embedded into concrete.

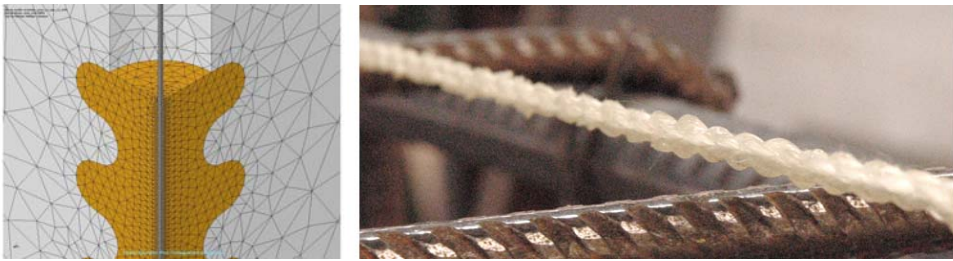


Fig. 13. Sensor coating. On the left, FEM figure of the sensor developed at LCPC; On the right, the sensor actually made by the IDIL company from the theoretical model.

4.2 Temperature and strain discrimination

In the aim of simultaneously estimate T and ε , one of the more instinctive consists in using two fibres in the same sensing cable, one being strain-free, and the other being bound with the material. Then the first is only submitted to temperature changes and can be used to compensate numerically its effects on the measurement of the second. These kind of cable is commercially available, but it has to be carefully used. Indeed, since the cable is embedded in the material, it is very difficult for the user to guaranty that the first fibre remains strain free during all the sensor lifetime.

Thus, two different parameters p_1 and p_2 are measured by optical methods in the same fibre. Both are varying linearly with temperature and strain, resulting in the following system:

$$\begin{pmatrix} p_1 \\ p_2 \end{pmatrix} = \begin{pmatrix} C_{T1} & C_{\varepsilon1} \\ C_{T2} & C_{\varepsilon2} \end{pmatrix} \begin{pmatrix} \Delta T \\ \varepsilon \end{pmatrix} \quad (13)$$

Then temperature and strain can be estimated, inverting the previous system as it follows:

$$\begin{pmatrix} \Delta T \\ \varepsilon \end{pmatrix} = \frac{1}{D} \begin{pmatrix} C_{\varepsilon 2} & -C_{\varepsilon 1} \\ -C_{T 2} & C_{T 1} \end{pmatrix} \begin{pmatrix} p_1 \\ p_2 \end{pmatrix} \quad (14)$$

Where $D = C_{T1}C_{\varepsilon 2} - C_{\varepsilon 1}C_{T2}$ is the discriminator of the system matrix. The uncertainties $u(T)$ and $u(\varepsilon)$ on T and ε method are then linked to uncertainties $u(p_1)$ and $u(p_2)$ on associated to parameters directly measured p_1 and p_2 . Thus, assuming all the calibration coefficient are perfectly well known:

$$u(\Delta T) = \frac{1}{|D|} \left[|C_{\varepsilon 2} u(p_1)| + |C_{\varepsilon 1} u(p_2)| \right] \quad (15)$$

$$u(\varepsilon) = \frac{1}{|D|} \left[|C_{T 2} u(p_1)| + |C_{T 1} u(p_2)| \right] \quad (16)$$

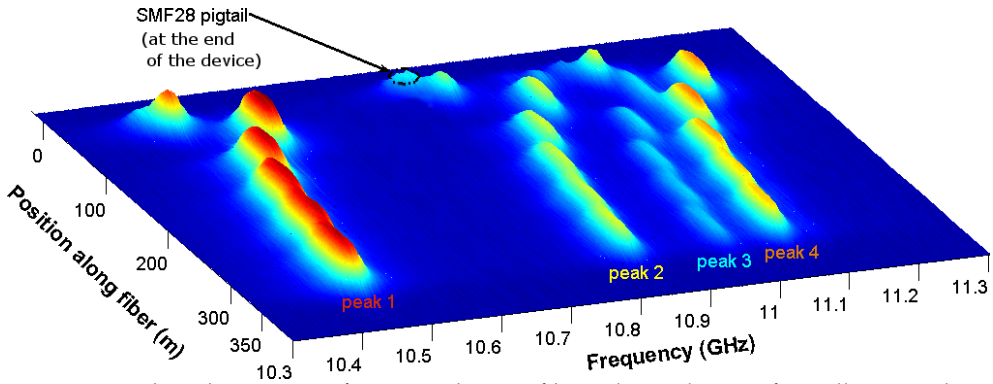


Fig. 14. Distributed spectrum of a strained LEAF fibre. The evolution of 4 Brillouin peaks is clearly visible (Lanticq, 2008a).

As Large Effective Area Fibre (LEAF) have several significant Brillouin peaks at $1.55 \mu\text{m}$ wavelength, we decided to investigate the suitability of the two of its four peaks to perform simultaneous measurements. To do so, we estimated coefficients C_{Ti} and $C_{\varepsilon i}$ during experimental calibration. One can see on Fig. 14 distributed Brillouin spectrum measurement of a strained LEAF fibre performed with the same experiment as those on Fig. 5. Highest value of $|D|$ were obtained with first and third peaks. Since $|D| = 10^{-3} \text{ MHz}^2 \cdot \text{C}^{-1}$ we estimated uncertainties on T and ε , assuming $u(v_i) = 2 \text{ MHz}$ (typical value):

$$u(\Delta T) = 35 \text{ }^\circ\text{C} \quad (17)$$

$$u(\varepsilon) = 700 \mu\varepsilon \quad (18)$$

Equations (17) and (18) prove that LEAF fibre is not suitable for simultaneous measurement. Moreover recent works (Zou et al., 2008a) (Zou et al., 2008b) have tended to prove that no solid fibre seems efficient to separate temperature and strain with the use of two Brillouin frequencies.

Then, one can think about using Raman and Brillouin distributed measurement in the same fibre, but Brillouin sensing requires monomode fibre whereas Raman measurements reach an optimal efficiency in multimode fibres (Farahani & Gogolla, 1999). It is possible to design a cable with two fibres (monomode and multimode) but two interrogating systems are necessary and cost would be important.

More promising results have been highlighted using polarisation maintaining fibres: The second parameter is then the local beat length. In this case, the interrogating systems must have a high spatial resolution because beat length is as low as 5 mm in this kind of fibre. Either B-OCDA (Zou et al., 2008b) or OFDR (Froggatt et al., 2006) systems have been implemented for simultaneous measurement and gave very promising result. Nevertheless those apparatus were made of polarisation maintaining components, much more costly. In addition, in the most part of civil engineering structures, temperature gradients are very weak (compared to strain ones), and consequently only a few temperature sensors are necessary to monitor this parameter. Thus, the need of multiplexing is less critical, and standard sensors such as resistive temperature detectors or thermocouples can be regarded as acceptable solution for users.

5. Conclusion

To conclude, we propose the outline of what would be a modern distributed strain monitoring system. In section 4. we demonstrate that time-domain based systems constitutes the only suitable technical solution for kilometre-scale instrumentation. However high-resolution can be complementarily used in small parts of the sensing line, if something has been detected in it. To do so, it is necessary to give an access to the end user in the aim of plugging the high resolution device (HR system on Fig. 15). For better localisation of measurement points, markers can be introduces regularly along the sensing line. Finally, as temperature often varies slowly spatially, a few temperature sensors could be enough to compensate the temperature effect on strain measurement systems. But in certain cases, as bridges, temperature can vary as much in the structures as it must be monitored by distributed measurements. That is why simultaneous strain and temperature sensing methods are still today a very intense research topic.

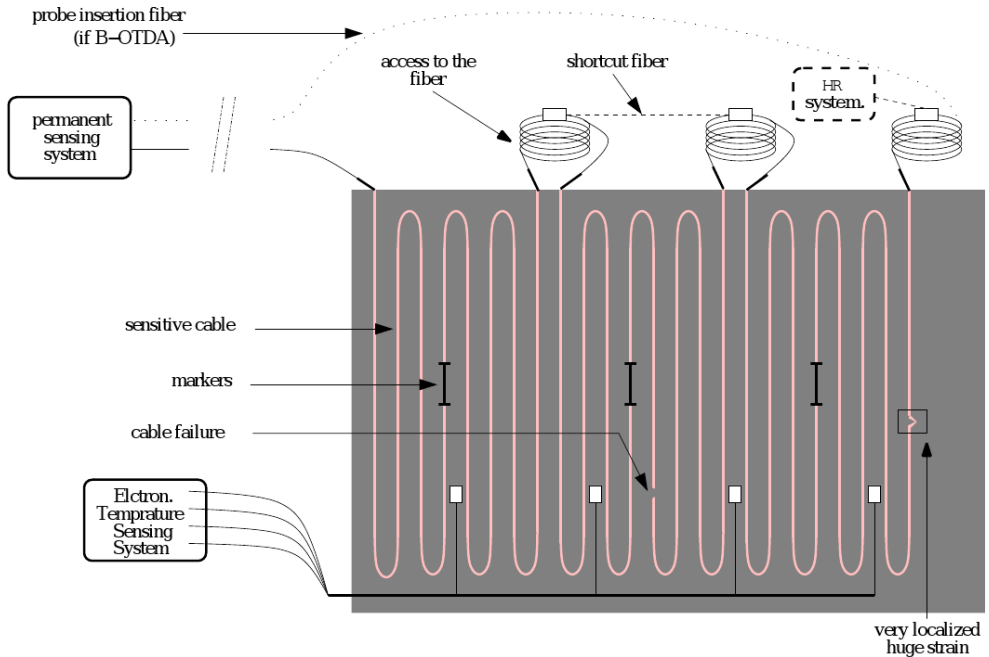


Fig. 15. Modern instrumentation scheme for SHM applications.

6. References

- Ansari, F. & Libo, Y. (1998) "Mechanics of bond and interface shear transfer in optical fibre sensors", *Journal of Engineering Mechanics*, Vol. 124, No. 4, 385-394.
- Barnoski, M. K. & Jensen, S.M. (1976) "Fibre waveguides: a novel technique for investigating attenuation characteristics" *Applied Optics* Vol. 15, No. 9.
- Branko Glisic & Daniele Inaudi (2007) *Fibre Optic Methods for Structural Health Monitoring*, Wiley & Sons, ISBN 978-0470-06142-8.
- Caussignac, JM.; Dupont, J. & Chau, B.; (2002), "Design of optical fibre sensors for smart concrete structures" *Proceedings of the First European Workshop of Structural Health Monitoring (SHM2002)*, 585-591, Cachan, France.
- Choquet, P.; Juneau, F.; Bessette, J.; (2000) "New generation of Fabry-Perot fiber optic sensors for monitoring of structures" *Proceedings of SPIE's 7th annual International Symposium on Smart Structures and materials*, Newport Beach, USA.
- Crunelle, C.; Wuilpart, M.; Caucheteur, C.; & Mégret, P.; (2009) "A quasi-distributed temperature sensor interrogated by a wavelength-sensitive optical time-domain reflectometer" *Measurement Science Technology*, Vol. 20, No 2, 027001.
- Delépine-Lesoille, S. ; Merliot, E. ; Boulay, C. ; Quétel, L.; Delaveau, M. ; Courteville, A. (2006) "Quasi-distributed optical fibre extensometers for continuous embedding into concrete". *Smart Structures and Materials*, 931-938.

- Dewynter, V. et al. (2007) "Underground tunnelling monitoring based on sensitive optical fibre cable and Brillouin reflectometry", *3rd Int. Conf. on Structural Health Monitoring of Intelligent Infrastructure*, Vancouver, Canada.
- Dubois, J.-P. ; Delépine-Lesoille, S.; Tran, V.-H. ; Buschaert, S. ; Mayer, S. ; Henault, J.-M.; Salin, J. & Moreau, G. (2009) "Raman versus Brillouin optical fiber distributed temperature sensing: an outdoor comparison", *4th International Conference on Structural Health Monitoring on Intelligent Infrastructure (SHMII-4)*, Zurich, Switzerland.
- Duck, G. & LeBlanc, M. (2000) "Arbitrary strain transfer from a host to an embedded fibre-optic sensor", *Smart Materials and Structures*, Vol. 9, No. 4, 492-497.
- Farahani, M.A.; Gogolla, T. (1999) "Spontaneous Raman scattering in optical fibers with modulated probe light for distributed temperature Raman remote sensing. *Journal of Lightwave Technology*, Vol. 17, No. 8, 1379.
- Fellay, A.; Thévenaz, L.; Facchini, M.; Nikles, M.; and Robert, P. (1997) "Distributed sensing using stimulated Brillouin scattering : towards ultimate resolution." *In Proceedings of Optical Fiber Sensors Conference*, Vol. 16, pages 324-327.
- Froggatt, M. & Moore J. (1998) "High-spatial-resolution distributed strain measurement in optical fibre with Rayleigh scatter", *Applied Optics* Vol. 37, No. 10.
- Froggatt, M.; Gifford, D.; Kreger, S.; Wolfe, M.; & Soller, B. (2006) "Distributed Strain and Temperature Discrimination in Unaltered Polarization Maintaining Fiber," *in 18th Optical Fiber Sensors Conference, OSA Technical Digest (CD) (Optical Society of America, 2006)*, paper ThC5. Cancun, Mexico.
- Fry, J.-J. (2004) "Détection de fuite sur les digues par acquisition de profils de température le long d'une fibre optique" *Sécurité des digues fluviales et de navigation*, November 25-26, Orléans, France.
- Garus, D.; Krebber K.; Schliep, F. & Gogolla, T. (1996) "Distributed sensing technique based on Brillouin optical-fiber frequency-domain analysis". *Optics Letters*, Vol. 21, No. 17, 1402-1404.
- Glisic, B. & Inaudi, D. (2007) *Fibre Optic Methods for Structural Health Monitoring*, John Wiley & Sons.
- Glombitza, U. & Brinkmeyer, E. (1993) "Coherent frequency-domain reflectometry for characterization of single-mode integrated-optical waveguides". *Journal of Lightwave Technology*, Vol. 11, No. 8, 1377-1384.
- Hénault J.-M. (2006) "Mesure de température distribuée par fibre optique et effet Raman: Détection de fuites dans les digues." *Journée mesure de température, Mesurexpo*, October 17, Paris, France.
- Honda, N. ; Inoue, M. ; Araki, N. & Azuma, Y. (2009) "New Optical Fiber Line Testing System Function for Highly Accurate Facility Location Using Brillouin Frequency Shift Assigned Optical Fiber," *in Optical Fiber Communication Conference, OSA Technical Digest (CD) (Optical Society of America, 2009)*, paper OWU3.
- Hotate, K. & Hasegawa, T. (2000) "Measurement of Brillouin gain spectrum distribution along an optical fiber using a correlation-based technique proposal, experiment and simulation". *IEICE TRANSACTIONS on Electronics*, Vol. E83-C, No. 3, 405-412.
- Imai, M.; Sako, Y.; Miura, S.; Miyamoto, Y.; Ong, S.L. & Hotate, K. (2003) "Dynamic Health Monitoring for a building model using a BOCDA based fibre optic distributed sensor" *Structural health monitoring and Intelligent Infrastructure*, Vol. 1, 241-46.

- Inaudi, D. & Glisic, B. (2006). "Reliability and field testing of distributed strain and temperature sensors." *SPIE Smart Structures and Materials Conference, San Diego, USA. 2006* ; Vol. 6167, pp 61671D. SPIE.
- Kister, G.; Winter, D.; Tetlow, J.; Barnes, R.; Mays, G. & Fernando, G.F. (2005). "Structural integrity monitoring of reinforced concrete structures. part 1 : evaluation of protection systems for extrinsic fibre fabry-perot sensors." *Engineering Structures*, Vol. 27, No. 3, 411-419.
- Koyamada, Y.; Imahama, M.; Kubota, K.; Hogari, K. (2009) "Fibre-Optic Distributed Strain and Temperature sensing With Very High Measurand Resolution Over Long Range Using Coherent OTDR." *Journal of Lightwave Technology*, Vol. 27, No. 9, 1142-1146.
- Kurashima, T. & Tateda, M. (1990). "Thermal effects on the Brillouin frequency shift in jacketed optical silica fibres." *Applied Optics*, Vol. 29, No. 15, 2219-2222.
- Lanticq, V. ; Quiertant, M.; Merliot, E. & Delepine-Lesoille, S. (2008) "Brillouin sensing cable: Design and experimental validation" *IEEE Sensors Journal*, Vol. 8, No. 7, 1194-1201.
- Lanticq, V. (2009a) *Mesure répartie de température et de déformation par diffusion Brillouin : De la fibre optique au capteur pour le génie civil*. PhD Thesis, Télécom- Paristech, France.
- Lanticq, V.; Bourgeois, E.; Magnien, P.; Dieleman, L.; Vincelas, G.; Sang, A. & Delepine-Lesoille, S. (2009b). "Soil-embedded optical fiber sensing cable interrogated by Brillouin optical time-domain reflectometry (B-OTDR) and optical frequency-domain reflectometry (OFDR) for embedded cavity detection and sinkhole warning system." *Measurement Science and Technology*, Vol. 20, No. 3, 034018-034028.
- Lee, C. & Chiang, P.W. (2001) "Utilization of a dispersion-shifted fibre for simultaneous measurement of distributed strain and temperature through Brillouin frequency shift" *IEEE Photonic Technology Letters*, Vol. 13, 1094-1097.
- Lee, C. ; Suh, K. & Landry, T. (2008) "The implementation of self calibration techniques in Raman backscatter based fibre optic distributed temperature system (DTS) technology" *Transmission and Distribution Conference and Exposition*. 1 – 6.
- Liu, Z. & Kim, A.K. (2003) "Review of Recent Developments in Fire Detection Technologies" *Journal of Fire Protection Engineering*, Vol. 13, No. 2, 129-151.
- Lo, Y.-L. & Xu, S.-H. (2007) *Sensors and Actuators*, Vol. A 136, 238-243.
- Lopez-Higuera, J. M. (2002) *Handbook of Optical Fibre Sensing Technology*, John Wiley & Sons.
- Niklès M., Thévenaz L. & Robert P.A. (1997) "Brillouin Gain Spectrum Characterization in Single-Mode Optical Fibres" *Journal of Lightwave Technology*, Vol. 15, No. 10, 1842-1851.
- Okabe, Y.; Tanaka, N. & Takeda, N. (2002) "Effect of fiber coating on crack detection in carbon fiber reinforced plastic composites using fiber Bragg grating sensors" *Smart Mater. Struct.*, Vol. 11, 892-898.
- Ou, J.P.; Li, H. & Z.D. Duan (2005), *Proceedings of the second International Conference on Structural Health Monitoring and Intelligent Infrastructure*, ISBN 0 415 39652 2, Shenzhe China, November 2005, Taylor & Francis, London.
- Rajesh, M.; Geetha, K.; Sheeba, M.; Radhakrishnan, P.; Vallabhan, C.P.G. & and Nampoori. V.P.N. (2006) "A fibre optic smart sensor for studying the setting characteristics of various grades of cement." *Optics and Lasers in Engineering*, Vol. 44, No. 5, 486- 493.
- Rogers A. (1999) "Distributed optical-fibre sensing", *Measurement Science Technology*, pp. 75-99.

- Song, K.Y.; He, Z.; & Hotate, K. (2006) "Distributed strain measurement with millimeter-order spatial resolution based on Brillouin optical correlation domain analysis" *Optics Letters*, Vol. 31, No. 17, 2526-2528.
- Wade, S.A.; Grattan, K.T.V.; McKinley, B.; Boswell, L.F. & D'Mello, C. (2004). "Incorporation of fibre-optic sensors in concrete specimens: testing and evaluation." *IEEE Sensors Journal*, Vol. 4, No. 1, 127-134.
- Wan, K.T. & Leung, C.K.Y. (2007) "Fibre optic sensor for the monitoring of mixed mode cracks in structures" *Sensors and Actuators* Vol. A 135, 370-380.
- Winter, D.; Tetlow, J.; Hameed, A.; Leng, J.; Barnes, R.; Kister, G.; Mays, G.; Talbot, J. & Fernando, G. F. (2002) "Structural integrity monitoring of concrete structures using optical fibre sensors", *Proceedings of the First European Workshop of Structural Health Monitoring (SHM2002)*, 615-622, Cachan France.
- Zou, L. & Bao, X. (2004) "Dependance of the Brillouin frequency shift on strain and temperature in a photonic crystal fibre" *Optics Letters*, Vol. 29, 1485-1487.
- Zou, L.; Bao, X.; Wan, Y. & Chen, L. (2005) "Coherent Probe-pump-based Brillouin Sensor for Centimeter-crack Detection" *Optics Letters*, Vol. 30, 370-72.
- Zou, W.; He, Z. & Hotate, K.; (2008a) "Investigation of strain- and temperature-dependences of brillouin frequency shifts in geo2-doped optical fibers". *Journal of Lightwave Technology*, Vol. 26, No. 13, 1854-1861.
- Zou, W.; He, Z. & Hotate, K.; (2008b) "Stimulated brillouin scattering in f-doped optical fibers and its dependences on strain and temperature." *Conference on Optical Fiber communication/National Fiber Optic Engineers Conference, 2008. OFC/NFOEC 2008* pp.1-3.
- Zou, W.; He, Z. & Hotate, K.; (2008c) "Fiber-optic Brillouin distributed discrimination of strain and temperature with 11-cm spatial resolution using correlation-based continuous-wave technique." *34th European Conference on Optical Communication, 2008. ECOC 2008*. Brussels, Belgium.

Finding hydrogen leaks by means of the fiber Bragg gratings technology

Marc Debliquy ⁽¹⁾, Driss Lahem ⁽²⁾, Christophe Caucheteur ⁽¹⁾,

Patrice Megret ⁽¹⁾

⁽¹⁾*Université de Mons*

Belgium

⁽²⁾*Materia Nova*

Belgium

1. Introduction

Hydrogen participates to a wide range of chemical processes and it also appears during energy production and transport. It is widely used in aerospace applications where it acts as fuel for rockets. Nowadays, hydrogen is considered as an alternative source of energy for automotive applications and many developments are currently carried out on hydrogen fuel cells or engines. If these developments succeed economically, there will be an increased demand for hydrogen. With its high diffusivity, hydrogen is an extremely flammable gas. In air, it can burn at concentrations from about 4% with a flame velocity almost ten times higher than that of natural gas. Therefore, for security reasons, hydrogen leak detectors are highly important in industrial and practical applications.

In this frame, optical fiber sensors are particularly interesting in comparison with other technologies such as pellistors or semiconductor sensors (Yu&Yin, 2002). Indeed, optical fiber sensors offer unique advantages such as immunity to electromagnetic interference, light weight, flexibility, stability, high temperature tolerance, and even durability against high radiation environments. A single optical fiber can also offer distributed or quasi-distributed sensing, which is not possible with other sensing methods.

Among the different optical fiber sensor configurations, a great deal of the researches has been devoted to fiber Bragg gratings (FBGs) since they have been rapidly considered as excellent sensor elements, able to measure static and dynamic fields such as temperature, strain and pressure (Kersey et al. 1997; Othonos&Kalli, 1999). FBGs covered with Palladium have been widely investigated in the past for hydrogen detection (Sutapun et al., 1999; Tang et al., 1999; Peng et al. 1999; Maier, 2006). The sensing mechanism is based on the swelling of the Palladium coating, resulting in a stress on the grating. This sensor configuration suffers from a main drawback that is a quite long response time leading to a hysteresis effect between the responses obtained for increasing and decreasing hydrogen concentrations. Furthermore, the behaviour of such sensors in air environment is not known since all previous studies presented results of experiments conducted in nitrogen environment and mainly dedicated to aerospace applications.

We propose here a completely new hydrogen FBG-based sensor covered by a catalytic sensitive layer made of a ceramic doped with noble metal. In presence of hydrogen in air, an exothermic reaction occurs in the sensitive layer and leads to an increase of temperature measured by the FBG through a shift of its central wavelength. The obtained sensor response is linear and without hysteresis. The response is also selective and extremely fast for both increasing and decreasing hydrogen concentrations. The sensor has been tested in wet air and a very good sensitivity has been obtained whatever the relative humidity level of the environment.

The applications aimed are essentially hydrogen detection in air for the monitoring of storage places and pipe lines.

2. Generalities on Bragg gratings.

This paragraph summarizes the important concepts necessary to understand the principles of the presented hydrogen sensors.

2.1 Basic principle of fiber Bragg gratings

A fiber Bragg grating, called FBG, is a periodic and permanent modification of the core refractive index value along an optical fiber (Othonos & Kalli, 1999; Kashyap, 1999). This modification is generally obtained by exposing the core of a photosensitive optical fiber to an intense UV interference pattern. A fiber Bragg grating is defined by several physical parameters (figure 1). The grating length L is the optical fiber length along which the refractive index modulation is realized. The periodicity and the amplitude of the refractive index modulation are defined by Λ and δn , respectively.

The order of magnitude of these parameters typically varies from 0.2 μm to 100 μm for Λ , from a few mm to a few tens of cm for L and from 10^{-5} to 10^{-3} for δn . The inscription of such a perturbation in the fiber core induces light coupling between two counter-propagating modes. This mode coupling is produced for some wavelengths around the Bragg wavelength defined by the Bragg condition:

$$\lambda_{\text{Bragg}} = 2 \cdot n_{\text{eff}} \cdot \Lambda \quad (1)$$

As shown on figure 1, a fiber Bragg grating acts as a selective mirror in wavelength around the Bragg wavelength for which there exists an energy transfer from the forward-going to the backward-going fundamental core mode. Physically, for each period of the fiber Bragg grating, a weak Fresnel reflection is produced due to a variation of the refractive index value. An important reflection is obtained when all the weak contributions add in phase. This condition is respected for the Bragg wavelength.

The grating planes are subject to temperature and strain perturbations, which modify the phase matching condition and lead to wavelength dependent reflectivity. Therefore tracking the wavelength at which the Bragg reflection occurs is the way to obtain the magnitude of the external perturbation.

For instance, the Bragg wavelength is influenced by the temperature or the stain applied to the fiber. One understands immediately the interest of these gratings to prepare temperature or strain sensors.

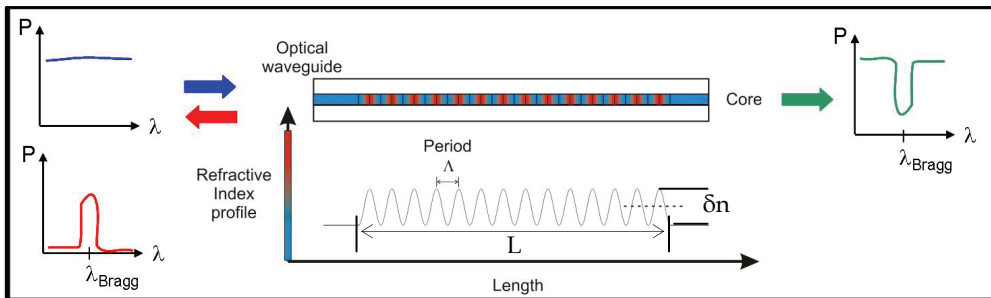


Fig. 1. Operating principle of a fiber Bragg grating.

A fiber Bragg grating is also able to couple light from a propagating mode to another mode characterized by a propagation constant that matches the spatial periodicity of the grating. This may result in coupling between the fundamental core mode and cladding or radiation modes. This coupling phenomenon is exploited in tilted fiber Bragg gratings.

It is also possible to manufacture fiber gratings that are transmissive so that they couple light between core and forward-going cladding modes. In this case the phase matching condition dictates a long grating periodicity of the order of several hundred microns. These components are known as long period fiber gratings LPFG.

2.2 Photosensitivity in optical fibers.

Photosensitivity of an optical fiber corresponds to its propensity to locally modify its core refractive index value when it is exposed to light with a wavelength and an intensity that depend on the core material.

Although photosensitivity is a very important property of an optical fiber, the complete mechanism responsible for this phenomenon is not yet fully understood. A lot of work is still in progress to better explain this phenomenon and to improve its knowledge. The study of the different mechanisms responsible for the optical fiber photosensitivity falls outside the scope of this document. This phenomenon was observed for a large number of fiber materials but is very important in germanium doped silica fibers. The photosensitivity is associated to the defects induced by germanium in the silica lattice. That is why these germanium doped fibers remain the most used for preparing Bragg gratings.

Pure silica SiO_2 is an amorphous material characterized by a tetrahedral structure. Each oxygen atom links the silicon atoms of two adjacent structural molecules and is then shared by two tetrahedral units, as shown in figure 2(a). The combination of the different units forms a quasi-random structure (see figure 2 (b)).

The structure of germanium-doped silica is linked to that of pure silica since germanium, like silicon, is an element of the fourth group in the Mendeleev table of elements. A germanium atom can thus replace a silicon atom in the structure represented in figure 2.

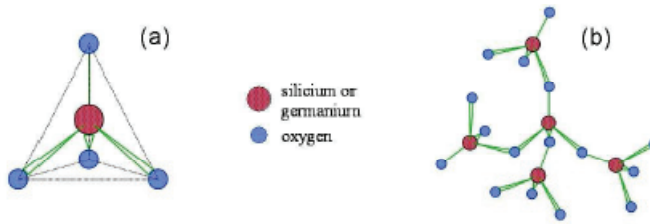


Fig. 2. Tetrahedral structure of silica

The defects that are present in the structure are called color centers. Contrarily to silica that only exists in the form SiO_2 , the two forms GeO and GeO_2 are stable and can be present in germanium-doped silica. The GeO defect, called germanium oxygen-deficient center (GODC), is often found in the structure of germanium-doped optical fiber. When it is present, the germanium or silicon atom is linked to only 3 oxygen atoms instead of 4 in the ideal structure and a bond is directly realized with a germanium atom (Ge-Si or Ge-Ge). This defect is characterized by an absorption band centered around 240 nm. The energy required to break the bond is around 5 eV.

There also exists a second type of structure of GODC. In this case, a germanium atom is bonded with only two oxygen atoms so that two electrons are free. This defect also presents an absorption peak at 240 nm. In their model, D.Hand and P. Russel link the mechanism of refractive index change to the photoinduced absorption change (Hand&Russel, 1990). This absorption creates new permanent defects that lead to a modification of the refractive index value. The modification of the absorption spectrum affects of course the refractive index since these values are linked by the Kramers-Kronig relationship (Russel&Hand, 1991).

It is in practice possible to obtain an important concentration of these two kinds of defects by reducing the quantity of oxygen during the fabrication process of the optical fiber.

There are substantial experimental evidences supporting the mechanism put forward by D. Hand and P. Russel in which the resultant color-centers are responsible for changes in the UV absorption spectrum of the glass and the refractive index change follows the Kramers-Kronig relationship. Many experiments support the GeE' defect center to be responsible for photosensitivity (Atkins et al., 1993; Tsai et al., 1993). However, the color center model cannot satisfactorily explain the behavior of all fiber types and the dopants used to modify the core refractive index. An alternative model based on glass densification induced by photoionization of the Ge defects has also found experimental support. This alternative model was proposed by M. Sceats and coworkers in 1993 (Sceats et al., 1993). The compaction/densification model is based on laser irradiation-induced density changes that result in refractive index changes. Irradiation by laser light at 248 nm has been shown to induce thermally reversible, linear compaction in amorphous silica, leading to refractive index changes. The model thus takes into account the presence of important stresses inside the optical fiber: mechanical, thermal stress coming from the optical fiber manufacturing process. These stresses can be relaxed by UV irradiation. The breaking of the bonds by UV irradiation (D. Hand and P. Russel mechanism) can also be responsible for the stress relaxing as this process causes a local density increase inside the optical fiber and a modification of the refractive index. Its exact contribution under various experimental conditions has still to be further investigated.

2.3 Techniques used to increase photosensitivity

Since the discovery of photosensitivity and its impact on the creation of fiber Bragg gratings, there has been considerable effort in understanding and increasing the photosensitivity in optical fibers. Standard single-mode optical fibers (3% germanium in the core) typically present index changes of about 3.10^{-5} . The addition of various co-dopants in germanosilicate optical fibers has resulted in photosensitivity enhancement. In particular, boron co-doping can lead to a saturated refractive index change about 4 times larger than that obtained in pure germanosilicate optical fibers. Sensitization techniques have also been developed for writing highly reflective gratings in germanosilicate optical fibers. An increase of the photoinduced refractive index modulation to values of the order of 10^{-3} and higher has been obtained via hydrogenation or flame brushing. These techniques consist in increasing the charge in hydrogen in the fiber core before grating inscription. For the hydrogenation (hydrogen loading) technique (Lemaire et al., 1993), optical fibers are placed in hydrogen gas environment at temperatures ranging from 20 °C to 75 °C and pressures from 20 atm to 750 atm, which results in diffusion of hydrogen molecules into the fiber core. Depending on the temperature and pressure values, the hydrogenation process can last from several hours to several days or even several weeks. During the UV irradiation, hydrogen allows the creation of GODC since it combines with oxygen atoms in order to form OH radicals. As hydrogen rapidly diffuses out of the optical fiber at ambient temperature, hydrogen-loaded optical fibers have to be maintained at low temperature prior to the fiber grating manufacturing process. Deuterium can also be used instead of hydrogen in order to avoid enhancement of the absorption peak of the OH bond around 1380 nm. This leads to the formation of OD radicals.

In the flame brushing technique (Bilodeau et al., 1993), the region of the optical fiber to be photosensitized is brushed repeatedly by a flame fueled with hydrogen and a small amount of oxygen, reaching a temperature of about 1700 °C. The photosensitization process takes approximately 20 minutes. At this very high temperature, hydrogen diffuses into the fiber core and reacts with the germanosilicate glass to produce GODC. This reaction creates a strong absorption band at 240 nm and leads to a highly photosensitive core. The flame brushing technique allows hydrogenation at ambient pressure but it can only be used locally as the flame is generally very small.

2.4 Temperature and mechanical strain sensitivities of uniform fiber Bragg gratings

The Bragg wavelength depends on the effective refractive index of the core and the spatial periodicity of the grating. These two parameters are affected by changes in strain and temperature. In particular, the effective refractive index is modified through the thermo-optic and strain-optic effect, respectively. Hence, from equation (1), the shift in the Bragg wavelength $\Delta\lambda_{\text{Bragg}}$ due to strain $\Delta\epsilon$ and temperature ΔT variations is given by:

$$\Delta\lambda_{\text{Bragg}} = 2 \left(\Lambda \frac{dn_{\text{eff}}}{dT} + n_{\text{eff}} \frac{d\Lambda}{dT} \right) \Delta T + 2 \left(\Lambda \frac{dn_{\text{eff}}}{d\epsilon} + n_{\text{eff}} \frac{d\Lambda}{d\epsilon} \right) \Delta\epsilon \quad (2)$$

The first term in Equation (2) represents the effect of temperature on the Bragg wavelength. The shift of the Bragg wavelength due to thermal expansion comes from the modification of the grating spacing and the refractive index. The relative wavelength shift due to a temperature change ΔT can be written as:

$$\frac{\Delta\lambda_{\text{Bragg}}}{\Delta T} = \lambda_{\text{Bragg}} \left(\frac{1}{n_{\text{eff}}} \frac{dn_{\text{eff}}}{dT} + \frac{1}{\Lambda} \frac{d\Lambda}{dT} \right) \quad (3)$$

where

$\frac{1}{n_{eff}} \frac{dn_{eff}}{dT}$ is the thermo-optic coefficient, which is approximately equal to $8.6 \cdot 10^{-6} \text{ K}^{-1}$ for

germanium doped silica core optical fiber (Othonos & Kalli, 1999).

$\frac{1}{\Lambda} \frac{d\Lambda}{dT}$ is the thermal coefficient of the optical fiber, which is approximately equal to $0.55 \cdot 10^{-6}$

K^{-1} for silica (Othonos & Kalli, 1999).

Clearly the refractive index change is the dominant effect. The order of magnitude of temperature sensitivity of the Bragg wavelength around 1550 nm is $10 \text{ pm}/^\circ\text{C}$.

Figure 3 shows the experimental evolutions of the Bragg wavelength as a function of temperature for a 1 cm long uniform fiber Bragg grating. The grating was placed inside a thermal chamber regulated in temperature with an accuracy of the order of $0.1 \text{ }^\circ\text{C}$.

The evolution is linear with a slope computed equal to $10.23 \text{ pm}/^\circ\text{C}$.

Experiments were carried out for increasing and decreasing perturbations.

As shown in figure 3, no hysteresis was obtained, which is very important for sensing purposes.

The second term in equation (2) represents the effect of longitudinal strain on an optical fiber. It corresponds to a change in the grating periodicity and the strain-optic induced change in the refractive index. By defining the strain as $\epsilon = \Delta\Lambda / \Lambda$, the change of the grating periodicity can be related to the applied strain since

$$\Lambda_s = \Lambda + \Delta\Lambda = \Lambda(1 + \epsilon) \tag{4}$$

where Λ_s represents the modified grating period after the application of the perturbation.

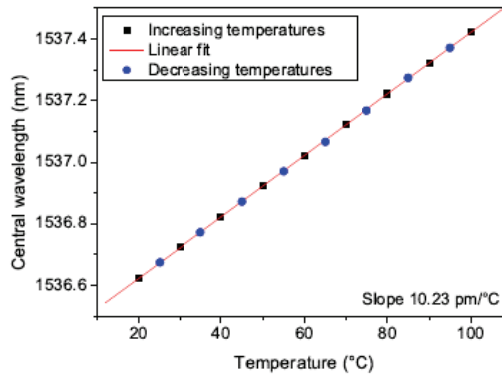


Fig. 3. Evolution of the peak wavelength as a function of temperature changes

The elasto-optic effect relates the refractive index change to the applied strain (Yarif, 1983):

$$\Delta n_{ij} = \Delta \left(\frac{1}{n_{eff}^2} \right)_{ijj} = \sum_{i=1}^6 \sum_{j=1}^6 p_{ij} \epsilon_{ij} \tag{5}$$

where Δn_{ij} is the change in the electric impermeability tensor, ϵ_j are the strain components and p_{ij} are the elements of the elasto-optic tensor. The form of the elasto-optic tensor, but not the magnitude of the coefficients p_{ij} can be derived from the symmetry of the material under

consideration. In its most general form, there are 36 different coefficients p_{ij} . For the class of isotropic materials, to which silica glass belongs, this number is reduced to two independent coefficients p_{11} and p_{12} (Yarif, 1983).

The magnitudes of the individual coefficients p_{ij} are dependent on the material considered. For pure bulk silica it was found that typical values measured at 628 nm are $p_{11}=0.121$ and $p_{12}=0.270$ (Bertholds & Dandliker, 1988). These values are often used when computing the influence of mechanical perturbations such as elongation and lateral compression of optical fibers. However due to the presence of doping elements in the core, the effective values for fibers may be different from those for bulk silica. Measurements on single-mode optical fibers at 628 nm yielded values of $p_{11}=0.113$ and $p_{12}=0.252$, respectively (Barlow, D. Payne, 1983). An error on these values of approximately 5% is possible because of the uncertainty on the value of the Poisson's ratio of the optical fiber.

Assuming that the grating is strained in the z direction only and that the fiber material follows Hooke's law, we obtain the shift of Bragg wavelength for an applied strain:

$$\Delta\lambda_{Bragg} = \lambda_{Bragg}(1 - p_e)\Delta\epsilon \quad (6)$$

$$p_e = \frac{n_{eff}^2}{2} [p_{12} - \nu(p_{11} + p_{12})] \quad (7)$$

where ν is the Poisson's ratio.

Substitution of parameters ($p_{11}=0.113$, $p_{12}=0.252$, $\nu=0.16$ and $n_{eff}=1.482$) in equations (6) and (7) gives a strain-optic constant $p_e=0.21$ and a sensitivity around 1550 nm of 1.2 pm/ $\mu\epsilon$.

2.5 Advantages of fiber Bragg grating sensors

The first fiber Bragg grating sensor was reported in 1989 by W. Morey and coworkers (Morey et al., 1989). The development of the external writing technique has considerably increased the interest in fiber Bragg grating sensors. This interest comes from the great potential that they have for a large number of sensing applications where are required measurements of strain and temperature (Morey et al., 1989), pressure (Xu et al., 1994), acceleration (Therault et al., 1996), high magnetic field (Kersey & Marrone, 1994) and force (Bjerkkan et al., 1996).

As already understood, fiber Bragg gratings are intrinsic optical sensors which modify the characteristic spectrum of an incident light signal since their physical parameters are affected by the external perturbation. The most widely used principle of operation of fiber Bragg grating sensors is to monitor the shift in wavelength of the reflected signal as a function of the external parameter to be measured.

The main advantage of fiber Bragg grating sensors is that the measurand information is wavelength-encoded. This property makes the sensor self-referencing and independent of fluctuating light levels. The system is therefore immune to source power and connector losses that affect many other types of optical fiber sensors. The very low insertion loss and narrowband wavelength reflection of fiber Bragg gratings offer convenient serial multiplexing along a single-mode optical fiber. There are further advantages of fiber Bragg gratings over conventional electrical strain gauges, such as linearity in response over many orders of magnitude. Many of them are intrinsic to the properties of optical fibers: immunity to electromagnetic interferences, light weight, flexibility, stability, high temperature tolerance and even durability in high radiation environments, which all contribute to obtain reproducible measurements. The small diameter of the optical fiber and the small length of fiber Bragg gratings make them compatible with applications for which slightly intrusive

probes are required, such as in the human body for temperature and/or chemical species profiling. Furthermore, fiber Bragg gratings can be easily embedded into materials to provide damage detection or internal strain field mapping. Fiber Bragg grating sensors are therefore very important components for the development of smart structure technology and for monitoring composite material curing and response. Nowadays such sensors offer real-time monitoring of civil structures and aerospace applications (Othonos & Kalli, 1999).

2.6 Long Period Fiber Gratings

We give here the basic theory of long period fiber gratings LPFG in order to have a fundamental understanding of the coupling mechanisms of such gratings in single mode optical fiber (Erdogan, 1997).

Let us note that long period fiber gratings are not Bragg gratings but they offer a lot of applications in sensing and will be used for chemical sensing purposes. The period of the refractive index modulation for a LPFG lies in the range 500 μm instead of 500 nm for a FBG. The operating principle of long period fiber gratings proposed by A. Vengsarkar and coworkers is illustrated in figure 4 (Vengsarkar et al., 1996). It can be seen that light vehiculated by the fundamental core mode is perturbed by the presence of the grating in the fiber core and is coupled to forward-going cladding modes. For long period fiber gratings, the difference between the propagation constant of the guided mode and the phase vector of the grating equals the propagation constant of one or more cladding modes at appropriate wavelengths.

Cladding modes result from the radiation modes that are trapped by the cladding-air interface. These modes attenuate rapidly due to bends in the fiber and absorption of cladding.

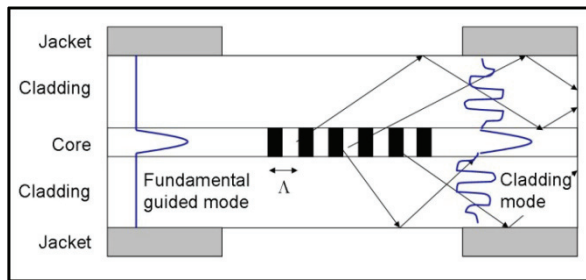


Fig. 4. Coupling of the fundamental guided mode to cladding modes in a long period fiber grating (not in scale)

Light at the phase-matched wavelengths is then lost from the fiber. For typical long period fiber gratings, more than one cladding mode can satisfy the phase-matching condition at different wavelengths and the guided mode can also be coupled to all those cladding modes. Typical transmitted spectra are thus composed of several cladding modes resonances. The important point is that these gratings can couple light out of the core. This has two consequences: energy can be given to the external medium and the transmission spectrum of the LPFG are very sensitive to refractive index changes of the external medium. These LPFG are therefore used to detect refractive index changes of the surrounding medium.

As in the case of uniform fiber Bragg gratings, LPFG's are sensitive to external parameters, in particular: temperature, strain or bending (James&Tatam, 2003). The sensitivity of long period fiber gratings characteristics to environmental parameters is influenced by the grating period (Bhatia, 1999) and by the optical fiber composition (Shima et al., 1997). However it is also influenced by the cladding modes to which coupling takes place. This combination of influences allows the design of long period fiber gratings that have a range of possible responses to a particular measurand beyond temperature and strain. A single long period fiber grating can indeed be characterized by attenuation bands that have a positive sensitivity to a measurand, others that are insensitive and others that have a negative sensitivity to the measurand. In summary, it is possible to finetune the sensitivity to temperature or strain by changing the geometry of the grating and the wavelength range. The refractive index sensitivity of long period fiber gratings comes from the dependence of the phase matching condition on the effective refractive indices of the cladding modes. They are indeed function of the difference between the surrounding refractive index and the cladding refractive index. The central wavelengths of the attenuation bands are thus dependent on the surrounding refractive index, providing that the cladding has a higher refractive index than the surrounding medium.

The sensitivity to refractive index changes is spectrally manifested by central wavelength shifts and by changes in the minimum transmission value of the attenuation bands. The highest sensitivity is obtained for higher order modes and occurs for refractive index values close to that of the cladding (Patrick et al., 1998).

When the surrounding refractive index value matches that of the cladding, the cladding appears to be of infinite extent and a broadband radiation modes coupling with no distinct attenuation bands is obtained. When the surrounding refractive index is higher than that of the cladding, the central wavelengths of the attenuation bands present a considerably reduced sensitivity (Lee et al., 1997; Duhem et al., 1998).

A change in the form of the transmitted spectrum is however obtained since the peak to peak amplitudes of the attenuation resonances is reduced. In such a situation, the presence of attenuation bands is no longer due to the total internal reflection at the cladding/surrounding medium interface but comes from the Fresnel reflection that yields to attenuated cladding modes (Duhem et al., 1998).

The refractive index sensitivity has been exploited in a lot of applications such as chemical concentration sensing, liquid level sensing and even biosensing (James&Tatam, 2003).

3. Preparation of fiber gratings

This paragraph will shortly explain the most often used techniques to prepare fiber gratings eg to achieve the refraction index modulation in the core of the fiber thanks to the photosensitivity effect.

There are essentially 4 methods : interferometric method, phase mask, point to point and amplitude mask technique.

3.1 Interferometric method

For the interometric method (figure 5), also called transverse holographic technique (Meltz et al., 1989), one uses interferometer that splits the incoming UV laser light (at 244 nm) into two beams of equal intensity that were subsequently recombined in the core region of the

side exposed optical fiber to form an interference pattern, inducing a permanent refractive index modulation in the core. Furthermore, the periodicity of the refractive index modulation depends on the angle of recombination of the two beams. In each path of the free-space interferometer, a cylindrical lens focused the light onto the optical fiber.

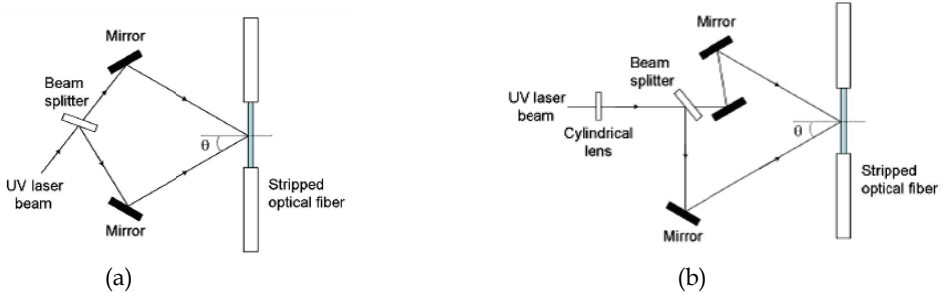


Fig. 5. General amplitude-splitting interferometer (a) and improved version (b).

An improvement to the amplitude-splitting interferometer is shown in figure 5 (b). Indeed, in the first interferometer proposed by G. Meltz, the UV writing laser light is split into equal intensity beams that recombine after having undergone a different number of reflections in each optical path. Consequently the interfering beams acquire different polarization orientations, which results in a low-quality fringe pattern for laser beams having low spatial coherence. This problem is eliminated in the new implementation of the interferometer since it compensates for the beam splitter reflection by including a second mirror in one of the optical paths. The total number of reflections is the same in the two arms, which ensures that the two interfering beams are identical. A cylindrical lens is also used to focus the interfering beams to a fine line matching the fiber core. The resulting intensity obtained at the fiber core is higher and yields to an improvement of the grating fabrication.

The grating periodicity Δ , which is identical to the periodicity of the interference fringe pattern, depends on both the irradiation wavelength λ_{UV} and the half angle between the intersecting UV beams θ . The period of the grating is then given by the following relationship (8):

$$\Delta = \frac{\lambda_{UV}}{2 \sin \theta} \quad (8)$$

One of the advantages of the holographic technique is its flexibility. Indeed, it is possible to inscribe gratings of different lengths and to modify the period through varying the angle θ . The main inconvenient is the instability towards vibrations and air movements. This method is difficult to use for mass production.

3.2 The phase mask technique

The phase mask technique is one of the most effective methods for inscribing fiber Bragg gratings in photosensitive optical fiber. This technique uses a diffractive optical element called phase mask to spatially modulate the UV writing beam. A phase mask is a relief grating realized in a pure fused silica plate. The significant features of the phase mask are the grooves realized into a UV-transmitting silica mask plate, with a carefully controlled mark-space ratio as well as etch depth. The profile of the periodic relief grating is chosen

such that when a UV beam is incident on the phase mask, the zero-order diffracted beam is suppressed to less than a few percent (typically less than 3%) of the transmitted power. This is done by action on the depth of the interference fringes. In addition, the diffracted plus and minus first orders are maximized with more than 35% of the transmitted power for each of these diffraction orders. A near-field interference pattern is then produced by the interference of the plus and minus first-order diffracted beams. The periodicity of the fringes is one half that of the phase mask. Hence, one given phase mask yields only one Bragg wavelength. The interference pattern photo-prints a refractive index modulation in the fiber core that is placed in close proximity to the phase mask, as shown in figure 6.

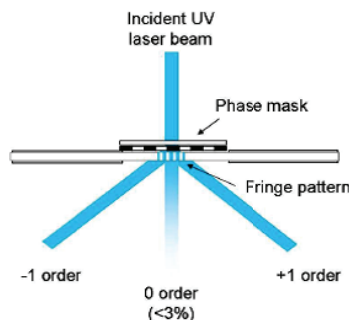


Fig. 6. Schematic of a phase mask used for fiber Bragg gratings inscription.

A cylindrical lens can also be used to focus the fringe pattern in the fiber core and to maximize the power density. The earliest experiments using the phase mask technique were performed by K.O. Hill and coworkers in 1993 (Hill et al., 1993). Since this original demonstration, the phase mask technique has been developed to a point where the inscription of nearly 100% reflective gratings is now routine with moderate UV optical power. Furthermore it is now possible to fabricate non uniform grating structures using the phase mask technique with specific phase masks.

The phase mask technique greatly reduces the complexity of the fiber grating fabrication system. The simplicity of using only one optical element provides a robust and stable method for the production of high quality fiber Bragg gratings. Since the optical fiber is placed directly behind the phase mask in the near field of the diffracting UV beams, stability problems due to mechanical vibrations are minimized. However, this technique is not flexible as the period of the gratings and the maximum length of the grating are fixed by the mask. Different masks are needed when the Bragg wavelength needs to be modified.

3.3 The point to point technique

The point to point technique is accomplished by inducing a change in the core refractive index corresponding to a grating plane one step at a time along the fiber core. This method is used to prepare long period gratings. This technique can also be applied to manufacture short period gratings when the spot is sufficiently focused (waist of the order of $0.25 \mu\text{m}$) but it then requires a very stable and precise submicron translation system. In a typical experimental set-up, the UV laser beam passes through a slit before being focused on the core of an optical fiber, as shown in figure 7. As a result, the core refractive index in the

irradiated fiber section is changed locally. The fiber is then translated through a distance Λ corresponding to the grating period, in a direction parallel to the fiber axis. This process is repeated to form the grating structure in the fiber core. Depending on the grating length, the manufacturing process can be relatively long. Consequently, errors in the grating spacing due to thermal effects and/or small variations in the optical fiber strain can occur.

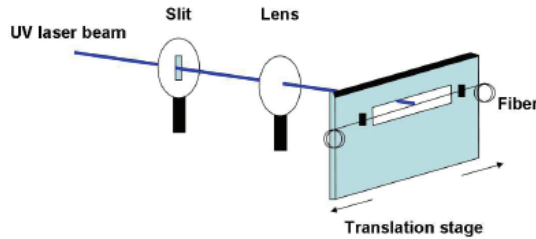


Fig. 7. Operating principle of the point to point technique.

3.4 Amplitude mask technique

The amplitude mask technique consists in placing a metal mask (generally in copper) in front of the optical fiber. The mask contains a pattern that is identically reproduced on the single mode optical fiber during the UV beam translation so that the periodicity of the obtained gratings is equivalent to that of the metal mask. To obtain a modification of the grating periodicity, it is thus required to use different metal masks.

4. Description of the hydrogen sensors

The different sensors consist in Uniform Fiber Bragg Gratings and/or Long Period Bragg Gratings covered with a sensitive layer that reacts with hydrogen (Caucheteur et al., 2008a). The sensitive layer consists in Platinum doped tungsten trioxide nano-lamellae.

The idea is to use the exothermic effect due to the combustion of H_2 on the surface of the sensitive coating which acts as a catalyst thanks to the following reactions (9 et 10):

The overall reaction is the combustion of hydrogen and WO_3 is not consumed.

The reaction heat of hydrogen combustion in normal conditions is 57.8 kcal/mol.



4.1 Preparation of the Bragg gratings

Uniform FBGs and long period fiber gratings (LPFGs) were inscribed into standard single mode fiber by means of a frequency-doubled Argon-ion laser emitting at 244 nm. Prior to the UV exposure, the optical fiber was hydrogen-loaded at 70 °C and 200 atm during 48 hours. After the inscription, the gratings were annealed at 100 °C during 24 hours in order to stabilize their properties. Every grating was written in the middle of a 5 cm long stripped region of the optical fiber. The sensitive layer was deposited uniformly along the stripped region using the dip-coating technique, thus ensuring the same experimental conditions for all the gratings. As further explained, LPFGs were used for their radiative properties since

they are transmissive gratings that couple light from the fiber core to the cladding (James & Tatam, 2003).

4.2 Realization of the sensitive layer

Nano-sized tungsten oxide powder was prepared using sol-gel method (Okazaki et al., 2003; Caucheteur et al., 2008). To start, aqueous sol-gel of tungstic acid (H_2WO_4) was prepared from Na_2WO_4 with protonated cation-exchange resin. In a first stage, a gel consisting of $\text{WO}_3 \cdot \text{H}_2\text{O}$ was formed. The gel was washed, centrifuged several times with distilled water and dried in air at 60°C for 6h. The powder consisting in nano-lamellae of tungsten oxide with high specific surface area (figure 8) is finally obtained. Appropriate amounts of hexachloroplatinic acid (H_2PtCl_6) solution were added to the obtained powder. The mixture was finally annealed at 500°C for 1h in order to obtain WO_3 doped with Pt on its surface. At the end of the process, the active layer consists of WO_3 nano-lamellae (squares of about $1\ \mu\text{m} \times 1\ \mu\text{m} \times 50\ \text{nm}$) with Pt dispersed on their surface. The molar ratio Pt/W was about 1/14. After deposition on a substrate, a microporous structure is obtained with high specific area and high catalytic activity.

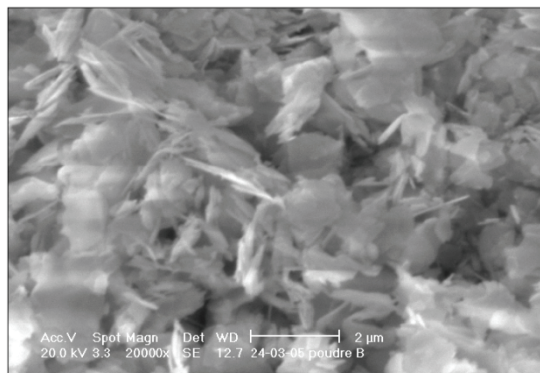


Fig. 8. Scanning Electron Microscopy image of the tungsten trioxide powder used in the sensitive layer. (Caucheteur et al., 2008 b)

4.3 Deposition of the sensitive layer on the fiber Bragg gratings

Prior to the deposition of the layer, the optical fiber was cleaned. The sensitive layer was then deposited, by using dip-coating technique, on the stripped optical fiber at a place where an FBG was written. The nanopowder of platinum doped tungsten oxide was mixed with a solvent (ethanol) so that the optical fiber could be immersed into the solution. Then the solvent evaporated at room temperature and the sensitive layer remained fixed on the optical fiber. The thickness of the deposited layer was measured of the order of 3 microns.

4. Experimental set-up

The set-up used to test the H_2 sensors in different air environments of various relative humidity levels is depicted in figure 9. A bubbler filled with distilled water is used to

control the relative humidity level of air between 0 and 90 %. Three mass flow controllers provided a mixture of air and hydrogen with variable H_2 concentrations from 0 to 4 % (the error on the determination of the H_2 concentration being equal to 0.05 %). The gas chamber was made of a 20 cm long and 1.5 cm wide glass cylinder with an inlet and an outlet to allow the gas mixtures flow through the chamber. Temperature and gas flow were continuously monitored. The amplitude spectrum of the tested gratings was measured by means of an ASE source covering the C+L bands (1520 - 1620 nm) and an optical spectrum analyzer (OSA) with an accuracy of 15 pm.

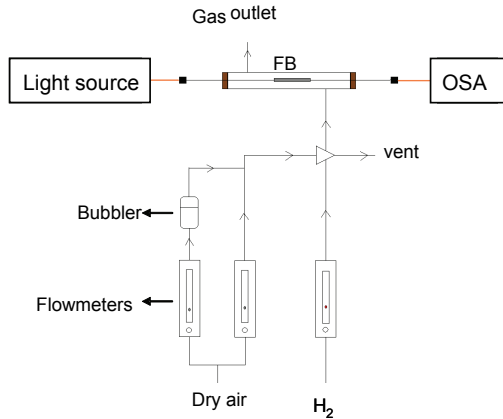


Fig. 9. Schematic of the experimental set-up used to test the H_2 fiber grating sensors.

5. Results

The response to hydrogen injections of sensors in different configurations was followed.

FBG of various lengths and hybrid LPFG+FBG structures were studied.

The effect of ambient temperature and relative humidity on the response were also checked for the different configurations.

5.1 Uniform Bragg gratings.

Figure 10 presents the results obtained on the transmitted spectrum of a 4 cm long FBG subjected to different H_2 concentrations in dry air at room temperature (20 °C). In presence of H_2 in air, a shift of the Bragg wavelength to the right appears due to the exothermic reaction that occurs between H_2 molecules and O_2 molecules inside the sensitive layer. The chemical reaction occurring in the sensitive layer is the oxidation of the H_2 molecules that generates H_2O molecules. For a 2 % concentration of H_2 in dry air, the measured wavelength shift is equal to 4 nm. It is equivalent to an increase of temperature around the FBG of about 400 °C since the temperature sensitivity of the FBG is of the order of 10 pm/°C.

It is important to mention that the exothermic reaction is initiated inside the sensitive layer when an energy threshold is reached. It is indeed required to bring sufficient energy so that the chemical reaction can be initiated. For the 4 cm long FBG tested above, the threshold in terms of H_2 concentration is equal to 1.0 % in dry air. That means that, for the first

measurement cycle realized for increasing H₂ concentrations, the grating did not react to H₂ concentrations below 1%. Then, once the chemical reaction has been initiated, it reacted to concentrations smaller than 1%, as shown on figure 4. Moreover, it was observed that the concentration threshold depended on the length of the grating. The threshold is bigger if the grating is shorter (figure 11). This is a very important feature of our sensor that limits its practical applications. That is why we have tried to quantify it as well as possible.

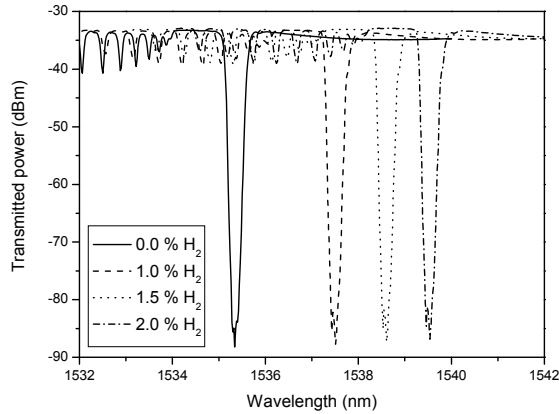


Fig. 10. Transmitted spectrum of a 4 cm long FBG in response to different H₂ concentrations in dry air at 20 °C.

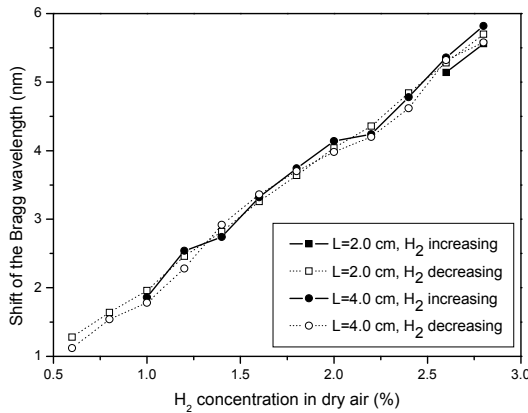


Fig. 11. Shift of the Bragg wavelength as function of the H₂ concentration in dry air at ambient temperature for different physical lengths of the gratings.

For that purpose, different strongly reflective uniform gratings characterized by different physical lengths were tested. The gratings were inscribed with the same velocity for the UV beam sweep along the phase mask and consequently, the longer gratings were more exposed to the UV interference pattern than the shorter gratings. The longest gratings (that are also the strongest in terms of coupling coefficient) were characterized by the presence of

important cladding modes resonances below the Bragg wavelength in the transmitted spectrum (approximately 3 dB of peak to peak amplitude for the low order cladding modes) as can be seen on figure 3, which demonstrates their strong coupling characteristics. Table 1 summarizes the results obtained in terms of detection threshold of H₂ concentrations for a set of 7 FBGs. The data were recorded for H₂ concentrations ranging from 0 to 3% and increasing by step of 0.1%.

Grating length (cm)	Threshold (% H ₂)
0.5	No response up to 3%
1.0	~ 3.0
2.0	~ 2.5
2.5	~ 1.6
3.0	~ 1.4
3.5	~ 1.2
4.0	~ 1.0

Table 1. Thresholds for the detection of H₂ in dry air as function of the grating length during the first measurement cycle at room temperature.

These results reveal that the physical length of the inscribed grating influences the detection threshold of H₂ concentrations. Longer gratings allow for a reduction of the threshold. This comes from the fact that, as they are characterized by a strong coupling to both the backward going core mode and cladding modes, long gratings deliver some energy to the cladding that is finally collected by the sensitive layer and contributes to decrease the H₂ concentrations required to reach the threshold. This mechanism is possible since the refractive index modulation of the sensitive layer is higher than that of pure silica. Consequently, light that is outcoupled from the core of the fiber is guided into the sensitive layer and allows to initiate the chemical reaction between H₂ and O₂ molecules for small H₂ concentrations.

Figure 12 shows the wavelength shifts measured for all the tested gratings in response to increasing and decreasing H₂ concentrations. The plain curves were obtained for increasing H₂ concentrations (during the first measurement cycle) whereas the dotted curves were obtained for decreasing H₂ concentrations. The wavelength shifts were then converted to temperature variations around the tested FBGs (figure 13).

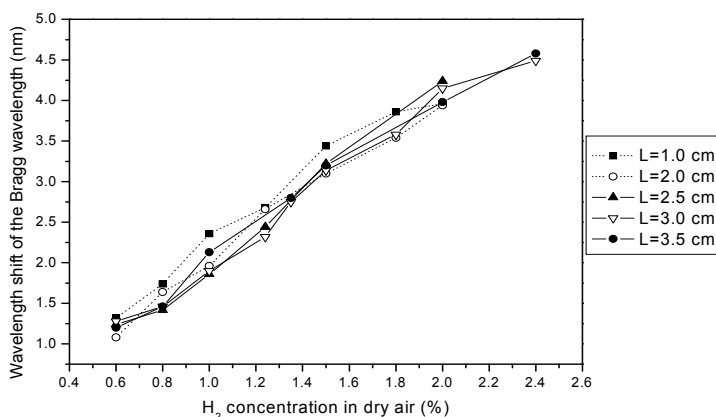


Fig. 12. Shift of the Bragg wavelength as function of the H₂ concentration in dry air at ambient temperature for different physical length of the gratings.

The results obtained from these experiments demonstrate that the grating length has no influence on the temperature delivered by the chemical reaction. The sensitivity of the sensor (the slope of the curve) is thus not dependent on the grating physical properties as expected since the reached temperature mainly depends on the hydrogen concentration.

Another important feature is the linear behaviour obtained in response to varying H₂ concentrations. Moreover, the data obtained for increasing H₂ concentrations match those obtained for decreasing H₂ concentrations so that there is no hysteresis in the sensor response. This characteristic is surely obtained owing to the very small response time (less than 4 seconds) of the sensor to varying H₂ concentrations.

The H₂-FBG sensors were also tested in wet air environments and the obtained results demonstrated that the threshold of detection of hydrogen concentration increases when the relative humidity level increases. For the 2.5 cm long FBG sensor, the threshold increased from 1.5 % to 3 % when the relative humidity level was changed from 0 % to 50 %. For the 4 cm long FBG, it increased from 1.0% to 1.5% when the relative humidity level was changed from 0 % to 90 %. This increase attributed to the presence of H₂O molecules adsorbed on the surface that tend to inhibit the reaction given in (9). The sensitivity to H₂ concentrations did not change in wet air in comparison to that obtained in dry air because, as long as the threshold is passed, the temperature on the sensor is high enough to desorb the water molecules adsorbed on the surface and the reaction takes place as if water were not present. Indeed the temperature is higher than 100 °C when the reaction is ignited.

However, as shown on figure 14, the sensitivity in response to H₂ concentrations did not change in wet air in comparison to that obtained in dry air. The differences between the temperatures reached in dry air and in 50 % wet air all fell within ± 20 °C whatever the hydrogen concentration value.

Low temperature environments also led to an increase of the threshold value. At -30 °C, the detection threshold reached 1.8 % for the 4 cm long FBG. This value is still well below the 4 % explosion limit and it can be accepted in our applications.

The selectivity of the sensitive layer was tested with other gases such as carbon monoxide, methane and pure nitrogen. No answer was obtained, demonstrating that this sensor is specific to the detection of hydrogen in air.

These results can be rationalized by a simple model : the response of the sensor can be understood by examination of the heat flows exchanged on the sensitive layer surface in the presence of H_2 .

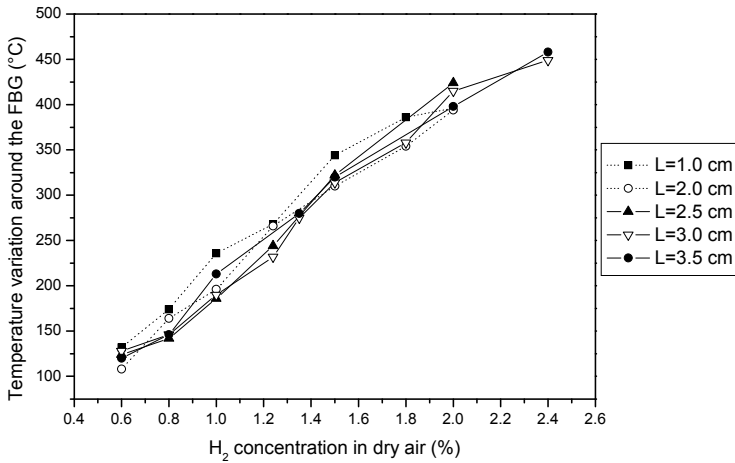


Fig. 13. Temperature variation around the FBG as function of the H₂ concentration in dry air at ambient temperature for different physical length of the gratings.

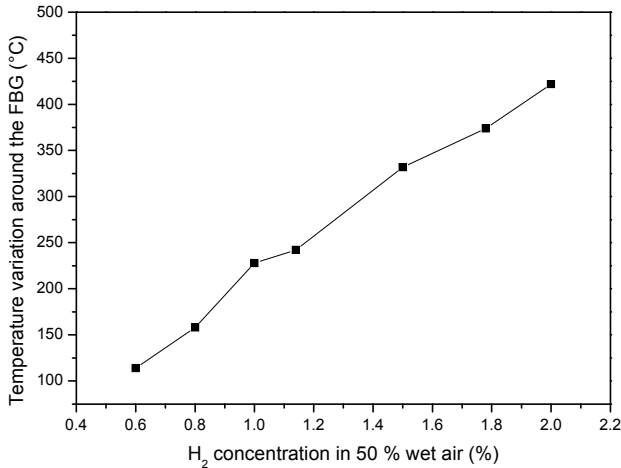


Fig. 14. Temperature variation around the 2.5 cm long FBG as function of the H₂ concentration in 50 % wet air at ambient temperature.

When the sensitive layer is in contact with a gas mixture of air and hydrogen, the oxidation of H_2 molecules by O_2 molecules contained in air occurs on its surface. This reaction is exothermic so that the temperature locally increases around the gratings. H_2 sensing is therefore based on the monitoring of the resonance wavelength shift induced by the temperature change. This reaction requires an activation energy equal to 0.15 eV (Appel et al., 2004). The temperature experienced by the grating results from the equilibrium between the heat flow delivered by the exothermic reaction $-\varphi_r$ and the heat flow lost by exchange with the surrounding medium φ_{th} . In a very good approximation, we may consider that φ_{th} is dominated by radiation so that it can be expressed by:

$$\varphi_{th} = \varepsilon\sigma(T^4 - T_e^4) \quad (11)$$

where ε is the emissivity of the WO_3 layer (close to 0.9 as it was estimated from infrared measurement of a surface of WO_3 heated to a known temperature), σ is the Stefan-Boltzmann constant ($5.673 \cdot 10^{-8} \text{ W}/(\text{m}^2\cdot\text{K}^4)$), T is the absolute temperature measured by the grating and T_e is the absolute ambient temperature. φ_r is defined as :

$$\varphi_r = v \cdot (-\Delta H_r) \quad (12)$$

$$v = k \cdot C_{H_2} \quad (13)$$

$$k = k_0 \cdot \exp\left(-\frac{E_a}{RT}\right) \quad (14)$$

where v is the reaction rate and $-\Delta H_r$ is the reaction heat and is equal to 57.8 kcal/mol. The reaction rate v is proportional to the concentration of hydrogen C_{H_2} and depends on the temperature through the usual Arrhenius formula. E_a is the activation energy (0.15 eV), R is the gas constant equal to 8.31 J/(mol.K). k_0 depends on the amount of Pt per surface unit and reflects the sensitive layer efficiency. Its value is not precisely known in practice. Using Eq. (1) and (2), the sensor behavior can be semi-quantitatively simulated from the condition $\varphi_{th}=\varphi_r$ for different operating conditions. Figure 15 shows simulation results obtained for different ambient temperatures and for different sensitive layer efficiencies (the parameters put in the model were not optimized to exactly simulate the experimental results, reasonable values were used to qualitatively explain the observed results). Conformingly to our experiments, one can see on figure 15 that the detection threshold increases when both the ambient temperature and the sensitive layer efficiency decrease. Decreasing k_0 gives the same qualitative effect as a humidity level increase since water molecules tend to inhibit the exothermic reaction occurring on the sensitive layer. Hence, it may explain the increase of the threshold level. However, for the global evolution, as the temperature increases while hydrogen reacts, the adsorbed water molecules disappear from the surface and the occupied reaction sites are released and can participate to the reaction. Consequently, as soon as the temperature exceeds 60 °C, the effect of water almost vanishes and the equilibrium response remains the same as in absence of water.

Due to the activation energy (0.15 eV) of the chemical reaction, there exists a minimum of H_2 concentration below which the reaction will not start. In other words, there exists a threshold value in terms of H_2 concentration below which the sensor does not react. In practice, this threshold value can be decreased thanks to an external energy contribution. This could be done for instance by a local heating of the sensitive layer. One efficient way to do this is to exploit the light energy transported by the optical fiber. Indeed, at 1550 nm, the photon energy is about 0.7 eV and consequently, light that would be coupled from the core of the optical fiber towards the sensitive layer could favor the reaction for lower H_2

concentrations. This coupling mechanism is possible since the refractive index of the sensitive layer is slightly higher than that of pure silica. This explains the effect of the size of the grating. This effect was not simulated so far in our simple analysis.

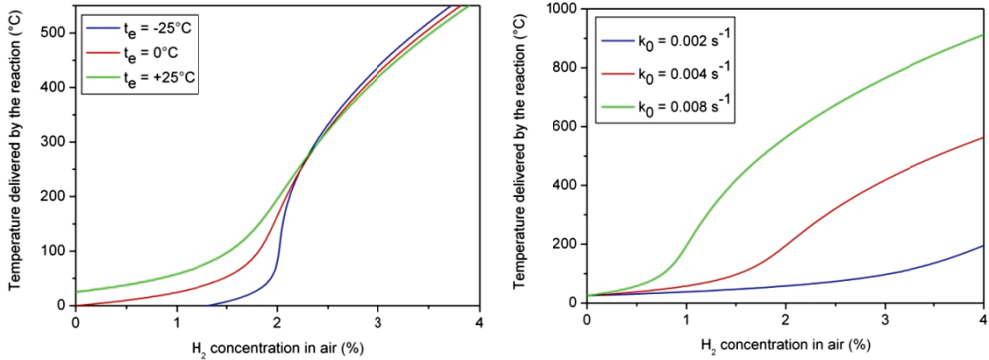


Fig. 15. Sensor responses simulated for different ambient temperatures (left - $k_0=0.004\text{ s}^{-1}$) and for different sensitive layer efficiencies (right - $t_e=25^\circ\text{C}$).

5.2 Hybrid structure LPFG+FBG

In the previous paragraph, we have demonstrated the possibility to decrease the threshold value to 1 % in dry air with strongly reflective uniform FBGs. However, in that case, the FBGs are so strong that the accurate measurement of their Bragg wavelength is impossible (falls in the noise). Moreover, a drastic increase of the threshold was obtained in wet air and for temperatures below 0°C , which strongly limits the use of uniform FBGs for H₂ sensing.

To avoid the limitations of uniform FBGs, a hybrid configuration consisting of the superimposition of a uniform FBG within an LPFG is presented. This solution takes profit of the light coupling to the cladding modes induced by the LPFG. Indeed, as the refractive index of the sensitive layer, consisting essentially in WO_3 , is slightly higher than that of pure silica, the light outcoupled in the cladding penetrates the sensitive layer and its energy (photon energy around $1550\text{ nm} \sim 0.7\text{ eV}$) favors the exothermic reaction.

The FBG is used as a probe to reflect the temperature change. The sensing mechanism is therefore based on the monitoring of the wavelength shift due to a temperature change in the reflected spectrum of the uniform FBG.

Both kinds of gratings were designed to minimize the detection threshold. The periodicity of the LPFG was chosen so as to obtain a strong resonance band (light coupled to the cladding) inside the spectral range of the optical source. A periodicity of $475\text{ }\mu\text{m}$ allowed us to obtain such a feature. A 1 cm long 545 nm period uniform FBG was then superimposed on the 3 cm long LPFG so as to obtain a point sensor. As shown in figure 16, it was written at the extremity of the LPFG to take a maximum profit of the light coupling provided by the LPFG. Figure 16 also shows the transmitted and reflected spectra of a typical hybrid configuration. Our first experiments consisted in testing the behavior of hybrid configurations composed of 3 cm long LPFGs characterized by different refractive index modulations, yielding various transmission losses in the C+L bands. The LPFGs were inscribed with the same optical power (55 mW) but different exposure times (translation velocity of the UV beam

along the exposed fiber length set to 0.5 cm/s) so that the laser fluence was modified between the different inscriptions. In any case, the FBGs were characterized by a transmission loss of about 12 dB.

The radiating efficiency of every coated LPFG was evaluated by computing the ratio between the injected and transmitted optical powers integrated over the LPFG resonance bandwidth. The difference between these two quantities indeed reveals the total amount of radiated optical power. In addition, an examination of the fiber surface with an IR camera revealed that the radiation extends on a few centimeters beyond the LPFG end and is not uniform along the grating length. Hence, only a part of the total radiated power can be collected by the sensitive layer and is useful to favor the exothermic reaction. From our experiments, this part was roughly estimated to the third of the total radiated power. Figure 17 shows that the LPFG radiating efficiency increases with respect to the exposure time.

In particular, with the LPFG characterized by a 15 dB transmission loss, more than 60 % of the injected light is coupled out of the fiber core. For this grating and with the ASE source used here, we approximated to 0.2 mW the optical power collected by the sensitive layer. This quantity corresponds to about $1.5 \cdot 10^{20}$ photons/(s.m²), which is sufficient to favor the reaction with respect to the total number of H₂ adsorption sites per surface unit of the sensitive layer (estimated to 10^{19} /m² of fiber). The exact quantum efficiency is currently unknown and the involved mechanisms are thus being investigated.

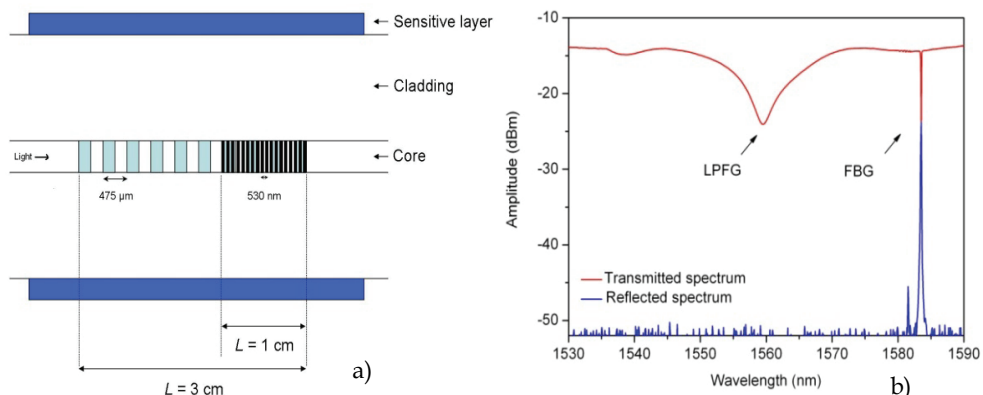


Fig. 16. Uniform FBG superimposed in a LPFG for H₂ detection (a) and transmitted/reflected spectra of this hybrid sensor on the C+L bands (b).

Figure 18 confirms the threshold reduction obtained provided by LPFGs. With the LPFG characterized by a 15 dB loss, the threshold has been measured equal to 0.6 % of H₂ concentration instead of 3 % with the equivalent single uniform FBG. It must be noticed that for all graphs, the response (wavelength shift versus concentration) is approximately the same, yielding the same sensitivity. This is due to the fact that the response is directly linked to the temperature reached thanks to the exothermic reaction. For all sensors, the response is linear and reversible, with a mean sensitivity equal to 198 pm per 0.1 % of H₂ concentration, which is easy to detect with a standard instrumentation. The sensor response time was measured of about one second for H₂ concentrations above the detection threshold.

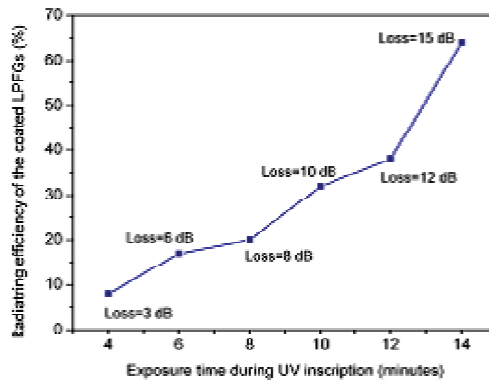


Fig. 17. Radiating efficiency as a function of the exposure time and corresponding LPFG transmission loss in the C+L bands.

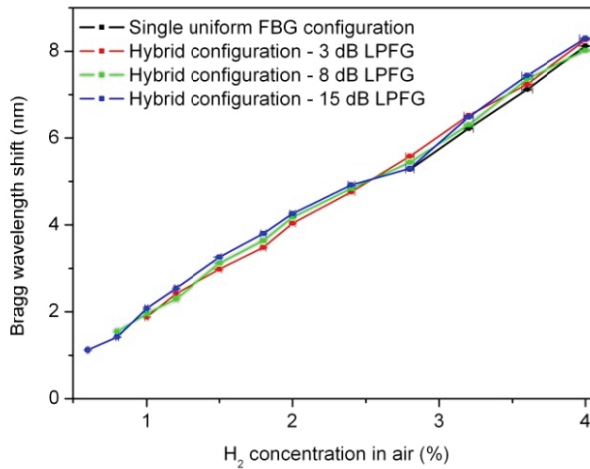


Fig. 18. Bragg wavelength shift as a function of the H₂ concentration in dry air for a single uniform FBG and hybrid gratings with various LPFGs.

The sensor behavior was also tested in wet air environments and at various temperatures. Figure 19 presents the Bragg wavelength shift of a hybrid sensor (configuration with the LPFG characterized by the 15 dB transmission loss) due to the H₂ concentration in different wet air environments. The H₂ detection threshold increases as the relative humidity level increases.

In 90 % wet air, the threshold has been measured equal to 0.9 % H₂ concentration. This is a clear improvement in comparison to a single 1 cm long uniform FBG sensor for which the threshold value has been measured higher than 3 % in 90 % wet air.

Finally, figure 20 confirms that a surrounding temperature decrease limits the sensor performances since more energy is required to initiate the exothermic reaction for a given H₂

concentration. However, while a single FBG is not sensitive to H₂ concentrations up to 4.0 % at -50 °C, the hybrid configuration presents a detection threshold equal to 1.5 %.

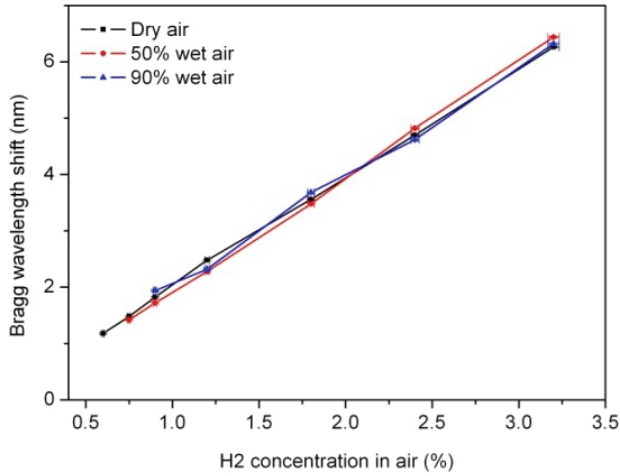


Fig. 19. Bragg wavelength shift as a function of the H₂ concentration in wet air for a hybrid sensor.

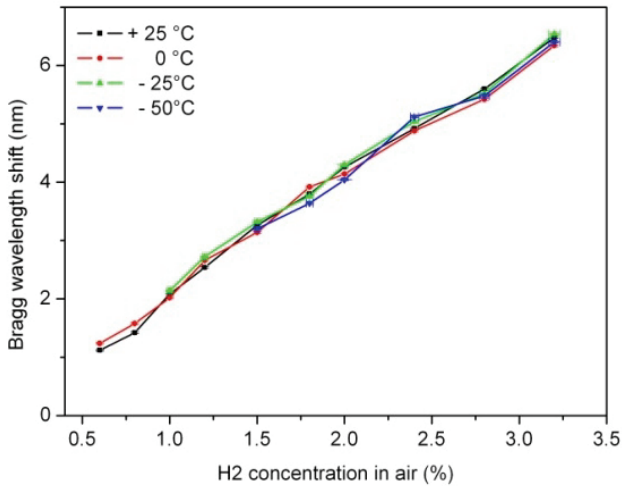


Fig. 20. Bragg wavelength shift as a function of the H₂ concentration at different temperatures.

Hence, in comparison to the use of single FBGs, the hybrid configuration presents the important advantage to decrease the detection threshold value for any experimental conditions. This feature is linked to the use of LPFGs and is possible without increasing the

optical source power density. It thus allows to work with a standard optical source (total power of 15 mW in our case), which keeps as low as possible the sensor price. Let us also mention that using uniform FBGs as probes instead of LPFGs presents two assets. First, the sensor response is encoded in the Bragg wavelength and is therefore not influenced by bending effects, which is not the case for LPFGs. Second, while the resonance band of an LPFG extends on several tens of nanometers (complicating the realization of quasi-distributed sensors with such gratings), a wavelength window of several nanometers is sufficient to record the reflected spectrum evolution of uniform FBGs. Consequently, thanks to the presence of uniform FBGs, the hybrid configuration can be used in frequency multiplexed systems. In particular, with LPFGs characterized by a transmission loss of 3 dB, up to 15 hybrid sensors can be cascaded along an optical fiber in the range of the used ASE source.

6. Conclusions and future work

In this chapter, a novel sensor is presented that is able to measure hydrogen leaks in air by means of optical fibers. The sensor is composed of a fiber Bragg grating covered by a catalytic sensitive layer. In presence of hydrogen in air, an exothermic reaction between H_2 molecules and O_2 molecules takes place on the sensitive layer, leading to an increase of temperature around the Bragg grating. The detection of H_2 concentrations is thus based on the monitoring of the Bragg wavelength shift in response to temperature changes.

Our sensor offers a very good sensitivity and a very fast response. It is selective to hydrogen and presents a rapid, linear response without hysteresis, which constitute very important sensor characteristics. It is also compatible with frequency multiplexing and can consequently allow for the realization of quasi-distributed sensors.

However, in its basic configuration, this sensor suffers from the presence of a detection threshold that limits the range of H_2 concentrations that it can detect. The possibility to decrease this threshold by working with highly reflective gratings has been shown.

The most elegant solution consists in superimposed hybrid fiber gratings coated with a catalytic sensitive layer that heats the gratings in the presence of hydrogen in air. In this hybrid configuration, the LPFG provided a light energy coupling to the sensitive layer to decrease the H_2 detection threshold while the FBG was used to track the temperature increase. Very good sensing performances have been reported: fast response, high sensitivity, reversibility, frequency multiplexing capability and H_2 concentrations detection well below the explosion limit of 4 %, whatever the relative humidity level and for temperatures down to $-50\text{ }^\circ\text{C}$.

These hybrid configurations will be further studied in order to minimize the reaction threshold. Future work on these sensors would be to get full understanding and modeling of the sensor and then optimization of the sensor in order to minimize the detection limit imposed by the reaction threshold.

7. References

- Appel C., Mantzaras J., Schaeren R., Bombach R. and Inaen A., "Catalytic combustion of hydrogen-air mixtures over platine: validation of hetero/homogeneous chemical reaction schemes," *Clean Air* 5, 21-44 (2004).
- Atkins R., Mizrahi V., Erdogan T. (1993), "248-nm induced vacuum UV spectral changes in optical fiber preform cores: Support for a colour centre model of photosensitivity" , *Electronics Letters*, vol. 29, num. 22, pp. 385-387, 1993.
- Barlow A., Payne D. (1983), "The stress-optic effect in optical fibers" , *Journal of Quantum Electronics*, vol. 19, num. 5, pp. 834-839, 1983.
- Bhatia V. (1999), "Applications of long-period gratings to single and multiparameter sensing" , *Optics Express*, vol. 4, pp. 457-466, 1999.
- Bertholds A., Dandliker R. (1988), *J. of Lightwave Technology*, vol. 6, num. 1, pp. 17-20, 1988.
- Bilodeau F., Malo B., Albert J., Johnson D., Hill K., Hibino Y., Abe M., Kawachi M.(1993), "Photosensitization of optical fiber and silica-on-silicon/silica waveguides" , *Optics Letters*, vol. 18, num. 12, pp. 953-955, 1993.
- Bjerkkan L., Hjelme D., Johannessen K. (1996), "Bragg grating sensor demodulation scheme using a semiconductor laser for measuring slamming forces of marine vehicle modes" , *Proceedings of the 11th International Conference on Optical Fiber Sensors*, pp. 236-239, 1996.
- Caucheteur C., Debliquy M., Lahem D., Mégret P. (2008), 'Hydrogen leak optical sensor using radiating fiber gratings', *proceedings IEEE Sensors Conference*, Lecce, Italy, 27/10-29/10, 2008 (2008/08/27) pp 1281-1285. a)
- Caucheteur C., Debliquy M., Lahem D. and Mégret P. (2008), "Catalytic fiber Bragg grating sensor for hydrogen leak detection in air," *IEEE Photon. Technol. Lett.* 20, 96-98 (2008). b)
- Duhem O., Henninot J.-F., Warenghem M., Douay M. (1998), "Demonstration of long-period grating efficient couplings with an external medium of a refractive index higher than that of silica" , *Applied Optics*, vol. 37, pp. 7223-7228, 1998.
- Erdogan T. (1997), "Cladding-mode resonances in short- and long-period fiber grating filters" , *Journal of the Optical Society of America A*, vol. 14, num. 8, pp. 1760-1773, 1997.
- Hand D., Russel P.(1990) ,"Photoinduced refractive-index changes in germanosilicate fibers" , *Optics Letters*, vol. 15, num. 2, pp. 102-104, 1990.
- Hill K., Malo B., Bilodeau F., Johnson D., Albert J. (1993), "Bragg gratings fabricated in monomode photosensitive optical fiber by UV exposure through a phase mask" , *Applied Physics Letters*, vol. 62, pp. 1035-1037, 1993.
- James S., Tatam R. (2003), "Optical fiber long-period grating sensors: characteristics and application" , *Measurement Science and Technology*, vol. 14,pp. R49-R61, 2003.
- Kashyap R., *Fiber Bragg gratings*, Academic Press, 1999.
- Kersey A., Marrone M. (1994), "Fiber Bragg high-magnetic-field probe" , *Proceedings of the 10th International Conference on Optical Fiber Sensors*, pp. 53-56, 1994.
- Kersey A.D., Davis M.A., Patrick H.J., LeBlanc M., Koo K.P., Askins C.G., Putnam M.A., Friebele E. J.(1997) "Fiber Bragg grating sensors", *IEEE Journal of Lightwave Technology* 15, pp 1442-1463, 1997.

- Lee B., Liu Y., Lee S., Choi S., Jang J. (1997), "Displacements of the resonant peaks of a long-period fiber grating induced by a change of ambient refractive index", *Optics Letters*, Vol. 2, pp. 1769-1771, 1997.
- Lemaire P., Atkins R., Mizrahi V., Reed W. (1993), "High pressure H₂ loading as a technique for achieving ultrahigh UV photosensitivity and thermal sensitivity in GeO₂ doped optical fibers", *Electronics Letters*, vol. 29, pp. 1191-1193, 1993.
- Meltz G., Morey W., Glenn W. (1989), "Formation of Bragg gratings in optical fibers by a transverse holographic method", *Optics Letters*, vol. 14, num. 15, pp. 823-825, 1989.
- Morey W., Meltz G., Glenn W. (1989), "Fiber optic Bragg grating sensors", *Proceedings of SPIE*, pp. 98-107, 1989.
- Othonos A., Kalli K. (1999) "*Fiber Bragg gratings: Fundamentals and applications in telecommunications and sensing*", Artech House, Norwood, MA, 1999.
- Okazaki S., Nakagawa H., Asakura S., Tomiuchi Y., Tsuji N., Murayama H., Yashiya M. (2003), "Sensing characteristics of an optical fiber sensor for hydrogen leak", *Sensors and Actuators B* **93**, pp 142-147, 2003.
- Patrick H., Chang C., Vohra S. (1997), "Long period fiber gratings for structural bend sensing", *Electronics Letters*, vol. 33, pp. 1893-1894, 1997.
- Patrick H., Kersey A., Bucholtz F. (1998), "Analysis of the response of long period fiber gratings to external index of refraction", *Journal of Lightwave Technology*, vol. 16, pp. 1606-1642, 1998.
- Russel P., Hand D. (1991), "Optically-induced creation, transformation and organisation of defects and colour-centres in optical fibers", *Proceedings of the SPIE International Workshop on Photoinduced Self-Organization Effects in Optical Fiber*, pp. 47-54, Quebec City, Canada, 1991.
- Sceats M., Atkins G., Poole S. (1993), "Photo-induced index changes in optical fibers", *Annual Reviews in Material Science*, vol. 23, pp. 381-410, 1993.
- Shima K., Himeno K., Sakai T., Okude S., Wada A. (1997), "A novel temperature-insensitive long-period grating using boron-codoped germanosilicate core-fiber", *Proceedings of the International Conference on Optical Fiber Communications*, pp. 347-348, 1997.
- Theriault S., Hill K., Bilodeau F., Johnson D., Albert J. (1996), "High-g accelerometer based on an in-fiber Bragg grating sensor", *Proceedings of the 11th International Conference on Optical Fiber Sensors*, pp. 196-199, 1996.
- Tsai T., Friebele E., Griscom D. (1993), "Thermal stability of photoinduced gratings and paramagnetic centers in Ge- and Ge/P-doped silica optical fibers", *Optics Letters*, vol. 18, num. 12, pp. 935-937, 1993.
- Vengsarkar A., Lemaire P., Judkins J., Bhatia V., Erdogan T., Sipe J. (1996), "Long-period fiber gratings as band-rejection filters", *Journal of Lightwave Technology*, vol. 14, num. 1, pp. 58-65, 1996.
- Xu M., Geiger H., Dakin J. (1994), "Optical in-fiber grating high pressure sensor", *Electronics Letters*, vol. 29, pp. 398-399, 1994.
- Yariv A., Yeh P. (1983), *Optical waves in crystals: propagation and control of laser radiation*, John Wiley and Sons, 1983.
- Yu F.T.S., Yin S., Yu Y.T.S. (2002), *Fiber Optic Sensors*, Marcel Dekker Inc., USA, 2002.

Fiber Optic Chemical Sensors based on Single-Walled Carbon Nanotubes: Perspectives and Challenges

Marco Consales¹, Antonello Cutolo¹, Michele Penza², Patrizia Aversa²,
Michele Giordano³ and Andrea Cusano¹

¹ *Optoelectronic Division, University of Sannio, Benevento, Italy*

² *Department of Physical Technologies and New Materials, ENEA, Brindisi, Italy*

³ *Institute for Composite and Biomedical Materials, CNR, Portici, Italy*

1. Introduction

Carbon nanotubes (CNTs) have become a highly-studied material class in recent years for numerous applications in nanoscience and nanotechnology due to their outstanding physical and chemical properties. High chemical reactivity, excellent mechanical strength but ultra-light weight, high thermal stability, high electron mobility, rich electronic properties, high aspect ratio, hollow nanostructure, large surface area make CNTs an ideal platform for many nanomaterial micro/nano-systems and process control practical applications. Conceptually, carbon nanotubes are viewed as rolled-up structures at nanoscale into seamless cylinders of single or multiple sheets of graphene to engineering single-walled and coaxial multi-walled carbon nanotubes, respectively. Generally, the diameter of a single nanotube ranges from 1 to 5 nanometers; while the bundles of roped multiple nanotubes have a diameter varying in the range of 5-100 nm. These one-dimensional nanostructured carbon allotropes have been applying to explore their potential in chemical gas sensing and biosensing.

This chapter reviews the development of high performance opto-chemical sensors based on the integration of CNTs with the optical fiber technology. The paper starts with an overview of the CNT amazing features and their exploitation as highly adsorbent nano-scale materials for chemical sensing. The attention is then focused on the operating principle, fabrication and characterization of fiber optic chemo-sensors in the Fabry-Perot type reflectometric configuration, realized by means of the deposition of a thin sensitive layer of single-walled carbon nanotubes (SWCNTs)-based material on the distal end of standard silica optical fibers (SOFs). This is followed by an extensive review of the excellent room temperature sensing capabilities of the realized SWCNT sensors against Volatile Organic Compounds (VOCs) in different environments (air and water). The experimental results here reported reveal that ppm and sub-ppm chemical detection limits, low response times as well as fast and complete recovery of the sensor responses have been obtained in most of the investigated cases. This evidences the great potentialities of the proposed photonic sensors

based on SWCNTs and their feasibility to be successfully employed for practical environmental monitoring applications, both in vapor or liquid phase. Furthermore, the use of SWCNT-based nanocomposites as novel sensitive fiber coatings is proposed to enhance the chemical sensing performance and improve the adhesion of CNTs to the fiber surface. It will also be shown how the typical poor selectivity of SWCNTs-based sensors towards a given chemical specie can be overcome by using standard pattern recognition techniques applied to fiber optic sensor arrays, exploiting both the static and dynamical features of the single sensor responses.

2. Chemical sensors for environmental monitoring

Environmental monitoring is required to protect the public and the environment from toxic contaminants and pathogens that can be released into a variety of media including air, soil, and water. Air pollutants include sulfur dioxide, carbon monoxide, nitrogen dioxide, and VOCs, which originate from sources such as vehicle emissions, power plants, refineries, and industrial and laboratory processes. Soil and water contaminants can be classified as microbiological, radioactive, inorganic, synthetic organic, and VOCs. Pesticide and herbicides are applied directly to plants and soils, and incidental releases of other contaminants can originate from spills, leaking pipes, underground storage tanks, waste dumps, and waste repositories. Some of these contaminants can persist for many years and migrate through large regions of soil until they reach water resources, where they may present an ecological or human-health threat. The current monitoring methods are mainly based on off-site laboratory analyses and are costly and time-consuming. In addition, limitations in sampling and analytical techniques occur (Wilson et al., 1995; Looney and Falta, 2000). For this reason, a need exists for accurate, inexpensive, continuous and long-term monitoring of environmental contaminants using sensors that can be operated on site.

Chemical sensors can be in most cases schematically described as composed of a sensitive part which, interacting with the surrounding environment, collects and concentrate molecules at or within the surface undergoing physical changes, and of an opportune transducer that converts into an interpretable and quantifiable term such modification of the sensing part. The heart of the chemical sensor is the sensitive element which is the interface between transducer and external environment so that the nature, the selectivity and sensitivity of the sensor depends upon these interactive materials. Good materials to use as sensing part should optimize specific interactions with a target analyte or narrow class of analytes, should provide a fast and reversible diffusion of the penetrants, small recovery times and should maintain the physical state so as the geometry over several cycles of use, in order to avoid hysteretic effects, and thus to ensure the reproducibility (Grate & Abram, 1991). Candidate materials for chemical sensors include polymers, organic monolayers, ceramics, metals semiconductors, nanostructured and porous materials (nanomaterials, molecular sieves, sol-gels, aerogels), biomolecules and combination thereof.

The natural step following the selective recognition of an analyte from the sensitive layer is the signal transduction, and thus the choice of an opportune technique to read the physical or chemical changes occurring at the sensing part. Transducing approaches can include mechanical (acoustic wave, micromechanical), electrochemical, optical, thermal, and electronic types. Each has strengths and weaknesses relative to the particular application.

Each transduction principle can be implemented in a variety of configurations, and fabricated by multiple approaches, resulting in many different sensing platforms.

A number of chemical sensors have been developed for environmental monitoring applications, a classification of which can be carried out upon their principal physics and operating mechanisms. The most exploited transduction principles in chemical sensing are the mass change and the resistivity/conductivity change of the sensitive element occurring on exposure to and consequent sorption of molecules of target environmental analytes. The first physical parameter is in many cases measured by the shift in the resonant frequency of an oscillating piezoelectric crystal. Depending on the kind of vibrational wave propagated in the crystal, a mass sensor can be classified as Quartz Crystal Microbalance (QCM) or Surface Acoustic Wave (SAW) sensor (Hartman et al., 1994; Kepley et al., 1992; Penza et al., 2006_a). They typically use a thin polymeric film as sensitive layer (Grate, 2000), however SAW and QCM-based chemical sensors using other sensitive coatings have been proposed (Zhang et al., 2004; Penza et al., 2005_a). Instead, resistivity/conductivity changes are typically detected by conductometric measurement carried out on sensitive materials (mainly semiconducting metal oxides and conjugated polymers) deposited between two electrodes. These sensor technologies carry the name of Metal Oxide Semiconductors (MOS) and Conductive Organic Polymer (COP) sensors (James et al., 2005). During the last two decades, however, a remarkable interest has been also focused on optical transduction principles for the measurement of chemical and biological quantities (Baldini et al., 2006). A large variety of devices based on optical methods have been used in chemical sensing and biosensing including ellipsometry, spectroscopy (luminescence, phosphorescence, fluorescence, Raman), interferometry (white light interferometry, modal interferometry in optical waveguide structures), spectroscopy of guided modes in optical waveguide structures (grating coupler, resonant mirror), and surface plasmon resonance (Wolfbeis, 2004; Zudans et al., 2004; Steinberg et al., 2003; Orellana, 2004; Homola et al., 1999; Mignani et al., 2005; Arregui et al., 2003; Brecht & Gauglitz, 1995; Gauglitz, 1996; Boisdé, 1996). In these sensors a desired quantity is determined by measuring refractive index, absorbance and fluorescence properties of analyte molecules or of a chemo-optical transducing medium. Optical fiber sensors are also very attractive in chemical sensing applications due to some unique characteristics deriving by the use of optical fibers, one of the most outstanding characteristic of which is their ability to transmit light over large distances with low losses allowing a sensor head to be remotely located from the instrumentation. This feature is particularly useful for sensing in harsh environments where hazardous chemicals may be present or extremes in temperature occur. In addition the small size, light weight and high flexibility of fibres allow access to areas that would be otherwise difficult to reach.

Provided the optical power density are within certain limits, fiber optic chemical sensors are much safer in explosive environments compared with sensors involving electrical signals, where a spark may trigger a gas explosion. Optical signals are immune to electrical or magnetic interference from, for examples, power lines and electrical machinery. Furthermore optical fibers have the capability of carrying a huge amount of information, much greater than that carried by electrical wires. Fiber optic sensing is very versatile, since the intensity, wavelength, phase and polarization of light can all be exploited as measurement parameters, and several wavelengths launched in the same fiber in either direction form independent signals. This gives the possibility to monitor several chemicals with the same fiber sensor or even simultaneously monitor unwanted environment

parameter variations which could drastically affect the chemical concentration measurements, such as the temperature or disturbance of the fiber. Multiplexing of fiber optic systems is also relatively easy, allowing expensive source or analysis instrumentation to be shared among a number of sites.

This contribution reviews the integration of carbon nanotubes as advanced sensitive coatings with optical fiber technology for the development of high performance opto-chemical sensors exploitable for several environmental monitoring applications. In particular, the excellent sensing capabilities of the realized photonic chemo-sensors against VOCs and other pollutants in air and water, at room temperature, will be reviewed.

2.1 Carbon nanotubes: advanced materials for chemical sensing

The search for new advanced materials is an important area of contemporary research in numerous disciplines of science. Great attention has been paid in recent years to nanostructured materials of different chemical composition, produced as nanoparticles, nanowires or nanotubes. Similarly, there has already been great interest in their preparation, properties and applications in the literature. As matter of fact, with the development of nano-science and nano-technology, a large number of literatures on one-dimensional nanostructured materials, including tubes, rods, belts, and wires in this area, have been published every year (Huang & Choi, 2007). These materials have their unique structures which are dominated by a wire-like structure whose diameter varies over a broad range from several tens of nanometers to a micrometer. In particular, carbon-based nanostructures exhibit unique properties and morphological flexibility, which renders them inherently multifunctional and compatible with organic and inorganic systems.

Carbon nanotubes (CNTs), discovered by Iijima in 1991 (Iijima, 1991) are at the forefront of the novel nanoscale investigations and nanostructure effects due to their unique electronic, chemical, structural, optical, mechanical and thermal properties depending on their specific hollow nanostructure with surface-arranged carbon atoms organized in rolled one-dimensional seamless tubes (Dresselhaus et al., 2001; Dai, 2002). They are considered as a new form of pure carbon, and can essentially be thought of as layers of graphite rolled-up into a tube to form a cylinder with diameter of few nanometers and length ranging from 1 to 100 microns. To date, CNTs are building blocks considered as the most promising functional nanomaterial for future miniaturized gas nanosensors due to their hollow nanostructure and high specific surface area which provide attractive characteristics for gas sensing applications. In fact, due to their unique morphology, CNTs possess the excellent capability to reversibly adsorb molecules of environmental pollutants undergoing a modulation of their electrical, geometrical and optical properties, such as conductivity, refractive index, thickness etc. CNTs can be distinguished in SWCNTs or multi-walled carbon nanotubes (MWCNTs) depending on whether only one layer or many layers of graphite are concentrically rolled up together, and can behave either as metallic or semiconducting, depending upon their diameter and chirality (the way the hexagons are arranged along the tubule axis) (Terrones, 2003). SWCNTs are a very important variety of carbon nanotube because they exhibit important electrical and sensing properties that are not shared by the MWCNTs variants. The purity of the CNTs affects their sensing performance, thus efficient purification protocols to remove metallic impurities and amorphous carbon particles have been developed as well (Penza et al., 2007_a).

2.2 Chemical sensors based on carbon nanotubes: state of the art

The special geometry of carbon nanotubes and their characteristic of being all surface reacting materials offer great potential applications as chemical sensor devices with excellent sensitivities and fast responses (Riu et al., 2008). Most of the sensors based on CNTs are field effect transistors (FET), since much interest has been focused in the past on the study of the changes in their electrical properties as a consequence of the interaction with gaseous and VOC molecules: many studies have shown that although carbon nanotubes are robust and inert structures, their electrical properties are extremely sensitive to the effects of charge transfer and chemical doping by various molecules. The electronic structures of target molecules near the semiconducting nanotubes cause measurable changes to the nanotubes electrical conductivity. Nanosensors based on changes in electrical conductance are highly sensitive, but they are also limited by factors such as their inability to identify analytes with low adsorption energies, poor diffusion kinetics and poor charge transfer with CNTs (Modi et al., 2003).

Kong et al. (Kong et al., 2000) were probably the first to show that CNTs can be used in chemical sensors since exposing SWCNTs to electron withdrawing (e.g. NO₂) or donating (e.g. NH₃) gaseous molecules dramatically increases or decreases the electrical resistance of SWCNTs in the transistor scheme. In addition CNTs-based sensors demonstrated a fast response and a higher sensitivity than, for example, solid-state sensors at room temperature. More or less in the same period, it was demonstrated that the electrical conductance of SWCNTs could be modified in presence of O₂ (Collins et al., 2000). The effect of the adsorption of several gas compounds in SWCNTs was also described (Sumanasekera et al., 2000), as well as those of water vapor on the electrical resistance of a SWCNT (Zahab et al., 2000). Shortly afterwards, Fujiwara et al. (Fujiwara et al., 2001) studied the N₂ and O₂ adsorption properties of SWCNT bundles and their structures. All these studies opened the door to the development of chemical sensors based on CNTs.

Sensing devices based not only on the changes in the electrical properties of CNTs but also on other principles were proposed. For example, bundles of SWCNTs (Adu et al., 2001) have measured the thermoelectric qualitative response to a variety of gases (He, N₂, H₂, O₂ and NH₃). Sumanasekera et al. (Sumanasekera et al., 2002) created a thermoelectric chemical sensor to measure the easily detectable and reversible thermoelectric power changes of SWCNTs when they are in contact with He, N₂ and H₂. Chopra et al. (Chopra et al., 2003) developed a circular disk resonator coated with SWCNTs using a conductive epoxy, which selectively detects the qualitative presence of several gases (NH₃, CO, Ar, N₂ and O₂) due to changes in the dielectric constant and shifts in the resonant frequency.

Wei et al. (Wei et al., 2003) demonstrated a gas sensor depositing CNT bundles onto a piezoelectric quartz crystal. This sensor detected CO, NO₂, H₂ and N₂ by detecting changes in oscillation frequency and was more effective at higher temperatures (200 °C). Penza et al. (Penza et al., 2004_a) developed SAW and QCM sensor coated with SWCNTs and MWCNTs and used them to detect VOCs such as ethanol, ethylacetate and toluene by measuring the downshift in the resonance frequency of the acoustic transducers.

Carbon nanotubes can be easily functionalized with molecules enabling the specific interaction with target chemicals thus improving the typically low selectivity of CNTs-based devices. In this way, different types of sensors based on molecular recognition interactions can be developed, allowing the development of nanosensors that are highly selective and sensitive. Chen et al. (Chen et al., 2003) used a non-covalent functionalized FET based on

SWCNTs for selectively recognizing target proteins in solution. Azanian et al. (Azamian et al., 2002) immobilized glucose oxidase on SWCNTs and enhanced the catalytic signal by more than one order of magnitude compared to that of an activated macro-carbon electrode. Zhao et al. (Zhao et al., 2002) worked with horseradish peroxidase and Sotiropoulou et al. (Sotiropoulou et al., 2003) worked with enzymes. Barone et al. (Barone et al., 2002) developed a device for β -D-glucose sensing in solution phase. They also showed two distinct mechanisms of signal transduction: fluorescence and charge transfer.

Recently, further interest has also been devoted to the possibility to change the optical and/or geometrical properties of SWCNTs upon adsorption of target analyte molecules, enabling to exploit such materials for the development of opto-chemical sensors for numerous environmental monitoring application, from chemical detection in air and water (Consales et al., 2006_a; Penza et al., 2004_b; Penza et al., 2005_b; Cusano et al., 2006_a; Consales et al., 2007_a) to hydrogen detection at cryogenic temperatures suitable for aerospace applications (Cusano et al., 2006_b). In particular, the possibility of exploiting such materials in conjunction with the optical fiber technology could enable the development of optoelectronic noses and tongues capable of air and water quality monitoring, characterized by ppm and sub-ppm resolutions, good recovery features and fast responses, as it will be seen in section 4 and 5.

3. Opto-chemical sensors in reflectometric configuration

The reflectometric configuration is essentially based on a low finesse and extrinsic Fabry-Perot (FP) interferometer and, as schematically shown in Fig. 1, uses a thin sensitive film deposited at the distal end of a properly cut and prepared SOF to produce a FP cavity. The first mirror is given by the fiber/sensitive layer interface whereas the second one is given by the sensitive layer/external medium interface.

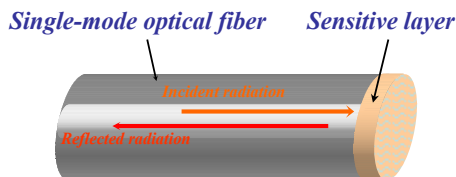


Fig. 1. Schematic view of the Fabry-Perot-based configuration.

First described in 1899 by Fabry and Perot (Fabry & Perot, 1899), the interferometer known by their names makes use of multiple reflections between two closely spaced surfaces. In fact the light is partially reflected each time it reaches the second surface, resulting in multiple offset beams which can interfere with each other. The amount of light reflected at the first interface can be calculated as the sum of the multiple reflected beams and is strongly influenced even by very small changes of the distance between the two surfaces (the sensitive layer thickness) or its optical properties (the sensitive layer refractive index) (Dakin & Culshaw, 1988). This explains the massive use of such configuration in fiber optic-based sensing in the two past decades, especially for the detection and measurements of various physical, chemical and biomedical parameters (Jackson, 1994; Chan et al., 1994). All

these characteristics, combined with the possibility of integrating a number of sensitive materials with the optical fibers by means of very simple, low cost and versatile deposition techniques make it one of the most attractive and useful optoelectronic configuration especially suitable for practical applications.

The principle of operation of an optoelectronic sensor in reflectometric configuration relies thus on the fact that a modulation of the intensity of light reflected at the fiber-sensing overlay interface occurs due to changes in layer thickness (d_{film}) and complex refractive index (\tilde{n}_{film}). As matter of fact the fiber-film reflectance can be expressed as (Macleod, 2001):

$$R = \left| \frac{r_{12} + r_{23} \cdot e^{-i\tilde{k}_{film}}}{1 + r_{12} \cdot r_{23} \cdot e^{-i\tilde{k}_{film}}} \right|^2 \quad (1)$$

with:

$$r_{12} = \frac{n_f - \tilde{n}_{film}}{n_f + \tilde{n}_{film}}; r_{23} = \frac{\tilde{n}_{film} - n_{ext}}{\tilde{n}_{film} + n_{ext}} \quad (2)$$

$$\tilde{k}_{film} = \frac{2\pi \cdot (2 \cdot \tilde{n}_{film} \cdot d_{film})}{\lambda} = \frac{4\pi \cdot n \cdot d_{film}}{\lambda} - i \frac{4\pi \cdot k \cdot d_{film}}{\lambda} = \beta_{film} - i\alpha \cdot d_{film}$$

where $\tilde{n}_{film} = n - i \cdot k$, $\alpha = 4\pi k/\lambda$ is the overlay absorption coefficient, n_f and n_{ext} are the optical fiber and external medium refractive index, and λ is the optical wavelength. Thus, the reflectance changes due to the chemical interaction between sensing overlay and target analyte can be expressed as follows:

$$\Delta R = \left(\frac{\partial R}{\partial n} \right) \cdot \Delta n + \left(\frac{\partial R}{\partial \alpha} \right) \cdot \Delta \alpha + \left(\frac{\partial R}{\partial d_{film}} \right) \cdot \Delta d_{film} = S_n \cdot \Delta n + S_\alpha \cdot \Delta \alpha + S_d \cdot \Delta d_{film} \quad (3)$$

where S_n , S_α and S_d are the sensitivities against the variations of the effective refractive index, the absorption coefficient and the overlay thickness, respectively. They strongly depend upon the geometrical and electro-optical properties of the sensitive nanocoatings and upon the environmental condition (for example vapor or liquid phase), and for this reason they have to be properly considered case by case. In particular, several effects could be involved to promote a reflectance change as a consequence of the analyte molecule adsorption within the sensitive overlay: first of all, swelling of the SWCNT nano-composite overlay that leads to a consequent increase of the film thickness; also, refractive index variations are expected due to the film density variation as expressed by the Lorentz-Lorentz law (Kingery et al., 1976). In addition, according to the plasma optic effect (Wooten, 1972; Soref & Bennet, 1987; Heinrich, 1990) a change either in the real part of the refractive index or in the absorption coefficient could be possible as a consequence of the free carrier concentration change induced by charge transfer mechanisms during analyte sorption. Modifications of film reflectance could be also possible due to optical absorption changes induced by chemical interaction with target analyte. In addition, it is noteworthy that, when very low chemical concentrations are considered (as in this work), it can be assumed that the analyte molecule adsorption occurs at constant overlay thickness ($\Delta d_{film}=0$ in (3)).

3.1 Optoelectronic interrogation system

An important issue to address when dealing with sensors is the design and development of a proper demodulation unit able to provide a continuous interrogation of single or multiple sensor probes by minimizing size, complexity and increasing the cost effectiveness. So far, a variety of schemes have been proposed for the interrogation of a fiber optic sensor based on the FP cavity, the most used ones relying on spectrum-modulating approach and single wavelength reflectometry (Kersey & Dandridge, 2001). Here the attention has been focused on this last technique, which is simple to implement and requires just few widespread commercial and low-cost optoelectronic components while preserving excellent performance. In addition it enables the fabrication of cost-effective, reliable, robust and portable equipments, which are factors of crucial importance for in-situ and long-term monitoring applications and for the desired technology transfer to the market. The typical interrogation scheme enabling the reflectance monitoring of a FP cavity realized on the distal end of an optical fiber is shown in Fig. 2 (Consaes et al., 2007_b).

It basically involves a superluminescent light emitting diode (with central wavelength $\lambda=1310$ nm and a bandwidth of approx. 40 nm), a 2x2 coupler and two photodetectors. It provides an output signal I that is proportional to the fiber-film interface reflectance R and that is insensitive to eventual fluctuations of the optical power levels along the whole measurement chain. As matter of fact, emitted light is splitted by the coupler and directed to the sensing probe (where partial reflection occurs) and to the first photoreceiver, whose output thus consists of an electrical signal (V_{source}) proportional to the power emitted by the source (P_{source}). Reflected light is directed through the coupler to the second photoreceiver which responds with an electrical signal (V_{signal}) proportional to P_{source} and to the overlay reflectance (R). The intensity compensation is obtained by considering the ratio between the voltage signals at the two photoreceivers:

$$I = \frac{V_{signal}}{V_{source}} = \alpha \cdot R \quad (4)$$

where α is a constant accounting for all the set-up parameters. In the followings, the relative change of the sensor output $\Delta I/I_0$ is considered (where I_0 is the output signal in the reference or initial condition), which, in turn, corresponds to the relative reflectance change occurring at the fiber-sensitive layer interface ($\Delta R/R_0$). Synchronous detection is typically implemented to enhance the system performance, by amplitude modulating the light source at 500 Hz and retrieving the photodetector voltages by using a dual channel lock-in amplifier. The minimum $\Delta R/R_0$ that can be detected by means of this interrogation system, calculated considering the maximum scattering on the sensor response in a steady-state level for a time interval of at least 10 minutes, is typically in the range $1\text{-}6 \cdot 10^{-4}$. In addition, a Time Division Multiplexing (TDM) approach is typically exploited to perform the quasi-simultaneous interrogation of up to eight optical probes by means of a fiber optic switch.

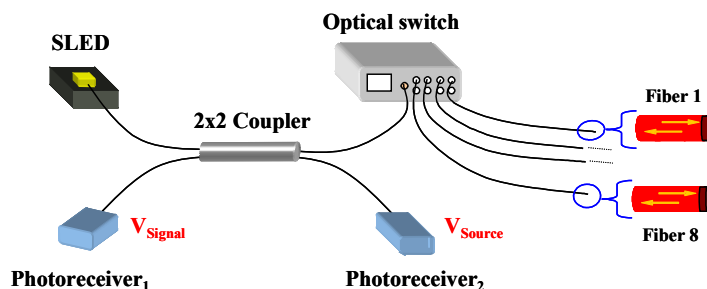


Fig. 2. Schematic illustration of the typical interrogation scheme adopted for the single wavelength reflectance monitoring of an optical cavity realized upon the fiber tip

3.2 Opto-chemical sensor fabrication

The realization of thin films of SWCNTs with a controllable thickness is an important basis for the future development of their scientific understanding and technological applications. Proper manipulation techniques are required for applying thin-films of carbon nanotubes on substrates that do not allow direct grow methods. Although various proposals exist for their incorporation into devices, in single tube or thin film architectures (Bachtold et al., 2001), here the Langmuir Blodgett (LB) technique has been chosen as way to transfer nanometer-scale layers of SWCNTs upon either bare optical fibers or Cadmium Arachidate (CdA) buffer-linker material, previously deposited (by the same technique) upon the fiber end in order to improve the carbon nanotubes adhesion on the sensors surface. The CdA has been chosen as buffer material due to its peculiar amphiphilic molecular structure suitable for LB deposition process (Takamoto et al., 2001; Di Luccio et al., 2004).

The LB-technique is one of the most promising techniques for preparing such thin films as it enables the precise control of the monolayer thickness, homogeneous deposition of the monolayer over large areas and the possibility of making multilayer structures with varying layer composition (Roberts, 1990). An additional advantage of the LB technique is that monolayers can be transferred on almost any kind of solid substrate. However these advantages have to be traded with the low speed of the deposition procedure as well as the limited number of materials suitable for this technique. As represented in Fig. 3, the molecules of the films to deposit are firstly dispersed onto the surface of a sub-phase, typically oriented with the hydrophobic part upwards and with the hydrophilic one immersed in water. Subsequently, a reduction of the surface area occupied by each molecule is performed by means of moving barriers in order to produce a solid phase of a given surface pressure in which the molecules are densely packed forming an highly ordered array (James & Tatam, 2006). From this phase the molecules can be transferred to a properly cleaned and prepared solid substrate by its dipping through the condensed Langmuir layer. As the solid phase is reached only at high surface pressures, a continuous reduction of the moving barriers is performed when the molecules are transferred from the sub-phase to the substrate in order to keep the surface pressure constant, ensuring that the solid phase is maintained. Repeated dipping of the same substrate are also possible, resulting in the deposition of a thin film one monolayer at a time.

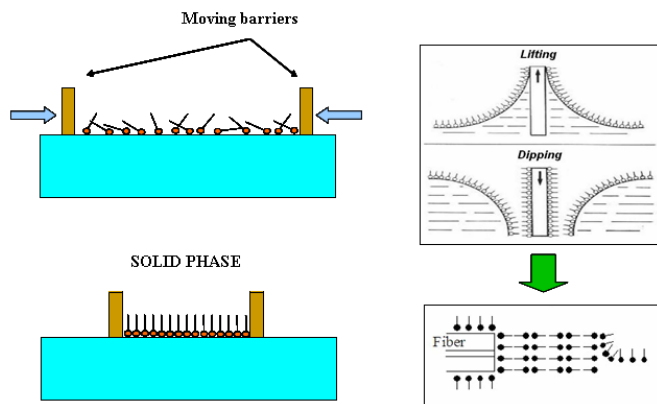


Fig. 3. Schematic representation of the Langmuir-Blodgett deposition procedure.

For CdA buffer multilayer deposition, a solution (0.953 mg/ml) of arachidic acid [$\text{CH}_3(\text{CH}_2)_{18}\text{COOH}$] in chloroform is typically spread onto a sub-phase of deionized water (18 M Ω) containing 10^{-4} M cadmium chloride (CdCl_2). The sub-phase pH is kept constant at a value of 6.0, with the temperature fixed at 23°C. The monolayer is compressed with a barrier rate of 15 mm/min up to a surface pressure of 27 mN/m. The single layer is deposited on the SOF with a vertical dipping rate of 12 mm/min. After a proper drying of 24 hours, the coated fiber is ready for the deposition of the CNT sensing layers.

For SWCNT film deposition, a solution (0.2 mg/ml) of SWCNT pristine material in chloroform is spread onto a sub-phase constituted by deionized water (18 M Ω) with 10^{-4} M of CdCl_2 . The sub-phase pH and the temperature are kept constant at values of 6.0 and 23°C, respectively. The monolayer is compressed with a barrier rate of 15 mm/min up to a surface pressure of 45 mN/m. The single layer is deposited on the SOF surface, either bare or already coated by 20 monolayers of CdA (Penza et al., 2005_b), with a dipping rate of 3 mm/min. After a proper drying of 12 hours overnight, the sensing multilayers deposited are ready for the experimental testing. The raw pristine material of commercial SWCNTs has always been used as-bought, without any purification treatment. The samples are prepared by sonicating SWCNT suspension in chloroform for 1 hour at room temperature prior to the deposition. It is also noteworthy that before the LB deposition procedure the SOFs are previously accurately polished from the acrylic protection and cleaved with a precision cleaver in order to obtain a smooth and plane surface. Then, they are washed in chloroform and dried with gaseous nitrogen to be ready for the deposition. The number of deposited CdA and/or SWCNT monolayers are controlled by choosing how many times the substrate is dipped inside or lifted from the solution containing the monolayer to transfer.

3.3 Structural and morphological characterization of SWCNT overlays

The rational design of a chemical sensor and of its performance is something which is possible only if the sensitive material properties and the way they are affected by different deposition parameters or ambient conditions are well known and understood. To this aim an extensive characterization of the as-bought SWCNT powders as well as of the deposited LB SWCNT films has been carried out in order to investigate their structural and

morphological features. Such characterization involved X-ray diffraction (XRD) and Raman Spectroscopy analyses, High-Resolution Transmission Electron Microscopy (HRTEM) and Scanning Electron Microscopy (SEM) observations. In particular, in Fig. 4.a is reported the typical XRD spectrum of as-bought SWCNT powder (1 mg) material. The pattern exhibits a well-defined graphite-like (002) diffraction peak at $2\theta = 26.5^\circ$, and a broad band centered at lower $2\theta = 22^\circ$ from amorphous carbon or non-nanotube carbon material.

Further XRD analyses performed on CdA multilayers on glass substrates evidenced a CdA monolayer spacing of about 2.8 nm for cadmium arachidate. The same measurements, performed with a SWCNT multilayer, revealed a carbon nanotubes monolayer spacing of about 2.0 nm (Penza et al., 2005_b). Also Raman spectroscopy analyses have been conducted to characterize the fabricated LB films based on SWCNTs already deposited on the SOF tip. To this aim, a Raman microscope functioning in backscattering configuration employing a HeNe laser (633 nm) and 50x and 100x objective lenses was used. The results are shown in Fig. 4.b, where the typical Raman spectrum of a SWCNT film is reported. The characteristic multi-peak feature "G-band" at about 1580 cm^{-1} , corresponding to carbon atoms vibration tangentially with respect to the nanotube walls (Saito et al., 1998), together with the less remarkable disorder-induced "D-band" peak typically in the range $1300\text{--}1400\text{ cm}^{-1}$, representing the degree of defects or dangling bonds, can be easily revealed.

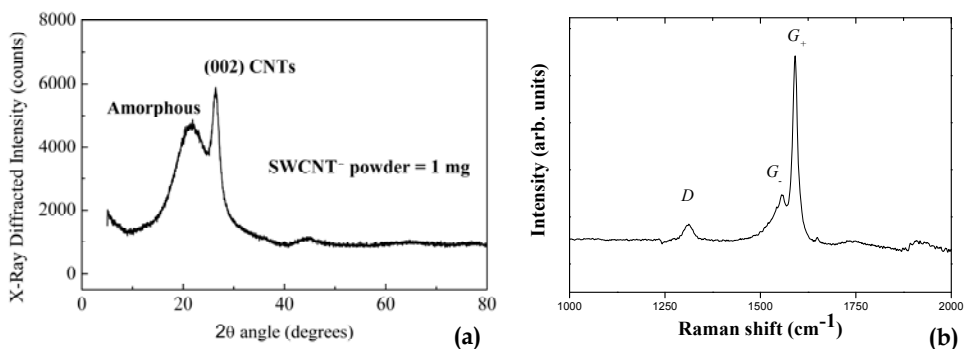


Fig. 4. (a) X-ray diffraction spectrum obtained from HiPco SWCNT powder (1 mg) and (b) typical Raman spectrum of a LB SWCNT film directly deposited on the optical fiber tip.

In particular the observation of the two most intense G peaks (labelled G⁺ and G⁻) confirm the single-walled nature of the carbon tubes while their predominant semiconducting behavior can be derived by the Lorentzian lineshape of the G⁻ feature which, on the contrary, is broadened for metallic SWCNTs (Saito et al., 1998). In addition, the large ratio of G to D peaks give us an indication of an ordered structure of the deposited SWCNT overlay. It is worth noting that, since the Raman studies have been performed on SWCNT film already deposited on the fiber end-face, the results shown also confirm their successful integration with optical fiber technology. The HRTEM images of a SWCNT powder, reported in Fig. 5 at (a) low and (b) high magnification, confirm the nanometric dimension of the carbon tubes and reveal the presence between them of some Fe metal particles, a typical catalyst used in the HiPco production process of carbon nanotubes.

Finally, in Fig. 5.c is reported the typical SEM images of CdA-buffered LB SWCNT films deposited upon a SOF tip. It demonstrates once more the success of the integration of carbon nanotubes with the optical fiber and reveals their attitude to adhere one to each other forming bundles or ropes with a spaghetti-like arrangement.

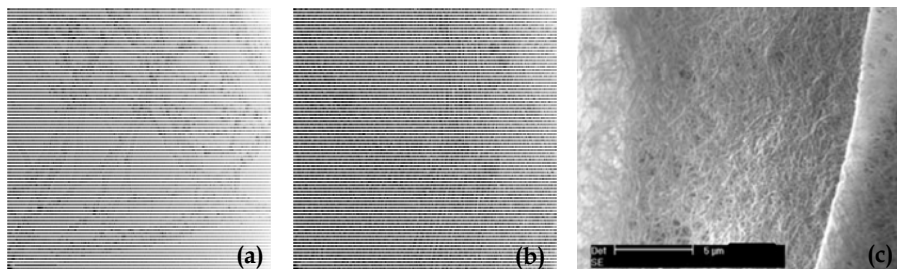


Fig. 5. HRTEM images of SWCNT powder at (a) low and (b) high magnification and (c) SEM images of CdA-buffered SWCNT LB films deposited on a SOF tip.

4. Environmental monitoring applications: Experimental Results

In the following we report the results obtained during the last years of research focused on the development of SWCNTs-based fiber optic chemo-sensors. In particular, we focus our attention on chemical trace detection in air and water, at room temperature. The strong potentiality of this novel SWCNTs-based fiber optic sensing technology to be employed for numerous practical environmental monitoring application is clearly demonstrated.

4.1 Room temperature detection of VOCs in air

The investigation and characterization of the VOC detection performance of SWCNTs-coated opto-chemical sensors has been carried out by means of an experimental setup ad hoc designed and realized, a schematic representation of which is reported in Fig. 6.

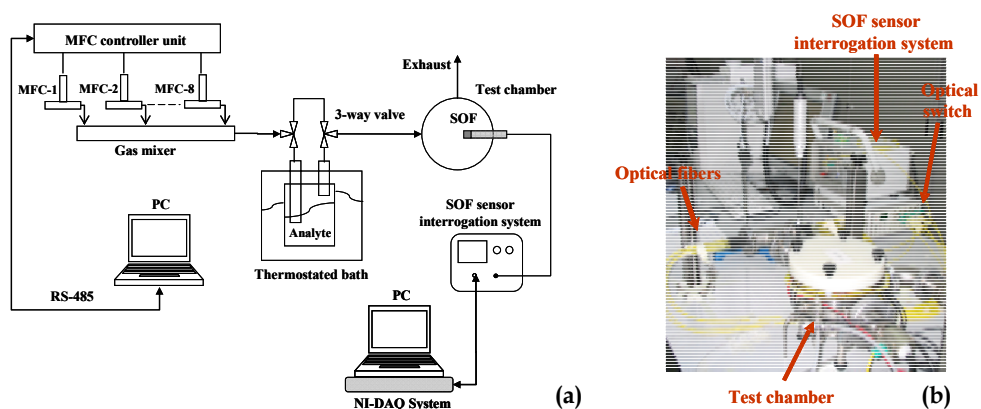


Fig. 6. Experimental setup used for the vapor testing.

In particular the optical fiber probes are located in a properly designed test chamber realized in stainless steel. The volume of the test chamber was 1200 ml, the total flow rate per exposure has been kept constant at 1000 ml/min and the vapors have been generated by the bubbling method. The gas flow rate has been controlled by a mass flow-meter driven by a controller-unit communicating with a PC via standard RS-485 serial bus. The controller unit was able to drive up to eight different gas-channels, and the gas flow rate in each gas-channel was regulated by a dedicated mass flow meter with a full scale of the mass flow ranging from 10 to 1000 ml/min. Numerous tests have been performed by using nitrogen or dry air as reference and carrier gas to transport the generated vapors inside the test ambient: dry air has been chosen because of the higher stability demonstrated by the optical fiber sensor signals. All the experiments have been conducted at room temperature.

The capability of SWCNT overlays of undergoing changes in their complex refractive index and thickness as consequence of the adsorption of target analyte molecules was demonstrated for the first time in 2004 (Penza et al., 2004). In that case LB films consisting of SWCNT bundles were transferred upon the optical fiber tip by using a buffer LB multilayer of CdA pre-deposited on the sensor surface in order to promote the CNT adhesion. The fabricated probes were exploited for the detection of several VOCs, such as isopropanol, methanol, ethanol, toluene and xylene. However, in 2005, multilayers of SWCNTs with different thicknesses were successfully deposited directly upon the optical fiber surface by a modification of the LB process (Consales et al., 2006_b), resulting in an improvement of the sensing performance of the un-buffered configuration with respect to the buffered case, especially in term of sensor sensitivity. As an example, Fig. 7 shows the highest $\Delta R/R_0$ exhibited by a fiber optic probe coated with 4 SWCNT monolayers (namely SOF-4) when exposed to 30-minutes decreasing concentration pulses of xylene vapors with respect to the counterpart optoelectronic sensor arranged in the CdA buffered configuration (2 monolayers of SWCNTs deposited onto 20 monolayers of CdA). In both cases, significant reflectance changes occurred on analyte exposure as consequence of the variation in the SWCNT overlay refractive index promoted by toluene molecules adsorption.

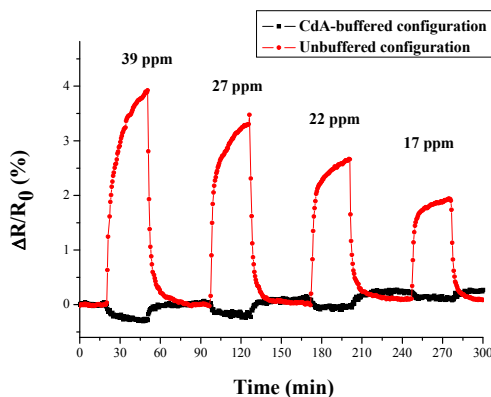


Fig. 7. $\Delta R/R_0$ occurred on xylene vapor exposure to CdA-buffered and un-buffered SWCNTs-based opto-chemical sensors, at room temperature.

Both sensors exhibited the capability of detecting the chemical under investigation at ppm traces combined with fast response, complete reversibility (enabling the reuse of the sensor after a given measurement) and a marked response time dependence on analyte concentration. However the sensor SOF-4 provided response changes more than one order of magnitude higher than the ones provided by the counterpart probe in the CdA-buffered configuration. In light of this results, strong interest was devoted to the investigation of the sensing capabilities of SWCNTs-based opto-chemical sensors arranged in the un-buffered configuration against several VOCs.

In Fig. 8.a are reported the results of toluene vapor testing carried out by exposing the probe SOF-4 to four toluene pulses with concentration in the range 54-93 ppm. The results obtained confirmed the behavior of the fiber optic sensor exhibited during xylene testing: as matter of fact, also in this case a $\Delta R/R_0$ increase on exposure was observed as consequence of analyte molecule adsorption. A less pronounced dependence of the response time on toluene concentration was noticed, revealing that different adsorption dynamics occur depending on the VOC under investigation. Also, a slight drift in the signal baseline can be recognized, due to little thermal changes in the not perfectly thermo-stated test chamber.

In order to investigate the reliability of the proposed transducers, a repeatability test has been carried out for the same fiber optic sensor. The results are shown in Fig. 8.b, where the $\Delta R/R_0$ occurred as consequence of two xylene exposures at 21 ppm are reported. As evident, the opto-chemical probe demonstrated high repeatability and reliability also at very low analyte concentrations.

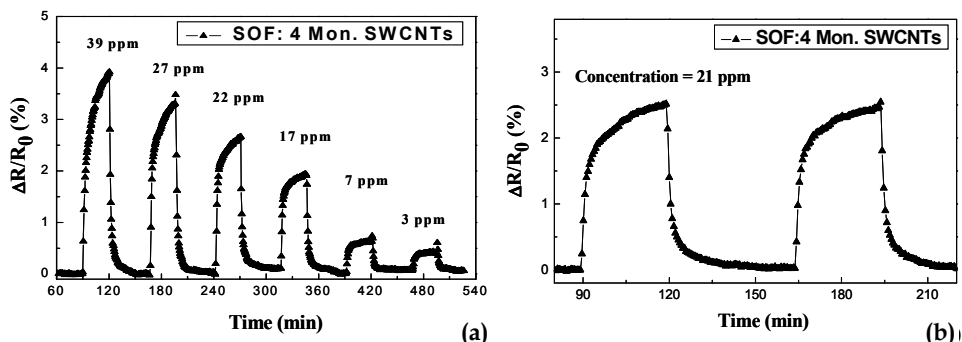


Fig. 8. (a) Response of sensor SOF-4 to toluene vapors at room temperature and (b) repeatability test performed exposing the same sensor to 2 pulses of xylene vapors (21 ppm).

These results have to be considered at constant temperature, because no thermal variation occurred meanwhile. However it is evident that monitoring of thermal drifts and compensation of their effects on sensor response are strictly required to not affect the system performance. Temperature monitoring could be implemented by means of proper fiber bragg grating temperature sensors, which could be either separately inserted within the test ambient or integrated with the optical fiber probe (Cusano et al., 2004). Similarly, CNTs-based fiber optic chemo-sensors demonstrated a relevant sensitivity also to humidity changes (Consales et al., 2006_b), thus revealing the necessity of proper calibrations and compensations of the sensor response, especially when high accuracy is requested.

In Fig. 9 have been reported the calibration curves of sensor SOF-4 obtained against toluene and xylene vapors, which revealed an almost linear behavior in the investigated concentration ranges. In addition, by comparing sensor sensitivities to both analytes, calculated as relative reflectance change upon concentration unit ($S_{analyte}=(\Delta R/R_0)/C$) (D'Amico & Di Natale, 2001) a SOF sensitivity to xylene ($S_{xylene}=1.1 \cdot 10^{-3} \text{ ppm}^{-1}$) more than two times higher than that to toluene ($S_{toluene}=4.7 \cdot 10^{-4} \text{ ppm}^{-1}$) has been found. Considering the minimum $\Delta R/R_0$ achievable with the exploited interrogation unit, a resolution of approx. 290 ppb and 120 ppb have been estimated for toluene and xylene, respectively.

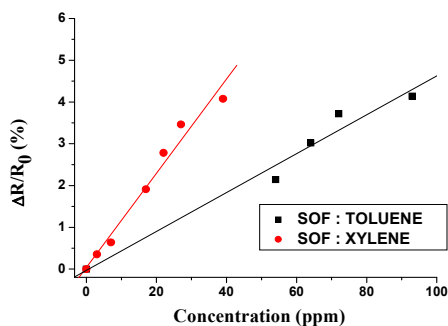


Fig. 9. Calibration curves of sensor SOF-4, exposed to toluene and xylene vapors.

This excellent resolutions are more than three orders of magnitude higher than that obtained by means of a fluorosiloxane polymer-based Surface Plasmon Resonance (SPR) optical fiber sensor (900 ppm and 190 ppm, respectively for toluene and xylene) (Abdelghani & Jaffrezic-Renault, 2001), and more than two orders of magnitude higher than that provided by a multimodal optical fiber sensor sensitized by phenyl-modified porous silica (100 ppm and 20 ppm, respectively) (Abdelmalek et al., 1999).

4.1.1 Influence of monolayers number and CdA buffer on sensor sensitivity

Here, the influence of the number of SWCNT monolayers on the sensor performance are discussed. The differences between the sensing capability of buffered and un-buffered configurations are also better discussed. To this aim, four opto-chemical sensors coated by different numbers of monolayers, directly deposited on bare substrates and also buffered by 20 LB monolayers of CdA, have been simultaneously exposed to toluene and xylene vapors. Fig. 10.a reports the $\Delta R/R_0$ versus toluene concentration for all the tested sensors. It can be seen that a sensitivity increase has been obtained by passing from 2 ($0.9 \cdot 10^{-4} \text{ ppm}^{-1}$) to 4 SWCNT monolayers ($4.7 \cdot 10^{-4} \text{ ppm}^{-1}$). On the contrary, the optical chemo-sensor coated by a higher number of monolayers (12), and thus by a thicker SWCNT film, exhibited a negative sensitivity ($-0.7 \cdot 10^{-4} \text{ ppm}^{-1}$). This means that for this sensor the fiber-film interface reflectance decreases on exposure. This is due to the fact that the film reflectance, and thus also the sensor sensitivity, is strongly dependent on the thickness and refractive index of the CNT overlay, in accordance with (1). As a matter of the fact, depending on the geometric features of the film deposited atop the optical fiber, either positive or negative sensitivities to a target analyte can be obtained.

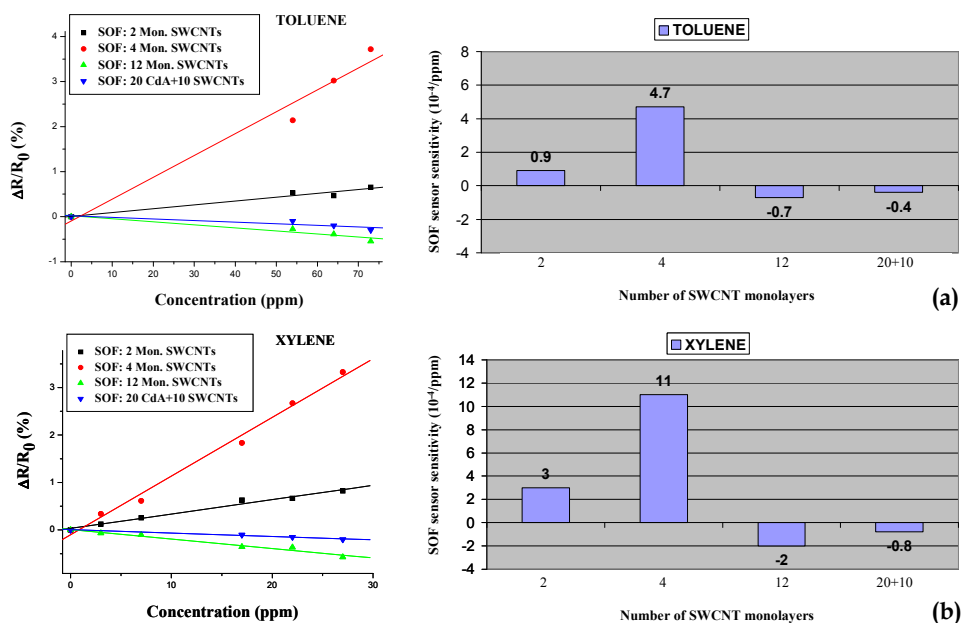


Fig. 10. Calibration curves and sensitivities obtained by exposing four fiber optic sensors coated by a different number of SWCNT monolayers to (a) toluene and (b) xylene vapors.

For the same reason, the CdA buffer multilayer, whose optical properties are quite similar to those of the standard optical fibers, and thus not optimized for the particular configuration exploited, dramatically decreases the sensitivity of optical fiber sensors ($-0.4 \cdot 10^{-4}$ ppm $^{-1}$). It is noteworthy, however, that by choosing a buffer-linker material whose optical and geometrical features (such as the multilayer thickness and refractive index) are well optimized for the specific configuration, one could be able to strongly enhance the SOF sensor performance. From Fig. 10.b it can be seen that the four fiber optic chemo-sensors exhibited the same behaviors also in case of xylene vapor testing: hence, it demonstrates that the inversion of the optoelectronic sensor sensitivities is not due to the particular analyte tested, but to the optical configuration exploited. This feature could be very useful for pattern recognition analysis in case of multi-transducer approaches, where complementary sensors are exploited to improve the analyte discrimination (Penza et al., 2005_b).

4.1.2 Response and recovery time analysis

As the experimental results revealed a dependence of sensor response times (and as consequence of the adsorption/desorption dynamics) on analyte concentration, a detailed analysis of response and recovery times of sensor SOF-4 has been performed (Consales et al., 2007_b) by its exposure to different concentration pulses of toluene and xylene vapors (the exposure time was 30 minutes). The response (recovery) time has been calculated as the time the output signal needed to pass from 10% to 90% (from 90% to 10%) of the total signal variation. The results obtained for both chemicals are quite similar and revealed the attitude

of response time to increases with analyte concentration while the recovery time is quite constant. In particular, the minimum response time in case of toluene, obtained for 54 ppm, was approx. 7 minutes while the maximum one, obtained for 93 ppm, was approx. 11 minutes. The recovery time was as low as approx. 5 minutes. Slower responses were observed in case of xylene exposure, for which the SOF response times increased from approx. 4 minutes (3 ppm) to approx. 18 minutes (39 ppm), and the recovery time was approx. 6 minutes. This could be ascribed to a different adsorption kinetic of the two analyte molecules inside the CNT sensitive nanocoatings. It is noteworthy, however, that the response times of the proposed fiber optic chemo-sensors are relatively good taking into account the volume of the test chamber and the total flow rate per exposure. It is also important noting that although these times could be reduced by depositing a lower amount of carbon nanotubes on the SOF tip, the choice of the geometric features of the sensitive overlay has to be made by considering the trade-off that exists between sensor sensitivity and response (and recovery) time (Consales et al., 2007_b).

4.2 Towards fiber optic tongue: chemical trace detection in water

In this section the attention has been focused on the feasibility of exploiting the excellent sensing properties of CNTs for the development of high performance optoelectronic sensors capable of chemical trace detection in aqueous environments, at room temperature.

A schematic view of the experimental setup exploited for chemical trace detection in water is reported in Fig. 11.a. The SWCNTs-based opto-chemical transducers have been inserted in a beaker containing pure water. The presence within the test ambient of the analyte under investigation has been promoted by its injection inside the beaker. The injected volume has been chosen, each time, in order to obtain the desired analyte concentration. The polluted water has been continuously stirred to ensure maximum dispersion of analyte. In addition, after each exposure, the capabilities of SOF sensors to recover the initial steady state level have been investigated by restoring the initial condition of pure water: pure water has been continuously injected in the test chamber, while the contaminated water, previously present in it, contemporarily stilled out.

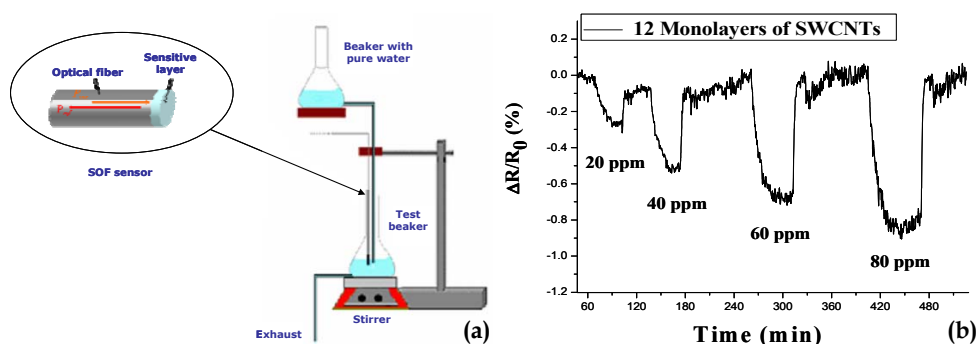


Fig. 11. (a) Experimental setup exploited for chemical trace detection in water and (b) $\Delta R/R_0$ occurred to the sensor SOF-12 on toluene injections, at room temperature.

The results obtained exposing a SOF sensor coated by 12 monolayers of SWCNTs (SOF-12) to several injections of toluene in water, with concentrations in the range 20-80ppm (calculated as $\mu\text{l/l}$), are shown in Fig. 11.b. They revealed a sensitivity in air higher (approx. $1.5 \cdot 10^{-4} \text{ ppm}^{-1}$) than that obtained in case of water environment (approx. $1.2 \cdot 10^{-4} \text{ ppm}^{-1}$). The differences can be ascribed to the dependence of the reflectance upon the surrounding refractive index combined to different adsorption characteristics occurring in liquid environment, especially if the kinetic is diffusion limited.

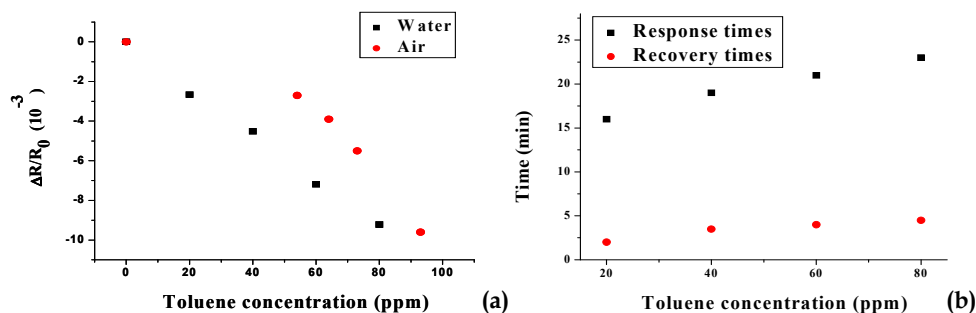


Fig. 12. (a) Calibration curves of sensor SOF-12 against toluene in air and aqueous environments and (b) characteristic times of the same sensor on toluene exposure in water.

Taking into account the sensitivity of the sensor against toluene and considering the $\Delta R/R_{0min}$ ($6 \cdot 10^{-4}$) obtainable with the exploited instrumentation, a resolution of 5 ppm has been estimated. Finally, an analysis of the response (t_{10-90}) and recovery (t_{10-90}) times of the optical probes has been carried out. The results obtained for the detection in water are shown in Fig. 12.b and reveal characteristic times slightly dependent on analyte concentration, with the mean response time (approx. 20 min.) higher than the mean recovery one (approx. 4 min.). A clear difference has been found with respect to the characteristic times obtained in case of in air detection, where the same sensor exhibited mean response and recovery times (towards toluene) of approx. 8 and 28 min., respectively.

4.3 Discussion

Here, a brief discussion concerning some of the typical drawbacks arising from the use of carbon nanotubes as sensitive elements of reflectometric optical fiber sensors is carried out, which evidences some currently unsolved matters, but, at the same time, opens the way to further investigations and research activities. First of all, the attitude of SWCNTs to randomly distribute in tangled networks of nanotubular chains and densely aggregate mats causes a not very high repeatability of the distribution of carbon nanotubes upon the sensor surface as well as their optical properties. These drawbacks could be overcome by means of an alignment of the carbon nanotubes onto the sensor substrate, which should provide a better and almost predictable SWCNT distribution upon them (Yoo et al., 2005).

The adhesion of the carbon nanotubes to the fiber substrate also requires further investigations and improvements, especially when the SWCNTs-based sensors are exploited for in water chemical detection applications, for which particularly hard operating conditions could even promote a detachment of the sensitive overlay from the optical fiber

tip. A first attempt to improve the adhesion of SWCNT overlays to the distal end of the optical fibers is reported in the next section and relies on their embedding in CdA host-matrix in order to obtain nanocomposites with tailored amount of nanotube filler contents. Finally, another issue to address is related to the poor selectivity of the proposed SWCNTs-based sensors towards a given chemical specie. This means that in case of a multicomponent gas mixture with interfering analytes, the information provided by the sensors could be ambiguous and no straightforward information about the test environment could be achieved. This is a very common aspect in chemical sensing applications as demonstrated by the strong effort which is currently devoted by the researchers on how to improve the sensor discrimination ability among different analytes. Basically, there are two possible approaches in the attempt to increase the chemical sensor selectivity, and both have to be followed in synergy. The first one is a direct approach which relies on the sensitive layer functionalization in order to have an higher affinity of the material towards specific chemical species (Balasubramanian & Burghard, 2005). The second one is based on the use of a hybrid system composed of multiple transducers coated by the same material (or, in the most general case, by different materials) in the form of an array. Here, sensors with a poor selective response, when considered collectively, provide unique patterns typical for each analyte. The generated response patterns are interpreted by pattern-recognition algorithm for the selective detection (Zarcomb & Stretter, 1984). Section 5 is focused on this last approach: in particular it will be shown that the use of standard pattern recognition techniques, such as the Principal Component Analysis (PCA), applied on both the static and dynamic responses of the single sensor of a fiber optic sensor array enables to significantly enhance the discrimination ability of the SWCNTs-based optoelectronic sensors.

5. SWCNTs-based nanocomposites as advanced nano-coatings

As already discussed in section 4.3, the adhesion of carbon nanotubes to the fiber substrate and the poor repeatability of the deposition process (especially concerning the distribution of the tubes upon the fiber tip as well as the optical properties of the fabricated layer) represent two important issues to improve for an extensive exploitation of the proposed SWCNTs-based opto-chemical sensors for practical applications and for their effective transfer to the market. The alignment of carbon nanotubes upon the sensor substrate as well as the embedding of controlled quantity of them inside a host-matrix of a foreign material for the synthesis of nanocomposites with tailored amount of nanotube filler contents have been identified as possible ways to overcome these drawbacks. In fact, the CdA was used in the past as buffer-linker material to promote the adhesion of SWCNT thin films to the fiber end-face. Here the attention has been focused on the latter solution. In particular, the sensing performance of fiber optic chemo-sensors based on nanocomposite overlays of SWCNTs embedded in a CdA matrix have been investigated against several chemicals both in gaseous (hydrocarbons, alcohols and NO₂) and liquid phase (toluene and xylene), at room temperature.

5.1 CdA/SWCNTs-based sensors fabrication and characterization

The Langmuir-Blodgett deposition process has been exploited again as a way to transfer thin films of SWCNTs-based nanocomposites upon the distal end of properly prepared single-mode optical fibers. The CdA has been chosen as host-matrix material to incorporate

the SWCNTs in the nanocomposite due to its peculiar amphiphilic molecular structure suitable for LB deposition process and because of the know-how already experienced by the authors in the integration of such material and the optical fiber transducers (Penza et al., 2005_b; Cusano et al., 2006_b). Two separate solutions of arachidic acid in chloroform and SWCNTs in chloroform have been mixed in order to prepare a final solution of chloroform with arachidic acid (0.25 mg/ml) and SWCNTs (0.19 mg/ml). The concentrations and the volumes of the initial solutions were chosen to obtain a weight percentage of the filler component (SWCNTs) with respect to the matrix-component (CdA) of approximately 75 wt. %. However, different concentrations of arachidic acid and SWCNTs in the final solution could also be exploited for the preparation of composites with different weight percentages. The mixed solution was then accurately dispersed and stirred in an ultrasonic bath for 1 h. Subsequently, 160 μ l of the mixed solution were spread onto a sub-phase constituted by acetate buffer with CdCl₂ 10⁻⁴ M. The pH and the temperature of the sub-phase were kept constant at 6.0 and 20° C, respectively. The monolayer of the nanocomposite was compressed with a barrier rate of 15 mm/min up to a surface pressure of 27 mN/m. The single composite monolayer was deposited upon the fiber surface with a dipping rate of 14 mm/min. The optical fibers used for the deposition have been previously accurately polished from the acrylic protection and cleaved with a precision cleaver. Then, they have been washed in chloroform remove any residual coating. Repeated dipping of the fiber substrates through the condensed Langmuir layer have been performed, resulting in the deposition of multilayered CdA/SWCNT films one monolayer at a time. Fig. 13 shows the typical SEM photograms, at (a) low and (b) high magnification, of a multilayer constituted by 20 monolayers of CdA/SWCNT nanocomposite at 27 wt. % (deposited upon a glass substrate). The typical bundle disposition of the carbon nanotubes together with their good cadmium arachidate-assisted adhesion to the surface can be easily observed. A detailed morphological and structural characterization of the carbon nanotubes-based composites deposited by the LB method has been carried out by Penza et al. (Penza et al., 2006_b). Instead, here, the results of Raman spectroscopy analysis are reported, conducted with the aim of characterizing the fabricated nanolayers of CdA/SWCNTs (already deposited on the optical fiber tip) and compare them with the standard SWCNTs one. To achieve this purpose, a Raman microscope functioning in backscattering configuration employing a HeNe laser (633 nm) and 50x and 100x objective lenses was used.

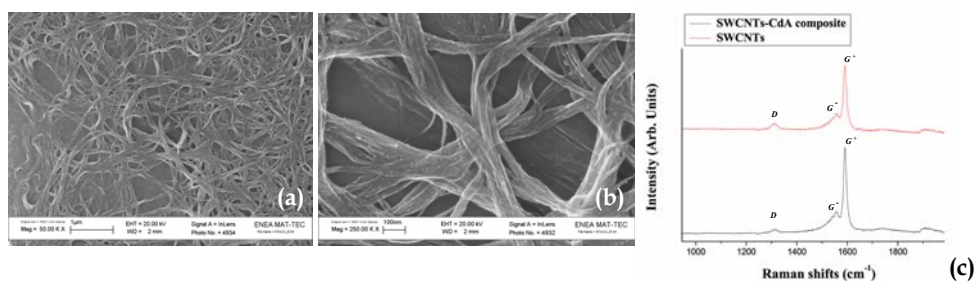


Fig. 13. SEM image of a CdA/SWCNT overlay with a filler content percentage of 27 wt.%, at (a) high and (b) low magnification, deposited upon a glass substrate; (c) Raman spectra of SWCNT and CdA/SWCNT LB overlays directly deposited on the optical fiber end-face.

The results are shown in Fig. 13.c, where the typical Raman spectra of SWCNTs and CNT-based composite layers, already deposited upon the fiber end-face, have been reported. No significant differences between the two recorded spectra can be observed, thus evidencing that no degradation of the CNT occurred due to their inclusion within the CdA matrix.

5.2 VOC detection in air at room temperature

The room temperature sensing performance of the fabricated probes have been investigated both in air and water environments and have been compared with those obtained with the same transducers coated by un-buffered SWCNT overlays. Here the attention is focused on trace detection of four VOCs (toluene, xylene, ethanol and isopropanol) and one gas (NO_2) by using a sample coated by 10 monolayers of nanotubes-based composite with a SWCNT filler weight percentage of approximately 25 wt.%. The results are shown in Fig. 14, where, in particular, the $\Delta R/R_0$ occurred on exposure to toluene and ethanol vapors have been reported. The analyte adsorption within the SWCNTs-based nanocomposite overlay was able to induce a significant increase of the fiber-film reflectance as consequence of the complex refractive index change in the FP sensing cavity. The experimental data clearly reveal the capability to detect very low concentrations of the tested pollutants at ppm levels, as well as its quite good attitude to recover the initial baseline signal upon the complete analyte molecule desorption. This feature is of great importance for chemical sensing since it enables the sensor to be easily and quickly reused after a given measurement, avoiding ad hoc cleaning procedures, that are costly and time-consuming. In particular, the sensor exhibited a complete and fast reversibility of the response in case of toluene exposure, however this is not the case of ethanol test for which the reference signal corresponding to the condition of uncontaminated ambient is not fully recovered. This behavior was also observed on isopropanol exposure and could be attributed to the higher polarity of this kind of chemical species (alcohols). Different xylene and ethanol sensitivities have been measured for the CdA/SWCNTs-based fiber probe (approx. $1.3 \cdot 10^{-3} \text{ppm}^{-1}$ and approx. $5 \cdot 10^{-4} \text{ppm}^{-1}$, respectively). In addition, the different response dynamic can be attributed mainly to the different diffusivities of toluene and ethanol molecules within the nanocomposite overlay.

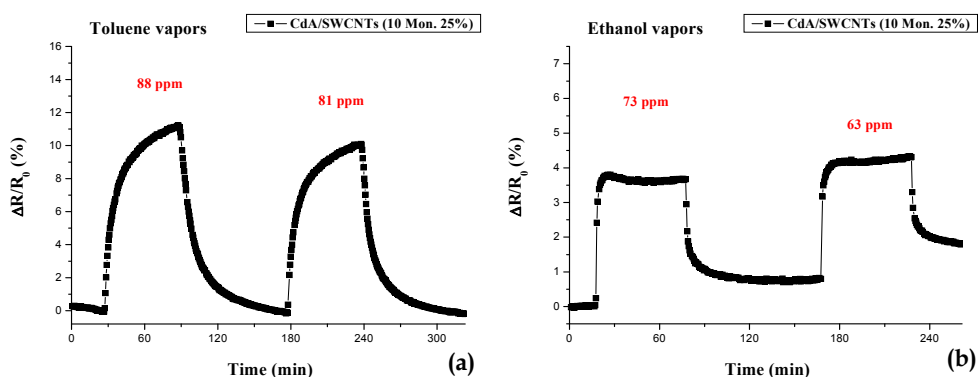


Fig. 14. Time response of the photonic sensor coated by 10 monolayers of CdA/SWCNT nanocomposite (25 wt. %) to (a) toluene and (b) ethanol vapors, at room temperature.

Fig. 15.a reports the response of the same CdA/SWCNTs-based sensor to five NO_2 pulses with concentrations in the range 1-10 ppm. Also in this case the sensor turned out to be capable of detecting very small traces of the gas under test and, similarly to what observed for alcohol detection, a baseline shift occurred upon multiple exposures of NO_2 . However, in this case the drift is thought to be mainly caused by the fact that the time extent between two successive NO_2 exposures is not sufficiently high to let the sensor to completely recover its initial baseline. This is demonstrated by the fact that after the last exposure the baseline value is similar to the one recorded before the first exposure. Combined with this effect, a slight drift of the baseline intensity is also present, that could be attributed to a strongest interaction between NO_2 and CdA/SWCNT overlay. Also a chemical modification of the overlay could be possible. In both cases, a modification of the nanocomposite refractive index is expected. The same can be said for the case of ethanol adsorption. It is also worth noting that for NO_2 detection the fiber optic transducer exhibited a $\Delta R/R_0$ of opposite sign with respect to that observed in case of vapor detection. This interesting behavior has been observed also for the fiber optic sensors in the standard configuration (i.e. fiber optic coated by pure SWCNTs), and could be ascribed to the electrical nature of the analyte under investigation, electron donor (vapors) or acceptor (NO_2). In particular it could be due to the influence that the charge transfer induced by the analyte molecule adsorption within the sensitive material has on the optical properties of SWCNTs-based overlay itself. In light of this consideration, the plasma optic effect (Wooten, 1972; Soref & Bennet, 1987; Heinrich, 1990) is also being considered, that allows one to relate the modulation of the optical properties of sensitive overlays (refractive index and absorption coefficient) to the changes in its free carrier concentration. In order to better clarify this aspect, further measurements are currently in progress involving more analytes with varying charge transfer properties as well as transducers with different principles of operation (mainly resistive, capacitive and mass-sensitive) coated by the same SWCNTs-based materials. However, to support our conjecture, preliminary experiments have been conducted with the aim of measuring the electrical response of a SWCNTs-based composite layer upon NO_2 exposure.

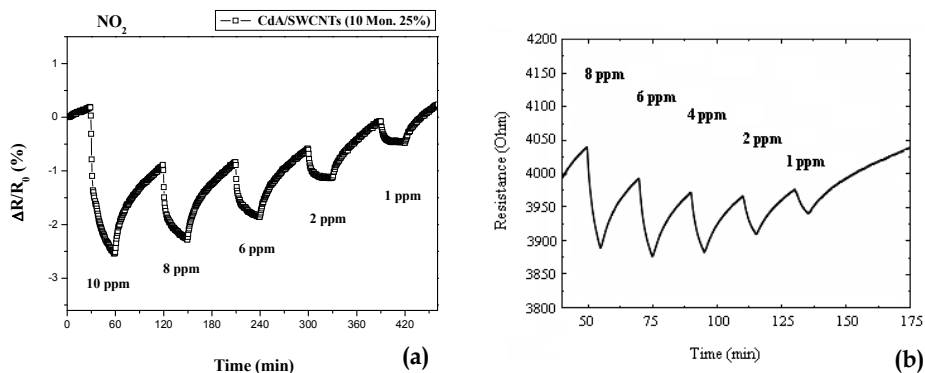


Fig. 15. (a) $\Delta R/R_0$ of the opto-chemical sensor coated by 10 nanocomposite monolayers (25 wt. %) and (b) electrical resistance versus time of a CdA/SWCNT thin film on exposure to different concentrations of gaseous NO_2 , at room temperature.

To this aim, a direct measure of the d.c. electrical conductance of the composite films deposited onto rough alumina (5.0 mm length \times 5.0 mm width \times 0.5 mm thickness) substrates with 200 μm pitch interdigitated Cr/Au (20 nm/200 nm thick) pattern by means of two-pole probe method with an electrometer (Keithley 617) has been carried out.

Fig. 15.b reports the typical time response of the electrical resistance of a LB layer of CdA/SWCNTs composite upon exposure of NO_2 , at room temperature. As expected, it decreases when the composite film is exposed to the oxidizing NO_2 gas. In particular, electron charge transfer occurs from SWCNTs-based composite to NO_2 because of the electron-accepting power of the NO_2 molecules. Thus, the NO_2 gas depletes electrons from the SWCNTs-based composite, increases the concentration of electrical holes in the p-type SWCNTs-based composite, hence causing the electrical resistance to decrease. Even if a partial desorption and an un-reached saturation level can be observed, similarly to the case of optical sensors, however a clear electrical response modulated by the gas adsorption is demonstrated, revealing that a charge transfer effectively occurs between the realized LB SWCNT overlays and the analyte under investigation.

Furthermore, an almost linear behavior in the sensor calibration curves (reported in Fig. 16) has been found towards most of the tested chemicals in the investigated ranges, as well as a higher sensitivities (see Fig. 17.a) in case of exposure to aromatic hydrocarbons ($3.2 \cdot 10^{-3} \text{ ppm}^{-1}$ and $1.3 \cdot 10^{-3} \text{ ppm}^{-1}$ respectively for xylene and toluene) than to alcohols ($5 \cdot 10^{-4} \text{ ppm}^{-1}$ and $4 \cdot 10^{-4} \text{ ppm}^{-1}$ respectively for isopropanol and ethanol). In addition the sensitivity towards NO_2 was of approx. $-1.3 \cdot 10^{-3} \text{ ppm}^{-1}$. By considering the minimum detectable $\Delta R/R_0$ achievable with the exploited interrogation system, resolutions (calculated as $\Delta R/R_{0\text{min}}/C$, where C is the analyte concentration) in the range 30-80 ppb and 200-250 ppb have been estimated respectively for hydrocarbon and alcohol detection, while the minimum concentration of NO_2 that can be detected turned out to be approx. 80 ppb.

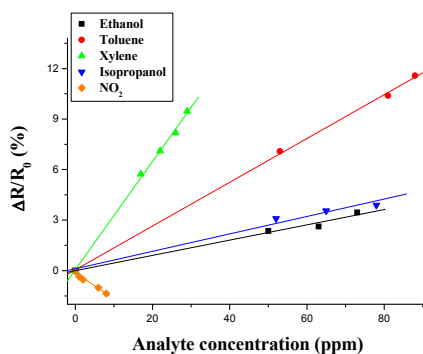


Fig. 16. Sensor characteristic curves obtained for the five tested chemicals.

Moreover, the analysis of the mean response time revealed that the CdA/SWCNT composite-based sensor provides a faster response (see Fig. 17.b) in case of alcohol exposure (8 and 9 minutes, respectively) than in the hydrocarbon one (33 and 31 minutes, respectively). In particular, the ratio between the mean response time in case of toluene and ethanol detection is approx. 3.4, while the one obtained with standard SWCNTs is approx. 15. This means that the presence of the CdA matrix not only slows the sensor response down but also leads to significant differences in the adsorption dynamics of the two

analytes. In addition, since the diffusivity depends upon the exploited SWCNT filler content, it is expected that variations in the SWCNT weight percentage within the CdA matrix could be able promote differences in the sensor response times. In order to investigate this aspect, further experimental measurements will be performed, involving sensors with different wt. percentages of CNTs.

The opto-chemical sensors based on CdA/SWCNTs exhibited quite high response times; this could be mainly due to the fact that the molecules of the target analyte adsorb not only at the side-wall of the carbon nanotubes, but also in the interstitial sites between the tubes (Fujiwara et al., 2001). In particular, in case of film consisting of bundles of SWCNTs, the latter contribution could significantly slow down the sensor response times (Kong et al., 2000). However it is worth noting that these times are comparable with those obtained by means of many sensors based on different transducing principles (conductometric, resonator, mass-sensitive sensors, etc.) but integrating the same sensitive materials (Kong et al., 2000, Chopra et al., 2003, Penza et al., 2005_b, Lucci et al., 2005). Also, it can be attributed to the presence of the CdA matrix and thus to the diffusion rates of analyte molecules inside the CNT composite. It is also important noting that the content of SWCNTs within it can also influence the diffusion times and the sensor sensitivity (as already reported for the electrical case with CdA/SWCNTs-based SAW sensors (Penza et al., 2006_b; Penza et al., 2007_b). These aspects, however, are still under investigation. The bar plots reported in Fig. 17 can be used also to compare the sensing performance of the nanocomposite-based probe with the results obtained with that coated by 10 monolayers of SWCNTs directly deposited atop the fiber end: the use of the novel CdA/SWCNT nanocomposite coatings not only improves the sensor robustness, but also significantly enhances its sensitivity.

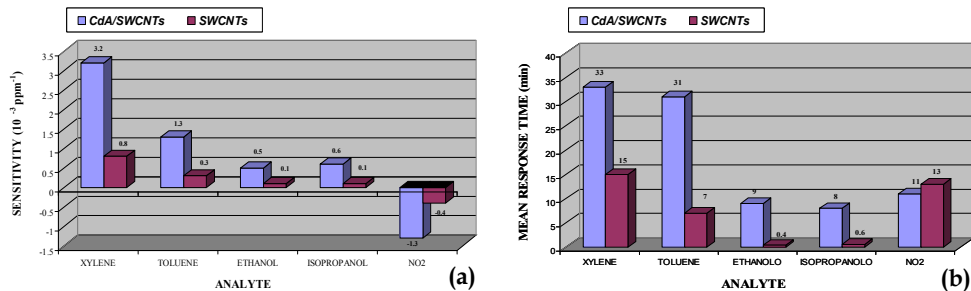


Fig. 17. Comparison between sensitivity and mean response times of the CdA/SWCNTs and SWCNTs based fiber optic sensing configurations obtained for the five tested chemicals.

The bar plots reported in Fig. 17 can be used also to compare the sensing performance of the nanocomposite-based probe with the results obtained with the probe coated by ten monolayers of SWCNTs directly deposited upon the fiber end. It can be clearly observed that the use of the novel CdA/SWCNT nanocomposite coatings not only promotes a better adhesion of the carbon tube to the fiber sensor surface but also significantly enhances the sensitivity of the proposed chemo-optical sensors. As matter of fact, sensor sensitivity from three to seven times higher have been observed for the investigated chemicals with respect to the counterpart optoelectronic sensor directly coated by SWCNTs. However much lower

response times have been obtained in most of the cases, probably due to the fact that the presence of the CdA matrix influences the analyte molecule diffusion times.

5.3 Chemical trace detection in aqueous environments

Once verified their excellent VOC adsorption capabilities in air at room temperature, the sensing characteristics of the CdA/SWCNT nanocomposites have been investigated also for hydrocarbon detection in aqueous environment. To this aim, a fiber optic chemo-sensor coated by 20 monolayers of CdA/SWCNT nanocomposite was exploited for the detection of low concentrations of toluene and xylene in water. In Fig. 18.a have been reported the transient responses of the fiber optic probe as a consequence of several toluene injections with concentrations ranging from 20 to 100 ppm ($\mu\text{l/l}$). Differently from the air case, a significant reflectance decrease occurred on analyte adsorption within the sensing nanolayer. This could be ascribed to the different SWCNTs-filler content used in this case and, as consequence, to a different refractive index of the sensitive overlay as well as to the dependence of the reflectance on the surrounding refractive index (in accordance with (1) and (2)) combined with the different adsorption characteristics occurring in the two environments. In addition, a good repeatability has been observed in the sensor response when exposed to two successive 100 ppm xylene injections.

Similar results were obtained also in case of xylene detection measurements carried out considering the same concentration range. The calibration curves (reporting the sensor output versus the analyte concentration) are shown in Fig. 18.b. They demonstrate that also for the detection in aqueous ambient a linear dependence exists between the fiber-film reflectance change and the concentration of the two organic analytes.

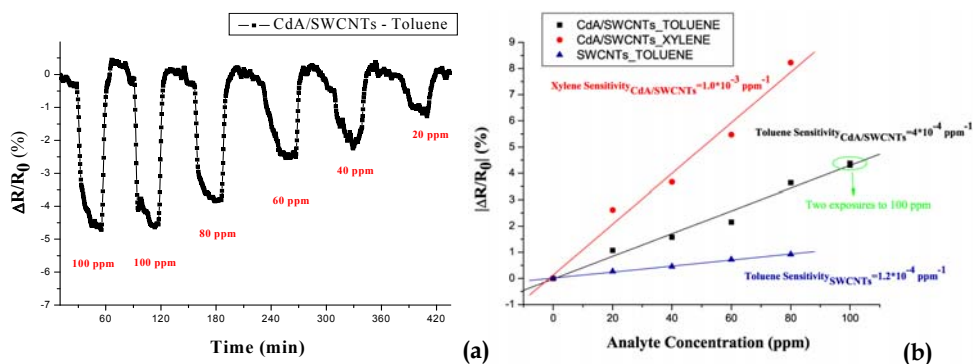


Fig. 18. (a) Time responses of a sensor coated by 20 CdA/SWCNTs monolayers (75 wt. %) to toluene in water and (b) calibration curves obtained in case of toluene and xylene injections.

In addition, the typical higher affinity of carbon nanotubes-based sensors towards xylene (the sensor sensitivity is $1.0 \cdot 10^{-3} \text{ ppm}^{-1}$) than toluene ($4 \cdot 10^{-4} \text{ ppm}^{-1}$) was confirmed. The sensor resolution obtained in this case are respectively of approx. 0.6 and 1.5 ppm. In addition, to compare the performance of the proposed sensor with those obtained with the one coated by a SWCNT layer, the characteristic curves of the standard SWCNTs-based transducers against toluene in water have also been reported in figure 18.b. The results

clearly reveal that a significant enhancement in the sensor sensitivity can be obtained by the use of SWCNTs-based composite ($4 \cdot 10^{-4}$ ppm⁻¹) with respect to the standard carbon nanotube counterpart ($1.2 \cdot 10^{-4}$ ppm⁻¹).

6. Improving the discrimination ability of SWCNTs-based chemo-sensors

As already discussed in section 4.3, one of the major concerns with chemical sensors is how to improve their discrimination ability among different analytes. In fact, we are still far away from having synthetic and tunable materials able to mimic the tremendous molecular recognition capability of the biological receptors such as enzymes.

Between the two possible approaches typically exploited by the researchers (mentioned in section 4.3) our attention has been focused on the use of sensor arrays composed of low-selective elements combined with pattern recognition algorithms. As matter of fact, in the following we will show the results obtained by applying the PCA on the responses of an array composed of optical chemo-sensors coated by different SWCNTs-based overlays. They will reveal the ability of the photonic sensor array to clearly discriminate among different analytes, either in vapor or gaseous phase.

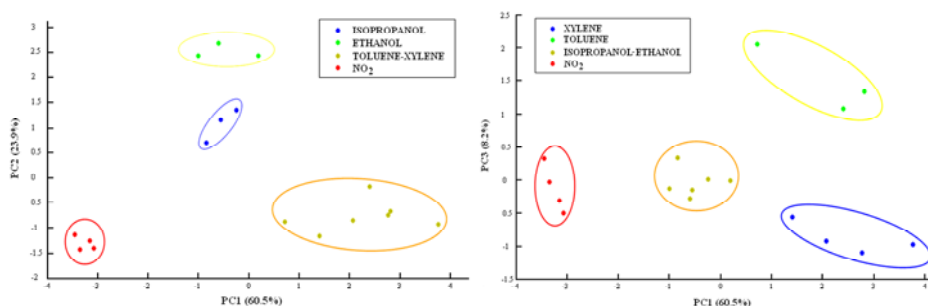
PCA is a powerful, linear, supervised, pattern recognition technique used as a mathematical tool for analyzing, classifying and reducing the dimensionality of numerical datasets in a multivariate problem (Gardner & Bartlett, 1999). It typically decomposes the primary data matrix (made of a given number of measurements or experimental points) by projecting the multi-dimensional dataset onto a new coordinate base formed by the orthogonal directions with data maximum variance. The eigenvectors of the data matrix are called principal components (PCs) and are uncorrelated among them. The PCs are ordered so that PC₁ displays the greatest amount of variance, followed by the next greatest PC₂ and so on. The magnitude of each eigenvector is expressed by its own eigenvalue, which gives a measure of the variance related to that principal component. As a result of the coordinates change, a data dimensionality reduction to the most significant PCs and an elimination of the less important ones can be achieved without considerable information losses. The main features of PCA analysis are the coordinates of the data in the new base (scores plot) and the contribution to each component of the sensors (loads plot). The scores plot is usually used for studying the classification of the data clusters; while the loads plot can be used for giving information on the relative importance of the sensors to each principal component and their mutual correlation. In this PCA study, the array is composed of the two optical chemo-sensors, coated by ten monolayers of standard SWCNTs and CdA/SWCNTs composite (25 wt. %), whose performance against toluene, xylene, ethanol, isopropanol and NO₂ have been analyzed in section 5.1 (and summarized in Fig. 17). In addition, since we noticed a strong influence of the tested analyte specie on the dynamic behavior of the sensor output (for example the responses to ethanol and isopropanol exhibited a marked overshoot as well as a much faster increase, on exposure, than those to alcohols and NO₂) we applied the PCA both on the static and transient parameters of the response curve (as reported in table 1).

Input data of primary matrix are obtained extracting, for each sensor, the parameters P1-P5 by the responses to different exposures of the five analytes. The PCA was applied to a data-matrix composed by 10 columns (2 sensors x 5 parameters P) and 17 rows (17 measurements x all 5 analytes). Data are further processed by the correlation matrix (centered and standardized data to remove inadvertent weighting that arise to arbitrary units).

	Parameter	Description
P1	$\Delta R/R_0$	Relative reflectance change at the equilibrium
P2	$\Delta R/R_{0_Max}$	Maximum relative reflectance change
P3	$\Delta R/R_{0_3\text{ mins.}}$	Relative reflectance change after 3 minutes
P4	t_{10-90}	Response time
P5	t_{max}	Time needed to reach the maximum $\Delta R/R_0$

Table 1. Parameters extracted from the transient response curve

In Fig. 19 are reported the obtained score plots in the PC1-PC2 and PC1-PC3 planes, revealing that the largest part of information has been reduced to the first PC (60.5%), which is also the most important in the discrimination of the clusters. PC2 comprises a lower amount of information (23.9%) while PC3 only the 8.2%, for a cumulative variance of 92.6%. From score plots it can be seen that NO_2 is the most distinguishable analyte (its samples have the longer distance from those of the other analytes); this can be mainly ascribed to the fact that it is the only one for which both elements of fiber optic sensor array exhibited negative reflectance changes. It also turned out that, the score plot in the plane PC1-PC2 enables one to discriminate between NO_2 , ethanol, isopropanol and hydrocarbon in general, since toluene and xylene samples are clustered together. The same occurs for ethanol and isopropanol in the plane PC1-PC3. However, all tested chemicals (either vapors or gas) can be clearly discriminate in the PC1-PC2-PC3 space indicating that this sensor array provides a high discrimination power to these species. This demonstrates that selected features are very powerful for analyte discrimination purposes in the case-study. The results here reported evidence the strong potentiality of the integration of CNTs-based materials with fiber optic technology towards the realization of high-performance SWCNT optoelectronic noses and tongues exploitable for practical environmental monitoring applications.

Fig. 19. PCA score plot of toluene, xylene, ethanol, isopropanol and NO_2 of the data matrix obtained from static and transient responses of CNT-based fiber optic sensors array.

7. Conclusion and future prospects

In conclusion, in this paper the combination of advanced nanostructured coatings based on single-walled carbon nanotubes with the optical fiber technology for the development of high performance opto-chemical sensors has been reviewed. The sensitive material integration has been performed by the customization of the well known molecular engineered Langmuir-Blodgett deposition technique, that has here been used to transfer

ultra-thin layers based on SWCNTs upon the distal end of silica optical fibers. The adopted optical configuration is based on an extrinsic low-finesse Fabry-Perot interferometer, with its principle of operation relying, therefore, on the measurement of the changes in the amount of power reflected at the fiber-film interface occurring as a consequence of the changes in the optical (complex refractive index) and geometrical properties (thickness) of the sensitive elements. Such modifications are, in turn, caused by the interaction of the sensing layers with the target analyte molecules present in the environment.

Since the heart of a chemical sensor is the sensitive layer, from which the main performance of the sensing device derives, a strong effort has been devoted to the investigation of the carbon nanotube overlays features. For this reason, extensive structural and morphological characterizations either of the as-bought SWCNT powders or of the deposited LB SWCNT films have been carried out by means of X-ray diffraction and Raman Spectroscopy analyses, HRTEM and SEM observations. They confirmed the nanostructured dimensions of the exploited class of sensitive material as well as its successful transferring upon the optical fiber surface. The realized chemical sensors have been tested against VOCs and other pollutants either in air or aqueous environments, at room temperature. In most of the investigated cases the fiber optic chemo-sensors coated by SWCNTs demonstrated their strong potentiality as well the ability of detecting environmental pollutants around or well below the ppm threshold. The sensing performance of the proposed opto-chemical probes can be easily tailored by a proper choice of the number of SWCNT monolayers. This choice, however, has to be made by taking account of the trade-off between sensor sensitivity and response time. Furthermore, the use of CdA/SWCNTs-based nanocomposites as novel sensitive nanocoatings has also been presented, revealing their strong potentiality to be successfully employed for chemical sensing both in liquid and gas phase. In addition, preliminary results have been presented demonstrating that it is possible to improve the discrimination ability of SWCNTs-based opto-chemical sensors towards a given chemical specie (thus overcoming their typical poor selectivity) by using standard pattern recognition techniques applied on fiber optic sensor arrays, exploiting both the static and transient features of the single sensor responses.

8. References

- Abdelghani A. and Jaffrezic-Renault N. (2001). SPR fibre sensor sensitized by fluorosiloxane polymers. *Sensors and Actuators B*, 74, 117-123.
- Abdelmalek F., Chovelon J.M., Lacroix M., Jaffrezic-Renault N., Matejec V. (1999). Optical fibre sensors sensitized by phenyl-modified porous silica prepared by sol-gel. *Sensors and Actuators B*, 56, 234-242.
- Adu C.K.W., Sumanasekera G.U., Pradhan B.K., Romero H.E., Eklund P.C.(2001). Carbon nanotubes: A thermoelectric nano-nose. *Chemical Physics Letters*, 337, 31-35.
- Arregui, F. J., Matias I.R., Claus R.O. (2003). Optical Fiber Gas Sensors Based on Hydrophobic Alumina Thin Films Formed by the Electrostatic Self-Assembly Monolayer Process. *IEEE Sensors Journal*. 3, 1, 56-61.
- Azamian B.R. Davis J.J., Coleman K.S., C. Bagshaw C., Green M.L.H. (2002). Bioelectrochemical single-walled carbon nanotubes. *Journal of the American Chemical Society*, 124, 12664.

- Bachtold A., Hadley P., Nakanishi T., Dekker C. (2001). Logic Circuits with Carbon Nanotube Transistors. *Science*, 294, 1317-1320.
- Balasubramanian K. & Burghard M. (2005). Chemically Functionalized Carbon Nanotubes. *Small*, 1, 180-192.
- Baldini F., Chester A.N., Homola J., Martellucci S. (2006). *Optical Chemical Sensors*. NATO Science Series II: Mathematics, Physics and Chemistry, North Atlantic Treaty Organization, Springer, ISBN: 1402046103
- Barone P.W., Baik S., Heller D.A., Strano M.S. (2005). Near-infrared optical sensors based on single-walled carbon nanotubes. *Nature Materials*, 4, 86-92.
- Boisde G. & Harmer A. (1996). *Chemical and Biochemical Sensing with Optical Fibers and Waveguides*. Artech House, Boston, ISBN: 0890067376.
- Brecht A. & Gauglitz G. (1995). Optical probes and transducers. *Biosensors and Bioelectronics* 10, 923-936.
- Chan M. A., Collins S. D., Smith R. L. (1994). A micromachined pressure sensor with fiber-optic interferometric readout. *Sensors and Actuators A*, 43, 1-3, 196-201.
- Chen R.J., Bangsaruntip S., Drouvalakis K.A., Kam N.W.S., Shim M., Li Y., Kim W., Utz P.J., Dai H. (2003). Noncovalent functionalization of carbon nanotubes for highly specific electronic biosensors. *Proc. of the National Academy of Sciences*, 100, 4984-4989.
- Chopra S., McGuire K., Gothard N., Rao A.M., Pham A. (2003). Selective gas detection using a carbon nanotube sensor. *Applied Physics Letters*, 83, 2280.
- Collins P.G., Bradley K., Ishigami M., Zettl A., (2000) .Extreme oxygen sensitivity of electronic. properties of carbon nanotubes. *Science*, 287, 1801-1804.
- Consales M., Campopiano S., Cutolo A., Penza M., Aversa P., Cassano G., Giordano M., Cusano A., (2006_a) .Carbon nanotubes thin films fiber optic and acoustic VOCs sensors: performances analysis. *Sensors and Actuators B*, 118 232-242.
- Consales M., Campopiano S., Cutolo A., Penza M., Aversa P., Cassano G., Giordano M., Cusano A. (2006_b). Sensing properties of buffered and not buffered carbon nanotubes by fibre optic and acoustic sensors", *Measurement Science and Technology*, 17, 1220-1228.
- Consales M., Crescitelli A., Campopiano S., Cutolo A., Penza M., Aversa P., Giordano M., Cusano A., (2007_a) .Chemical Detection in Water by Single-Walled Carbon Nanotubes-based Optical Fiber Sensors. *IEEE Sensors Journals*, 7, 7, 1004-1005.
- Consales M., (2007_b). Carbon Nanotubes Coated Acoustic and Optical VOCs Sensors: Towards the Tailoring of the Sensing Performances. *IEEE Transactions on Nanotechnology*, 6, 601-612.
- Cusano A., Persiano G.V., Russo M., Giordano M. (2004). Novel Optoelectronic Sensing System for Thin Polymer Films Glass Transition Investigation. *IEEE Sensors Journal*, 4, 6, 837-844.
- Cusano A., Pisco M., Consales M., Cutolo A., Giordano M., Penza M., Aversa P., Capodici L., Campopiano S., (2006_a). Novel Optochemical Sensors Based on Hollow Fibers and Single Walled Carbon Nanotubes. *IEEE Photonics Technology Letters*, 18, 22, 2431-2433.
- Cusano A., Consales M., Cutolo A., Penza M., Aversa P., Giordano M., Guemes A. (2006_b) .Optical probes based on optical fibers and single-walled carbon nanotubes for hydrogen detection at cryogenic temperatures. *Applied Physics Letters*, 89, 201106.

- Dai H. (2002). Carbon nanotubes: synthesis, integration, and properties. *Accounts of Chemical Research*, 35, 1035-1044.
- Dakin J. & Culshaw B. (1988). *Optical Fiber Sensors: Principle and Components*. Artech House, Boston, MA, ISBN: 0890063176.
- D'Amico A. & Di Natale C. (2001). A contribution on some basic definitions of sensors properties. *IEEE Sensors Journal*, 1, 3, 183-190.
- Di Luccio T., Antolini F., Aversa P., Scalia G., Tapfer L. (2004). Structural and morphological investigation of Langmuir-Blodgett SWCNT/behenic acid multilayers. *Carbon*, 42, 5-6, 1119-1122.
- Dresselhaus M. S., Dresselhaus G., Avouris Ph., (2001). *Carbon Nanotubes: Synthesis, Structure, Properties, and Applications*. Topics in Applied Physics, Vol. 80, Springer, Berlin, ISBN: 3540410864.
- Fabry C. & Perot A. (1899). Théorie et applications d'une nouvelle méthode de spectroscopie interférentielle. *Annales de Chimie et de Physique*, 16, 115-44
- Fujiwara A., Ishii K., Suematsu H., Kataura H., Maniwa Y., Suzuki S., Achiba Y. (2001). Gas adsorption in the inside and outside of single-walled carbon nanotubes. *Chemical Physics Letters*. 336, 205-211.
- Gauglitz G. (1996). Opto-Chemical and Opto-Immuno Sensors. *Sensor Update*, Vol. 1, VCH, Weinheim.
- Grate J.W. & Abraham M.H. (1991). Solubility interactions and the selection of sorbent coating materials for chemical sensors and sensor arrays. *Sensors and Actuators B*, 3, 85-111.
- Grate J. W. (2000). Acoustic Wave Microsensor Arrays for Vapor Sensing. *Chemical Reviews*, 100, 7, 2627-2648.
- Hartmann J., Auge J. Hauptmann P. (1994). Using the quartz crystal microbalance principles for gas detection with reversible and irreversible sensors. *Sensors and Actuators B*, 19, 1-3, 429-433.
- Heinrich H.K. (1990). Picosecond non invasive optical detection of internal electrical signals in flip-hip-mounted silicon integrated circuits. *IBM Journal of Research and Development*, 34, 162-172.
- Homola J., Yee S. S., Gauglitz G. (2007). Surface plasmon resonance sensors: review. *Sensors and Actuators B*, 54 3-15.
- Huang X.J. & Choi Y.K. (2007). Chemical sensors based on nanostructured materials. *Sensors and Actuators B*, 122, 659-671.
- Iijima S. (1991). Helical microtubules of graphitic carbon. *Nature*, 354, 56-58.
- Jackson D. A. (1994). Recent progress in monomode fibre-optic sensors. *Measurement Science and Technology*, 5, 621-638.
- James D., Scott S.M., Ali Z., O'Hare W.T. (2005). Chemical sensors for electronic nosesystems. *Microchimica Acta*, 149, 1-17.
- James S.W., Tatam R.P. (2006). Fibre optic sensors with nano-structured coatings, *Journal of Optics A.: Pure and Applied Optics*, 8, S430-S444.
- Kersey A.D. & Dandridge A. (1990). Applications of Fiber-optic Sensors. *IEEE Transactions on components, hybrid and manufacturing technology*, 13, 1, 137-143.
- Kingery W.D., Bowen H.K., Uhlmann D.R. (1976). in: *Introduction to Ceramics*, Wiley & Sons, New York.

- Kong J., Franklin N.R., Zhou C., Chapline M.G., Peng S., Cho K., Dai H. (2000). Nanotube molecular wires as chemical sensors. *Science*, 287, 622-625.
- Kepley L.J., Crooks R.M., Ricco A.J. (1992). A selective SAW-based organophosphonate chemical sensor employing a self-assembled, composite monolayer: a new paradigm for sensor design. *Analytical Chemistry*, 64, 3191-3193.
- Looney B.B. & Falta R.W. (2000). *Vadose zone Science and Technology Solutions*. Battelle Press, Columbus, OH.
- Lucci M., Regoliosi P., Reale A., Di Carlo A., Orlanducci S., Tamburri E., Terranova M.L., Lugli P., Di Natale C., D'Amico A., Paolesse R. (2005). Gas sensing using single wall carbon nanotubes ordered with dielectrophoresis. *Sensors and Actuators B*, 111-112, 181-186.
- Macleod H. A. (2001). Thin Film Optical Filters, 3rd Edition. *Institute of Physics Publishing*, Bristol and Philadelphia.
- Mignani A.G., Ciaccheri L., Cimato A., Attilio C., Smith P.R., (2005). Spectral nephelometry for the geographic classification of Italian extra virgin olive oils. *Sensors and Actuators B*, 111-112, 363-369.
- Modi A., Koratkar N., Lass E., Wei B., Ajayan P.M., (2003). Miniaturized gas ionization sensors using carbon nanotubes. *Nature*, 424, 171-174.
- Orellana G. (2004). Luminescent optical sensors. *Analytical and Bioanalytical Chemistry*, 379, 3, 344-346.
- Penza M., Antolini F., Vittori Antisari M. (2004_a). Carbon nanotubes as SAW chemical sensors materials. *Sensors and Actuators B*, 100, 47-59.
- Penza M., Cassano G., Aversa P., Antolini F., Cusano A., Cutolo M., Giordano M., Nicolais L. (2004_b). Alcohol detection using carbon nanotubes acoustic and optical sensors. *Applied Physics Letters*, 85, 12, 2379-2381.
- Penza M., Cassano G., Aversa P., Antolini F., Cusano A., Consales M., Giordano M., Nicolais L. (2005_a). Carbon nanotubes-coated multi-transducing sensors for VOCs detection. *Sensors and Actuators B*, 111-112, 171-180
- Penza M., Cassano G., Aversa P., Cusano A., Cutolo M., Giordano M., Nicolais L. (2005_b). Carbon nanotube acoustic and optical sensors for volatile organic compound detection. *Nanotechnology*, 16, 2536-2547.
- Penza M., Cassano G., Aversa P., Cusano A., Consales M., Giordano M., Nicolais L. (2006_a). Acoustic and Optical VOCs Sensors Incorporating Carbon Nanotubes. *IEEE Sensors Journal*, 6, 4, 867-875.
- Penza M., Tagliente M.A., Aversa P., Cassano G., Capodiecchi L. (2006_b). Single-walled carbon nanotubes nanocomposite microacoustic organic vapor sensors. *Materials Science and Engineering C*, 26, 1165-1170.
- Penza M., Tagliente M.A., Aversa P., Re M., Cassano G. (2007_a). The effect of purification of single-walled carbon nanotube bundles on the alcohol sensitivity of nanocomposite Langmuir-Blodgett films for SAW sensing applications. *Nanotechnology*, 18, 185502.
- Penza M., Aversa P., Cassano G., Wlodarski W., Kalantar-Zadeh K. (2007_b). Layered SAW gas sensor with single-walled carbon nanotube-based nanocomposite coating. *Sensors and Actuators B*, 127, 168-178.
- Riu J., Maroto A., Rius F.X. (2006). Nanosensors in environmental analysis. *Talanta*, 69, 288-301.
- Roberts G. (1990). *Langmuir-Blodgett Films*. Plenum Press, New York ISBN: 0306433168.

- Saito R., Dresselhaus G., Dresselhaus M.S. (1998). *Physical Properties of Carbon Nanotubes*. Imperial College Press, London, ISBN: 1860942237.
- Soref R. & Bennet B.R. (1987). Electrooptical effects in Silicon. *IEEE Journal of Quantum Electronics*, 23, 123-129.
- Sotiropoulou S., Gavalas V., Vamvataki V., Chaniotakis N.A., (2003). Novel carbon materials in biosensor systems. *Biosensors and Bioelectronics*, 18 (2003) 211.
- Steinberg I.M., Lobnik A., Wolfbeis O.S., (2003). Characterisation of an optical sensor membrane based on the metal ion indicator Pyrocatechol Violet. *Sensors and actuators B*, 90, 230-235.
- Sumanasekera G.U., Adu C.K.W., Fang S., Eklund P.C., (2000). Effects of gas adsorption and collisions on electrical transport in single-walled carbon nanotubes. *Physical Review Letters*, 85, 1096-1099.
- Sumanasekera G.U., Pradhan B.K., Romero H.E., Adu C.K.W., Foley H.C., Eklund P.C. (2002). Thermoelectric Chemical Sensors Based on Single-walled Carbon Nanotubes. *Molecular Crystals and Liquid Crystals*, 387, 31-37.
- Takamoto D.Y., Aydil E., Zasadzinski J. A., Ivanova A.T., Schwartz D.K., Yang T., Cremer P.S. (2001). Stable Ordering in Langmuir-Blodgett Films. *Science*, 293, 5533, 1292-1295.
- Terrones M. (2003). Science and technology of the twenty-first century: Synthesis, Properties, and Applications of Carbon Nanotubes. *Annual Review of Materials Research*, 33, 419-501.
- Wei B.Y., Lin C.S., Lin H.M. (2003). Examining the Gas-Sensing Behaviors of Carbon Nanotubes Using a Piezoelectric Quartz Crystal Microbalance. *Sensors and Materials*, 15, 177-190.
- Wilson L.G., Everett L.G., Cullen S.J. (1995). *Handbook of Vadose Zone Characterization & Monitoring*. CRC Press, Boca Raton, FL, ISBN: 0873716108.
- Wolfbeis O.S. (2004). Fiber-optic chemical sensors and biosensors. *Analytical Chemistry*, 76, 3269-3284.
- Wolfbeis O.S. (1991). *Fiber Optic Chemical Sensors and Biosensors. Vol. II*, CRC Press, Boca Raton ISBN: 0849355095.
- Wooten F. (1972). *Optical Properties of Solids*, Academic Press, New York, ISBN: 0127634509.
- Yoo S., Jung Y., Lee D.S., Han W.T., Oh K., Murakami Y., Edamura T., Maruyama S. (2005). Optical anisotropy in single-walled carbon nanotubes. *Optics Letters*, 30, 3201-3203.
- Zahab A., Spina L., Poncharal P., Marliere C. (2000). Water-vapor effect on the electrical conductivity of a single-walled carbon nanotube mat", *Physical Review B*, 62, 10000.
- Zarcomb S. & Stretter J.R. (1984). Theoretical basis for identification and measurement of air contaminants using an array of sensors having partially overlapping sensitivities. *Sensors and Actuators*, 6, 225-243.
- Zhang J., Hu J., Zhu Z.Q., Gong H., O'Shea S.J., (2004). Quartz crystal microbalance coated with sol-gel-derived indium-tin oxide thin films as gas sensor for NO detection. *Colloids and Surfaces A: Physicochemical and Engineering Aspects*, Vol. 236, 1-3, 23-30.
- Zhao Q., Frogley M.D., Wagner H.D. (2002). Direction-sensitive stress measurements with carbon nanotube sensors. *Polymers for Advanced Technologies*, 13, 10-12, 759-764.
- Zudans I., Heineman W.R., Seliskar C.J. (2004). In situ measurements of chemical sensor film dynamics by spectroscopic ellipsometry. Three case studies. *Thin Solid Films*, Vol. 455-456, 1, 710-715.

Low Cost Multi-fiber Model Distributed Optical Fiber Sensor

Chuanong Wang
*National Institute of Aerospace
Hampton, VA, USA*

1. Introduction

1.1 Review on Techniques of Distributed Optical Fiber Sensors

Distributed optical fiber sensors are usable in many applications including stress monitoring of large structures such as buildings, bridges, dams, storage tanks, aircraft and also temperature profiling in electric power system, leakage detection in pipelines, etc. The researches on distributed optical fiber sensor are backward to 1970s (B. Lee, 2003; M. K. Barnoski & S. M. Jensen, 1976). Distributed optical fiber sensors are typically classed into intrinsic distributed optical fiber sensor and quasi-distributed optical fiber sensor. One of the most popular intrinsic distributed optical fiber sensors is optical time-domain reflectometry (OTDR) which is based on monitoring the Rayleigh backscattering along the fiber (M. Nakazawa, 1983). Based on the basic OTDR concept, various distributed sensing approaches were developed (A. J. Rogers, 1980; M. Zaboli & P. Bassi, 1983). OTDR has become a standard technique for testing optical fiber links and fault location in optical fiber communications. Furthermore, Raman OTDR, Brillouin OTDR and optical frequency-domain reflectometry (OFDR) (J. P. Dakin et al, 1985; M. Tateda, 1990; W. Eickhoff & R. Ulrich, 1981) are also developed and OTDR has found widespread applications in many fields (L. Thevenaz & M. Facchini, 1999). Concerning quasi-distributed optical fiber sensor, fiber bragg gratings (FBG) sensors are well developed and have been commercially manufactured and practically adopted on some bridges and dams (W. W. Morey et al, 1990; W. L. Schulz et al, 1998).

1.2 Needs in Lower Cost Distributed Optical Fiber Sensors

Distributed optical fiber sensors offer many advantages over traditional sensor techniques especially in long distance distributed parameters measurement and electric critical environments. Moreover, optical fiber is a low cost medium which is essentially important for the sensors popular applications. Nowadays, fiber sensors can be found in long distance power line systems, in buildings, bridges, dams, vehicles and even aircrafts. However, most of distributed optical fiber sensor systems which are considered for a very long distance (generally over kilometers) are very costly. This is because the instruments for the light source and signal detections are very complex and costly. And in traditional distributed optical fiber sensor system, the signal detection and processing have been a

complex problem. For examples, Rayleigh OTDR has the disadvantage of a weak signal which has to be integrated over many pulses and leads to a long response time. Raman OTDR is more serious because Raman scattering coefficient is about three orders of magnitude weaker than that of the Rayleigh (J. P. Dakin et al, 1985). Although several improving approaches are proposed to enhance the capability of detecting the weak backscattering signal (J. K. A. Everard, 1987), the fundamental limitation of conventional OTDR brings many difficulties on signal detection where great bandwidth leads to low signal noise ratio. Brillouin OTDR and OFDR not only have very weak scattering signals but also need coherent detection which makes the total system more sophisticated. FBG sensor, which integrates many fiber Bragg gratings in a single fiber, is based on wavelength division multiplexing technique and needs complex techniques for manufacturing. Therefore, all the current distributed optical fiber sensing techniques are based on complex signal detection and processing techniques which leads to sophisticated instruments such as reflectometry and interferometer. The entire sensing systems are complex and costly. In the applications of distributed optical fiber sensors, the cost of sensor systems limits the application of distributed optical fiber sensor to the objectives only having great importance. Actually, optical fiber sensors are desired in most structures which need distributed parameter measurement. There are wide needs of distributed optical fiber sensors in middle length (several meters to several hundred meters) with simpler system and lower cost.

1.3 Multi-fiber Model Sensor Concept

In recent years, a new technique was developed motivated by the low cost applications in middle distance range (C. Wang & K. Shida, 2006, 2007). The concept of new technique is to use light coupling between multi-fiber (generally two fibers) and the attenuation of light over fibers for distributed sensing. Basically, the sensor uses transmission light active fiber for localized deformation measurement and the coupling light from active fiber to passive fiber for position information. The output of sensor can be detected by photodiodes with a simple preamp circuit. The principle of the new sensor eliminates all the critical requirements on light source and signal detection as in conventional OTDR and FBG sensors. Therefore, the light source and signal detection circuit are very simple and low cost. Although more fibers are used, the total sensor system cost is greatly reduced because the cost of light source and signal detection instrument are greatly reduced.

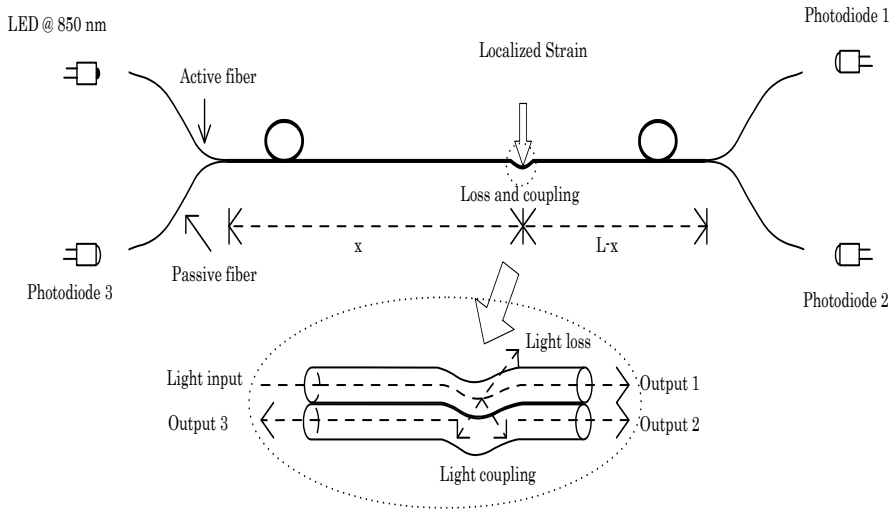


Fig. 1. Structure and principle of the multi-fiber model sensor.

The sensor here is different with evanescent wave coupling based sensors where the evanescent wave power in the cladding of single model optical fiber is quite weak. We use multi-model fibers for both active fiber and passive fiber. This multi-fiber model sensor is a new attempt for distributed optical fiber sensor except the techniques reviewed above. The idea is confirmed by the prototype sensors. The theoretical model and analysis on maximum length and spatial resolution are also studied.

2. Principle, Theory, Design of Intrinsic Distributed Multi-fiber Model Sensor

2.1 Structure and Principle of Sensor

As illustrated in Fig.1, the sensor is composed of two fibers. The first fiber is defined as the active fiber with light propagating within it. The second fiber is defined as the passive fiber which has no active light inside in common state and is designed to receive coupling light from the active fiber passively. The transmission rate of the active fiber is sensitive to the strain applied on it. By analyzing the output of active fiber, strain value can be measured. The response of the active fiber to strain has no dependency on the strain position. When localized strain is applied on the two fibers, light couples from the active fiber to the passive fiber at the strain applied point. The coupled light propagates along the passive fiber in the direction of both forward and backward. The outputs at the two ends of the passive fiber (output 2 and output 3) are used for strain position determination. Distributed sensing is based on the passive fiber attenuation. Fiber attenuation may be caused by absorbency, scattering, disfigurement of structure, bending and so on. The transmission characteristics of a fiber are usually given in terms of attenuation for a given wavelength (or range) and over a given length. The elementary experimental experience gives the relation of transmission rate and attenuation coefficient as follow:

$$T_r = \frac{P_{out}}{P_{in}} = 10^{-\frac{L \cdot \alpha}{10}} \quad (1)$$

where, α is attenuation coefficient, L is the length of fiber, P_{in} is the input light intensity, P_{out} is the output light intensity, T_r is the transmission rate. Obviously, the transmission rate of fiber has dependency on attenuation coefficient and length of fiber. When attenuation coefficient is fixed, the transmission rate is only related to the length of fiber. Therefore, if light is limited into a fiber at a certain point of the medium part, the output light intensities at two ends have dependency on the light incident position. Concerning the proposed sensor in this paper, different strain positions result in different outputs at the two ends of the passive fiber. By analyzing the output light intensities at the two ends of passive fiber, the position of strain can be determined. Attenuation coefficient of common fiber is generally smaller than 10 dB/km in the communication systems and has the theoretical limit of 0.2 dB/km. In our study, the passive fiber is designed to have condign attenuation coefficient which is greater than common fiber.

2.2 Light Source and Signal Detection Circuit

We use a LED (Hamamatsu Co. L7560) as the light source of the active fiber which has a peak wavelength at 850 nm. The typical coupled light power of 30 μ W is taken as the effective light emitting power of LED for analysis. Three photodiodes (Centronic Co. OSD1-5T) are used as the light detectors which has peak responsivity of 0.45 A/W at wavelength of 850 nm. The noise equivalent power (NEP) of the photodiodes is 25 fW. AD549 is used for the preamp of photodiodes which has a low offset drift by temperature of 20 μ V/ $^{\circ}$ C. The preamp electric circuit is shown in Fig. 2. The principle of the preamp electric circuit gives the expression of output voltage as follow:

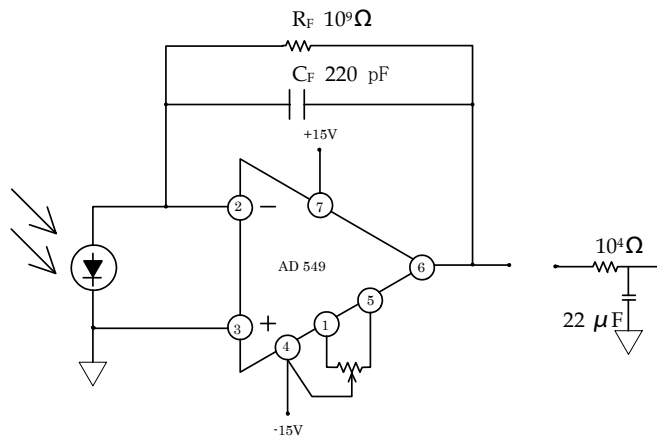


Fig. 2. Electric circuit for photodiode signal amplifying.

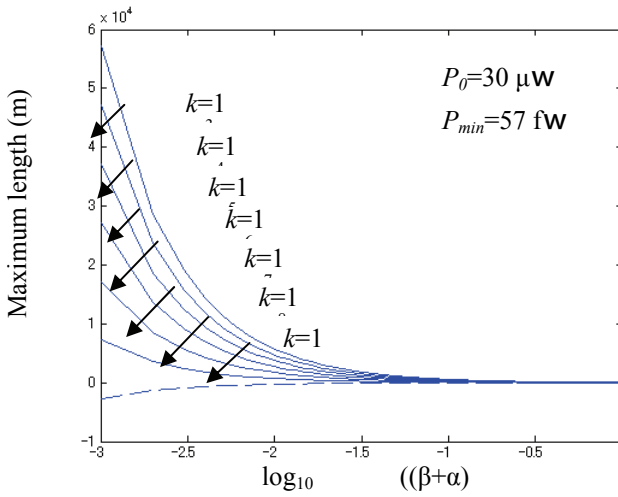


Fig. 3. Length limit of multi-fiber model sensor with different coupling coefficients.

$$V_{out} = P \times R \times \frac{R_F}{1 + j \cdot (f / f_p)} \tag{2}$$

where P is the light power incident on the photodiode surface in Watts and R is the photodiode peak responsivity of 0.45 A/W, f is signal frequency and f_p is the 3 dB cutoff frequency equals to:

$$f_p = \frac{1}{2\pi \cdot R_F \cdot C_F} \tag{3}$$

C_F sets the signal bandwidth to 0.7 Hz with R_F and also limits the peak in noise gain that multiplies the op amp input voltage noise contribution. A single pole filter at the amplifier output limits the op amp output voltage noise bandwidth to 0.7 Hz which improves the preamplifier's signal to noise ratio by a factor of three. Noise limits the signal resolution obtainable by the preamp. The photodiode preamp circuit in Fig. 2 can detect a signal current of 26 fA rms. Since the photodiode has responsivity of 0.45 A/W, the minimum detectable light power is 57 fW which is about double of the photodiodes noise equivalent power (NEP) 25 fW. The dynamic range of the preamp can be adjusted in practical applications.

2.3 Theory and Analysis on Limit Parameters

The maximum length of double-fiber distributed optical fiber sensor is restricted by the output light power at the passive fiber ends and the minimum detectable light power by photodiode preamp. From the principle of sensor, the emitting light intensities at the tow ends of passive fiber can be expressed as follow:

$$P_f = P_0 \cdot k_e \cdot 10^{\frac{\alpha \cdot x}{10}} \cdot k_s \cdot k_f \cdot 10^{\frac{\beta(L-x)}{10}} \tag{4}$$

$$P_b = P_0 \cdot k_e \cdot 10^{-\frac{\alpha \cdot x}{10}} \cdot k_s \cdot k_b \cdot 10^{-\frac{\beta \cdot x}{10}} \quad (5)$$

where

- P_f emitting light intensity at forward end of passive fiber;
- P_b emitting light intensity at backward end of passive fiber;
- P_0 effective emitting light intensity of LED;
- k_e input end coupling coefficient;
- a attenuation coefficient of active fiber;
- x position of localized strain;
- k_s coupling coefficient from active fiber to passive fiber by strain;
- k_f fraction of light propagating forward within the passive fiber;
- k_b fraction of light propagating backward within the passive fiber;
- β attenuation coefficient of passive fiber.

Since the double ended outputs of passive fiber are used for position sensing, the length limiting conditions are that $P_f > P_{min}$ at position of $x = 0$ and $P_b > P_{min}$ at position of $x = L$. Educing (4) and (5) by these limiting conditions, we can get the length limiting equations as follow:

$$L < \frac{10}{\beta} \log_{10} \left(\frac{P_0 \cdot k_e \cdot k_s \cdot k_f}{P_{min}} \right) \quad (6)$$

$$L < \frac{10}{\beta + \alpha} \log_{10} \left(\frac{P_0 \cdot k_e \cdot k_s \cdot k_b}{P_{min}} \right) \quad (7)$$

where, P_{min} is the minimum detectable light intensity by the preamp. The attenuation of active fiber is expected to be minimized while that of the passive fiber is quite greater. The attenuation is mainly caused by the passive fiber. Moreover because of the similarity of the output expressions at the two ends of the passive fiber, we can use (7) for the analysis of outputs at both ends.

The theoretical length limit to attenuation coefficient is shown in Fig. 3 where we define $k = k_e \cdot k_s \cdot k_f$ or $k = k_e \cdot k_s \cdot k_b$ as the total effective coupling coefficient. From the calculation results, we can see that lower attenuation coefficient and higher total effective coupling coefficient conduce to greater length limit. The length limit greatly depends on the total effective coupling coefficient k . In practical experiments, to nondestructive strain, k is at the factor of 10^{-7} - 10^{-3} and for destructive strain, k is at the factor of 10^{-3} - 10^{-2} . By designing appropriate attenuation coefficient of passive fiber, the fibers length can reach the level of kilometers which is meaningful for many applications in structure strain monitoring such as bridges and dams.

Because of the exponential attenuation of light propagating in fiber, the spatial resolution of the proposed sensor is non-uniform along the length of fiber. The minimum spatial resolution Δx by single end output is restricted by the conditions expressed as follow respectively:

$$P_f(x + \Delta x) - P_f(x) > P_{min} \quad (8)$$

$$P_b(x) - P_b(x + \Delta x) > P_{min} \quad (9)$$

where $P_f(x)$ and $P_b(x)$ are output light power at forward and backward end respectively corresponding to coupling position of x . From the above two equations, we can get the spatial resolution distribution along the fiber as follow:

$$\Delta x_f = \frac{10}{\beta - \alpha} \cdot \log_{10} \left[1 + \frac{P_{\min} \cdot 10^{\beta L} \cdot 10^{(\alpha - \beta)x}}{P_0 \cdot k_e \cdot k_s \cdot k_f} \right] \tag{10}$$

$$\Delta x_b = \frac{10}{\beta + \alpha} \cdot \log_{10} \left[1 - \frac{P_{\min} \cdot 10^{\beta L} \cdot 10^{(\alpha - \beta)x}}{P_0 \cdot k_e \cdot k_s \cdot k_b} \right]^{-1} \tag{11}$$

where Δx_f and Δx_b are the spatial resolutions determined by the single end output of forward and backward respectively. The spatial resolution distributions are greatly influenced by the parameters of k_f and k_b . In Fig. 4, we show the single end determined spatial resolution distributions under three groups of k_f and k_b . The length is 1000 m and (k_f, k_b) equals to (0.9, 0.1), (0.7, 0.3) and (0.5, 0.5) respectively. From (4) and (5), we can see that the outputs light intensities at both ends of the passive fiber have dependence on k_s , which is influenced by strain value. Therefore, dividing (4) by (5), we can get k_s independent equation as follow:

$$x = \frac{1}{2} \left[L + \frac{10}{\beta} \log_{10} \left(\frac{P_f}{P_b} \cdot \frac{k_b}{k_f} \right) \right] \tag{12}$$

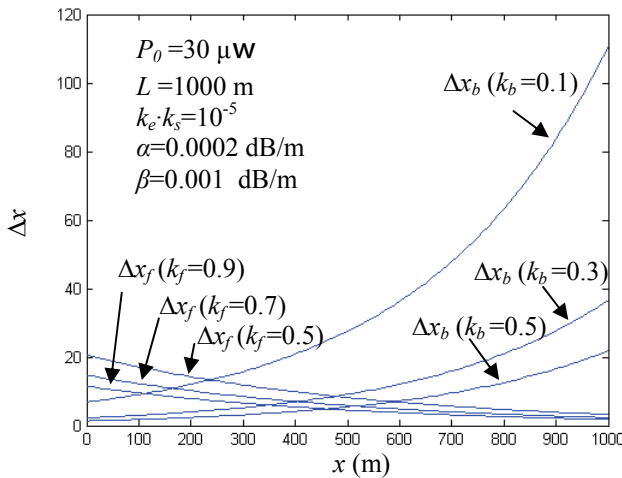


Fig. 4. Spatial resolution distribution by single end output.

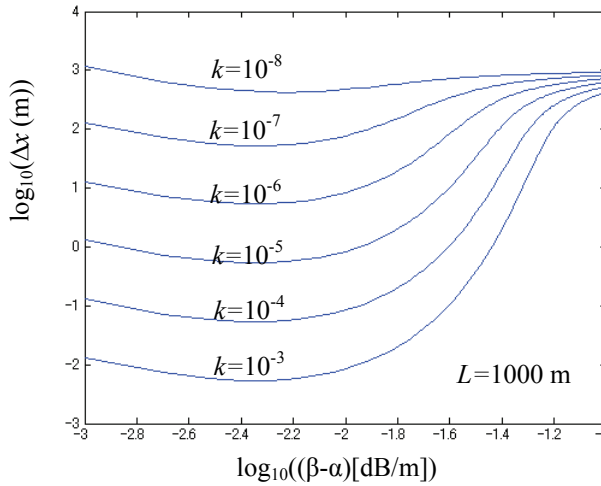


Fig. 5. Spatial resolution dependence on attenuation coefficient of passive fiber when $L = 1000$ m.

In (12), the strain position in theory has no dependency on k_s , the coupling coefficient between the two fibers. Actually, the strain value has influence on position sensitivity. Smaller strain value leads to less sensitivity to position and the position estimation is restricted by the detectable conditions. Since P_f and P_b have different individual sensitivity to position, the total spatial resolution is determined by the more sensitive one as follow:

$$\Delta x = \min\{\Delta x_f, \Delta x_b\} \quad (13)$$

From the spatial resolution distribution illustrated in Fig. 4, we can see that the total spatial resolution Δx has a maximum value at the point where Δx_f is equal to Δx_b . To nondestructive strain, the coupling light propagating forward within the passive fiber is much more than that of backward, the parameter k_f is quite greater than k_b . The total spatial resolution mainly depends on the forward end output. For convenience of analysis, we use the restricting condition expressed in (10) at point of $x=0$ for total spatial resolution analysis. This is a conservative condition and in theory the spatial resolution can be better. The total spatial resolution to attenuation coefficient is shown in Fig. 5 where we suppose the length is 1000 m. From the calculational results, we can know that, the attenuation coefficient has an optimization area for the best spatial resolution on a given length. Spatial resolution greatly depends on the total effective coupling coefficient k which is also illustrated in Fig. 5. From the figure, we can see that, if the total effective coupling coefficient k is at the level of 10^{-7} , it will be meaningless for the spatial resolution of hundred meters. When k changes from 10^{-6} to 10^{-5} , the spatial resolution can be promoted from tens of meters to the level of meter with appropriate attenuation coefficient. When k changes from 10^{-5} to 10^{-3} , the spatial resolution is furthermore promoted to centimeter level. In spite of other factors, higher coupling coefficient is propitious to the promotion of spatial resolution.

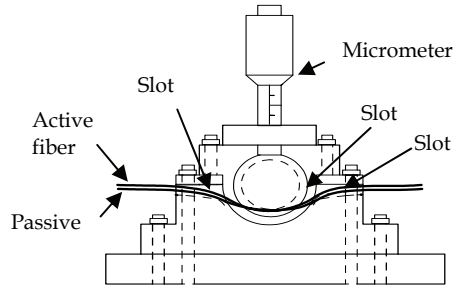


Fig. 6. Experimental micrometer controlled mechanism for strain.

However, in practical experiments, the high coupling coefficient is at cost of great destructive strain which leads to an unsteady relationship between k_f and k_b . As expressed in (12), the ratio of k_b to k_f has direct influence on the position value estimation. As a matter of fact, k_b and k_f are influence by strain value. To the same strain, the ratio of k_b to k_f is constant. To value changeable strain, k_f and k_b should be determined before the position estimation. It is more difficult for destructive strain with a high coupling coefficient than that of the nondestructive strain. Anyway, even in the area of nondestructive strain, spatial resolution can reach a level which is meaningful to many applications. All the above analysis is restricted by the given LED emitting light power $30 \mu\text{W}$ which has much space to be promoted. Greater light emitting power of light source contributes to promotion of length and spatial resolution and also decreases the influence of coupling coefficient. Optimized designing of the double-fiber model sensor is a tradeoff between the length and spatial resolution for attenuation coefficient of the passive fiber.

2.4 Experiments on Prototype Sensor

The prototype sensor is developed with a length of 4 meters. Two multi-model fibers are used for both the active and passive fiber with the attenuation coefficient of 0.007 dB/m and 3.5 dB/m respectively. The attenuation is mainly caused by the passive fiber and the attenuation caused by the active fiber can be ignored. A fiber light source aimed LED is used for light emitting. Three high sensitive photodiodes are used for light detection. AD549 is used for the preamp electric circuit and the preamp is designed to have a narrow bandwidth of 0.7 Hz together with a low-pass filter in order to promote the signal to noise ratio. A digital multimeter (KEITHLEY 2000) is used for voltage signal measurement and the data is automatically recorded by a computer. We use a micrometer controlled mechanism to apply strain on the two fibers as illustrated in Fig. 6. The mechanism uses a cylinder in radius of 1 cm to apply strain on fibers. Both of the cylinder and the base parts are machined with slots to hold the fibers. The two fibers keep vertical through the whole process of experiment. The applied strain on fibers can be precisely controlled to both nondestructive and destructive strain. Experiments are made in laboratory room with temperature roughly controlled. The transition process of LED and electric circuit are well considered by making experiments after waiting a period of time. The room light is well shielded to avoid noise caused by disorder light.

Light coupling coefficient includes the input end coupling coefficient k_e and the strain coupling coefficient k_s . The LED L7560 has a small lens integrated at the front part which is specially designed for light emitting into fiber. The input end coupling coefficient k_e is 0.462 under the conditions of our experiments. The light coupling coefficient between the two fibers k_s is an important parameter to the proposed sensor. The output light intensities of the passive fiber greatly depend on the light coupling coefficient, and consequently, the maximum length and the spatial resolution. The coupling coefficient is dependent on applied strain value. The experimental results of light coupling coefficient are shown in Fig. 7 where the k_{ef} and k_{eb} are the total effective coupling coefficient in forward and backward direction which are equal to $k_e k_s k_f$ and $k_e k_s k_b$ respectively. According to the deformation value of fibers, the applied strain can be divided into the nondestructive strain and the destructive strain. From the experimental results, we can see that, k changes from 10^{-5} to 10^{-3} in nondestructive strain area and changes from 10^{-3} to 10^{-2} in the destructive strain area. The theoretical maximum length can be up to the level of 10 km and the spatial resolution can be under the level of centimeter in spite of other factors.

Since (12) is independent from k_s , the effectiveness of position estimation will not be influenced by changes of light coupling coefficient k_s as long as the output light intensities are under the restricting conditions of length limit and spatial resolution. The ratio of backward propagating light and forward propagating light directly influence the position estimation as illustrated in (12). If the same strain is applied on different position of sensor, the ratio of k_b to k_f has the same value. Consequently, (12) works well for stain position estimation. However, if different strain values are applied, the ratio of k_b and k_f must be determined before strain position estimation.

As illustrated in Fig. 7, the effective coupling coefficient has different dependence on the strain value in the two areas of nondestructive and destructive strain. In the nondestructive strain area, both of the k_{ef} and k_{eb} have exponential form dependence

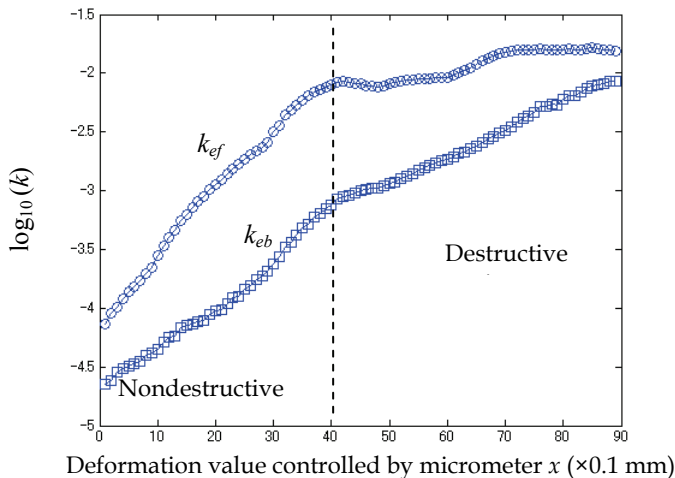


Fig. 7. Experimental results of light coupling coefficients.

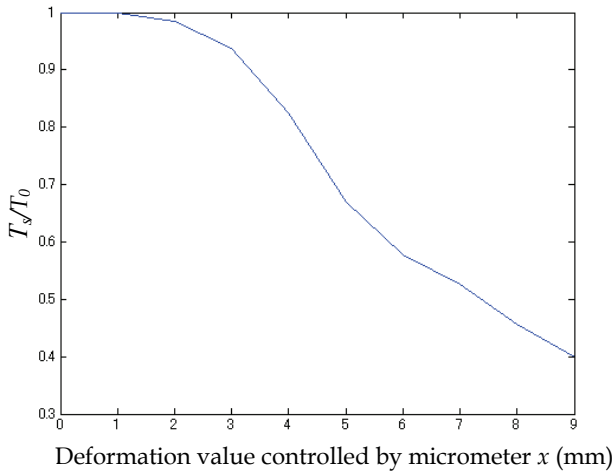


Fig. 8. Response of the active fiber transmission rate to strain value.

on strain value which can exponentially be modeled. In the destructive strain area, the forward effective coupling coefficient k_{ef} shows unstable dependence on strain value which brings difficulties for value estimation. Therefore, under current conditions, the proposed sensor is used in the area of nondestructive strain. Concerning the applications such as civil structure strain monitoring, it is of the same importance to detect the exceptional strain in the early stage with warning the accidental destructive strain.

The active fiber is used for strain value sensing. The response of active fiber transmission rate to the strain value is shown in Fig. 8, where T_s is the transmission rate of the active fiber with strain, T_0 is the original transmission rate. Although the active fiber used in our study is not specifically designed for pressure sensing, the active fiber has a sensitive response to the applied strain. Using the output of the active fiber, the strain value can be determined. In the area of nondestructive strain, the coupling coefficient can be consequently estimated. As a matter of fact, the transmission rate of the active fiber is not only dependent on the applied strain but also other factors, for example, ambient temperature and fiber eroding. The output of the active fiber includes all the perturbation on the fiber. However, strain can be indicated from other perturbations by the outputs of passive fiber. Moreover, the influence by ambient temperature is possible compensated by electrical circuit. The influence by localized high temperature area, for example, caused by fire, is another problems involved for further study.

In order to confirm the distributed sensing of the proposed sensor, we apply the localized nondestructive strain on the developed prototype sensor at different positions. In Fig. 9, we show the comparison of the practical experiment results and the theoretical curves predicted by (12), where the ratio of P_f to P_b is used for strain position estimation. From Fig. 9, we can see that, the experimental results are well coincident to the curves predicted by theoretical equation. The ratios of k_b to k_f under three strain values are experimentally tested to be 0.75, 0.57 and 0.43 respectively.

Concerning the strain position value reconstruction, we proposed the (12) which is confirmed by experimental results. Equation (12) eliminates the influence of k_s under the detectable conditions. But it is still influenced by the ratio of k_b to k_f . The

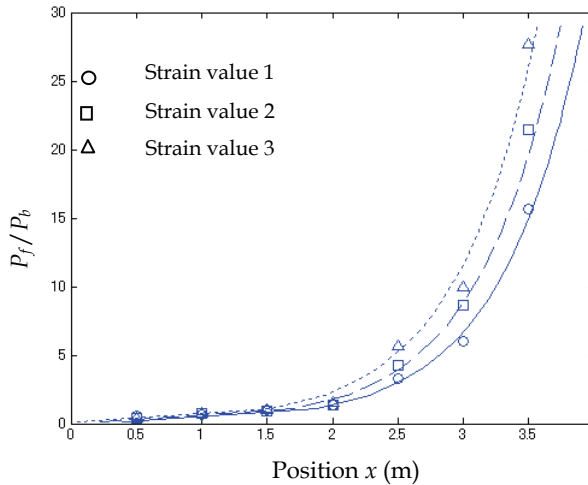


Fig. 9. Response of the passive fiber to distributed strain.

errors of position sensing mainly come from the estimation results of the ratio of k_b to k_f which can be modeled only in area of nondestructive strain. Therefore, the coupling model between the two fibers is of great importance to the proposed sensor. More precise model is achieved, the sensor provides better performance. When the ratio of k_b to k_f is fixed or experimentally measurable, the proposed sensor has great potential in spatial resolution and length. As another way, if the absolute value of k_{ef} can be determined, the strain position can be reconstructed by (4) individually. In Fig. 9, if the position goes on increasing, the

P_f / P_b will get sharp increase and it is not good for position sensing. However, the attenuation coefficient of passive fiber 3.5 dB/m is designed for 4 m length. To longer length, the attenuation coefficient of passive fiber has to be redesigned. As a matter of fact, optimizing and design of sensor need many strategies. To any given length applications, the response of passive fiber to strain position is expected to have similar form as shown in Fig. 9 with different x units.

As a result, the prototype sensor is effective to sense the distributed strain by the outputs of the passive fiber. The effectiveness of the proposed sensor is conformed. Moreover, both of the theoretical analysis and practical experiments are restricted by the given LED light emitting power 30 μ m in this period of study. By using light emitting power promoted light source, the sensor can achieve better performance.

3. Quasi-Distributed Multi-fiber Model Sensor

3.1 Principle and Configuration of Quasi-Distributed Sensor

In intrinsic distributed multi-fiber sensor, the coupling coefficients ratio in forward and backward direction is dependent on fibers' deformation form which is uncertain in practical applications. And also, the backward coupling coefficient is quite smaller than forward coupling coefficient which limits the position sensing. Quasi-distributed sensor uses the special designed mechanism as the sensing element and has steady deformation form controlled by the mechanism. The light direction influence on coupling coefficient is also removed by using light sources at both ends of the active fiber so that the sensor has the symmetrical coupling coefficients in the two directions of forward and backward along the fiber. As illustrated in Fig.10, the sensor is composed of two multimode fibers with discrete sensing elements arranged along them. The first fiber is the active fiber with active light propagating within it. The second fiber is the passive fiber which has no active light inside in common state and is designed to receive coupling light from the active fiber. Strain sensing is performed by the sensing elements which are discretely arranged along the fibers with given distance interval. When localized strain is applied on certain sensing element, the two fibers are forced to macro bending by the sensing element. The jacket layers of the two fibers are divested in the sensing element parts. Therefore, the macro bending makes light lose from the active fiber and partly couple into the passive fiber. The coupled light propagates along the passive fiber mainly in forward direction. Light sources are used at both ends of the active fiber. Using this method, the light direction influence on coupling coefficient is removed. The outputs at two ends of the passive fibers will not be influenced by light propagating direction in the active fiber. The sensing elements are machined to have symmetrical inner shape (along the fibers' center axis) and fixed bending radius. This is motivated by the making symmetrical deformation of fibers along their center axis. Consequently, the coupling coefficients in the two opposite directions can be equal. The two fibers have jacket layers to protect fibers and prevent light coupling in other places outside the sensing elements. Therefore, the light coupling between the two fibers is limited in the sensing elements and with fixed deformation form. Using this method, the deformation form influence on the coupling coefficient is removed.

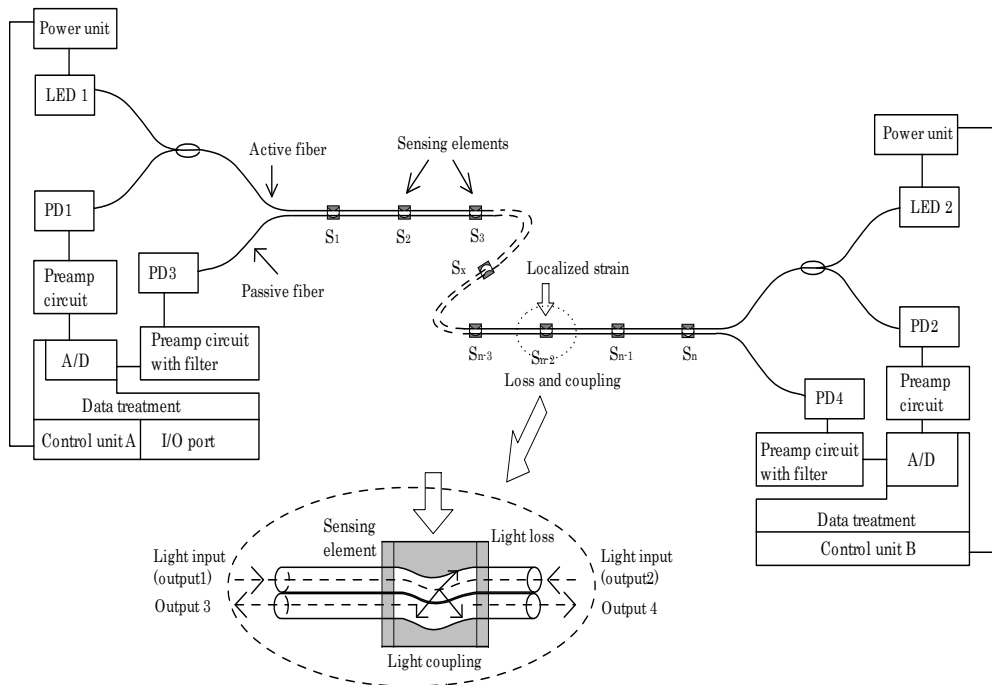


Fig. 10 Principle and configuration of the quasi-distributed sensor system

The sensor configuration is shown in Fig. 10. Two light-emitting-diodes (LED1 and LED2) are used as the light sources and two photo-diodes (PD1 and PD2) are used as the light detectors at two ends of the active fiber. The light-emitting-diode and photo-diode are connected to the active fiber by 3-dB coupler. Another two photo-diodes (PD3 and PD4) are used at the two ends of the passive fiber as the light signal detectors of the passive fiber. The circuit modules used in the sensor system are also illustrated in Fig. 10 including preamp circuits, filters, A/D converters, control units and power units.

As shown in Fig. 10, the driving circuits of the sensor system are divided into two parts which have different physical locations (at the two ends of the fibers). The active fiber (together with PD1 and PD2) is used not only for strain sensing and but also for handshaking commands and data communication between the two parts of the driving circuits. The working flow chart of sensor system is shown in Fig. 11. As the non-working state of the sensor system, the signal detection channel with PD2 keeps "listening" state to the active fiber output while other parts of the sensor system can be shut off in this state. Once measurement is started by manual operation or remote controlling signal, the control unit A firstly sends the "Start" command codes into the active fiber. The command codes are sent digitally by LED1 and are detected by PD2. Since the PD2 keeps listening to active fiber, the digit signals of "Start" command will be picked up by PD2. After the command is decoded, the control unit B makes the PD2 and PD4 ready for measurement signal detection and sends "Ready" command to active fiber by LED2. PD1 receives the "Ready"

command, and LED1 is turned on for a period of time ΔT as the light source for measurement. At this time, PD2 and PD4 can get continuous light signals but maybe not steady. The influence may come from the ambient temperature and transitional working state of LED. The control unit B evaluates the signal quality and makes the judgment. If the signal quality is not good, the control unit B will resend the "Ready" command and LED1 will be turned on again for repeated measurement. After the data from PD2 and PD4 are saved, the control unit B sends "Get ready" command to PD1. The control unit A makes PD1 and PD3 ready for measurement signal detection and then sends "Ready" to PD2. After the "Ready" command is received, LED2 is turned on for a time period of ΔT as the light source in opposite direction. Similar with the first step measurement, the control unit B evaluates the signal quality from PD1 and PD3 and makes the judgment whether to repeat the measurement or not. After the data from PD1 and PD3 are saved, control unit A sends "Data" command and the saved data of PD2 and PD4 in control unit B are transmitted to this side. Finally, all the data are processed by control unit A and it gives the final measurement results to I/O port of the sensor system.

Element	Fiber	Coupler	LED	Photodiode	Amplifier	μ Controller with A/D
Number	2	2	2	2	4	2
Note	Multi-mode	3 dB	30 μ W	25fW NEP	High	46 dB Dynamic Range

Table 1. Basic Elements of Sensor System

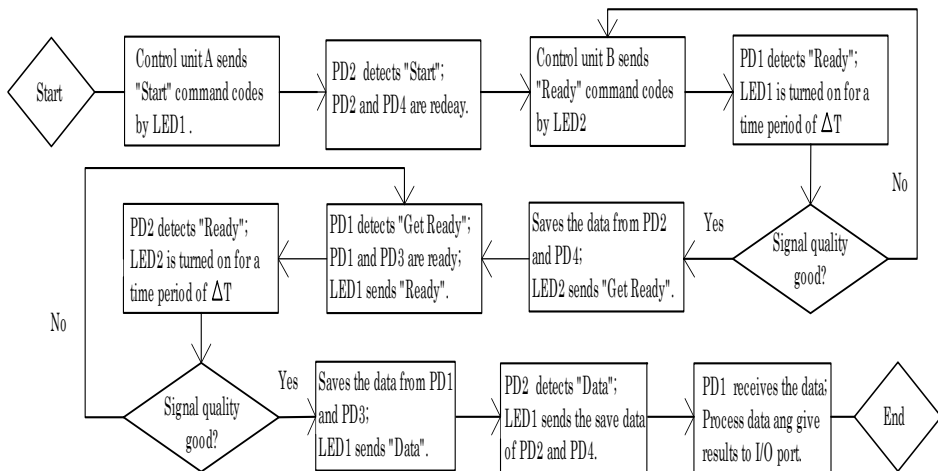


Fig. 11. Working flow chart of the sensor system

Using the active fiber as command communication medium, the sensor system can control the electric units in two physical positions without any additional signal channel. Since the control command is digital signal, the transmission rate change of active fiber caused by strain will not fail the communication as long as the light signal can be detected. Totally four

command can be coded by two bits data. The micro controller functions include control logic (two bits commands), control A/D, storing 4 numbers of data and communication for data upload to I/O. A simple micro controller can perform all the functions easily. It is noticeable that all the hardware in the sensor system from regular electrical and optical elements. There are no sophisticated circuits nor complex devices or special techniques used in the sensor system. The cost is dominated by the basic elements as listed in Table 1.

3.2 Theoretical Analysis on Limit Parameters

Double-ended light source gives symmetric coupling coefficient in the two direction of backward and forward. The output light power at the two ends of passive fiber can be expressed by equations (14) and (15) which is similar to but different with equations (4) and (5) in backward light power equation.

$$P_f = P_0 \cdot k_e \cdot 10^{-\frac{\alpha \cdot x}{10}} \cdot k_s \cdot 10^{-\frac{\beta(L-x)}{10}} \quad (14)$$

$$P_b = P_0 \cdot k_e \cdot 10^{-\frac{\alpha(L-x)}{10}} \cdot k_s \cdot 10^{-\frac{\beta \cdot x}{10}} \quad (15)$$

Since outputs of the passive fiber are used for position sensing, the length limiting conditions are that $P_f > P_{min}$ at position of $x = 0$ and $P_b > P_{min}$ at position of $x = L$. Here, P_{min} is the minimum detectable light power by photodiode preamp which is equal to n times of the noise equivalent power (NEP) and n is related to signal noise ratio. Because the symmetrical character of P_f and P_b , the two conditions are equivalent for theoretical length limit analysis. Educing equation (14) by this limiting condition, we can get the length limiting equation as follow:

$$L < \frac{10}{\beta} \log_{10} \left(\frac{P_0 \cdot k_e \cdot k_s}{NEP \cdot n} \right) \quad (16)$$

From equation (16), we get the theoretical length limit to passive fiber attenuation coefficient β , as shown in Fig. 12, where P_0 is equal to effective coupled light power of 30 μ W (LED L7560) and P_{min} values are 22 fW, 220 fW and 2.2 pW corresponding to R_F value of $10^{-9}\Omega$, $10^{-8}\Omega$ and $10^{-7}\Omega$ respectively. From the curves illustrated in Fig. 7, we know the sensor maximum length is dependent on the light coupling coefficient k_s , the passive fiber attenuation coefficient β and the P_{min} value of the light detection circuit. The k_s has been proved in the area of $10^{-5} \sim 10^{-2}$. By choosing appropriate attenuation coefficient for the passive fiber, the proposed sensor is possible to reach the level of kilometers. Given the conservative value of $P_{min} = 2.2$ pW, the maximum length is above kilometer when β is in the area of $10^{-3} \sim 10^{-2}$ dB/m.

The spatial resolution of the proposed sensor is determined by the sensing element interval. As the precondition of effective sensing, the sensing element interval Δd must be greater than the minimum spatial resolution Δx which is determined by sensor design parameters. The minimum spatial resolution Δx by single end output is restricted by the conditions as expressed in equation (7) and (8).

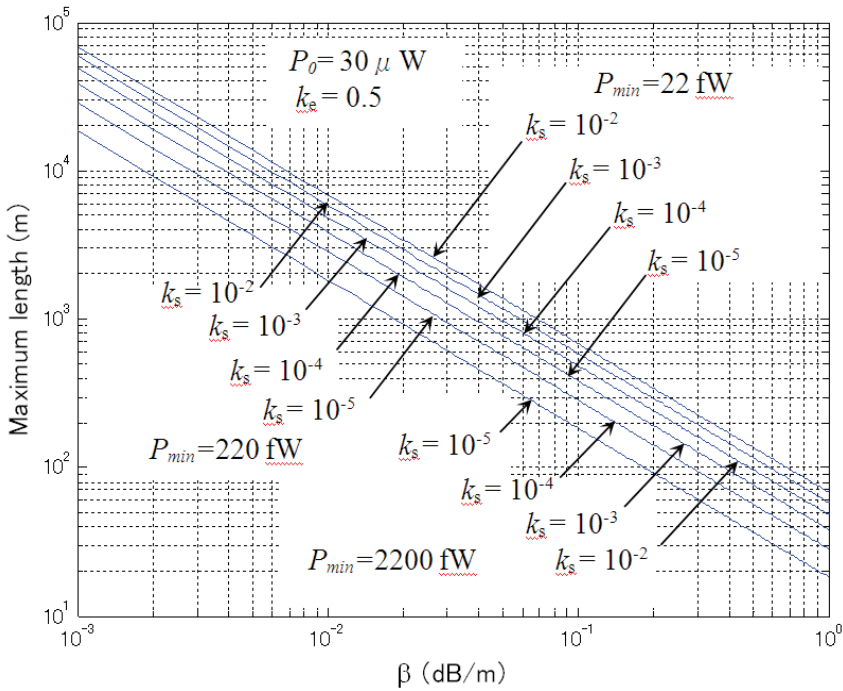


Fig. 12. Length limit of the sensor with different NEP

Similar with the analysis in Section 2.3, we can get the spatial resolution distribution along the fibers as shown in Fig. 13. Because of the exponential attenuation of light propagating in fiber, the spatial resolution of the proposed sensor is non-uniform along the fibers. Fig. 13 shows the single end determined spatial resolution along the fibers with given parameters of $L=1000$ m, $\alpha = 0.0002$ dB/m, $\beta = 0.001$ dB/m. From Fig. 13, we know that the spatial resolution changes in large area from hundreds of meters to millimeter and is greatly dependent on the coupling coefficient and P_{min} value.

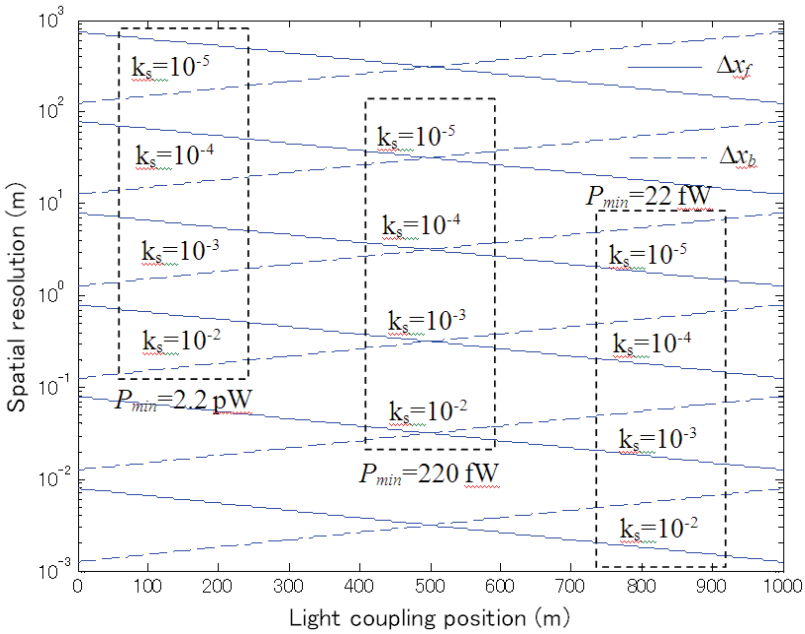


Fig. 13. Spatial resolution distribution along the fibers

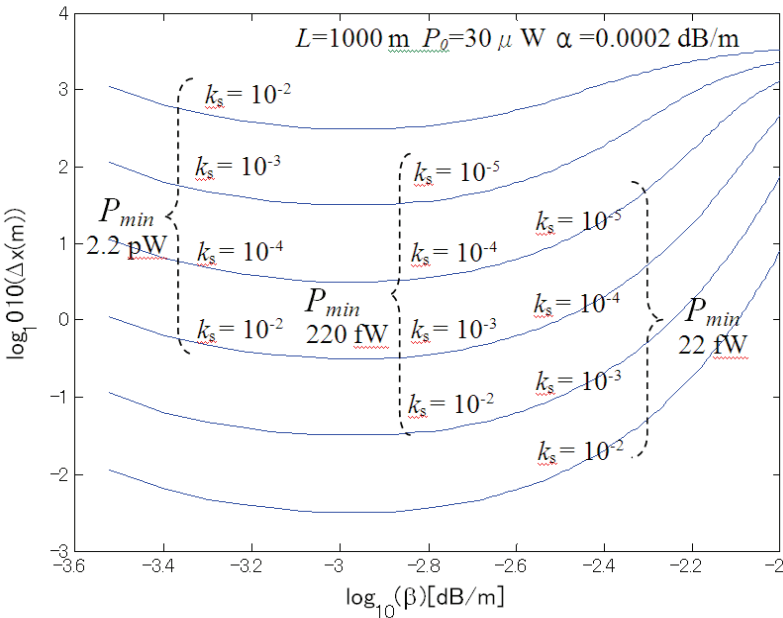


Fig. 14. Spatial resolution dependence on the attenuation coefficient β coupling coefficient k_s and NEP

Since the output light power at both ends of the passive fiber is dependent on the coupling coefficient k_s , we divide (14) by (15) and get position sensing function using double ended outputs as follow:

$$x = \frac{1}{2} \left[L + \frac{10}{\beta - \alpha} \log_{10} \left(\frac{P_f}{P_b} \right) \right] \tag{17}$$

In equation (17), the strain position has no dependence on the coupling coefficient k_s in theory. Actually, position sensing by (17) is still influenced by k_s in sensitivity and SNR value. The sensing is also restricted by the limiting conditions for the length and spatial resolution. From Fig. 13, we know that the maximum values of Δx is at the position of $x = L/2$. Using this conservative condition, we show the double ended outputs determined spatial resolution with different parameters of β , k_s and P_{min} in Fig. 14.

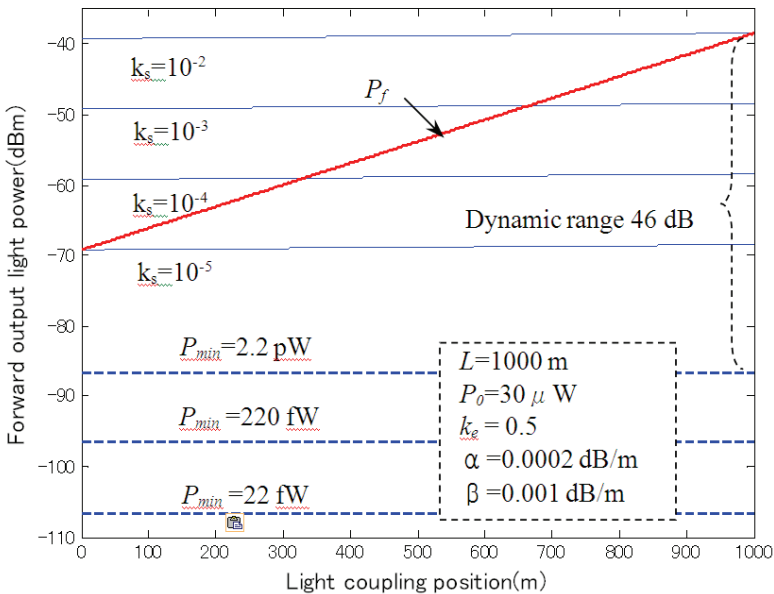


Fig. 15. Dynamic range of forward output light power of passive fiber

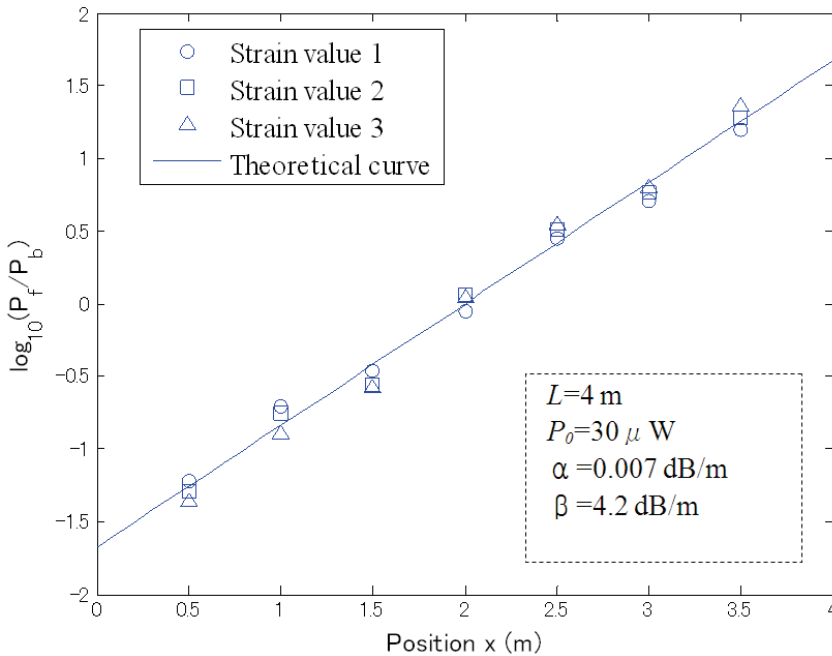


Fig. 16. Response of the passive fiber to distributed strain

The minimum spatial resolution are in the areas of (1 cm, 1 m) , (10 cm, 100 m) and (1 m, 1000 m) when the coupling coefficient value changes for 10^{-5} to 10^{-2} and P_{min} values are 22 fW, 220 fW and 2.2 pW respectively. As the limiting condition, sensing element interval should be greater than the minimum spatial resolution. According to specific needs, the sensing element interval can change in a large area from centimeters to hundreds meters.

The forward output light power of the passive fiber is shown in Fig. 15 with the given parameters values. The output light power is dependent on light coupling coefficient k_s and light attenuation in the two fibers. Under given conditions, the output light power has a dynamic range of 31 dB. The passive fiber attenuation coefficient value of 0.001 dB/m is chosen based on the length limit and spatial resolution analysis results for the length of 1000 m. The P_{min} lines of 2.2 pW, 220 fW and 22 fW are also shown in Fig. 15. From this figure, we can see that the passive fiber outputs have quite great safe space to the minimum detectable light power and the sensor can get quite great SNR value. A dynamic range of 46 dB (from -86 dBm to -38 dBm) is needed to be covered by the A/D converter for a minimum detectable light power of 2.2 pW. This can be realized using a 8-bit A/D converter (24 dB) and repetition increasing of 30 dB. Since the sensor use continuous signal form, there is no bandwidth requirement for both of light source and light detector. Within a bandwidth of 1 Hz, the signal can be detected by simple photodiode preamp circuit which can have a great dynamic range. All the performance parameters of the sensor are specially designed for specific applications requirements. For other circumstances, the sensor parameters values should be redesigned taking the specific applications considered.

3.3 Experiments and Results

In order to confirming the sensor, a prototype sensor is developed in the length of 4 m in laboratory. In Fig. 16, we show the experimental results in strain position sensing with the corresponding theoretical curves. Totally seven sensing elements are used which have uniform interval of 0.5 m. The parameters used in prototype sensor are as follows: $\alpha = 0.007$ dB/m, $\beta = 4.2$ dB/m, $P_{min} = 2.2$ mW ($R_F = 10^4 \Omega$). Three strain values are applied in the experiments which lead to different coupling coefficient value of k_s . From Fig. 16, we can see that, the position sensor results have no dependence on the strain value and the experimental results are well coincident to the curves predicted by theoretical equation (17). Using the double ended light source and sensing element, the sensor gets symmetrical outputs at the two ends of the passive fiber. It contributes the promotion of sensor performance parameters including length, spatial resolution and appropriate dynamic range and makes the proposed sensor possible for practical applications.

4. Discussions and Conclusions

4.1 Discussions

The multi-fiber model sensor has lower cost and simpler principle compared with other distributed optical sensor. The advantages of multi-fiber model sensor are discussed as following:

(1) There is no special structure in the fibers like bragg grating. There are also no special requirements for the optical fiber such as light wavelength, homochromy, interference, polarization and dispersion. A wide range of optical fiber can be the candidates in designing and fabricating sensors.

(2) The sensor has no critical requirements on light source and signal detection instruments. The sensor has light intensity based outputs for both of the active fiber and the passive fiber. By using continuous form signals, the sensor needs no great bandwidth for both of the light source and the light detector circuit. This is greatly helpful to improve the signal to noise ratio and sensor sensitivity and reduce the complexity and cost of signal detection hardware.

(3) The driving and control circuits are simple and low cost. Totally, four commands are used in handshake process which can be encoded by two bits. The digital pulses for handshake need neither critical up and down edges nor great bandwidth. The data saving and processing require only four numbers' memory space and simple calculation ability which can easily realized by a single chip.

Therefore, the sensor has the simple and low cost characters which will contribute to wider application of the optical fiber sensors. It is a competitive solution to distributed parameters measurement in medium length distance (several meters to kilometers).

The main limitation of the proposed sensor is the difficulty for multipoint measurement at the same time. But there are many circumstances where the first problem point is of the most interests, for example, the safety monitoring of civil structure. It is meaningful in many applications to alert and locate the first problem point. After appropriate modification, the sensor is possible to be used in submersion sensor, hot spot sensor, inner deformation sensor, position sensor and so on. The multi-fiber sensor makes the optical fiber sensor possible to be applied in wider circumstances where the conventional sensors may be not cost-effective. And it also makes complete the applications of distributed

optical fiber sensors in medium distance (several meters to 1 kilometer) as a low cost solution.

4.2 Conclusions

In this chapter, we introduced a novel quasi-distributed optical fiber for distributed strain monitoring. By using the coupling light between two multi-model fibers, the sensor gets output light intensity signals which can effectively be detected by photodiodes with common preamp circuit. The effectiveness of the sensor is practically confirmed. Theoretical analysis shows that the sensor's maximum length can reach the level of kilometers and the spatial resolution can reach the level of centimeters. In the distributed optical fiber sensor field, the proposed double-fiber model sensor is new attempt different from other techniques. Since the sensor uses neither sophisticated instruments nor any special techniques, the total systems can be realized with extremely low cost. It is meaningful to the widely needed on-line monitoring applications in many circumstances especially where the cost-effectiveness is critical limited.

5. References

- A. J. Rogers, "Polarization optical time domain reflectometry," *Electron. Lett.*, vol. 16, pp. 489-490, Jun. 1980.
- B. Lee, "Review of the present status of optical fiber sensors," *Opt. Fiber Technol.*, vol. 9, pp. 57-79, Apr. 2003.
- C. Wang and K. Shida, A novel multifunctional distributed optical fiber sensor based on attenuation, *Proc. IMTC'06*, pp. 2018-2023, April, 2006.
- C. Wang and K. Shida, A low cost double-fiber model distributed optical fiber sensor, *IEEE T. Instrum. Meas.*, Vol. 56, No. 4, August, 2007.
- C. Wang, Study on Multifunctional Sensors for Trucks Safety Monitoring, Ph.D Thesis of Saga University, September, 2007.
- J. P. Dakin, D.J. Pratt, G.W. Bibby, J. N. Ross, "Distributed optical fiber Raman temperature sensor using a semiconductor light source and detector," *Electron. Lett.*, vol. 21, pp. 569-570, Jun. 1985.
- J. K. A. Everard, Novel signal techniques for enhanced OTDR sensors, *Proc. SPIE*, vol. 798, pp. 42-46, Mar. 1987.
- L. Thevenaz, M. Facchini, Monitoring of large structures using distributed Brillouin fiber sensing, *Proc. OFS'13*, pp. 345-348, 1999.
- M. K. Barnoski and S. M. Jensen, Fiber waveguides: A novel technique for investigating attenuation characteristics, *Appl. Opt.*, vol. 15, pp. 2112-2115, 1976.
- M. Nakazawa, Rayleigh backscattering theory for single-mode optical fibers, *Opt. Soc. Am.*, vol. 73, no. 9, pp. 1175-1180, Sep. 1983.
- M. Zaboli, P. Bassi, High spatial resolution OTDR attenuation measurement by a correlation technique, *Appl. Opt.*, vol. 22, pp. 3680-3681, Dec. 1983.
- M. Tateda, First measurement of strain distribution along field installed optical fibers using Brillouin spectroscopy, *J. Lightwave Technol.*, vol. 8, pp. 1269-1272, 1990.
- W. Eickhoff and R. Ulrich, Optical frequency domain reflectometry in single-mode fiber, *Appl. Phys. Lett.*, vol. 39, pp.693-695, Nov. 1981.

- W. W. Morey, G. Meltz, and W. H. Glenn, Fiber Bragg grating sensors, *Proc. SPIE*, vol. 1169, pp. 98-107, Jan. 1990.
- W. L. Schulz, E. Udd, J. M. Seim, and G. E. McGill, Advanced fibre grating strain sensor systems for bridges, structures, and highways, *Proc. SPIE*, vol. 3325, pp. 212-221, 1998.

Potentialities of multimode fibres as transmission support for multiservice applications: from the wired small office/home office network to the hybrid radio over fibre concept

Christophe Lethien, Christophe Loyez,
Jean-Pierre Vilcot and Paul Alain Rolland
*IEMN CNRS UMR 8520 (Institut d'Electronique, de Microélectronique et de Nanotechnologie) and IRCICA FR CNRS 3024 (Institut de Recherche sur les Composants logiciels et matériels pour l'Information et la Communication Avancée),
Université des Sciences et Technologies de Lille,
France*

1. Introduction

The aim of this chapter is to demonstrate the high potentialities of the multimode fibre to be used as transmission media for multiservice applications inside a building or even in-house (Small Office/Home Office). Most of the building networks are based on multimode fibre topology (90%) for high speed (10Gbps) - short range (<300m) optical networks. A significant increase of the data rate through the corporate Network or the Internet has been observed, due mainly to the explosion of the media exchange (music, Video on Demand (VOD), big data files,...). The IEEE802.3 Gigabit Ethernet Standard is becoming the commonly installed standard in an office network while some specific applications will require a high data rate transmission (for ex. 10Gbps). Moreover, the deployment of the Fibre To The Home concept has been already launched all over the world (Europe, United State, Asia...) under the acronym "triple play" (data, voice and TV over IP). The easy handling and connection of multimode fibre coupled to the high bandwidth capacities open the way to the "Do It Yourself" concept (DIY) for the subscriber.

The first part of this chapter deals with the description of the different candidates able to provide a low cost solution and to support the increase of the data rate through longer range. The description will focus on the fabrication processes, the physical properties and the optical performances (attenuation, optical bandwidth, numerical aperture...) obtained for glass multimode fibre (GMMF) as well as polymer ones (PMMF). In order to satisfy the growing demand of the 10Gbps applications, some manufacturers of optical fibre such as Draka Comteq, Corning or OFS optics have developed new Extended Bandwidth GMMF allowing to transmit high throughput signals (10Gbps) through more than 1000m. These

fibres - principally optimized for an 850nm wavelength operation - exhibit a high Bandwidth-Length product (>6GHz.km) and the well known (more than 30 years old) fabrication process of the GMMF allows to obtain glass fibres with high purity and optimized index profile. These glass multimode fibres enable to reach a good trade-off between cost and performance. Nevertheless, in order to decrease the connection cost of an optical LAN, novel optical fibres less brittle and more flexible than silica ones, based on polymer materials (the PolyMethylMethAcrylate PMMA (Plexiglass) or the fluoropolymer Cytop® (CYclic Transparent Optical Polymer)), have been developed by Asahi Glass and Chromis Fibreoptics. The high attenuation of the polymer based optical fibres as well as their intermodal dispersion induce link length limitation that should reasonably restrict their use to home applications where, by the way, their easy handling should drive to the DIY concept.

GMMF or PMMF exhibit a high transmission capacity when high fibre bandwidth and Coarse Wavelength Division Multiplexing (CWDM) technique are combined and the concept of multiservice application is born around this idea. In fact, the idea is to re-use the existing baseband Ethernet network that is already deployed inside buildings to simultaneously transmit other services thanks to wavelength multiplexing: this is the topic of the second part of this chapter. The improvement of the indoor coverage of wireless communications signals using carrier frequencies up to 10GHz (radiocellular (GSM, DCS, EDGE, UMTS), WLAN (IEEE 802.11a, b, g,...) and WPAN (Bluetooth, Zigbee, UWB) standards...) between different offices located in a building could be realized with the radio over fibre (RoF) concept. RoF concept allows to transport by optical means a radio signal from a central office to multiple remote access points through a fibre network in order to extend the wireless range and to provide a high quality of service (QoS) in term of data rate. Each access point is composed of E/O and O/E converters for the bidirectional transmission as well as active and passive RF devices (amplifier, coupler, circulator...). The required O/E and E/O components are available. Most of them have been developed for GbE or 10GbE applications. Concerning the RF electronics, it has been developed for the different wireless systems under investigation. Different implementations that are able to transmit such signals using multimode fibre (GMMF and PMMF) will be described as well as the obtained performance (Error Vector Magnitude, eye diagram...). Using Ultra Coarse Wavelength Multiplexing (i.e. 850 nm and 1300nm) which is affordable using WDM multimode couplers, the radio over fibre technology can be coupled to the digital baseband transmission on the same multimode fibre converting so this support to a multi-service transmission media. Results of simultaneous transmission experiments will illustrate this aspect.

A last application of WDM use consists in the optical powering of the remote access points that has already been demonstrated over GMMF and can be considered as another complementary service.

All of these topics will be described in this chapter.

1. Physical links (fabrication processes, physical properties...) dealing with the further developments on the Glass Multimode Fibre (GMMF) and the new development on the Polymer Multimode Fibre (PMMF)
2. Wired links using baseband signals (topology, performance...)
3. Radio over multimode fibre systems (topology, performance...)

- 4. Multi-services application: Optical Powering of remote access points in Radio over Fibre systems and simultaneous transmission of baseband and radio signals

2. Description of the multimode propagation channel: from the glass fibre world to the polymer optical fibre concept

The fibres used for optical telecommunications are made of dielectric materials (here, glass or polymer) having the functionality to confine and to guide visible and infrared light over long distances. Generally, an optical fibre is composed of two concentric dielectric tubes (the core and the cladding) each of them with a specific permittivity (or refractive index) value or profile. Under some conditions, the guided propagation of the light along the fibre axis is realized; it occurs in the material having the highest refractive index (fibre core).

Regarding to the core diameter, we can define either singlemode or multimode fibres: the modal behaviour of these two fibres is related to the number of modes propagating inside the fibre core. In this chapter, we focus only on the multimode fibres due to the easiness of connection, relative large modal bandwidth available over short range (typically inside a building) and the fibre compatibility with the low cost infra-red Vertical Cavity Surface Emitting Laser (VCSEL). Because of the large core diameter of such fibres, a large number of modes propagate inside the core where the multipath propagation is governed by the refractive index profile.

The light propagate into the multimode fibre core only if the incident light in front of the fibre's input facet is concentrated inside an acceptance cone (fig. 1) defined as the Numerical Aperture (NA).

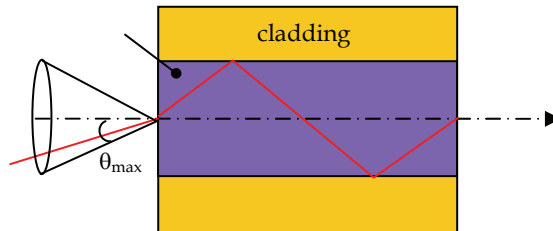


Fig. 1. Definition of the numerical aperture (NA)

The NA is related to the refractive index difference and is independent of the refractive index profile as defined in the relationship (1):

$$NA = \sin(\theta_{max}) = \sqrt{n_{core}^2 - n_{cladding}^2} \tag{1}$$

From the geometric optics point of view, two different kinds of multimode fibres can be distinguished¹:

¹ The ring fibres as well as the W shape fibres do not fill with the application field of this chapter.

- the step index fibre having a step variation (fig. 2a) of the refractive index profile in the transverse plane: the rays inside the fibre core propagate by total internal reflection at the core/cladding interface (fig. 2c)
- the graded index fibre, where the index profile (fig 2b) is optimized to reduce the delays between the fastest fundamental mode (close to the fibre axis) and the higher order modes as shown in fig 2d. This graded index profile allows the enhancement of the modal bandwidth and different optimizations have been and are made to get the different types of multimode fibres particular behaviours.

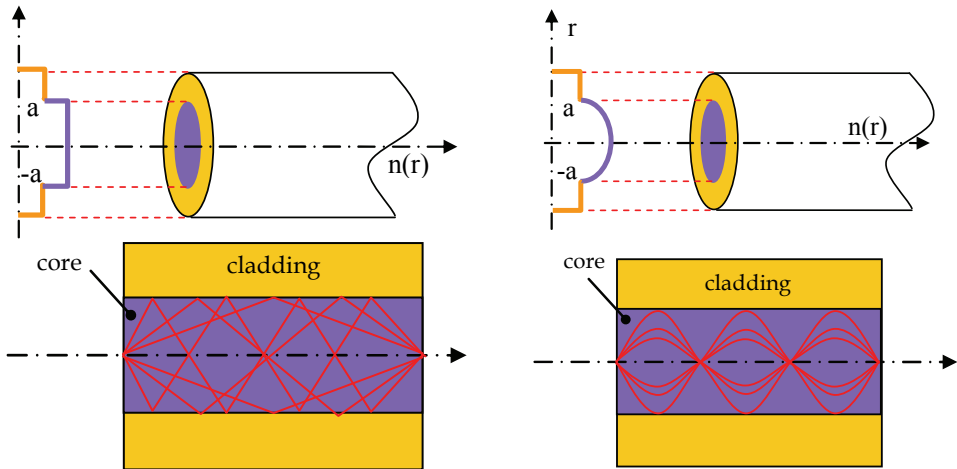


Fig. 2. Refractive index profile of step index fibre (a) and graded index fibre (b). Ray tracing of the multimode propagation inside a step index fibre (c) and a graded index fibre (d).

The graded index profile variation is described by the equation (2).

$$n(r) = \begin{cases} n_{core} \cdot \left(1 - 2\Delta \left(\frac{r}{a} \right)^g \right)^{1/2} & \text{if } 0 \leq r \leq a \\ n_{cladding} & r \geq a \end{cases} \quad (2)$$

where n_{core} and $n_{cladding}$ are respectively the refractive index of the core and the cladding parts of the fibre and a the core radius. The constant Δ is defined by the relationship (3).

$$\Delta = \frac{n_{core}^2 - n_{cladding}^2}{n_{core}^2} \quad (3)$$

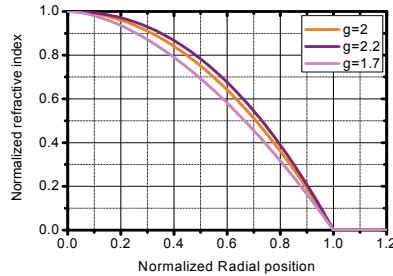


Fig. 3. Refractive index profile as a function of the core index exponent (gradient index type fibre)

In case of graded index fibre, the refractive index profile is determined by the g factor called the core index exponent. In case of the g factor is very close to 2, we define parabolic index or square law multimode fibre (fig. 3).

The ray optics theory does not take into account the relative values of both wavelength (λ) and diameter of the finite ray (Φ_{ray}): the full description of the multimode fibre propagation would be completed with the evaluation of the intensity distribution within the light beam. With the use of the Maxwell formalism related to the wave description for lightwave, the electromagnetic field (E, H) distribution inside the fibre is given by the solutions of the eigenvalue equation (4).

$$\Delta \begin{Bmatrix} E \\ H \end{Bmatrix} + (\omega^2 \mu_0 \epsilon_0 n^2 - \beta^2) \begin{Bmatrix} E \\ H \end{Bmatrix} = 0 \tag{4}$$

where ω and β represent respectively the pulsation and the propagation constant and μ_0 and ϵ_0 , vacuum permeability and permittivity.

Theses solutions represent the mode field distribution not only in the core but also in the cladding. The full resolution of the eigenvalue equation does not cover the field of this chapter but the mode notion had to be introduced. The authors invite the reader to refer to ref [Miller, 1979] describing a detailed resolution of the equation (4). Nevertheless, the total number of propagating modes (N) inside a multimode fibre having a cylindrical revolution and defined by the core radius (a), the refractive index difference (Δ) and the core index exponent (g) is given by the equation (5) whatever the index profile is and by the equation (6) in case of step index profile ($g \rightarrow \infty$):

$$N = \frac{V^2}{2} \cdot \frac{g}{g+2} \tag{5}$$

and

$$N_{step} \approx \frac{V^2}{2} \tag{6}$$

where V represent the normalized cut-off frequency given by the relationship (7).

$$V = \frac{2\pi a}{\lambda} \cdot NA \quad (7)$$

We can notice that the total number of modes is correlated to the core diameter, the numerical aperture, the operating wavelength and the core index exponent. The mode field distribution could be evaluated thanks to the use of the near field distribution measurement. From the communication point of view, an optical pulse travelling over an optical fibre is attenuated and spread due to respectively the material transparency of the fibre core and the fibre dispersion. Regarding to, respectively, the input optical power (P_0) and output optical power (P_L) after fibre propagation (length: L), the fibre attenuation (α) is given by the equation (8). The fibre attenuation α is generally referred to the operating wavelength in the fibre datasheets and could be evaluated over a large spectral range.

$$\alpha = \frac{10}{L} \cdot \log_{10} \left(\frac{P_0}{P_L} \right) \quad (8)$$

The fibre dispersion, that is responsible for the pulse broadening in a multimode fibre, is correlated to:

- the chromatic dispersion
- the intermodal dispersion (owing to the number of propagation modes)

If only one mode is considered (only considering chromatic dispersion), the temporal broadening of an input pulse is induced both by the material dispersion $M(\lambda)$, the spectral width ($\Delta\lambda$) of the light source and the fibre length (L) according to the formula (9).

$$\Delta t_{chromatic} = M(\lambda) \cdot \Delta\lambda \cdot L \quad (9)$$

In multimode fibre communication, the pulse broadening effects related to the intermodal dispersion are determined by both, the number of modes excited in the fibre core and the coupled power into each of these modes. Even if the main part of the optical power is coupled to the fundamental mode group LP_{01} , several groups of higher order modes propagate through the fibre with different optical paths leading to a spreading of the arrival time at the receiver side (fig. 4). The effects on the fibre bandwidth due to the intermodal dispersion caused by the different group velocities of the various modes (or groups of modes) can be minimized by optimizing the index profile versus different criteria (operating wavelength, signal bandwidth, propagation length,...).

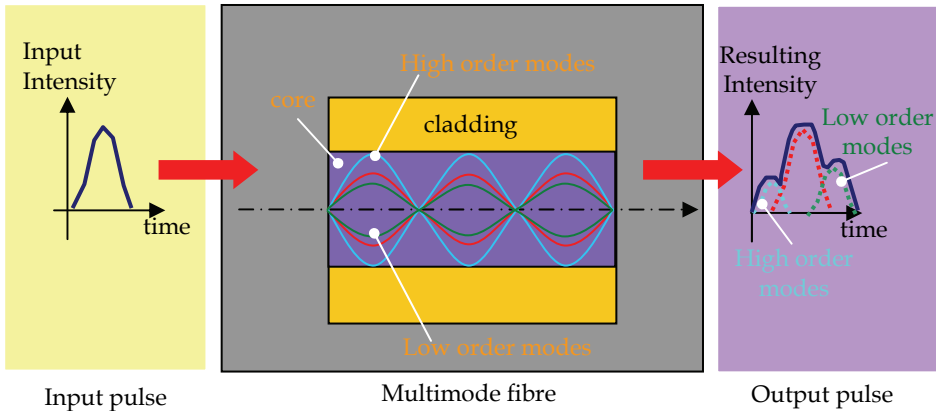


Fig. 4. Illustration of the intermodal dispersion over a multimode fibre

Depending on this index profile and so the wavelength, mode groups propagate at different velocities and the difference in travel time between the fastest and the slowest mode groups is known as the Differential Mode Delays (DMD). On fig. 5, is represented a typical DMD chart showing the pulse spreading after propagation for different launching position at the input fibre facet ($0\mu\text{m}$ means launching just in the centre of the fibre, $20\mu\text{m}$ means launching at $20\mu\text{m}$ away from the centre, launching being made by a small spot).

This DMD parameter is very important in multimode fibre communication and needs to be reduced in order to increase the bandwidth/length product of multimode fibres. The DMD measurements allow to qualify the modal bandwidth of the multimode fibre and has been calculated thanks to the formula (10) derived from [TIA-455-220-A]:

$$DMD = \frac{[T_{slow} - T_{fast}] - \Delta T_{Short_length}}{length} \quad (10)$$

where T_{slow} and T_{fast} represents the trailing edge of the slowest resultant pulse and the leading edge of the fastest resultant pulse measured at 25% of the threshold (Fig. 5). ΔT_{short_length} represents the pulse width (at 25% from the threshold value) obtained on a short length of fibre and the length term is used to normalize the DMD parameter by the fibre length. The DMD is related to the Effective Modal Bandwidth (EMB, also known under laser bandwidth) and the calculated effective modal bandwidth (EMBc, dealing with the “worst case EMB”) defined in the fibre’s datasheets.

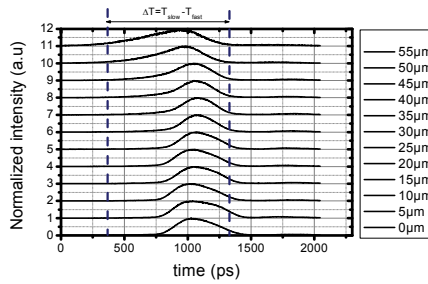


Fig. 5. DMD scanning of a polymer fibre having a 120µm core diameter [Lethien, 2008]

Contrary to single mode fibre (SMF), the modal bandwidth of multimode fibre depends strongly on the spatial distribution of the optical power and so on the modal launching conditions (see DMD chart on Fig. 5). In order to study the evolution of the fibre bandwidth regarding to the launch conditions, a high dynamic range (30dB) test setup [Lethien, 2008] allows the measurement of the response of multimode fibres in both time and frequency domains. Due to the high attenuation of several types of fibres, the test setup must also be designed minimizing extra optical losses. The test setup consists in a picosecond pulse laser (Hamamatsu PLP-10: central wavelength: 850 nm, spectral width: 4nm, pulse width: 70 ps typ.) coupled to free space optics that allow modifying the mode launching conditions at the input of the fibre under test (FUT) (Fig. 6).

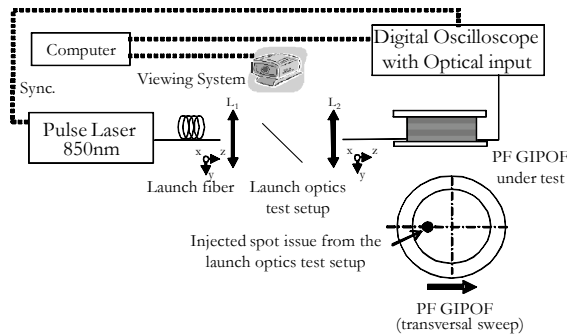


Fig. 6. Bandwidth measurement test setup at 850nm

This launching optics is composed of a launch fibre (SMF, 9 µm core, NA=0.11), two lenses, two 3-axis high precision positioners, one beamsplitter and a viewing system connected to a computer. This optical bench induces 5dB optical losses from the output of the laser source to the input of the FUT. The position of the injection spot regarding to the fibre core is displayed via the viewing system which is disposed on one light path issued from the beamsplitter. The fig. 7 illustrates the displacement of the injection spot on the input facet of the FUT. On the two pictures on the left side, the injection spot is outside the fibre core. This latter fibre is illuminated from its output facet by a visible light source. On the two pictures

on the right side, the spot is launched inside the fibre core and the intensity of the back-illuminating light has been adjusted in order to distinguish the injection spot from the fibre core.



Fig. 7. Offset launch of a restricted spot into a fibre core. From left to right, this injection spot is going from outside the core up to its centre.

Based on the Lagrange-Helmholtz invariant calculus, the diameter of the launched spot as well as its numerical aperture have been determined regarding to the core diameter ($\Phi_{\text{Launch-fibre}}$), the NA ($NA_{\text{Launch-fibre}}$) of the launch fibre and the focal length, f_1 and f_2 , of, respectively, lenses L_1 and L_2 as described in (11) and (12):

$$\phi_{\text{launched-spot}} = \phi_{\text{launch-fiber}} \cdot \frac{f_1}{f_2} \tag{11}$$

$$NA_{\text{launched-spot}} = NA_{\text{launch-fiber}} \cdot \frac{f_1}{f_2} \tag{12}$$

By using the adequate optical lenses and regarding to the available launch fibre (single mode fibre, 50 μm and 62.5 μm core diameter glass multimode fibres...), Any launching conditions, from the overfilled launch (OFL) condition (LED condition) to the restricted mode launch (RML) condition can be then simulated. The OFL conditions are used to define the OFL modal bandwidth and the RML conditions deal with both the DMD and the EMB measurements.

Time domain analysis of the output signal issued from the multimode fibre is made using an optical sampling oscilloscope; this analysis can be converted into the frequency domain using FFT (Fast Fourier Transform). The fibre bandwidth is obtained by de-embedding the frequency domain results issued from the tested length of multimode fibres from the results obtained on a short fibre length (1 m).

2.1 The Glass Multimode Fibre (GMMF): further developments

2.1.1 Manufacturing processes of GMMF

A glass multimode fibre is generally composed of a SiO_2 core doped with Ge surrounded by a SiO_2 undoped cladding layer. The aim of this part is not to present the much known glasses material but to review the three different processes involved by the 3 main manufacturer of glass multimode fibres. Most of the optical fibre is fabricated by the so-called preform methods consisting in realizing a glass rod with diameter from 1cm up to 10cm and nearly 1m length. The optical fibre is then pulled thanks to a fibre drawing tower. The heating of the preform close to the melting point in the furnace localized at the top of the drawing tower allows to pull a thin fibre where the core diameter can be adjusted

according to the pulling speed and the furnace temperature (fig. 8).

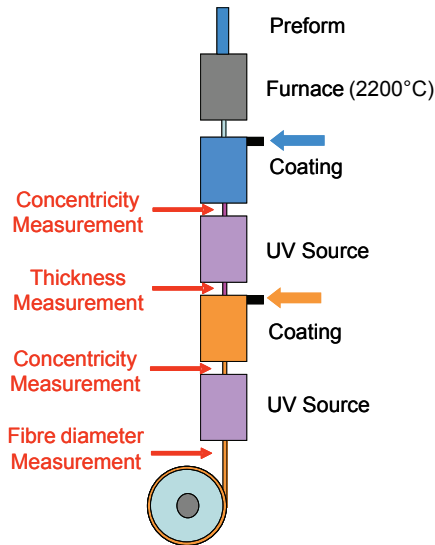
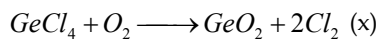
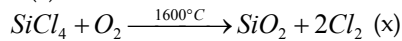


Fig. 8. Overview of a fibre drawing tower

Currently, several processes could be used to manufacture the preform before the fibre pulling:

- The Modified Chemical Vapour Deposition (MCVD) or just called CVD process developed by OFS' optics [MCVD OFS]
- The Plasma-activated Chemical Vapour Deposition (PCVD) process used by Draka Comteq [PCVD Draka]
- The Outside Vapour Deposition (OVD) manufacturing process used by Corning [OVD Corning]

The MCVD process (fig. 9a) is a patented process developed at Bell Labs in the 1970s. A mixture of ultra-pure gases composed by oxygen (O_2), silicon tetrachloride ($SiCl_4$), germanium tetrachloride ($GeCl_4$) and freon (C_2F_6) is sent inside a rotating high purity quartz tube which is heated from an outside source at a temperature close to $1600^\circ C$ (flame). The chemical reactions occurring inside the quartz tube induce the formation of glass soot, resulting to the coating deposition of a thin layer of doped glass particles inside the tube as described in equation (x) and (x).



Then, the mixture of gases is progressively adjusted inside the tube and the process is done again layer by layer to form the complex structure of the fibre core (in case of gradient doping). Once the tube composed by the glass material is collapsed by heating it at $2000^\circ C$, the preform is then fully fabricated and ready for the pulling. Nevertheless, the index profile has to be controlled in order to avoid defects such as centre dips or centre line spike which significantly degrade the DMD and effective modal bandwidth performance.

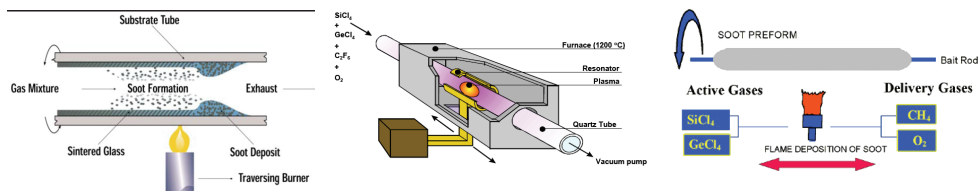


Fig. 9. Description of the MCVD [MCVD OFS], PCVD [PCVD Praka] and OVD [OVD Corning] manufacturing processes

The PCVD [Kuyt, 1999] process (fig. 9b) is similar to the MCVD method: the heating of the deposition region is now realized thanks to the use of microwaves instead of a burner (flame) to form reactive plasma used for the glass deposition.

Unlike the two processes dedicated to inside vapour deposition (external flame or plasma), the Outside Vapour Deposition (OVD) manufacturing process used by Corning consists in forming sequential layers of glass soot around a rotating target rod plunged in a mixture of gases (fig. 9c). The target rod travels through a traversing burner and reacts in the flame to form SiO_2 and GeO_2 fine soot particles. Firstly, the core material (doped silica) is deposited followed by the pure silica cladding. Both the core and the cladding materials are vapor-deposited. With the use of this OVD process, Corning can exhibit the high purity of the entire preform. When deposition is complete, the bait rod is removed from the center of the porous preform, and the preform is placed into a consolidation furnace. During the consolidation process, the water vapour is removed from the preform. This high-temperature consolidation step sinters the preform into a solid, dense, and transparent glass. Regarding to the available manufacturing process to fabricate GMMF and to the Corning point of view, the OVD process seems to provide the best uniformity in term of EMB performance (better refractive index control than the MCVD and PCVD processes). A study performed by Corning [Lopez, 2008] has reported recently that the EMB from GMMF produced by MCVD process demonstrate a 13% difference value contrary to 3% average difference for the ones produced with the OVD process. The presence of centreline dips in the refractive index profile is attenuated with the OVD process contrary to the in vapour deposition processes leading (PCVD, MCVD) to the improvement of the EMB (reduction of the DMD phenomena) as well as the transmission performance.

2.1.2 State of the art of the GMMF according to the modal bandwidth

This part deals with the comparison between the GMMF performance available on the market in term of EMB and attenuation. The GMMF are standardized by the International Electrotechnical Commission (IEC), the International Standards Organization (ISO) and the Telecommunications Industry Association (TIA). The properties of the GMMF [IEC 60793-2-10 - TIA 492AAAA - TIA 492AAAB - TIA 492AAAC - TIA 492AAAD - ISO 11801] issued from the main manufacturers Draka Communications, Corning and OFS optics, especially the OFL bandwidth (MHz.km), the high performance EMB (MHz.km), the numerical aperture, the core/cladding diameters (μm) and the GMMF attenuations (dB/km), are summarized in the table 1 [Draka - Corning - OFS optics].

	IEC	ISO	TIA	Core/ cladding diameters(μm)	α 850nm (dB/km)	α 1300nm (dB/km)	OFL 850nm (MHz.km)	OFL 1300nm (MHz.km)	EMB 850nm (MHz.km)	NA
HiCap	A1b	OM1+	492AAAAA	62.5/125	2.7	0.6	200	600	-	0.275
HiCap	A1a.1	OM2+	492AAAB	50/125	2.2	0.5	600	1200	-	0.2
MaxCap300	A1a.2	OM3	492AAAGA	50/125	2.2	0.5	1500	500	2000	0.2
MaxCap 550	A1a.3	OM4	492AAAD-A	50/125	2.2	0.5	3500	500	4700	0.2
Infinicor CL 1000	A1b	OM1	492AAAAA	62.5/125	2.9	0.6	200	500	385	0.275
Infinicor 300	A1b	OM1	492AAAAA	62.5/125	2.9	0.6	200	500	220	0.275
Infinicor 600	A1a.1	OM2	492AAAB	50/125	2.3	0.6	500	500	510	0.2
Infinicor SXi	A1a.1	OM2	492AAAB	50/125	2.3	0.6	700	500	850	0.2
Infinicor SX+	A1a.2	OM3	492AAAGA	50/125	2.3	0.6	1500	500	2000	0.2
Infinicor eSX+	A1a.2	OM4	492AAAGA	50/125	2.3	0.6	1500	500	4700	0.2
OFS Laser optimized 62.5	A1b	OM1	492AAAAA	62.5/125	2.9	0.6	220	500	-	0.275
OFS Laser optimized 62.5 XL	A1b	OM1	492AAAAA	62.5/125	2.9	0.6	350	500	-	0.275
OFS LaserWave® G+	A1a.1	OM2	492AAAB	50/125	2.3	0.6	700	500	950	0.2
OFS LaserWave® 300	A1a.2	OM3	492AAAGA	50/125	2.3	0.6	1500	500	2000	0.2
OFS LaserWave® 550	A1a.3	OM4	492AAAD-A	50/125	2.3	0.6	3500	500	4700	0.2

Table 1. Summary of current glass multimode fibre properties

The high potentialities of the GMMF described in the table 1 allow to investigate high data rate over long haul transmission with low cost architecture and commercial off the shelf devices.

2.2 The Polymer Multimode Fibre (PMMF): new concept

Only the PMMF with a graded index profile and designed to be used for the telecommunications will be considered in this paragraph.

2.2.1 Properties of the graded index PMMF

The thermoplastic PMMA (Polymethylmethacrylate) has been the first material used for the PMMF fabrication. Known under the acronym Plexiglass®, the PMMA is an organic compound having an amorphous structure of the polymerized material and a glass transition temperature (T_g) close to 100°C. The Plexiglass® is composed of several MMA monomers, each of them showing 8 C-H bonds as described in fig. 10a. The 6th and 5th harmonic waves (occurring at 627nm and 736nm respectively) of the MMA monomer are responsible for the high level of attenuation of the PMMA based PMMF especially from the visible to the infra-red spectral ranges (110dB/km at 650nm). In order to decrease the intrinsic absorption of the PMMA based PMMF resulting particularly from the vibrational overtones, the idea is to perform the partial or complete substitution of the hydrogen compound by heavy atoms like deuterium (also called heavy hydrogen ^2H , a stable isotope of hydrogen having twice the atomic mass of the hydrogen atom) or fluorine atoms. Even if the use of heavy hydrogen induces a significant improvement of the fibre attenuation [Koike, 1996] over the visible spectrum (one order of magnitude), the deuterium based PMMF are very sensitive to the water vapour in the ambient air which is absorbed by the core material leading to an increase of the attenuation².

² In fact, the deuterium is progressively replaced by hydrogen atoms resulting from the water vapour contamination inside the fibre.

Thanks to the use of fluorine atoms to realize the core material, it would be possible to reject the absorption bands (C-F bonds) of the used material into the infra-red spectra, far away from the telecommunication window (850nm - 1550nm). Regarding to the available [Murofushi, 1996] polymer materials (PTFE, PFA...)³, the minimum fibre absorption has been obtained by Asahi Glass Company (AGC) from Japan with the use of the cyclic transparent optical polymer (CYTOP®) which contains only C-F bonds as shown in fig. 10b. The CYTOP® material is an amorphous fluoropolymer having a T_g close to 108°C and where the graded index variation inside the fibre core is realized by copolymerisation of two monomers and by a doping process (interfacial-gel polymerization method).

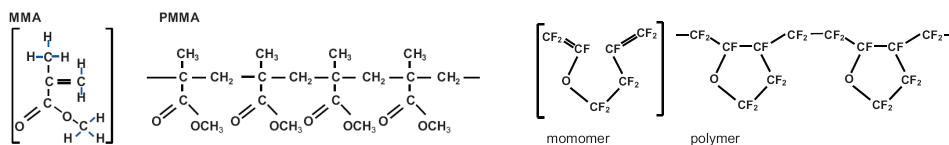


Fig. 10. Molecular geometry and bonding of the Plexiglas® (a) and the CYTOP® (b) materials

Nevertheless, even if the fibre attenuation is going to decrease till 15dB/km at 1300nm (fig. 11) with the use of the CYTOP® material, the calculated attenuation [Murofushi, 1996] threshold is not yet reached mainly due to the extrinsic losses induced by the fabrication process (impurities owing to the gas, material crystallization (scattering centres), contamination and so on). Moreover, the fluorination method using the CYTOP® material is generally expensive due to the complicated reaction steps induced during the material synthesis [Koike, 2009]. Recently, Koike *et al* [koike, 2009] have proposed the use of a partially fluorinated polymer P3FMA (poly (2, 2, 2- trifluoroethyl methacrylate)) to decrease the vibrational absorption due to C-H bonds in PMMA fibres. Thanks to this polymer, an attenuation close to 71dB/km at 650nm has been reached with P3FMA based PMMF. Several manufacturing processes have been reported for the graded index PMMF fabrication and a little synthesis is done for the three following processes:

- the interfacial gel polymerization technique
- the centrifuging process and the combined copolymerization/rotating methods
- the extrusion of several layers

³ PTFE : polytetrafluoroethylene and PFA : tetrafluoroethylene - perfluoroalkylvinyl - ether

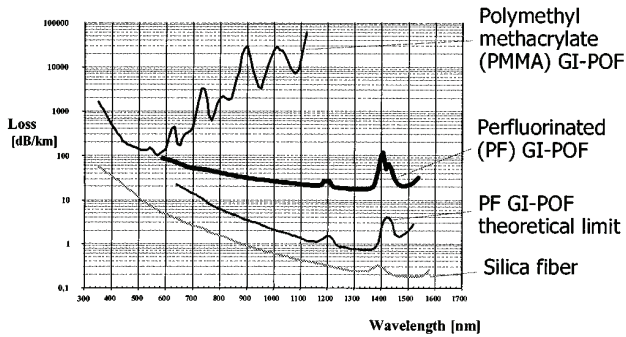


Fig. 11. Spectral attenuation of the graded index PMMF as compared to glass fibre [Van den Boom *et al*, 2001]

Koike *et al* [Koike, 2002 – Koike, 1995] from the Keio University (Japan) have developed the interfacial gel polymerization method to realize the preform (fig. 11). A mixture composed of two kinds of monomers (a classical one and a dopant) has been inserted in a tube (diameter equivalent to the preform diameter) and heated at 80°C to be preliminary liquefied. During this process, the formation of a gel layer is done in the inner wall of the tube (polymer gel phase) and the smaller size monomer diffuses from the edge of the tube to the centre in order to form the graded index profile. The graded index profile is correlated to the dopant distribution inside the preform.

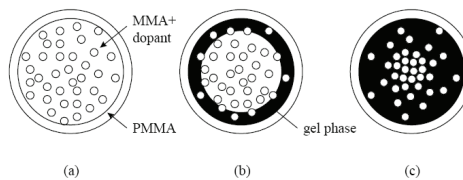


Fig. 12. Interfacial gel polymerization method used by Koike *et al* [Koike, 2002 – Koike, 1995]

Owing to the density difference between the two monomers, the centrifuging method [Duijnhoven, 1999] could be used to produce PMMF preforms. More specifically, a gravitational field is used in the process to generate and to fix compositional gradients in homogeneous mixtures of monomers, mixtures of polymers and polymer-monomer mixtures according to the molecular weight. In this manufacturing method, the rotation speed is kept below 25000 rotations per min (rpm).

The South Korea firm Optimedia head by C.W Park has developed a graded index PMMF based on the PMMA material [Park, 2006] with the use of the copolymerization/rotating methods. Here, a mixture of polymers is filled inside a tube before a polymerisation done either by UV exposure or the increase of temperature. The rotation of the filled tube is only done to provide a symmetrical UV exposure and so a uniform polymerization of the material used to make the preform (fig. 12a).

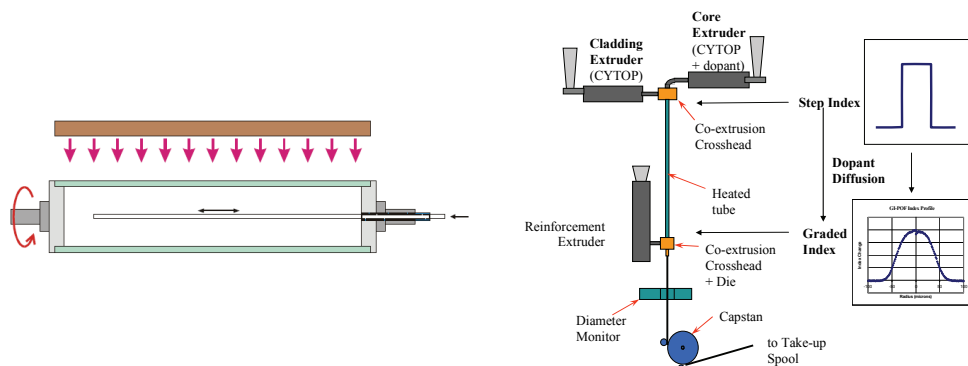


Fig. 13. Manufacturing processes used by Optimedia (Copolymerization [Park, 2006]) and Chromis fiberoptics (co-extrusion process [White, 2005])

The Chromis fiberoptics company head by W. White has performed the fabrication of PMMF based on the CYTOP® material with the use of the co-extrusion process. Two extruders containing respectively the CYTOP® material for the cladding and the CYTOP® fluoropolymer including dopant for the core are used to fill a heated tube (fig. 12b). Owing to the thermally polymerization, the dopant diffuse from the centre to the outer edge in order to form the graded index profile [White, 2005].

2.2.2 Overview of the different polymer fibres used in telecommunication for in building transmission

The fibre length inside a building is generally limited to 300m [Bennet, 2004] and for the application field of this chapter (High data rate baseband transmission, radio over fibre systems) the CYTOP® based PMMF seems to present the suitable properties to achieve the link budget requirement. In fact, the relative low attenuation (~40dB/km) in the expected spectral range [850nm - 1300nm] contrary to the PMMA based PMMF (more than 100dB/km in the visible range) as well as their bandwidth allow using them to design high speed and low losses small office/home office networks. Currently, two manufacturers have been identified for supplying the perfluorinated graded index polymer optical fibres. Asahi Glass Company has commercialized the Lucina PMMF in early 2000 with the use of the interfacial gel polymerization method and good attenuation and bandwidth performance has been obtained (table 2). This fibre has a 120µm core diameter and a numerical aperture close to 0.185. Since April 2009, AGC company has proposed the so named Lucina-X PMMF that includes a double cladding in order to decrease the sensitivity of such fibres to bending effects. Since 2005, Chromis Fiberoptics has developed the co-extrusion process to draw the perfluorinated graded index PMMF. This process is well adapted to mass production. The core diameter of such PMMF [Chromis - Asahi Glass] varies from 50µm up to 120µm (table 2). Actually, only the 120µm core diameter based PMMF Lucina and GigaPOF-120SR have been standardized under the A4G category. A PMMF based on a 62.5µm core diameter has been standardized under the A4h acronym but this type of PMMF has only a 245µm cladding diameter contrary to the GigaPOF-62SR. An update of the IEC-60793-2-40

document [IEC-60793-2-40] will allow to standardize the 50µm and 62.5µm based PMMF from Chromis Fiberoptics manufacturer.

	IEC	ISO	TIA	Core/ cladding diameters (µm)	α 850nm (dB/km)	α 1300nm (dB/km)	OFL 850nm (MHz.km)	OFL 1300nm (MHz.km)	EMB 850nm (MHz.km)	NA
Lucina	A4g	-	-	120/490	18	18	350	-	-	0.185
Lucina - X	A4g	-	-	120/490	18	18	350	-	-	0.185
GigaPOF-50SR				50/490	40	40	300	-	-	0.19
GigaPOF-62SR	A4h?			62.5/490	40	40	300	-	-	0.19
GigaPOF-120SR	A4g	-	-	120/490	40	40	300	-	-	0.185

Table 2. Overview of the commercially available PMMF

To conclude on the glass and the polymer multimode fibres, some backscattering traces realised on 4 PMMF and 1 GMMF are presented.

The backscattering technique (fig. 13) has been used to localize the defects in the fibre core and to determine the fibre length. The main intensity peak, due to the Fresnel reflection of the propagated light at the end of the fibre (polymer or glass/air interface at the connector), is localized close to 200m for all the fibres. Defects are materialized by the smaller backscattering peaks that appear all along the propagation. The PMMF issued from the Chromis Fiberoptics manufacturer (more particularly the 50µm sample) exhibit so some defects unlike the PMMF from the Asahi Glass (Lucina). The Draka GMMF Maxcap550 exhibits an uniform shape due to the low spectral attenuation and the absence of scattering losses in the fibre core.

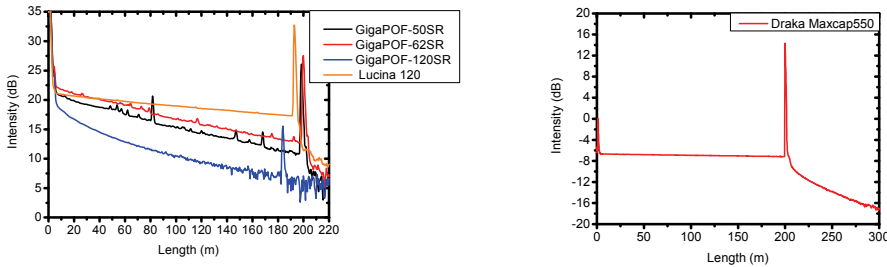


Fig. 14. Backscattering traces of the Lucina (PMMF) and the Chromis Fiberoptics fibres (PMMF) as compared to the Draka Maxcap550 (GMMF)

In spite of the attenuation, the PMMF are very challenging due to their easiness of connection. No expensive tools are required to provide a clean facet of the fibre contrary to the silica fibre world. Clip-on connectors have been developed by Nexans and Chromis Fiberoptics to be fixed on the external coating of the PMMF which favour the *Do it Yourself* concept. Nevertheless, the bandwidth potentialities of the PMMF do not reach the GMMF especially with the deployment of the new OM4 fibre designed for high speed and long haul distribution (1km) inside a fibre network. The PMMF attenuation needs also to be improved in order to increase the link budget and to be competitive against the GMMF.

Nevertheless, regarding to the promising material dispersion, the PMMF based on the CYTOP® material should provide better performance in term of bandwidth capacities. The fig. 14 presents the dispersion of the three materials used to develop either GMMF or PMMF.

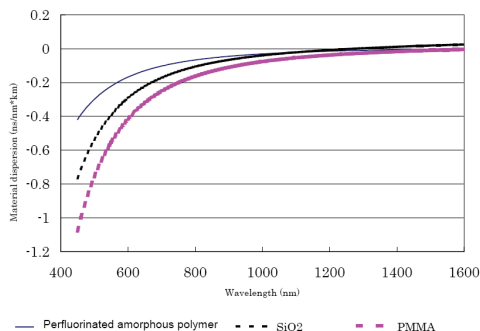


Fig. 15. Comparative study of material dispersion used in GMMF and PMMF [Asahi Glass]

3. Optical transmission of baseband multi-gigabit signals over multimode fibres

3.1 Multi-gigabit transmission over the GMMF

In 2002, Pepeljugosky *et al* [Pepeljugoski, 2002] have demonstrated the potential of high modal bandwidth GMMF to be used for a 15.6Gbps transmission over 1km at 850nm. Successful transmission of 20Gbps over 200m is also reported with the same fibre at 850nm. The 40Gbps transmission over high modal bandwidth GMMF has been reported by Matthijsse *et al* [Matthijsse, 2006] at 1300nm over more than 400m link length. A special fibre has been pulled to optimize the bandwidth at 1300nm (5.3GHz.km) and several launch conditions have been tested from the centre launch to the radial overfill launch. A singlemode to multimode fibre coupling is realized at the emission and a multimode fibre taper is used at the receiver side in order to focus the light issued from the multimode fibre core (50µm diameter) to the active area of the used photodiode (~14µm). Good 40Gbps transmission performances were so reported over 40nm wavelength window which demonstrated the huge tolerance of the operating wavelength when using such high modal bandwidth GMMF inside a high data rate fibre network.

3.2 Multi-gigabit transmission over the PMMF

The high attenuation of the polymer based optical fibres as well as their intermodal dispersion induce link length limitation particularly at 850nm. In fact, Pedrotti *et al* [Pedrotti, 2006] report the state of art of the multi-gigabit transmission over PMMF: most of the presented works exhibit a bit rate-length product less than 1Gbps.km. Li *et al* [Li, 1999] report a high bit rate-length product but with the use of APD receivers not compatible with low cost systems. Giaretta *et al* [Giaretta, 2000] have realized an 11Gbps transmission over a range less than 100m by using a 1300nm FP laser and coupling optics which are not suited

for a low cost 10Gbps optical network.

In [Lethien, 2008], it has been proposed to investigate the use of conventional low cost devices such as VCSEL (Vertical Cavity Surface Emitting Laser) and PIN photodiodes with plastic fibre in order to have a pragmatic approach of the future high speed optical network. Phyworks technology [Phyworks], based on the use of Electronic Dispersion Compensation devices (EDC) placed at the electrical output of a conventional photoreceiver (here, a GaAs photodiode), has been used. The EDC technology allows overcoming the modal dispersion of the multimode fibres either in glass or polymer. Phyworks company wants to produce 10Gbps TX/RX module including VCSEL TOSA (Transceiver Optical SubAssembly) and driver for the TX part and photodiode ROSA (Receiver Optical SubAssembly), EDC and transimpedance amplifier (TIA) chips for the RX part with target price of less than 200\$ per module. The coupling pair EDC/TIA cost should be around 55\$ (low cost devices contrary to the ones used in the previous studies [Pedrotti, 2006], [Li, 1999], [Giaretta, 2000]). The EDC technology is a cost effective solution to struggle the intermodal dispersion inherent to the optical link based on the multimode fibre. The Phyworks serial EDC replaces the existing Clock Data Recovery (CDR) of a classical XFP transceiver.

The transmission of a 10.3125Gbps baseband signal over 4 polymer fibres (GigaPOF50-SR, GigaPOF62-SR, GigaPOF120-SR and Lucina) have been performed (fig. 15). As mentioned previously, the study done by Giaretta *et al* [Giaretta, 2000] has been achieved at 1300nm and with a 130 μ m core diameter PF GIPOF. This fibre has been excited in restricted mode launch conditions with the use of a single mode fibre coupled to the 1300nm laser in order to decrease intermodal dispersion effects. Moreover, in order not to induce mode filtering at the receiver and to reduce the coupling losses due to the large core diameter of the fibre, Giaretta *et al* have used a collimating lens and a focusing lens inducing 4.8dB coupling losses.

The study reported by Lethien *et al* [Lethien2, 2008] is realized at 850nm (low cost 10G XFP transceiver) and without adaptive optics due to the fibre core diameter. In order to exhibit the power dispersion penalties for all the fibres under test, we have measured the BER as a function of the received optical power in the back-to-back case and by inserting the required length corresponding to the 4 fibres under test.

The BER measurements realized on the GigaPOF50-SR PF fibre did not provide goods results (no error free in all case even if we remove the optical attenuator due to a default of concentricity of the fibre core regarding to the cladding). The exhibited power dispersion penalties are summarized for a BER= 10^{-9} in the table 3.

	From Chromis fiberoptics manufacturer			From AGC Manufacturer
Fiber type	50A	62.5A	120A	120B
With EDC	-	3.5	4	3.5
Without EDC	-	6	>9	9

Table 3. Measurement of the power dispersion penalties (dB) of the optical link

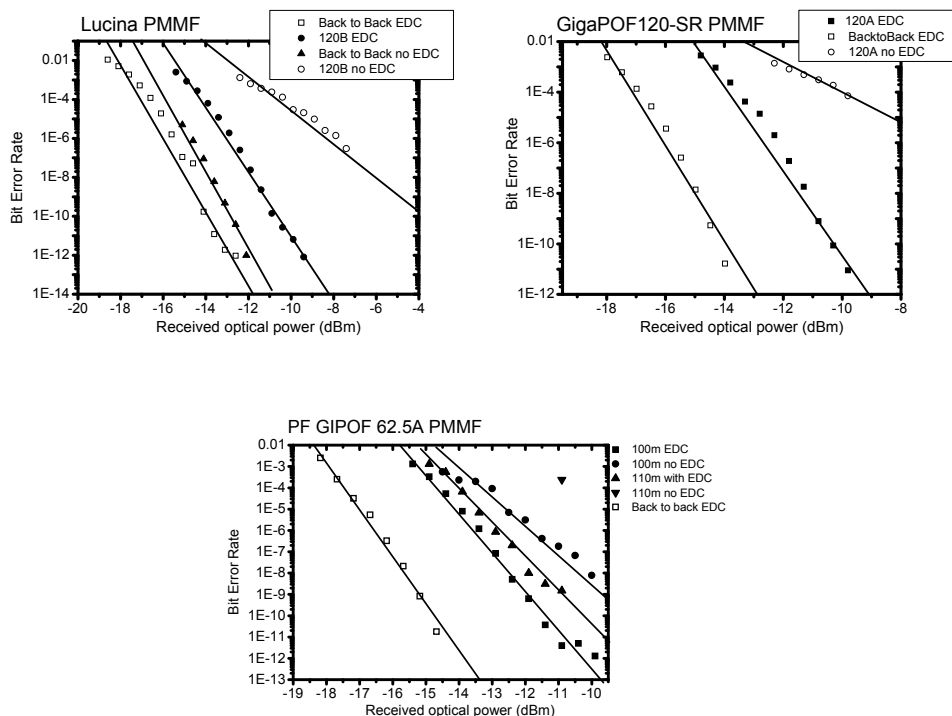


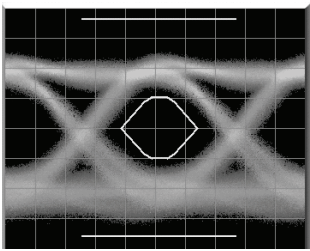
Fig. 16. BER as a function of the received optical power

The 3 presented PMMF coupled to an EDC device exhibit power dispersion penalties around 4dB. These penalties are inherent to the modal bandwidth of the fibre. As described in the datasheets of the Picolight XFP module, the worst case distance range of a 10.3125Gbps signal over a 50/125 GMMF with a Bandwidth-length product of 400MHz.km (500MHz.km) is 66m (82m). These BL products have been given in order to have a comparative reference with the measured modal bandwidth of the 4 PMMF under test. As mentioned previously, the 50µm based PMMF cannot transmit such kind of high bit rate signal. The two 120µm core diameter PMMF exhibit a power dispersion penalties around 3.5dB with the use of an EDC device and 9dB without dispersion compensation.

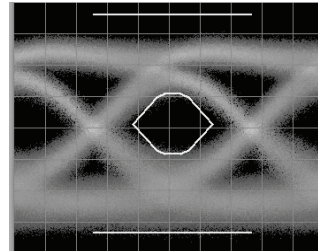
The number of propagation modes in an optical fibre depends on the core diameter. The 120µm PMMF owns a larger core diameter than the 62.5µm based PMMF. By the way, the propagated modes in the 120µm - core fibre are much numerous in that case. The intermodal dispersion in the large core PMMF is then much higher than in the GigaPOF62-SR fibre. These results have been demonstrated by the power dispersion penalties measurement in between the two fibres without the use of an EDC device (5dB for the 62.5µm PMMF compared to 9dB for the 120µm PMMF). Nevertheless, all these power dispersion penalties have been induced not only by the modal bandwidth limitations of the

fibre but also by a mode filtering at the receiver (active area # $70\mu\text{m}$).

The transmission of a 10Gbps signal has been achieved over 100m of the $62.5\mu\text{m}$ core diameter PMMF with a $\text{BER}=10^{-12}$. The length of the optical link realized with the used fibre is higher than the range of the optical link based on GMMF provided in the datasheets of the Picolight module (BL product # 400-500MHz.km – length 66m/82m). The additional range gained with the use of an EDC device at the photoreceiver side is equal to 18m which demonstrated the potential of the dispersion compensation devices coupled with the $62.5\mu\text{m}$ core diameter based perfluorinated based PMMF. In the fig. 16, the mask testing measurements regarding to the transceivers type including and not EDC devices are performed on the GigaPOF62-SR (100m length). By using the conventional photoreceiver (RX part of the low cost Picolight XFP), the BER is closed to 10^{-7} and set around 3.10^{-12} with the use of the EDC device. The eye opening is then higher with the use of the EDC device. It has been shown that the EDC device enhances the signal quality by reducing the intersymbol interference phenomena which demonstrates without any doubt the potential of this kind of device.



GigaPOF62 with EDC



GigaPOF62 without EDC

Fig. 17. 10GBase-SR mask testing of the 62.5A PF GIPOF

The 40Gbps transmission over 30m of the GigaPof-50SR both at 1550nm and 850nm has already been reported by [Polley, 2007]. An increase of the link length is then realized by the same group and similar transmission over the perfluorinated based PMMF having a core diameter value close to $50\mu\text{m}$ has been yet demonstrated by Polley *et al* [Polley, 2008]. The link is limited to 100m and the laser is a FP laser operating at 1315nm.

In 2007, a precise comparative study between GMMF and PMMF has been performed regarding to the sensitivity of such fibres to the offset launch for data rate close to 40Gbps and link length less than 100m [Schöllmann, 2007]. The feasibility of error free transmission at 1550nm with either 100m of GMMF (OM3 type) or 50m of PMMF (GigaPOF50-SR) is so demonstrated for 40Gbps signal. To obtain such results, offset launches close to $\pm 3\mu\text{m}$ for the GMMF and $\pm 10\mu\text{m}$ for the PMMF have been exhibited.

4. Radio over Fibre (RoF) systems

Radio over Fibre (RoF) systems use optical carriers to distribute micro- or millimeter-wave signals. Contrary to the previous part dedicated to baseband signals, the RoF concept deals with narrow band or broadband signals exhibiting a modulation bandwidth between several MHz (for narrow band signal) to more than 500MHz for the future Ultra Wide Band signals. In spite of the reduced bandwidth, high data rates combined with portability could be obtained. Such systems are used on applications, such radars, on several kilometres spans. An interesting use of these systems in telecommunications is to distribute wireless telecom signals all over an indoor or shadowed area. In that case, multiple access points are needed on a coverage zone that is typically less than 1km diameter wide. The concept is then declined as a picocellular system in which each elementary cell covers a maximum of some hundreds of meters. But most of time, these elementary cells will cover a unique space or room (fig. 17). The coverage of a building can then be done using a central office which receives/emits signals either by radio or fibre optics systems and distributes them to a multitude of remote antenna units which are optically fed. These remote antenna units deliver the downlink signals and receive the uplink ones within their dedicated picocell area.

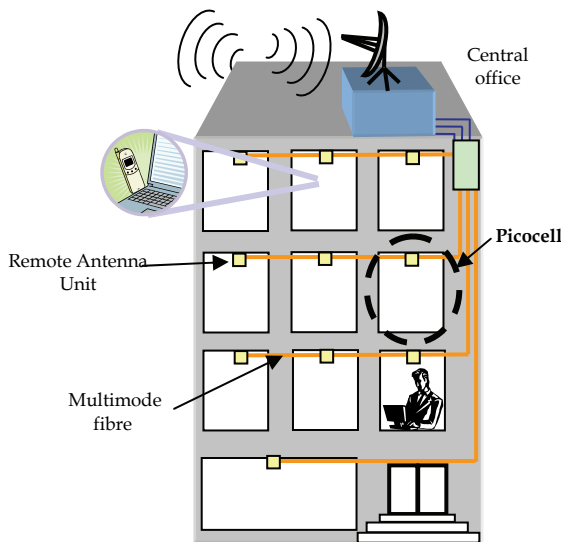


Fig. 18. Schematic of radio over fibre picocellular indoor system.

Two kinds of systems can be distinguished. The first one deals with RF signals having a carrier frequency up to 10GHz and is mainly dedicated to the optical transport of wireless communication bands, wireless signals. In that case, the RoF system acts as a relay for these signals. The second one is more advanced and is based on an optically generated micro- or even millimetre wave signal (up to 60GHz frequency bands); the achievable data rate could be then as high as several hundred of Mbps and up to the Gbps. These systems are dedicated to the transfer of huge amount of data within the same building such as hospitals

or banks. They can act as stand-alone internal systems without any external connections. This application field dealing with the millimetre wave RoF system is covered in another chapter of this book.

An overview of the wireless signals used in a radio over fibre systems will be performed just before the description of the RoF topologies and RoF systems.

4.1 Evolution of the Wireless communications networks

The radio over fibre concept complies with the radio spectrum dedicated to broadcast and wireless applications having a carrier frequency up to 1GHz (AM and FM radios, TV broadcast...). The RoF system covers also the microwave as well as the millimetre waves (radiocellular, WLAN, WPAN...) with carrier frequency from 1GHz up to 100GHz.

From a radio frequency point of view, a radio signal is disturbed when the propagation is done in a confined space, for example inside a building or a tunnel. The aim of a RoF deployment is either to improve the indoor coverage of a wireless signal or to increase the connectivity of an ad-hoc network. This chapter focuses only on wireless standards mainly created by the major normalization organisms (IEEE, ETSI, 3GPP, 3GPP2...) and generally divided into three main categories depending on the application field:

- the radio-mobile signals
- the Wireless Local Area Network (WLAN) standard
- the Wireless Personal Area Network (WPAN) standard

The radiocellular concept deals firstly with the deployment of the 2nd generation of mobile equipment (ME). Depending of the country where the mobile network is implemented, several standards have been investigated. The 2nd generation of the radio-mobile standard (IS-136 ; GSM ; PDC and PDC-P ; cdmaoneA) has a data rate limited to 14.4kbps except for the PDC with 30kbps value.

Before the deployment of the 3rd generation, an intermediary step is added and known under the 2.5 generation (IS-136+; GSM/GPRS or GSM/HSCSD ; cdmaoneB; cdma2000 phase 1) in order to provide furthers services requiring much data rate (internet, video exchange...). Theoretically, the data rate is close to 100kbps. The EDGE radiocellular standard corresponding to an improvement of the GSM one is used for data transmission at 384kbps. The 3rd generation of mobile networks is deployed with throughput up to 2Mbps all over the world for responding both to the exponential growing of video media exchanges and the internet traffic. The main problem is related to the inter-operability between the different standards deployed all over the world (IS-136HS, UMTS, cdma200 phase 2). The convergence of the three last cited standards is known under the HSDPA and HSUPA acronyms (High Speed Downlink/Uplink Packet Access) linked to the 3.5th generation deployment: the data rate is close to 14.4Mbps. In 2010, a new emerging standard is going to be deployed as the future radio-mobile standard. The Long Term Evolution (LTE) represents the future of the UMTS standard as it evolves from an architecture supporting both circuit-switched and packet-switched communications to an all-IP, packet-only system. The so-called LTE is related to the 3.9th generation and provides throughput up to 300Mbps with a specific quality of services (QoS) depending on the mobile speed (Optimized performance for low mobile speeds from 0 to 15 km/h - supported with high performance from 15 to 120 km/h - functional from 120 to 350 km/h). The QoS of mobile communications with speed comprising between 350 to 500 km/h is currently under

consideration. Regarding to all the radio-mobile generations, the carrier frequency of such wireless networks is comprised between 900MHz and 2.62GHz.

The indoor coverage of a signal issued from a Wireless Local Area Networks (WLAN) is very sensitive to the material used to fabricate the building. The main WLAN standard is the Wireless-Fidelity, known under the acronym WiFi or IEEE802.11. Several declinations of such standard are related to the data rates and the operating frequency. The table 4 summarizes the basic properties of the WiFi standardized by the IEEE organism. The data rate varies from 11Mbps up to 54Mbps depending on the standard release. The IEEE802.11a has been used in United States. The IEEE802.11b and IEEE802.11g are dedicated to Europe. The radio range is generally close to 140m in free space configuration and is reduced for in building communications (35m) as well as the bit rate.

	IEEE802.11a	IEEE802.11b	IEEE802.11g
Carrier frequency	5.825 GHz	2.412 GHz	2.412 GHz
Modulation scheme	64QAM - OFDM	CCK - DSSS	64QAM - OFDM
Data rate	54Mbps	11Mbps	54Mbps
filter	BT = 0.5	BT = 0.5	BT = 0.5

Table 4. Overview of the IEEE802.11 standard

In June 2009, the IEEE802.11n will be expected to propose high data rate (250Mbps) and long range transmission inside a building (more than 70m) especially thanks to the use of multiple antennas (Multiple Input Multiple Output system (MIMO)).

In order to develop personal network without cable (Wireless Personal Area Network - WPAN) for computer office applications or radio mobile systems, several protocol have been created either for low or high data rates transmission. A standard created by Ericsson in 1994 (Bluetooth) for low bit rate wireless communication has been used over the unlicensed ISM band (2.4GHz). The data rate is close to 3Mbps and the radio range is limited to 10m when emitting less than 1mW RF power level. Launched by Nokia, the Wibree has been created to provide a short radio range (5m) and low data rate standard with a fewer consumption than the Bluetooth (better than a 50 factor). The Wibree is unfortunately incompatible with the Bluetooth and since June 2007, a fusion between the two standards has been created over the "Bluetooth ultra low power". An oriented low consumption wireless sensor networks (WSN) standard known under the acronym Zigbee (IEEE802.15.4) and using the ISM 2.4GHz unlicensed frequency bands in Europe has been used for domotic applications. The data rate is well limited to 250kbps and a new modulation scheme is under development with the use of ultra wide band concept.

The Ultra-Wideband standard (UWB) is becoming the common wireless technology for short haul - high data rate wireless communications and sensor networks. Regulated by the Federal Communications Commission (FCC) in the USA since April 2002, the UWB technology operating in the frequency range between 3.1GHz up to 10.6GHz and two proposals of this standard have been investigated by laboratories and manufacturers depending on the modulation schemes in the IEEE 802.15.3a working group. The standardization of the high data rate (>200Mbps) ultra-wideband technologies has been firstly studied. The Direct Sequence (DS) and the Multiband Orthogonal Frequency-Domain Multiplexing (MB-OFDM) ultra-wideband technologies are in competition and the

supporting organizations who support each proposal continue to promote them outside of the IEEE task group. The DS-UWB [Yao, 2007] is based on the use of the position, amplitude or phase modulation of a sub-nanosecond pulse and is supported by the UWB Forum. The standard jointly published by the Wimedia alliance and the Multiband OFDM alliance defines the specifications of the OFDM physical layer and is known under the name ECMA-368 (ISO specifications). This ECMA Standard [ECMA 368, 2007] specifies the ultra-wideband physical layer (PHY) and medium access control (MAC) sublayer for a high-speed short haul wireless network, utilizing the frequency range described above and supporting data rates of up to 480 Mbps. The ECMA-368 standard is divided into 14 unlicensed bands, each with a bandwidth of 528 MHz (fig. 18). The first 12 bands are then grouped into 4 band groups, each of them being composed of 3 frequency bands. The last two bands are grouped into a fifth band group. The sixth band group consists of bands 9 to 11 which overlaps band groups 3 and 4. The Wimedia standard uses the MB-OFDM modulation scheme to transmit information through a wireless personal area network (WPAN). A total of 110 sub-carriers (100 data carriers and 10 guard carriers) are used per band. In addition, 12 pilot subcarriers that allow for coherent detection bring out a total of 122 subcarriers spaced 4.125MHz apart. The occupied bandwidth is nominally 528MHz and the signal subcarrier could hop in frequency according to predetermined patterns known as Time-Frequency Code (TFC). The MB-OFDM UWB standard provides throughput from 53.3Mbps up to 480Mbps depending on the modulation schemes over 2m to 10m range. The power spectral density is closed to -41dBm/MHz over the UWB spectrum. QPSK modulation is used for data rates up to 200Mbps and Dual Carrier Modulation (DCM) scheme is dedicated to 320, 400 and 480Mbps throughput: the DCM modulation consists in the grouping of 4 bits onto two separate constellation maps to obtain the same structure that of a 16QAM modulation scheme. Each of these 16QAM constellations is then modulated onto two subcarriers spaced 206MHz apart allowing to decrease the probability that both suffer simultaneously from fading. Since March 2007, the ECMA-368 standard has been recognized as the ISO/IEC 26907 international standard (ISO/IEC 26907:2007 Information technology -- Telecommunications and information exchange between systems -- High Rate Ultra Wideband PHY and MAC Standard).

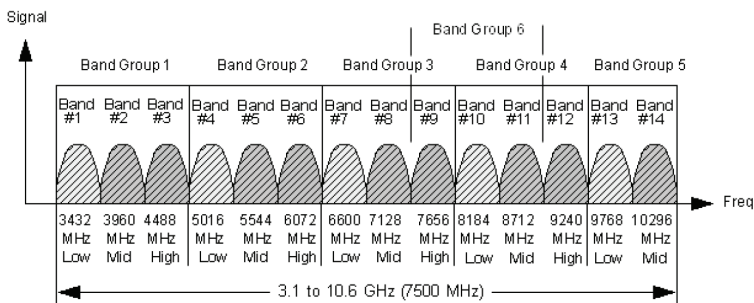


Fig. 19. Allocation of the frequency bands for UWB band groups [2]. Each band has a 528MHz bandwidth and central frequency is indicated.

All the radio standards presented in this part could be evaluated with the use of modulation quality metrics such as the Error Vector Magnitude or the Relative Constellation Error (RCE) given by the standardization organisms (ex: IEEE, ETSI...). The Error Vector Magnitude - expressed in percentage or dB - is defined as the vector difference at a given time in between an ideal reference signal and the measured signal submitted to residual noise and distortion induced by the radio over fibre system (fig. 19).

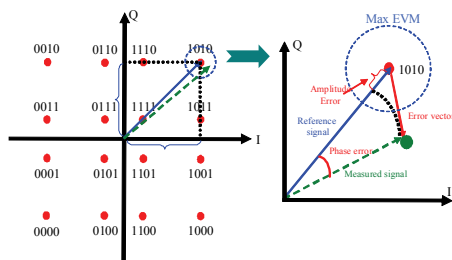


Fig. 20. 16 QAM modulation scheme and schematic view of the Error Vector Magnitude parameter

As mentioned previously, the improvement of the indoor coverage of all the presented standards could be realized with the use of the radio over fibre concept and the main topologies are described in the next part.

4.2 Topologies used for the distribution of radio signal over the optical fibres

According to A. Seeds point of view [Seeds, 2002], the availability of the first semiconductor lasers and electro-optic modulators combined with the development of the low loss silica optical fibres (either singlemode or multimode) as well as the development of PIN and avalanche photodetectors since 30 years has lead to the birth of the radio over fibre technology. For indoor or shadow area coverage of radio communications systems, picocellular RoF systems are fine alternatives since they allow distributing signals where global distribution systems are ineffective. Their coverage range is some tens to hundred meters. A typical system uses a base station which optically fed remote antenna units with the RF signal which is modulated on the optical carrier. Since the coverage is rather small, electromagnetic pollution can be greatly reduced since emitted RF power can be 30 dB lower than for classical systems, i.e. 20 mW in spite of 20W. This optical carrier is carried on optical fibre up to the remote antenna units. The application field of this chapter is related to the multimode fibre either in glass or polymer and whatever the optical carrier and wavelength are, the transmission of signals can be achieved using three main schemes.

4.2.1 Baseband over fibre (BB over Fibre)

The radio signal is received and the data are extracted (A/D) as a binary sequence in the central office. These data are used to modulate the optical emitter (EO). At the remote antenna unit, once detected (OE) they are converted (D/A) to modulate a RF carrier (provided by a Local Oscillator that is locally generated) (fig. 20). These data are use to modulate the optical emitter (EO). At the remote antenna unit, once detected (OE) they

modulate again (D/A) a RF carrier (provide by a Local Oscillator) that is locally generated (fig. 20). This topology adds complexity and cost in each remote antenna due to the embedded required electronics. Anyway, it is the less stringent on optical link requirements since only the data stream (less than 1Gbps data rate) is carried on it. The GMMF or PMMF fibres are considered to be the low cost solution here but obviously SMF can be used with an increase in the connection cost. Transceivers are here digital transceivers as used in GbE transmission.

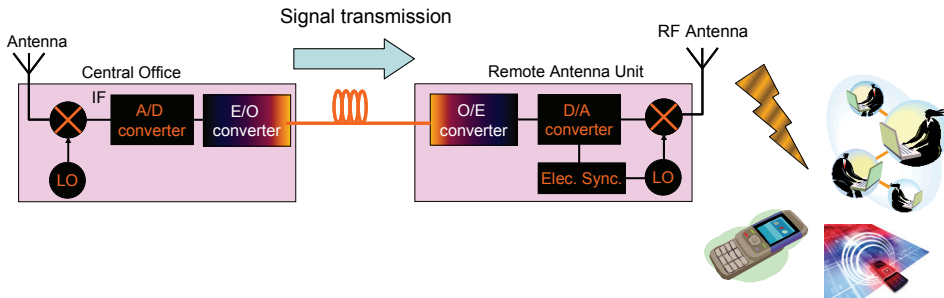


Fig. 21. Data over fibre transmission scheme

4.2.2 Intermediate Frequency over Fibre (IF over Fibre)

The radio signal is down-converted to a lower frequency and the resulting IF signal is sent through the fibre. At the remote antenna unit, this IF signal is mixed with a local oscillator one to re-generate the RF signal (fig. 21). This scheme adds lower complexity at remote antenna units that the previous one since only RF circuitry is needed. We are now dealing with an analog optical transmission link. The same comment as above concerning the type of fibre that can be used can be made.

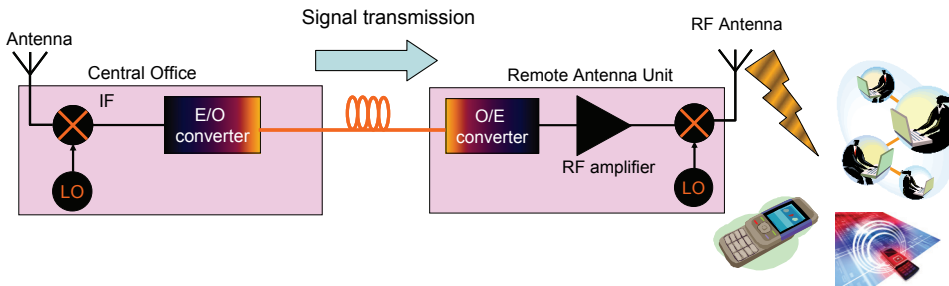


Fig. 22. IF over fibre transmission scheme

4.2.3 RadioFrequency over Fibre (RF over Fibre)

This is the simplest way of implementation as well as the lower cost for the remote antenna units. The RF signal directly modulates the emitter and is directly re-emitted at the remote antenna unit (fig. 22). But this scheme requires enhanced performance for the optical emitters and receivers since they have to transmit the carrier frequency of the radio signals.

If that one is roughly below 10 GHz, this transmission scheme shall be affordable, above 10 GHz, IF over fibre scheme shall be considered as a more potential cost effective solution.

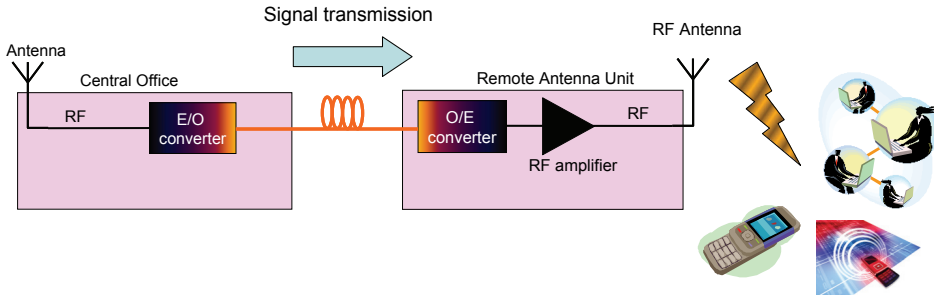


Fig. 23. RF over fibre transmission scheme

4.2.4 Architecture of a bidirectional access point

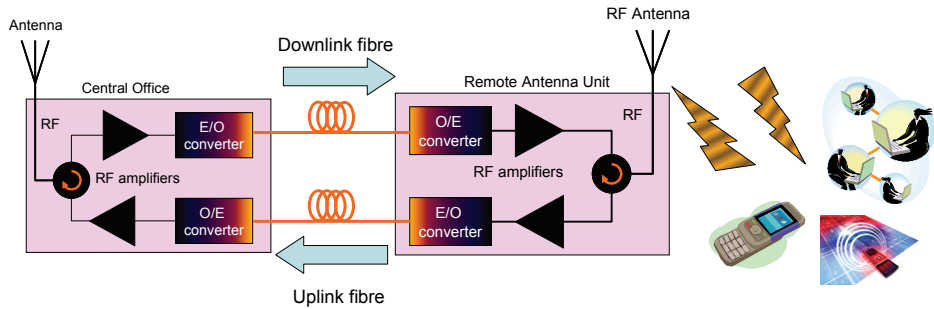


Fig. 24. Schematic view of a bidirectional access point

In order to realize the bidirectional aspect of the radio link (up and downlink), the remote antenna unit has to integrate both an E/O emitter, an O/E receiver and the RF circuitry able to achieve the corresponding topologies (BB over fibre, IF over fibre and RF over fibre). In the fig. 23, the easiest RF over fibre topology is described just with the use of a RF circulator to separate the up and down streams. Regarding to the link budget of such RoF system (mainly 30dB RF losses), RF amplification has to be done to overcome the RF losses either in downlink with the use of a Medium Power Amplifier (MPA) or with a Low Noise Amplifier (LNA) able to provide a small noise factor for the uplink.

4.3 State of the art of the Radio over multimode fibres system

The previous part has demonstrated the potential of the radio over multimode fibre technology to improve the indoor coverage of radio signals between different offices located in a building where a multimode fibre based network has been already deployed. As described, the radio over fibre (RoF) technology allows to optically transport a radio signal through an optical fibre and so to extend the wireless range beyond 10m. The pragmatic approach of these studies, based on the use of multimode fibres either in glass or polymer

associated with commercial off the shelf (COTS) devices (Vertical Cavity Surface Emitting Laser (VCSEL) and photodiode), induces the use of the intensity modulation - direct detection technique (IM-DD) without sophisticated architecture.

In the following, we will consider in most of the case the RF over fibre topology since it is potentially THE low cost solution owing to the fact that very few electronics are required within the remote antenna units. This solution will be even more effective if transmission can be done on multimode fibre that constitutes the main part of the pre-installed fibres in buildings for gigabit Ethernet applications. The modal characteristic of this kind of fibre restricts the system bandwidth but high modal bandwidth multimode fibres have been developed as described previously. Therefore, Wake *et al* [Wake, 2001] demonstrated that it is possible to overcome this limitation even transmitting complex modulation schemes (32 QAM) having a bit rate of 10Mbps on a RF sub-carrier (2 GHz) through 1 km of GMMF OM2 at 1.3 μ m. On fig. 24, the constellation as well as the eye diagrams of such a signal is represented before and after the optical transmission. As it can be observed, no real degradation appears even considering the bandwidth of the optical fibre is 500MHz.km. This work is considered as the beginnings of the radio over multimode fibre concept.

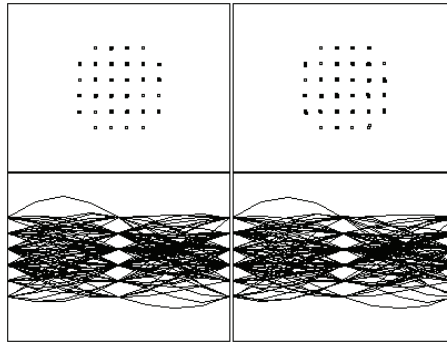


Fig. 25. IQ Constellation (top) and eye (bottom) diagrams of a 32 QAM signal on 2 GHz RF carrier before (left) and after (right) its transmission on a GMMF based RoF system [Wake, 2001]

4.3.1 RoF system developed with GMMF

The joined researches lead both by the University of Cambridge and the University College London in the Friday (Fibre Radio for In-building Distributed Antenna sYstems) project are focused on the market dealing with the extended coverage of second generation (2G), 3G mobile and WLAN networks in deployment areas such as corporate office buildings, shopping centres and airports [Wake, 2002]. The indoor coverage of such signals can only be improved using distributed antenna systems (DAS) within the building since the signal penetration from outside base stations is unreliable (fig. 25). In the Friday project, the exploitation of low-cost solutions (850nm VCSELs and subcarrier transmissions over pre-installed multi-mode fibre (MMF)) is performed to design and implement a low-cost and multi-services fibre-based DAS (GSM (900MHz and 1800MHz), UMTS (2GHz) and WLAN (5-6GHz)). The topology used for optically deport both the IEEE802.11a and IEEE802.11g

WLAN standards in the Friday project is presented on the fig. 25.

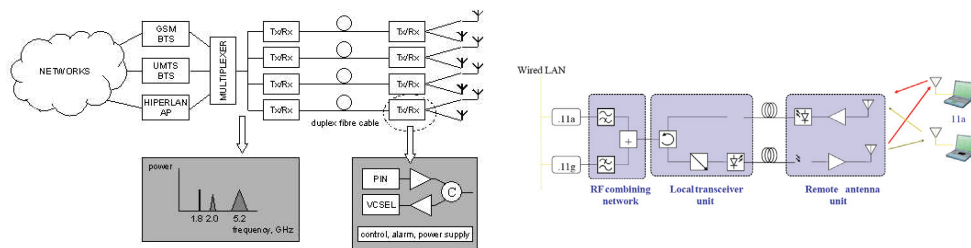


Fig. 26. RoF topology used in the Friday project (left) and for the WLAN standards (right)

Tyler *et al* have demonstrated the possibility [Tyler, 2002] to use the low bandwidth GMMF having a core diameter of $62.5\mu\text{m}$ for achieving the transmission of a 2.5Gbps Sub-Carrier Modulated signal (SCM) over 300-m length at 1300nm.

Chia *et al*. [Chia, 2003] have reported the transmission performance (error vector magnitude (EVM) variation) of the 50- μm -core high bandwidth MMF (2000 MHz km at 850 nm) used in radio-over-fiber systems (RoF) for WLAN IEEE 802.11 a/b/g signals. Hartmann *et al*. have done some studies dealing with an RoF system operating at 1300 nm with $62.5\text{-}\mu\text{m}$ -core MMF (500MHz km) for WLAN distribution system [Hartmann, 2004]. The performance (frequency response, spurious-free dynamic range, link gain, and noise figure) of two RF links using two $50\mu\text{m}$ -core MMF have been compared by Carlson *et al*. for the transmission of wireless telecom and local area networks signals at 840 nm [Carlsson, 2004].

In [Lethien, 2005] the transmission of digital signal modulated on radio-frequency subcarriers through GMMF by using low-cost 850nm vertical-cavity surface-emitting lasers and $50\mu\text{m}/62.5\mu\text{m}$ core matched receptacle photodiodes. Several mobile telecommunication (GSM, UMTS FDD) and WLAN standards (IEEE802.11a, b, g) have been transmitted over the OM2 Corning Infinicor 600 and the Corning Infinicor SXi (BL product at 850nm: 500MHz.km and 1500MHz.km) and high bandwidth OM3 Infinicor SX+ (BL product at 850nm: 2000MHz.km) GMMF. Several fibre lengths (100, 300m and 600 m) have been tested in an RF over fibre transmission scheme.. Characterization has been carried out to exhibit the error vector magnitude (EVM) variation as a function of fibre type and length. EVM minor to IEEE requirements are obtained for all standards being tested such as IEEE 802.11 g with 1.8% root-mean-square for 300 m of $50\mu\text{m}$ -OM2 GMMF at 850 nm as shown in the fig. 26. The UMTS transmission over GMMF and using a singlemode VCSEL has been realized by [Persson, 2006]. An EVM value close to 3% is reported in this paper when using the OM3 type GMMF in a link operating at 850nm. In [Nkansah, 2006], the performance measurements of different combinations of digital enhanced cordless telecommunications packet radio service, global system for mobile communications, universal mobile telecommunication service, and IEEE802.11g (54 Mbps) signals in a dual band configuration has been performed (fig. 27). The RoF system consists in the use of the RF over fibre topology with 300 m OM2 GMMF combined with low cost 850nm COTS VCSEL and photodiode.

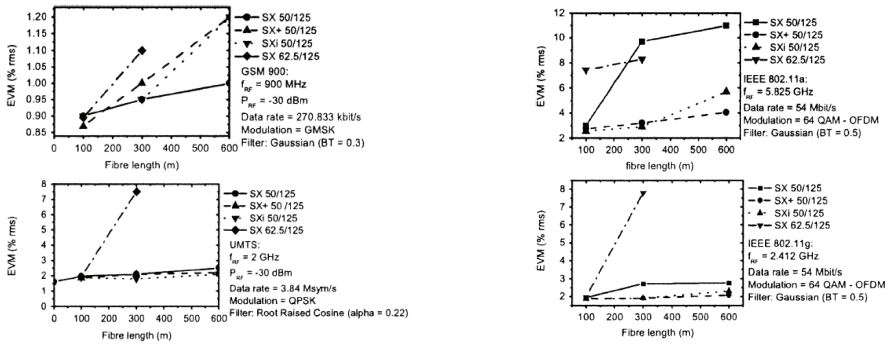


Fig. 27. Error Vector Magnitude as a function of the fibre length for the GSM, UMTS, IEEE802.11a and IEEE802.11g standards [Lethien, 2005]

The feasibility of such a system is demonstrated with error vector magnitude measurements which are within the required specifications. Inexpensive and omnidirectional multiband antennas were used in the wireless path. EVM has been evaluated both for the transmission of UMTS and IEEE802.11g standards over 300m OM2 GMMF followed by 4m wireless transmission. 8.8% and 4.7% EVM values are respectively obtained for the UMTS and the WiFi at the central unit in the uplink configuration.

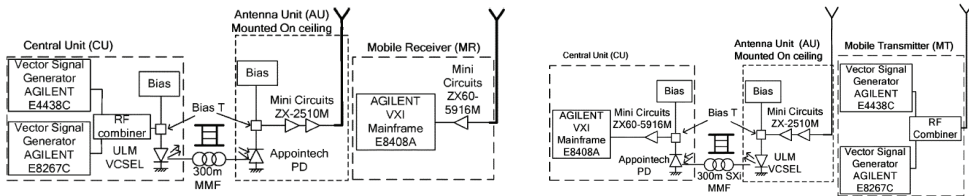


Fig. 28. Downlink (left) and uplink (right) configuration of a simultaneous transmission of dual band radio standards [Nkansah, 2006]

Today, one of the interesting topic concerns the feasibility of using the RoF concept to optically deliver the ultra-wide band signal to achieve long haul and high speed hybrid network. Previous studies have been already achieved on the UWB radio over fibre system but have been limited to one type of glass fibre (singlemode fibre: [Tabatabai, 2006] and multimode fibre [Yee, 2007], [Guo, 2008]) and packet error ratio (PER) measurement. In [Ben Ezra, 2008] paper, a theoretical modelling of a 4GHz Ultrawide Band (UWB RoF) radio over multimode fibre link operating at 850nm is presented as well as the experimental measurement over GMMF having a length more than 500m. The PER has been evaluated as a function of the fibre length. A 1m wireless path strongly degrades the overall performance of the used system developed in the framework of the UROOF European project (Photonic components for UWB over optical fiber IST-5-033615). Pizzinat *et al* [Pizzinat, 2007] have demonstrated the possibility of transmitting a MB OFDM UWB signal having a data rate of 1.92Gbps over 500m link length composed of the OM2 GMMF (BL product: 700MHz.km at 850nm). The measured BER in the two different frequency bands of the transmitted signal

(3.1GHz - 4.7GHz or 6 to 7.6GHz) are respectively 10^{-8} and 10^{-6} , values obtained with TOSA and ROSA devices (Transmitted or Received Optical Sub-Assembly) inserted in a point to point topology. The feasibility of a multipoint to multipoint architecture has been demonstrated by Pizzinat *et al* [Pizzinat, 2008] for the distribution of UWB MB OFDM signal over multimode fibre with low cost devices.

4.3.2 RoF system developed with PMMF

Regarding to the PMMF available on the market, only the perfluorinated CYTOP® based PMMF is used for the distribution of radio signals over optical multimode fibre, mainly owing to its relative low attenuation in the infrared domain (contrary to the Plexiglas based PMMF). The use of the PMMF in RoF systems is mainly exploited by two different groups localized on the one hand in Eindhoven University of Technology (The Netherlands) and on the other hand, in the University of Lille 1 (France).

Koonen's group [Koonen, 2008] has developed a special topology based on optical frequency multiplication (OFM) to transmit radio signal over the Lucina fibre as described in figure 28. The so called OFM technique is based on FM to IM conversion and is very robust against modal dispersion occurring in multimode fibre communication.

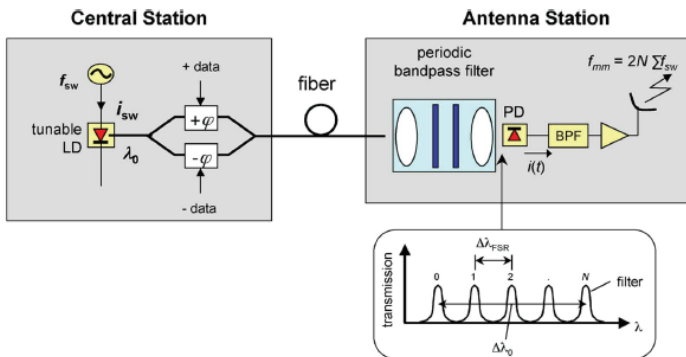


Fig. 29. Overview of the OFM method [Koonen, 2008]

The wavelength of a tunable optical source is periodically swept over a range $\Delta\lambda_0$ in the central station. The antenna station is composed of a periodic optical band-pass filter where the band-pass transmission peaks are spaced by the wavelength free spectral range ($\Delta\lambda_{FSR}$). The light issued from the frequency sweeping optical source goes back and forth inside the cavity of the band-pass filter resulting in the presence of transmission peaks. Light intensity bursts are then detected on the photodiode. A microwave signal is so generated at the fundamental frequency and also higher harmonics. An electrical band-pass filter (BPF) is used to select the specific harmonic allowing the propagation of the pure radiofrequency signal thanks to the antenna. A Mach Zehnder intensity modulator is used to modulate the frequency-swept optical carrier with the data stream: the resulting signal is not affected by the OFM process and is considered as the envelope of the optical sweeping signal before the photodetection. This OFM process could be used also with the GMMF.

In [Lethien, 2006], the improvement of the indoor coverage of radiocellular signals such as GSM and UMTS has been realized with the use of the Lucina fibre in a RoF topology based

on the IMDD technique. The EVM has been evaluated after the transmission over a GMMF and PMMF in order to exhibit a different behaviour of the two fibres regarding to the radio signals. The results show that, the Lucina fibre constitutes without any doubt a promising candidate in RoF system using COTS components dedicated for GMMF. Moreover, because of its higher core diameter, PMMF does not induce modal noise penalties as occurred in GMMF link [Ishigure, 2003] and the alignment is also less critical what reduces the cost of the optical active and passive devices including the installation and maintenance costs of the connections. Its higher flexibility based on “plastic” material offers a great advantage compared to the silica fibre which is more brittle. Nevertheless, the higher core diameter of the fibre with respect to the active area of some high speed detectors is the cause of an additional power penalty.

Lethien *et al* [Lethien, 2009] has demonstrated the potential of GMMF and PMMF to transmit the Wimedia MB OFDM UWB standard over more than 1km and 200m respectively for the GMMF and the PMMF. The influence of the fibres properties (attenuation, bandwidth/length product...) on the link quality (fig. 29) has been performed and two different behaviours regarding to the core material have been exhibited.

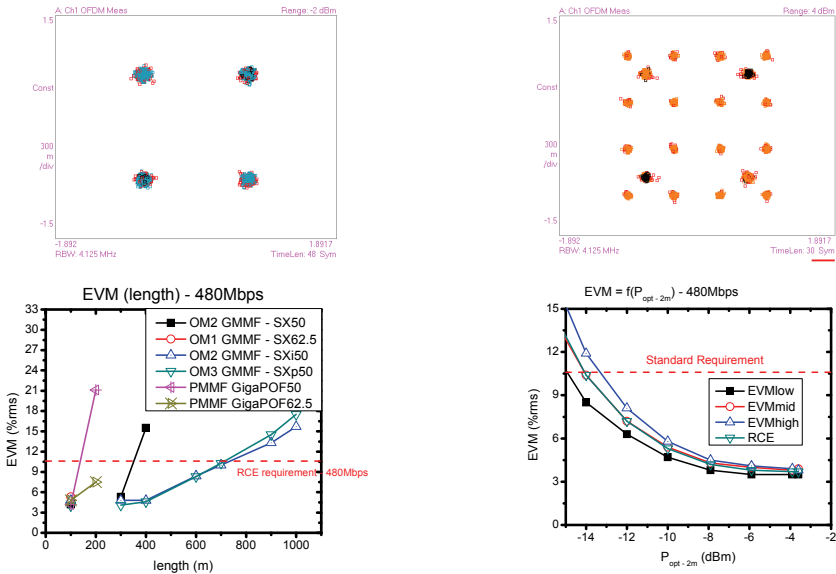


Fig. 30. IQ constellation diagrams (QPSK and Dual Carrier Modulation schemes) and evolution of the EVM as a function of the fibre length and the fibre attenuation

By using this preinstalled multimode fibre Ethernet networks, it would be possible to use the high potential of the fibre bandwidth coupled with the wavelength division multiplexing technique to successfully transmit multi-services application without impairments aiming to obtain a low cost infrastructure in term of service integration. The successful transmission on a single GMMF of the IEEE802.11g signal with the optical power used to supply the remote access points (principally composed by a laser, a photodiode and RF amplifier) is also reported by Wake *et al* [Wake, 2008] thanks to the use of the

wavelength multiplexing method. The so obtained EVMs with electrical or optical power supplies are in the same order of magnitude.

The simultaneous transmission of a digital 10GbE signal and a radiofrequency MultiBand Orthogonal Frequency Division Multiplexing Ultra-Wide Band (band group 5) MB-OFDM UWB signal at 480 Mbps has been successfully achieved over 1.1km fiber length without any error and with RCE less than 5.5% rms, respectively by Lethien *et al* [Lethien2, 2009, Lethien3, 2009]. Concerning the radio signal, an additional 1-meter long wireless path has also been demonstrated that led to an RCE value of 7.2%.

5. Conclusion

This chapter describes an overview of the potentialities of the multimode fibre either in glass or polymer to be used for multi-services applications. The state of art of the existing GMMF and PMMF has been done with the advantages and drawbacks of the used core material. The manufacturing processes of such multimode fibres have been described to exhibit the fibre performances obtained regarding to the used processes. The transmission of multi-gigabits signal over both PMMF and GMMF is also reported for short range/high data rate wired networks. Moreover, the radio over fibre concept is introduced for the improvement of the indoor coverage of wireless signal in shadowed area with low cost and unsophisticated topologies. It has been demonstrated in this chapter that the multimode fibre constitutes, without any doubt, a promising candidate for home office/small office applications.

6. References

- [Asahi Glass] Datasheets of the Asahi Glass Perfluorinated GIPOF "Lucina™", http://www.agc.co.jp/english/rd_e/e_lucina.html, 2009 (Tokyo, Japan)
- [Ben Ezra, 2008] Y. Ben Ezra *et al*, "Experimental and theoretical investigation of the multiband OFDM Ultra Wideband Radio over multimode fiber transmission", in proceedings of the 2008 IEEE International conference on ultra-wideband (ICUWB 2008), vol. 3, pp 55-58.
- [Bennet, 2004], M. Bennett, A. Flatman, B. Tolley, "Broad Market Potential of 10Gb/s Ethernet on FDDI grade MM Fiber," IEEE802.3, (2004), http://www.ieee802.org/3/tutorial/mar04/10GMMF_SG_v031604a.pdf
- [Carlsson, 2004] C. Carlsson, A. Larsson, and A. Alping, "RF transmission over multimode fibers using VCSELs—Comparing standard and high bandwidth multimode fibers," J. Lightw. Technol., vol. 22, no. 7, pp. 1694–1700, Jul. 2004.
- [Chia, 2003] M. Y. W. Chia *et al*, "Radio over multimode fiber transmission for wireless LAN using VCSELs," Electron. Lett., vol. 39, no. 15, pp. 1143–1144, 2003.
- [Chromis] Datasheets of the Chromis Perfluorinated GIPOF "GigaPOF", <http://www.chromisfiber.com/products.htm>, 2009 (Warren, USA)
- [Corning] Datasheets of the Corning™ fibers, http://www.corning.com/opticalfiber/products/infinicor_fibers.aspx, May 2008 (New York, USA)
- [Draka] Datasheets of the Draka fibers, http://www.draka.com/draka/DrakaComteq/Drakafibre/Languages/English/Navigation/Markets&Products/Technical_Suppo

- rt/Datasheets/DCOF_MaxCap-550.pdf, September 2008 (Amsterdam, The Netherlands)
- [Duijnhoven, 1999] Franciscus G.H. van Duijnhoven, "Gradient refractive index polymers produced in a centrifugal field : preparation, characterisation and properties", - Eindhoven : Technische Universiteit Eindhoven, 1999. Proefschrift. - ISBN 90-386-2581-2, <http://alexandria.tue.nl/extra3/proefschrift/boeken/9902697.pdf>
- [ECMA 368, 2007] Standard ECMA-368, "High Rate UltraWideband PHY and MAC Standard," 2nd edition, (December 2007), <http://www.ecma-international.org/publications/standards/Ecma-368.htm>
- [Giaretta, 2000] G. Giaretta et. al. "High-Speed (11 Gbit/s) Data Transmission Using Perfluorinated Graded-Index Polymer Optical Fibers for Short Interconnects (<100m)," *IEEE Photon. Tech. Lett.* **12**, 347-349 (March 2000)
- [Guo, 2008] Y.-X. Guo, V. H. Pham, M.-L. Yee, L. C. Ong, B. Luo, "Performance evaluation for WiMedia Ultra-Wide Band simultaneous Transmission with wireless LAN over cable and Fiber," in *Proceedings of IEEE Radio and Wireless Symposium (IEEE, 2008)*, pp 259-262
- [Hartmann, 2004] P. Hartmann, X. Qian, R. V. Penty, and I. H. White, "Broadband multimode fiber (MMF) based IEEE 802.11a/b/g WLAN distribution system," in *Microwave Photonics Conf. Proc. (MWP 2004)*, 2004, pp. 173-180.
- [IEC 60793-2-10] Standard IEC 60793-2-10, "Optical fibres - Part 2-10: Product specifications - Sectional specification for category A1 multimode fibres", (June 2007),
- [IEC 60793-2-40] Standard IEC 60793-2-40, "Product specifications - Sectional specification for category A4 multimode fibres," 2nd edition, (March 2006), <http://webstore.iec.ch/webstore/webstore.nsf/artnum/035855>
- [Ishigure, 1998] T. Ishigure *et al* "High bandwidth low loss Graded index polymer optical fibre for near infrared use", *ECOC 1998*, Madrid (Spain), September 1998
- [Ishigure, 2003] T. Ishigure, K. Makino, S. Tanaka and Y. Koike, "High-Bandwidth Graded Index Polymer Optical Fiber enabling Power Penalty-Free Gigabit data transmission", *Journal of Lightwave Technology*, vol. 21, no. 11, November 2003, pp 2923-2930
- [ISO 11801] Standard ISO 11801, "ISO 11801 - INFORMATION TECHNOLOGY - GENERIC CABLING FOR CUSTOMER PREMISES"
- [Koike, 1995] Koike *et al*, "High-bandwidth, high-numerical aperture graded-index polymer optical fiber", *JOURNAL OF LIGHTWAVE TECHNOLOGY*, VOL. 13, NO. 8, August 1995 pp 1686-1691
- [Koike, 1996] Y. Koike: "Status of POF in Japan", *POF'1996*, Paris 22.-24.10.1996, pp. 1-8
- [Koike, 1997] Y. Koike: „Progress in Plastic Fiber Technology“, *OFC'1997*, Dallas, pp. 103-108
- [Koike, 2002] Koike *et al*, "High-Bandwidth Graded-Index Polymer Optical Fiber With High-Temperature Stability", *JOURNAL OF LIGHTWAVE TECHNOLOGY*, VOL. 20, NO. 8, AUGUST 2002 pp 1443-1448
- [Koike, 2009] Kotaro Koike and Yasuhiro Koike, "Design of Low-loss Graded Index Plastic Optical Fibre Based on Partially Fluorinated Methacrylate Polymer", *IEEE Journal of Lightwave Technology*, Vol. 27, No. 1, January 2009

- [Koonen, 2008] A.M.J. Koonen et al, "Radio over MMF technique - pat II: Microwave to millimetre wave systems", IEEE/OSA Journal of Lightwave Technology, vol. 26, no. 15, august 2008, pp 2396-2408
- [Kuyt, 1999] G. Kuyt, P. Pleunis, A. van Bergen, and R. van Laere, "PCVD graded index multimode fibers for gigabit speed datacom applications using laser sources," in Proc. EuroCable , 1999, pp. 222-229.
- [Lopez, 2008] M. Lopez and P. Ronco, "Advantages of the Corning optical fiber manufacturing process", white paper, available online at www.corning.com/WorkArea/downloadasset.aspx?id=10869
- [Lethien, 2005] LETHIEN C., LOYEZ C., VILCOT J.P., « Potentials of radio over multimode fiber systems for the in-buildings coverage of mobile and wireless LAN applications", IEEE Photonics Technol. Lett., 17, 12 (2005) 2793-2795
- [Lethien, 2006] LETHIEN C., GOFFIN A., VILCOT J.P., LOYEZ C., "Radio over fibre systems using perfluorinated graded index polymer optical fibre", Microw. Opt. Technol. Lett., 48, 6 (2006) 1197-1199
- [Lethien1, 2008] C. Lethien, C. Loyez, J-P. Vilcot and A. Goffin, "Differential Mode Delay measurements of the fluorinated based Graded Index Polymer Optical Fibre", IEEE Photonics Technology Letters, Vol. 20, No. 18, pp 1584 - 1586, September 2008
- [Lethien2, 2008] C. Lethien et al, "Potential of the polymer optical fibers deployed in a 10Gbps small office/home office network", Opt. Express, 16, 15 (2008), pp 11266-11274
- [Lethien, 2009] CHRISTOPHE LETHIEN, CHRISTOPHE LOYEZ, JEAN-PIERRE VILCOT, RÉDHA KASSI, NATHALIE ROLLAND, CATHY SION AND PAUL ALAIN ROLLAND, "Review of glass and polymer multimode fibers used in a Wimedia UltraWide Band MB-OFDM radio over fiber system", IEEE/OSA Journal of Lightwave Technology, vol 27, no 10 (2009), pp 1320-1331
- [Lethien2, 2009] LETHIEN C., LOYEZ C., VILCOT J.P., ROLLAND P.A., "High modal bandwidth glass multimode fibers used for the simultaneous transmission of 10GbE and band group 5 MB-OFDM ultra-wide band signals", in proceeding of the European Workshop on Photonic Solutions for Wireless, Access and in-house Networks, Duisburg, Germany, may 18-20, 2009
- [Lethien3, 2009] LETHIEN C., LOYEZ C., VILCOT J.P., P.A. ROLLAND, "Multi-service applications on high modal bandwidth glass multimode fiber", IET Electron. Lett., 45, 18 (2009), pp 951-952 (august 27, 2009)
- [Li, 1999] W. Li et. al. "Record 2.5 Gbit/s 550 m GIPOF Transmission experiments at 840 and 1310 nm wavelength", in *Proceedings of POF1999*, (China, July 13-16, 1999), pp 60-63
- [Matthijsse, 2006] P. Matthijsse et al, "Multimode fiber enabling 40 Gbit/s multi-mode transmission over distances >400m", in proceedings of the OFC 2006, OW1-13
- [MCVD OFS] D. Mazzarese, "Manufacturing multimode fiber: Precise control of production and testing ensures high performance", white paper, available online at www.ofsoptics.com/resources/fibermpgpaper.pdf
- [Miller, 1979], S.E. Miller et al, "Optical Fiber telecommunications", 1979, Academic Press, ISBN : 0-12-497350-7
- [Murofushi, 1996] M. Murofushi: "Low loss perfluorinated POF", POF'1996, Paris, 22.-24.10.1996

- [Nkansah, 2006] NKANSAH A., DAS A., LETHIEN C., VILCOT J.P., GOMES N.J., GARCIA I.J., BATCHELOR J.C., WAKE D., Simultaneous dual band transmission over multimode fiber-fed indoor wireless network, *IEEE Microw. Wirel. Compon. Lett.*, 16, 11 (2006) 627-629
- [OFS optics] Datasheets of the OFS optics fibers, www.ofsoptics.com/resources/multimodeselectionguide%20.pdf, 2009 (Norcross, USA)
- [OVD Corning] P. Bell and T. Wiggs, "Multimode fibre and the vapour deposition manufacturing process outside vapour deposition vs. Inside vapour deposition", white paper, available online at www.corning.com/WorkArea/downloadasset.aspx?id=7029
- [PCVD Draka] PCVD based fibre production, available online at www.thor.edu/kvasir/2-draka.pdf
- [Park, 2006] S. W. Park, "Production, properties and future of PMMA-GI-POF", 21. Meeting of the ITG-SC 5.4.1, Oldenburg, 12.05.2006
- [Pedrotti, 2006] K. D. Pedrotti, R. P. Dahlgren, J. A. Wysocki, S. E. Ralph, R. Gandhi and A. Polley, "Multi-gigabit transmission over POF," in *Proceedings of POF World West*, (Santa Clara, June 21-22, 2006)
- [Pepeljugoski, 2002] P. Pepeljugoski *et al* "15.6-Gb/s Transmission over 1km of netw generation multimode fiber", *IEEE PHOTONICS TECHNOLOGY LETTERS*, VOL. 14, NO. 5, MAY 2002, pp 717-719
- [Persson, 2006] Persson, K.-A. Carlsson, C. Alping, A. Haglund, A. Gustavsson, J.S. Modh, P. Larsson, A., "WCDMA radio-over-fibre transmission experiment using singlemode VCSEL and multimode fibre", *IEE Electronics Letters*, Vol. 42, No 6, pp 372-374, march 2006
- [Phyworks] Description of the Phyworks technology, <http://www.phyworks-ic.com/technology.asp>
- [Pizzinat, 2007] Anna Pizzinat, Pierre Urvoas and Benoit Charbonnier, "1.92Gbit/s MB-OFDM Ultra Wide Band Radio Transmission over low bandwidth multimode fiber", in proceeding of the Optical Fiber Communication and the National Fiber Optic Engineers Conference 2007 (OFC/NFOEC 2007), 25-29 March 2007, pp 1 - 3
- [Pizzinat, 2008] A. Pizzinat *et al*, « Low cost Transparent radio over fibre system for UWB based home network », in proceeding of ECOC 2008, 21-25 september 2008, Brussels (Belgium)
- [Polley, 2007] A. Polley, R. J. Gandhi, and S. E. Ralph, "40Gbps links using plastic optical fiber," in *Proc OFC, Anaheim, 2007*, OMR5
- [Polley, 2008] A. Polley and Prof. Stephen E. Ralph, "100 m, 40 Gb/s Plastic Optical Fiber Link", in proceeding of OFC/NFOEC 2008, OWB2
- [Schöllmann, 2007] Stefan Schöllmann *et al*, "First Experimental Transmission over 50 m GI-POF at 40 Gb/s for Variable Launching Offsets", in *Proceedings of the 33rd European Conference on Optical Communications*, September 16-20, 2007, Berlin, Germany
- [Seeds, 2002] Alwyn J. Seeds, "Microwave photonics", *IEEE TRANSACTIONS ON MICROWAVE THEORY AND TECHNIQUES*, VOL. 50, NO. 3, MARCH 2002, pp 877 - 887

- [Tabatabai, 2006] F. Tabatabai, H. Al-Raweshidy, "Performance evaluation for WLAN and UWB using radio over fibre," in Proceedings of the 9th European Conference on Wireless Technology (IEEE, 2006), pp. 147-149
- [TIA-455-220-A] TIA-455-220-A, "Differential Mode Delay Measurement of Multimode fibre in the time domain", January 03
- [TIA 492AAAA] Standard TIA 492AAAA, "Detail Specification for 62.5-Micrometer Core Diameter/125-Micrometer Cladding Diameter Class Ia Graded-Index Multimode Optical Fibers", (January 1998)
- [TIA 492AAAB] Standard TIA 492AAAB, "Detail Specification for 50-Micrometer Core Diameter/125-Micrometer Cladding Diameter Class Ia Graded-Index Multimode Optical Fibers", (November 1998)
- [TIA 492AAAC] Standard TIA 492AAAC, "Detail Specification for 850-nm Laser-Optimized, 50-um Core Diameter/125-um Cladding Diameter Class Ia Graded-Index Multimode Optical Fibers, (January 2003)
- [TIA-492AAAD], Standard TIA 492AAAD, "OM4 fiber specification", in preparation
- [Van den Boom et al, 2001] Van den Boom H.P.A et al, "High-Capacity Transmission Over Polymer Optical Fibre", IEEE JOURNAL ON SELECTED TOPICS IN QUANTUM ELECTRONICS, VOL. 7, NO. 3, MAY/JUNE 2001
- [Tyler, 2002] Tyler E J, M Webster, R V Penty and I H White, "Subcarrier modulated transmission of 2.5Gb/s over 300m of 62.5µm-core diameter multimode fibre", IEEE Photon. Technol. Lett., Dec 2002
- [Wake, 2001] WAKE D., DUPONT S., LETHIEN C., VILCOT J.P., DECOSTER D., "Radio frequency transmission of 32 QAM signals over multimode fibre for distributed antenna system applications", Electron. Lett., 37, 17 (2001) 1087-1089
- [Wake, 2002] Wake, D, "Trends and prospects for radio over fibre picocells", in proceedings of MWP 2002. International Topical Meeting on Microwave Photonics, 5-8 Nov. 2002 Page(s):21 - 24
- [Wake, 2008] DAVID WAKE, CHRISTOPHE LETHIEN, CATHY SION, JEAN-PIERRE VILCOT AND NATHAN J.GOMES, "An Optically Powered Radio over Fiber Remote Unit using Wavelength Division Multiplexing", in proceedings of the IEEE International Microwave Photonics conference and the Asia-Pacific Microwave Photonics conference (IEEE MWP2008/APMP2008), September 30th - October 3rd 2008, Gold Coast (Australia)
- [White, 2005], W. White, "New Perspectives on the Advantages of GI-POF", POF 2005, Hong Kong, September 2005
- [Yao, 2007] J. Yao, F. Zeng, Q. Wang, "Photonic generation of Ultrawideband signals," Journal of Lightwave Technology, 25, 11, 3219-3235 (November 2007)
- [Yee, 2007] M.-L. Yee, Y.-X. Guo, V. H. Pham, L. C. Ong, "WiMedia Ultra-Wide Band Transmission in Radio over Fiber using Multimode Fiber," in Proceedings of the 20th Annual Meeting of the IEEE Lasers and Electro-Optics Society (IEEE, 2007), pp 335-336

An overview of radio over fibre systems for 60-GHz wireless local area networks and alternative solutions based on polymer multimode fibres

Christophe Loyez, Christophe Lethien,
Jean-Pierre Vilcot and Nathalie Rolland

*Institut d'Electronique, de Microélectronique et de Nanotechnologie, UMR CNRS 8520
Villeneuve d'Ascq, FRANCE*

1. Introduction

This chapter deals with innovative optical systems specific to the high-data-rate hybrid networks operating in the millimetre-wave frequency band. With the incoming of high-data-rate communications protocols, the Radio Frequency (RF) systems operating in the near 60-GHz frequency band are a current alternative to the conventional Ultra Wide Band (UWB) technologies which are limited by drastic power regulations (-41dBm/MHz). To enhance the connectivity of the 60-GHz Wireless LANs, a vast amount of Radio over Fibre (RoF) systems have been developed by the international research community and their performances are demonstrated for data rate in the range of several hundredths of Mbps. Most of them are based on Single Mode Fibres (SMF) assuming that an obvious optical transmission of the 60-GHz carrier signal is required: this chapter will detail the main principles of usual SMF RoF systems. In particular, such systems have to meet specific requirements concerning the access points to prevent degradation performance due to limitations such as the chromatic dispersion inherent to the optical fibre and owing to the phase-noise of the 60-GHz signal. We conclude the compliance of the SMF RoF systems with low-cost applications is still difficult due to the sensitivity of SMF regarding to a misalignment between the fibre core and the active area of the electro-optic and opto-electronic converters. The weak tolerance regarding to an offset launch increases the connection cost. To get rid of the limitations described above, we propose alternative solutions to SMF techniques assuming that the optical transmission of the 60-GHz carrier signal is not necessary required. These solutions for hybrid optical-wireless networks are based on Polymer MultiMode Fibres (PMMF) and include novel monolithically integrated 60-GHz RF systems. The following topics will be detailed in this chapter:

- the usual topologies and requirements of 60-GHz SMF RoF systems.
- a first alternative based on a subcarrier radio signal transmission over PMMF for 60-GHz WLAN using a phase-noise cancellation technique

-a second one involving an impulse system for 60-GHz wireless networks based on PMMF.

2. 60-GHz RoF system based on Single Mode Fibres

2.1 Topologies of 60 GHz SMF RoF systems

The most popular topologies of 60-GHz RoF systems are still today based on SMF solutions. The aim of such architectures is to transmit efficiently a millimetre-wave signal over a few dozen of kilometres. This objective is motivated by the fact the 60 GHz frequency sources have to meet strong requirements of phase-noise and frequency stability which are not compliant with a real integration of the access points. The characteristics of these SMF systems are described by the figure 1. The millimetre-wave signal cannot directly modulate the bias current of usual lasers having limited modulation bandwidth. By the way, an external modulation is achieved in most of the SMF topologies involving Optical External Modulators (OEM) such as an Electro-Absorption Modulator or an interferometric Mach-Zehnder Modulator (Vegas Olmos 2008). The modulated optical signal suffers from the chromatic dispersion which induces severe link budget penalties even if the photodetector (PD) owns a sufficient detection bandwidth. Several techniques have been investigated to overcome this limitation. We can note the chromatic dispersion compensation and the achievement of single Sideband optical sources (Woo-Kyung Kim 2008). To relax the constraints of frequency bandwidth, solutions performing the optical transmission of sub-harmonic Local Oscillator signals on SMF have been developed. Good performances are obtained for most of these SMF solutions which are well suited for inter-building optical transmission.

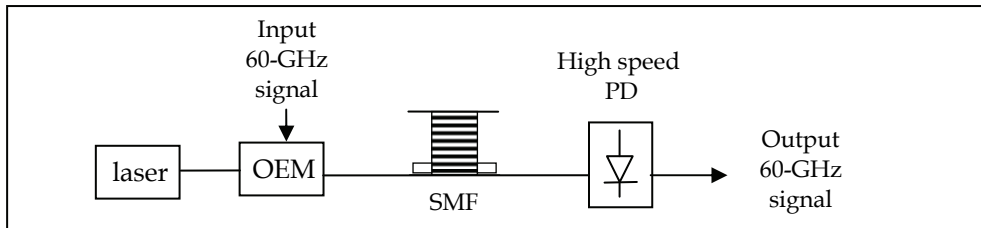


Fig. 1. 60-GHz RoF SMF system

2.2 Evolution towards PMMF systems

For short distances in the range of a few hundredth of meters, alternative solutions based on PMMF optical solutions can be used especially for in-building communication. Polymer fibre has been chosen since its easy handling and connection is a real asset compared to the silica fibre: clip-on connector has been developed as to be fixed directly on the external coating of the polymer fibre without the use of expensive tools like in the silica fibre world. Even if these polymer optical fibres exhibit some drawbacks - main one is its high attenuation -, they are well matched to a small office/home office environment use and open the road of the "do it yourself" concept. The chapter titled "Potentialities of multimode fibres as transmission support for multiservice applications: from the wired

small office/home office network to the hybrid radio over fibre concept'' summarizes the properties of such a fibre.

The techniques describe hereafter overcome the phase-noise limitation and enable the use of fully integrated oscillator in access points, such as MMIC (Monolithic Microwave Integrated Circuit) oscillators which exhibits a die size less than 1mm^2 . Then, the optical transmission of the 60-GHz local oscillator is not the most interesting solution since fibre-radio systems based on a simple RF architecture using optical COTS (commercial off the shelf) components can be efficient.

3. Self-heterodyne system

3.1 Overall description

This first topology includes a self-heterodyne device based on the RF transmission of an additional signal carrier. This topology is depicted by the figure 2: a Vector Signal Generator generates the desired data signal (modulation scheme, data rate) on a 500 MHz subcarrier signal. 500 MHz is chosen to be compatible with the Vector Signal Analyser (VSA) performance, even though a PMMF (62.5 μm core diameter) could transmit microwave signal at higher frequencies due to its high optical bandwidth. Before the optical transmission, Transmitter / Receiver (T/R) modules performs the 60-GHz radio transmission of the resulting subcarrier signal. These modules described hereafter include a phase-noise cancellation technique. At the output of the receiver, this recovered IF signal directly modulates the current of a 850 nm distributed feedback laser. The optical signal is transmitted through the PMMF before to be collected by a multimode pigtailed photodiode. Then, a vector signal analyser measures the rms EVM of the recovered signal. The used PMMF is a perfluorinated graded index polymer optical fibre (PF GIPOF). This one has a 100 m length and owns a bandwidth-length product close to 600MHz.km

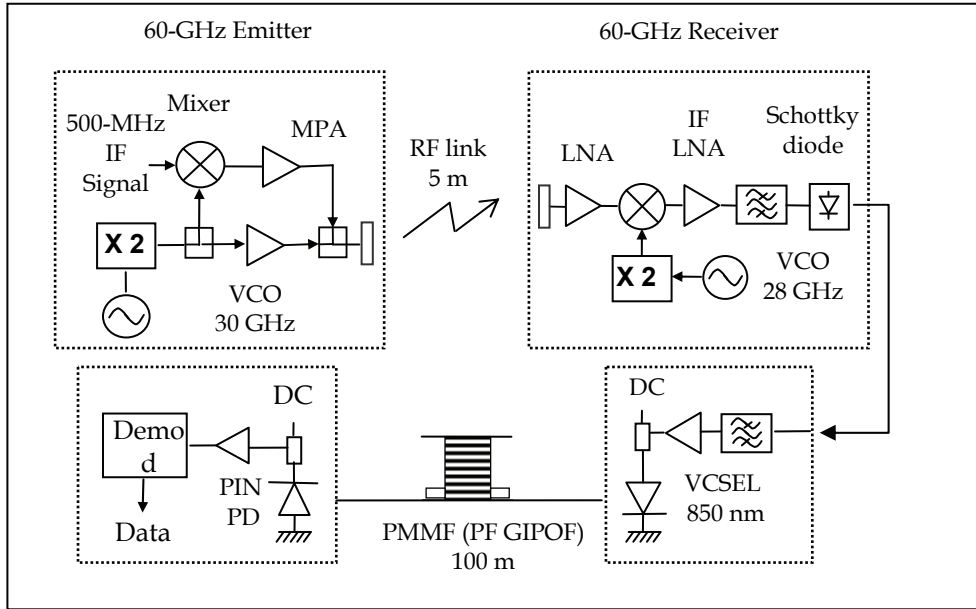


Fig. 2. Self-heterodyne / IF over MMF system

3.2 60GHz T/R modules including the phase-noise cancellation technique

In order to cancel the phase-noise, two RF signals with correlated phases are transmitted in order to perform a frequency mixing between them in the receiver. Exploiting the large amount of spectral resources of the 60 GHz band, this kind of solution has already been reported (Shoji 2002). Nevertheless, such systems had, up to now, the drawback of degrading the Carrier-to-Noise power Ratio of the recovered signal. In comparison with a conventional system including LOs with excellent phase-noise, this degradation is at least of 9 dB. The architecture of our system cancels the phase-noise without significant degradation of the CNR. This system is lightly different from a conventional heterodyne system, especially for the transmitter which is designed to transmit an additional signal $S_c(t)$. Nevertheless, this architecture is still convenient since it takes advantage of the naturally strong power of the LO pump signal. Figure 2 describes in details the transceiver topology. Before the up-conversion of the IF signal $S_{IF}(t) = A_0 \cos(2\pi \cdot f_{IF}t + \phi_{IF}(t))$ with $f_{IF} = 500$ MHz, the LO signal is separated in two paths. The first path provides a pump signal to up-convert the IF signal as in a conventional heterodyne transmitter. The second path delivers the LO signal which is amplified before emission. By this way, we control the power of each signal and we prevent the power amplifier from compression due to the additional signal. The global emitted signal is then expressed as follows:

$$S(t) = S_C(t) + S_{RF}(t) = A \cos(\omega_c t + \phi_c(t)) + A \cos((\omega_c + \omega_{RF})t + \phi_{RF}(t)) \tag{1}$$

with :

$$f_c = \frac{\omega_c}{2\pi} = 60 \text{ GHz and } f_{RF} = \frac{\omega_{RF}}{2\pi} = f_c + f_{IF} = 59.5 \text{ GHz}$$

Assuming that the phase-noise is much lower for the IF signal than for the LO, the correlation between the signals is verified. The signal propagation is performed with directive antennas. The receiver presents a conventional topology. After propagation, the two transmitted signals are down-converted by using a LO whose phase-noise can be very detrimental. During these operations, the phase-noise of the two resulting signals $S'_C(t)$ and $S'_{RF}(t)$ increases but the phase correlation between them is not affected. The global signal $S'(t)$ is then described by the expression (2) :

$$S'(t) = S'_C(t) + S'_{RF}(t) = A' \cos((\omega_c - \omega_{LO})t + \phi'_c(t)) + A' \cos((\omega_c + \omega_{IF} - \omega_{LO})t + \phi'_{RF}(t))$$

$\phi'_c(t)$: Cumulated phase-noise contributions of T/R local oscillators.

$$\phi'_{RF}(t) = \phi'_c(t) + \phi_{FI}(t) + \phi_0 ; f_{OL} = \frac{\omega_{OL}}{2\pi} = 56 \text{ GHz} \tag{2}$$

Then, an IF mixer based on a polarized Schottky diode performs a frequency mixing between the two input signals $S'_C(t)$ and $S'_{RF}(t)$. After a low-pass filtering, the recovered IF signal $m(t)$ is then expressed by the equation (3) :

$$m(t) = S'(t)^2 * h_{IF}(t) = A'^2 \cos(\omega_{IF}t + \phi_{IF}(t) + \phi_0) \tag{3}$$

This brief theoretical analysis shows that the Schottky diode mixer acts well as a cancellation device of phase-noise by recovering the original signal without contributions of the T/R LOs. To verify experimentally the cancellation of phase-noise, the T/R modules described above have been achieved by using a MMIC technology. In a first place, the T/R LOs were replaced by synthesized signal generators. Figure 3 presents characteristics of the input signal. The signals $S'_C(t)$ and $S'_{RF}(t)$ cumulate the phase-noise of T/R LOs as shown figures 4 and 5. We can note the strong similarity between the two spectral densities due to the phase correlation. The input signal levels are adjusted to ensure an equal power emission P_T equal to 5 dBm for both the signal $S'_{RF}(t)$ and $S'_C(t)$. The cumulate gain of the T/R antennas, $G_T(\text{dB})$ and $G_R(\text{dB})$, is around 16 dB. Up to the input of the Schottky diode, the power equality of the $S'_C(t)$ and $S'_{RF}(t)$ signals is preserved using a broadband IF LNA. After the Schottky diode mixer, the phase-noise of the resulting signal $m(t)$ drops drastically as illustrated the figure 6, which shows that the cancellation of local oscillator phase-noise has been performed successfully. The only difference between the input and output signals is due to the thermal noise $Geq.Feq.k.To = -112 \text{ dBc/Hz}$ in this case.

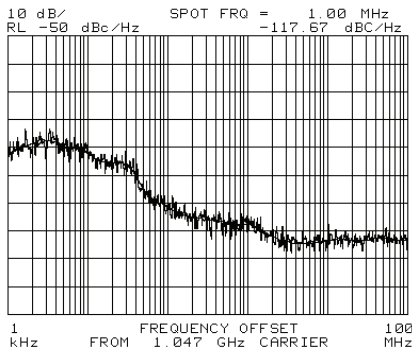


Fig. 3. Phase noise of the Input IF signal

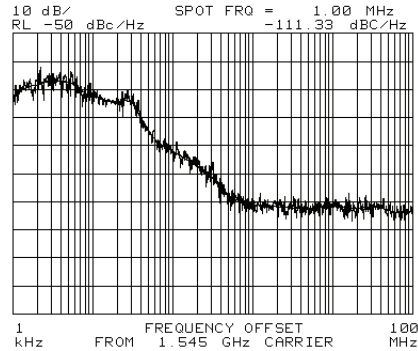


Fig. 4. Phase noise of the signal $S'_C(t)$

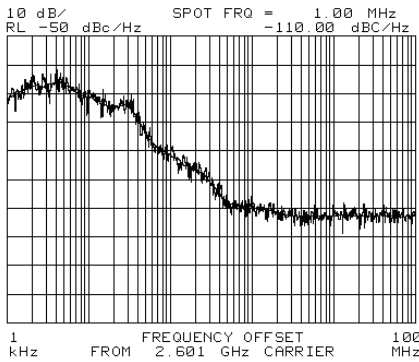


Fig. 5. Phase noise of the signal $S_{RF}'(t)$

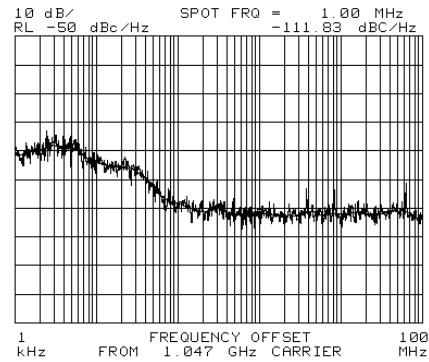


Fig. 6. Phase noise of the output signal $m(t)$

As announced by the equation (3), the residual phase-noise is only the fact of the properties of the signal $S_{IF}(t)$ and drops below -90 dBc/Hz at 10 kHz off-carrier. Such performances are very attractive in millimeter band. Secondly, MMIC VCOs associated to a frequency multiplication module were used as T/R LOs.

Even if these characteristics of phase-noise are very mitigated by additional parasitic signals, the phase-noise of the output signal $m(t)$ is still rigorously unchanged. This result shows that MMIC VCOs with degraded characteristics of phase-noise can be included as LO in T/R modules by using this approach.

3.3 Noise Figure considerations and Carrier to Noise Ratio Measurements

The comparison of phase-noise between the $S_{RF}'(t)$ and $m(t)$ signals, respectively plotted in figures 5 and 6, shows a strongly similar contribution of the thermal noise equal to -112 dBc/Hz. This means that the CNR level remains unchanged before and after the cancellation device. In this part, we deal with the conversion losses L_d of the Schottky diode mixer and its impact on the noise figure F_{eq} of the receiver. In particular, we detail the appropriate design to prevent noise figure and, by the way, CNR degradations. As described by the Friis formula (4), the power gain and noise figure of each component are needed to determine F_{eq} .

$$F_{eq} = F_{LNA} + \frac{(F_{MIX} - 1)}{G_{LNA}} + \frac{(F_{LNA_IF} - 1)}{G_{LNA} \cdot G_{MIX}} + \frac{(F_{det} - 1)}{G_{LNA} \cdot G_{MIX} \cdot G_{LNA_IF}} + \frac{(F_{MPA_IF} - 1)}{G_{LNA} \cdot G_{MIX} \cdot G_{LNA_IF} \cdot G_d} \quad (4)$$

$$P_{IN} = P_T \cdot G_T \cdot G_R \cdot \left(\frac{\lambda}{4\pi \cdot R^2} \right) \cdot G_{LNA} \cdot G_{MIX} \cdot G_{LNA_IF} \quad (5)$$

These data are summarized in Table 1. The RF LNA and mixer are designed to reduce the noise figure F_{eq} . For a conventional receiver, the value F_{eq} would be around 6 dB. In the case of this system, the conversion losses L_d have to be measured.

Component	LNA	Mixer	LNA_IF	Diode Mixer	MPA_IF
Gain (dB)	40	-12	GLNA_IF	Gd = - Ld	20
Noise Factor (dB)	6	15	3	Fd	3

Table 2. Gain and noise figure of components in the receiver

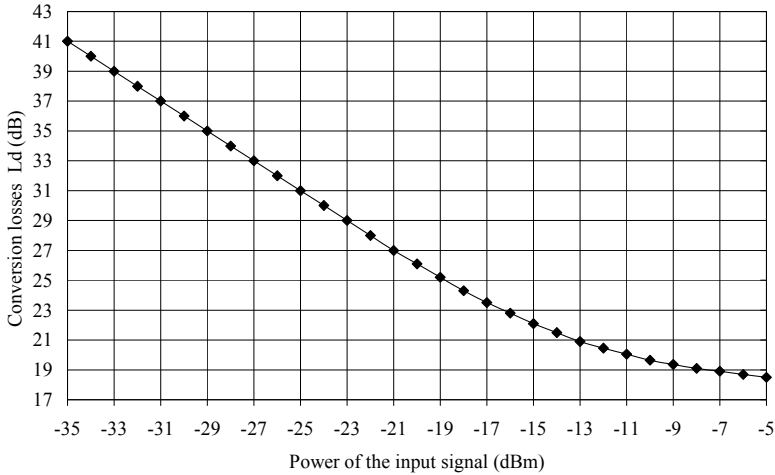


Fig. 7. Conversion losses Ld of Schottky diode mixer

The Schottky diode mixer presents important conversion losses, especially for a low input power. Figure 7 displays these conversion losses, L_d , versus the input signal power P_{in} . The link budget, expressed by equation (5) and applied to these experimental results, concludes that the conversion losses L_d could reach up to 40 dB for a propagation distance of 15 meters. As a consequence, such conversion losses had to be taken into account in the receiver design concerning the noise figure.

According to the results described above, the Friis formula (4) and the link budget (5) enable to calculate the degradation of the noise figure F_{eq} versus the propagation distance. Concerning the noise figure F_d of the Schottky diode mixer, we assumed $F_d = L_d + 9$ dB when the power equality of the two input signals, $S_c(t)$ and $S'_{RF}(t)$, is ensured. In these conditions, a gain of LNA equal to 15 dB allows a transmission distance of 15 meters with a F_{eq} degradation less than 1 dB.

This approach of the receiver design prevents theoretically the noise figure from an additional damage due to the cancellation. To confirm these results experimentally, measurements of the CNR, versus the propagation distance, have been achieved respectively for the $S_{RF}(t)$ and $m(t)$ signals. For these measurements, we integrated the approximate spectral power noise density in considering an equivalent noise bandwidth of 25 MHz. In figure 8, these experimental results confirm that the CNR of the received signal undergoes no significant degradation due to the phase-noise cancellation.

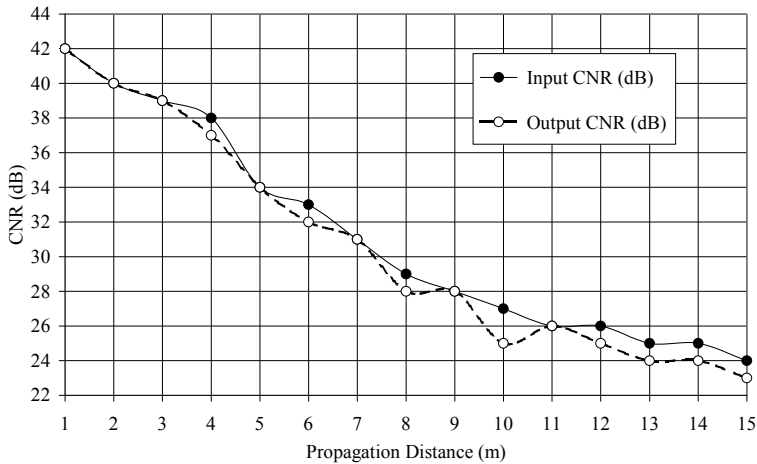


Fig. 8. CNR Measurements

3.4 EVM measurements

The 500 MHz modulated subcarrier is generated by a vector signal generator. The modulation schemes are QPSK, 16QAM and 64QAM allowing data-rates up to 300 Mbps. The T/R base-band filters are root raised-cosine filters with a roll-off factor $\alpha = 0.35$. The recovered signal is analysed by using a vector signal analyser. Experimental results of rms EVM for different modulation schemes are promising. We can note that these results are not strongly limited by the optical link. The EVM measurements have been performed as a function of the RF range. The results corresponding to RF range equal to 5 meters are presented hereafter: EVM results are less than 6.5% value for a QPSK 100 Mbps transmission. Since a direct QPSK 100 Mbps link between the ESG and the VSA leads to EVM results in the range of 4% to 5%, the degradation of the signal quality due to the overall transmission is not significant. Reaching such results using only MMIC VCOs is unrealisable without phase-noise cancellation technique. To transmit higher data rate, 16QAM modulation is tested up to 200 Mbps. For this case, EVM results never exceed 6.5 % even though measurement of a direct link provides EVM in range of 3.5%. The constellation diagram of figure 9 shows that this weak degradation is only due to thermal noise and non-linear behaviour of the 60-GHz transceiver. No alteration due to phase-noise can be observed, verifying the performance of phase-noise cancellation technique. To reach data rates of 300 Mbps, 64QAM modulation scheme is used. Once again, the phase-noise cancellation is applied and thermal noise and non-linearities are the only degradation factors. EVM results are in the range of 6 %: they are very promising and can be greatly enhanced by using a RF system having a better 1dB compression point. It will be then possible to transmit RF signals with the same power level (5dBm) but with a more important back-off.

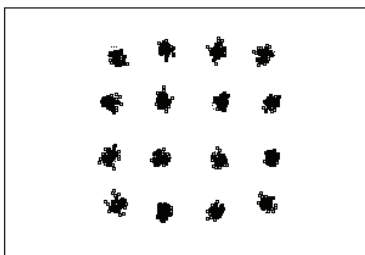


Fig. 9. Constellation Diagram (16QAM - 200 Mbps)

3.5 Multiple access strategy

A weak spectral efficiency is the only drawback of the topology detailed above. Furthermore, the multiple access strategy of such a technique is reduced to Frequency Division Multiple Access (FDMA). To reduce the spectral bandwidth of a channel, it is worth transmitting the additional carrier with a frequency f_c very close to one limit of the RF signal spectrum. Further works are in progress to achieve high-data-rate FDMA systems having an excellent trade-off between channel capacity and architecture compactness.

4. 60-GHZ Frequency Up-Converted Impulse System

4.1 Physical and MAC layers considerations

Concerning the physical layer, the main characteristic of this 60-GHz system is to inhibit the impact of both the LO phase-noise and the system non-linearities on signal quality. By the way, the Pulse Position Modulation (PPM) technique applied to sub-nanosecond pulses that are up-converted in the 60-GHz band is an attractive solution: the data information supported by the pulse position can not be affected by any phase deviation or power saturation. Furthermore, the use of sub-nanosecond pulses performs a wide spread spectrum which robustness against signal fading due to multi-path propagation has already been widely reported. Another consideration is relative to the Medium Access Control (MAC) layer: contention-based protocols such as CSMA/CA (Carrier Sense Multiple Access with Collision Avoidance) present suitable abilities for ad hoc network performance (Sobrinho 1999). To multiplex the radio-communications, we use such protocols based on a Time Hopping (TH) technique which takes advantage of the characteristics of the UWB pulses (Bo Hu 2005). Figure 9 illustrates the PPM and TH operations for a specific time interval.

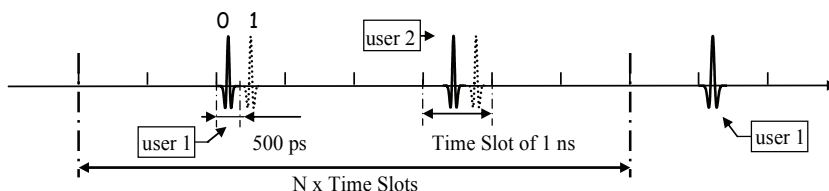


Fig. 10. PPM and TH technique using sub-ns pulses

4.2 Overall topology

The overall topology is depicted in the figure 10. The RF emitter and receiver include MMICs realized with different pHEMTs from OMMIC foundry (ft up to 120 GHz). The main component of the emitter is a pulse generator. This generator consists of a high-speed NOR logic gate associated to a varactor diode which enables to delay the relative position of generated pulses. The 60-GHz carrier signal is generated by a 30-GHz VCO associated to a frequency doubler. The frequency up-conversion of the sub-nanosecond pulses is obtained by modulating the amplitude of the 60-GHz OL signal. This Amplitude Modulation (AM) is performed by a switch having a SPDT (Single-Pole Double-Throw) topology and ensuring an isolation of more than 23 dB. The RF modulated signal is then amplified using a Medium Power Amplifier (MPA) which provides an output power of 16 dBm. The receiver includes a low noise amplifier, a RF detector and a correlator. The Low-Noise Amplifier has a Noise Figure equal to 6.5 dB and a power gain of 42 dB at 60-GHz. The RF detector performs the envelope detection of 60-GHz up-converted IR-UWB pulses. Next, the correlator mainly consists of a matched filter and a fast sampling and hold amplifier (SHA). Another pulses generator is used to trig this SHA. This second pulses generator is synchronised with the incoming signal by using a specific synchronisation technique which renders output binary data (Deparis 2006).

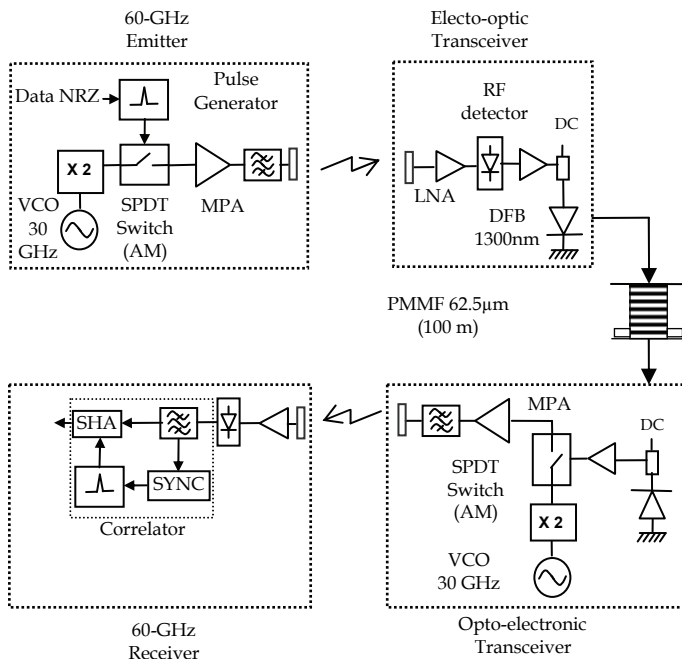


Fig. 11. multi-hops opto-RF transmission

4.3 Experimental Set-Up and Results

The multi-hop transmission is described in Figure 10: the binary data stream is provided by a data timing generator Tektronix. These data modulate the pulse position of a first transmitter operating at 60 GHz. After the MPA, the time evolution of the RF signal is measured and shows an isolation between the ON-state and the OFF-state greater than 20 dB. The pulse width is close to 300 ps and corresponds to a good trade-off between channel capacity and spectral band filling: the narrowness of the pulse width enables to decrease the probability of collisions between users and offers a sufficient spread spectrum to prevent signal fading due to multipath propagation. The radiated signal has a peak power of 22 dBm and is transmitted over a range of 4 meters. The emitter and receiver antennas have a 3dB aperture beam-width equal to 60 degrees. The RF part of the electro-optic transceiver is only composed by a LNA and a detector enabling to recover the pulse envelope. Then, these pulses modulate the intensity of a Distributed Feedback Laser (DFB) operating at 1300nm. The intensity modulated optical signal is transmitted through a PMMF based on perfluorinated polymer and having a core diameter close to 62.5 μm . The measured optical power after 100 m link length is -4dBm (optical).

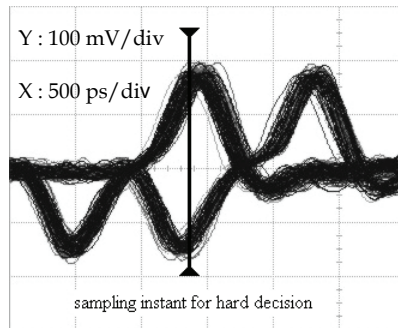


Fig. 12. Eye diagram of received PPM signal

A low cost PIN photodiode followed by a DC-6GHz amplifier delivers the sub-nanosecond pulses to the RF part of the optoelectronic transceiver. Recovered pulses modulate a second 60-GHz LO signal. The modulated signal is amplified in the same manner as for the first hop. Once again, the modulated RF signal is transmitted over a distance of 4 meters. Same antennas as for the first RF hop are used. The MMW receiver, as the first one, is only composed by a LNA and a detector which enables to recover the pulse envelope. At this stage, the eye diagram of the received pulse stream can be observed in Figure 11. The eye aperture shows the high quality of the multi-hop transmission. These results are quantified by BER measurements on a logic analysis system: for a data rate of 100 Mbps, BER measurements reach values greater than 10^{-6} and validate by this way the MMW RoF system performance. Further experimental results have been led successfully for data rates up to 200 Mbps with BER measurements under the threshold value of 10^{-6} without using additional signal processing.

5. Conclusion

In this chapter, we have presented two innovative hybrid systems based on specific 60-GHz wireless systems. The compliance of these systems with opto-RF transceivers has been experimentally demonstrated, proposing by the way two efficient alternatives to 60-GHz SMF RoF systems. Lower cost optical solutions, i.e. 62.5 μ m core polymer fibre and IM-DD technique, were used.

We have detailed an unidirectional transmission by using a PMMF based optical link operating at 1300nm. Assuming the low material dispersion properties (and so the potential high bandwidth) of the PMMF in a wide wavelength range (from 800nm to 1400nm), the bidirectional transmission could be performed by using the Wavelength Division Multiplexing (WDM) technique available for the Glass Multimode Fibre.

6. References

- Bo Hu; Beaulieu, N.C ; *Accurate performance evaluation of time-hopping and direct-sequence UWB systems in multi-user interference*, IEEE Transactions on Communications, Volume 53, Issue 6, June 2005 Page(s):1053 - 1062
- Deparis, N.; Boe, A.; Loyez, C.; Rolland, N.; Rolland, P.A.; *Receiver and Synchronization for UWB impulse radio signals*, 2006 IEEE MTT-S - 11-16 June 2006- San Francisco, California
- Shoji, Y.; Hamaguchi, K.; Ogawa, H.; *Millimeter-wave remote self-heterodyne system for extremely stable and low-cost broad-band signal transmission*, IEEE Transactions on Microwave Theory and Techniques, Volume 50, Issue 6, June 2002 Page(s):1458 - 1468
- Sobrinho, J.L.; Krishnakumar, A.S.; *Quality-of-service in ad hoc carrier sense multiple access wireless networks*, IEEE Journal on Selected Areas in Communications, Volume 17, Issue 8, Aug. 1999 Page(s):1353 - 1368
- Vegas Olmos, J.J.; Kuri, T.; Sono, T.; Tamura, K.; Toda, H.; Kitayama, K.-i.; *Reconfigurable 2.5-Gb/s Baseband and 60-GHz (155-Mb/s) Millimeter-Waveband Radio-Over-Fiber (Interleaving) Access Network*, Journal of Lightwave Technology, Volume 26, Issue 15, Aug.1, 2008 Page(s):2506 - 2512
- Woo-Kyung, Kim; Woo-Jin Jeong; Soon-Woo Kwon; Myoung-Keun Song; Geun-Sik Son; Woo-Seok Yang; Hyung-Man Lee; Han-Young Lee; *60 GHz Optical Carrier Generation Using a Domain Reversed LiNb2O3 Optical Modulator*, Journal of Lightwave Technology, Volume 26, Issue 14, July15, 2008 Page(s):2269 - 2273

Application of Graded-Index Plastic Optical Fiber in broadband access networks

Jianjun Yu

*NEC Laboratories America
jianjun@nec-labs.com, USA*

1. Introduction

The explosive growth of broadband multimedia applications, such as video streaming, high-definition television (HDTV), video on demand, and interactive games, a huge demand for bandwidth has been imposed on the access infrastructure. The next generation access solutions have to be cost efficient to provide huge bandwidth. However, to gain this bandwidth usually needs high performance and high cost optical and electrical components. To reduce the cost is the main motivation for researchers, carriers and equipment providers. Fortunately, people have found some good solutions. Specially, newly developed plastic optical fiber (POF) has been demonstrated that it can be used to provide huge bandwidth and low insertion loss by some special design. Recently, graded index POF (GI-POF) has demonstrated that it can provide over 40GHz bandwidth. Some advanced modulation formats can also be employed to extend the bandwidth of the GI-POF further. Directly modulated laser with special optical filtering technique can generate a laser to increase the dispersion tolerance and extend the transmission distance of signal in GI-POF. Optical orthogonal frequency division multiplexing signal (OFDM) can be used to transmit signal in narrow bandwidth so that it can be also used to increase the bandwidth of the GI-POF. In this chapter, we will review these new techniques and report our latest results.

2. Access optical network

Access networks connect business and residential premises to metropolitan area networks (MANs) or wide area networks (WANs). Because of the explosive growth of broadband multimedia applications, such as video streaming, high-definition television (HDTV), video on demand, and interactive games, a huge demand for bandwidth has been imposed on the access infrastructure. As DWDM technology was developed for the long haul network and gigabit Ethernet for the local area network (LAN), access networks tend to be the bottle neck for end-to-end broadband applications. Today, the two most popular access network solutions are digital subscriber loop (xDSL) technologies deployed by telephone companies, and cable modems from cable companies. These access technologies do not have comparable bandwidth capability with Gigabit Ethernet and have limitations in providing high quality integrated services, including video, voice, and data. Unlike metro and long-

haul networks, access networks must serve a more diverse and cost sensitive customer base. End users may range from individual homes, to corporate premises, to hotels, and services must therefore be provisioned accordingly. Data, voice, and video must be offered over the same high-speed connection with guarantees on quality of service (QoS), and the ability to upgrade bandwidth and purchase content on a needed basis. Therefore, the next generation access solutions have to be cost efficient when providing more bandwidth.

In the so-called FTTx access networks, optical fiber replaces copper in the distribution network. For example, in fiber to the curb (FTTC) or home (FTTH), the capacity of access networks is sufficiently increased to provide broadband services to subscribers. Because of the cost sensitivity of access networks, passive optical networks (PONs) are considered to be the most promising technology as they can provide reliable yet integrated data, voice, and video services to end users at bandwidths far exceeding current access technologies. Unlike other access networks, PONs are point to multipoint networks capable of transmitting over 20 kilometers of single mode fiber. PONs can offer symmetrical data transmission on both the upstream and downstream links, allowing the end user to provide Internet services such as music file sharing and Web hosting. In addition to providing a good alternative, PONs represent an excellent evolutionary path for current access technologies such as cable and DSL. By using passive components (such as optical splitters and couplers) and eliminating regenerators and active equipment normally used in fiber networks, PONs reduce the installation and maintenance costs of fiber as well as connector termination space. These costs still require laying fiber, which makes PONs more expensive to install. However, since fiber is not bandwidth limited but loss limited (as opposed to copper wires, cable, and wireless), the potential performance gains and long-term prospects make PONs well-suited for new neighborhoods or installations.

PONs typically fall under 2 groups: ATM PON (APON) and Gigabit PON (GPON) from Full Service Access Network (FSAN) and the International Telecommunication Union – Telecommunication Standardization Sector (ITU-T); and Ethernet PON (EPON) from IEEE 802.11ah Ethernet in the first mile (EFM) working group. In the APON and BPON specifications, ATM is used as the native protocol data unit (PDU), which implies protocol conversion between Ethernet and ATM is needed. EPON combines low-cost Ethernet equipment and low cost passive optical components, and has therefore attracted more attention in recent years.

Current access technologies represent a significant bottleneck in bandwidth and service quality between a high-speed residential/enterprise network and a largely overbuilt core backbone network. Backbone networks are provisioned for operation under worst-case scenarios of link failures, and thus backbone links are lightly loaded most of the time. In addition, high capacity routers and ultra-high capacity fiber links have created a true broadband architecture. However, large backbones are not the whole the equation; distribution of that connectivity to individual enterprises and homes is just as critical for meeting the huge demand for more bandwidth (Fig. 1). Unfortunately, the cost of deploying true broadband access networks with current technologies remains prohibitive. This in turn makes it difficult to support end-to-end Quality of Service (QoS) for a wide variety of applications, particularly non-elastic applications such as voice, video, and multimedia that cannot tolerate variable or excessive delay or data loss.

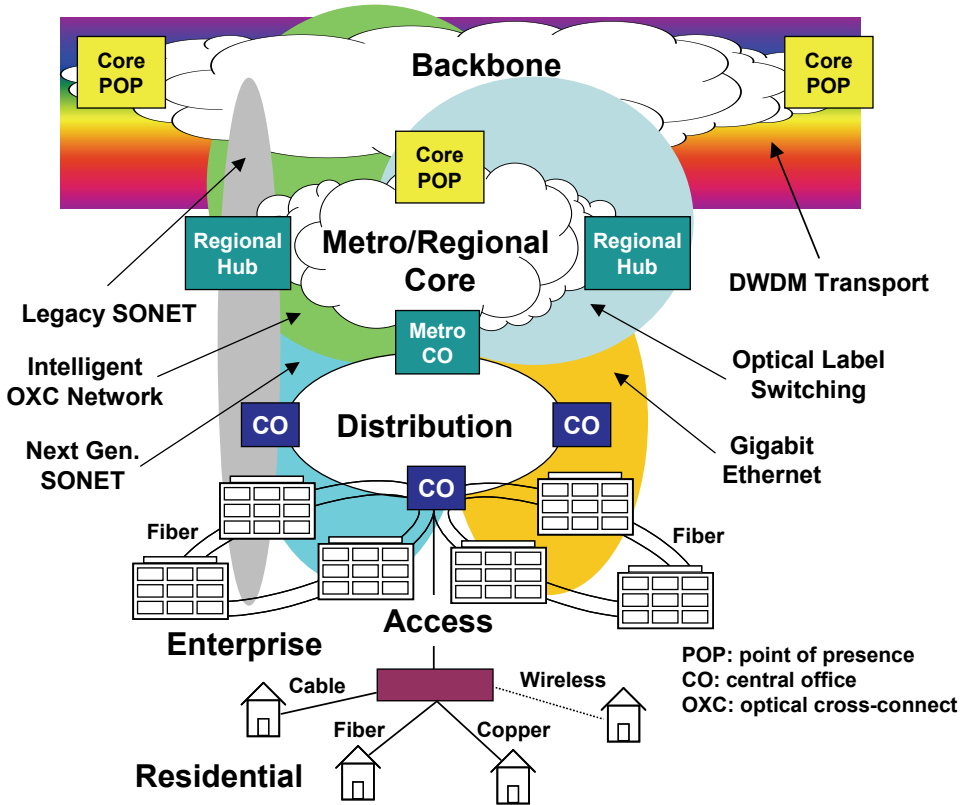


Fig. 1. Distributing optical backbone connectivity to enterprises and homes.

2.1 Existing Access Solutions

When it comes to access networks, network operators have a difficult choice among competing technologies - Digital Subscriber Line (DSL), cable, optical, and fixed wireless. Key considerations to the choice include deployment cost and time, service range, and performance. The most widely deployed solutions today are DSL and cable modem networks, which have a combined total of roughly 25 million users by the end of 2003. Although they offer better performance over 56 Kbit/s dial-up telephone lines, they are not true broadband solutions for several reasons. For instance, they may not be able to provide enough bandwidth for emerging services such as content-rich services, media storage, peer-to-peer services, multi-player games with audio/video chat to teammates, streaming content, on-line collaboration, high-definition video-on-demand, and interactive TV services. In addition, fast Web-page download still poses a significant challenge, particularly with rich, engaging, and value-added information involving high-resolution DVD video streaming, multimedia animation or photo quality images. Finally, only a handful of users can access multimedia files at the same time, which is in stark contrast to direct broadcast TV services. To encourage broad use, a true broadband solution must be scalable to thousands of users and must have the ability to create an ultra-fast Web-page download

effect, superior to turning the pages of a book or flipping program channels on a TV, regardless of the content.

A major weakness of both DSL and cable modem technologies is that they are built on top of existing access infrastructures not optimized for data traffic. In cable modem networks, RF channels that are left over after accommodating legacy analog TV services are dedicated for data. DSL networks do not allow sufficient data rates at required distances due to signal distortion and crosstalk. Most network operators have come to realize that a new, data-centric solution is necessary, most likely optimized over the Internet Protocol (IP) platform. The new solution should be inexpensive, simple, scalable, and capable of delivering integrated voice, video, and data services to the end-user over a single network.

2.2 Ethernet for the First Mile

Ethernet for the First Mile (EFM) is an effort to extend Ethernet's reach over the first-mile access link between end-users and carriers, and make Ethernet a low-cost broadband alternative to technologies such as DSL and cable. The motivation for doing this is sound since there are currently over 500 million Ethernet ports deployed globally and it is advantageous to preserve the native Ethernet frame format rather than terminate it and remap its payload into another layer 2 protocol (e.g., Point-to-Point Protocol, PPP). The EFM specifications are developed by the IEEE 802.3ah Task Force (<http://www.ieee802.org/3/efm>), which was formed in November 2000. The draft standard (version 3.0 was issued on January 2004) includes *physical layer* specifications for copper, fiber point-to-point, fiber point-to-multipoint topologies. It is supported by the EFM Alliance or EFMA (www.efmalliance.org), a vendor consortium formed in December 2001 to:

- Promote industry awareness and acceptance of EFM standard;
- Contribute technical resources to facilitate standard development;
- Provide resources for multi-vendor interoperability.

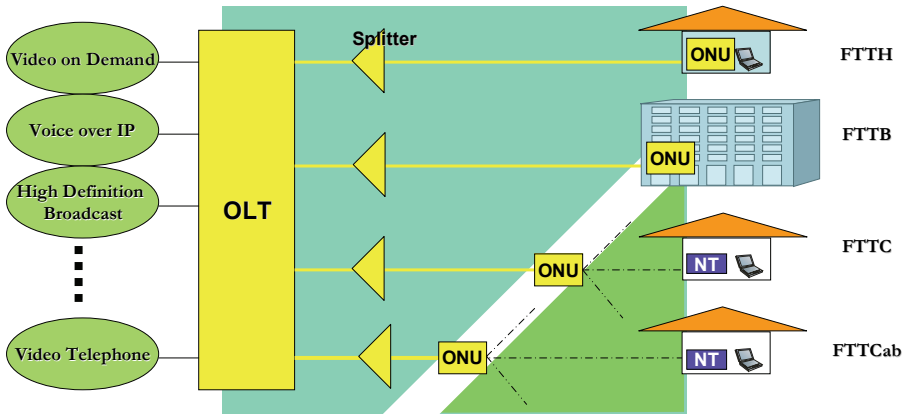
2.3 Broadband Optical Access

DSL or cable-modem access provides benefits of installed infrastructure, virtually eliminating deployment costs. If fixed wireless access is chosen, network providers gain the benefit of quick and flexible deployment. However, these access methods may suffer bottlenecks in bandwidth-on-demand performance and service range. For example, cable networks are susceptible to ingress noise, DSL systems can be plagued with significant crosstalk, and unprotected broadcast wireless links are prone to security breach and interference. Furthermore, current DSL and cable deployments tend to have a much higher transmission rate on the downstream link, which restricts Internet applications to mostly Web browsing and file downloads.

While wireless access is excellent for bandwidth scalability in terms of the number of users, optical access is excellent for bandwidth provisioning per user. Furthermore, the longer reach offered by optical access potentially leads to more subscribers. Optical access networks offer symmetrical data transmission on both the upstream and downstream links, allowing the end user to provide Internet services such as music/video file sharing and Web hosting. In addition to providing a good alternative, such networks represent an excellent evolutionary path for current access technologies. These costs still require laying fiber, which makes optical access networks more expensive to install. However, since fiber is not

bandwidth limited but loss limited (as opposed to copper wires, cable, and wireless), the potential performance gains and long-term prospects make optical access networks well-suited for new neighborhoods or installations. In addition, there are innovative solutions for deploying fiber in the last mile, even in established neighborhoods. For example, instead of investing in expensive dedicated fiber conduits, existing sanitary sewers, storm drains, waterlines, and natural gas lines that reach the premises of many end users can be exploited. Fiber can be housed in these utilities by forming creative business partnerships among optical fiber owners, service providers, utility pipe owners, vendors, and city municipalities. Access networks should be scalable in bandwidth provisionable per-user. To be scalable with number of subscribers, it is highly important to identify architectures that allow low equipment cost per subscriber. As new applications appear and demand higher bandwidth, the network should be gracefully upgraded. It is important to be able to perform an incremental upgrade where only the subscribers requiring higher bandwidth are upgraded, not the entire network. Since the lifespan of optical fiber plant is longer compared to copper or coaxial cables, it is expected that the optical network will be upgraded multiple times during its lifetime. As such, it is important to design access architectures that allow seamless upgrade. In addition, the deployment of fibers between residences can be used to connect end-users directly, forming an autonomous communication network among residential end-users, thereby improving the overall service reliability through provision of redundant data paths similar to the multihop wireless architecture described in the previous section.

2.4 Passive Optical Networks



FTTH: Fiber to the Home FTTB: Fiber to the Building
FTTC: Fiber to the Curb FTTCab: Fiber to the Cabinet

Fig. 2. Typical Passive Optical Access Network.

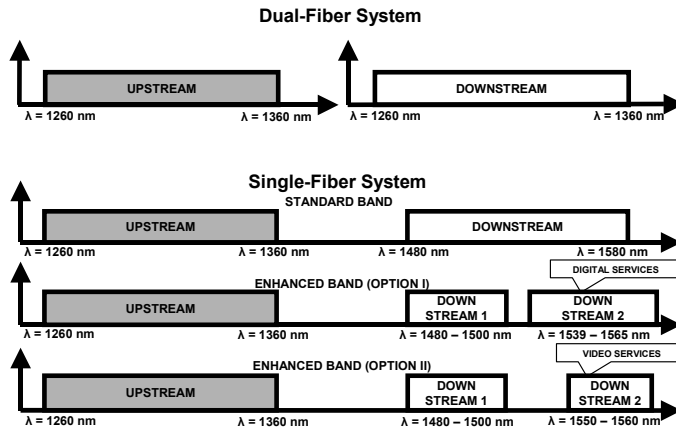


Fig. 3. Upstream and downstream optical bands for dual and single-fiber PONs.

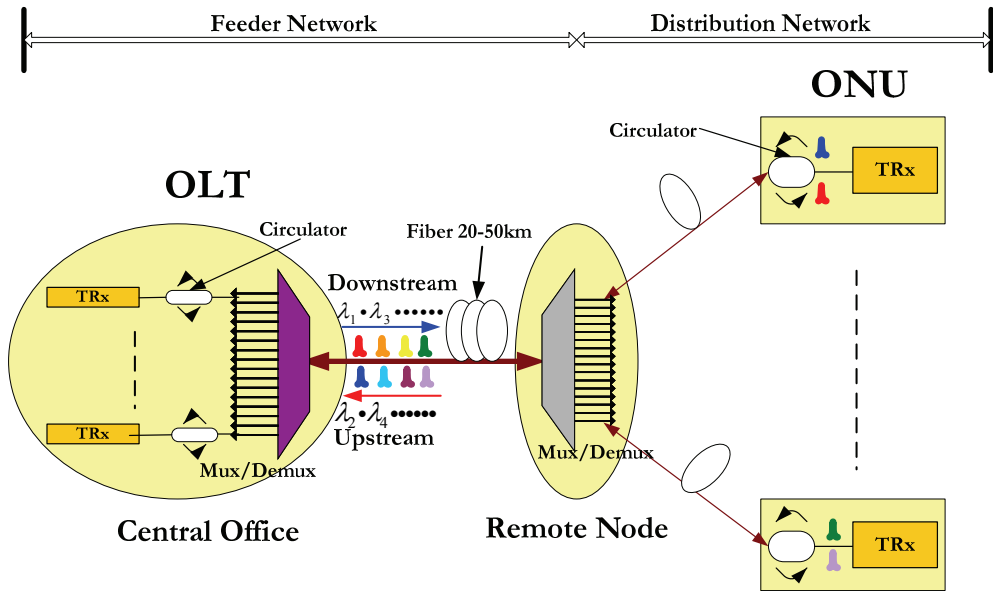


Fig. 4. The detailed architecture between OLT and ONU

Passive optical network (PON) is a technology viewed by many as an attractive solution to the last mile problem as PONs can provide reliable yet integrated data, voice, and video services to end users at bandwidths far exceeding current access technologies. Unlike other access networks, PONs are point to multipoint networks capable of transmitting over 20 kilometers of single-mode fiber. As shown in Fig. 2, a PON minimizes the number of optical transceivers, central office terminations, and fiber deployment compared to point-to-point and curb-switched fiber solutions. By using passive components (such as optical splitters and couplers) and eliminating regenerators and active equipment normally used in fiber

networks (e.g., curb switches, optical amplifiers), PONs reduce the installation and maintenance costs of fiber as well as connector termination space. The general PON architecture consists of the Optical Line Terminator (OLT) on the service provider side and Optical Network Unit (ONU) (or sometimes the Optical Network Terminal) on the user side (Fig. 3). The ONUs are connected to the OLT through one shared fiber and can take different FTTx configurations e.g., Fiber to the Home (FTTH), Fiber to the Curb (FTTC), and more recently Fiber to the Premise (FTTP). The upstream and downstream optical bands specified by ITU-T for dual and single-fiber PONs are shown in Fig. 4.

PONs typically fall under two groups: ATM PONs (APONs) and Ethernet PONs (EPONs). APON is supported by FSAN and ITU-T due to its connection-oriented QoS feature and extensive legacy deployment in backbone networks. EPON is standardized by the IEEE 802.3ah Ethernet in the First Mile (EFM) Task Force. EPONs leverage on low cost, high performance, silicon-based optical Ethernet transceivers. With the growing trend of GigE and 10GigE in the metro and local area networks, EPONs ensure that IP/Ethernet packets start and terminate as IP/Ethernet packets without expensive and time consuming protocol conversion, or tedious connection setup.

2.5 Wavelength Division Multiplexing Optical Access

Wavelength Division Multiplexing (WDM) is a high capacity and efficient optical signal transmission technology that is prevalent in long-haul backbone applications, but is now emerging in Metropolitan Area Networks (MAN). WDM uses multiple wavelengths of light, each wavelength corresponding to a distinct optical channel (also known as lightpath or lamda, λ), to transmit information over a single fiber optic cable simultaneously. Current backbone commercial WDM systems have been increased up to 40 (100GHz spacing), 80 (50GHz spacing) in C-band or 160 wavelengths in C+L-band on a single fiber. It is an economical alternative to installing more fibers and a means to dramatically provide higher capacity.

Current demand of bandwidth is nearly approaching the limit of transmission capacity of copper-based technologies like Digital Subscriber Line (DSL) or cable modem. Although based on aforementioned TDMA PON has the ability to provide up to 1-2.5Gb/s, burst mode reception at OLT and the clock synchronization of different ONUs have already been the main barrier to limit the TDMA mechanism up to higher signal rates. Therefore, WDM has been considered as a transition path from the current access technologies to the ultimate access solution. WDM itself inherits many advantages from the WDM technology of backbone or metro area such as large capacity, data transparent, multi-service, easy management, network security, and upgradability. And also combined the merits of PON network, WDM PON has been considered as future-proof ideal solution. Regarding the wavelength assignment for WDM PON, there are two choices: Coarse WDM (CWDM) or Dense WDM (DWDM). CWDM utilizes 18 wavelengths from 1270nm to 1610nm covering O, E, S, C, L-band with a wide channel spacing 20nm, therefore, athermal AWG and uncooled laser sources are good enough. Low cost is the most attractive advantage for CWDM. However, the elimination of strong absorption at the water peak in E-band and the need for effective all band amplification become the two critical issues that must be addressed in order to longer reach. On the other hand, DWDM achieves greater spectral efficiency using 50/100GHz channel spacing and with commercially available fiber-based

EDFA, can be scalable in distance and number of users, which makes it a better upgrade option in the long-term future.

WDM optical access is a future-proof last mile technology with enough flexibility to support new, unforeseen applications. WDM switching can dynamically offer each end user a unique optical wavelength for data transmission as well as the possibility of wavelength reuse and aggregation, thereby ensuring scalability in bandwidth assignment. For instance, heavy users (e.g., corporate users) may be assigned a single wavelength whereas light users (e.g., residential users) may share a single wavelength (Fig. 2), all on a single fiber. Based on wavelength switched scheme, in a WDM PON network, the OLT contains a multi-wavelength source used to send signals across different wavelengths. In the remote node, an optical switch (MUX/DEMUX) selects out one or more associated wavelengths and transmits them to the subscriber ONU as shown in Fig.4 in detail. We are also witnessing the exciting convergence of WDM and Ethernet, the most notable example being the National LambdaRail or NRL (www.nationallambdarail.org), which is a high-speed, experimental 40-wavelength DWDM optical testbed developed to rival the scale of research provided by the Arpanet (the Internet's precursor) in the 1960s. NRL is the first wide-area use of 10 Gbit/s switched Ethernet and is based on a routed IP network. It is owned by the university community, thanks to the plunge in dark fiber prices over the last 4 years.

2.6 Enabling Technologies of WDM PON Optical devices

One of the biggest challenges for successful DWDM PON deployment is the adoption of cost effective light source components. It is desirable to have tunable laser sources which not only support network provisioning and reconfigurability, but also minimize the production costs and backup stock numbers in the carrier's network. Several sources exist: 1) tunable VCSEL, although long wavelength (C-band) VCSEL are not yet mature up to now, it will be an ideal candidate since it has the potential for high-level system integration characteristics; 2) Spectrum-slicing using a broadband incoherent light source such as a LED may be used to realize the wavelength independent ONT. The LED can be fabricated at a low cost and modulated directly. However, its output power and modulation speed are insufficient for high speed operation; 3) a wavelength locked Fabry-Perot laser diode (F-P LD) with external spectrum spliced amplified spontaneous emission (ASE) injection was proposed recently. By injecting spectrum-sliced broadband light source (BLS) into a F-P LD, the laser is forced to operate in a quasi single mode and the mode partition noise of the F-P LD is suppressed. Although modulation index, bias current and the power of external optical excitation must be carefully chosen to maximize the efficiency, it is a promising solution to reduce cost.

Another key problem involves the survivability of the optical access network. Compared to ring networks as used in SONET/SDH, the tree-and-branch structure used in PONs is more vulnerable to single points of failures due to its topology and the lack of an alternative redundant path. If a fiber link from the RN and to the ONU is broken, the affected ONU will become unreachable from the OLT. Thus, the protection and restoration will be indispensable to provide high availability. This field is still relatively new and only few bidirectional self-healing WDM PON architectures have been proposed. These architectures utilize two different wavelength bands for the neighboring WDM PON's and cyclic property of arrayed wavelength grating (AWG).

3. Plastic optical fiber

3.1 Regular plastic optical fiber

Currently, different types of optical fiber are employed in the field. These types of fiber mainly include quartz optical fiber, glass optical fiber and plastic optical fiber. Quartz optical fiber is suitable for long distance transmission (over 1km). The quartz optical fiber has two types: single mode and multi-mode with different core area. The telecommunication fiber is usually single mode fiber due to requirement of high bandwidth, small dispersion and polarization mode dispersion. For office networks, multi-mode fiber can be employed due to low-cost. Glass optical fiber is mainly used along with POF for lighting. While for polymethylmethacrylate (PMMA) plastic optical fiber (POF), it is used for short-distance electronic appliances and cars.

POF is an optical fiber which is made out of plastic. POF typically uses PMMA (acrylic), a general-purpose resin, as the core material, and fluorinated polymers for the clad material. In large diameter fibers, the core comprises 96% of the cross section to allow the transmission of light. The core size of POF is in some cases 100 times larger than glass fiber. Although quartz fiber is widely used for infrastructures and fiber to the home, POF has been called the "consumer" optical fiber because the fiber and associated optical links, connectors, and installation are all inexpensive. In relation to the future request of high-speed home networking, there has been an increasing interest in POF as a possible option for next-generation Gigabit/s links inside the house. For telecommunications, the more difficult-to-use glass optical fiber is more common. This fiber has a core made of germania-doped silica. Although the actual cost of glass fibers are lower than plastic fiber, their installed cost is much higher due to the special handling and installation techniques required.

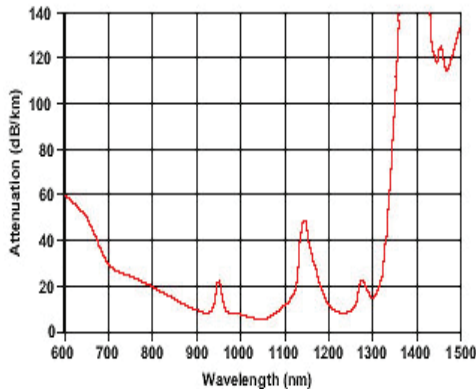


Fig. 5. GI-POF attenuation.

3.2 Graded-Index Polymer Optical Fiber (GI-POF)

Perfluorinated graded-index polymer optical fibers (GI-POFs) can provide large bandwidth and low attenuation (60dB/km) at 850–1300nm, so it is a good replacement and a low cost alternative to traditional glass. With ease of use and affordability, GI-POFs make an excellent choice for the installation of high performance fiber networks. In addition, GI-

POFs provide a higher transmission bandwidth than any other type of plastic optical fiber. Recently, a few 40Gb/s transmission experiments have been demonstrated. Until recently, all commercially available POFs have been fabricated from non-fluorinated polymers such as PMMA and, as a result, have had a refractive index that changes in steps. Although inexpensive, these fibers are characterized by large modal dispersion and typically operate at 530nm or 650nm, which is well outside of standard communication wavelengths (850nm or 1300nm), which is where high-speed transceivers are readily available. Due to the high attenuation in the near infrared, these fibers are restricted to low performance (<100Mb/s), short range (<50m) applications in the visible region. With the advent of an amorphous perfluorinated polymer, polyperfluoro-butenylvinylether (commercially known as CYTOP®), the limitations presented by step-index POFs have been overcome. Perfluorinated fiber exhibits very low attenuation in the near infrared (~10dB/km) as shown in Fig. 5. Moreover, since the perfluorinated optical fiber can be constructed with a graded refractive index, it is capable of supporting bandwidths that are 100 times larger than those provided by conventional POFs. This is due to the interplay between high mode coupling, low material dispersion, and differential mode attenuation. Unlike conventional glass fibers, which suffer from high interconnection and receiver costs, perfluorinated GI-POFs are easy to install. To add a connector to a glass fiber, the fiber needs to be cleaved using an expensive, specialized tool. Then, epoxy is used to attach the fiber to the connector hardware. Finally, the assembled connector must be polished. In contrast, the GI-POF can be terminated using simple and inexpensive tools, connectors are crimped on, and polishing occurs in mere seconds, leading to a high quality optical link in a fraction of the time. Moreover, GI-POFs are compatible with standard multimode glass fiber transceivers. As an example, Table 2 lists the specification of the commercial GI-POF from Thorlabs.

Fiber model	50SR	62SR	120SR
Attenuation at 850nm	<60dB/km		
Attenuation at 850nm	<60dB/km		
Bandwidth at 850nm	>300MHz·km		
Numerical aperture	0.190±0.015	0.190±0.015	0.190±0.015
Macrobend loss	<0.25dB	<0.35dB	<0.60dB
Zero dispersion wavelength	1200~1650nm		
Dispersion slope	<0.06ps/nm ² ·km		
Core diameter	50±5µm	62.5±/-5µm	120±/-10µm
Cladding diameter	490±/-5µm		
Temperature induced attenuation at 850nm (-20 to +70°C)	<5dB/km		

Table 2. specification of Thorlab's GI-POF.

Since 2006, a few world records by employing GI-POF have been achieved. The optical fiber communication conference (OFC) 2006, Georgia Tech's researchers reported that 30Gb/s on/off keying (OOK) signals are transmitted over 30m GI-POF. In ECOC 2007, Schollmann et al., reported the 40Gb/s OOK signals are delivered over 50m GI-POF with new designed multi-mode high-speed receiver. In OFC 2008, Yu in NEC Labs America reported 42.8Gb/s optical signal generated by chirped managed laser transmission over 100m GI-POF. In

ECOC 2008, Yu in NEC Labs America demonstrated 16Gb/s OFDM signal transmission over 50m GI-POF. In OFC 2009, Yang reported 40Gb/s signal transmission over 100m GI-POF based on discrete multimode modulation. By using the new spectral efficiency modulation format, such as CML and OFDM, can furthermore increase the bandwidth of the GI-POF.

4. Enabling techniques to expand the bandwidth of GI-POF

4.1 Chirped Management Laser

The demand of bandwidth for Internet traffic and access networks in the premises are rapidly increasing, fueled by video and graphic-rich applications. Therefore, the data rate at 40-Gb/s per channel is expanding to next-generation optical access networks and very-short-reach (VSR) optical links. Unlike long-haul and metro networks, access and VSR networks require low hardware cost and low operation expenses to make the transmission technology attractive and practical. Currently, there is a growing interest in utilizing directly modulated lasers (DMLs) in cost-sensitive metro and access optical links because of their potentially low cost, compact size, low power consumption, and high output power characteristics when compared with other transmitter sources using external modulation (EM) scheme such as electro-absorption modulator (EAM) or Mach-Zehnder modulator (MZM). As it is well known, however, DMLs are the carrier density modulation via drive current, giving rise to inherent and highly component-specific frequency chirp, i.e., a residual phase modulation (PM) accompanying the desired intensity modulation (IM). This chirp results in broad spectrum that severely limits the maximum transmission distance within ~20 and ~2-km SSMF for 10 and 40 Gb/s without dispersion compensation because of its interaction with fiber dispersion along the transmission link. One way to overcome this issue is to use the special fiber with a negative dispersion characteristic, which is a good choice to take advantage of the positive chirp characteristics of DMLs to increase the reach without dispersion compensation modules that can cost as much as the transmission fiber. However, it is only suitable to new deployment of optical transport system but not fit to upgrade and change of the installed base of metro fiber links.

Chirp-managed laser (CML) can provide a good optical source for access systems. In order to support high dispersion tolerance, a DFB laser biased at high direct current (DC) far above the threshold is used, digital data directly modulate this DFB laser, and a suitable optical filter is used to control the phase between the adjacent bits. The additional benefits of the higher bias are high output power, wide modulation bandwidth, low timing jitter, and suppressed transient chirp. CML technology simultaneously meets two market needs: (1) the data rate upgrade from 2.5 to 10 Gb/s, even to 40 Gb/s, in the emerging metro market, and (2) the migration of small form factor pluggable optics from short reach to high-performance long reach and WDM links. The directly modulated signals have low extinction ratio (ER) and an accompanying adiabatic chirp. An optical spectrum reshaping (OSR) filter is placed at the laser output to perform frequency modulation (FM) to amplitude modulation (AM) conversion to increase the ER and convert the slowly-varying adiabatically chirped pulses to flat-topped chirp pulses with abrupt phase transitions [9]. The output of the CML has been shown to have tolerance to both negative and positive dispersion for 10-Gb/s optical links.

The CML technique has been applied in 10-Gb/s data links with 200-km transmission over SMF without dispersion compensation and 675-km transmission using a combination of electronic dispersion compensation (EDC) and tunable dispersion compensating modules at the receiver. We have developed a 40-Gb/s CML transmitter with high dispersion tolerance using a simple combination of a directly modulated DFB laser and the subsequent conventional optical filter.

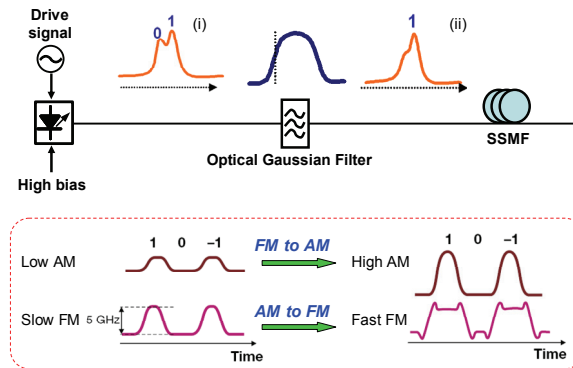


Fig. 6. Schematic of chirped-managed DML transmitter.

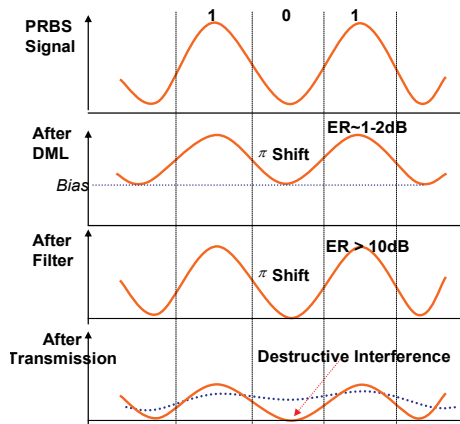


Fig. 7. Schematic of signal waveform.

4.2 The Principle of the CML Transmitter

4.2.1 Chirp Characteristics of DMLs

The performance of DMLs strongly depends on the characteristics of the laser frequency chirp. At high data rates ($\geq 2.5\text{Gbit/s}$), the frequency chirp of DMLs has two major components: the transient chirp and the adiabatic chirp. At lower data rates, the thermal

chirp becomes dominant. Here we focus on high data rate operation. The chirp $\Delta\nu(t)$ of a DML is related to the laser output optical power $P(t)$ through the expression

$$\Delta\nu(t) = \frac{\alpha}{4\pi} \left(\frac{d}{dt} [\ln(P(t))] + \kappa P(t) \right), \quad (1)$$

Where α is the linewidth enhancement factor and κ is the adiabatic chirp coefficient. In (1), the first term is a structure-independent transient chirp, and the second term is a structure-dependent adiabatic chirp. DMLs can be classified as transient or adiabatic chirp dominated. Transient chirp dominated DMLs exhibit significantly more overshoot and ringing in output power and frequency deviations. The frequency difference between steady-state "1"s and "0"s is relatively small. On the other hand, adiabatic chirp dominated DMLs exhibit damped oscillations and large frequency difference between steady-state "1"s and "0"s. In the equation (1), the output power $P(t)$ is related to the photon density $S(t)$ through the relation:

$$P(t) = \frac{V\eta h\nu}{2\Gamma\tau_p} S(t) \quad (2)$$

And the photon density $S(t)$ is determined by the well-known small signal single mode laser rate equations in the simple form as follows:

$$\frac{dS(t)}{dt} = \frac{\Gamma g_0(N(t) - N_0)}{1 + \varepsilon S(t)} S(t) - \frac{S(t)}{\tau_p} + \frac{\Gamma\beta N(t)}{\tau_c}, \quad (3)$$

$$\frac{dN(t)}{dt} = \frac{I(t)}{eV} - \frac{N(t)}{\tau_c} - \frac{g_0(N(t) - N_0)}{1 + \varepsilon S(t)} S(t), \quad (4)$$

$$\frac{d\phi}{dt} = \frac{\alpha}{2} \left[\Gamma g_0(N(t) - N_0) - \frac{1}{\tau_p} \right], \quad (5)$$

Where $I(t)$ is the current waveform injected in the active layer, $N(t)$ is the carrier density, ν is the optical frequency, h is the Planck's constant, η is the differential quantum efficiency, Γ is the confinement factor, N_0 is the carrier density at transparency, β is the fraction of spontaneous emission noise coupled into the lasing mode, g_0 is the differential gain coefficient, ε is the nonlinear gain compression factor (gain saturation coefficient), τ_p is the photon lifetime, τ_c is the carrier lifetime, V is the volume of the active layer and α is the same as in Eq. 1, i.e. the linewidth enhancement factor. It should be noticed that, in a first approximation, static temperature (25°C) dependence of the value of each parameter has been ignored here. From Eqs. 1-5, we can see that the minimum number of parameters that have to be estimated is ten ($\Gamma, V, N_0, \beta, g_0, \varepsilon, \tau_p, \tau_c, \eta, \alpha$) in addition to the lasing wavelength λ . In the (1), the α parameter can be calculated as well as the adiabatic chirp coefficient κ , which is directly related to the nonlinear gain compression factor:

$$\kappa = \frac{2\Gamma}{\eta h\nu V} \varepsilon. \quad (6)$$

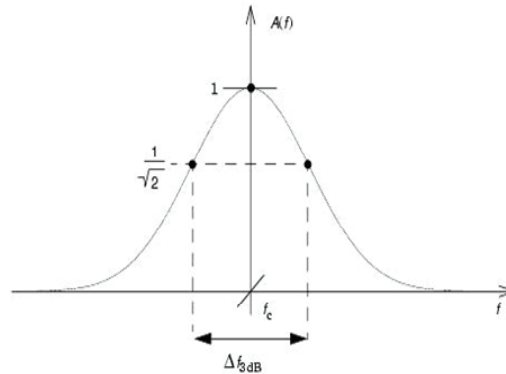


Fig. 8. Transfer function of the Gaussian filter.

Therefore, based on the Eqs. 1-6 of the chirp model (already including the drive current (DC) bias), we can design the parameters of the DMLs to offer suitable chirp response for the generation of the phase correlation.

4.2.2 Operating Principle

The high dispersion tolerance is mainly because of the phase-correlative modulation among the adjacent bits via precisely controlling the frequency chirp in the DML modulation. The adiabatic chirp makes the “1” bits blue shifted relative to the “0” bits. By controlling the modulation depth, the phase flip between 0 and π in the middle of the space bit could be realized, which leads to the destructive interference between the energies on either side of the middle of the space after the dispersion-induced broad spectrum. The π out of phase is the key to the dispersion tolerance. This resulting phase correlation and destructive interference along the fiber transmission are similar to that for optical duobinary modulation, but here, we don’t require pre-coder, encoder, and external modulator in the transmitter side and the decoder in the receiver side.

The CML transmitter comprises a DML and the subsequent optical filter, the schematic diagram is shown in Fig. 6. The DML is a high-speed standard DFB laser, the optical filter is a conventional bandpass filter. The highly chirp-controlled modulation creates two distinct frequency peaks in Fig. 6 inset (i). The main function of the filter is to increase the extinction ratio by passing the “1” bits while attenuating “0” bits in inset (ii), and simultaneously suppress the transient chirp and shape it into the top-flatted chirp. To realize the proper phase flip between the bits, much higher driven bias compared to the conventional direct modulation is employed. The additional benefits of the higher bias are high output power and wide modulation bandwidth due to the high operation point. We can also achieve the stable single mode operation and low timing jitter, and make the laser be the adiabatic chirp dominated via suppression of the transient chirp because the working condition is far away from the threshold of the laser. For a 40-Gb/s data rate, the pulse width is 25 ps, to get the π phase shift, adiabatic chirp need to be equal to $\frac{\pi}{2\pi \times 25 \text{ ps}} = 20 \text{ GHz}$, that means the “1”

bit has 20 GHz blue shift relative to entire “0” bit. The generation of suitable adiabatic chirp

by adjusting bias and laser parameters is the first step to achieve the higher dispersion tolerance, which is due to the AM to FM conversion ("1" bit has blue shift due to the higher intensity compared to "0" bits). However, this results in a low extinction ratio (ER~1-2 dB) accompanying the higher bias. Therefore, a subsequent optical filter is employed to perform the FM to AM conversion by passing the "1" bits and attenuating the "0" bits for increasing the ER. Considering the 1 0 1 bit sequence, the original binary signal, the directly modulated signal, the filtered signal and the transmitted signal are shown in Fig. 7. The change of correlative phase flips and ER are also shown here. It is clearly seen that the eye would close and the original bit could not be recognized (the dashed line in "after transmission") without the destructive interference between the adjacent "1" bits.

4.2.3 Optimization Parameters of the Optical Filter

Since the filter plays an important part in the CML generation, we study the optimization parameters of the optical filter. The subsequent optical filter has two main functions: one is to perform the FM to AM conversion by passing the "1" bits and attenuating the "0" bits for increasing the ER. Additional effect of the optical filter is to suppress the transient chirp and shape it into the top-flatted chirp waveform for keeping the π out of phase difference during the "0" bit. In dependence on the specific application, the filter design includes development of the filter with prescribed magnitude and phase response. Various types of optical filters can be a candidate for optimal OSR filter:

- 1) Butterworth: Maximally flat magnitude response in the pass band, the disadvantage is some overshoot and ringing in step response.
- 2) Chebyshev: Better rate of attenuation beyond the pass-band than Butterworth, the disadvantage is considerably more ringing in step response than Butterworth.
- 3) Bessel: A uniform time delay within pass band and the best step response with minimal overshoot or ringing. The advantage is slower initial rate of attenuation beyond the pass band compared with Butterworth and other filters.
- 4) Rectangular and Trapezoid: Ideal selectivity, absolutely flat magnitude and phase of the frequency response. The disadvantage is that it requires truncation of the impulse response and signal delay at simulations with periodic boundary conditions.
- 5) Gaussian: Smooth transfer function without dispersion, more importantly, it is easily implemented to the real design and application in optical communication systems.

Based on the above mentioned reasons, we select the Gaussian filter type in our simulation model. The Gaussian filter transfer characteristic is determined by the parameter bandwidth

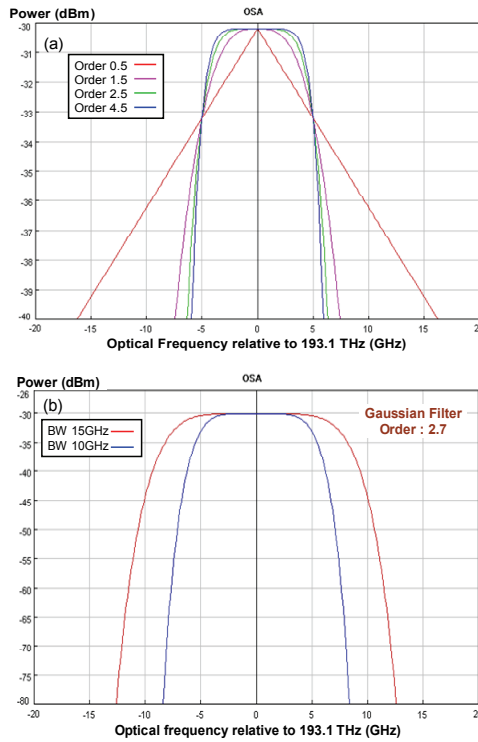


Fig. 9. Transfer characteristics of bandpass optical Gaussian filters. (a) Gaussian filter with different orders and the same 3 dB bandwidth, (b) Gaussian filter with different bandwidths and the same order.

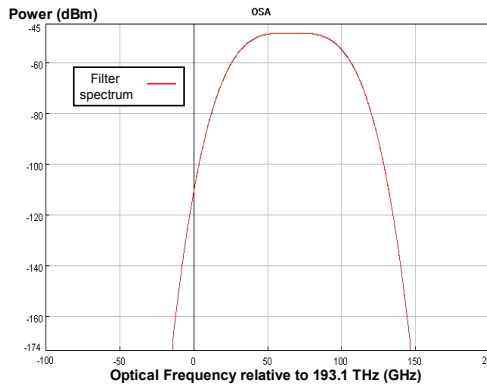


Fig. 10. Transfer spectrum for 40Gb/s signals

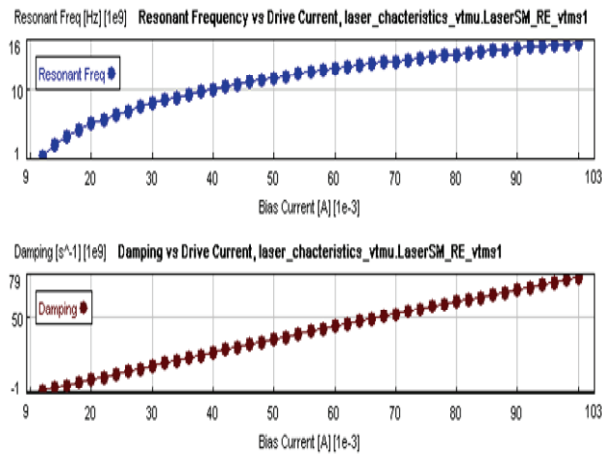


Fig. 11. Resonant frequency and damping as functions of bias current

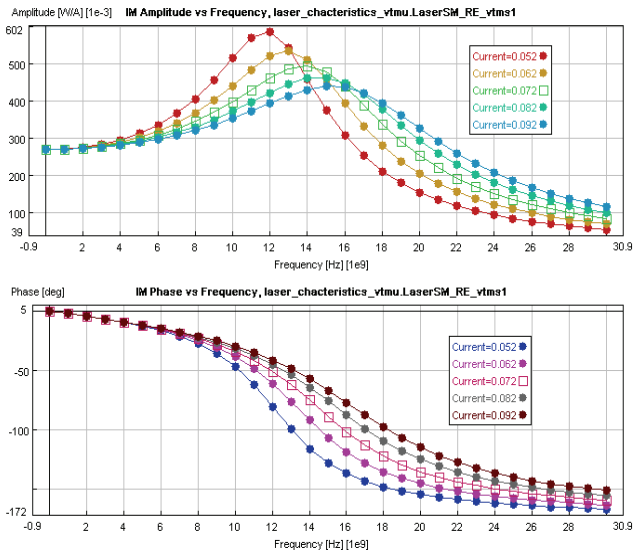


Fig. 12. Amplitude and phase response in the DML intensity modulation

(Δf_{3dB}), central frequency (f_c) and Gaussian order (n) of the filter, the expression is shown in (7):

$$T(f) = \exp \left(-\ln \sqrt{2} \left(\frac{f - f_c}{f_g} \right)^{(2n)} \right) \tag{7}$$

with the assumption of vanishing phase and $f_g = \frac{\Delta f_{3dB}}{2}$.

Filter order sets the attenuation rate at transition from pass band to stop band. Fig. 8 shows the basic transfer function of the Gaussian filter.

As mentioned before, passing the signal through the edge of the filter not only improves the ER but also produces vestigial sideband (VSB) effect, which adds blue transient chirp at the "1" to "0" and "0" to "1" transitions, further improving the eye opening after fiber dispersion. The VSB filtering reduces the information bandwidth as well. Fig. 9(a) and 9(b) shows the transfer spectrum of this Gaussian optical filter in the different of order and bandwidths set, respectively. It is noted that the Gaussian order can be set as the non-integer value. It is clearly seen that the top becomes flat and the roll-off response is very sharp. Regarding the 40-Gb/s signals, we simulate the best transfer spectrum with the bandwidth of 54 GHz and Gaussian order of 1.7. The transfer spectrum is shown in Fig. 10.

4.2.4 Parameters Optimization of DML (Laser Model)

A typical single-mode dynamic laser model (LaserSM_RE module in VPI) based on standard rate equations is used in the simulation. This module simulates the dynamics and noise characteristics of a directly-modulated single-mode laser driven by an electrical current waveform. The model describes the evolution of optical power, phase and carrier density averaged over the whole laser cavity. The model is ideal for modeling metro transmission systems using directly-modulated lasers, as it takes into account the relaxation oscillation, turn-on jitter, laser chirp, intensity and phase noise which can significantly affect the system performance. The chirp control in this directly modulated transmitter comes from two important sections: (1) Generating proper chirp frequency in the laser; (2) chirp filtering and conversion in the subsequent optical filters. We provide the theoretical analysis for the proper chirp generation (adiabatic chirp) in the laser with very high bias. According to the analysis of the chirp model, we performed the multi-parameters sweeping so as to find the optimized laser structure which is suitable to get the π out of phase for the transmission of the directly modulated signals. The results are provided below in table1:

Column Name	Units	Value
Emission Frequency	Hz	193.1e12
Reference Power	W	6.0e-3
Laser Chip Length	m	200e-6
Linear Material Gain Coefficient	m ²	9e-20
Transparency Carrier Density	1/m ³	1.5e24
Confinement Factor		0.3
Group Effective Index		4.0
Material Linewidth Enhancement Factor		3.5
Left Facet Reflectivity		0.3
Right Facet Reflectivity		0.3

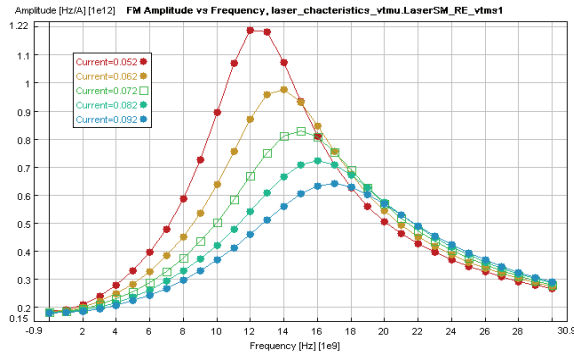
Bimolecular Recombination Coefficient	m^3/s	1.0e-16
Spontaneous Emission Factor		1.0e-4
Nonlinear Gain Coefficient		3.0e-23

Table 1. Summary of laser intrinsic parameters

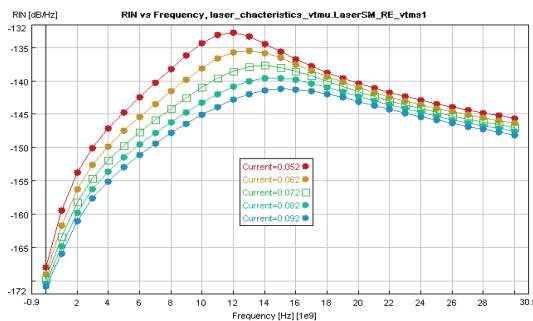
All the parameters above are used for 10-Gb/s signals, regarding 40-Gb/s signals, the drive amplitude is 21 mA and the bias is 85 mA, the nonlinear gain coefficient is changed into 5.0e-23, others keep the same as parameters for 10-Gb/s signals.

4.2.5 Bias current related characteristics

Compared with the conventional DML, the lower threshold is required because we need to bias this laser roughly 5~6 times threshold. Because of inaccuracy of the results below the threshold operation, the sweep is generated above the laser threshold for obtaining the whole working conditions. The resonant frequency and damping as a function of bias current are shown in Fig. 11. It generally increases with increasing the bias current. At the operating range of 60-80 mA bias, the slope of these two curves keeps almost stable.



(a) Frequency response



(b) RIN response

Fig. 13. Frequency modulation response and relative intensity noise spectrum.

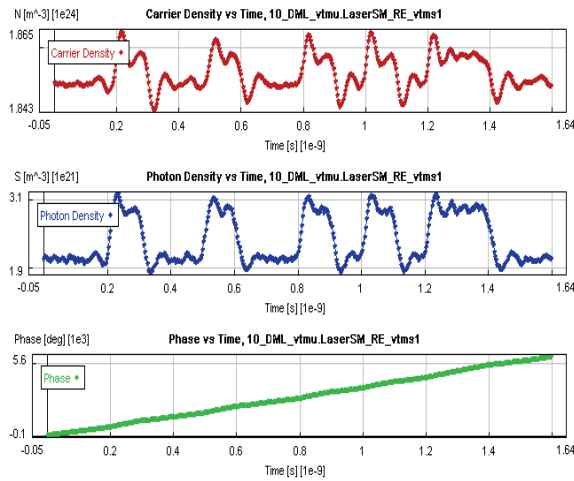


Fig. 14. Internal states as functions of time.

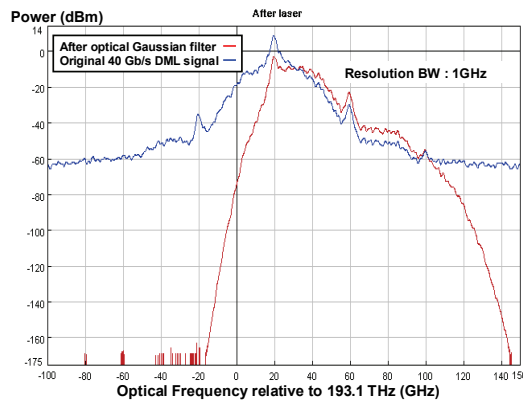


Fig. 15. 40-Gb/s signal spectra before and after optical filtering.

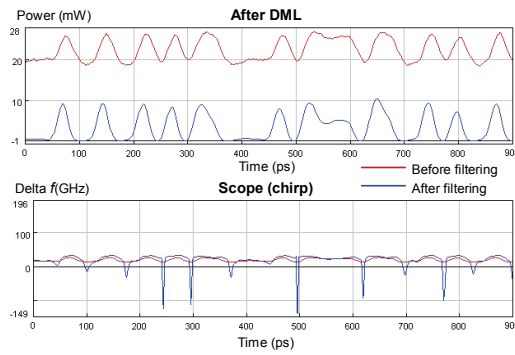
4.2.6 Frequency related characteristics

Figure 12 shows the small-signal intensity modulation amplitude and phase response computed at different bias currents. These response curves can be compared with measured data and used to assist in fitting the model parameter to real devices. At 14 GHz, the laser has the maximum amplitude response at the operation point of 72 mA. It is shown in Fig. 13 that the small-signal frequency modulation response and the relative intensity noise spectrum of the laser at different bias current. The frequency response increases with the optical emitted power, the 3-dB bandwidth at the bias of 72mA is larger than 10GHz and the peak of resonant frequency is 15 GHz. From the (b) in Fig. 13, the relative intensity noise (RIN) is low enough at resonant frequency of 14 GHz at the bias of 72 mA.

4.2.7 Time related characteristics

The carrier, the photon density and the phase of the optical field as a function of time are shown in Fig. 14. These results are based on the internal states of the rate equation model. We can see that the carrier and photon density have the transient change at the drop and down of the optical pulse, which is directly related to the transient chirp. And the photon density, the optical power, is the key to the conversion from amplitude modulation to frequency modulation via the adiabatic chirp. As shown in Fig. 15, the direct modulation leads to the broader spectrum compared with the external modulation scheme. Fig. 16 shows simulation results of signal waveform and chirp response at the output of this DML, after the Gaussian filter and eye diagrams after transmission. The drive amplitude to this DML is 21 mA and the bias is 85 mA. It is clearly seen that the chirp response is flat top, and the eye diagrams are wide open over 15-km SSMF transmission.

(a)



(b)

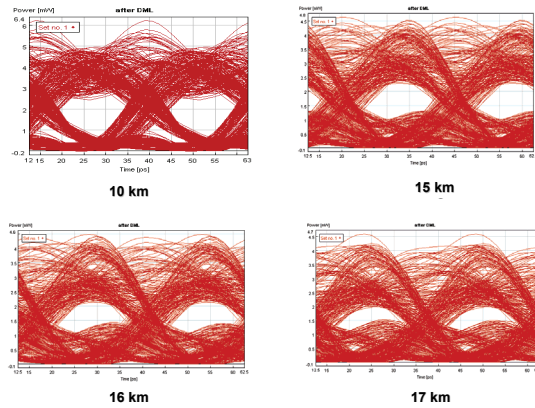


Fig. 16. (a) Waveform and flat-topped chirp and (b) eye diagrams in different distance for 40-Gb/s signals.

4.3 CML transmission performance

The experimental setup is shown in Fig. 17. A commercially available DFB laser at 1548.9 nm is directly modulated at 40-Gb/s using a PRBS with a word length of 2^7-1 or $2^{31}-1$

generated from SHF 50 GHz pattern generator (SHF 12100B). The laser is biased at 94 mA and driven by 2.7 V (peak-to-peak) to produce 9 dBm average power and ~ 11 GHz of adiabatic chirp. The bias and drive voltage are optimized for the best BER performance after transmission. After the DML, a tunable optical filter (TOF) with 3-dB bandwidth of 0.32 nm and 20-dB bandwidth of 0.76 nm is used as the OSR filter to generate the desired chirp-managed signals. The optical eye diagrams before and after the filter are inserted in Fig. 18. The extinction ratio of the DML output before the OSR filter is 1.3 dB and increased to 5 dB, after the OSR filter. The optical spectra before and after the OSR filter are shown in Fig. 19. After the OSR filter, the CML signal is launched into different lengths of standard SMF-28 fiber. The dispersion and loss at

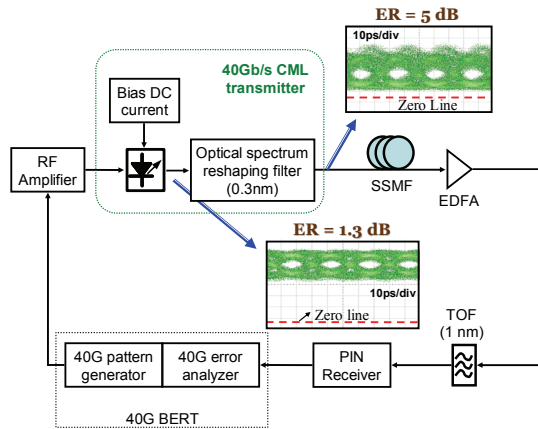


Fig. 17. Chirp-managed 40-Gb/s transmission experimental setup. (TOF: tunable optical filter.)

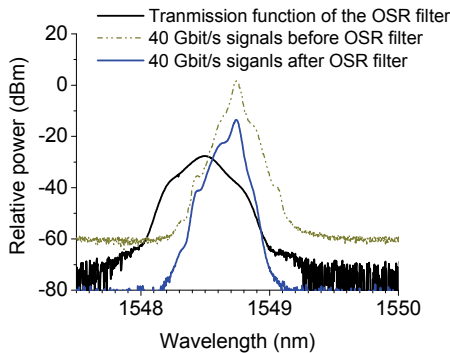


Fig. 18. Received optical spectra with 0.01-nm resolution before and after OSR filter.

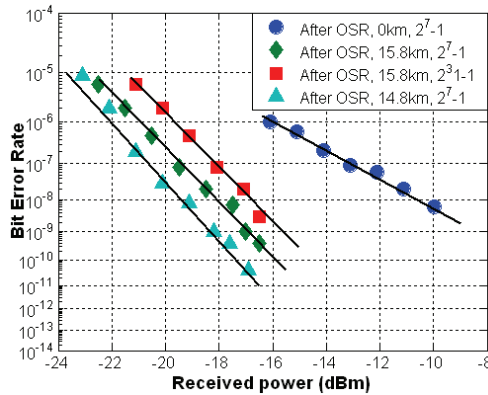


Fig. 19. Measured BER curves of 40-Gb/s CML signals in different distance and PRBS length.

1548.9 nm of this fiber are 17 ps/nm/km and 0.2 dB/km, respectively. The receiver consists of an EDFA pre-amplifier and a 50 GHz PIN photodiode. Another TOF with 3-dB bandwidth of 1.4 nm is used to reduce amplified spontaneous emission (ASE) noise from the EDFA. A SHF 50 GHz error analyzer (SHF11100A) is used to measure the BER performance. The clock signals for the SHF error analyzer are directly obtained from the pattern generator. Fig. 19 shows the BER performance for the 40-Gb/s CML signals transmission over different fiber lengths with different patterns. When the PRBS pattern is 2^7-1 , the receive sensitivity at a BER of 10^{-9} after transmission over 14.8 km and 15.8 km are -17.6 and -16.5 dBm, respectively. Increasing the pattern length to $2^{31}-1$, the BER increases to 10^{-8} after transmission over 15.8 km at -16.5 dBm received power. The pattern dependence penalty is mainly due to the low frequency thermal chirp of the DFB, which is not compensated in this experiment.

4.4 Transmission over Graded-Index Plastic Optical Fiber

In the above section, we have reported the application of the chirp-managed transmitter operating at 42.8-Gb/s data rate over standard SMF without dispersion compensation. In this section, we demonstrate that GI-POF can transmit 40Gb/s signal with a BER smaller than 2×10^{-3} .

The experimental configuration is shown schematically in Fig. 20. The CML transmitter setup, including the driving voltage of the laser, and the OSR filter is kept similar as these in Fig. 16. The optical spectra with 0.01-nm resolution before and after OSR filter are shown in Fig. 20 insets (a) and (b). After the OSR filter and EDFA, the CML signal is launched into 100-m commercially available GI-POF (GigaPOF-50SR, Thorlabs) for transmission.

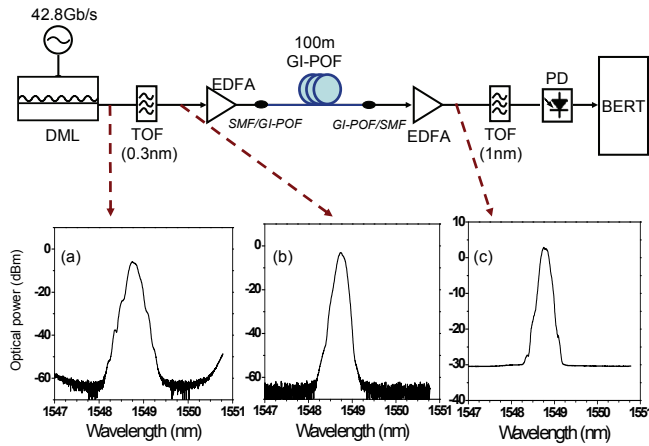


Fig. 20. Schematic of experimental setup for the chirp-managed signal transmission over 100 m GI-POF at 42.8 Gb/s. Inset: received optical spectrum (0.01 nm). (a): Before OSR filter; (b): After OSR filter; (c): After 100m GI-POF.

Due to the lack of a photodiode with multi-mode input and a bandwidth up to 40 GHz, we use a regular photodiode with single-mode input and bandwidth of 45 GHz. Therefore, there is additional insertion loss when we connect the GI-POF with the SMF-28. The coupler loss from GI-POF to SMF-28 is approximately 10 dB. The signal power launched into GI-POF is 23 dBm, and the output power after the 100-m GI-POF is -4 dBm. The insertion loss is over 27 dB, however, the insertion loss at this wavelength can be largely reduced when the laser is operated at 1310 nm or 850 nm. After coupling with the SMF-28, the optical power is -14 dBm. The receiver consists of an EDFA preamplifier and a 45 GHz high-speed single-mode coupled photodiode. The received optical spectrum after preamplifier is shown in Fig. 20 inset (c). Another TOF with 3-dB bandwidth of 1 nm is used to reduce ASE noise from the EDFA. A commercial error analyzer is used to measure BER performance while the clock signals for the error analyzer are directly obtained from the pattern generator. We evaluate the optical signal-to-noise ratio (OSNR) requirement for this CML laser at 42.8-Gb/s as shown in Fig. 20. The measurement results show that the required OSNR for the 42.8-Gb/s CML signal is 24.8 dB (0.1 nm) when the BER equals to 2×10^{-3} .

Fig. 21 shows the measured BER performance and the corresponding eye diagrams after 100-m GI-POF transmission at different bit rates, including 34, 36, 40 and 42.8 Gb/s. For the CML signal before transmission, the lowest BERs are 3×10^{-6} and 1×10^{-7} at the bit rate of 42.8 and 40-Gb/s, respectively. After transmission over 100-m GI-POF, the BER value is raised from 1.0×10^{-9} to 3.6×10^{-4} while the bit rate increased from 34 Gb/s to 42.8 Gb/s. Even if the bit rate is 42.8 Gb/s, error-free transmission can be realized at the BER of 3.6×10^{-4} using FEC modules.

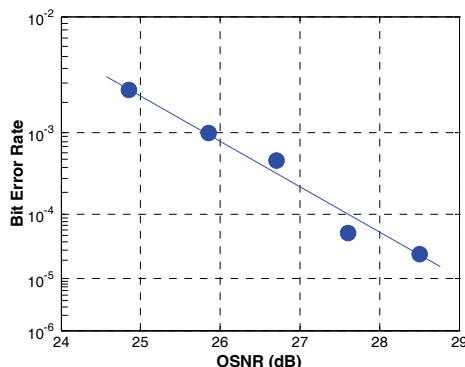


Fig. 21. Measured BER as a function of OSNR for the CML signal at 42.8 Gb/s before transmission.

4.5 OFDM technique and application in POF system

4.5.1 OFDM technique

Orthogonal frequency division multiplexing (OFDM) is a particular frequency-division multiplexing (FDM) scheme utilized a digital multi-carrier modulation method. Every portion of input data is transmitted on one of the available closely-spaced orthogonal subcarriers. OFDM is divided into several parallel data up and down streams or channels. Sub-carriers are modulated with conventional digital modulation schemes (such as Quadrature Amplitude Modulation (QAM) or Phase Shift Keying (PSK)) at a low symbol rate, which can maintain total data rates similar to conventional single-carrier modulation schemes at the same bandwidth.

The primary advantage of OFDM over single-carrier schemes is its ability to conquer severe channel conditions, especially the Multi-Path Effect. Channel equalization is simplified because it could be viewed as using a lot of slowly modulated narrowband signals rather than one rapidly modulated wideband signal. The low symbol rate makes the use of a guard interval between symbols affordable, which makes it possible to handle time-spreading and eliminates inter-symbol interference (ISI). This mechanism also facilitates the design of single-carrier networks, where several adjacent transmitters send the same signal simultaneously at the same frequency, as the signals from multiple transmitters could be combined constructively, rather than interfering that would typically occur in a traditional single-carrier system.

The first OFDM experiments were presented in the 1960s' military radio link. At that time, actual civil use of OFDM was limited and the practicability of the concept was questioned. When the digital communication and integrated circuit chip have been tremendously promoted, OFDM are developed as a popular scheme for broadband digital communication, whether wireless or over copper wires, adopted in applications such as digital television and audio broadcasting. Over the last decade, OFDM is exploited for wireless communication system, and also becoming a basic technique for next generation broadband wireless access network. Today it is proved in practice that traditional wireless communication systems, like TDMA, FDMA or even CDMA are not capable of meeting the

required criteria because of their inherent limitations. This is the reason why a large amount of research effort in radio communications is focused on multicarrier transmission methods, and these techniques are now considered the only way to support future demands. OFDM/OFDMA is the criteria technique of Long Term Evolution (LTE) which is the extension of 3GPP (3rd Generation Partnership Project).

In recent years, seamless integrated wired and wireless access technology is becoming an interesting research subject. A significant solution of this subject is OFDM radio frequency signal transmission over fiber. Radio-Over-Fiber (ROF) has well known scheme for distributing RF and microwave signals, such as low transmission loss and wide bandwidth. OFDM is more and more attractive in optical communication application, which appears in a large number of optical researches, such as long-haul transmission and WDM-PON. The combination of OFDM and ROF is increasing the high-speed wireless data transmission and video distribution in future broadband access network.

People are paying more attention to do channel optimization in optical domain, such as dispersion shift fiber or dispersion compensating fiber. However, electrical optimization is more effective to make received OFDM-ROF signal better. For instance, pilots that are padded into OFDM symbol can equalize noises and phase distortions of received signal. OFDM-QPSK baseband signal transmitted over 50 km SSMF by 60-GHz ROF technique is used to prove the effect of electrical equalization. The received QPSK constellations without and with equalization are shown in Fig.22 (a) and (b). In this demonstration, 60 of 64 sub-carriers are used to transmit data with QPSK modulation; pilots are carried by the other 4 sub-carriers. Coarse channel estimation is achieved from received pilots. Fig.22 (a) depicts QPSK constellation with severe noises and phase distortion caused by dispersion and nonlinear effect. Great impact of electrical equalization which compensates signal's distortions is shown in Fig. 22 (b).

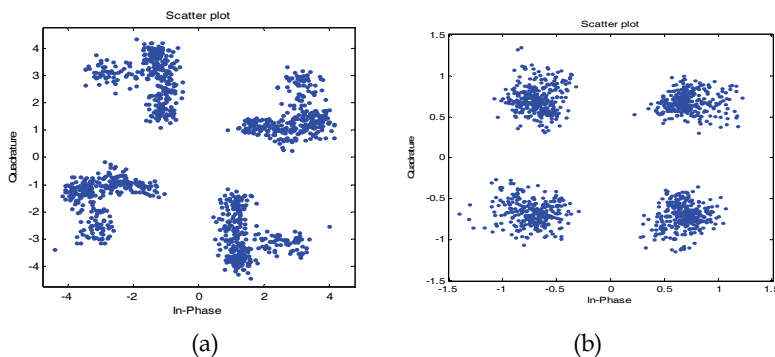


Fig. 22. QPSK constellations without (a) and with (b) equalization.

4.5.2 Optical OFDM Signals over GI-POF

In this section we will experimentally demonstrate the transmission of upconverted 16Gbit/s OFDM signals on 24GHz microwave carrier over 50m GI-POF at 1310nm.

The experimental setup of the proposed OFDM signals transmission over GI-POF is shown in Fig. 23. The lightwave from the DFB laser-diode (LD) at 1310nm with the output power around 10dBm is modulated by an intensity modulator (IM) driven by up-converted OFDM

signals. The 16Gbit/s OFDM signals are generated by OFDM transmitter and then up-converted to 24GHz to realize RF-OFDM signals via an electrical mixer. The up-converted spectrum is inserted in Fig. 21. We can see that the bandwidth of the OFDM signal is 8GHz. The OFDM baseband signal is generated offline and uploaded into a Tektronix AWG7102. The waveforms produced by the arbitrary wave generator (AWG) are continuously output at a sample rate of 20GHz (8bits DAC, 4GHz bandwidth). The FFT size is 256, from which 200 channels are used for data transmission, 55 channels at high frequencies are set to zero for over-sampling, and one channel in the middle of the OFDM spectrum is set to zero for DC in baseband. 10 training sequences are applied for each 150 OFDM-symbol frame in order to enable phase noise compensation. At the output of the AWG, the low-pass filter (LPF) with 5GHz bandwidth is used to remove the high-spectral components. Subsequently, the RF-pilot tone is created by inserting a small DC offset before an analogue I/Q mixer is used to up-convert the OFDM signal from the baseband to an 8.5GHz intermediate frequency (IF). The electrical spectrum of the original signal is shown in Fig. 24(a)

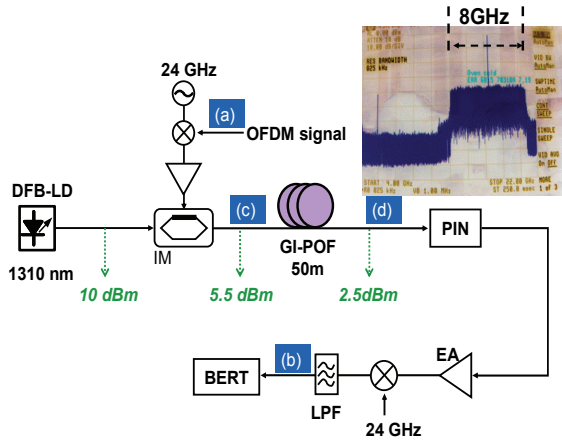


Fig. 23. Experimental configuration for 16Gb/s OFDM transmission over GI-POF. EA: electrical amplifier; IM: intensity modulator; GI-POF: graded-index plastic optical fiber; PIN: receiver; LPF: low pass filter. Inset: electrical spectrum of the OFDM signal after up-conversion.

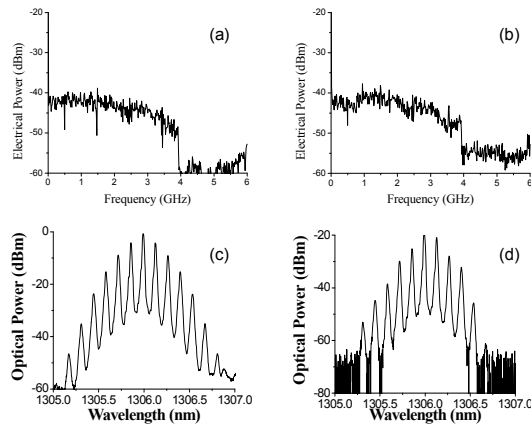


Fig. 24. Received electrical spectra: (a) after arbitrary waveform generator, (b) after LPF; received optical spectra with 0.01nm resolution: (c) before, and (d) after GI-POF at the point (a)-(d) in Fig. 1, respectively.

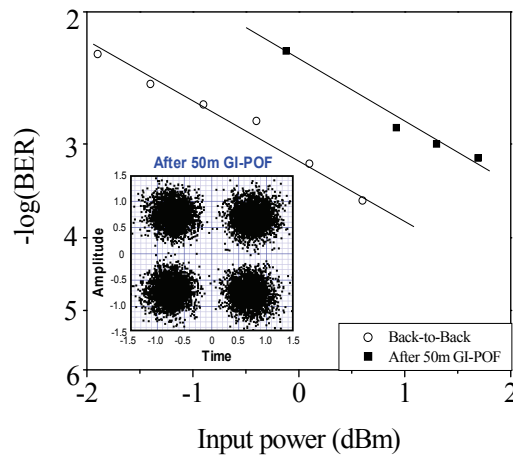


Fig. 25. Measured BER curves and the constellation figure of back-to-back and after 50m GI-POF.

that was measured at the point (a) in Fig. 23. The IM is driven by the OFDM signals to create double sideband (DSB) optical signals. The bias and the power of the RF signals are carefully adjusted to obtain proper power ratio between the optical carrier and the first-order sideband signals. The optical spectrum with 0.01nm resolution after the intensity modulator is shown in Fig. 24(c). After IM, the signal was launched into 50m of commercially available GI-POF for transmission. The core of the GI-POF is 50 μm with 60dB/km attenuation at 1300 nm. The signal power launched and output of GI-POF was 5.5 and 2.5dBm. The optical spectrum after transmission is presented in Fig. 24(d). A PIN

receiver is used in the receiver side with the bandwidth of 29GHz and a 50 μ m multimode-coupled input. Before low pass filter (LPF), a 24GHz electrical LO signal is mixed to down-convert the electrical signal to its baseband form. The down-converted signals are sampled with a real-time oscilloscope (Tektronix 6154C) and processed off-line. The electrical spectrum of down-converted signals is shown in Fig. 24(b). The measured BER of back-to-back and after transmission is shown in Fig. 25 and the constellation figure after 50m GI-POF is inserted. One million bits have been evaluated for all values of BER reported in this work. We can see that there exists signal degradation after 50m GI-POF. But the BER is still lower than 1×10^{-3} , which is below the limitation of forward error correction (FEC) at 2×10^{-3} . The main reason is the degradation of optical signal-to-noise- ratio (OSNR) from the fiber with an insertion loss of 3dB and modal dispersion.

5. Conclusions

We have reviewed broadband optical access networks to provide the needed bandwidth and flexible connectivity for future Internet users. For transmission fiber in broadband optical access network, GI-POF can be used to provide up to 40Gb/s huge bandwidth and low insertion loss by some special design. New modulation format signals can further extend the transmission distance of the signal in the GI-POF. Directly modulated laser with special optical filtering technique can generate a laser to increase the dispersion tolerance, and further more increase the bandwidth of the GI-POF. We have demonstrated that this 40Gb/s CML signals can be transmitted in GI-POF over 100m distance with BER smaller than FEC limitation. We have proposed and experimentally demonstrated a transmission system with ultra-bandwidth up to 16Gbit/s OFDM signals over 50m GI-POF. The experimental results illustrate that the transmission over GI-POF degrades the optical signal performance due to the reduction of OSNR in the fiber link. However, this system still can realize error-free transmission when the FEC is used.

6. Acknowledgement

Author likes to thank Prof. G. K. Chang, Dr. B. Bing, Dr. Y-K. Yeo, Dr. C. Xiao, Dr. M. Huang, Dr. H. Muhammad and Dr. A. Chowdhury and Dr. Z. Jia from Georgia Institute of Technology and Dr. T. Wang from NEC Laboratories America for their great contribution for these research results.

7. References

- A. Polley, R. J. Gandhi, and S. E. Ralph (2007). 40Gbps links using plastic optical fiber, In *Proc. of OFC 2007, OMR5*.
- A. Weinert (2002). Plastic Optical Fibers. *Publicis MCD Verlag*, Munich 1999
- B. Bing and G. K. Chang. Chapter 2: The Last Mile, the Edge, and the Backbone, in *Broadband Last-Mile Technologies*, N. Jayant (ed.), *CRC Press*, USA, 2005, ISBN: 0824758862.
- B. Dagens, A. Martinez, D. Make, O. L. Gouezigou, J. G. Provost, V. Sallet, K. Merghem, J. C. Harmand, A. Ramdane and B. Thedrez (2005). Floor Free 10-Gb/s Transmission

- With Directly Modulated GaInNAs-GaAs 1.35-um Laser for Metropolitan Applications, *IEEE Photon. Technol. Lett.*, 17 (5), 971-973..
- B. R. Saltzberg (1967). Performance of an efficient parallel data transmission system, *IEEE Transactions on Communications Technology*, 15 (6), 805-811.
- Bahai, A. R. S., Saltzberg, B. R., Ergen, M. (2004)., *Multi Carrier Digital Communications: Theory and Applications of OFDM*, Springer.
- C.-J. Chae, E. Wong, R.S. Tucker (2002). Optical CSMA/CD media access scheme for Ethernet over passive optical network, *IEEE Photon. Tech. Lett.*, 14(5), 711-13.
- D. J. Shin, D.K.Jung, H.S. Shin, S.B. Park, H.S. Kim, S.H. Kim, Seongtaek Hwang, E.H. Lee, J.K. Lee, Y.K. Oh, and Y.J. Oh (2005). AWG misalignment tolerance of 16×155 Mb/s WDM-PON based on ASE-injected FP-LDs, *Proc OFC'05*, JWA54.
- D. Mahgerefteh, D. Mahgerefteh, Y. Matsui, C. Liao, B. Johnson, D. Walker, X. Zheng, Z.F. Fan, K. McCallion and P. Tayebati (2005). Error-free 250km transmission in standard fibre using compact 10 Gbit/s chirp-managed directly modulated lasers (CML) at 1550nm , *Electron. Lett.*, 41(9), 543-544.
- D. Qian, J. Yu, J. Hu, L. Zong, L. Xu, T. Wang (2008), 8x11.5Gbit/s OFDM transmission over 1000km SSMF using conventional DFB lasers and direct-detection, in *Proc. of OFC 2008*, OMM3.
- D. Qian, J. Yu, J. Hu, P. N. Ji, T. Wang (2008). 11.5-Gb/s OFDM transmission over 640km SSMF using directly modulated laser, in *Proc. of ECOC 2008*, Mo. 3. E. 4.
- E. S. Son, K. H. Han, J. H. Lee, and Y. C. Chung (2005). Survivable Network Architectures for WDM PON, *OFC'05*, OF14.
- G. Giaretta, W. White, M. Wegmuller, and T. Onishi (200). High Speed (11 Gbit/s) Data Transmission Using Perfluorinated Graded-Index Polymer Optical Fibers for Short Interconnects (<100 m), *IEEE Photonics Tech. Lett.*, 12(3), 347-349.
- G. Kramer, B. Mukherjee, G. Pesavento (2002). IPACT: a dynamic protocol for an Ethernet PON (EPON), *IEEE Communications Magazine*, 40(2), 74 - 80.
- H. J. Thiele, P. J. Winzer, J. H. Sinsky, L. W. Stulz, L. E. Nelson, F. Fidler (2004). 160-Gb/s CWDM Capacity Upgrade Using 2.5-Gb/s Rated Uncooled Directly Modulated Lasers, *IEEE Photon. Technol. Lett.*, 16 (10), 2389-2391.
- H. Yang, S. C. J. Lee, E. Tangdiongga, F. Breyer, S. Randel, and A. M. J. Koonen (2009). 40-Gb/s Transmission over 100m Graded-Index Plastic Optical Fiber based on Discrete Multitone Modulation, in *Proc. of OFC 2009*, PDPD8.
- <http://www.thorlabs.com/Thorcat/16600/16678-M01.pdf>.
- I. Tomkos, I. Roudas, R. Hesse, N. Antoniadis, A. Boskovic, R. Vodhanel (2001). Extraction of Laser rate equations parameters for representative simulations of metropolitan-area transmission systems and networks, *Optics Communications*, 194(1-3), 109-129.
- IEEE P802.3ba 40Gb/s and 100Gb/s Ethernet Task Force* [Online]. Available: <http://www.ieee802.org/3/ba/>
- IEEE Standard for a High-Performance Serial Bus - Amendment 2: 1394b-2002.
- IEEE Standard for a High-Performance Serial Bus 1394-1995. *IEEE Press*, 1996
- ITU-T Standards G.983.1 to G.983.8, Broadband optical access systems based on passive optical networks (PONs).
- ITU-T Standards G.984.1 to G.984.2, Gigabit-capable passive optical networks (GPON).

- J. Downie, I. Tomkos, N. Antoniadis, A. Boskovic (2002). Effects of Filter Concatenation for Directly Modulated Transmission Lasers at 2.5 and 10Gb/s, *IEEE J. Lightwave Technol.*, 20 (2), 218-228.
- J. K. Jeyapalan (2003). Municipal Optical Fiber Through Existing Sewers, Storm Drains, Waterlines, and Gas Pipes May Complete the Last Mile, in proc. of ASCE, 708-726, available from: http://www.agc.org/content/public/PDF/Municipal_Uilities/Municipal_fiber.pdf.
- J. Krauser, P. E. Zamzow, O. Ziemann (2002). POF, Polymer Optical Fiber for data communications", *Springer-Verlag/Sci-Tech/Trade*; edition 1.
- J. Morgado, and A. Cartaxo (2003). Directly Modulated Laser Parameters Optimization for Metropolitan Area Networks Utilizing Negative Dispersion Fibers, *IEEE J. Select. Topics Quantum Electron.*, 9(5), 1315-1324.
- J. Xie, S. Jiang, Y. Jiang (2004), A dynamic bandwidth allocation scheme for differentiated services in EPONs, *IEEE Communications Magazine*, 42(8), 32 - 39.
- J. Yu (2008), 42.8 Gb/s Chirp-Managed Signal Transmission over 100 m Graded-Index Plastic Optical Fiber, in *Proc. of OFC 2008*, PDP-28.
- J. Yu, D. Qian, M. Huang, Z. Jia, G. K. Chang, T Wang (2008). 16Gbit/s radio OFDM signals over graded-index plastic optical fiber, in *Proc. Of ECOC 2008*, P. 6. 16.
- J. Yu, M. F. Huang, P. N. Ji, and T. Wang (2008). 42.8 Gb/s Chirp-Managed Signal Transmission Over 100 m Graded-Index Plastic Optical Fiber, in *Proc OFC, 2008*, PDP 28.
- J. Yu, M. Huang, D. Qian, L. Chen, G. K. Chang (2008). Centralized Lightwave WDM-PON Employing 16-QAM Intensity Modulated OFDM Downstream and OOK Modulated Upstream Signals, *IEEE Photonics Technology Letters*, 20(18), 1545 - 1547.
- J. Yu, P.N. Ji, Z. Jia, T. Wang, X. Zheng, Y. Matsui, D. Mahgerefteh, K. McCallion, Z.F. Fan and P. Tayebati (2007). 42.8 Gbit/s chirp-managed signal transmission over 20km standard SMF at 1550nm without DCF, *Electronic Lett.*, 43(23) .
- J. Zheng, H. T. Mouftah (2005). Media access control for Ethernet passive optical networks: an overview, *IEEE communications magazine*, 43(2), 145-150.
- J.-R. Burie, P. Andre, M. Riet, S. Vuye, P. Berdager, E Dumont, O. Le Gouezigou, N. Kauffmann, A. Konczykowska, S. Lamy and D. De la Grandiere (2002). Mux-driver-EAM in single module - a solution for ultra-high bit rate applications *Electronic Lett.*, 38(14), 740-741.
- K. D. Pedrotti, R. P. Dahlgren, J. A. Wysocki, S. E. Ralph, R. Gandhi and A. Polley (2006). Multi-gigabit transmission over POF, *POF World West*, 21-22.
- K. Fazel and S. Kaiser (2008), *Multi-Carrier and Spread Spectrum Systems: From OFDM and MC-CDMA to LTE and WiMAX*, 2nd Edition, John Wiley & Sons, 2008, ISBN 978-0-470-99821-2.
- K. Sato, S. Kuwahara, Y. Miyamoto, and N. Shimizu (2002). 40Gb/s direct modulation of distributed feedback laser for very-short-reach optical links, *Electron. Lett.*, 38 (15), 816-817.
- Leeper, David G (2007)., "WiFi - The Nimble Musician in Your Laptop", *IEEE Computer Magazine -- How Things Work*, April, 2007, pp 108-110.
- M. Asai, R. Hirose, A. Kondo, and Y. Koike (2007). High-Bandwidth Graded-Index Plastic Optical Fiber by the Dopant Diffusion Coextrusion Process, *J. Lightwave Technol.*, 25 (10), 3062-3067.

- M. Feuer, S. Y. Huang, S. Woodward, O. Coskun and M. Boroditsky (2003). Electronic Dispersion Compensation for a 10-Gb/s Link Using a Directly Modulated Laser, *IEEE Photon. Technol. Lett.*, 15(12), 1788-1790.
- M. Jones (2007), *start: Running Ethernet over plastic optical fiber*
- M. P. McGarry, M. Maier, M. Reisslein (2004). Ethernet PONs: a survey of dynamic bandwidth allocation (DBA) algorithms, *IEEE communications magazine*, 42(8), 8-15.
- Mitsubishi International Corporation, 655 3rd Ave. - New York, N.Y. 10017 (www.pofeska.com)
- NSF Workshop Report (2004). Residential Broadband Revisited: Research Challenges in Residential Networks, Broadband Access, and Applications.
- O. Ziemann, J. Krauser, P. E. Zamzow, W. Daum (2008). POF Handbook - Optical Short Range Transmission Systems. 2nd ed., *Springer*, 884 p. 491 illus. in color, ISBN: 978-3-540-76628-5.
- P. Hoehner, S. Kaiser, P. Robertson (1997). Two-dimensional pilot-symbol-aided channel estimation by Wienerfiltering, *IEEE International Conference on Acoustics, Speech, and Signal Processing, ICASSP-97*.
- P. N. Ji, J. Yu, Z. Jia, T. Wang, X. Zheng, Y. Matsui, D. Mahgerefteh, K. McCallion, Z. F. Fan, and P. Tayebati (2007). Chirp-Managed 42.8 Gbit/s Transmission over 20 km Standard SMF without DCF Using Directly Modulated Laser, *in Proc ECOC 2007*, 10.4.6.
- P. Robertson, S. Kaiser (1999). The effects of Doppler spreads in OFDM(A) mobile radio systems, *Vehicular Technology Conference*.
- P.S. Chow, J.M. Cioffi, and J.A.C. Bingham (1995). A Practical Discrete Multitone Transceiver Loading Algorithm for Data Transmission over Spectrally Shaped Channels, *IEEE Trans. Commun.*, 43(2), 773-775
- R. Ramaswami and K. Sivarajan (2002). Optical Networks: A Practical Perspective, *Morgan Kaufmann*.
- R. W. Chang (1966). Synthesis of band-limited orthogonal signals for multi-channel data transmission, *Bell System Technical Journal* 46, 1775-1796.
- R. W. Chang, and R. A. Gibbey (1968). A theoretical study of performance of an orthogonal multiplexing data transmission scheme, *IEEE Transactions on Communications Technology*, 16 (4), 529-540.
- S. Blake, D. Blake, M. Carlson, E. Davies, Z. Wang, W. Weiss (1998), An architecture for differentiated services, *IETF RFC 2475*.
- S. Chandrasekhar, C. R. Doerr, L. L. Buhl, D. Mahgerefteh, Y. Matsui, B. Johnson, C. Liao, X. Zheng, K. McCallion, Z. Fan, and P. Tayebati (2005). Flexible transport at 10-Gb/s from 0 to 675 km (11500ps/nm) using a chirp-managed laser, no DCF, and a dynamically adjustable dispersion compensating receiver, *in Proc OFC 2005*, PDP30.
- S. Coleri, M. Ergen, A. Puri, A. Bahai (2002). Channel estimation techniques based on pilot arrangement in OFDM systems. *IEEE Transactions on Broadcasting*, 48(3), 223-229.
- S. I. Najafi (1996). Glass Integrated Optics and Fiber Devices, *Soc. of Photo Optical*.
- S. Schöllmann (2007), First Experimental Transmission over 50 m GI-POF at 40Gb/s for Variable Launching Offsets, *in Proc. of ECOC 2007*, PDP 3.7.

- S.-B. Park, D. K. Jung, D. J. Shin, H. S. Shin, S. Hwang, Y. J. Oh, and C. S. Shim (2005). Bidirectional Wavelength-Division-Multiplexing Self-Healing Passive Optical Network, in *Proc. of OFC'05*, JWA57.
- S.C.J. Lee (2007). 24-Gb/s Transmission over 730 m of Multimode Fiber by Direct Modulation of an 850-nm VCSEL using Discrete Multi-tone Modulation, in *Proc. of OFC 2007*, PDP6.
- S.-M. Lee, K.-M. Choi, S.-G. Mun, J.-H. Moon, and C.-H. Lee (2005). Dense WDM-PON based on Wavelength Locked Fabry-Perot Lasers, in *Proc. of OFC'05*, paper JWA55.
- T. de Couasnon, R. Monnier, J. B. Rault (1994). OFDM for digital TV broadcasting, Signal processing, (ELSEVIER) 39 (1994) 1-32
- T. Ishigure, M. Kano, and Y. Koike (2000). Which Is a More Serious Factor to the Bandwidth of GI-POF: Differential Mode Attenuation or Mode Coupling? *J. Lightwave Technol.*, 18 (7), 959-965.
- T. Ishigure, Y. Koike (2003). Design of POF for Gigabit Transmission, in *Proc. Of POF Conf.* 2-5.
- U. Schelinski, M. Scholles, G. Muellritter (2003). Consumer Networking Infrastructure Based on IEEE 1394b, *International Conference on Consumer Electronics (ICCE)*.
- W. Daum, J. Krauser, P. E. Zamzow, O. Ziemann(2002), POF Polymer Optical Fibers for Data Communication, *Springer*.
- W. R. White, M. Dueser, W.A. Reed, and T. Onishi (1999). Intermodal Dispersion and Mode Coupling in Perfluorinated Graded-Index Plastic Optical Fiber, *IEEE Photon. Tech. Lett.*, 11 (7), 997-999.
- Y. Luo, N. Ansari (2005). Bandwidth allocation for multiservice access on EPONs, *IEEE communications magazine*, 43(2), 16-21.
- Y. Matsui, D. Mahgerefteh, X. Zheng, C. Liao, Z. F. Fan, K. McCallion, and P. Tayebati (2006), Chirp-Managed Directly Modulated Laser (CML), *IEEE Photon. Technol. Lett.*, 18 (2), 385-387.
- Z. Jia, J. Yu, and G. K. Chang (2007). Chirp-Managed Directly-Modulated DFB Laser, *Recent Patents on Engineering*, 1, 43-47.

High-Speed, High-Power, and High Responsivity Photodiode for Radio-Over-Fiber (ROF) Communication

J.-W. Shi, F.-M. Kuo and Y.-S. Wu

*Department of Electrical Engineering, National Central University
Taiwan*

1. Introduction

The tremendous increase in the required volume of wireless data-transmission has stimulated attention on ways to use the millimeter wave (MMW) bands above 60GHz (V-band) or above 100GHz (W-band) as the carrier frequency for the realization of systems with very high transmission data rates in excess of many gigabits-per-second [1,2]. Unfortunately, there is a large propagation loss of the MMW signal in the >W-band or V-band frequencies, whether in free space or in a coaxial cable. One promising solution to this problem is the radio-over-fiber (ROF) technique [1-3], where the MMW signal is distributed through a lossless optical fiber and then radiated over the last-mile to the user-end. High-speed, high responsivity, and high-power photodiodes (PD) serve as a key component in photonic MMW communication systems [1] for transducing the intense optical power to high-power MMW power. The saturation current-bandwidth product is thus a key parameter for evaluating the performance of high-power photodiodes (PD) for such applications, especially when the operating frequency is around 100GHz or higher. By increasing the saturation current of the PD, we can boost the injected optical power and further increase the maximum available MMW power. The burden imposed on the MMW power amplifier can thus be relaxed [4,5]. Recently, a research group at NTT reported excellent results for a 10Gb/s wireless link at 120GHz, achieved by using a high-power uni-traveling-carrier photodiode (UTC-PD) based photonic transmitter [1,2].

There are two approaches to improve the high-power performance of PDs. One is to distribute and uniform the photocurrents along the edge-coupled PDs to minimize the thermal problem [6] and space-charge screening effect [4,5] by improving the geometric structure of optical and electrical waveguides, such as, evanescently-coupled photodiode (ECPD) [7-9]; the other is to minimize the space-charge screening effect in the photo-absorption volume by changing the structure or material of epitaxial layers, such as UTC-PD [4,5], partially depleted absorber photodiode (PDP) [10], and separated-transport-recombination photodiode (STR-PD) [11]. In this chapter, we reviewed our recent works on InP and GaAs based high-power photodiodes, which can overcome the above-mentioned problems and achieve state-of-the-art output power without seriously sacrificing the

responsivity and speed performance.

2. Geometric Structure of High-power, High-responsivity, and High-speed Photodiode

2.1 Introduction

Figure 1 (a) and (b) shows the cross-sectional view of vertical-illuminated PDs (VPD) and WGPD, respectively. Compared with the structure of typical VPDs, the structure of the edge-coupled waveguide photodiode WGPD [4] has attracted a lot of attention due to its superior bandwidth-responsivity product performance [4]. In VPDs structure, the direction of carrier transport is parallel with the direction of incident photon and in order to shorten the carrier drift-time inside the absorption regime, we must decrease the absorption layer thickness and the responsivity performance will thus be sacrificed for high-speed performance. On the other hand, in WGPD structure, the direction of carrier transport is perpendicular to the direction of incident photon and we can still use a thin absorption layer ($<200\text{nm}$) to absorb the edge-coupling photon completely by using a proper length of active waveguide, however, its maximum output photocurrent is seriously limited, due to the problem of saturation at the input-end of device [4]. Figure 2 shows the conceptual diagram of input-end-saturation problem in WGPD. As can be seen, most of the incident photon will be absorbed near the input-end of WGPD and the high density of photo-generated carriers would thus saturate the device output power. There are two major trends being followed to improve the high-power performance of the WGPD. One is to distribute and make uniform the photocurrents by improving the structure of optical and electrical waveguides, such as research into the velocity matched distributed photodetector (VMDP) [12] and the other is evanescently-coupled photodiode (ECPD) [7-9]. As can be seen in Figure 2, the incident photon is launched to the bottom passive optical waveguide of ECPD and gradually coupled to the upper active absorption region. Because the gradually coupling process into the absorption regime, the distribution of photo-generated carriers thus becomes more uniform and the problem of input-end saturation in traditional WGPD can thus be minimized. Recently, several research groups have demonstrated the state-of-the-art performance of ECPDs with a short coupling length ($\sim 20\mu\text{m}$) and partially depleted absorber [8,9]. However, the tolerance of the cleaved coupling length of such devices is very small (less than $5\mu\text{m}$) and different coupling lengths have a serious effect on the responsivity performance [8]. This problem can be overcome by dry etching a deep trench to precisely define the waveguide length [13]. However, any roughness on the dry-etched

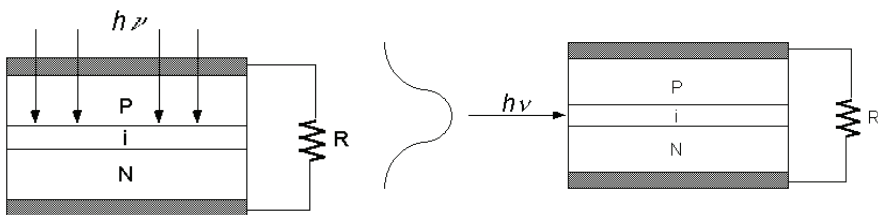


Fig. 1. Schematic diagram of a p-i-n based VPD (a) and WGPD (b) structure.

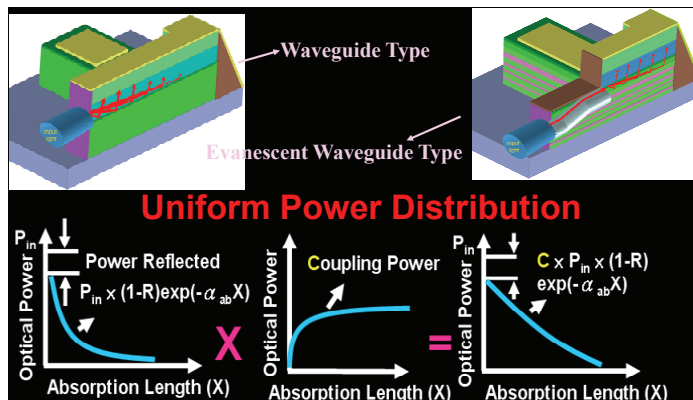


Fig. 2. The conceptual diagram of launched optical wave in the input-end of WGPLD structure and ECPD structure

facets can degrade the responsivity performance. Other groups have also developed photodiodes with an asymmetric twin waveguide (tapered) structure to improve the cleaving tolerance and achieve high responsivity performance [7] but the misalignment between these twin waveguides and the optical scattering loss, which is induced by very long waveguide lengths ($>700\mu\text{m}$), can both seriously affect the responsivity [7]. In addition, by integrating an edge-coupled PD with a leaky optical waveguide, is another possible solution to increase the tolerance of the cleaving process [12], although the electrical bandwidth performance may be sacrificed for the high responsivity performance, due to the fact that a much larger photo-absorption volume than that of the traditional WGPLD is necessary to completely absorb the diluted optical power [4,12]. In this chapter, we reviewed our recent works [14,15], which can overcome the above-mentioned problems of ECPD and achieve the goal of high-bandwidth, high-responsivity, and high saturation power. At first, we combined a partially p-doped photo-absorption layer with a leaky optical waveguide and a distributed-bragg-reflector (DBR) in the structure of an edge-coupled photodiode. The integrated DBR mirror can fold the injected optical path and enhance the responsivity performance without increasing the device-absorption-length. The demonstrated device can achieve superior performance in terms of bandwidth, saturation power, and quantum efficiency for the control, without DBR mirrors. Furthermore, the responsivity performance of our demonstrated device is much less sensitive to the cleaved coupling length than is that of the ECPD (7% vs. 30% [8]). The another structure we demonstrated for solving the problems of ECPD is the dual-step evanescently-coupled waveguide photodiode [15] (DECPD). By separating the fiber-guide region and coupling-guide region into different parts of the optical waveguide [15], the dependence of the responsivity on the cleaved-length can be minimized, nor is a long ($\sim 700\mu\text{m}$) passive waveguide with complex tapered stages any longer necessary.

2.2 Leaky-Waveguide PDs

In order to determine the influence of DBR mirrors on the responsivity performance of photodiodes, two kinds of device, with the same geometry and epi-layer structures, but with and without DBR mirrors, were fabricated. The DBR mirror device has twice the reflected input optical power and absorption of the folded optical power. Thus, compared with the DBR device, the control device requires a much longer device-absorption-length, which results in poorer speed performance. The cross-sectional view and top-view of the demonstrated devices are given in Figure 3 and the inset shows the fabricated DBR mirror.

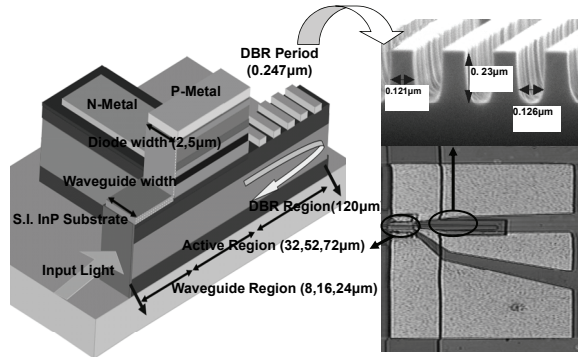


Fig. 3. The cross-sectional and top views of the demonstrated devices. The inset pictures the fabricated DBR mirrors.

The DBR mirror pairs (500 pairs), as labeled in Figure 3, are designed to produce a reflection maximum at around the 1550nm wavelength regime. The leaky optical waveguide used was composed of two lower undoped InGaAsP core layers, a thin heavily doped n-type InP etching stop layer, an In_{0.53}Ga_{0.47}As based photo-absorption layer, 0.3μm undoped and 0.2μm p-doped in thickness, and a topmost p-type InP cladding

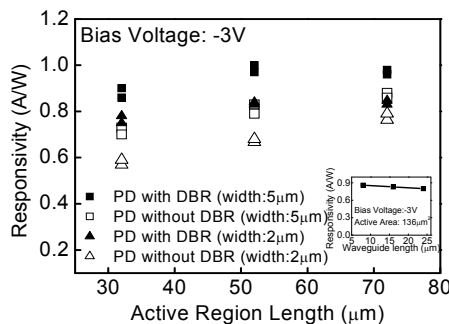


Fig. 4. The measured responsivity of both devices (with and without DBR mirrors) versus length of active diodes. The bias voltage is fixed at -3V and the waveguide widths of both

devices are $2\mu\text{m}$ and $5\mu\text{m}$. The inset shows the measured responsivities of DBR devices with the same active area ($136\mu\text{m}^2$) and different cleaved lengths of passive optical waveguide.

structure, without DBR mirrors, is around $200\mu\text{m}$, and the theoretical calculated RC-limited bandwidth is just around 10GHz , in the case of a 50Ω load. By the incorporation of highly reflective DBR mirrors into our optical leaky waveguide, the required absorption-length can be shortened, meaning a superior bandwidth-responsivity performance product. The partially p-doped photo-absorption layer, shortens the thickness of the depletion layer and significantly increases the saturation current of the PD [10]. Figure 4 shows the measured maximum responsivity of both devices vs. the active diode lengths with different waveguide widths ($2\mu\text{m}$ and $5\mu\text{m}$). We can clearly see that all devices with DBR mirrors and different waveguide widths exhibit a much higher responsivity than that of the control device without DBR. The inset shows the measured responsivity of the DBR device vs. the cleaved waveguide length. We can clearly see that the measured responsivity is almost independent of the cleaved length. In comparison with the reported ECPD results, the measured responsivity will vary much more significantly (from $\sim 0.7\text{A/W}$ to $\sim 1\text{A/W}$) when the cleaved length increases from $10\mu\text{m}$ to $20\mu\text{m}$ [7]. As shown in this figure, for a device with a DBR mirror, the achieved responsivity can be as high as 0.9A/W . Furthermore, our demonstrated device does not exhibit serious wavelength selectivity, which is a serious problem for the resonant-cavity-enhanced PD (RCEPD) [12]. This is because our cavity length is much longer than the operating wavelength and that an AR coating is applied to the input facet. The bandwidth and saturation current were measured with a heterodyne beating system. The traces shown in figure 5 (a) were from devices with and without DBR mirrors, with different active areas ($96\mu\text{m}^2$ and $136\mu\text{m}^2$) and almost similar responsivity performance (0.8 vs. 0.7A/W). Both devices were measured under the same dc bias voltage (-3V) and output photocurrent (5mA). Compared with the control, the device with DBR mirrors not only has higher electrical bandwidth performance ($\sim 40\text{GHz}$ vs. $\sim 30\text{GHz}$) but also produces higher bandwidth-responsivity ($\sim 32\text{GHz}\cdot\text{A/W}$ vs. $\sim 21\text{GHz}\cdot\text{A/W}$). Figure 5 (b) shows the measured frequency responses of devices with DBR mirrors and different active areas ($96\mu\text{m}^2$ and $160\mu\text{m}^2$) under a -3V bias voltage and a fixed 15mA output photocurrent. Even under such a high output photocurrent (15mA), both devices achieved

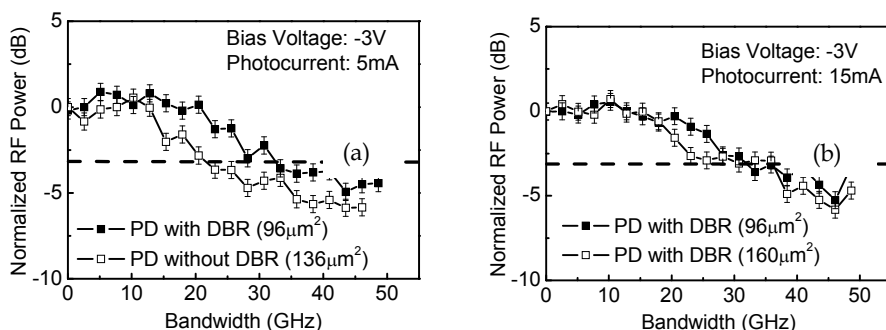


Fig. 5. (a) The measured frequency responses of devices under a fixed dc bias voltage (-3V) and output photocurrent (5mA). The active area of the devices, with and without DBR, is

$96\mu\text{m}^2$ and $136\mu\text{m}^2$, respectively. (b) The measured frequency responses of devices with DBR mirrors and two different active areas ($96\mu\text{m}^2$ and $160\mu\text{m}^2$) under a fixed output photocurrent (15mA) and dc bias voltage (-3V).

an electrical bandwidth of around 40GHz. The high responsivity (0.8A/W and 0.9A/W) and high electrical bandwidth ($\sim 40\text{GHz}$) that the demonstrated devices achieved under high current operation ensure their suitability for application to 40Gbit/sec analog and digital fiber communication systems. As compared to the results shown in Figure 5, we can clearly see that although the DBR device has larger active area than those of the control device ($160\mu\text{m}^2$ vs. $136\mu\text{m}^2$), the electrical bandwidth performance is still much better ($\sim 40\text{GHz}$ vs. $\sim 30\text{GHz}$) even under a much higher output photocurrent (15mA vs. 5mA). The superior high-power performance of the DBR device to the control device can possibly be attributed to its more uniform distribution of photo-generated carriers, because of the folded photo-absorption process. Figure 6 represents the photo-generated RF power versus dc photocurrent of devices under a fixed dc bias voltage (-3V). The ideal relation between the RF power of a 100% modulated large-signal and the average current with a 50Ω load is also plotted as a straight line for reference. As shown in this figure, DBR devices with a smaller geometric size ($96\mu\text{m}^2$ vs. $160\mu\text{m}^2$) can have a slightly larger photo-generated RF power under the same photocurrent, due to having a larger RC limited bandwidth. Furthermore, we can clearly see that the two DBR devices have a higher saturation current ($\sim 18\text{mA}$ vs. $\sim 15\text{mA}$) and RF power (6.4dBm vs. 2dBm) than that of the control devices with a $136\mu\text{m}^2$ active area, due to their superior high power performance as discussed in Figure 3 and 4. The values achieved for RF power (6.4dBm), saturation photocurrent ($\sim 18\text{mA}$), responsivity (0.8A/W), and electrical bandwidth ($\sim 40\text{GHz}$) are comparable with the ECPD with PDP structure [16].

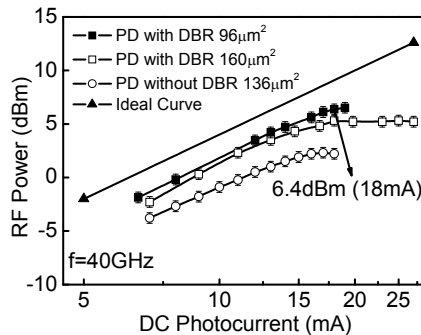


Fig. 6. The RF power versus dc photocurrent of both devices (with and without DBR) with three different active areas (squares: $96\mu\text{m}^2$, open squares: $160\mu\text{m}^2$, open circles: $136\mu\text{m}^2$) under a fixed 40GHz operating frequency and dc bias voltage (-3V).

2.3 Dual-Step Evanescently-Coupled Uni-Traveling-Carrier Photodiodes

A cross-sectional schematic diagram and the top view of the demonstrated DECPD are shown in Figures 7(a) and (b), respectively. Figure 7(c) shows a top view of the DECPD after zooming in on

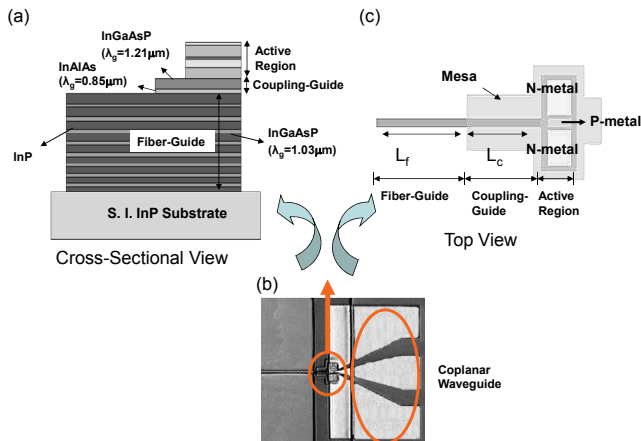


Fig. 7. (a) Cross-sectional view and (b) top-view of the demonstrated DECPD; (c) shows the top-view after zooming in on the active part of device. T and λ_g represents the thickness and bandgap wavelength of the specified epi-layer, respectively.

its active region. As shown in Figure 7(a), the first step in the bottom of our ECPD is a single-mode fiber-guide while the second step is the coupling-guide region. The lengths (L_f and L_c) of these two regions are marked in Figure 7(c). The fiber-guide is composed of nine InGaAsP layers, whose thicknesses increase from 100nm (bottom) to 314nm (top), in increments of 30nm, interspersed between the 80-nm-thick InP layers. In order to achieve low polarization dependence, low coupling loss, and maintain single-mode propagation, (which can benefit integration with other active or passive components in the planar-lightwave-circuit [17]), the index difference and thickness between InGaAsP and InP layers and the width ($\sim 5\mu\text{m}$) and depth ($\sim 3\mu\text{m}$) of the cross-section of our fiber-guide are all optimized using commercial three-dimensional (3-D) beam propagation method software (BPM). The insets to Figure 8 show the simulated mode spectrum and mode profile of light that propagates in the single-mode fiber-guide. Obviously, there is one significant dominant peak, of nearly 89% of the total input power, in this inset, which indicates that our fiber-guide can only support one mode (single-mode) propagation. We can thus understand that as the injected light couples into the upper coupling-guide region, it is always transferred with the same optical mode shape, regardless of the value of L_f , which is determined by the cleaving process. The second step in our passive waveguide is the coupling-guide region, which is composed of two n-doped InGaAsP ($1 \times 10^{18} \text{cm}^{-3}$) optical matching layers [8,9], for optical power coupling to the absorption region and good n-type ohmic contacts. The length of this coupling region L_c is precisely defined by the mask design rather than by the cleaving process. We can thus optimize L_c to achieve complete optical absorption for different active areas (lengths). Figure 8 shows the simulated optical

power distributions in our demonstrated devices. The simulated two DECPDs have the same active areas ($76\mu\text{m}^2$) and active lengths ($20\mu\text{m}$), but different L_c ($20\mu\text{m}$ and $35\mu\text{m}$). The values of L_f obtained during the simulation are both around $300\mu\text{m}$.

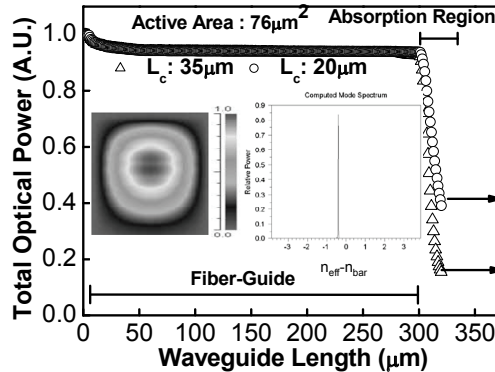


Fig. 8. Simulated optical power distributions without considering the optical scattering loss for devices with different coupling lengths and a fixed active area ($76\mu\text{m}^2$). Triangle: $L_c=35\mu\text{m}$; circle: $L_c=20\mu\text{m}$. The arrowheads indicate the residual optical power after propagation through the active length ($20\mu\text{m}$). The insets show simulated cross-sectional views of the optical mode and mode spectrum in the fiber-guide region.

We can clearly see that by optimizing the value of L_c to be $35\mu\text{m}$, the injected optical power for the active area (length) can be absorbed completely. The optimized values of L_c for devices with three different active areas; $56\mu\text{m}^2$, $76\mu\text{m}^2$, and $116\mu\text{m}^2$, and a fixed waveguide width $2\mu\text{m}$, are $40\mu\text{m}$, $35\mu\text{m}$, and $25\mu\text{m}$, respectively. The active absorption region of our device has a typical UTC-PD structure [5]. The abrupt graded p-type doping profile ($2.5 \times 10^{17} \text{cm}^{-3}$ to $3 \times 10^{18} \text{cm}^{-3}$) in the absorption region is expected to minimize the speedy degradation phenomenon of our UTC-PD, especially when operating under a low output photocurrent [5]. Figure 9 shows the measured responsivity of our devices under a fixed bias voltage -3V and different polarization states versus different fiber-guide (cleaved) lengths L_f . The L_c of all the measured devices is fixed at $40\mu\text{m}$. We can clearly see that the responsivity decreases as L_f increases, which may be attributed to the increase of optical scattering loss with L_f . The measured responsivity of our devices, which have the same $76\mu\text{m}^2$ ($56\mu\text{m}^2$) active area and different fiber-guide lengths (from $20\mu\text{m}$ to $50\mu\text{m}$), is as high as around 1A/W (0.9A/W). The responsivity of the reported ECPD will oscillate seriously with the cleaved length (from $\sim 0.7\text{A/W}$ to $\sim 1\text{A/W}$ for cleaved lengths varying in the same range, $20\mu\text{m}$ to $50\mu\text{m}$) [8,9]. We can thus conclude that, not only does our device demonstrate device high responsivity ($\sim 1\text{A/W}$), but the cleaving tolerance is much higher (\sim around $50\mu\text{m}$) than that of reported planar multi-mode ECPDs [8,9].

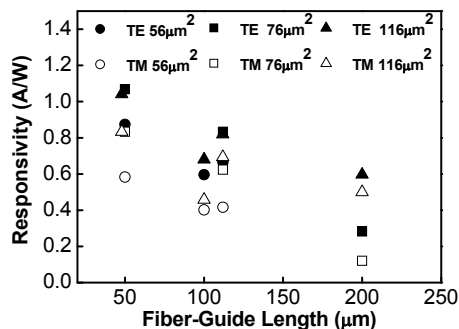


Fig. 9. Measured responsivity versus different L_f for devices with different active areas under a fixed bias voltage -3V.

The bandwidth and saturation current are measured with a heterodyne beating system. Figure 10 shows the measured frequency responses of the DECPD with different active areas under a fixed -1V bias voltage and a fixed photocurrent 5mA. The achieved 3-dB bandwidths of devices with active areas of 56μm², 76μm², and 116μm² are around 60GHz, 50GHz, and 40GHz, respectively. The inset to Figure 10 shows the measured frequency responses of a device with an 116μm² active area under different reverse bias voltages and a small output photocurrent (0.5mA). We can clearly see that the speed performance of device is not degraded, even given such a small output photocurrent density (0.43kA/cm²) and different bias voltages. The past results reported for UTC-PDs indicate that they usually exhibit degradation of speed performance under low output photocurrent [5,18], which is an issue for high-speed fiber communication system [19]. The abrupt graded p-type doping profile in the absorption region of our device means that the static built-in electric field (1.6 to 19kV/cm) is around the critical field for the overshoot-velocity of the electrons. This in turn means that a smaller self-

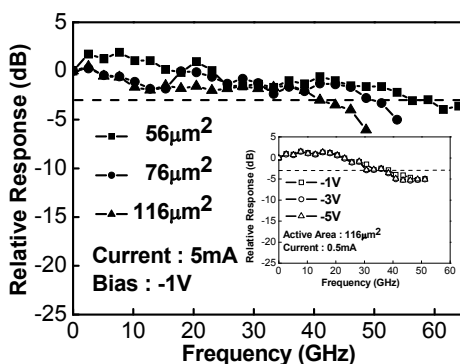


Fig. 10. Measured frequency responses of devices with different active areas under a fixed dc bias voltage (-1V) and a fixed output photocurrent (5mA). The inset shows the device

with an $116\mu\text{m}^2$ active area measured under three different dc bias voltages (-1V, -3V, and -5V) and much lower output photocurrent (0.5mA)

induced field (photocurrent density) will be required to accelerate an electron to near its overshoot-velocity, thereby minimizing the problem of bandwidth degradation under low currents. Figure 11 shows the photo-generated RF power of the devices with (a) $56\mu\text{m}^2$, and (b) $116\mu\text{m}^2$ active areas. The three traces show the results measured under three different bias voltages (-1V, -2V, and -3V). The operating frequency is fixed at 60GHz and 40GHz for (a) and (b), respectively. The ideal relation between the RF power of a 100% modulated large-signal and the average current on a 50Ω load is also plotted as a straight line for reference. The maximum values of the RF power and dc photocurrent of the device with a $56\mu\text{m}^2$ active area are limited by the thermal failure of the device. On the other hand, for a device with a larger active area ($116\mu\text{m}^2$), significant saturation occurs at around 19mA photocurrent. The observed thermal-damage in our small device ($56\mu\text{m}^2$) may be attributed to its larger electrical and thermal resistance, compared with that of a large device ($116\mu\text{m}^2$). The values obtained for saturation current-bandwidth are around 780mA-GHz for both devices. In comparison with other reported high-performance ECPDs with a 25Ω effective load [20] or partially depleted absorbers (PDA)-ECPDs [16] with a 50Ω load, our demonstrated device can achieve a comparable bandwidth-responsivity (54GHz-A/W vs. 60GHz-A/W [20] and 40GHz-A/W [16]), and a higher saturation current-bandwidth performance (780mA-GHz vs. 520mA-GHz [20] and 680mA-GHz [16]).

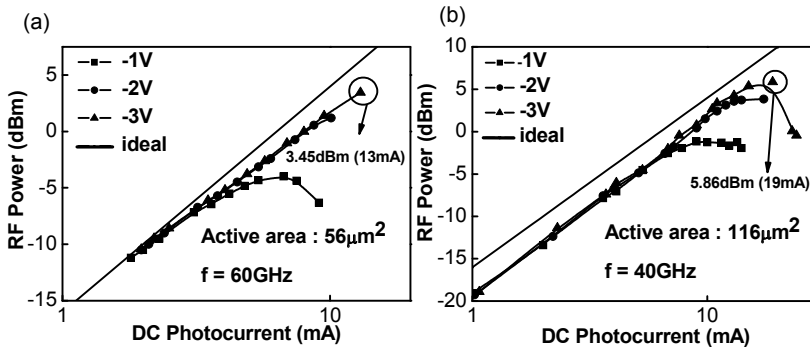


Fig. 11. The RF power versus dc photocurrent of both devices (with and without DBR) with three different active areas (squares: $96\mu\text{m}^2$, open squares: $160\mu\text{m}^2$, open circles: $136\mu\text{m}^2$) under a fixed 40GHz operating frequency and dc bias voltage (-3V).

3. Epitaxial Layer Structure of High-Power Photodiodes

3.1 Introduction

Ultra-high-speed and high-output-power performances are two main trends in the progress of all semiconductor-based devices for telecommunication. However, in most cases, speed and power performances are usually two-trade off parameters in the design of these devices, which include ultra-high speed PDs [4]. By properly down scaling the photo-

absorption volumes of PDs, ultra-high speed performances can be achieved, due to the reduction of parasitic capacitance and resistance in PDs. However, the small photo-absorption volume ($\sim 1\mu m^3$) would cause a high density of photo-generated free carriers and induce a strong space charge field that screens the external applied bias field. The electrical bandwidth would thus seriously degrade due to the reduction in drift velocity of photo-generated carriers [4,5]. There are two major ways to increase the output saturation current (power) and electrical bandwidth product performances, the one is to distribute the photocurrents along edge-coupled PDs, such as the velocity matched distributed photodetector (VMDP) [12] and ECPD as we discussed before, the other is to shorten the carrier drift-time in the active photo-absorption volume, such as UTC-PD [4,5] and seperated-transport-recombintaion PD (STR-PD) [11]. In this chapter, we will introduce the fundamental trade-off between speed and power of ultra-high speed PDs, review the previous reported ultra-high speed/power PDs, and also our recent work about PD with state-of-the-art saturation current-bandwidth product performance.

3.2 Space-Charge-Screening (SCS) Effect in Photodidoe

Field-screening is a fundamental mechanism that limits the output power and electrical bandwidth of PDs under high optical power illumination. A simple model illustrates physical phenomena that mitigate field-screening effects in high-speed PDs, as discussed below. Filed screening arises when the dipole due to spatial separation of photo-generated charges, significantly reduces the drift field. This is especially serious when the photo-generated hole resides in the photo-absorption volume, due to its low mobility and the existence of hetero-structure barriers in p-i-n PDs as illustrated in Figure 12.

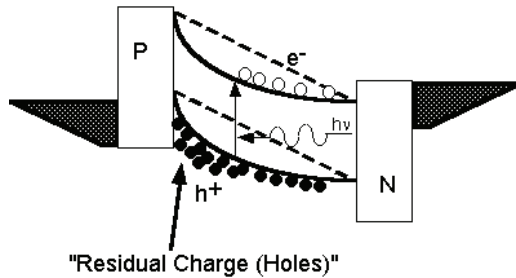


Fig. 12. The serious space-charge screening is originated from hole storage in photo-absorption volume.

The electric field in the photo-absorption layer is the sum of the built-in field (E_b), the field due to photo-generated free charges (E_f), and the fields of waves originating elsewhere and propagating inside the structure (E_w), $E = E_b + E_f + E_w$. The space charge field is found by Gauss’s law and is proportional to the charge area density. For simplicity and clarity, the built-in field and the charge densities of the electrons and holes are approximated as rectangle functions in Figure 13. Figure 13 shows three sets of conceptual graphs at successive times after photo-generation of electrons and holes in the photo-absorption volume by a short optical pulse. The upper plot shows the photo-generated charge densities,

and the lower plots show the net electric field in the absorption region. Electron and hole velocities are assumed equal. The field resulting from the separation of the free charges opposes the built-in field, and if the charge density is large enough, may actually cancel it, as shown in the third set of graphs. Further, besides these, from the above figures, we can clearly see that the region with the least electric field is near the center of absorption region, where the carriers, especially for the case of hole, in the low-field region will travel slow, causing a slow component in the device photocurrent response. Field-screening is said to occur when the device response is perceptibly affected.

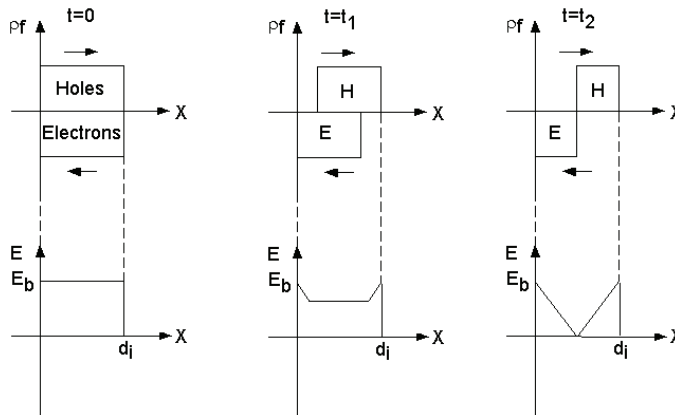


Fig. 13. Conceptual illustration of field-screening mechanism. Simplified electron and hole distributions and net electric fields in the depletion region are plotted at three times after photo-generation by a short optical pulse.

$$E_{eff} = \left(\frac{V_{bais} - Z_{load} \times J \times A + V_{bi}}{D} \right) - \left(\frac{J \times D}{V_{hole} \times \epsilon} \right) \quad (1)$$

$$V_{hole} = V_{pl} \times \tanh \left(\frac{\mu_h \times E_{eff}}{V_{pl}} \right) \quad (2)$$

Symbol	Quantity & Value
E_{eff}	Effective electric field intensity (V/m)
V_{bais}	Applied voltage (V)
A	Active area of photodiode
J	Generated current density (A/m^2)
V_{bi}	Built-in voltage of diode (0.7 V)
D	Depletion layer thickness(m)
ϵ	Dielectric Constant of InGaAs (1.23×10^{-10} F/m)
V_{hole}	Hole Velocity (m/s)
V_{pl}	Maximum Hole Velocity (4.8×10^4 m/s)
μ_h	Hole Mobility ($60 \text{ cm}^2/Vs$)
Z_{load}	Load Impedance (50Ω)

Table 1. Symbols and quantities for equation (1) & (2)

Eq. 1 and 2 is the transcendental equation for solving the net magnitude of electric field in the photo-absorption region and the drift velocity of photo-generated hole, respectively. The

physical meanings and values of each parameter are given in Table 1. We can clearly see that in order to increase the E_{eff} and saturation current of photodiode, we must reduce the depletion layer thickness (D) or increase the carrier drift-velocity (V_{hole}). By increasing the drift-velocity of photo-generated carriers, such as with the structure of a UTC-PD, is one way to minimize the SCS effect. Excellent high-speed and high-power performance has been demonstrated [4,5] in UTC-PD. Figure 14 shows the conceptual band diagram of UTC-PD. Compared with the traditional p-i-n structure, the photo-absorption layer in the UTC-PD is a p-type doped epi layer instead of an intrinsic layer, thus the photo-generated holes will relax to the p contact metal directly without drift, diffusion or accumulation in photo-absorption layer, which will cause serious bandwidth degradation due to the space-charge screening effect. The photo-generated electrons in the absorption layer will diffuse into an intrinsic layer. In order to reduce the diffusion time of electrons in p-type layer, graded-doped or graded-bandgap absorption layers have been demonstrated in UTC-PDs [4,5] as in the n-p-n hetero-junction bipolar transistor (HBT) devices. Without the poor transport properties, such as low mobility and low drift velocity of the photo-generated holes, high power-bandwidth product performance of VPD type, WGPD type, and distributed type UTC-PDs have been demonstrated [4,5,21].

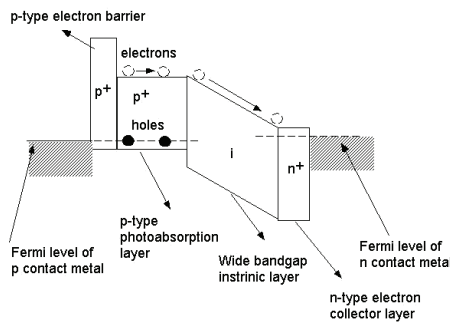


Fig. 14. The conceptual band diagram of UTC-PD

3.3 Near-Ballistic Uni-Traveling Carrier Photodiode (NBUTC-PD)

The structure of UTC-PD, as discussed before, has attracted much attention due to its excellent speed and output power performance. However, such a device usually suffers from the problem of bandwidth degradation under high dc external bias voltage [4,5] due to both the high electric field existing at the junction of the collector (C) and photo-absorption (P) layer, and the decrease in the overshoot drift-velocity of photo-generated electrons. One possible way to enhance the speed performance of UTC-PD is to reduce the externally applied bias voltage and let the value of the electric field in the C-P junction approximately for the critical field, which will enhance the drift-velocity of photo-generated electrons [4,5]. However, under such low reverse bias voltage (around -1V for 200nm collector), the field-screening effect, which originates from the difference in polarity between the output ac voltage across the standard 50Ω load and the dc bias voltage, will seriously limit the maximum output photocurrent of the UTC-PD. Near-ballistic UTC-PD (NBUTC-PD) with state-of-the-art performance has been demonstrated to overcome the above-mentioned problems [22,23]. By inserting an additional delta-doped p+ charge layer and an electric-

field-suffer layer into the collector layer, we can produce an appropriate value of electric field in most of the collector layers so as to sustain a peak velocity of photo-generated electrons under certain ranges of bias voltage and output photocurrent.

Figure 15 shows the conceptual band diagram of InP based NBUTC-PD. The major difference in the epi-layer structure between the UTC-PD and the demonstrated NBUTC-PD is the additional planar-doped p^+ $\text{In}_{0.52}\text{Al}_{0.48}\text{As}$ charge layer and the 100nm thick undoped $\text{In}_{0.52}\text{Al}_{0.48}\text{As}$ electric-field-suffered layer (E). The basic working principle of the NBUTC-PD is similar to that of the reported "Ballistic Collection Transistor (BCT)" [24], whose near-ballistic transport property has been verified through Monte Carlo simulations and experiments [25]. By introducing the proper planar doping density ($5 \times 10^{14}\text{cm}^{-2}$) into the depleted p^+ charge layer, the maximum electric field in the $\text{In}_{0.52}\text{Al}_{0.15}\text{Ga}_{0.33}\text{As}$ collector layer can be controlled to produce an appropriate value (around 40kV/cm at -5V bias) to sustain the overshoot velocity of the photo-generated electrons under a certain range of bias

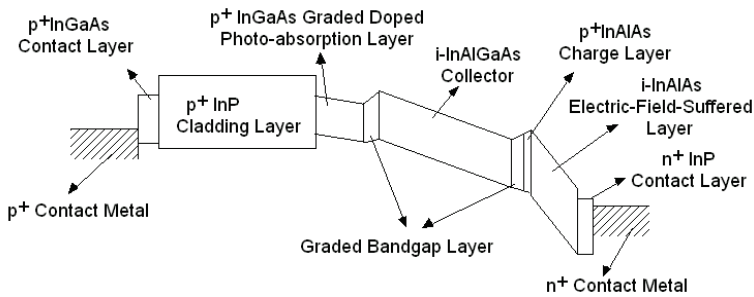


Fig. 15. The conceptual band diagram of NBUTC-PD

voltages and output photocurrents. The adopted graded p-type doping profile of the P layer can produce a built-in electric field (1.6 to 19kV/cm) around the critical field for the electron overshoot velocity. This means that a small self-induced field (photocurrent density) will be required to accelerate an electron to near its overshoot-velocity in the P layer [15]. Through this special P and C two-layer design, near-ballistic-transport of photo-generated electrons throughout the whole epi-layer structure can thus be expected. NBUTC-PDs with ECPD and back-side illuminated VPD structures [22,23] have both been demonstrated. Both kinds of structure have demonstrated excellent speed and power performance.

Figure 16 (a), (b) shows cross-sectional view and top views of the demonstrated NBUTC-PD with ECPD structure, respectively. The optical waveguide structure of our demonstrated NBUTC-PD is based on the reported high-performance planar evanescently-coupled photodiode as discussed before [8,9]. Extremely high responsivity of 1.01A/W and 1.02A/W was achieved with $150\mu\text{m}^2$ and $200\mu\text{m}^2$ active areas, respectively. The responsivity of the device with an $8\mu\text{m}$ waveguide/diode width and $40\mu\text{m}$ ($320\mu\text{m}^2$ active area) absorption length could be further improved to 1.14A/W . To our knowledge, these are the highest values ever reported for the responsivity of high-speed and high power UTC-PDs [4,5]. Figure 17 shows the typical frequency responses of the device with a $200\mu\text{m}^2$ active area under different levels of the output photocurrent (0.5mA, 5mA, and 20mA) and a fixed dc bias voltages (-5V). One can clearly see that under 0.5 and 5mA operation, the electrical

bandwidth was around 40GHz. When the photocurrent reached 20mA, the bandwidth of device increased to 50GHz. Figure 18 shows the measured and fitted frequency responses of the device with a 320 μm^2 active area under 10mA and 15mA

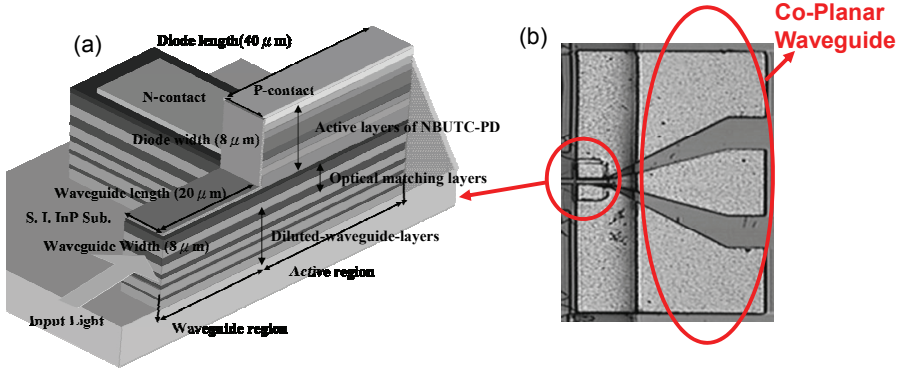


Fig. 16. Cross-sectional view (a) and top-view (b) of NBUTC-PD, which incorporates with an evanescently-coupled optical waveguide.

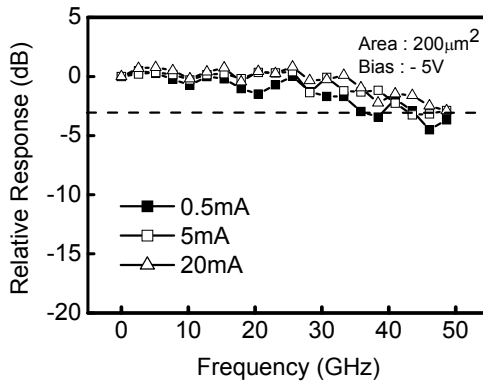


Fig. 17. The measured frequency responses of the device with a 200 μm^2 active area under different levels of the output photocurrent and a fixed dc bias voltage (-5V). (square: 0.5mA; open square: 5mA; open triangular: 20mA).

output photocurrent values. The dc bias voltage was fixed at -4V. According to our simulation results, the bandwidth improvement under high current operation (15mA) is associated to the reduction of the transport time as discussed above and the ac capacitance [18]. The total capacitance is reduced due to the subtraction of the differential ac capacitance $I_C \times \left(\frac{d\tau_c}{dV_{ac}} \right)$, proportional to the current, from the depletion capacitance [13,18]. Where, V_{ac} is the output ac voltage of device, I_C is the photocurrent, and τ_c is the

electron drift time. For the case of demonstrated device, such effect should be significant due to that under near-ballistic transport, the variation of drift-velocity (time) vs. the electric field (V_{ac}) is obvious, according to the reported field dependence electron drift velocity of III-V semiconductors. On the other hand, for the case of UTC-PD operated in the velocity-saturation regime, such effect can almost be neglected due to the fact that electron velocity is insensitive to the electric field. In our bandwidth simulation model, we thus used different

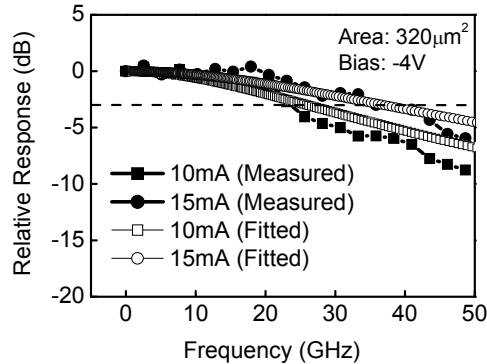
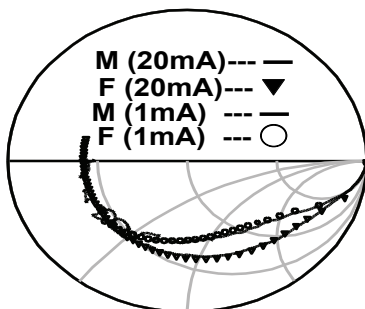


Fig. 18. The measured and fitted frequency responses of the device with a $320\mu\text{m}^2$ active area under different output photocurrent values and a fixed dc bias voltage (-4V) (square: measured trace under 10mA operation; circle: measured trace under 15mA operation; open square: fitted trace under 10mA operation; open circle: fitted trace under 15mA operation.).

drift-velocities and the variation of slopes of electron drift-velocity vs. the electric field in $\text{In}_{0.53}\text{Ga}_{0.47}\text{As}$ material to roughly estimate the reduction of total capacitance and fit the measured frequency responses. Figure 19 shows the fitted and measured microwave S_{22} parameters of NBUTC-PD with a $320\mu\text{m}^2$ active region for a broad frequency range (from 40 MHz to 50 GHz) under two different output photocurrents (1mA and 20mA) and a fixed bias voltage of -5V . The obvious difference between the S_{22} parameters under low and high photocurrents indicates the variation of the elements' values in the equivalent-circuit-model. Under high current operation (20mA), the traces of S_{22} in the Smith-Chart are closer to the S_{22} traces of the case of ideal open-circuit than the measured S_{22} trace under low current operation (1mA) are, which implies a significant improvement in the microwave characteristics of device. This phenomenon has never been observed before in the traditional p-i-n PD. The measured frequency responses of the S_{22} parameters of ordinary PDs or UTC-PD are usually insensitive to their output photocurrent [26]. As compared with the reported UTC-PD [4,5], NBUTC-PD can achieve almost the same electrical bandwidth (around 40GHz), even with a much larger device size ($320\mu\text{m}^2$ vs. $\sim 120\mu\text{m}^2$), and responsivity. This implies that the NBUTC-PD can achieve better output power and responsivity performance with a larger device size without sacrificing speed seriously due to the superior transport property of photo-generated electrons. The traces shown in Figure20 represent the photo-generated RF power vs. dc photocurrent of the NBUTC-PD under different bias voltages (-1V , -3V , and -5V).



Frequency (DC to 50.00GHz)

Fig. 19. The measured and the fitted S_{22} parameters of the device with a $320\mu\text{m}^2$ active area under different levels of output photocurrent (1mA and 20mA) and a fixed dc bias voltage (-5V). The two solid lines represent the measured S_{22} under 1mA and 20mA. Traces with open circle and close triangle symbols represent the fitted results under 1mA and 20mA, respectively.

The operating frequency was fixed at 40GHz. The ideal relation between the RF power of a 100% modulated large-signal and the average current on a 50Ω load is also plotted as a straight line for reference. For the case of a -5V bias, the traces of the device with different active areas ($200\mu\text{m}^2$ and $320\mu\text{m}^2$) are also shown for the purpose of comparison. Since, the bandwidth of the device with a $320\mu\text{m}^2$ active area increases as the photocurrent increases significantly under a -5V bias, the output RF power is closer to the ideal line than is the case with a low photocurrent.

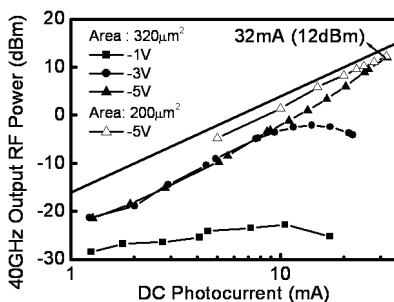


Fig. 20. RF power versus dc photocurrent of the devices with different active areas under different reverse bias voltages (square: -1V, circle: -3V, triangle (open triangle): -5V) at a 40GHz operating frequency. The ideal relation between the RF power and current on a 50Ω load is plotted as a straight line for reference purpose.

As compared to the structure of ECPD, the VPD structure may have further improved high-power performance due to that the input-end saturation problem can be eliminated. However, its responsivity may be poorer. Fortunately, when the operation frequency is over 100GHz, the maximum output saturation power from PD becomes a key issue instead of efficiency due to that the over 100GHz MMW power amplifier still remains a challenge. The

key point to pursue the ultimate high saturation current-bandwidth product of the PD is to downscale the area of the photo-absorption active area and the thickness of the depletion layer. However, device-heating [6] and high parasitic resistance could become problems, which would seriously limit the saturation current of a PD with such a small active area ($\sim 10\mu\text{m}^2$). It has been demonstrated that such problems can be minimized by the incorporation of flip-chip bonding structures or an epitaxial layer transferring process [27]. Figures 21 (a) to (d) show the top view of the NBUTC-PD with VPD structure before flip-chip bonding, cross-sectional views of the device, the flip-chip bonded NBUTC-PD, and the layout of the flip-chip bonding pedestal, respectively. The details of the geometric structure of the back-side illuminated NBUTC-PD are similar to those described in our previous work [25]. Figure 22 (a) and (b) shows the measured O-E frequency response and measured output photocurrent vs. MMW power of NBUTC-PD with a $144\mu\text{m}^2$ active area, respectively. The measured saturation-current bandwidth product is a record-high, over $4070\text{mA}\cdot\text{GHz}$ ($>110\text{GHz}$, 37mA). This is superior to all values reported for high-performance evanescently-coupled p-i-n PDs ($624\text{mA}\cdot\text{GHz}$, 120GHz , 5.2mA) [20], parallel-fed traveling wave photodetectors ($1760\text{mA}\cdot\text{GHz}$, 80GHz , 22mA), [17], and UTC-PDs ($>2380\text{mA}\cdot\text{GHz}$ [4], ($2500\text{mA}\cdot\text{GHz}$ [28])) under the similar heterodyne-beating CW-measurement.

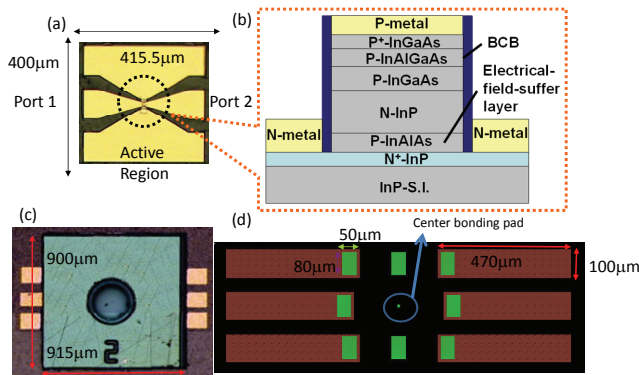


Fig. 21. (a) Top-view of the NBUTC-PD, (b) conceptual cross-sectional view of the NBUTC-PD (c) NBUTC-PD after flip-chip bonding, (d) and flip-chip bonding pedestal.

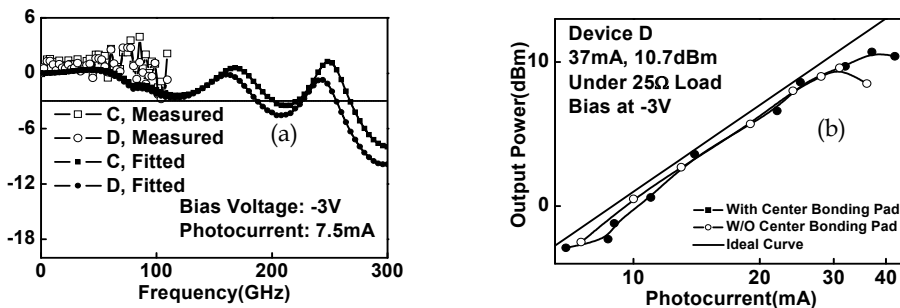


Fig. 22. (a) The measured and fitted O-E frequency response of NBUTC-PD with VPD structure. Device C and D have $100\mu\text{m}^2$ and $144\mu\text{m}^2$ active areas, respectively.

3.4 Partially-Depleted PDs

Thinning the absorption layer thickness [4] or using the p-type absorption layer [4,5], such as the case of UTC-PD, are both possible ways to increase the saturation power of PD, however, the quantum efficiency performance of PDs are usually sacrificed due to its thin intrinsic layer or the recombination process of photo-generated carriers in the photo-absorption layer with p-type dopant [1,11]. Recently, some research groups have demonstrated a new photodiode design that combines the depleted and neutral absorption layers (p-type doping) to maximize the bandwidth-efficiency product of photodiode [10]. Excellent bandwidth

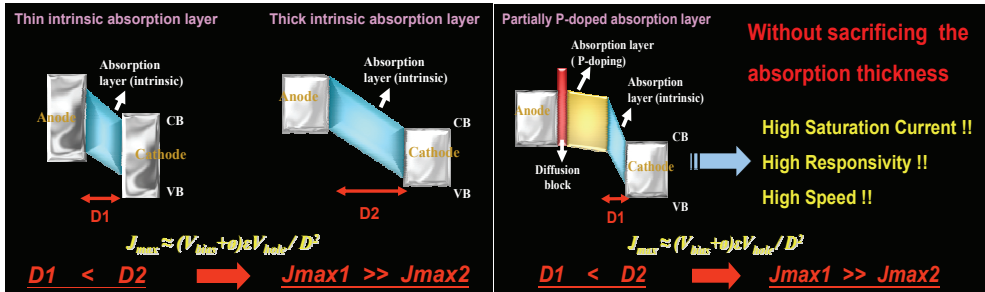


Fig. 23. The conceptual picture, which illustrate why that the PDP structure can have higher saturation current than that of a traditional p-i-n diode.

(over 50GHz) and efficiency performance (0.98A/W) have been demonstrated by use of such technique with the structure of vertical-illuminated PD. Figure 23 shows the conceptual band diagram of a partially depleted PD (PDP) and a traditional PD with a pure intrinsic absorption layer. We can clearly see that by replacing some part of intrinsic absorption layer with p-type doping layer, the depletion layer thickness can be downscaled and the drift-time of photo-generated hole can be effectively reduced. The diffusion time of electron in the p-type absorption layer is not an issue due to that it can be minimized by use of the graded doping profile to create a built-in electric field and accelerate the diffusion process. Such technique has already been reported in the UTC-PD structure [4,5]. Furthermore, the PDP structure can have superior responsivity performance to the high-power PD by downsampling the absorption layer thickness. ECPD with PDP structure as active photodiode [9] have already been demonstrated. In order to study the influence of

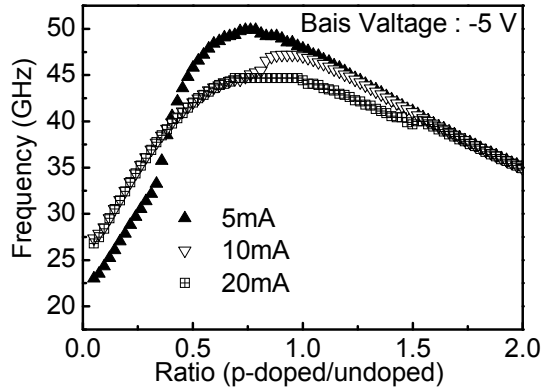


Fig. 24. The simulated electrical bandwidth vs. the ratio of p-doped photo-absorption layer thickness to undoped photo-absorption layer thickness under different operation current (5, 10, 20 mA). The thickness of InGaAs photo-absorption layer is fixed at 500nm.

partially p-doped photo-absorption layers on the high power performance of photodiode, two kinds of devices, which have the same structures of epi-layers except for the photo-absorption active region, were fabricated. Device A has the graded partially p-doped photo-absorption layer to accelerate the drift velocity of photo-generated electrons and device B has a pure intrinsic photo-absorption layer. The ratio of p-doped to undoped layer thickness of device A has been optimized due to the trade-off between RC time constant and drift time of photo-generated carriers [29]. Figure 24 shows the simulation result. As can be seen, by choosing that the ratio of p-type layer thickness over the total absorption layer thickness, which is fixed at $0.5\mu\text{m}$, equals to 0.5, we can get a optimized speed performance. The measured DC responsivity of both devices are the same as 1A/W . The measured frequency responses and $f_{3\text{dB}}$ electrical bandwidths of device A and B are shown in Fig. 25 (a). Device A and B have the same sizes of active area ($150\mu\text{m}^2$) under the same dc bias voltage (-1V) and output photocurrent (5.5mA). According to the measurement results, we can clearly see that device A with partially p-doped photo-absorption layer has superior electrical bandwidth

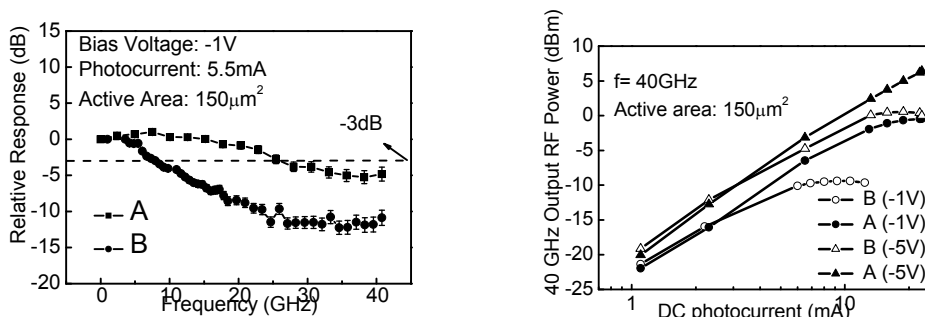


Fig. 25. (a) The measured frequency responses of device A and B under the same high output current (5.5mA) and dc bias voltage (-1V). The active area of device A and B is about 150 μm² (b) RF power versus dc photocurrent of device A and device B under different reverse bias voltages (close triangle: -5V of device A, open triangle: -5V of device B, close circle: -1V of device A, open circle: -1V of device B) at 40GHz operating frequency. The active area of both devices is 150 μm².

performance (~26GHz vs. ~8GHz) especially under high current (5.5mA) and low bias voltage operation (-1V). Fig. 25 (b) shows the photo-generated RF power versus dc photocurrent of device A and B with the same active area (150 μm²) under different reverse bias voltages (-1V and -5V). As this figure indicates, both devices exhibit significant saturation behaviors under low bias voltage (-1V) and high current operation (~10mA). Besides, device A has significant higher values of RF saturation power than device B especially under low dc bias voltage (-1V). These measurement results, as shown in Fig. 23 to 25, indicate that the technique of partially p-doped photo-absorption layer will enhance the speed and output power performance of photodiode significantly without sacrificing the responsivity performance. Furthermore, as compared to downscale the thickness of intrinsic InGaAs photo-absorption layer directly, this demonstrated technique would not increase the device absorption length or sacrifice the responsivity.

3.5 Separated-Transport-Recombination PDs

Based on equation 1, downscaling the depletion layer thickness is the most straightforward way to increase the saturation power of a photodiode [4,11] due to the shortening of carrier drift-time. However, PDs with thin depletion layers usually suffer from the problems of low quantum efficiency and very limited RC bandwidth. As discussed before, PDP structure is one kind of structure to overcome the above-mentioned problems, however, its speed performance may still be limited by the drift-diffusion time of carriers. A novel p-i-n photodiode structure: the Separated-Transport-Recombination photodiode (STR-PD), which can greatly relieve the trade-offs among output saturation power, quantum efficiency, and electrical bandwidth performance, have been demonstrated to further improve the speed performance [11]. In the demonstrated GaAs based STR-PD, the LTG-GaAs layer, which has an extremely short carrier lifetime (less than 1ps) [30], is adopted to serve as the recombination center in the active photo-absorption region and further break the bandwidth

limitation of drift-diffusion time of photo-generated carriers. Figure 26 shows a conceptual band diagram of the STR-PD. The LTG-GaAs layer with an extremely short

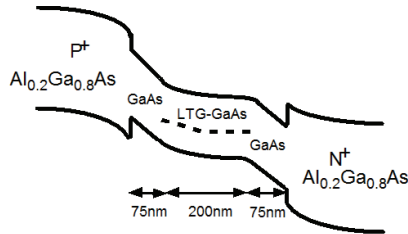


Fig. 26. The conceptual band diagram of the demonstrated STR-PD.

carrier lifetime [30] serves as a recombination center sandwiched between two high quality GaAs based photo-absorption layers. As shown in Fig. 26, the external applied electric field is concentrated in the two GaAs layers due to the high defect density and field-screening effect of the inserted LTG-GaAs layer [11]. These two photo-absorption layers can, thus, be treated as a “transport layer” or “depletion layer” in our structure due to their much higher mobility compared to LTG-GaAs and the concentration of the applied electric field. To recombine the photo-generated carriers, which exhibit low drift-velocity under high current operation, the position of this inserted LTG-GaAs based layer is located near the center of the photo-absorption region [4]. Under optical illumination, most of the photo-generated electrons in the transport layer, which is near the P⁺ Al_{0.2}Ga_{0.8}As layer, will be injected into the LTG-GaAs layer and will recombine with the photo-generated hole from the other side of transport layer. The effective carrier-drift distance in the STR-PD will be roughly approximated by the thickness of the one-sided GaAs based photo-absorption (depletion) layer, which can be thinned down to shorten the drift-time of photo-generated carriers and increase the output saturation current. In our structure, the trade-off between the output saturation current and R-C bandwidth limitation can also be relieved significantly due to the increase in the thickness of the total intrinsic (i) layer, which is composed of undoped GaAs and LTG-GaAs layers with high resistivity, and to the reduction of the device capacitance without affecting the carrier drift-time. Compared with the traditional p-i-n photodiode, it can minimize the RC bandwidth limitation by increasing the thickness of the intrinsic photo-absorption layer directly. However, the drift-time will be increased and the output saturation power will be seriously degraded [4]. Due to the separation of the transport layer (GaAs) from the recombination layer (LTG-GaAs) in our STR-PD structure, the applied electric field will be concentrated in the two GaAs based transport layers, and the problems of low drift-velocity and lifetime increasing effect of the LTG-GaAs based layer can, thus, be compromised [31,32]. In order to study the influence of the recombination layers on the high power performance of photodiodes, two kinds of devices, which have the same epi-layer structure except for the photo-absorption active region, were fabricated. As shown in Fig. 26, device A has an LTG-GaAs-based recombination layer with a 200nm thickness in the center of the photo-absorption region, and the thickness of the surrounding GaAs layer is 75nm. Device B has a pure GaAs based photo-absorption layer with a 350nm thickness, which is around five times thicker than the effective carrier-drift distance of device A (350nm vs. 75nm). The two types of fabricated devices have the same geometry of the WSPD, which can achieve bandwidth-efficiency product performance superior to that of

VPDs as discussed before. A mode-locked Ti:sapphire laser, which has a center wavelength of 850nm, as the light source for dc photocurrent and ac transient measurements. Figure 27 (a) and (b) shows the FWHM of the measured impulse responses versus reverse bias voltage, respectively. As the diagrams indicate, device A achieved better speed performance than device B especially under a high output photocurrent and low dc bias voltage. Furthermore, we can clearly see that in the case of device A, the measured FWHM was insensitive to both the reverse bias voltages (-1 ~ -7V) and input optical power (0.02mW, 0.4mW). As shown in Fig. 27(b), the lifetime increasing effect of the traditional LTG-GaAs based p-i-n photodiode under a high dc bias voltage [30] is eliminated in our novel structure due to the concentration of the applied electric field in the GaAs based transport layers.

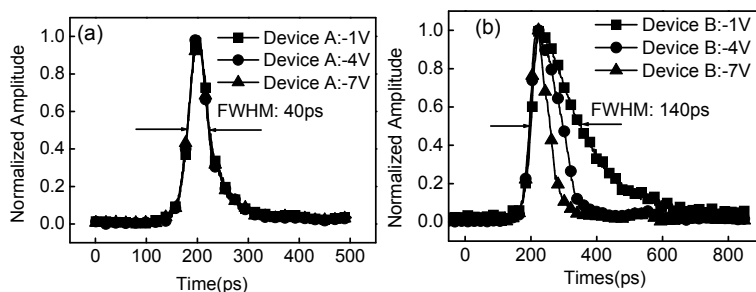


Fig. 27. The normalized impulse responses of device A (a) and device B (b) with a $400\mu\text{m}^2$ active area under a fixed optical pumping power (0.4mW) and different reverse bias voltages (-1V, -4V, -7V).

4. The Application of High-Power PDs to ROF Communication System

4.1 High-Power PD for RoF Communication and Nonlinear Photodetection Scheme

As discussed in the introduction, the “killer application” of high power PD is in the RoF communication system. In this system, high-power PD is used for converting the intense optical power to strong MMW signal and then radiating it to the user-end in last-mile. Photonic transmitter [2, 33-35] (PT), which is composed of a high-power PD and printed-circuit antenna, has thus been demonstrated to match such application. Furthermore, the nonlinear photodetection scheme [36,37] of high-power PD is usually adopted in RoF system to eliminate the necessity of MMW electronic mixer and remote signal re-generation [38]. In this section, we will review several kinds of photonic transmitter and introduce the nonlinear operation of NBUTC-PD based PT for the application of W-band RoF system.

4.2 Photonic Transmitter

Figure 28 (a) and (b) shows a top view of the demonstrated PTs through the use of flip-chip bonding (hybrid) and monolithic integration of PDs with antenna, respectively.

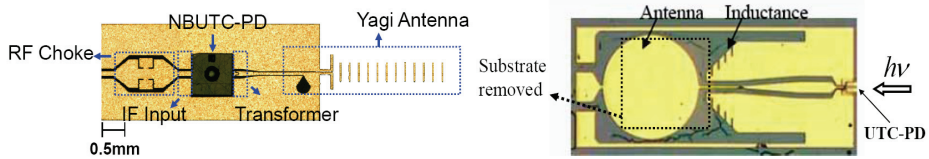


Fig. 28. (a) Top-view of the flip-chip bonding and (b) monolithic integrated photonic transmitters.

In Fig. 28 (a), the integrated active PD is NBUTC-PD, and the passive antenna is quasi-Yagi antenna with end-fire pattern [35]. The active NBUTC-PD is flip-chip bonded with antenna on an AlN substrate. As compared to the reported UTC-PD based PT with taper-slot antenna (TSA) also with end-fire pattern, the size of our quasi-Yagi antenna [39] has comparable directivity (~ 10 dB) and is more compact than that of TSA. In addition, the quasi-yagi antenna is more immune to the substrate-modes, which should be a serious issue of antenna when the operating frequency is over 100GHz, than those of other kinds of planar antenna, such as dipole, slot, and TSA [40]. In Figure 31, the integrated active PD is STR-PD and the antenna is circular disk monopole antenna with broadside pattern [41]. By use of such PT under 850nm femto-second Ti:sapphire mode-locked laser excitation, high radiated peak power without using Si substrate-lens can be achieved [34]. As discussed before, NBUTC-PD has strong bias dependent speed performance. By use of such characteristics, high-power and low up-conversion-loss optoelectronic mixer, which is used for nonlinear photodetection system [36], has been demonstrated [35,42]. Compared with UTC-PD based OE mixer, NBUTC-PD based OE mixer can have wide operation (up-conversion) bandwidth due to the forward bias operation is eliminated [43]. Figure 29 shows the system setup of BPSK and QPSK RoF wireless data transmission system. In such system, the NBUTC-PD based PT, as shown in Figure 28(a), is adopted to convert the optical LO signal at 100GHz to electrical and the electrical QPSK and BPSK data signal is injected onto the NBUTC-PD and the bias point of device is thus modulated by injected signal. The QPSK or BPSK data signal is then up-converted to W-band and radiated to the receiver end. Compared to the traditional On-Off Keying (OOK) data transmission process [1] using a PT, the modulation format of the BPSK and QPSK techniques allows for higher spectral efficiency and is compatible with today's wireless communication systems. In order to realize the goal of free-space data transmission, a high-performance W-band optical photonic source [44] is installed in such system. The inset to Figure 29 shows the output optical spectrum from this optical source. As can be seen, the optical harmonic distortion suppression ratio is 18 dB, and is limited by the bandwidth of our dual-parallel E-O modulator (i.e., 10 GHz) [44]. This source is much less noisy than the two-laser heterodyne-beating system, which was used for device characterization. During the experiment, the BPSK signal is a 1.25Gbit/sec pseudo random bit sequence (PRBS) $2^{31}-1$ signal. The 0.625Gbit/sec QPSK signal is generated by an arbitrary waveform generator (AWG) at a data rate of 625Mb/s. The receiver end is composed of a W-band horn antenna, a W-band low-noise-amplifier (LNA), and a fast W-band power detector to detect the envelope and phase of data signal. The signal detected by the power detector is boosted by an IF amplifier

and then fed into a high-speed real time scope prior to performing off-line signal processing.

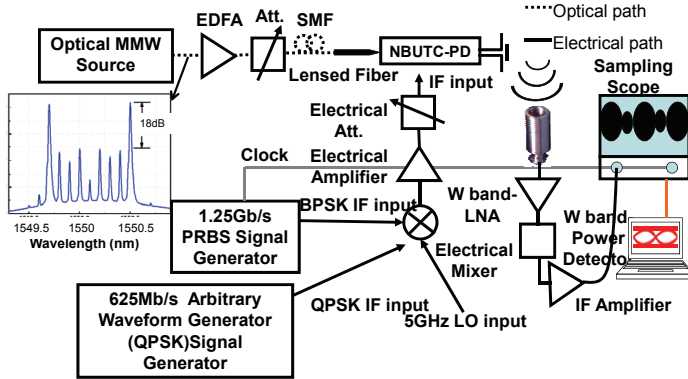


Fig. 29. The system setup for BPSK or QPSK data transmission.

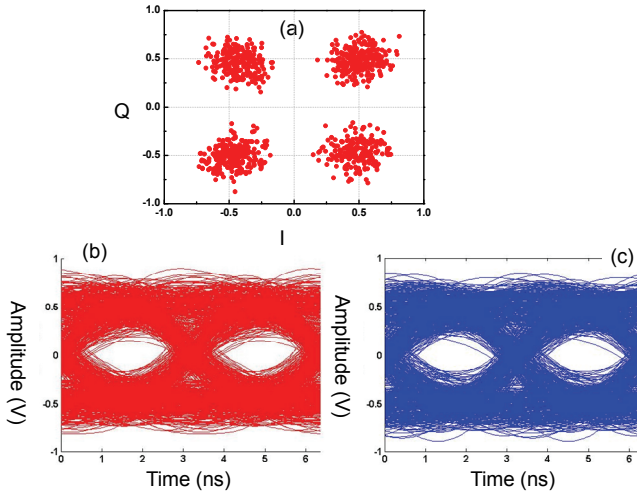


Fig. 30. (a) Constellation of the 0.625-Gb/sec QPSK signal. Eye diagrams of the 0.625-Gb/s QPSK signal: (b) I; (c) Q.

Figure 30 (a) shows the constellation of the received 0.625-Gb/s QPSK signal when the output photocurrent is 10mA; while (b) and (c) show the digital signal processing (DSP) reconstructed I and Q eye diagrams. The corresponding EVM is around 24.7%.

5. Conclusion

The motivation for developing high-power and high-speed PDs arises from the power and speed limitations on conventional p-i-n PDs. There are two approaches to improve the high-power performance of PDs without downscaling the device active area aggressively and seriously sacrificing its responsivity. One is to distribute and uniform the photocurrents along the edge-coupled PDs by improving the geometric structure of optical and electrical waveguides, such as, evanescently-coupled photodiode (ECPD); the other is to minimize the space-charge effect in the photo-absorption volume by changing the structure or material of epitaxial layers, such as UTC-PD, PDP, and STR-PD.

In this book chapter, at first, we discussed the geometric structures of high-power PD. In order to overcome the significant variation of quantum efficiency vs. cleaved length in the traditional ECPD, two kinds of structure have been discussed. One is DECPD and the other is the leaky-waveguide with DBR mirror. In the structure of DECPD, the fiber-coupling waveguide and absorption-layer coupling waveguide is separated in space and the cleaved tolerance can thus be greatly improved. With respect to the structure of leaky-waveguide PD with DBR mirror, it can reduce the required photo-absorption volume due to the optical path is folded and the improvement in O-E bandwidth. Excellent high-responsivity and high-saturation-current-bandwidth product performance have been demonstrated by use of both structures.

In the second part of this chapter, we discuss the mechanism of saturation of PD under high-power operation and disclose several kinds of high-power PDs to overcome the limitation of high-power performance. The key issue to improve the high-power performance of PD is to shorten the carrier drift time inside the absorption region. There are two possible ways to realize this goal; one is to increase the drift-velocity of photo-generated carriers and the other is to directly downscale the depletion layer thickness. By eliminating the slow hole-transport in the UTC-PD, the effective carrier drift-velocity is improved and excellent high-speed and high-power performance has been demonstrated. By further increasing the electron drift-velocity in UTC-PD, the NBUTC-PD structure has demonstrated superior saturation-current bandwidth product with high responsivity. Although to directly downscale the depletion layer thickness is the most straightforward way to improve high-power performance of PD, its RC-limited bandwidth and responsivity performance are usually sacrificed. In order to release the trade-off among depletion layer thickness, RC-limited bandwidth, and responsivity performance of PDs, STR-PD and PDP structures have been demonstrated. By inserting a p-type region and a material with extremely short lifetime ($<1\text{ps}$) in the absorption region of PDP and STR-PD, respectively, superior high-power performance of both structure to traditional p-i-n PDs have both been demonstrated. In the third part of this chapter, we discussed the application of one kind of high-power PD: NBUTC-PD, and photonic transmitter to the RoF communication system. By use of the bias modulation technique on NBUTC-PD, the QPSK and BPSK wireless data transmission at 100GHz frequency has been successfully demonstrated.

6. References

- [1] A. Hirata, T. Kosugi, H. Takahashi, R. Yamaguchi, F. Nakajima, T. Furuta, H. Ito, H. Sugahara, Y. Sato, and T. Nagatsuma, "120-GHz-Band Millimeter-Wave Photonic Wireless Link for 10-Gb/s Data Transmission," *IEEE Trans. Microwave Theory Tech.*, vol. 54, pp. 1937-1944, May, 2006.
- [2] A. Hirata, H. Ishii, and T. Nagatsuma, "Design and Characterization of a 120-GHz Millimeter-Wave Antenna for Integrated Photonic Transmitters," *IEEE Trans. Microwave Theory Tech.*, vol. 49, pp. 2157-2162, Nov. 2001.
- [3] A. J. Seeds and K. J. Williams, "Microwave Photonics," *J. of Lightwave Technol.*, vol. 24, pp. 4628-4641, Dec, 2006.
- [4] K. Kato, "Ultrawide-Band/High-Frequency Photodetectors," *IEEE Trans. Microwave Theory Tech.*, vol. 47, pp. 1265-1281, Jul., 1999.
- [5] H. Ito, S. Kodama, Y. Muramoto, T. Furuta, T. Nagatsuma, T. Ishibashi, "High-Speed and High-Output InP-InGaAs Unitraveling-Carrier Photodiodes," *IEEE J. of Sel. Topics in Quantum Electronics*, vol. 10, pp. 709-727, Jul., 2004.
- [6] T. H. Stievater and K. J. Williams, "Thermally Induced Nonlinearities in High-Speed p-i-n Photodetectors," *IEEE Photon. Technol. Lett.*, vol. 16, pp. 239-241, Jan., 2004.
- [7] F. Xia, J. K. Thomson, M. R. Gokhale, P. V. Studenkov, J. Wei, W. Lin, and S. R. Forrest, "A asymmetric twin-waveguide high-bandwidth photodiode using a lateral taper coupler," *IEEE Photon. Technol. Lett.*, vol. 13, pp. 845-847, Aug., 2001.
- [8] S. Demiguel, N. Li, X. Li, X. Zheng, J. Kim, J. C. Campbell, H. Lu, and A. Anselm, "Very High-Responsivity Evanescently Coupled Photodiodes Integrating a Short Planar Multimode Waveguide for High-Speed Applications," *IEEE Photon. Technol. Lett.*, vol. 15, pp.1761-1763, Dec., 2003.
- [9] Y.-S. Wu, J.-W. Shi, J.-Y. Wu, F.-H. Huang, Y.-J. Chan, Y.-L. Huang, and R. Xuan "High Performance Evanescently Edge Coupled Photodiodes with Partially p-Doped Photo-absorption Layer at 1.55 μ m Wavelength" *IEEE Photon. Tech. Lett* vol. 17, pp.878-880, April, 2005.
- [10] X. Li, N. Li, S. Demiguel, X. Zheng, J. C. Campbell, H. H. Tan, and C. Jagadish, "A Partially Depleted Absorber Photodiode With Graded Doping Injection Regions," *IEEE Photon. Technol. Lett.*, vol. 16, pp.2326-2328, Oct., 2004.
- [11] J.-W. Shi, H.-C. Hsu, F.-H. Huang, W.-S. Liu, J.-I. Chyi, Ja-Yu Lu, Chi-Kuang Sun, and Ci-Liang Pan, "Separated-Transport-Recombination p-i-n Photodiode for High-speed and High-power Performance" *IEEE Photon. Technol. Lett.*, vol. 17, pp. 1722-1724, Aug., 2005.
- [12] L. Y. Lin, M. C. Wu, T. Itoh, T. A. Vang, R. E. Muller, D. L. Sivco, and A. Y. Cho, "High-power High-speed Photodetectors Design, Analysis, and Experiment Demonstration," *IEEE Trans. Microwave Theory Tech.*, vol. 45, pp. 1320-1331, Aug., 1997.
- [13] M. Achouche, V. Magnin, J. Harari, F. Lelarge, E. Derouin, C. Jany, D. Carpentier, F. Blache, and D. Decoster, "High performance evanescent edge coupled waveguide unitraveling-carrier photodiodes for >40-Gb/s optical receivers," *IEEE Photon. Technol. Lett.*, vol. 16, pp. 584-586, Feb., 2004.
- [14] W.-Y. Chiu, J.-W. Shi, W.-K. Wang, Y.-S. Wu, Y.-J. Chan, Y.-L. Huang, and R. Xuan, "Leaky-Wave Photodiodes with a Partially p-Doped Absorption Layer and a Distributed-Bragg-Reflector (DBR) for High-Power and High-Bandwidth-

- Responsivity Product Performance" *IEEE Photon. Technol. Lett.*, vol. 18, pp. 1323-1325, June, 2006.
- [15]Y.-S. Wu, J.-W. Shi, P.-H. Chiu, and Wei Lin "High-Performance Dual-Step Evanescently-Coupled Uni-Traveling-Carrier Photodiodes" *IEEE Photon. Technol. Lett.*, vol. 19, pp. 1682-1684, 2007.
- [16]S. Demiguel, X. Li, N. Li, H. Chan, J. C. Campbell, J. Wei and A. Anselm, "High-Responsivity High-speed and High-power Partially Depleted Absorber Waveguide Photodiodes with Relaxed Coupling Tolerance" in *Proc. OFC 2005*, vol. 3, pp.WQ2-1-WQ2-3.
- [17]A. Beling, J. C. Campbell, H.-G. Bach, G. G. Mekonnen, and D. Schmidt, "Parallel-Fed Traveling Wave Photodetector for >100-GHz Applications," *J. of Lightwave Technol.*, vol. 26, pp. 16-20, Jan., 2008.
- [18]Y.-S. Wu, J.-W. Shi, and P.-H. Chiu "Analytical Modeling of a High-Performance Near-Ballistic Uni-Traveling-Carrier Photodiode at a 1.55 μ m Wavelength," *IEEE Photon. Technol. Lett.*, vol. 18, pp. 938-940, April, 2006.
- [19]E. Lach and K. Schuh, "Recent Advances in Ultrahigh Bit Rate ETDM Transmission Systems," *J. Lightwave Technol.*, vol. 24, pp. 4455-4467, Dec., 2006.
- [20]A. Beling, Heinz-Gunter Bach, G. G. Mekonnen, R. Kunkel, and D. Schmidt, "Miniaturized waveguide-integrated p-i-n photodetector with 120-GHz bandwidth and high responsivity," *IEEE Photon. Technol. Lett.*, vol. 17, pp. 2152-2154, Oct., 2005.
- [21]Y. Hirota, T. Hirono, T. Ishibashi, and H. Ito, "Traveling-Wave Photodetector for 1.55 μ m Wavelength Fabricated with Uni-Taveling-Carrier Photodiodes" *Appl. Phys. Lett.*, vol. 78, pp. 3767-3769, 2001.
- [22]J.-W. Shi, C.-Y. Wu, Y.-S. Wu, P.-H. Chiu, and C.-C. Hong, High-Speed, High-Responsivity, and High-Power Performance of Near- Ballistic Uni-Traveling-Carrier Photodiode at 1.55 μ m Wavelength,"*IEEE Photon. Technol. Lett.*, vol. 17, pp. 1929-1931, Sep., 2005.
- [23]Y.-S. Wu, and J.-W. Shi, "Dynamic Analysis of High-Power and High-Speed Near-Ballistic Unitraveling Carrier Photodiodes at W-Band," *IEEE Photon. Technol. Lett.*, vol. 20, pp. 1160-1162, July, 200
- [24]T. Ishibashi and Y. Yamauchi, "A Possible Near-Ballistic Collection in an AlGaAs/GaAs HBT with a Modified Collector Structure," *IEEE Trans. on Electron Devices*, vol. 35, pp. 401-404, April, 1988.
- [25]T. Ishibashi, "Nonequilibrium Electron Transport HBTs," *IEEE Trans. on Electron Devices*, vol. 48, pp. 2595-2604, Nov., 2001.
- [26]G. Wang, T. Tokumitsu, I. Hanawa, K. Sato, and M. Kobayashi, "A Time-Delay Equivalent-Circuit Model of Ultrafast p-i-n Photodiodes", *IEEE Trans. Microwave Theory Tech.*, vol. 51, pp. 1227-1233, April, 2003.
- [27]N. Li, H. Chen, N. Duan, M. Liu, S. Demiguel, R. Sidhu, A. L. Holmes, Jr., and J. C. Campbell, "High Power Photodiode Wafer Bonded to Si Using Au With Improved Responsivity and Output Power" *IEEE Photon. Technol. Lett*, vol. 18, pp. 2526-2528, Dec., 2006.
- [28]N. Li, X. Li, S. Demiguel, X. Zheng, J. C. Campbell, D. A. Tulchinsky, K. J. Williams, T. D. Ishiki, G. S. Kinsey, and R. Sudharsanan, "High-Saturation-Current Charge-Compensated InGaAs-InP Uni-Traveling-Carrier Photodiode," *IEEE Photon. Technol. Lett.*, vol. 16, Mar., pp.864-866, 2004.

- [29]Y.-S. Wu, J.-W. Shi, J.-Y. Wu, F.-H. Huang, Y.-J. Chan, Y.-L. Huang, and R. Xuan, "Design and Demonstration of High-Power and High-Speed Evanescently Coupled Photodiodes with Partially p-Doped Photo-absorption Layer" *Conference on Laser and Electro-Optics (CLEO/QELS'2005)*, USA, OSA Technical Digest, CMGG1, 2005.
- [30]S. Gupta, J. F. Whitaker, and G. A. Mourou, "Ultrafast Carrier Dynamics in III-V Semiconductors Grown by Molecular-Beam Epitaxy at Very Low Substrate Temperatures," *IEEE J. of Quantum Electronics*, vol. 28, pp.2464-2472, Oct., 1992.
- [31]Y. J. Chiu, S. B. Fleischer, and J. E. Bowers, "High-Speed Low-Temperature-Grown GaAs p-i-n Traveling-Wave Photodetector," *IEEE Photon. Technol. Lett.*, vol. 10, pp.1012-1014, July, 1998.
- [32]N. Zamdmer, Qing Hu, K. A. McIntosh, and S. Verghese, " Increase in Response Time of Low-Temperature-Grown GaAs Photoconductive Switches at High Voltage Bias" *Appl. Phys. Lett.*, vol. 75, pp. 2313-2315, Oct., 1999.
- [33]Yu-Tai Li, J.-W. Shi, Ci-Ling Pan, C.-H. Chiu, W.- S. Liu, Nan-Wei Chen, C.-K. Sun, and J.-I. Chyi, "Sub-THz Photonic-Transmitters Based on Separated-Transport-Recombination Photodiodes and a Micromachined Slot Antenna" *IEEE Photon. Technol. Lett.*, vol. 19, pp. 840-842, June, 2007.
- [34]Yu-Tai Li, J.-W. Shi, C.-Y. Huang, N.-W. Chen, S.-H. Chen, J.-I. Chyi, and Ci-Ling Pan, "Characterization of Sub-THz Photonic-Transmitters Based on GaAs/AlGaAs Uni-Traveling Carrier Photodiodes and Substrate-Removed Broadband Antennas for Impulse-Radio Communication," *IEEE Photon. Technol. Lett.*, vol. 20, pp.1342-1344, Aug., 2008.
- [35]Y. S. Wu, N. W. Chen, and J. W. Shi, "A W-Band Photonic Transmitter/Mixer Based on High-Power Near-Ballistic Uni-Traveling-Carrier Photodiode (NBUTC-PD)," *IEEE Photon. Technol. Lett.*, vol. 20, pp. 1799-1801, Nov., 2008.
- [36]M. Tsuchiya, and T. Hosida, "Nonlinear Photodetection Scheme and Its System Applications to Fiber-Optic Millimeter-Wave Wireless Down-Links" *IEEE Trans. Microwave Theory Tech.*, vol. 47, 1999.
- [37]H. Fushimi, T. Furuta, T. Ishibashi, and H. Ito, "Photoresponse Nonlinearity of a Uni-Traveling-Carrier Photodiode and Its Application to Optoelectronic Millimeter-Wave Mixing in 60GHz Band," *Jpn. J. Appl. Phys.*, vol. 43, pp. L966-L968, July, 2004.
- [38]H.-C. Chien, A. Chowdhury, Z. Jai, Y.-T. Hsueh, and G.-K. Chang, "Long-Reach 60-GHz Mm-Wave Optical-Wireless Access Network Using Remote Signal Regeneration and Upconversion," in *Proc. ECOC 2008, Brussels, Belgium, Germany*, Sep., 2008, vol. 2, pp. 137-138.
- [39]N. Kaneda, W. R. Deal, Y. Qian, R. Waterhouse, and T. Itoh, "A broadband planar quasi-Yagi antenna," *IEEE Trans. on Antennas and Propagation*, vol. 50, pp. 1158-1160, Aug., 2002.
- [40]G. M. Rebeiz, "Millimeter-wave and terahertz integrated circuit antennas," *Proceedings of IEEE*, vol. 80, pp. 1748-1770, 1992.
- [41]Y.-C. Liang and N.-W. Chen, "An ultra-broadband coplanar waveguide-fed circular monopole antenna," *EuCAP 2007*, Edinburgh, UK, Nov., 2007.
- [42]J.-W. Shi, Y.-S. Wu, and Y.-S. Lin, "Near-Ballistic Uni-Traveling-Carrier Photodiode Based V-band Optoelectronic Mixers with Internal Up-Conversion-Gain, Wide Modulation Bandwidth, and Very High Operation Current Performance," *IEEE Photon. Technol. Lett.*, vol. 20, pp. 939-941, June, 2008.

- [43]A. Hirata, T. Furuta, H. Ito, and T. Nagatsuma, "10-Gb/s Millimeter-Wave Signal Generation Using Photodiode Bias Modulation," *J. of Lightwave Technol.*, vol. 24, pp. 1725–1731, April. 2006.
- [44]P. T. Shih, C. T. Lin, W. J. Jiang, E. Z. Wong, J. Chen, S. Chi, Y. -S. Wu, F. -M. Kuo, N. -W. Chen, and J. -W. Shi, "W-Band Vector Signal Generation via Optical Millimeter-Wave Generation and Direct Modulation of NBUTC-PD," *Proc. OFC 2009, San Diego, CA, USA, March, 2009*, pp. OWP4.

Ultrawideband-over-fiber technologies with directly-modulated semiconductor lasers

Víctor Torres-Company¹, Kamau Prince², Xianbin Yu²,
Timothy Braidwood Gibbon² and Idelfonso Tafur Monroy²

*¹Departament de Física, Universitat Jaume I
ES-12071 Castelló, Spain*

*¹Department of Electrical and Computer Engineering, McGill University
H3A 2A7 Montreal, Canada*

*²Department of Photonics Engineering, Technical University of Denmark
DK 2800 Lyngby, Denmark*

1. Introduction

In the last few years, there has been a growing interest in the generation of ultrawideband (UWB) radio-frequency (RF) signals. Due to the high-data-rate capabilities, low power consumption and immunity to multi-path fading, these pulses have an unprecedented opportunity to impact radio communication systems in personal area networks, and promise as well substantial applications in radar, safety, and biomedicine. The UWB RF spectrum was regulated between the 3.1 and 10.6 GHz band with a power spectral density of -41.3dBm/MHz , according to the Federal Communications Commission (FCC) of the United States. Later, Asian and also European regulations stated similar masks (Porcine et al., 2003; Di Benedetto et al., 2006). Any signal to be considered as UWB must have an RF spectral bandwidth greater than 500 MHz or a fractional bandwidth greater than 20%. Due to these strict regulations concerning the power levels, UWB systems for wireless communications are constrained to operate over few tens of meters. In addition, this huge spectrum challenges most of the current electronics devices aiming to provide arbitrary waveform generation and simplicity in a single low-cost platform.

However, the synergy between UWB and fiber technologies offers an alternative solution, providing uninterrupted service over different networks, while still preserving the high-data-rate capabilities. Moreover, UWB-over-fiber technology opens the possibility to generate the UWB compliant signals directly in the optical domain, thus relaxing the requirements for high-frequency electrical components.

In this Chapter, we review the basic notions of UWB-compliant signals and several widespread all-optical solutions for their generation and distribution. The central core of the Chapter will focus on simple techniques for the generation of doublet and monocycle UWB impulses, particularly those exploiting the dynamics of gain-switched semiconductor laser sources. Finally, we discuss new areas of research in this rapidly evolving field.

2. Review of photonically assisted UWB signal generation

The normalized version (in dB) FCC regulated UWB mask for indoor applications is depicted in Fig. 1 (right column) in dashed line, together with several electrical signals in time and their corresponding RF spectrum. As one can notice, a Gaussian electrical impulse does not satisfy the UWB requirements because it exhibits a high amount of energy at low frequencies. However, monocycle and doublet pulses, corresponding to first- and second-order derivation of Gaussian impulses, start to fit better into the UWB domain. Although they do not strictly fall into the FCC mask, an extra electronic filter could be placed before the transmitting antenna in order to achieve the UWB compliant pulse. Actually, the UWB radiating antenna helps to reduce this low frequency content. Although not a perfect solution, most researchers have focused into the generation of this kind of pulses because of their relative simplicity. A higher-order UWB pulse matches the mask without the need of filtering, but their generation requires more advanced techniques.

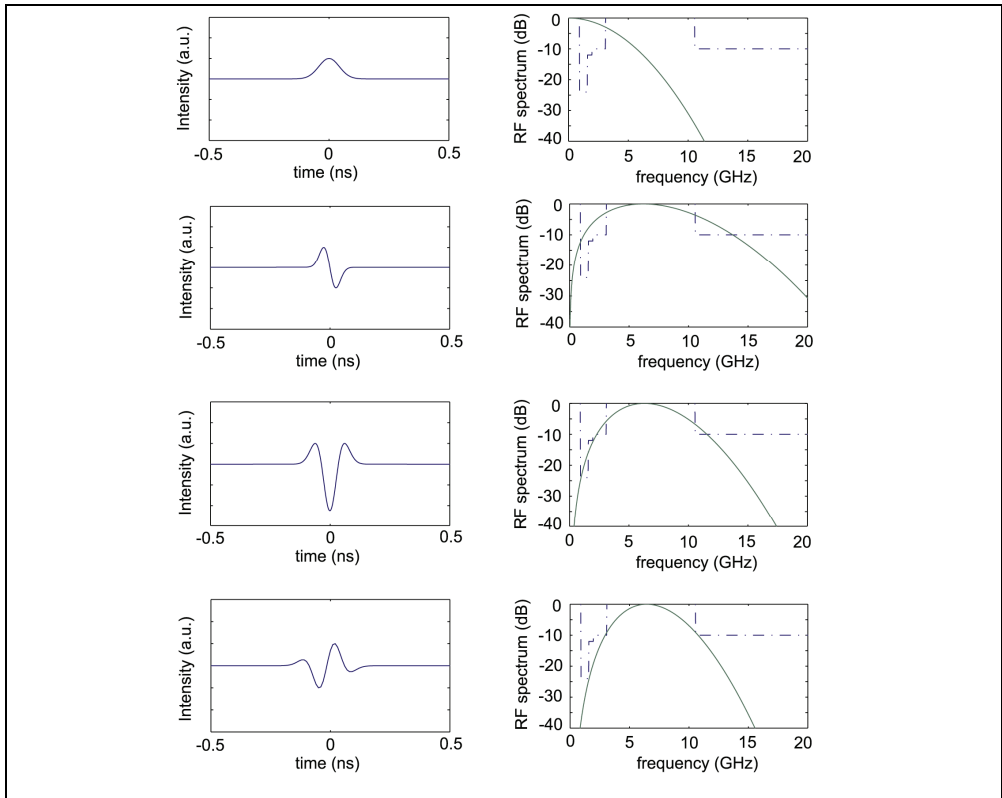


Fig. 1. Different impulse signals in time (left column) and their corresponding RF spectra (right column). The FCC UWB normalized mask is displayed in dashed line.

In this section we aim to review some of the work previously published on optical approaches for UWB signal generation. The list of references does not pretend to be

exhaustive, but it gives a flavour of the research trend in this topic from a historical and intuitive perspective.

2.1 Dispersion-induced frequency-to-time mapping

The first photonic approaches about generation of UWB pulses focused on the technique now known as “frequency-to-time mapping”. This solution aims at synthesizing the power spectrum of an ultrashort optical pulse and subsequently launching the signal into a linear dispersive medium. Because each frequency component travels at a different group velocity, after a certain amount of dispersion, the output intensity pulse becomes a scaled replica of the synthesized power spectrum (Fetterman et al. 1979; Tong et al. 1997). The scaling factor is provided by the group-delay-dispersion (GDD) coefficient of the dispersive medium (Muriel et al. 1999). Larger amounts of dispersion do not change the shape of the pulse, only increase the scale. The electrical UWB impulse is subsequently obtained by ideal photodetection. Due to the scaling factor capabilities, this technique for arbitrary waveform generation allows for entering into the low-frequency regime. An added advantage of this technique is that when a single-mode optical fiber is used as the stretching element, the signal is generated and transported in the same optical component without the need for chromatic dispersion compensation.

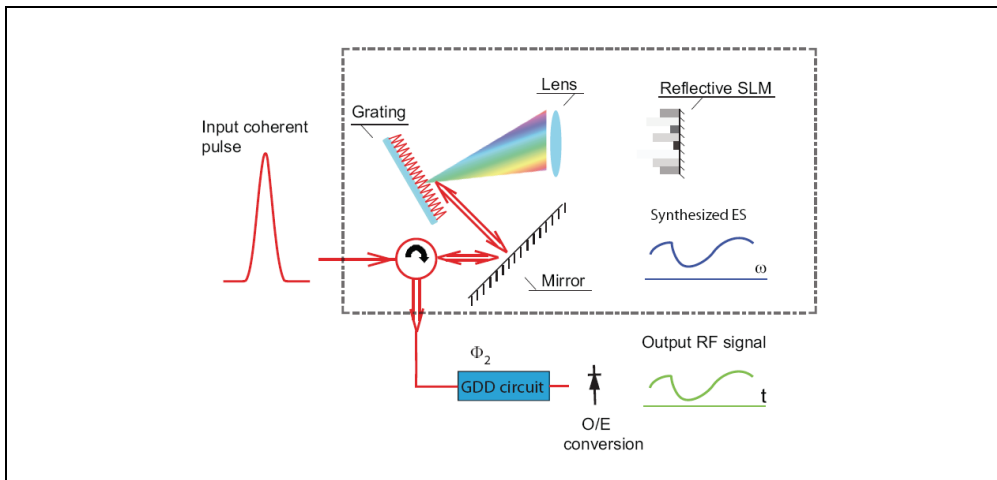


Fig. 2. Example of arbitrary microwave waveform generation based on Fourier transform pulse shaping and dispersion induced frequency-to-time mapping.

The first demonstration used a supercontinuum light source and a Fourier transform pulse shaper for the spectrum synthesizer (Chou et al., 2003). Later on, this technique incorporated a closed loop enabling rapid waveform design thanks to the reconfigurability of the spatial light modulator used in the pulse shaper (Lin et al., 2005). The high flexibility and resolution of this technique allow for the elimination of undesired ripples (apodization) and optimization of the RF spectrum of the signal to satisfy the FCC spectral regulations with a precision better than that offered by monocycle or doublet impulses (McKinney et al. 2006). More recently, fiber filters have been used to replace the Fourier transform shaper device,

leading to a more compact setup, but at the expense of sacrificing the reconfigurability capabilities (Wang et al. 2007). A recent solution deserves a special mention (Abtahi et al., 2008). There, an all-fiber reconfigurable optical filter, together with differential photodetection, permits obtaining Gaussian, monocycle, doublet and higher-order UWB impulses in a single device just by tuning a simple band-pass optical filter.

Although this frequency-to-time mapping technique provides an impressive flexibility in the synthesis of the UWB RF spectrum, the use of a broadband laser pulse as optical source restricts the repetition rate to a few MHz. A recent solution replaces the mode-locked laser by a broadband incoherent light source (Torres-Company et al., 2008). However, in this case, the shaping is performed on the averaged intensity profile, which means that because of the incoherent nature of the approach, there are uncontrolled changes in the pulse to pulse shape (Torres-Company et al., 2007).

2.2 Nonlinear optics

The first alternative approaches to the frequency-to-time mapping made use of the cross-phase modulation effect either in a highly nonlinear fiber (HNLF) (Zeng et al., 2007) or in a semiconductor optical amplifier (SOA) (Dong et al., 2007). The idea behind this is to induce a frequency chirp with a Gaussian pump pulse on a continuous wave (CW) probe laser. This phase modulation can be transformed into intensity modulation by using an appropriate optical band-pass filter. A nice feature of this system is that it permits the control of the polarity of the generated UWB pulse just by tuning the wavelength of the CW to fit in the positive or negative slope region of the optical Gaussian filter. Optimized spectral filters lead to a better control of the shape of the pulse, extending the technique to include doublet impulses too (Zeng et al., 2007). However, the HNLF approach still requires of a high-power laser pulse as pump signal to induce the chirping on the CW probe. On the other hand, the monocycle impulses generated using the SOA approach deviate from the ideal shape due to undesired effects such as the chirping in the dynamics of the process.

A recent approach has demonstrated the generation of generating UWB monocycle impulses with polarity control using sum-frequency generation (SFG) in a periodically-poled lithium niobate waveguide. This system provides a compact device and does not require a femtosecond light source (Wang et al., 2009). Doublet impulses could in principle be generated as well. However, the required power levels to excite SFG in the waveguide are still very high, leading to a low-efficiency global process.

2.3 Microwave photonic filtering design

Microwave photonics is nowadays a well-established research field. In general terms, it aims to provide processing functions of RF and microwave signals that are difficult to achieve using purely electronic approaches (Capmany and Novak, 2007). One of the most widely explored aspects of microwave photonics is radio-frequency filtering (Capmany et al., 2005). The advantages offered by photonics are reconfigurability, high bandwidth, immunity to electromagnetic interference, high-speed processing, and potential integrability with fiber optics technology. In a photonic microwave filter, the input RF signal modulates an optical source, the modulated optical waveform is then processed in a photonic circuit, and finally the signal is recovered back in the electrical domain by optoelectronic (O/E) conversion (Capmany et al., 2005). In the former approaches, filtering functions were implemented

using “positive” taps only, which implies that the filter is always pass-band at low frequencies. This drawback may be solved, e.g., by employing alternative modulation formats combined with differential photodetection, or nonlinear effects in either SOAs or SMFs (You and Minasian, 2004; Minasian, 2004; Capmany et al., 2005).

It has been recently recognized that monocycle impulses can be generated by filtering a Gaussian electrical impulse in a two-tap (one positive and another negative) microwave photonic filter; whereas doublet impulses are obtained in a three-tap configuration (two-positives and another negative and vice versa) (Yao, 2007). This general rule permits to recover the previous research work on incoherent filter design with positive and negative taps for the particular problem of UWB signal generation. Microwave photonic filters featuring reconfigurability are the preferred ones because they provide extra control on the UWB generated signal. In addition, since many of the synthesized filters require the use of a single-mode-fiber to achieve the required delays, the system generates and transports the signal simultaneously.

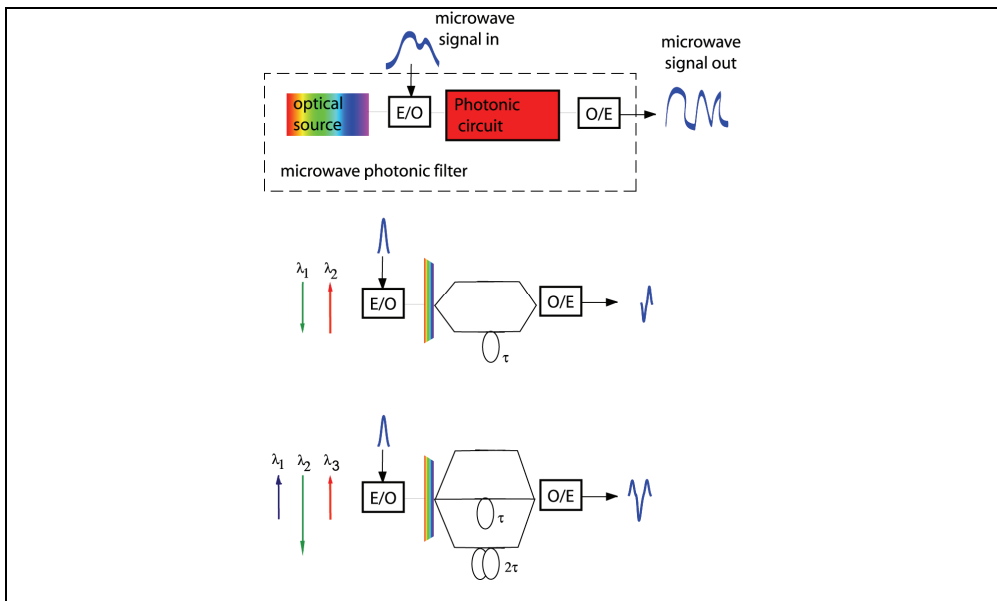


Fig. 3. General concept of a microwave photonic filter. Scheme for the generation of a monocycle and doublet with a microwave photonic filter with positive and negative taps.

For example, we mention the generation of monocycle and doublet impulses based on cross-gain modulation (XGM) in an SOA (Wang et al., 2006). XGM was one of the first approaches that recognized the capabilities to generate negative taps in a microwave photonic filter (Coppinger et al., 1997). Other approaches include the use of a polarization modulator and birefringent fibers (Yao & Wang, 2007) or the bias dependence with the wavelength in an electro-optic modulator (Li et al., 2008; Vidal et al. 2005). A very recent approach (Bolea et al., 2009) deals with the performance of an N-tap microwave photonic filter implemented with two EOMs and several switches (Capmany et al. 2003). Although the performance of

this microwave filter is more complex than the previous setups, the reconfiguration capabilities and the possibilities to implement alternative modulation schemes to ON-OFF keying makes the system very promising for UWB-over-fiber technologies.

3. UWB signal generation based on semiconductor laser dynamics

In this section we report an alternative photonic technique to generate UWB pulses. It involves the use of a distributed feedback (DFB) laser whose driving current is modulated by an electrical data signal (Torres-Company et al., 2008b; Torres-Company et al., 2008c). With respect to previous approaches, our configuration offers an efficient solution in terms of power consumption and constitutes a low-cost alternative, since there are no optical nonlinear processes involved requiring extra light sources or additional active optical devices. Our approach requires a single optical light source and avoids the use of external electro-optic modulation. It is worth mentioning that a previous reported work (Lin & Chen, 2006) used a current modulated Fabry-Perot laser for the generation of UWB signals. However, unlike in our approach, the frequency chirp was not used for achieving UWB signal generation. Instead, monocycle pulses were obtained by O/E conversion and subsequent differentiation performed in the electrical domain.

With our setup, monocycle or doublet pulse shapes can be achieved. Although the experimental arrangement is the same in both cases, the physical mechanism behind is different. The general setup consists on a DFB semiconductor laser, a 12.5 Gb/s bit pattern generator, and a spectral pass-band optical filter. The DFB laser is nominally specified for operation at 10 Gb/s, but the driving data signal was selected at the maximum bit rate. The output pulse from the laser is spectrally filtered by the band-pass filter, which had a Gaussian profile and a FWHM of 0.3 nm. The way of selecting the UWB-pulse shape is by adjusting the bias voltage applied to the laser, the amplitude of the data driving signal and the tunable filter. There are two sets of parameters that lead to either monocycle or doublet shapes. We now proceed to formulate a heuristic explanation for each of the different physical phenomenon behind this achievement.

3.1 Monocycle generation using the chirping effect

In this case, the laser is forward biased far from the threshold, and a relatively low value of modulating amplitude is selected. The laser dynamics is found in the linear region of the Power-Intensity curve. The key is that, as a result of the changes in the carrier population, the refractive index also changes, leading to a phase-modulation changing with time (Agrawal, 2002). Therefore, in the small-signal case the laser pulse becomes highly chirped, with an instantaneous frequency resembling the shape of a monocycle. Then, as heuristically explained in Fig. 4, the process of chirp-to-intensity conversion can be achieved by using a spectrally linear optical filter. This behavior is obtained approximately by placing our Gaussian bandpass filter at the linear slope region.

Of course, this is just a heuristic explanation and instantaneous frequencies do not always exist in the spectrum of a coherent signal (Mandel, 1974). Even more, the case displayed in Fig. 4 is only valid for phase-only modulated signals. However, let us formulate mathematically our problem. The complex field of the frequency-chirped pulse is filtered by a linear optical filter $H(\omega) = A(\omega + \omega_s)$, where A is a real constant that determines the slope of

the filter and ω_s denotes the vertical offset from the zero-crossing point. The temporal envelope at the output of the filter is given by

$$\psi_{\text{out}}(t) = i A [\psi'_{\text{in}}(t) - i \omega_s \psi_{\text{in}}(t)] \quad (1)$$

where the prime denotes temporal derivation and $\psi_{\text{in}}(t)$ is the input temporal envelope. We have taken into account that $FT^{-1}[-i \omega \Psi_{\text{in}}(\omega)] = \psi'_{\text{in}}(t)$, where $\Psi_{\text{in}}(\omega) = FT[\psi_{\text{in}}(t)]$, with FT and FT^{-1} denoting Fourier and inverse Fourier transformation, respectively. We can always rewrite the input envelope as $\psi_{\text{in}}(t) = I_{\text{in}}^{1/2}(t) \exp[-i \varphi_{\text{in}}(t)]$, where $\varphi_{\text{in}}(t)$ and $I_{\text{in}}(t)$ denote the phase and normalized intensity modulation, respectively. We now assume that the frequency modulation dominates respect to the intensity modulation, but its contribution value is less than the corresponding frequency offset of the filter, i.e., $|I_{\text{in}}'(t)| \ll |\varphi_{\text{in}}'(t)| \ll \omega_s$. With this assumption, and after some algebra, the optical intensity at the output of the filter can be approximated to

$$I_{\text{out}}(t) \approx 2 A^2 \omega_s I_{\text{in}}(t) [\varphi_{\text{in}}'(t) + \omega_s/2]. \quad (2)$$

The above equation establishes that the light intensity at the output of the optical filter is given essentially by the frequency chirp of the input optical pulse if the intensity profile is relatively smooth. The derivation of Eq. (2) accounts for the heuristic explanation provided in Fig. 4.

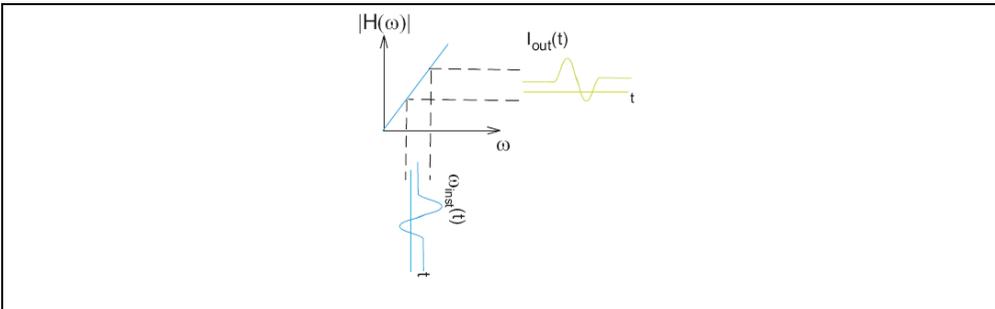


Fig. 4. Schematic overview of chirp-to-intensity conversion.

To test this approach we have built the setup corresponding to Fig. 5. The laser was biased at 67 mA, a value far from the threshold of 30 mA, and the bit pattern generator produced a sequence of one "1" followed by seven "0" with a peak-to-peak voltage of 0.57 V. The measured intensity and chirp are displayed at Fig. 6(a) in solid and dashed line, respectively. For the measurement of the chirp we employed the transport-of-intensity equation procedure (Dorrer, 2005), for which an SMF of 0.415km was used. We can appreciate the monocycle-like profile of the chirp. The spectrum corresponding to the laser and the filter, when located at the optimal point to achieve the monocycle shape, are displayed together in Fig. 6(b). The average optical power level before and after the filter was measured to be 5.6dBm and -9.1 dBm, respectively.

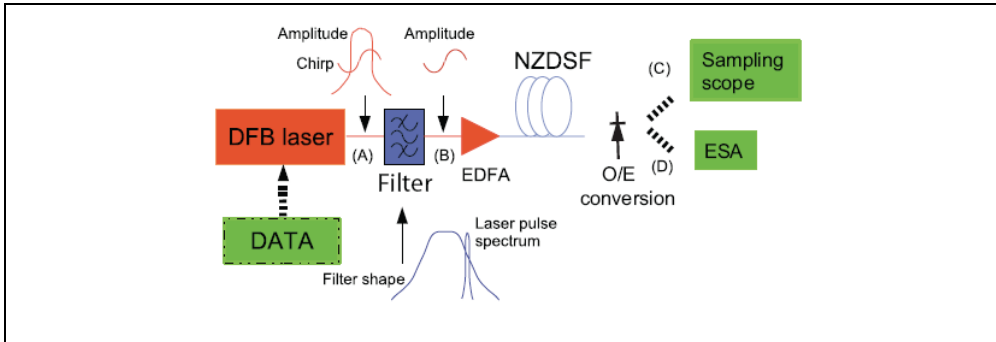


Fig. 5. Experimental setup to achieve monocycle UWB pulses based on chirp-to-intensity conversion.

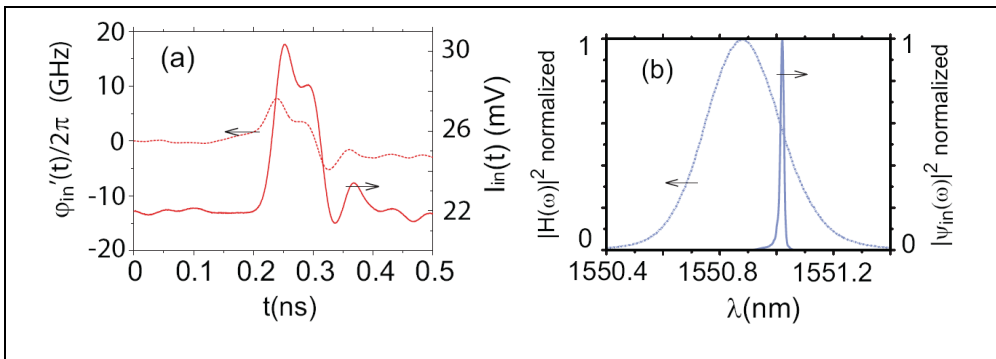


Fig. 6. (a) Input laser intensity pulse in amplitude (solid line) and chirp (dotted line) and (b) normalized spectrum of laser pulse (solid line) and amplitude filter (dotted line).

In order to test the validity of the signal for UWB communications we performed an additional transmission experiment. The optical signal is amplified by an Erbium-doped fiber amplifier (EDFA) and propagated through 20 km of non-zero dispersion shifted fiber (NZDSF) with 4.5dB loss and 5 ps/nm/km dispersion. This dispersion leads to a GDD parameter very low to distort the achieved UWB pulse. The intensity waveform at the output is detected by a 10GHz bandwidth photodiode (PD) which intrinsically assists in smoothing undesired high-frequency RF components that do not fall into the UWB range. The resultant electrical signal is measured in the RF domain by an electrical spectrum analyzer (ESA) with a resolution of 1MHz, and in the time domain by a sampling oscilloscope. The EDFA is adjusted so that the receiver gets an average optical input power of -0.5 dBm. Figure 7 shows the measured resultant UWB signal consisting of a monocycle-like pulse in time and frequency domain. For the frequency domain picture, we selected a repetition rate of 390.6MHz (a "1" followed by 32 "0") so that the achieved spectral shape is properly sampled. As it can be appreciated, the RF spectrum spreads over the UWB region. Due to the monocycle-like waveform, non-disregarding low-frequency content still remains, which can be minimized by reducing the power into the photodiode with some extra attenuator.

the RF spectrum of this waveform with the 10 GHz bandwidth PD and verified that it was not UWB compliant. However, we were able to produce the required pulse characteristics by passing this laser pulse through the same Gaussian spectral filter as before, but at a different operation point. In Fig. 9(b) we show the output laser spectrum (blue solid line) and the filter profile placed in the optimal position to achieve the doublet shape. As we can see, the high-frequency optical components are smoothed. It should be mentioned that previously-reported approaches for optical filtering of gain-switched lasers tried to avoid this overshooting effect and aimed to generate bellshaped ultrashort waveforms (Nakazawa et al. 1990; Niemi et al. 2001). Our goal here is instead to optimize the intensity profile so that this waveform can be exploited for UWB RF signal generation. After the optical filtering, we converted the optical signal into the electrical domain with a 10 GHz bandwidth PD, and succeeded in generating a doublet-like UWB impulse, as shown by the green line in Fig. 10 (a).

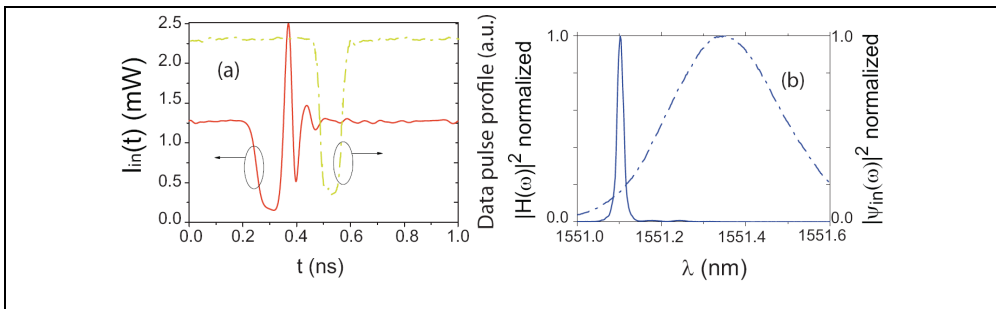


Fig. 9. (a) Intensity laser profile (red solid line) and electrical data signal (green dashed line). The temporal scale has a different origin for the electrical and optical signals. (b) Normalized spectrum of laser pulse (solid line) and amplitude filter (dotted line).

In order to verify the usefulness of this method we performed an additional experiment for propagating the signal through an optical fiber link. For this evaluation, the signal needed to be amplified after optical filtering and the O/E converter was placed at the receiver. As indicated in Fig. 8(b), the fiber link is comprised of two stages. We first propagated the signal through two SMF coils of 44km length each. Then the optical signal was further amplified and propagated through 30 km of NZDSF as well as 13km of DCF, matched to compensate for the dispersion introduced by the SMF in the first stage. This constitutes a total optical link length of 118 km, which represents the largest distance ever reported for UWB signal distribution, to the best of our knowledge. The output optical pulse is detected with the 10GHz bandwidth photodiode and measured simultaneously in the time domain with a sampling oscilloscope, and in frequency domain with an ESA with 1MHz measurement resolution. The achieved signal is displayed in Figs. 10(b) and (c). It possesses a central frequency of 7 GHz and has a 10 dB bandwidth of 10.2 GHz, hence a fractional bandwidth of 146 %. The pulse duration was measured to be 236 ps. Comparison of Figs. 10(a) and (b) indicates that there is no significant distortion of the UWB pulse during propagation. The spikes in Fig. 10c are due to the fact that we introduced a data sequence of one "1" followed by sixteen "0", so that the RF spectrum of a single UWB pulse is conveniently sampled at 0.78 GHz for illustration purposes. We achieved higher data

transmission rates with this optical pulse shape, up to a soft limit related to the output UWB pulse duration. We have successfully transmitted similar pulses at 3.12 GHz over this fiber link.

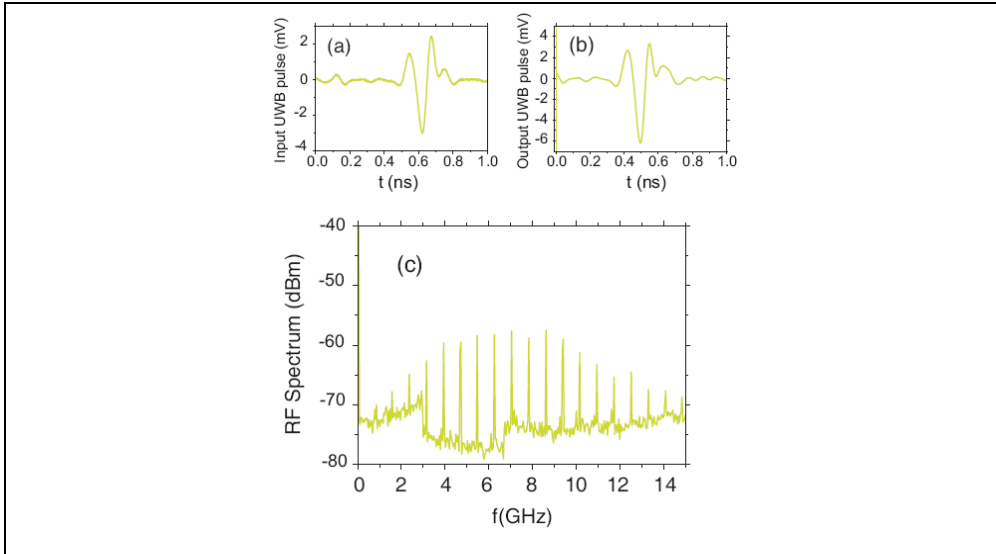


Fig. 10. Generated UWB doublet in (a) time domain before transmission; (b) after propagation in the 118 km fiber link and (c) spectral domain.

4. Current trends in photonically assisted UWB-over-fiber

4.1 Advanced modulation formats

Most of the discussion carried out through the Chapter has dealt with the generation of direct sequence (DS) UWB impulses assuming an ON-OFF keying modulation format. However, different modulation schemes such as pulse-position-modulation, pulse-polarity modulation, orthogonal pulse modulation or amplitude pulse modulation are being investigated. For instance, DS code division multiple access (DS-CDMA) is a widespread technique in multiple-user wireless communications. In this direction, several photonic approaches for bi-phase coded UWB impulse generation exist. We mention, for example, the use of phase-to-amplitude conversion in multichannel fiber gratings (Dai and Yao, 2008); a spectral filter in a Sagnac loop (Li et al., 2007); or polarization modulation (Ou et al., 2008). A recent solution based on a higher-order multi-tap reconfigurable microwave photonic filter features most of the previous modulation formats in a single platform (Bolea et al., 2009).

Another approach worth mentioning is the generation of direct-sequence binary phase shift keying (DS-BPSK) modulated UWB signals based on the overshooting effect in a distributed feedback (DFB) laser (Yu et al., 2009). The experimental setup is shown in Fig. 11. A continuous wave (CW) laser modulated by a 12.5 Gb/s Mach-Zehnder modulator (MZM) is injected into the first-order lasing side mode of a DFB laser biased close to the threshold. As a consequence of this, the DFB laser experiences cross-gain modulation along with associated overshooting relaxation oscillations. The effect is similar to that described in

section 3.2, the difference being that the DFB laser is not directly modulated, but instead undergoes indirect optical cross-gain modulation. No optical pulse shaper is required, making this UWB generation technique particularly simple and attractive.

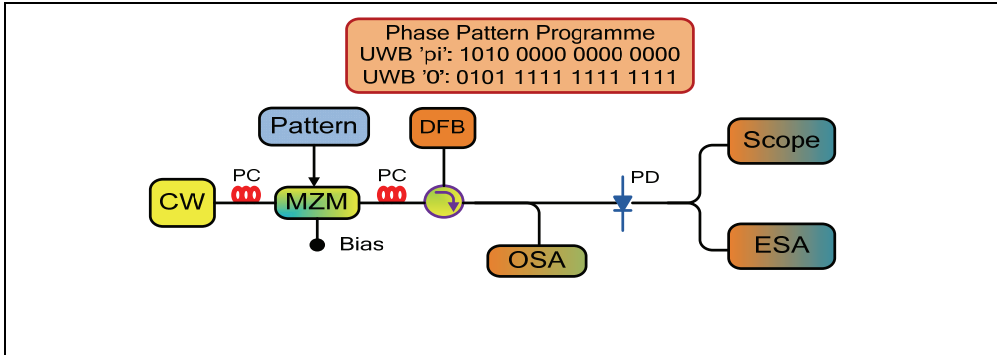


Fig. 11. The schematic configuration for generation of BPSK modulated UWB pulses. CW: continuous-wave laser, MZM: Mach-Zehnder modulator, PC: polarization controller, DFB: distributed feedback laser, OSA: optical spectrum analyzer, PD: photodiode, ESA: electrical spectrum analyzer.

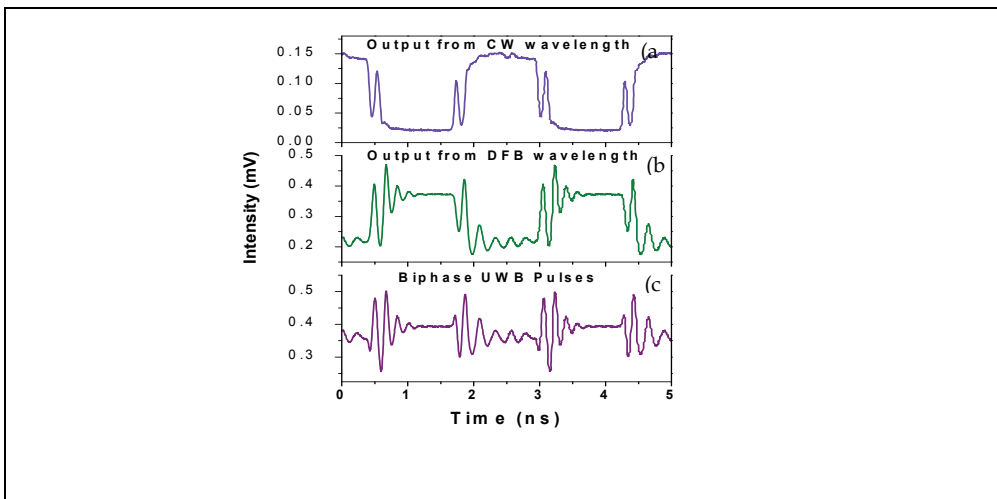


Fig. 12. (a) the output pattern from CW wavelength, (b) the output pattern from DFB wavelength, (c) the calculated biphase UWB pulses from summation of (a) and (b).

At the output of the circulator an UWB pulse is formed from the incoherent summation of the CW and DFB wavelengths. This is shown in Fig. 12, where Fig. 12(a) is the measured output pattern from CW wavelength, (b) is the measured output pattern from DFB wavelength, and (c) is the calculated biphase UWB pulses calculated from the summation of the measured signals of (a) and (b). Assuming the phase of the pulse generated by the 12.5 Gbit/s pattern '1010 0000 0000 0000' is π , and the phase of the pulse generated by

pattern '0101 1111 1111 1111' is 0, then it is evident from that binary phase shift keying coded pulses are generated.

Figure 13 shows the experimentally generated 781.25 Mb/s UWB signals in the time and frequency domains for the bit sequence 0 π 0 π . The electrical spectrum shows good compliance with the FCC mask. Use of externally injected DFB lasers is not limited to the generation of DS-BPSK UWB signals and has also been used for OOK UWB signals as well (Gibbon et al., 2009).

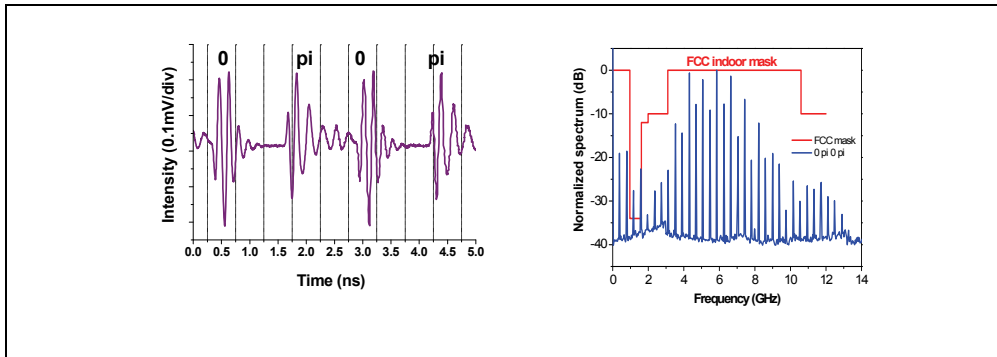


Fig. 13. The generated BPSK coded pulses in the time and frequency domains by using the pattern sequence 0 π 0 π .

4.2 UWB pulse shapes “on demand” and antenna distortion compensation

UWB is a wireless communication technology. Most of the previous approaches for photonic generation of UWB impulses assume that the photodetected signal is going to be transferred into the antenna without any significant degradation. However, as recently realized by several groups, this is not the case (McKinney et al., 2008; Abtahi et al., 2008b). The reason is that most UWB antennas do not have a perfect flat response into the UWB region specified by the FCC regulations. Besides, the wireless transmission and the receiver antenna also introduce appreciable changes in the phase and amplitude of the spectrum of the UWB signal. Therefore, the pulse measured at the photodiode is usually significantly different to the one measured at the receiver, thus limiting the range, speed and capabilities of the technology. However, most of these distortions are linear and can be compensated for by synthesizing a predistorted pulse (McKinney and Weiner, 2006; Abtahi et al., 2008b) or by post-compensating the pulse (Hamidi and Weiner, 2009), so that the received signal is a truly UWB impulse waveform.

To this aim, optical pulse shaping technology using either spatial light modulators or fiber Bragg gratings and the frequency-to-time mapping effect has been employed. This constitutes an excellent example of the capabilities of photonic approaches to overcome some of the problems that current electronics-based technology suffers.

4.3 Range extension of high bit rate UWB signals

The users' increasing demands on broadband and seamless services require that cellular voice and multimedia services are always available everywhere. Therefore, a system high bit

rate and long reach distance is highly desired for next generation networks to meet this requirement. In this case, the generation of high speed UWB signals and its range extension become more and more attractive. However, the communication range of UWB technology is limited due to the FCC mask and emission power level constraints. This becomes more critical as the data rate increases. Basically, the higher the data rate, the lower is the range. This provides a big challenge. Recently, a 500Mb/s UWB signal transmission over 65cm wireless distance has been demonstrated (Abtahi et al., 2008b), and a research group in Singapore demonstrated an experiment with 500 Mbps data rate wireless UWB transmission over 4m in 2003 (Peng et al., 2005).

Digital signal processing (DSP) technology has the well-known advantages of good noise tolerance, high sensitivity and high flexibility. DSP based receivers are expected to improve the wireless propagation performance and subsequently extend the range, which is an important feature to further enhance the usefulness of UWB based high-rate products.

5. Conclusions

UWB-over-fiber is an emerging research field offering an increased range of operation for this high-rate wireless technology. We have focused on simple photonic solutions based on semiconductor laser dynamics to generate UWB electrical impulses. In particular, we have demonstrated that monocycle and doublet impulses can be generated based on the chirping and overshooting effects, respectively. As basic equipment, we have used directly modulated laser and optical band-pass filtering with a Gaussian spectral profile. Although our approach constitutes a very simple solution, the price to pay is the low flexibility in the design of the pulse shape and the absence of reconfigurability capabilities. We have pointed out alternative solutions that feature different modulation formats and shapes, as well as reviewed some exciting possibilities enabled by photonic approaches.

6. Acknowledgments

This work has been partially funded by the Spanish Ministry of Science and Innovation (MCINN, research project FIS2007-62217) and the Convenio Universitat Jaume I-Fundació Caixa Castelló (project P1 1B2007-09). Victor Torres acknowledges the MCINN and Spanish Foundation for Science and Technology for a postdoctoral Fellowship. Timothy Gibbon acknowledges the Villum Kann Rasmussen Fonden for a postdoctoral Grant.

7. References

- Abtahi M.; Mirshafiei M.; Magné J.; Rusch L. A. & LaRochelle S. (2008). Ultra-wideband waveform generator based on optical pulse shaping and FBG tuning. *IEEE Photon. Technol. Lett.*, Vol. 20, No. 2, 135-137.
- Abtahi M.; Mirshafiei M.; LaRochelle S. & Rusch L. A. (2008). All-optical 500Mb/s UWB transceiver: an experimental demonstration. *J. Lightwave Technol.*, Vol. 26, No. 13, 2795-2802.
- Agrawal G. P. (2002). *Fiber-Optics Communication Systems*, John Wiley & sons, New York.

- Bolea M.; Mora J.; Ortega B. & Capmany J. (2009). Optical UWB pulse generator using an N tap microwave photonic filter and phase inversion adaptable to different pulse modulation formats. *Opt. Express*, Vol. 17, No. 7, 5023-5032.
- Capmany J.; Pastor D.; Martínez A.; Ortega B. & Sales S. (2003). Microwave photonic filters with negative coefficients based on phase inversion in an electro-optic modulator. *Opt. Lett.*, Vol. 28, No. 16, 1415-1417.
- Capmany J. & Novak D. (2007). Microwave photonics combines two worlds. *Nature Photon.*, Vol. 1, No. 6, 319-330.
- Capmany J.; Ortega B.; Pastor D. & Sales S. (2005). Discrete-time optical processing of microwave signals. *J. Lightwave Technol.*, Vol. 23, No. 2, 702-723.
- Chou J.; Han Y. & Jalali B. (2003). Adaptive RF- photonic arbitrary waveform generator. *IEEE Photon. Technol. Lett.*, Vol. 15, No. 4, 581-583.
- Coppinger F.; Yegnanarayanan S.; Trinh P. D. & Jalali B. (1997). All-optical incoherent negative taps for photonic signal processing. *Electron. Lett.*, Vol. 33, No. 11, 973-975.
- Dai Y. & Yao J. P. (2008). Optical generation of binary phase-coded direct-sequence UWB signals using a multichannel chirped fiber Bragg grating. *J. Lightwave Technol.*, Vol. 26, No. 15, 2513-2520.
- Di Benedetto M. -G.; Kaiser T.; Molish A. F.; Oppermann I. & Politano, C. (2006). *UWB Communication Systems: A Comprehensive Overview*, Hindawi Publishing, ISBN, New York.
- Dong J; Zhang X; Xu J.; Huang D.; Fu S. & Shum P. (2007). Ultrawideband monocycle generation using cross-phase modulation in a semiconductor optical amplifier. *Opt. Lett.*, Vol. 32, No. 10, 1223-1225.
- Dorrer C. (2005). Characterization of nonlinear phase shifts by use of the transport-of-intensity equation. *Opt. Lett.*, Vol. 30, No. 23, 3237-3239.
- Fetterman H. R.; Tannenwald P. E.; Parker C. D.; Melngailis J. & Williamson R. C. (1979). Real-time spectral analysis of far-infrared laser pulses using a SAW dispersive delay line. *Appl Phys. Lett.*, Vol. 34, No. 2, 123-125.
- Gibbon T. B.; Yu X; Zibar D. & Tafur Monroy I. (2009). Novel ultra-wideband photonic signal generation and transmission featuring digital signal processing bit error rate measurements. *OFC/NFOEC2009 Conference Proceedings*, California, USA, Paper: OTuB8.
- Hamidi E & Weiner A. M. (2009). Post-compensation of ultra-wideband antenna dispersion using microwave photonic phase filters and its applications to UWB systems. *IEEE Trans. Microw. Theory Techn.*, Vol. 57, No. 4, 890-898.
- Li J.; Xu K.; Fu S.; Wu J.; Lin J.; Tang M. & Shum P. (2007). Ultra-wideband pulse generation with flexible pulse shape and polarity control using a Sagnac interferometer-based intensity modulator. *Opt. Express*, Vol. 15, No. 26, 18156-18161.
- Li J.; Fu S.; Xu K.; Lin J.; Tang M. & Shum P. (2008). Photonic ultrawideband monocycle pulse generation using a single electro-optic modulator. *Opt. Lett.*, Vol. 33, No. 3, 288-290.
- Lin I. S.; McKinney J. D. & Weiner A. M. (2005). Photonic synthesis of broadband microwave arbitrary waveforms applicable to ultra-wideband communication. *IEEE Microw. Wireless Compon. Lett.*, Vol. 15, No. 4, 226-228.

- Lin W. P. & Chen Y. C. (2006). Design of a new optical impulse radio system for ultra-wideband wireless communications. *IEEE J. Sel. Top. Quantum Electron.*, Vol. 12, No. 4, 882-887.
- Mandel L. (1974). Interpretation of instantaneous frequencies. *Am. J. Phys.*, Vol. 42, No. 10, 840-846.
- McKinney J. D. & Weiner A. M. (2006). Compensation of the effects of antenna dispersion on UWB waveforms via optical pulse-shaping techniques. *IEEE Trans. Microw. Theory Techn.*, Vol. 54, No. 4, 1681-1682.
- McKinney J. D.; Lin I. S. & Weiner A. M. (2006). Shaping the power spectrum of ultra-wideband radio-frequency signals. *IEEE Trans. Microw. Theory Techn.*, Vol. 54, No. 12, 4247-4255.
- McKinney J. D.; Peroulis D. & Weiner A. M. (2008). Time-domain measurements of the frequency delay of broadband antennas. *IEEE Trans. Ant. Prop.*, Vol. 56, No. 1, 39-47.
- Minasian R. A. (2006). Photonic signal processing of microwave signals. *IEEE Trans. Microw. Theory Techn.*, Vol. 54, No. 2, 832-846.
- Muriel M. A.; Azaña J. & Carballar A. (1999). Real-time Fourier transformer based on fiber Bragg gratings. *Opt. Lett.*, Vol. 24, No. 1, 1-3.
- Nakazawa M.; Suzuki K. & Kimura Y. (1990). Transform-limited pulse generation in the gigahertz region from a gain-switched distributed-feedback laser diode using spectral windowing. *Opt. Lett.*, Vol. 15, No. 12, 715-717.
- Niemi T.; Zhang J. G. & Ludvigsen H. (2001). Effect of filtering on pulses generated with a gain-switched DFB laser. *Opt. Commun.*, Vol. 192, No. 3, 339-345.
- Ou P.; Zhang Y. & Zhang C.-H. (2008). Optical generation of binary phase-coded direct-sequence ultra-wideband signals by polarization modulation and FBG-based multi-channel frequency discriminator. *Opt Express*, Vol. 16, No. 7, 5130-5135.
- Peng X.; Png K. B.; Srivastava V. & Chin F. (2005) High Rate UWB Transmission with Range Extension, IEEE ICU 2005, Switzerland, (Invited paper).
- Porcine D.; Research P. & Hirt W. (2003). Ultra-wideband radio technology: potential and challenges ahead. *IEEE Commun. Mag.*, Vol. 41, No. 7, 66-74.
- Tong Y. C.; Chan L. Y. & Tsang H. K. (1997) Fiber dispersion or pulse spectrum measurement using a sampling oscilloscope. *Electron. Lett.* Vol. 33, No. 11, 823-825.
- Torres-Company V.; Lancis J. & Andrés P. (2007) Incoherent frequency-to-time mapping: application to incoherent pulse shaping. *J. Opt. Soc. Am. A.* Vol. 24, No. 3, 888-894.
- Torres-Company V.; Lancis J.; Andrés P. & Chen L. R. (2008) Reconfigurable RF-waveform generation based on incoherent filter design. *J. Lightwave Technol.* Vol. 26, No. 15, 2476-2483.
- Torres-Company V.; Prince K. & Monroy I. T. (2008b) Fiber transmission and generation of ultrawideband pulses by direct current modulation in semiconductor lasers and chirp-to-intensity conversion. *Opt. Lett.* Vol. 33, No. 3, 222-224.
- Torres-Company V.; Prince K. & Monroy I. T. (2008c) Ultrawideband pulse generation based on overshooting effect in gain-switched semiconductor laser. *IEEE Photon. Technol. Lett.* Vol. 20, No. 13, 1299-1301.
- Vidal B.; Corral J. L. & Martí J. (2005) All-optical WDM microwave filter with negative coefficients. *IEEE Photon. Technol. Lett.* Vol. 17, No. 3, 666-668.

- Wang Q.; Zeng F.; Blais S. & Yao J. P. (2006) Optical UWB monocycle pulse generation based on cross-gain modulation in a semiconductor optical amplifier. *Opt. Lett.* Vol. 31, No. 21, 3083-3086.
- Wang C.; Zeng F. & Yao J. P. (2007) All-fiber ultrawideband pulse generation based on spectral shaping and dispersion-induced frequency-to-time mapping. *IEEE Photon. Technol. Lett.* Vol. 19, No. 3, 137-139.
- Wang J.; Sun Q.; Sun J. & Zhang W. (2009) All-optical UWB pulse generation using sum-frequency generation in a PPLN waveguide. *Opt. Express* Vol. 17, No. 5, 3521-3530.
- Yao J. P. (2007) Photonic generation of ultrawideband signals. *J. Lightwave Technol.* Vol. 25, No. 11, 3219-3235.
- Yao J. P. & Wang Q. (2007) Photonic microwave bandpass filter with negative coefficients using a polarization modulator. *IEEE Photon. Technol. Lett.* Vol. 19, No. 9, 644-646.
- You N. S. & Minasian R. A. (2004) All-optical photonic signal processors with negative coefficients. *J. Lightwave Technol.* Vol. 22, No. 12, 2739-2742.
- Yu X; Gibbon T. B.; Zibar D. & Tafur Monroy I. (2009). A novel incoherent scheme for photonic generation of biphasic modulated UWB signals. *OFC/NFOEC2009 Conference Proceedings*, California, USA, Paper: JWA60.
- Zeng F.; Wang Q. & Yao J. P. (2007) All-optical UWB impulse generation based on cross-phase modulation and frequency discrimination. *Electron. Lett.* Vol. 43, No. 2, 121-122.

All Optical Generation and Processing of IR UWB Signals

Y. Ben Ezra, B.I. Lembrikov, M. Ran and M. Haridim
*Holon Institute of Technology (HIT),
 P.O.Box 305, 58102, 52 Golomb Str., Holon
 Israel*

1. Introduction

1.1 Impulse Radio (IR) Ultra Wideband (UWB) Communications

Ultra wideband (UWB) communication is a fast emerging technology that offers new opportunities such as high data rates, low equipment cost, low power, precise positioning capability and extremely low interference Ghawami (2005). A wide range of possible UWB communication system applications includes radars due to UWB ultra high precision ranging at the centimeter level, wireless personal area networks (WPAN), sensor networks, imaging systems, UWB positioning systems, etc. Yang (2004), Kshetrimayum (2009). From a commercial point of view, the high data rates are the most attractive feature of UWB systems for which speeds of over 100Mb/s have been demonstrated Ghawami (2005). There exist three main types of UWB technologies: impulse radio (IR UWB), direct sequence (DS UWB), and multi-band orthogonal frequency division multiplexing (MB OFDM) Ran (2009). IR UWB communication technique is essentially different from all other communication techniques because it is carrier free and uses for communication between transmitters and receivers very narrow radio frequency (RF) pulses generated from the UWB pulse generator, while traditional transmission systems transmit information by varying the power, frequency, and/or phase of a sinusoidal wave in a modulation process Kshetrimayum (2009), Yao (2007). Consequently, complicated frequency mixers and local oscillators for carrier frequency up and down conversion are not necessary Yao (2007). IR UWB modulation techniques are especially important because the UWB spectrum has been made available by the Federal Communication Commission (FCC) and it can be used with IRs developed to date Lin (2005).

Waveforms for IR UWB are designed to obtain a flat frequency response over the bandwidth of the pulse and to avoid a DC component. The large spectrum of a UWB signal may interfere with existing users. In order to keep this interference to the minimum, FCC specifies spectral masks for different applications, i.e. the allowed power output for specific frequencies Ghawami (2005). A contiguous bandwidth of 7.5GHz is available in the frequency interval of (3.1 – 10.6) GHz at a maximum power output of $-41.3dBm/MHz$ which is considered as extremely low Ghawami (2005). The power spectral density (PSD) of UWB systems defined as a ratio of the transmitted power P in watts and a signal bandwidth B in hertz is extremely low as compared to other communication systems due to the very wide bandwidth B of short pulses that are typically of nanosecond or picosecond order Ghawami (2005). The selection of the impulse signal type for IR UWB communication system is essential since it determines

the system performance Yao (2007). The fast switching in UWB systems results in a non-rectangular pulse shape which can be approximated by a zero-mean Gauss function $G(x)$ with a standard deviation σ Ghawami (2005)

$$G(x) = \frac{1}{\sqrt{2\pi\sigma^2}} \exp\left(-\frac{x^2}{2\sigma^2}\right) \quad (1)$$

A whole class of waveforms are called Gaussian waveforms due to their similarity to the Gauss function (1). The basis of these Gaussian waveforms is a Gaussian pulse given by Ghawami (2005)

$$y_{g1} = K_1 \exp\left(-\frac{t^2}{\tau^2}\right) \quad (2)$$

where $-\infty < t < \infty$, τ is the time-scaling factor, and K_1 is a constant. A Gaussian monocycle y_{g2} and a Gaussian doublet y_{g3} are given by the first and the second derivative of a Gaussian pulse, respectively Ghawami (2005)

$$y_{g2} = K_2 \left(-\frac{2t}{\tau^2}\right) \exp\left(-\frac{t^2}{\tau^2}\right); y_{g3} = K_3 \left(-\frac{2}{\tau^2}\right) \left(1 - \frac{2t^2}{\tau^2}\right) \exp\left(-\frac{t^2}{\tau^2}\right) \quad (3)$$

For the energies $E_{1,2,3}$ of the Gaussian pulses y_{g1} , y_{g2} , y_{g3} , the normalization constants $K_{1,2,3}$ can be evaluated as follows.

$$K_1 = \sqrt{\frac{E_1}{\tau\sqrt{\pi/2}}}; K_2 = \sqrt{\frac{\tau E_2}{\sqrt{\pi/2}}}; K_3 = \tau \sqrt{\frac{\tau E_3}{3\sqrt{\pi/2}}} \quad (4)$$

The spectra of the Gaussian pulses (2), (3) determined by their Fourier transforms $Y_{g1}(f)$, $Y_{g2}(f)$, $Y_{g3}(f)$, respectively, have the form Ghawami (2005)

$$Y_{g1}(f) = K_1 \tau \sqrt{\pi} \exp\left[-(\pi\tau f)^2\right] \quad (5)$$

$$Y_{g2}(f) = K_2 \tau \sqrt{\pi} (j2\pi f) \exp\left[-(\pi\tau f)^2\right] \quad (6)$$

$$Y_{g3}(f) = -K_3 (2\pi f)^2 \exp\left[-(\pi\tau f)^2\right] \quad (7)$$

Gaussian pulses are the most widely used waveforms due to their simplicity and achievability Yao (2007). The important property of the Gaussian pulses (2), (3) is that they are almost uniformly distributed over their frequency spectrum Ghawami (2005). UWB waveform can be generated by passing a Gaussian pulse through a bandpass filter acting similar to a first- or second-order differentiator Ghawami (2005), Yao (2007). However, it is difficult and expensive to generate such pulses with a fractional bandwidth greater than 100% at the central frequency of about 7GHz Yao (2007).

The current high data rate UWB systems are inherently limited to short-ranges of less than 10m due the constraints on allowed emission levels Yao (2007), Ran (2009). The transmission of high data rate UWB signals over larger distances of about 10 – 10000m is needed for broadband access technology. In order to increase the IR UWB transmission distances, a new concept combining the high data rate wireless short-range communications based on UWB technologies and the optical fiber technology has been proposed Ran (2009). This concept is called UWB radio over optical fibre (UROOF) Ran (2009). In this approach, the IR UWB signals of several GHz are superimposed on the optical continuous wave (CW) carrier and

transmitted transparently over an optical fiber Ran (2009), Yao (2007). The UROOF technology permits to avoid the high cost additional electronic components required for signal processing and makes it possible the integration of all the RF and optical transmitter/receiver components on a single chip. The overall combination of these features results in a cost-effective broadband system that can easily support 1Gb/s suitable for WPAN applications Ran (2009). Previously, most of the approaches to generating of IR UWB signals were based on electronic methods Wang (2006). UWB pulses can be generated electrically using electronic circuits such as a microwave ring filter, a microwave resonator-based bandpass filter, or a microwave differentiator Yao (2007). However, in order to distribute UWB signals over the optical fiber, it is desirable to generate these signals directly in the optical domain without extra electrical-to-optical (E/O) conversion Yao (2007). Recently, optically based methods of the Gaussian IR UWB monocycles and doublets generation for low-cost high-data rate UWB wireless systems have been proposed Lin (2005), Le Guennec (2007), Yao (2007), Zeng (April 2006), Zeng (October 2006), Zeng (2007). The advantages of these methods are following: the decreasing of interference between electrical devices, low loss and light weight of optical fibers Lin (2005), Yao (2007), Wang (2006). Below, in section 1.2, we consider the existing techniques of all-optical IR UWB generation.

1.2 Optical Techniques of IR UWB Generation

Optical IR UWB generation techniques are divided into 3 groups Yao (2007)

1. UWB pulse generation based on phase-modulation-to-intensity-modulation (PM-IM) conversion.
2. UWB pulse generation based on a photonic microwave delay line where the cross gain modulation (XGM) in a semiconductor optical amplifier (SOA) is used.
3. UWB pulse generation based on optical spectral shaping and dispersion-induced frequency-to-time mapping.

All these techniques can be implemented using fiber optic components such as an electro-optic phase modulator (EOM), a singlemode fiber (SMF), Erbium doped fiber amplifier (EDFA), a fiber Bragg grating (FBG) and a photodetector (PD) which provide the potential for integration based on integrated photonic circuits Yao (2007), Wang (2006), Zeng (April 2006), Zeng (October 2006). It should be noted that PM-IM conversion techniques are simpler than the techniques related to groups 2 and 3 while the approach based on the group 3 techniques has more flexibility in generating UWB pulses with arbitrary shapes Yao (2007). Recently novel UWB pulse generation techniques have been developed where UWB pulses were directly generated in the optical domain and distributed over optical fiber without the need for an extra E/O conversion Yao (2007).

In this work, we concentrate on the all-optical methods of UWB pulse generation based on nonlinear optical processes in SOA such as cross phase modulation (XPM) and XGM. Consider first the method based on XPM. The experimental setup for all-optical UWB doublet generation is shown in Fig. 1 Dong (2009). A probe CW signal is generated by CW laser diode at the wavelength $\lambda = 1550.56\text{nm}$ with a 1mW output power. A tunable laser emits CW light at $\lambda = 1558.7\text{nm}$ modulated by the Mach-Zehnder modulator (MZM) in order to form optical Gaussian pulses of the type (2). The bit pattern generator (BPG) drives the MZM at a repetition rate of 20Gb/s with a fixed pattern equivalent to a Gaussian pulse train $P_s(t)$ with a

repetition rate of 1.25GHz given by Dong (2009)

$$P_s(t) = \sum_{n=-\infty}^{\infty} \Omega(t - nT_r) \quad (8)$$

where $\Omega(t)$ is an ideal Gaussian waveform of the type (2) with a duty cycle of about 1/16 and full width at half maximum (FWHM) of about 50ps, and T_r is the pulse repetition interval. When the Gaussian pulses (8) and the probe signal are simultaneously fed into SOA, the probe signal will undergo both XGM and XPM, and the phase Φ_c is varying approximately proportionally to $P_s(t)$ Dong (2009)

$$\Phi_c = KP_s(t) + \Phi_0 \quad (9)$$

where K is the proportionality constant and Φ_0 is the initial phase. The chirp $\Delta\nu_c(t)$ of the probe signal is the first order derivative of the phase given by Dong (2009)

$$\Delta\nu_c(t) = -\frac{1}{2\pi} \frac{d\Phi_c}{dt} = -\frac{K}{2\pi} \frac{dP_s(t)}{dt} \quad (10)$$

The chirp (10) is a monocycle, according to definition (3). Its positive or negative value corresponds to blue or red shift of the probe wavelength, respectively Dong (2009). The SOA is followed by Gaussian optical blue shifted optical bandpass filter (OBF) and red shifted OBF forming the two polarity-reversed monocycle pulses with an opposite detuning to the probe carrier λ_c . Then, UWB doublet pulses can be obtained by combining the positive and negative monocycles with a proper delay Dong (2009). EDFA is necessary to amplify the output optical signal power due to large loss of OBFs, and OBF at the output with 1nm bandwidth is used in order to suppress the amplified spontaneous emission (ASE) noise Dong (2009).

The necessity of OBFs and EDFA makes the UWB pulse generation system based on XPM a costly one Dong (2009). Two polarity-reversed pulses can be obtained with a pump-probe scheme based on XGM in SOA where the time delay between the pump and probe waves is appropriately chosen. The experimental setup for the realization of such a scheme is shown in Fig. 2 Dong (2009). A CW probe light at λ_c and an optical Gaussian pulse train (8) at the wavelength λ_s are emitted by a CW laser diode and a tunable laser externally modulated by MZM, respectively, and launched into the SOA simultaneously. Two attenuators (ATIs) are used for the SOA input power adjustment. The CW probe signal obtains an inverted Gaussian shape due to XGM in the SOA. The peak of the Gaussian pulse and the pit of the probe signal at the SOA output are misaligned due to the non-uniform amplification which results in a monocycle shape without optical filter and time delay Dong (2009). A SMF section of 2.5 km serves as a dispersion medium in order to induce a group delay between the optical Gaussian pulse and the inverted probe light. Both positive and negative monocycle pulses can be obtained depending on the SMF group delay Dong (2009).

All-optical UWB pulse generation based on a hybrid of self phase modulation (SPM) and XGM, has also been demonstrated where the monocycle pulse is generated from a dark return-to-zero (RZ) signal and converted to a doublet pulse by injecting an additional probe signal with the SMF transmission Dong (2009).

An alternative approach based on optical cross polarization modulation has been recently proposed and demonstrated Chen (2008). Optical signal is cross-polarized modulated with simple electric pulses. An electrical pulse is used to drive an optical phase modulator (PM) where the phase shift between the two optical axes depends on the drive voltage V . If the

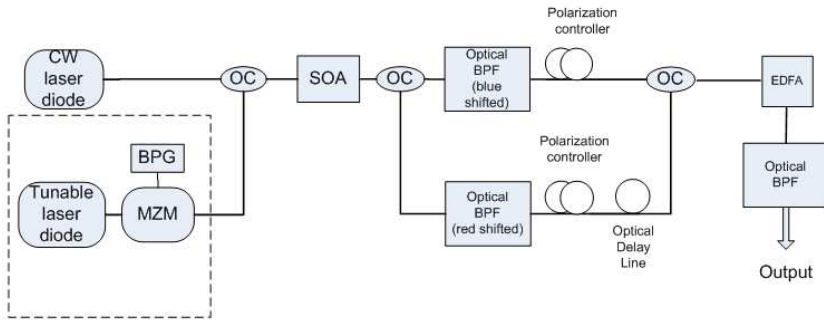


Fig. 1. Experimental setup for all-optical UWB generation based on XPM scheme (BPG: bit pattern generator; OC: optical coupler; MZM: Mach-Zehnder modulator; OBF: optical band-pass filter; ODL: optical delay line; PC: polarization controller)

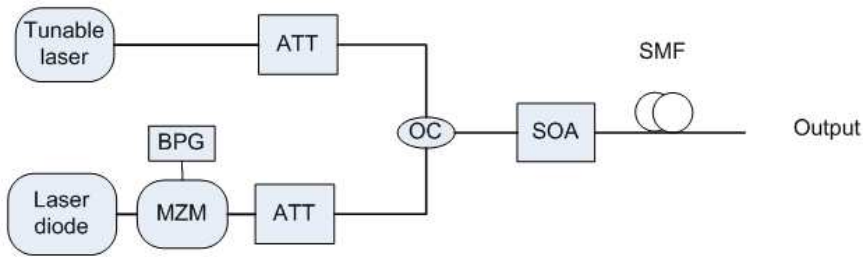


Fig. 2. Experimental setup for filter-free UWB generation based on XGM scheme (ATT: attenuator; SMF: single mode fiber; other abbreviations are similar to 1)

voltage $V = V_{\pi}$, then the polarization will rotate to the orthogonal direction at the output of PM. As a result, at the original input orientation there exists simultaneously a negative pulse. This process is called cross-polarization modulation (CPM) Chen (2008). Then, the monocycle pulses are obtained after a proper birefringence time delay and optical-to-electrical (O/E) conversion, and doublet pulses are obtained by using gain saturation and recovery processes in SOA Chen (2008).

The shortages of the proposed methods are the necessity of the sophisticated circuit for the generation of short electric Gaussian pulses, the use of EOM, and the need for a comparatively long SMF. Bulk SOAs are characterized by a comparatively low operation rate and high bias currents.

We proposed a theoretical analysis of a novel all-optical method of the IR UWB pulse generation in an integrated Mach-Zehnder interferometer (MZI) with quantum dot semiconductor optical amplifier (QD SOA) as an active element inserted into one arm of the integrated MZI which results in an intensity dependent optical signal interference at the output of MZI Ben Ezra (2008). The IR UWB pulse generation process is based both on XPM and on XGM in QD SOA characterized by an extremely high optical nonlinearity, low bias currents, and high operation rate Sugawara (2004). Unlike other proposed all-optical methods, we need not optical fibers, FBG and EOM substantially reducing the cost and complexity of a IR UWB generator. The IR UWB signals generated by the proposed QD SOA based MZI structure have the

form of the Gaussian doublet. The shape of the signal and its spectrum can be tailor-made for different applications by changing the QD SOA bias current and optical power.

Another novel approach of all-optical generation of UWB Gaussian monocycles and doublets is based on the system of two integrated unbalanced Mach-Zehnder Interferometers (MZIs) connected in parallel that does not contain any active elements. The MZIs are chosen in such a way that the phase difference of the interfering signals at the output is equal to π . Each one of the MZI is characterized by time delay differences τ and 2τ . As a result, at the output of the MZIs the interfering optical signals modulated by a Gaussian UWB pulse form the first-order difference approximating the Gaussian monocycle and the second-order difference approximating the Gaussian doublet. At the output of the system the UWB monocycles and doublets can be converted to a UWB signal by means of a homodyne detection where the local oscillator frequency ω_{LO} coincides with the optical carrier frequency ω Agrawal (2002). In such a case the homodyne detected signal is proportional to the UWB modulated optical signal amplitude Agrawal (2002), i.e. to the Gaussian monocycle or doublet in our case. The analysis shows that the performance of the proposed system is stable with respect to reasonable deviations of the MZI arm length and an input coupler ratio. The system can be made tunable by including into MZIs a tunable delay line.

We also discuss an all-optical signal processing based on wavelet transform (WT) applications. We proposed the implementation of the WT analysis for all-optical signal denoising, and all-optical passive generation of a so-called Mexican hat mother wavelet (MHMW) Rao (1998). The chapter is constructed as follows. The original results are presented in sections 2-6. The analysis of all-optical method of the IR UWB pulse generation in an integrated MZI with QD SOA can be divided into three stages. First, in section 2, we discuss the operation principle of unbalanced MZI (UMZI) containing QD SOA as a basic nonlinear component for the proposed scheme of all-optical IR UWB generation. Then, in section 3, ultra-fast nonlinear phenomena in QD SOA and are reviewed. Finally, in section 4, we present the simulation results for the IR UWB pulse generation in an integrated MZI with QD SOA. In sections 5 and 6, we propose a theory of all-optical passive generation of UWB Gaussian monocycles and doublets, all-optical passive generation of MHMW and all-optical signal denoising. The conclusions are presented in section 7.

2. Mach-Zehnder Interferometer (MZI) Containing Nonlinear Elements

There exist both all-fiber MZI Agrawal (2001) and monolithic integrated ones Joergensen (1996). The couplers at the input and output of MZI can have different power-splitting fractions, and two arms of MZI can have different lengths and propagation constants. Typically, in the linear case an input optical signal splits into two parts which acquire different phase if arm lengths are different. In such a case, MZI can be unbalanced since the two optical fields inside MZI have physically separated paths Agrawal (2001). Nonlinear applications of MZIs make use of the SPM- or XPM-induced phase shifts. The nonlinear response of an MZI can be switched from low to high or vice versa by changing the input peak power of the incident signal Agrawal (2001). The successful operation of integrated SOA-MZI structures in an essentially nonlinear regime providing wavelength conversion (WC), all-optical logic gate, and all-optical regeneration due to XGM has been demonstrated experimentally Chen (2002), Joergensen (1996), Kanellos (2007).

We discuss now the operation principle of the MZI containing in one arm a QD SOA as a nonlinear element. The block diagram of the proposed all-optical IR UWB pulse generator

consisting of CW laser, a pulsed laser, and MZI with a QD SOA in its upper arm is shown in Fig. 3 Ben Ezra (2008).

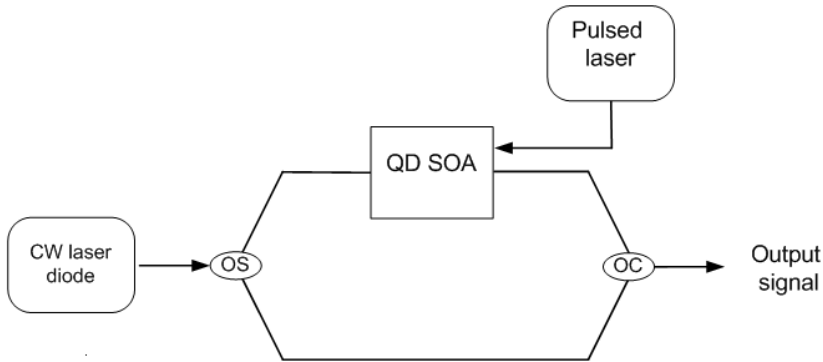


Fig. 3. Block diagram of the proposed IR UWB generator

A CW signal of a wavelength λ and an optical power P_0 is split by an optical splitter (OS) into two signals with equal optical power and fed into the two ports of the integrated MZI one of which contains a QD SOA. In QD SOA XGM gain and XPM phase shift are related due to the linewidth enhancement factor (LEF) α Agrawal (1989). The pulsed laser produces a train of short Gaussian pulses counter-propagating with respect to the input CW optical signal. The CW signal propagating through the upper arm of MZI transforms into the Gaussian pulse at the output of the MZI due to XPM and XGM with the train of Gaussian pulses whereas the optical signal in the linear lower arm of MZI remains CW. Both these pulses interfere at the output of MZI, and the output pulse shape is defined by the power dependent phase difference $\Delta\phi(t) = \phi_1(t) - \phi_2(t)$ where $\phi_{1,2}(t)$ are the phase shifts in the upper and lower arms of MZI, respectively. Evidently, the phase shift in lower arm of MZI is constant: $\phi_2 = \text{const}$. The MZI output optical power P_{out} is given by Wang (2004).

$$P_{out} = \frac{P_0}{4} \left[G_1(t) + G_2(t) - 2\sqrt{G_1(t)G_2(t)} \cos \Delta\phi(t) \right] \quad (11)$$

where $G_{1,2}(t)$ are amplification factors of the upper and lower arms of MZI. The upper arm amplification factor $\exp(g_{sat}L) \leq G_1(t) = \exp(gL) \leq \exp(g_0L)$ defined by the QD SOA gain g and its active region length L is limited by the saturation gain g_{sat} and the maximum modal gain g_0 typical for the linear regime. The linear lower arm amplification factor is simply unity $G_2 = 1$. The losses can be neglected due to a small length of integrated elements. Then the relation between the MZI phase shift and its amplification factor is given by $\Delta\phi(t) = -(\alpha/2) \ln G_1(t)$. The shape of the output pulse is determined by the time dependence of $G_1(t)$ both directly and through $\Delta\phi(t)$ according to equation (11) resulting in a Gaussian doublet under certain conditions determined by the QD SOA dynamics that will be discussed in section 3.

3. Ultra-fast Nonlinear Phenomena in QD SOA

In this section, we will discuss the structure and operation principles of QD SOA. We briefly review the QD specific properties, energy bands, and electron transitions responsible for the stimulated light emission and amplification in subsection 3.1. Theory of QD SOA operation based on the electron rate equations and photon propagation equation has been developed in a large number of works. See, for example, Berg (2004), Qasaimeh (2003), Qasaimeh (2004), Ben Ezra (September 2005), Ben Ezra (October 2005), Ben Ezra (2007) and references therein. It is considered in subsections 3.2 and 3.3.

3.1 Structure and Operation Principles of QD SOA

Quantization of of electron states in all three dimensions results in a creation of a novel physical object - a macroatom, or quantum dot (QD) containing a zero dimensional electron gas. Size quantization is significantly effective when the quantum dot three dimensions are of the same order of magnitude as the electron de Broglie wavelength Ustinov (2003). Detailed theoretical and experimental investigations of InAs/GaAs and InAs QDs electronic structure taking into account their shape (lens-shaped, pyramidal), size, composition profile, and production technique (Stranski-Krastanow, colloidal) have been carried out Bimberg (1999), Bányai (2005), Ustinov (2003). The different types of QDs based on different technologies and operating in different parts of spectrum are known such as In(Ga)As QDs grown on GaAs substrates, InAs QDs grown on InP substrates, and colloidal free-standing InAs QDs. In(Ga)As/GaAs QDs are characterized by emission at wavelengths no longer than $\lambda = 1.35\mu m$, while the InAs/InP structures have been proposed for emission at the usual telecommunication wavelength $\lambda = 1.55\mu m$.

A system of QDs can be approximated with a three energy level model in the conduction band containing a spin degenerate ground state GS, fourfold degenerate excited state (ES) with comparatively large energy separations of about $50 - 70meV$, and a narrow continuum wetting layer (WL). The electron WL is situated $150meV$ above the lowest electron energy level in the conduction band, i.e. GS and has a width of approximately $120meV$. In real cases, the QDs vary in size, shape, and local strain which leads to the fluctuations in the quantized energy levels and the inhomogeneous broadening in the optical transition energy. A Gaussian distribution may be used for the description of the QD sizes, and it shows that the discrete resonances merge into a continuous structure with widths around 10% Bányai (2005). The QDs and WL are surrounded by a barrier material which prevents direct coupling between QD layers. The absolute number of states in the WL is much larger than in the QDs. GS and ES in QDs are characterized by homogeneous and inhomogeneous broadening Bányai (2005). The homogeneous broadening caused by the scattering of the optically generated electrons and holes with imperfections, impurities, phonons, or through the radiative electron-hole pair recombination Bányai (2005) is about $15meV$ at room temperature.

The active region of a QD SOA is a layer including self-assembled InGaAs QDs on a GaAs substrate Sugawara (2004). Typically, the QD density per unit area is about $(10^{10} - 10^{11}) cm^{-2}$. The bias current is injected into the active layer including QDs, and the input optical signals are amplified via the stimulated emission or processed via the optical nonlinearity by QDs Sugawara (2004). The stimulated radiative transitions occur between GS and the valence band of QDs. A detailed theory of QD SOAs based on the density matrix approach has been developed in the pioneering work Sugawara (2004) where the linear and nonlinear optical responses of QD SOAs with arbitrary spectral and spatial distribution of quantum dots in active

region under the multimode light propagation have been considered. It has been shown theoretically that XGM takes place due to the coherent terms under the condition that the mode separation is comparable to or less than the polarization relaxation rate $|\omega_m - \omega_n| \leq \Gamma_g$ where $\omega_{m,n}$ are the mode frequencies and the relaxation time $\tau = \Gamma_g^{-1} = 130fs$ Sugawara (2004). XGM is also possible in the case of the incoherent nonlinear polarization, or the so-called incoherent spectral hole burning Sugawara (2004). It has been assumed that XGM occurred only for signals with a detuning limited by the comparatively small homogeneous broadening, and for this reason the ensemble of QDs should be divided into groups by their resonant frequency of the GS transition between the conduction and valence bands Sugawara (2004).

3.2 Rate Equations and Dynamics of QD SOA

The phenomenological approach to the QD SOA dynamics is based on the rate equations for the electron densities of GS, ES and for combined WL and barrier serving as a reservoir. It is determined by electrons, because of the much larger effective mass of holes and their smaller state spacing Berg (2004). The carrier dynamics is characterized by slow relaxation processes between WL and ES, and the rapidly varying coherent nonlinear population terms vanish after the averaging over the comparatively large relaxation time $\tau_{w2} \sim$ several ps from the two-dimensional WL to the ES. We have taken into account only incoherent population terms because for XGM between modes with the maximum detuning $\Delta\lambda_{\max} = 30nm$ within the especially important in optical communications conventional band (C-band) of $\lambda = (1530 \div 1565)nm$ the condition $\omega_1 - \omega_2 > \Gamma_g^{-1}$ is valid even for the lowest relaxation time from the ES to GS $\tau_{21} = 0.16ps$, and the rapidly varying coherent beating terms are insignificant Sugawara (2004). The direct carrier capture into the GS is neglected due to the fast intradot carrier relaxation and the large energy separation between the GS and the WL and it is assumed that the charge neutrality condition in the GS is valid. The rate equations account for both the fast transitions from WL to ES and GS and the slow dynamics of the spontaneous transitions and electron escape from ES back to WL Qasaimeh (2003), Qasaimeh (2004), Ben Ezra (2007). They have the form Qasaimeh (2003), Qasaimeh (2004), Ben Ezra (2007).

$$\frac{\partial N_w}{\partial t} = \frac{J}{eL_w} - \frac{N_w(1-h)}{\tau_{w2}} + \frac{N_w h}{\tau_{2w}} - \frac{N_w}{\tau_{wR}}, \quad (12)$$

$$\frac{\partial h}{\partial t} = \frac{N_w L_w (1-h)}{N_Q \tau_{w2}} - \frac{N_w L_w h}{N_Q \tau_{2w}} - \frac{(1-f)h}{\tau_{21}} + \frac{f(1-h)}{\tau_{12}}, \quad (13)$$

$$\begin{aligned} \frac{\partial f}{\partial t} &= \frac{(1-f)h}{\tau_{21}} - \frac{f(1-h)}{\tau_{12}} - \frac{f^2}{\tau_{1R}} \\ &- \frac{g_p L}{N_Q} (2f-1) S_p \frac{c}{\sqrt{\epsilon_r}} - \frac{g_s L}{N_Q} (2f-1) S_s \frac{c}{\sqrt{\epsilon_r}}. \end{aligned} \quad (14)$$

Here, S_p, S_s are the CW pump and on-off-keying (OOK) modulated signal wave photon densities, respectively, L is the length of SOA, g_p, g_s are the pump and signal wave modal gains, respectively, f is the electron occupation probability of GS, h is the electron occupation probability of ES, e is the electron charge, t is the time, τ_{2w} is the electron escape time from the ES to the WL, τ_{wR} is the spontaneous radiative lifetime in WL, τ_{1R} is the spontaneous radiative lifetime in QDs, N_Q is the surface density of QDs, N_w is the electron density in the WL, L_w is the effective thickness of the active layer, τ_{21} is the electron relaxation time from the ES to GS and

τ_{12} is the electron relaxation time from the GS to the ES, ϵ_r is the SOA material permittivity, c is the velocity of light in free space. The modal gain $g_{p,s}(\omega)$ is given by Uskov (2004)

$$g_{p,s}(\omega) = \frac{2\Gamma N_Q}{a} \int d\omega F(\omega) \sigma(\omega_0) (2f - 1) \quad (15)$$

where the number l of QD layers is assumed to be $l = 1$, the confinement factor Γ is assumed to be the same for both the signal and the pump waves, a is the mean size of QDs, $\sigma(\omega_0)$ is the cross section of interaction of photons of frequency ω_0 with carriers in QD at the transition frequency ω including the homogeneous broadening factor, $F(\omega)$ is the distribution of the transition frequency in the QD ensemble which is assumed to be Gaussian Qasaimieh (2004), Uskov (2004). It is related to the inhomogeneous broadening and it is described by the expression Uskov (2004)

$$F(\omega) = \frac{1}{\Delta\omega\sqrt{\pi}} \exp\left[-\frac{(\omega - \bar{\omega})^2}{(\Delta\omega)^2}\right] \quad (16)$$

where the parameter $\Delta\omega$ is related to the inhomogeneous linewidth $\gamma_{inhom} = 2\sqrt{\ln 2}\Delta\omega$, and $\bar{\omega}$ is the average transition frequency.

3.3 XGM and XPM in QD SOA

In order to describe adequately XGM and XPM in QD SOA we should take into account the interaction of QDs with optical signals. The optical signal propagation in a QD SOA is described by the following truncated equations for the slowly varying CW and pulse signals photon densities and phases $S_{CW,P} = P_{CW,P} / (\hbar\omega_{CW,P} (v_g)_{CW,P} A_{eff})$ and $\theta_{CW,P}$ Agrawal (1989).

$$\frac{\partial S_{CW,P}(z, \tau)}{\partial z} = (g_{CW,P} - \alpha_{int}) S_{CW,P}(z, \tau) \quad (17)$$

$$\frac{\partial \theta_{CW,P}}{\partial z} = -\frac{\alpha}{2} S_{CW,P} \quad (18)$$

Here $P_{CW,P}$ are the CW and pulse signal optical powers, respectively, A_{eff} is the QD SOA effective cross-section, $\omega_{CW,P}$, $(v_g)_{CW,P}$ are the CW and pulse signal group angular frequencies and velocities, respectively, $g_{CW,P}$ are the active medium (SOA) gains at the corresponding optical frequencies, α_{int} is the absorption coefficient of the SOA material. For the pulse propagation analysis, we replace the variables (z, t) with the retarded frame variables $(z, \tau = t \mp z/v_g)$. For optical pulses with a duration $T \gtrsim 10ps$ the optical radiation of the pulse is filling the entire active region of a QD SOA of the length $L \lesssim 1mm$ and the propagation effects can be neglected Gehrig (2002). Hence, in our case the photon densities

$$S_{CW,P}(z, \tau) = (S_{CW,P}(\tau))_{in} \exp\left[\int_0^z (g_{CW,P} - \alpha_{int}) dz'\right] \quad (19)$$

can be averaged over the QD SOA length L which yields

$$S_{CW,P}(\tau) = \frac{1}{L} (S_{CW,P}(\tau))_{in} \int_0^L dz \exp\left[\int_0^z (g_{CW,P} - \alpha_{int}) dz'\right] \quad (20)$$

Solution of equation (18) yields for the phases which should be inserted into MZI equation (11)

$$\theta_{CW,P}(\tau) = -(\alpha/2) \int_0^L dz g_{CW,P}. \quad (21)$$

The time-dependent variations of the carrier distributions in the QDs and WL result in the strong phase changes (18) during the light propagation in the QD SOA Gehrig (2002). System of equations (12)-(14) with the average pump and signal photon densities (20) and phases (21) constitutes a complete set of equations describing XGM and XPM in QD SOA related by the LEF α as it is seen from equations (17), (18) and (21).

4. Simulation Results for IR UWB Generation in MZI with QD SOA

The analytical solution of nonlinear and extremely complicated equations (12)-(14) in a closed form is hardly possible, and for this reason, the system of these equations has been solved numerically for the following typical values of the QD SOA parameters Ben Ezra (2007), Ben Ezra (2008). The QD SOA active region length L and width W are, respectively, $L = 2mm$, $W = 10\mu m$; the confinement factor $\Gamma = 3 \times 10^{-2}$, the maximum gain $g_{max} = 11.5cm^{-1}$, $\alpha_{int} = 3cm^{-1}$, the fastest relaxation time for the transitions between ES and GS is $\tau_{21} = 0.16ps$, while the largest relaxation time for the transition between ES and WL is about $\tau_{2w} \sim 1ns$. The simulation results for the output power Gaussian doublet and temporal variations of the optical signal power and phase in upper and lower arms of MZI are shown in Fig. 4.

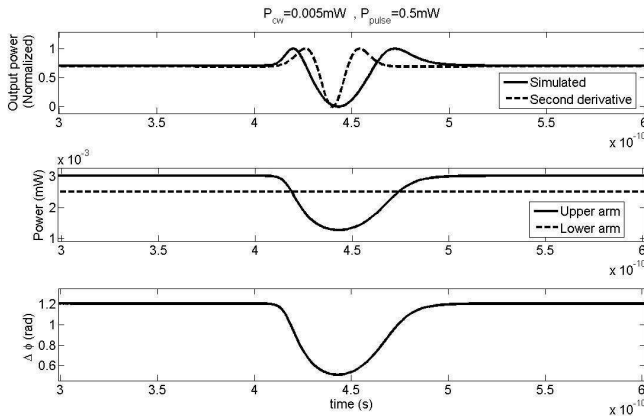


Fig. 4. Gaussian doublet of the output power pulse (solid line) and the second derivative of the Gaussian pulse (dashed line) for the pulsed laser optical power of $P_p = 0.5mW$ (upper box); optical signal power in the upper arm of MZI (middle box); phase difference $\Delta\phi$ (lower box)

At high Gaussian pulse power levels QD SOA passes to the nonlinear saturation regime where the amplification factor $G_1(t)$ and XPM phase shift $\Delta\phi(t)$ decrease to their minimum values. In this case, P_{out} also reaches its lowest level due to the maximum value of the oscillating term in equation (11). In such a case the XPM process is dominant, and the Gaussian doublet occurs as it is seen from Fig.4. The local maxima of the doublet can be explained by the dominant

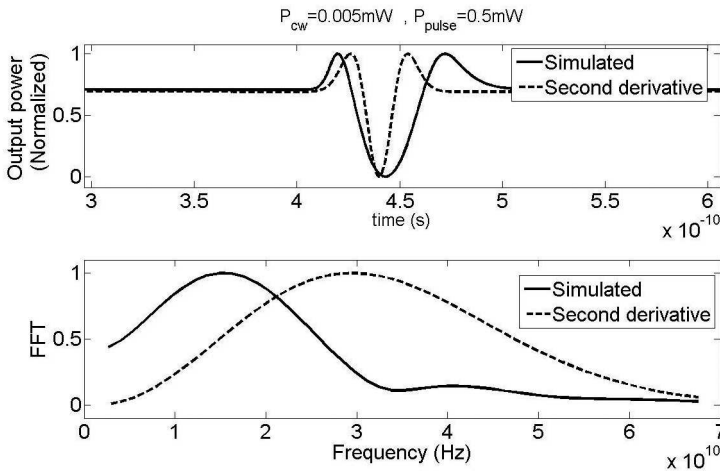


Fig. 5. Simulated Gaussian doublet (solid line) and the second derivative the standard Gaussian pulse (dashed line) (upper box); the spectra (FFTs) of the simulated IR UWB pulse (solid line) and second derivative of the standard Gaussian pulse (dashed line) (lower box)

role of XGM process in the regions of small variations of $\Delta\phi(t)$. In such a case, the variation of the oscillating term in equation (11) is negligible. This term is varying more slowly as compared to $G_1(t)$ because of the logarithmic form of the argument $\Delta\phi(t)$, except for the QD SOA saturation regime where $G_1(t)$ tends to its minimum value.

The simulated IR UWB doublet, second derivative of the standard Gaussian pulse and their fast Fourier transforms (FFTs), i.e. spectra are shown in Fig. 5. The spectrum of the simulated IR UWB signal manifests the filtering features of the proposed IR UWB generator Ghawami (2005). For the Gaussian pulse duration of about tens of picoseconds, the filtering behavior of the proposed IR UWB generator is caused by the fast transition relaxation time between GS and ES $\tau_{12} \sim 1\text{ps}$ in QD SOA limiting a rise time and a fall time of the pulse propagating through QD SOA. The operation rate of QD SOA is also strongly influenced by the SOA bias current and optical power Sugawara (2004), Ben Ezra (2007).

5. All-optical Passive Generation of IR UWB

UWB pulse generation techniques in optical domain discussed above are characterized by complicated and costly systems combining electronic and active nonlinear photonic elements such as SOA which are necessary for mixing and conversion of UWB modulated optical carriers with different optical frequencies. We propose an alternative method of all-optical generation of UWB Gaussian monocycles and doublets based on the system of two integrated unbalanced MZIs (UMZIs) connected in parallel that does not contain any active elements. The UMZIs are chosen in such a way that the phase difference of the interfering signals at the output is equal to π . Each one of the UMZIs is characterized by time delay differences τ and 2τ . As a result, at the output of the UMZIs the interfering optical signals UWB modulated by a Gaussian UWB pulse form the first-order difference approximating the Gaussian monocycle and the second-order difference approximating the Gaussian doublet. At the output of the system the UWB monocycles and doublets can be converted to a UWB signal by means

of a homodyne detection where the local oscillator frequency ω_{LO} coincides with the optical carrier frequency ω Agrawal (2002). In such a case the detected signal is proportional to the UWB modulated optical signal amplitude Agrawal (2002), i.e. to the Gaussian monocycle or doublet in our case. The system can be made tunable by including into UMZIs a tunable delay line.

The block diagram of the UMZIs is shown in Fig. 6. The UWB modulated optical carrier field at the system input is given by

$$E(t) = A(t) \exp[-i(\omega t + \phi)] \quad (22)$$

where $A(t)$ and ϕ are the amplitude and phase of the input signal, respectively. The signal (22) is split in the in the two equal parts at the input of the system, and then the each signal is split equally once more at the input of the both UMZIs. Assuming the delay time τ of the lower arm of the upper UMZI1 and of the upper arm of the lower UMZI2 and the delay time 2τ of the lower arm of the lower UMZI2 we can describe the interfering optical fields as follows.

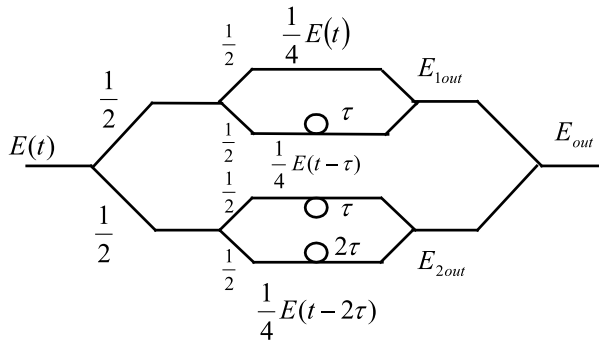


Fig. 6. The UMZIs connected in parallel

$$E_{1,2in} = \frac{1}{2}E(t); E_{1up} = \frac{1}{4}E(t); E_{1low} = \frac{1}{4}E(t - \tau) \quad (23)$$

$$E_{1out} = E_{1up} - E_{1low} = \frac{1}{4}[E(t) - E(t - \tau)] \quad (24)$$

$$E_{2up} = \frac{1}{4}E(t - \tau); E_{2low} = \frac{1}{4}E(t - 2\tau) \quad (25)$$

$$E_{2out} = E_{2up} - E_{2low} = \frac{1}{4}[E(t - \tau) - E(t - 2\tau)] \quad (26)$$

$$E_{out} = E_{1out} - E_{2out} = \frac{1}{4}[E(t) - 2E(t - \tau) + E(t - 2\tau)] \quad (27)$$

Equations (24)-(27) show that the output fields E_{1out} , E_{2out} of the UMZI1 and UMZI2, respectively, correspond to the first-order difference of the input signal $E(t)$, and the system output signal E_{out} corresponds to the second-order difference of $E(t)$ which represent the approximations of the first and second derivative of $E(t)$, respectively Yao (2007). In the case of the Gaussian UWB modulated input signal, the first derivative is the monocycle and second derivative is the doublet Ghawami (2005). In order to down-convert the output monocycle and doublet modulated optical signals, the coherent-detection technique is used where the

local oscillator frequency $\omega_{LO} = \omega$ Agrawal (2002). In order to improve the accuracy of the homodyne detection we use the same laser as a source of the externally UWB modulated optical signal and the CW optical signal. The block diagram of the system is shown in Fig. 7. The detector photocurrent $I(t)$ is given by Agrawal (2002)

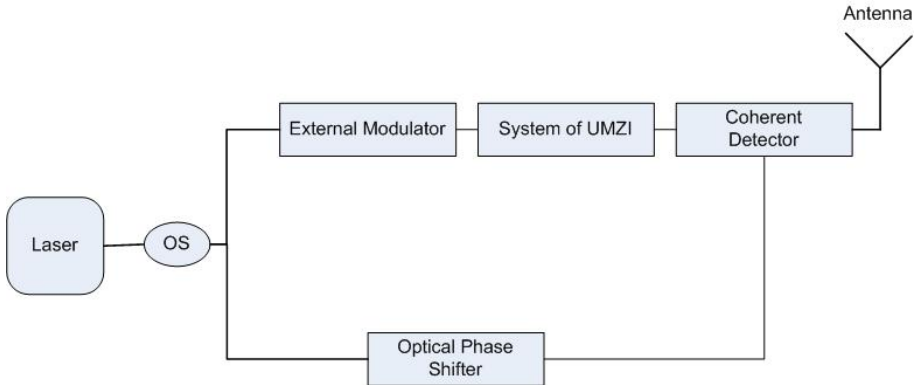


Fig. 7. Block diagram of UWB pulse photonic generation system

$$I(t) = R [P_{out} + P_{LO} + 2\sqrt{P_{out}P_{LO}} \cos(\phi_{out} - \phi_{LO})] \tag{28}$$

where R is the detector responsivity, $P_{out} = KA_{out}^2$, $P_{LO} = KA_{LO}^2$, A_{out} , A_{LO} , ϕ_{out} , ϕ_{LO} are the output signal and local oscillator optical powers, amplitudes and phases, respectively, K is a constant of proportionality. The phase difference $(\phi_{out} - \phi_{LO})$ can be eliminated by using a phase shifter. Then, the detected signal $I_H(t)$ is given by Agrawal (2002)

$$I_H(t) = 2R\sqrt{KP_{LO}}A_{out} \sim |E_{out}| \tag{29}$$

Equations (27) and (29) show that the detected signal $I_H(t)$ is proportional to the Gaussian doublet. Typically, the local oscillator power is much larger than the output signal, and optical losses in the MZI system can be neglected. For the typical values of $R = (0.4 - 0.9) A/W$ Agrawal (2002), $P_{LO} = 10mW$, $P_{out} = 0.1mW$ we obtain $I_H(t) \approx (0.8 - 1.8) mA$. The numerical simulations results for equations (24)-(27) are shown in Figs. 8, 9.

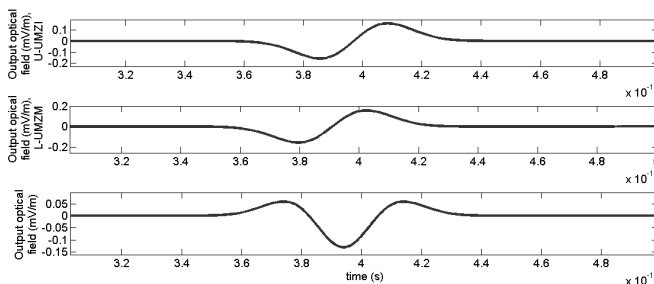


Fig. 8. Gaussian monocycles (the upper and middle boxes) and doublet (the lower box)

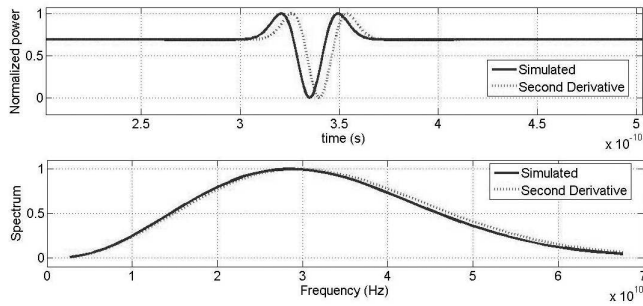


Fig. 9. Simulated Gaussian doublet at the output of the passive UNMZI system - solid line, the second derivative of Gaussian pulse - dashed line (the upper box); the spectra of the Gaussian doublet (solid line) and of the second derivative of Gaussian pulse (dashed line) (the lower box)

As it is seen from Fig. 8, the Gaussian monocycles and doublets can be optically generated by using the system of the passive UMZIs connected in parallel and coherent homodyne detector. Fig. 9 shows a satisfactory coincidence between the simulated Gaussian doublet and its spectrum and the calculated second derivative of the standard Gaussian pulse (3) and its spectrum.

Unlike the existing methods, the proposed method is based on the generation of the field pulses instead of the power pulses. The advantages of the proposed method are mainly related to the absence of the nonlinear active elements which results in the stability, simplicity and easy control of the proposed system.

6. All-optical Processing of UWB Signals

A wavelet transform (WT) involves time-frequency representation of nonstationary signals and can be successfully used in optical communications for signal processing operations such as an ultrafast image transmission, signal denoising, time-frequency multiplexing, spectral and temporal encoding Cincotti (2005). The use of WTs in optical communications can significantly improve a system capacity due to the two-dimensional processing capability of the multiresolution analysis (MRA) providing a high resolution at low frequency and low resolution at high frequency and permitting to localize a particular portion of the signal Cincotti (2005). The continuous WT (CWT) of a signal $s(t)$ is given by Rao (1998)

$$CWT_s(a, \tau) = \frac{1}{|a|} \int s(t) \Psi^* \left(\frac{t - \tau}{a} \right) dt \quad (30)$$

where a is a real scale parameter, τ is the translation factor, and $\psi(t)$ is the mother wavelet function. In digital signal processing and multiplexing the orthogonal wavelet series expansions or discrete WTs (DWTs) are more useful that can be obtained from CWT (30) when the scale and translation factors have discrete values. DWT decomposes the input signal at different scales and resolutions using bases localized in time and frequency domains and extracting specific information from the signal. Under certain conditions, a signal $s(t)$ can be represented

by a smoothed approximation at resolution 2^M given by Cincotti (2005)

$$s(t) = \sum_k 2^{-M/2} c_M[k] \phi(2^{-M}t - k\Delta\tau) + \sum_{l=1}^M \sum_k 2^{-l/2} d_l[k] \psi(2^{-l}t - k\Delta\tau) \quad (31)$$

where $\psi(t)$ is the mother wavelet function, $\phi(t)$ is the scaling function, $c_M[k]$ are the scaling/approximation coefficients, $d_l[k]$ the detail coefficients, and $\Delta\tau$ is the inverse of the signal free spectral range (FSR). The DWT decomposition (31) halves the time resolution and doubles the frequency band of original signal. In the case of the signal corruption by white Gaussian noise, the signal denoising scheme is based on the selective wavelet reconstruction since an inhomogeneous signal is described by a small number of wavelet coefficients while the white noise is distribute over a large number of coefficients Cincotti (2005).

Passive networks for a physical implementation of the discrete WT (DWT) can be based on passive MZIs described in section 5 with output asymmetric couplers Cincotti (2002). We propose a passive UMZI as a basic component for the all-optical passive generation of the Mexican hat mother wavelet (MHMW) and for the realization of the Haar wavelet decomposition which can be used for the all-optical signal denoising.

Using the system of passive UMZIs shown in Fig. 6 with the time delay $\Delta\tau$ instead of τ and applying equations (23)-(27) to the Gaussian input signal we indeed obtain the approximation of the Gaussian second derivative which is MHMW given by Rao (1998)

$$E(t) = (1 - t^2) \exp(-t^2) \quad (32)$$

The inverse MHMW corresponds to the doublet shown in Fig. 8.

Consider now the all-optical signal denoising. It is based on the Haar recursive decomposition with the quadrature mirror filter (QMF) coefficients $h[k]$ and $g[k]$. These coefficients can be realized by the digital filters given by

$$h[k] = \frac{1}{2} [\delta(k) + \delta(k+1)]; g[k] = \frac{1}{2} [\delta(k) - \delta(k+1)] \quad (33)$$

These filters can be implemented by the UMZI. In the case of low pass filter $h[k]$ the interference at the UMZI output should be constructive. In the opposite case of the high pass filter $g[k]$, the interference at the UMZI output should be destructive. We generated a noisy 10Gb/s NRZ optical signal. The eye diagram of this input signal is shown in Fig. 10. In order to carry out the denoising of the input NRZ signal we used a three stage cascade of the UMZIs of the type shown in Fig. 6 with FSR of $\Delta\tau$, $2\Delta\tau$, $3\Delta\tau$, respectively, which permits the realization of the three level Haar decomposition of the input signal. By eliminating the higher order detail components $d_l[k]$ we filter the noise components and simultaneously slightly reshape the input waveform itself. The eye diagram of the denoised signal is shown in Fig. and manifests a substantial improvement of the signal-to-noise ratio (SNR).

7. Conclusions

We have proposed a theoretical analysis of novel all-optical methods of the IR UWB signal generation.

1. We proposed a novel method of the IR UWB signal generation based on integrated MZI with a QD SOA as a nonlinear component. The generation mechanism is related to

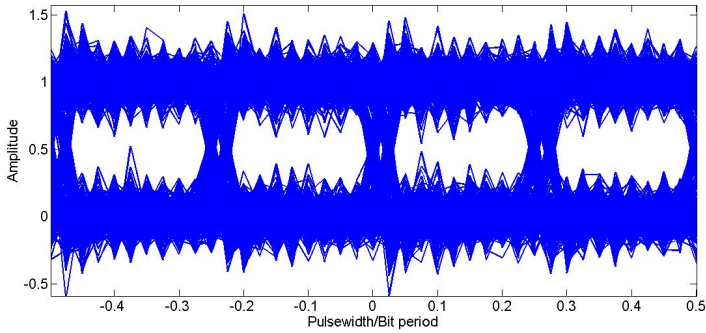


Fig. 10. The eye diagram of the input optical signal

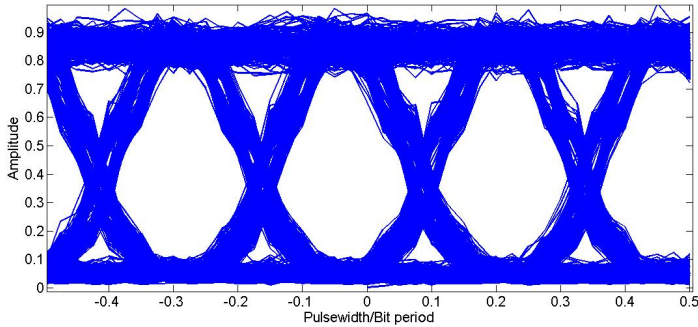


Fig. 11. The eye diagram of the optical signal after the wavelet denoising process

XPM and XGM phenomena in QD SOA Unlike other proposed all-optical methods, we need not optical fibers, FBG and EOM substantially reducing the cost and complexity of a IR UWB generator. The IR UWB signals generated by the proposed QD SOA based MZI structure have the form of the Gaussian doublet. The shape of the signal and its spectrum can be tailor-made for different applications by changing the QD SOA bias current and optical power.

2. We have shown theoretically that the Gaussian monocycles and doublets can be optically generated by using the system consisting of the passive UMZIs connected in parallel, and coherent homodyne detector. Unlike the existing methods, the proposed method is based on the generation of the field pulses instead of the power pulses and does not require nonlinear components.
3. We proposed the implementation scheme of the all-optical signal denoising and MHMW generation based on the system of the passive UMZIs.

8. References

- Agrawal, G.P. & Olsson, N.A. (1989). Self-phase modulation and spectral broadening of optical pulses in semiconductor laser amplifiers. *IEEE Journal of Quantum Electronics*, Vol. 25, No.11, (November 1989) 2297-2306, ISSN 0018-9197
- Agrawal, G.P. (2001). *Applications of Nonlinear Fiber Optics*. Academic Press, ISBN 0-12-045144-1, New York
- Agrawal, G.P. (2002). *Fiber-Optic Communication Systems*. Wiley, ISBN 0-471-21571-6, New York
- Bányai, L. & Koch, S. W. (2005). *Semiconductor Quantum Dots* (Second Edition). World Scientific, ISBN 9810213905, London,
- Ben-Ezra, Y.; Haridim, M. & Lembrikov, B. I. (2005). Theoretical analysis of gain-recovery time and chirp in QD-SOA. *IEEE Photonics Technology Letters*, Vol. 17, No. 9, (September 2005) 1803-1805, ISSN 1041-1135
- Ben-Ezra, Y.; Lembrikov, B. I. & Haridim, M. (2005). Acceleration of gain recovery and dynamics of electrons in QD-SOA. *IEEE Journal of Quantum Electronics*, Vol. 41, No. 10, (October 2005) 1268-1273, ISSN 0018-9197
- Ben-Ezra, Y.; Lembrikov, B. I. & Haridim, M. (2007). Specific features of XGM in QD-SOA. *IEEE Journal of Quantum Electronics*, Vol.43, No. 8, (August 2007) 730-737, ISSN 0018-9197
- Ben Ezra, Y.; Haridim, M.; Lembrikov, B.I. & Ran, M. (2008). Proposal for All-optical Generation of Ultra Wideband Impulse Radio Signals in Mach-Zehnder Interferometer with Quantum Dot Optical Amplifier. *IEEE Photonics Technology Letters*, Vol. 20, No. 7 (April 2008) 484-486, ISSN 1041-1135
- Berg, T.W.; Mørk, J. & Hvam, J.M. (2004). Gain dynamics and saturation in semiconductor quantum dot amplifiers. *New Journal of Physics*, Vol. 6, No. 178, (2004) 1-23, ISSN 1367-2630
- Bimberg, D.; Grundmann, M. & Ledentsov, N. N. (1999). *Quantum Dot Heterostructures*. John Wiley, ISBN 047 1973882, New York
- Chen, H.; Zhu, G.; Wang, Q.; Jaques, J.; Leuthold, J.; Picirilli, A.B. & Dutta, N.K. (2002). All-optical logic XOR using differential scheme and Mach-Zehnder interferometer. *Electronic Letters*, Vol. 38, No. 21, (October 2002) 1271-1273, ISSN 0013-5194
- Chen, H.; Chen, M.; Wang, T.; Li, M. & Xie, S. (2008). Methods for ultra-wideband pulse generation based on optical cross-polarization modulation. *Journal of Lightwave Technology*, Vol. 26, No. 15, (August 2008) 2492-2499, ISSN 0733-8724
- Cincotti, G. (2002). Fiber Wavelet Filters. *IEEE Journal of Quantum Electronics*, Vol. 38, No. 10, (October 2002) 1420-1427, ISSN 0018-9197
- Cincotti, G.; Moreolo, M.S. & Neri, A. (2005). Optical Wavelet Signals Processing and Multiplexing. *EURASIP Journal on Applied Signal Processing*, Vol. 2005, (January 2005) 1574-1583, ISSN 1110-8657
- Dong, J.; Zhang, X. & Huang (2009). All-optical ultra-wideband pulse generation based on semiconductor optical amplifiers. *Frontiers of Optoelectronics in China*, Vol. 2, No.1, (March 2009) 40-49, ISSN 1674-4128
- E. Gehrig, E. & O. Hess, O. (2002). Mesoscopic spatiotemporal theory for quantum-dot lasers. *Phys. Rev. A*, Vol. 65, No. 3, (March 2002) 033804-1-16, ISSN 1050-2947
- Ghavami, M.; Michael, L.B. & Kohno, R. (2005). *Ultra Wideband Signals and Systems in Communication Engineering*, Wiley, ISBN-10 0-470-86571-5(H/B), Chichester, England
- Joergensen, C. ; Danielsen, S.L.; Durhuus, T.; Mikkelsen, B. ; Stubkjaer, K.E.; Vodjdani, N.; Ratovelomanana, F.; Enard, A.; Glastre, G.; Rondi, D. & Blondeau, R. (1996). Wave-

- length conversion by optimized monolithic integrated Mach-Zender interferometer, *IEEE Photonics Technology Letters*, Vol. 8, No. 4, (April 1996) 521-523, ISSN 1041-1135
- Kanellos, G.T.; Petrantonakis, D.; Tsiokos, D.; Bakopoulos, P.; Zakyntinos, P.; Pleros, N.; Apostolopoulos, D.; Maxwell, G.; Poustie, A. & Avramopoulos, H. (2007). All-optical 3R burst-mode reception at 40 Gb/s using four integrated MZI switches. *Journal of Lightwave Technology*, Vol. 25, No. 1, (January 2007) 184-192, ISSN 0733-8724
- Kshetrimayum, R. S. (2009). An Introduction to UWB Communication Systems. *Potentials, IEEE*, Vol. 28, Issue 2, (March-April 2009) 9-13, ISSN 0278-6648
- Le Guennec, Y. & Gary, R. (2007). Optical frequency conversion for millimeter-wave ultra-wideband-over-fiber systems. *IEEE Photonics Technology Letters*, Vol. 19, No. 13, (July 2007) 996-998, ISSN 1041-1135
- Lin, W.-P. & Chen, J.-Y. (2005). Implementation of a new ultrawide-band impulse system, *IEEE Photonics Technology Letters*, Vol. 17, No. 11, (November 2005) 2418-2420, ISSN 1041-1135
- Qasaimeh, O. (2003). Optical gain and saturation characteristics quantum-dot semiconductor optical amplifiers. *IEEE J. of Quantum Electronics*, Vol. 39, No. 6, (June 2003) 793-798, ISSN 0018-9197
- Qasaimeh, O. (2004). Characteristics of cross-gain (XG) wavelength conversion in quantum dot semiconductor optical amplifiers. *IEEE Photonics Technology Letters*, Vol. 16, No. 2, (February 2004) 542-544, ISSN 1041-1135
- Ran, M; Ben Ezra, Y. & Lembrikov B.I. (2009). Ultra-wideband Radio-over-optical-fibre Technologies, In *Short-Range Wireless Communications*, Kraemer, R. & Katz, M. D. (Eds.), 271-327, Wiley, ISBN 978-0-470-69995-9 (H/B), Chichester, England
- Rao, R.M. & Bopardikar, A.S. (1998). *Wavelet Transforms. Introduction to Theory and Applications*. Addison-Wesley, ISBN-10: 020 16 34 635, Reading, Massachusetts
- Sugawara, M.; Ebe, H.; Hatori, N.; Ishida, M.; Arakawa, Y.; Akiyama, T.; Otsubo, K. & Nakata, Y. (2004) Theory of optical signal amplification and processing by quantum-dot semiconductor optical amplifiers. *Phys.Rev.B*, Vol. 69, No. 23 (June 2004) 235332-1-39, ISSN 1098-0121
- Uskov, A.V. ; Berg, T.W. & Mørk, J. (2004). Theory of pulse-train amplification without patterning effects in quantum-dot semiconductor optical amplifiers. *IEEE J. of Quantum Electronics*, Vol. 40, No. 3, (March 2004) 306-320, ISSN 0018-9197
- Ustinov, V.M.; Zhukov, A.E.; Egorov, A. Yu. & Maleev, N. A. (2003). *Quantum Dot Lasers*, Oxford University Press, ISBN 0 19 852679 2, Oxford
- Wang, Q.; Zhu, G.; Chen, H. ; Jaques, J. ; Leuthold, J.; Picirilli, A.B. & Dutta, N.K. (2004). Study of all-optical XOR using Mach-Zehnder interferometer and differential scheme. *IEEE J. of Quant. Electr.*, Vol. 40, No. 6, (June 2004) 703-710, ISSN 0018-9197
- Wang, Q. & Yao, J. (2006). UWB doublet generation using nonlinearly-biased electro-optic intensity modulator, *Electronic Letters*, Vol. 42, No. 22, (October 2006)1304-1305, ISSN 0013-5194
- Yang, L. & Giannakis, G.B. (2004). Ultra-Wideband Communications. *IEEE Signal Processing Magazine*, Vol. 21, No. 6; (November 2004) 26-54, ISSN 1053-5888
- Yao, J.; Zeng, F. & Wang, Q. (2007). Photonic generation of ultrawideband signals. *Journal of Lightwave Technology*, Vol. 25, No. 11, (November 2007) 3219-3235, ISSN 0733-8724
- Zeng, F. & Yao, J. (2006). An approach to ultrawideband pulse generation and distribution over optical fiber. *IEEE Photonics Technology Letters*, Vol. 18, No. 7, (April 2006) 823-825, ISSN 1041-1135

- Zeng, F. & Yao, J. (2006). Ultrawideband impulse radio signal generation using a high-speed electrooptic phase modulator and a fiber-Bragg-grating-based frequency discriminator. *IEEE Photonics Technology Letters*, Vol. 18, No. 19, (October 2006) 2062-2064, ISSN 1041-1135
- Zeng, F.; Wang, O. & Yao, J.P. (2007). All-optical UWB impulse generation based on cross-phase modulation and frequency discrimination. *Electronic Letters*, Vol. 43, No. 2, (January 2007) 119-121, ISSN 0013-5194

High Spectral Efficiency Optical Transmission of OFDM Ultra-wideband Signals beyond 40 Gb/s

B.I. Lembrikov, Y. Ben Ezra, M. Ran, M. Haridim
*Holon Institute of Technology (HIT),
 P.O.Box 305, 58102, 52 Golomb Str., Holon
 Israel*

1. Introduction

1.1 State of the Art of High Spectral Efficiency Transmission Techniques

1.1.1 Spectral Efficiency and Advanced Optical Modulation Formats

Modern optical communication systems fulfilling optical networking functionalities and operating at data rates of about 40Gb/s are now commercially available due to the rapid development of high-speed electronics and optical component technologies in recent years (Winzer, December 2006). In wavelength division multiplexing (WDM) systems the increase of system reach and capacity and, at the same time, the reduction of the cost per transported information bit are achieved by sharing optical components among many WDM channels (Winzer, May 2006). All shared optical components operate within limited wavelength windows, and consequently, WDM channels should be spaced as closely together as possible (Winzer, May 2006). Consequently, it is necessary to increase the system spectral efficiency (SE), or information spectral density defined as the ratio of net per-channel information data rate to WDM channel spacing and measured in $b/s/Hz$ (Bigo, 2004). For instance, transmission of 40Gb/s data information per WDM channel on the 100GHz International Telecommunication Union (ITU) frequency grid yields a SE of 0.4b/s/Hz (Winzer, May 2006). The cost per information bit can be also decreased by increasing of the per-channel data rates.

Progress in high SE, high capacity optically routed transport networks is defined by the following key technologies: (i) low-loss optical components such as transmission fiber, dispersion compensation devices, optical switching/routing elements; (ii) low-noise optical amplifiers; (iii) advanced optical fibers reducing nonlinearity and enabling higher signal launch powers; (iv) forward error correction (FEC); advanced modulation formats (Winzer, May 2006). At per-channel data rates of 40Gb/s and above special modulation formats and line coding are used to mitigate linear and nonlinear impairments from fiber-optic transmission and to achieve high spectral efficiencies in optically routed network scenarios (Winzer, December 2006). Record numbers of transmission distances and capacities in research laboratories reach up to 6100km and 6Tb/s, or 10000km and 1.6Tb/s which correspond to capacity-distance products of 36Pb/s · km and 16Pb/s · km, respectively (Winzer, May 2006).

The most common intensity data modulation format (DMF) is a binary nonreturn to zero (NRZ) on/off keying (OOK). However, it has a low SE. For this reason, other more advanced DMFs are proposed and developed such as binary chirped and chirp-free nonreturn

to zero (NRZ) and return to zero (RZ); vestigial sideband (VSB); single sideband (SSB); alternate chirped return to zero (ACRZ); dispersion supported transmission (DST), and multilevel amplitude-shift keying (M-ASK). Typical phase DMFs are binary and multilevel NRZ and RZ; differential phase-shift keying (DPSK), and differential quadrature phase-shift keying (DQPSK) (Winzer, December 2006). Polarization degree of freedom is mainly used to improve the propagation properties of a format, or in research experiments to increase spectral efficiency. The detailed analysis of these formats can be found in Ref. (Winzer, December 2006) and references therein.

1.1.2 Orthogonal Frequency Division Multiplexing (OFDM)

The optical communication system performance at high transmission data rate per channel approaching 100Gb/s strongly deteriorates due to the optical dispersion effects (Agrawal, 2002), (Shieh, 2008). Conventional dispersion compensation methods at these bit rates are costly, time-consuming, require precise optical fiber dispersion measurement and precise matching of the dispersion compensation across a broad wavelength range (Shieh, 2008). In particular, a dynamically reconfigurable network with a fast link setup makes the manual optical dispersion compensation impractical (Shieh, 2008). The recently proposed coherent optical orthogonal frequency division multiplexing (OFDM) can provide a solution of these problems (Shieh, 2008), (Armstrong, 2009). OFDM is a technique for transmitting data in parallel by using a large number of modulated carriers with the subcarrier frequencies chosen in such a way that they are orthogonal over one OFDM symbol period (Armstrong, 2009), (Couch II, 2001). DMFs mentioned above can be used in OFDM technology (Couch II, 2001). In the last decade, OFDM has emerged as the leading physical-layer interface in broadband wireless communication systems because it has the following advantages that are especially important for high data rate signal transmission (Shieh, 2008), (Armstrong, 2009).

1. In the case of OFDM, the intersymbol interference (ISI) caused by a dispersive channel is much smaller as compared to quadrature amplitude modulation (QAM), NRZ, and other conventional modulation schemes.
2. OFDM transfers the complexity of transmitters and receivers from the analog to the digital domain.

In OFDM the spectra of individual subcarriers overlap, but for linear channels the subcarriers can be demodulated without interference and without an analog filtering to separate the received subcarriers, due to the orthogonality property (Armstrong, 2009). Optical OFDM is based on electronic signal processing before the optical modulator and after the photo detector (PD). The sources of Optical OFDM solutions are divided into two groups (Armstrong, 2009).

1. For optical wireless, multimode fiber (MMF) systems, and plastic optical fiber systems characterized by many different optical modes the OFDM signal is represented by the intensity of the optical signal.
2. For SMF with only one mode of the signal the OFDM signal is represented by the optical field.

Coherent optical OFDM combines the advantages of coherent detection and OFDM modulation (Shieh, 2008). In particular, in the case of OFDM, the chromatic dispersion and polarization mode dispersion of the transmission system can be effectively estimated and mitigated,

and SE can be increased due to the partial overlapping of OFDM subcarrier spectra (Shieh, 2008).

OFDM has been thoroughly investigated in mobile communications in order to overcome hostile frequency-selective fading (Shieh, 2008). OFDM has been incorporated into a number of wireless network standards (802.11a/g WiFi, HiperLAN2, 802.16 WiMax) and digital audio and video broadcasting (DAB, DVB-T) (Shieh, 2008).

OFDM can be successfully applied to ultra wideband (UWB) signals transmission combining the advantages of the both technologies which results in a significant SE increase.

1.2 UWB OFDM Technology

UWB radio is a fast emerging technology widely used in wireless communications, networking, radar, imaging, and positioning systems (Yang, 2004). UWB characterizes transmission systems with instantaneous spectral occupancy in excess of 500MHz or a fractional bandwidth defined as B/f_c of more than 20%, where $B = f_H - f_L$ denotes the $-10dB$ bandwidth, and center frequencies $f_c = (f_H + f_L) / 2$, f_H , f_L are the upper and lower frequency of the $-10dB$ emission point, respectively (Yang, 2004). Historically, UWB radar systems were first developed mainly as a military tool due to their enhanced capability to penetrate through obstacles and ultra high precision ranging at the centimeter level (Ghavami, 2005), (Yang, 2004). Recently, UWB technology has been focused on consumer electronics and communications where UWB systems are characterized by low power, low cost, very high data rates, precise positioning capability and extremely low interference (Ghavami, 2005). For this reason, UWB technology is suitable for broadband services in the mass markets of wireless personal area networks (WPAN), and it is a promising candidate for such applications as accurate tracking and location, safety and homeland security. UWB technology may be implemented in the global positioning system (GPS) and wireless local area networks (WLAN) (Yang, 2004). A relatively new UWB technology application for communication is caused in particular by rapid advancement of semiconductor technology (Kshetrimayum, 2009).

The UWB technology development was stimulated in 2002 when Federal Communication Commission (FCC) released a spectral mask allowing operation of UWB radios at the noise floor, but over a huge bandwidth up to 7.5GHz (Yang, 2004). For UWB systems, the transmitted power is comparable to the level of parasitic emissions in a typical indoor environment being of the order 0.5mW (Kshetrimayum, 2009). For wireless communications, the FCC regulated power levels are below $-41.3dBm$ (Yang, 2004). Low power, short-range UWB communications are potentially capable of providing high spatial capacity. UWB connectivity may be used successfully in applications related to flexible location-aware communication networks (Yang, 2004). The general model of a single-link communication consists of a transmitter, a channel, and a receiver where the channel is the medium through which the transmitted data reaches a receiver (Kshetrimayum, 2009).

There exist three main types of UWB technologies: impulse radio (IR-UWB), direct sequence (DS-UWB), and multi-band OFDM (MB-OFDM) (Ran, 2009). In IR-UWB, information is carried by a set of narrow electromagnetic pulses. Their bandwidth is inversely proportional to the pulse width. Unlike conventional wireless communication systems that are based on carrier modulation, IR-UWB is essentially a baseband carrier free technology. The center frequency in IR-UWB is determined by the zero crossing rate of the pulse waveform. In general, waveforms for IR-UWB are designed to obtain a flat frequency response over the bandwidth of the pulse and to avoid a DC component. Various monocycle waveforms have been proposed to meet these characteristics including Gaussian, Raleigh, Laplacian and cubic. Various

DMFs may be used in the case of IR-UWB such as pulse amplitude modulation (PAM), pulse position modulation (PPM) and pulse shape modulation (PSM). DS-UWB is based on concepts of conventional DS spread spectrum (DS-SS). MB-OFDM is based on subdividing the UWB spectrum into 5 band groups and 14 sub-bands of 528MHz width composed of 128 sub-carriers OFDM signals, and each one is QPSK modulated.

The MB UWB OFDM technology combines the advantages of SE DMFs and OFDM. For this reason, recently, we proposed a new concept that combines the advantages of the high data rate wireless short-range communications based on UWB technologies, and in particular high SE, and the optical fiber communication technology (Ran, 2009). The fiber-optic communication systems can be applied in any area that requires transfer of information from one place to another (Agrawal, 2002). Their advantages are well known. For instance, the bandwidth of the modulated carrier can reach a few percent of the carrier frequency which provides the optical communication systems with the potential of carrying information at bit rates up to $1Tb/s$ (Agrawal, 2002). The fiber losses are extremely low compared to other channel materials exhibiting a minimum loss of about $0.2dB/km$ near the wavelength $\lambda = 1.55\mu m$ (Agrawal, 2002). The proposed concept enables the transmission of UWB radio signals over optical fibers by superimposing the UWB RF signals of several GHz on the optical continuous wave (CW) carrier. This concept is called UWB radio over fiber (UROOF). It has the following advantages:

1. The conversion process becomes transparent to the UWB modulation method.
2. The high costs of additional electronic components required for synchronization and other processes can be avoided.
3. The integration of all the RF and optical transmitter/receiver components on a single chip is possible.

UROOF technology can be successfully applied in the following areas (Ran, 2009).

1. UROOF technology can significantly improve WPAN by range extension up to 2-3 orders of magnitude.
2. Novel optical/wireless infrastructures can be developed capable of delivering broadband multimedia and above $1000Mb/s$ traffic to subscribers in remote areas.
3. UROOF technology can be used in security systems for collecting data from a large number of sensors and cameras equipped with UWB and transmitting it over optical infrastructures.

We proposed OFDM technology application to the high SE optical transmission of UWB signals beyond $40Gb/s$ (Ben-Ezra, 2008). The highly efficient method of RF and optical signal mixing is based on two different architectures: the parallel-RF/serial-optics architecture characterized by all-optical mixing for sub-carrier multiplexing, and the parallel-RF/parallel-optics architecture based on the array of $12 \times 10GHz$ components with directly modulated vertical cavity surface emitting lasers (VCSELs) and 12 multimode optical fibers. The main advantages of the both architectures are simplicity and low-cost implementation.

The original results are presented in Sections 2-6 of this work. The proposed novel parallel-RF/serial-optics and parallel-RF/parallel-optics architectures are considered in Section 2. In Section 3, the building blocks of these architectures are described. We discuss in detail the optical link model containing a directly modulated VCSEL as a transmitter, MMF, and a p-i-n diode as PD. A SiGe based optically controlled microwave convertor (OCMC) as a novel component for the UWB MB OFDM signal detection is developed in Section 4. Experimental and simulation results concerning the proposed MB UWB OFDM transmission system performance are presented in Section 5. Conclusions are presented in Section 6.

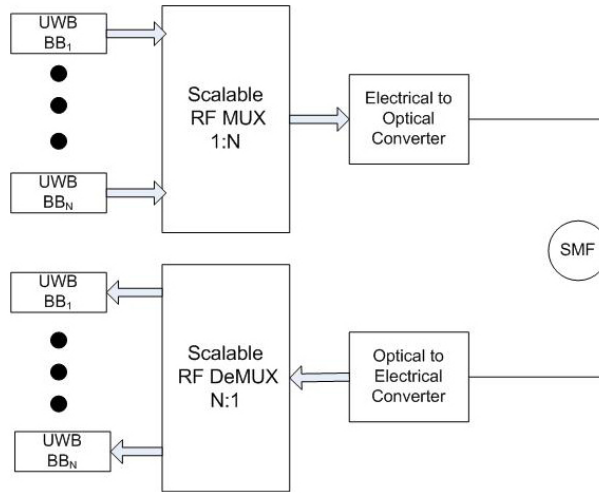


Fig. 1. 61.44Gb/s based on parallel RF/serial optics with $N = 128$ channels

2. Architecture of UWB OFDM Systems

In this section parallel and serial architectures of UWB OFDM systems are explored in order to construct multi-band OFDM signals capable of delivering a multi-gigabit analog signal. We address beyond 40Gb/s data rates by parallel transmission over more than 128 conventional baseband channels, each having 528MHz bandwidth.

2.1 Parallel RF/Serial Optic Architecture

A novel concept for a scalable radio-over-fiber (ROF) system enables to bring the bit rate up to 100Gb/s is shown in Fig. 1. The system is scalable in such a way that it enables various operations with channels and bands. It is necessary for development of novel optical/electrical (O/E) and electrical/optical (E/O) components and subsystems for the extended band UWB signal transmission over the fiber. For instance, photodetection up to 64GHz may be achieved through the lateral illumination and resonant-cavity-enhancement of SiGe heterojunction phototransistors (HPTs). Additionally, UWB and highly linear E/O modulator is needed for the implementation of the proposed architecture. SMF can be used in long-haul applications.

2.2 Parallel RF/Parallel Optics Architecture

In the alternative scheme of the parallel RF/parallel optics architecture shown in Fig. 2, each directly modulated low-cost multimode VCSEL with a 10 Gb/s bandwidth transmits its signal over a separate MMF. This architecture based on 12x10GHz transceiver for digital 100GbE was proposed in Ref. (IEEE). We enhanced this architecture for ROF applications. In contrast to the parallel RF/serial optics architecture with SMF suitable for long-haul applications, this version based on MMF is appropriate for short-range applications. The parallel RF/parallel optics architecture is expected to operate at wavelength $\lambda = 850nm$ over MMF of a length of about several hundred of meters. The input lanes are directly connected to 12 Laser Drivers (LDs), which are in turn connected to a 12-element VCSEL array. The output lanes are directly

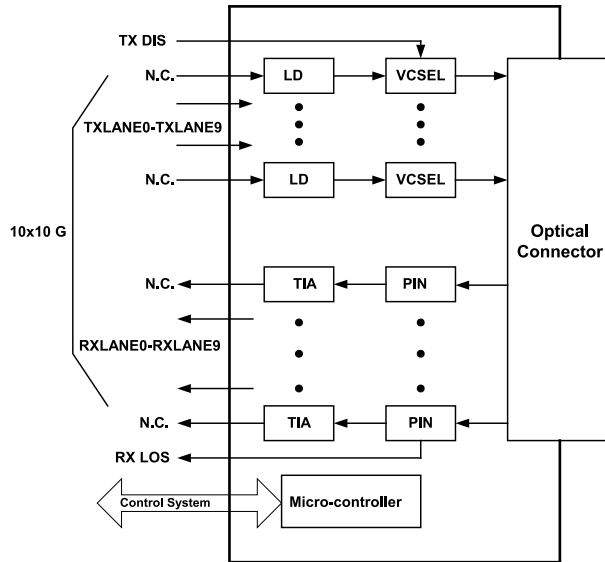


Fig. 2. 850 nm 400m 100Gb/s based on parallel RF/parallel optics

connected to a 12-element PIN-diode array. After the detection the RF signals are amplified by 12 transimpedance amplifiers (TIAs) as it is seen in Fig. 2.

3. Optical Link

In this section we consider the theoretical model of the optical link consisting of a transmitter, an optical fiber and a PD (Pepeljugoski, 2003). Transmitter, MMF and connections are the most important factors determining the 3-dB optical bandwidth of the link. The transmitter, VCSEL is a key device in local area networks using MMFs, and it possesses the following advantages: low power consumption; high-speed modulation with low driving current; narrow circular beam for direct fiber coupling; low cost and small packaging capability; single longitudinal mode operation with vertical microcavity (Koyama, 2006). The operational characteristics of directly modulated VCSEL are described by the rate equations for the photon density $P(t)$, electron density $N(t)$ and the phase $\phi(t)$ since the amplitude modulation in semiconductor lasers is accompanied by the phase modulation determined by the linewidth enhancement factor (LEF) α_c (Agrawal, 2002), (Pepeljugoski, 2003):

$$\frac{dP}{dt} = \left[\frac{\Gamma a (N - N_0)}{(1 + \epsilon p)} - \alpha_{tot} \right] v_g P - \frac{P}{\tau_p} + \frac{\beta \Gamma N}{\tau_e} + F_P(t) \tag{1}$$

$$\frac{dN}{dt} = \frac{I(t)}{qV} - \frac{v_g a (N - N_0)}{(1 + \epsilon p)} P - \frac{N}{\tau_e} - BN^2 - CN^3 + F_N(t) \tag{2}$$

$$\frac{d\phi}{dt} = \frac{1}{2} \alpha_c \left[\Gamma v_g a (N - N_0) - \frac{1}{\tau_p} \right] + F_\phi(t) \tag{3}$$

where a is the differential gain, N_0 is a transparency electron concentration, Γ is the confinement factor, v_g is the group velocity of light in the active region, V is the active region volume,

$\tau_{p,e}$ are the photon and electron lifetimes, respectively, ϵ is the gain compression factor, β is the spontaneous emission fraction coupled into a lasing mode, q is the electron charge, $I(t)$ is the VCSEL bias current, B is the bimolecular recombination factor, C is the Auger recombination factor, α_{tot} is the total loss coefficient given by

$$\alpha_{tot} = \alpha_{loss} + \frac{1}{L} \ln R \quad (4)$$

where α_{loss} is the VCSEL absorption coefficient, L is the VCSEL active region length, and R is the reflectivity of the mirrors. The terms $F_P(t)$, $F_N(t)$, $F_\phi(t)$ are the Langevin forces assumed to be Gaussian random processes. Single mode rate equations (1)-(3) have been found to be a very good approximation to the large signal behavior for MMF (Pepeljugoski, 2003).

The proposed model mainly concentrates on the signal degradation due to the intermodal dispersion because the largest part of the link power budget is consumed by pulse spreading caused by intermodal dispersion (Pepeljugoski, 2003). At the operating wavelength $\lambda = 850nm$, the $50\mu m$, 1% Δ MMF initially supports 19 mode groups, each of which can have its own group velocity v_g (Pepeljugoski, 2003). In actual MMFs there exists coupling between the modes due to the fiber imperfections. However, only the coupling of modes within a mode group is significant over the short length scales of hundreds of meters, while the modal dispersion between mode groups is neglected, and the coupling between them is absent (Pepeljugoski, 2003). The attenuation of the coupling modes within each group μ is described by the attenuation rate $\gamma_{\mu'}$, and the amplitude of a pulse launched into group μ is proportional to the factor $\exp(-\gamma_{\mu'}z)$ as it propagates through MMF (Pepeljugoski, 2003). As a result, the bandwidth and the MMF transfer function strongly depend on the excitation conditions determining how much power will be coupled into each mode group, and the signal at the receiver output is determined by the launch conditions, MMF properties, and the link configuration (Pepeljugoski, 2003).

The transverse modes of a VCSEL are assumed to be Gaussian beam modes $u_{pl}(r, \varphi, z, w_0, k)$ centered at the origin $r = 0$ of MMF and parallel to the z axis. They are given by (Pepeljugoski, 2003)

$$u_{pl}(r, \varphi, z, w_0, k) = \frac{w_0}{w} \left(\sqrt{2} \frac{r}{w} \right)^l L_p^l \left(2 \frac{r^2}{w^2} \right) \times \exp \left[-i \left(kz - \Phi_{pl} + l\varphi \right) - r^2 \left(\frac{1}{w^2} + \frac{ik}{2R} \right) \right] \quad (5)$$

where $p \geq 0$, $l \geq 0$ are the radial and angular mode numbers, w_0 is the spot size at the waist, $k = 2\pi/\lambda$ is the free space wavenumber, L_p^l are the generalized Laguerre polynomials, and

$$\Phi_{pl}(z, w_0, k) = (2p + l + 1) \arctan \left(\frac{2z}{kw_0^2} \right) \quad (6)$$

$$w(z, w_0, k) = w_0 \left[1 + \left(\frac{2z}{kw_0^2} \right)^2 \right]^{1/2}; R(z, w_0, k) = z \left[1 + \left(\frac{kw_0^2}{2z} \right)^2 \right] \quad (7)$$

For the few-moded VCSEL the Gaussian beam model is a reasonable approximation (Pepeljugoski, 2003). A VCSEL u_{pl} mode at the air-fiber interface is transformed into a different Gaussian beam mode which then excites the various modes $\psi_{lmvp}(r, \theta)$ of MMF corresponding

to the transverse components $E_{x,y}$ of the electric field in the fiber. The normalized modes $\psi_{lmvp}(r, \theta)$ are given by (Pepeljugoski, 2003)

$$\psi_{lmvp}(r, \theta) = f_{lm}(r) v(l\theta) \mathbf{p} \quad (8)$$

where $l \geq 0$ and $m > 0$ are the eigen-values of the radial and angular parts of (8), the index v denotes angular dependence $\sin l\theta$ or $\cos l\theta$, and polarization $\mathbf{p} = \mathbf{x}, \mathbf{y}$. The coupling amplitudes $a_{pl}^{\prime mv}$ of the incident Gaussian beam mode with the fiber mode $\psi_{lmvp}(r, \theta)$ are given by (Pepeljugoski, 2003)

$$a_{pl}^{\prime mv} = \int_A d^2x \psi_{lmvp}(x) u_{pl'}(x'', w'_0, k') \quad (9)$$

where the integration is carried out over the area A of the fiber end face. Assuming that impulses from the transmitter induced electric fields at the input end face of MMF have the form $\sum_{pl} c_{pl} u_{pl'}(x'', w'_0, k') \delta(t)$ we write the impulse response of MMF $h(z, t)$ (Pepeljugoski, 2003)

$$h(z, t) = \sum_{\mu} w_{\mu} \exp(-\gamma_{\mu} z) \delta(t - \tau_{\mu} z) \quad (10)$$

where c_{pl} are the complex amplitudes, $w_{\mu} = \sum_{lmv \in \mu} w_{lmv'}$ is the mode power distribution (MPD), and

$$w_{lmv'} = \sum_{pl'} |c_{pl'} a_{pl'}^{\prime mv}|^2 \quad (11)$$

A typical p-i-n PD is characterized by the quantum efficiency η and the bandwidth Δf given by (Agrawal, 2002), (Malyshev, 2004)

$$\eta = \frac{P_{abs}}{P_{opt}^{in}} = \zeta (1 - r) (1 - \exp(-\alpha_{PD} d)) \quad (12)$$

$$\Delta f = \left[\left(\frac{2\pi d}{3.5 \bar{v}_d} \right)^2 + \left(2\pi \epsilon_0 \epsilon_r S \frac{(R_s + R_l)}{d} \right)^2 \right]^{-1/2} \quad (13)$$

where ζ is p-i-n PD internal quantum efficiency close to unity, P_{opt}^{in} is the incident optical power at the input of PD, P_{abs} is the optical power absorbed in PD, r is the reflection coefficient of the PD surface, α_{PD} is the PD material absorption coefficient, and d is the thickness of the PD absorption intrinsic layer, \bar{v}_d is the average charge carrier drift velocity in the PD absorption intrinsic layer, ϵ_0 is the free space permittivity, ϵ_r is the PD permittivity, S is the PD photosensitive area, R_s, R_l are the series and load resistances in the PD equivalent circuit, respectively. The p-i-n PD bandwidth Δf is determined by the carrier transit time and RC time constant of the p-i-n PD equivalent circuit.

4. SiGe Technology Based Novel Microwave Photonic Component

The SiGe/Si structures are promising candidates for the high-speed optoelectronics receivers due to the high operation rate, comparatively optical high absorption coefficient, the possibility of operation in the near IR spectrum from 850nm to 1550nm, low noise and compatibility with Si based electronic components. We propose an analytical model of the thin layer SiGe/Si OCMC structure with a detecting layer thickness of about $d = (0.5 \div 2) \mu\text{m}$. The numerical estimations based on this model show that a bandwidth of at least 20GHz can be achieved.

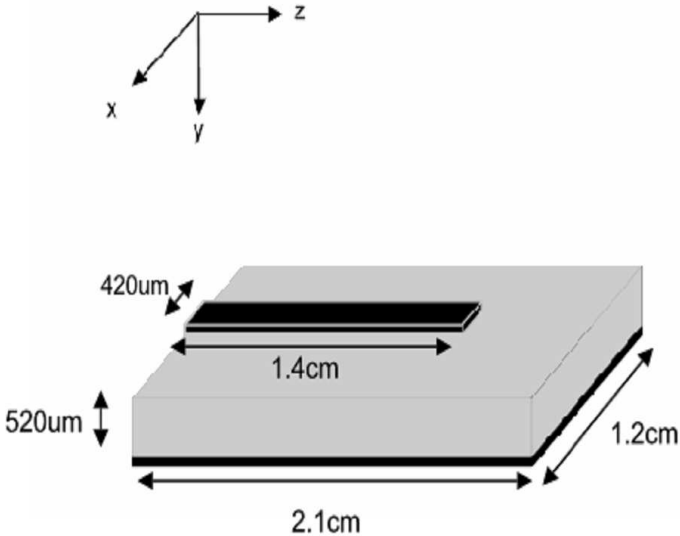


Fig. 3. Schematic view of an optically controlled microstrip converter (OCMC)

4.1 Physical Model of a SiGe Based OCMC

In UROOF technology, detection of the multiplexed MB OFDM UWB modulated optical signal is required. The down conversion from the optical domain to the UWB, or microwave (MW) domain can be modeled by an optically controlled load connected at the open end of a microstrip (MS) line. The direct optical control of MW devices and circuits is based on the physical process of carriers photo-generation within the device by the incident optical radiation having a photon energy $h\nu \geq E_g$ where h is the Planck constant, ν is the light frequency, and E_g is the semiconductor energy gap (Mathieu, 1998), (Seeds, 2002). As a result, the photo-induced electron-hole plasma produces a local change in the relative permittivity ϵ_r and conductivity σ of the substrate (Mathieu, 1998). The optical controlling technique has been successfully applied to MW devices such as directional couplers, phase shifters, attenuators, ultra-fast MW switches, etc. The advantages of this approach are following: low cost, low power consumption, high responsivity, flat spectral response over the desired band, low noise characteristics, possibility of creation of compact components which can be easily integrated with other electronic and photonics systems (Seeds, 2002).

Typically, optical control of MW devices is carried out in a steady-state regime. The down conversion from the optical domain to the MW domain can be modeled by an optically controlled load connected at the open end of the MS line. The conditions of the detection process are essentially different from the steady state optical control of the MS load. The input signal of the system in our case is the UWB modulated optical radiation fed from an optical fiber. Typically, the optical carrier power P_{opt} is comparatively low: $P_{opt} \sim 1mW$. For a multimode optical fiber with an optical beam radius $r_b \sim 10\mu m$, it yields a comparatively low intensity $I = P_{opt} / (\pi r_b^2) \sim 3W/mm^2$. In the proposed method we used OCMC consisting of an open ended MS line with a semiconducting substrate shown in Fig. 3. The optical beam, modulated by UWB RF signal, illuminates the substrate near the open end of the MS line.

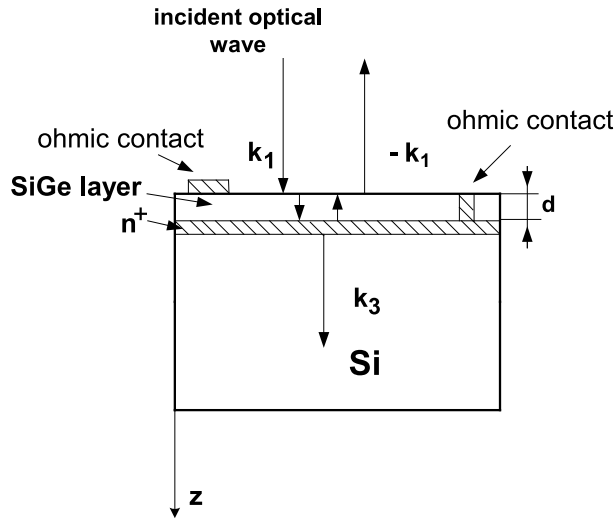


Fig. 4. Illuminated SiGe layer on a Si substrate

The efficiency of the optical-MW frequency down conversion depends on the ability to collect the photocarriers at the bottom contact. In the case of silicon technology, the thickness of conventional substrates is in the range of $350 - 500 \mu\text{m}$ which is very large compared to the diffusion length of the photocarriers $L_{n,p} = \sqrt{D_{n,p}\tau} \sim (10 \div 30) \mu\text{m}$. In the case of surface absorption characterized by large values of absorption coefficient α and consequently a very small absorption length $\sim \alpha^{-1}$, the effective photocarrier penetration depth is determined by the diffusion and drift properties of the photocarriers. The feasibility of the proposed OCMC device was experimentally verified by an open-ended MS line with $Z_0 = 50\Omega$ implemented on a high resistivity $\rho > 3000\Omega\text{cm}$ slightly p-type Si substrate shown in Fig. 3. The optical source was a tunable laser diode with wavelengths from $\lambda = 680$ up to $\lambda = 980\text{nm}$. It appeared to be that the results for the OCMC response function at the different levels of the optical power do not satisfy the requirements of the UWB RF signal detection.

An alternative approach has been proposed recently (Gupta, 2004), (Huang, 2006). It has been demonstrated experimentally that thin Ge-on-Si, or SiGe on Si layers of a thickness about one up to several micrometers can operate successfully as UWB RF signal detectors providing a bandwidth of about $(10 \div 20) \text{GHz}$ (Huang, 2006). For operation at longer wavelengths Ge-on-Si PDs with the bandwidth up to 21GHz at $\lambda = 1.31\mu\text{m}$ are attractive for monolithic optical receivers (Huang, 2006). A theoretical model of such thin film devices has not yet been developed to our best knowledge.

We have developed an analytical description of a SiGe/Si OCMC based on the photocarriers drift-diffusion model for photocarriers generated by a UWB modulated optical wave. Consider an infinite in the x, y directions layer of thickness d in the z direction placed on a semi-infinite in the z direction substrate presented in Fig. 4.

The electric and magnetic fields of the incident and reflected optical waves E_{1x}, H_{1y} in the free space $z < 0$, E_{2x}, H_{2y} in the layer $0 \leq z \leq d$, and E_{3x}, H_{3y} in the substrate $z > d$ are given by

$$z < 0 \rightarrow E_{1x} = [E_1^+ \exp(-ik_1z) + E_1^- \exp(ik_1z)]$$

$$\times \exp(i\omega_{opt}t) \quad (14)$$

$$H_{1y} = \frac{1}{Z_1} [E_1^+ \exp(-ik_1z) - E_1^- \exp(ik_1z)] \exp(i\omega_{opt}t) \quad (15)$$

$$0 \leq z \leq d \rightarrow E_{2x} = [E_2^+ \exp(-\gamma_2z) + E_2^- \exp(\gamma_2z)] \times \exp(i\omega_{opt}t) \quad (16)$$

$$H_{2y} = \frac{1}{Z_2} [E_2^+ \exp(-\gamma_2z) - E_2^- \exp(\gamma_2z)] \exp(i\omega_{opt}t) \quad (17)$$

$$z > d \rightarrow E_{3x} = E_3^+ \exp(-ik_3z) \exp(i\omega_{opt}t); \quad (18)$$

$$H_{3y} = \frac{1}{Z_3} E_3^+ \exp(-ik_3z) \quad (19)$$

Here the wave impedances of the media have the form

$$Z_1 = \sqrt{\frac{\mu_0}{\epsilon_0}} = 377\Omega; Z_2 = |Z_2| \exp i\theta; Z_3 = \sqrt{\frac{\mu_0}{\epsilon_0 \epsilon_{r3}}} \quad (20)$$

μ_0 is the free space permeability, the absorption layer wave impedance Z_2 is assumed to be complex, ϵ_{r3} is the permittivity of the substrate, ω_{opt} is the optical frequency,

$$k_1 = \frac{\omega}{c}, \gamma_2 = \frac{\alpha}{2} + i\beta, k_3 = \frac{\omega}{c} \sqrt{\epsilon_{r3}} \quad (21)$$

β is the propagation constant, and c is the speed of light in vacuum.

The standard solution of the boundary problem for the electric and magnetic fields in the layer between the surfaces $z = 0$ and $z = d$ yields the time averaged total optical intensity I_{opt}^{tot} in the layer consisting of the incident and reflected wave intensities $\langle P^+ \rangle$ and $\langle P^- \rangle$, respectively (Rao, 2000). It has the form

$$I_{opt}^{tot}(z) = \langle P^+ \rangle + \langle P^- \rangle \quad (22)$$

where

$$\begin{aligned} \langle P^+ \rangle &= \text{Re} \left(\frac{1}{2} E_{2x}^+(z, t) (H_{2y}^+(z, t))^* \right) \\ &= \text{Re} \left\{ \frac{|E_1^+|^2 \exp[-2 \text{Re}(\gamma_2)(z-d)] \left| 1 + \frac{Z_3}{Z_2} \right|^2}{2Z_2^* \left| \sinh(\gamma_2 d) \left[1 + \frac{Z_1 Z_3}{Z_2^2} \right] + \frac{(Z_1 + Z_3) \cosh(\gamma_2 d)}{Z_2} \right|^2} \right\} \end{aligned} \quad (23)$$

$$\begin{aligned} \langle P^- \rangle &= \text{Re} \left(\frac{1}{2} E_{2x}^-(z, t) (H_{2y}^-(z, t))^* \right) \\ &= \text{Re} \left\{ - \frac{|E_1^+|^2 \exp(2 \text{Re}(\gamma_2)(z-d)) \left| 1 - \frac{Z_3}{Z_2} \right|^2}{2Z_2^* \left| \sinh(\gamma_2 d) \left[1 + \frac{Z_1 Z_3}{Z_2^2} \right] + \frac{(Z_1 + Z_3) \cosh(\gamma_2 d)}{Z_2} \right|^2} \right\} \end{aligned} \quad (24)$$

Taking into account that according to (21) $2 \text{Re}(\gamma_2) = \alpha$ and substituting (23) and (24) into (22) we finally obtain

$$I_{opt}^{tot}(z) = I_0 \left[\frac{2Z_3 \cos \theta}{|Z_2|} \cosh(\alpha(z-d)) - \sinh(\alpha(z-d)) \left(1 + \frac{Z_3^2}{|Z_2|^2} \right) \right] \quad (25)$$

where

$$I_0 = \frac{2Z_1 P_{opt} \cos \theta}{A_{eff} |D|^2 |Z_2|}; P_{opt} = \frac{|E_1^+|^2 A_{eff}}{2Z_1}; A_{eff} = \pi r_b^2 \tag{26}$$

$$|D|^2 = \left| \sinh(\gamma_2 d) \left[1 + \frac{Z_1 Z_3}{Z_2^2} \right] + \frac{(Z_1 + Z_3)}{Z_2} \cosh(\gamma_2 d) \right|^2 \tag{27}$$

P_{opt} is the optical power of the incident wave in the free space $z < 0$, and r_b is the light beam radius. The explicit expression of $|D|^2$ in general case is hardly observable, and we do not present it here. It can be substantially simplified under the realistic quasi-resonance assumption for $\lambda_{opt} \sim 1\mu m$ and $d \sim (0.5 \div 2) \mu m$

$$\sin \beta d = 0, \beta d = \pi m, m = 1, 2, \dots \tag{28}$$

Then, a simplified expression of $|D|^2$ takes the form

$$\begin{aligned} |D|^2 &= \frac{(Z_1 + Z_3)^2}{|Z_2|^2} \cosh^2\left(\frac{\alpha}{2}d\right) + \sinh^2\left(\frac{\alpha}{2}d\right) \\ &+ \sinh^2\left(\frac{\alpha}{2}d\right) \left[1 + 2\frac{Z_1 Z_3 \cos 2\theta}{|Z_2|^2} + \frac{(Z_1 Z_3)^2}{|Z_2|^4} \right] \\ &+ \sinh(\alpha d) \frac{(Z_1 + Z_3) \cos \theta}{|Z_2|} \left[1 + \frac{Z_1 Z_3}{|Z_2|^2} \right] \end{aligned} \tag{29}$$

Now we evaluate the concentration of the photocarriers in the framework of the drift-diffusion model (Mathieu, 1998). The continuity equations for the photoinduced electron and hole concentrations $n(z, t)$ and $p(z, t)$ have the form, respectively,

$$\frac{\partial n}{\partial t} = n\mu_n \frac{\partial E}{\partial z} + \mu_n E \frac{\partial n}{\partial z} + D_n \frac{\partial^2 n}{\partial z^2} + g_n(z, t) - \frac{n - n_0}{\tau_n} \tag{30}$$

$$\frac{\partial p}{\partial t} = -p\mu_p \frac{\partial E}{\partial z} - \mu_p E \frac{\partial p}{\partial z} + D_p \frac{\partial^2 p}{\partial z^2} + g_p(z, t) - \frac{p - p_0}{\tau_p} \tag{31}$$

$$g_n(z, t) = g_p(z, t) = g(z, t) = \frac{\eta}{h\nu} \frac{\partial I(z, t)}{\partial z} \tag{32}$$

$$I(z, t) = I_{opt}^{tot}(z) [1 + f(t)] \tag{33}$$

Then the generation rates of electrons and holes $g_{n,p}(z, t) = g(z, t)$ can be written as follows

$$g(z, t) = g_0(z) + g_1(z, t); \tag{34}$$

$$g_0(z) = \frac{\eta}{h\nu} \frac{\partial I_{opt}^{tot}(z)}{\partial z} \tag{35}$$

$$g_1(z, t) = \frac{\eta}{h\nu} \frac{\partial I_{opt}^{tot}(z)}{\partial z} f(t) = g_0(z) f(t) \tag{36}$$

where $\tau_{n,p}$, $D_{n,p}$, $\mu_{n,p}$ are the lifetime, diffusion coefficients, and mobilities of electrons and holes, respectively, n_0 , p_0 are the equilibrium electron and hole concentrations, η is quantum

efficiency, E is the electrostatic field applied, and $f(t)$ is the UWB RF envelope of the optical carrier (25). Substituting (25) into equation (35) we obtain

$$g_0(z) = I_{01} \sinh(\alpha(z-d)) - I_{02} \cosh(\alpha(z-d)) \quad (37)$$

where

$$I_{01} = \frac{\eta\alpha}{hv} I_0 \frac{2Z_3 \cos\theta}{|Z_2|}; I_{02} = \frac{\eta\alpha}{hv} I_0 \left(1 + \frac{Z_3^2}{|Z_2|^2}\right) \quad (38)$$

Typically, in the photoinduced plasma, the electron and hole relaxation time is much smaller than the carrier lifetime, and electroneutrality condition can be applied (Gary, May 2006), (Gary, September 2006), (Mathieu, 1998).

$$n = p \quad (39)$$

At the illuminated surface of the semiconductor the strong injection mode and ambipolar diffusion are realized when $n \gg n_0, p_0$ so that the ambipolar mobility μ_a vanishes (Arnoud, 2002), (Arnoud, 2004)

$$\mu_a = \frac{\mu_n \mu_p (p-n)}{\mu_p p + \mu_n n} = 0 \quad (40)$$

In our case the thin layer is entirely occupied by the strong injection mode region. Under such conditions continuity equations (30), (31) reduce to the ambipolar diffusion equation (Mathieu, 1998)

$$\frac{\partial n}{\partial t} = D_a \frac{\partial^2 n}{\partial z^2} - \frac{n}{\tau} + g(z, t) \quad (41)$$

where it is assumed that $\tau_n = \tau_p = \tau$. According to expressions (34)-(36) we separate the steady-state and time dependent parts $n_{ph0}(z)$, $n_1(z, t)$ of the photocarrier concentration n .

$$n = n_{ph0}(z) + n_1(z, t) \quad (42)$$

Substituting (42) into equation (41) we obtain two equations for $n_{ph0}(z)$ and $n_1(z, t)$, respectively

$$D_a \frac{\partial^2 n_{ph0}}{\partial z^2} - \frac{n_{ph0}}{\tau} + g_0(z) = 0 \quad (43)$$

$$\frac{\partial n_1}{\partial t} = D_a \frac{\partial^2 n_1}{\partial z^2} - \frac{n_1}{\tau} + g_0(z) f(t) \quad (44)$$

where the ambipolar diffusion coefficient D_a is given by (Arnoud, 2002)

$$D_a = \frac{2D_n D_p}{(D_n + D_p)} \quad (45)$$

We use the boundary conditions of the mixed type, assuming a finite surface recombination velocity s_0 on the top surface $z = 0$ and a kind of an ohmic contact at the interface between the layer and the substrate which yields (Gary, May 2006)

$$\frac{\partial n}{\partial z} \Big|_{z=0} = \frac{s_0}{D_a} n(z=0); n(z=d) = 0 \quad (46)$$

We are interested in the time-dependent part of the photocarrier concentration $n_1(z, t)$ which is responsible for the UWB RF signal detection. Hence we should solve equation (44) with the

boundary conditions (46). In general case of the UWB RF signal $f(t)$ we carry out the Fourier transform of equation (44) with respect to time. We obtain

$$D_a \frac{\partial^2 N_1(z, \omega)}{\partial z^2} - \left(i\omega + \frac{1}{\tau} \right) N_1(z, \omega) + g_0(z) F(\omega) = 0 \quad (47)$$

where

$$N_1(z, \omega) = \int_{-\infty}^{\infty} n_1(z, t) \exp(-i\omega t) dt; F(\omega) = \int_{-\infty}^{\infty} f(t) \exp(-i\omega t) dt \quad (48)$$

The boundary conditions (46) can be applied to the general solution of (47). The result has the form.

$$\begin{aligned} N_1(z, \omega) &= \frac{F(\omega) \tau (1 - i\omega\tau)}{(\alpha^2 L_{aeq}^2 - 1) [1 + (\omega\tau)^2]} \\ &\times \left\{ -g_0(z) + \frac{1}{\left[\frac{1}{L_{aeq}} \cosh(d/L_{aeq}) + \frac{s_0}{D_a} \sinh(d/L_{aeq}) \right]} \right. \\ &\times \left[\left[\frac{\partial g_0}{\partial z}(0) - \frac{s_0}{D_a} g_0(0) \right] \sinh\left[\frac{(z-d)}{L_{aeq}} \right] \right. \\ &\left. \left. + g_0(d) \left[\frac{1}{L_{aeq}} \cosh\left(\frac{z}{L_{aeq}} \right) + \frac{s_0}{D_a} \sinh\left(\frac{z}{L_{aeq}} \right) \right] \right] \right\} \quad (49) \end{aligned}$$

where

$$L_{aeq}^2 = \frac{D_a \tau (1 - i\omega\tau)}{1 + (\omega\tau)^2} \quad (50)$$

4.2 Simulation and Design of a SiGe Based OCMC

Expression (49) for $N_1(z, \omega)$ averaged over the layer thickness d can be used as the frequency response of the illuminated layer when $f(t) = \delta(t)$ and consequently $F(\omega) = 1$. Using the explicit expression (37) for $g_0(z)$ we obtain

$$\begin{aligned} \bar{N}_1(\omega) &= \frac{1}{d} \int_0^d N_1(z, \omega) dz = \frac{F(\omega) \tau (1 - i\omega\tau)}{d (\alpha^2 L_{aeq}^2 - 1) [1 + (\omega\tau)^2]} \\ &\times \left\{ \frac{1}{\alpha} [I_{01} (\cosh(\alpha d) - 1) + I_{02} \sinh(\alpha d)] \right. \\ &\left. + \frac{1}{\left[\frac{1}{L_{aeq}} \cosh(d/L_{aeq}) + \frac{s_0}{D_a} \sinh(d/L_{aeq}) \right]} \right. \\ &\times \left[\left[\frac{\partial g_0}{\partial z}(0) - \frac{s_0}{D_a} g_0(0) \right] L_{aeq} \left[1 - \cosh\left(\frac{d}{L_{aeq}} \right) \right] \right. \\ &\left. \left. + g_0(d) \left[\sinh\left(\frac{d}{L_{aeq}} \right) + \frac{s_0 L_{aeq}}{D_a} \left(\cosh\left(\frac{d}{L_{aeq}} \right) - 1 \right) \right] \right] \right\} \end{aligned}$$

The results of the numerical evaluations of the response function $|\bar{N}_1(\omega)|$ for typical values of material parameters of SiGe on Si are presented in Fig. 5.

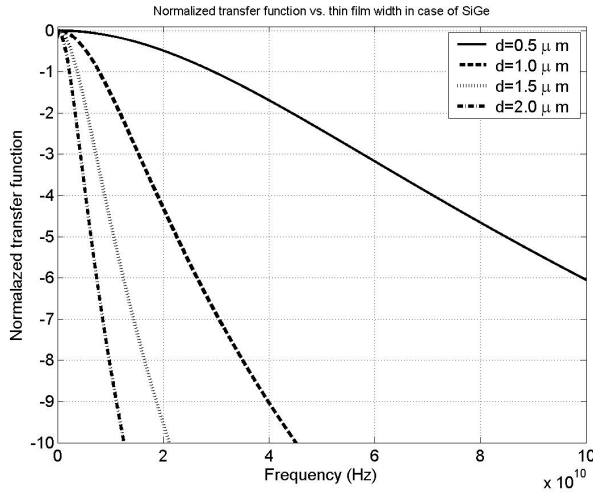


Fig. 5. Normalized transfer function $|\overline{N}_1(\omega)|$ for different SiGe layer thicknesses $d = 0.5; 1; 1.5; 2\mu m$

The power absorption coefficient of Si_xGe_{1-x} compounds is $\alpha \sim 10^3 cm^{-1}$ in the interval of $\lambda_{opt} \sim 850nm$. The electron mobility reaches its maximum value of $\mu_n = 7700cm^2 / (Vs)$ for $Si_{0.5}Ge_{0.5}$. For smaller concentrations of Ge the charge carrier mobilities are closer to those of a pure Ge, while in the opposite case they tend to the values of charge carrier mobilities in a pure Si.

5. Simulation and Experimental Results for UWB OFDM Transmission System Performance

5.1 Simulation Results

The numerical simulations have been carried out for the parallel RF/parallel optics architecture. We investigated the mixing of 10 RF channels each one with a 0.5GHz bandwidth. The resulting signal was applied to the multimode 10GHz VCSEL, the modulated optical signal was transmitted through the 50m MMF and at the output detected by the p-i-n PD. The simulation results are shown in Fig. 6.

The mixed RF spectrum at the VCSEL input, the modulated optical signal at the VCSEL output, and the detected RF spectrum are shown in the upper box, the middle box, and the lower box of Fig. 6, respectively. The internal structure of one of the RF channels located at 3.5GHz central frequency at the corresponding transmission stages is shown in Fig. 7. This channel includes 128 subcarriers and is transmitting 496Mb/s over 0.5GHz bandwidth. In order to study the dispersion influence on the quality of the transmitted MB OFDM signals we have carried out simulations for different MMF lengths. A short MMF with a length of 50m has an almost flat frequency response up to the frequency of 10GHz. The strongly inhomogeneous behavior in such a case in the vicinity of 10GHz is caused by the VCSEL bandwidth limitations. The p-i-n PD used in these measurements has the bandwidth of about 25GHz. The bandpass filter

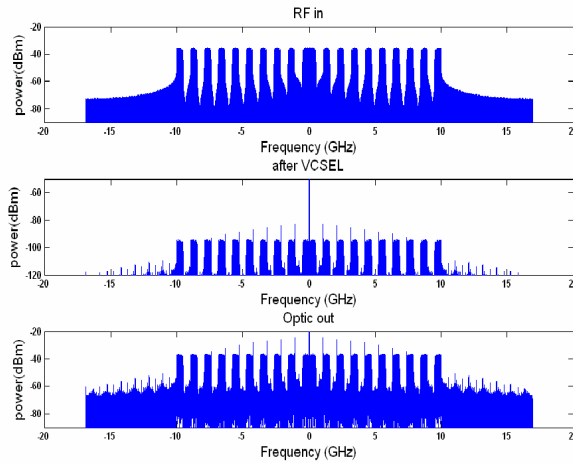


Fig. 6. The mixed RF channels spectrum before VCSEL (the upper box), after VCSEL (the middle box), and after the detection (the lower box)

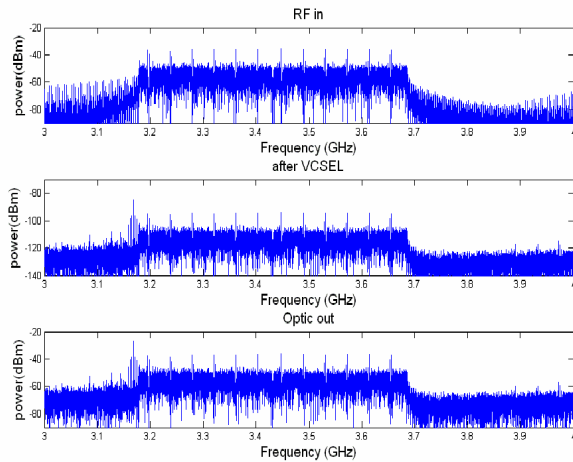


Fig. 7. The internal spectral structure of the individual UWB OFDM channel before VCSEL (the upper box), after VCSEL (the middle box), and after the detection (the lower box)

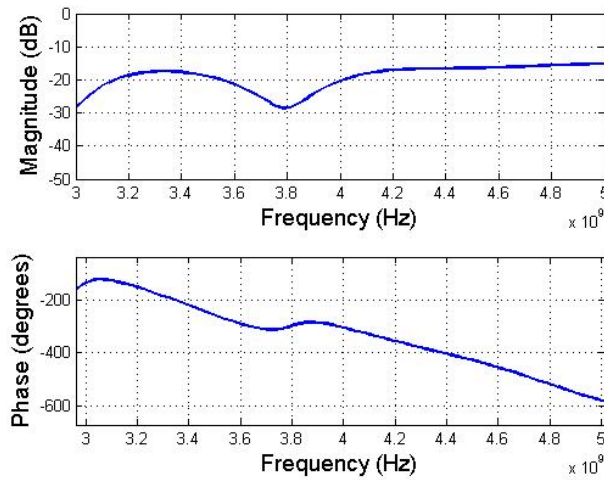


Fig. 8. The calculated magnitude (the upper box) and the phase (the lower box) of the 650m MMF transfer function

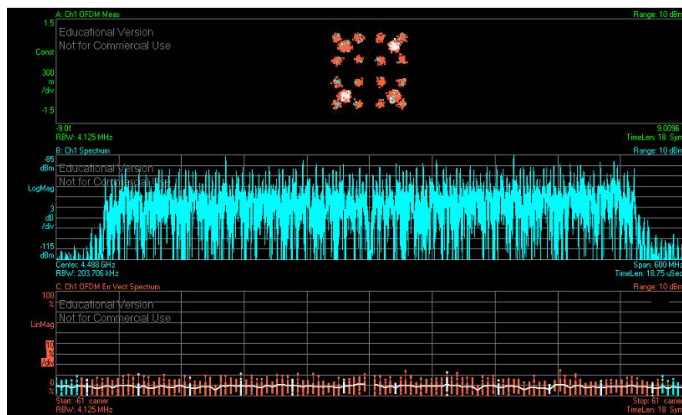


Fig. 9. Simulation results for the optical link response (MMF length 650m, TFC7 frequency interval 4.2 – 4.7GHz)

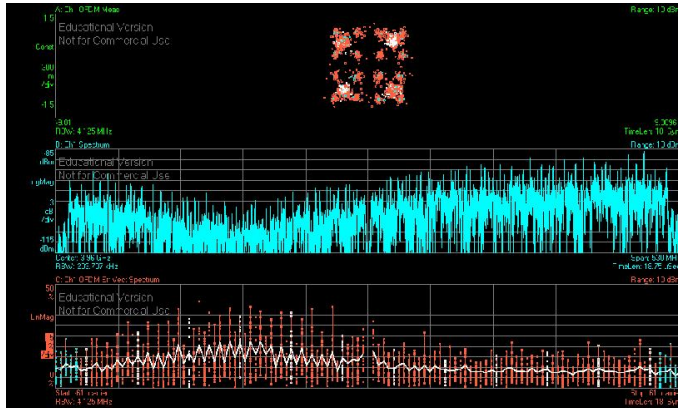


Fig. 10. Simulation results for the optical link response (MMF length $650m$, TFC6 frequency interval $3696 - 4224MHz$)

behavior of the MMF caused by the multimode dispersion is strongly manifested for longer MMFs. The magnitude and the phase of the $650m$ MMF are shown in Fig. 8.

The simulations have been carried out for the time frequency code 6 (TFC6) and TFC7 bands of MB OFDM UWB signals determined by the frequency intervals ($3696 \div 4224$) MHz and ($4224 \div 4752$) MHz, respectively. The simulation results for the frequency response and the constellation diagram of TFC6 and TFC7 MB OFDM signals transmitted through the $650m$ MMF are shown in Figs. 9, 10. In the TFC7 frequency range the transfer function magnitude curve is flat, and therefore the constellation diagram and the spectrum of the TFC7 MB OFDM signals are of high quality and not affected by the MMF dispersion as it is seen from Fig. 9. On the contrary, in the TFC6 frequency range the transfer function magnitude has a notch, and for this reason, the constellation and the spectrum of the TFC6 MB OFDM signals strongly deteriorate as it is seen from Fig. 10. Consequently, the transmission of the multiplexed MB OFDM signals is limited by the MMF length of about $100m$.

5.2 The Experimental Results for MB OFDM Signal Transmission

In our experiments, MB OFDM UWB signal was directly applied to the VCSEL and after propagation through the MMF was detected by the p-i-n PD. The objective of the measurements was to study the performance of the proposed link by means of the packet error rate (PER). The measurements have been carried out for the TFC5 determined by the frequency interval ($3168 \div 3696$) MHz, TFC6 and TFC7 bands of MB OFDM UWB signals. Fig. 11 presents the PER versus MMF length for the optical link.

The PER dependence versus the MMF length for the different MB OFDM UWB signals shows a peculiar behavior. The PER of the TFC7 band located at higher carrier frequency ($4.488GHz$) stays flat and has values of an order of magnitude of 10^{-6} for MMF lengths up to $1km$. However, the PER in the case of TFC5 band located at the $3.5GHz$ carrier frequency and the TFC6 band located at the $4.0GHz$ carrier frequency increases dramatically for the MMF lengths longer than $300m$.

In order to understand this behavior of the PER versus MMF length we have measured the MMF transfer function for different MMF lengths. The short MMF with a length of $10m$ has

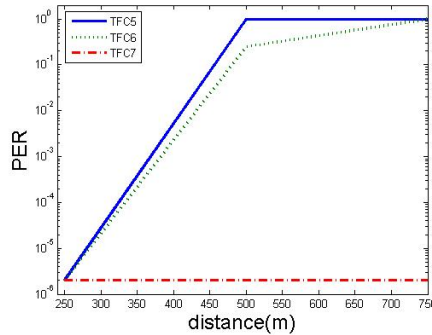


Fig. 11. The PER dependence on the MMF length for TFC5, TFC6, and TFC7 frequency bands for the optical link

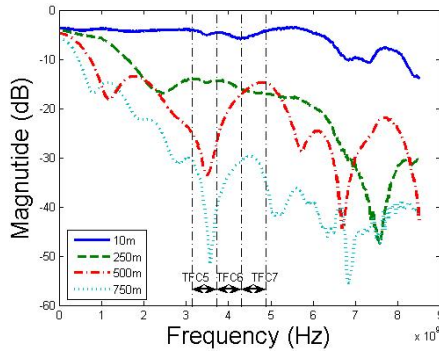


Fig. 12. The measurement results for the optical link frequency response

an almost flat frequency response up to the frequency of 10GHz as it is shown in Fig. 12. The strongly inhomogeneous behavior in such a case in the vicinity of 10GHz is caused by the VCSEL bandwidth limitations. The p-i-n PD used in these measurements has the bandwidth of about 25GHz. The bandpass filter behavior of the MMF caused by the multimode dispersion is strongly pronounced for longer MMFs.

According to Fig. 12, the MMF transfer function has strong notches in the frequency range of TFC5 band at the fiber lengths longer than 500m. These experimental results are in good accord with the simulations results mentioned above.

6. Conclusions

We proposed two possible architectures for high spectral efficiency optical transmission of OFDM UWB signals beyond 40Gb/s: the parallel RF/serial optics architecture and parallel RF/parallel optics architecture. We presented the detailed theoretical analysis and numerical results for a novel OCMC detecting device based on SiGe/Si structure. We have carried out numerical simulations for the parallel RF/parallel optics architecture and predicted its

highly quality performance. We investigated theoretically and experimentally the optical link consisted of the directly modulated VCSEL, MMF, and p-i-n PD.

7. References

- Agrawal, G.P. (2002) *Fiber-Optic Communication Systems*, Wiley, ISBN 0-471-21571-6, New York
- Armstrong, J. (2009). OFDM for Optical Communications, *IEEE Journal of Lightwave Technology*, Vol. 27, No. 3 (February 2009) 189-204, ISSN 0733-8724
- Arnould, J.-D.; Vilcot, A. & Meunier, G. (2002). Toward a Simulation of an Optically Controlled Microstrip Line at 10 GHz, *IEEE Trans. on Magnetics*, Vol. 38, No. 2, (March 2002) 681-684, ISSN 0018-9464.
- Arnould, J.-D.; R. Gary, R. & Vilcot, A. (2004). 3D Photo-induced Load Modeling for Optically Controlled Microstrip Line, *Microwave and Optical Technology Letters*, Vol. 40, No. 5 (March 2004) 356-359, ISSN 0895-2477
- Ben-Ezra, Y.; Ran, M.; Mahlab, U.; Lembrikov, B. I. & Haridim, M. (2008). High Spectral Efficiency Optical Transmission of OFDM Ultra-Wideband Signals beyond 40 Gb/s, *Proceedings of 10th Anniversary International Conference on Transparent Optical Networks (ICTON 2008)*, pp.186-189, ISBN 978-1-4244-2625-6, June 2008, National Institute of Telecommunications, Athens
- Bigo, S.(2004). Multiterabit DWDM terrestrial transmission with bandwidth-limiting optical filtering. *IEEE Journal of Selected Topics in Quantum Electronics*, Vol. 10, No. 2, (March/April 2004) 329-340, ISSN 1077-260X
- Couch II, L. W. (2001). *Digital and Analog Communication Systems*, Prentice Hall, ISBN 0-13-089630-6, Upper Saddle River, New Jersey
- Gary, R.; Arnould, J.-D. & Vilcot, A. (2006). Semi-analytical modeling and analysis in three dimensions of the optical carrier injection and diffusion in a semiconductor substrate, *Journal of Lightwave Technology*, Vol. 24, No. 5, (May 2006) 2163-2170, ISSN 0733-8724
- Gary, R.; Arnould, J.-D. & Vilcot, A. (2006). Semi-analytical computation and 3D modeling of the microwave photo-induced model in CPW technology. *Microwave and Optical Technology Letters*, Vol. 48, No. 9, (September 2006) 1718-1721, ISSN 0895-2477
- Ghavami, M.; Michael, L.B. & Kohno, R. (2005). *Ultra Wideband Signals and Systems in Communication Engineering*, Wiley, ISBN-10 0-470-86571-5(H/B), Chichester, England
- Gupta, A.; Levitan, S.P.; Selavo, L. & Chiarelli, D. M. (2004). High-speed optoelectronics receivers in SiGe, *Proceedings of the 17th International Conference on VLSI Design*, pp. 957-960, ISBN 0-7695-2072-3, Mumbai, India, January 2004, IEEE Computer Society, Washington, DC
- Huang, Z.; Kong, N.; Cuo, X.; Liu, M.; Duan, N.; Beck, A.L.; Banerjee, S.K. & Campbell, J. C. (2006). 21-GHz-bandwidth Germanium-on-Silicon photodiode using thin SiGe buffer layers, *IEEE Journal of Selected Topics in Quantum Electronics*, Vol. 12, No. 6, (November/December 2006) 1450-1454, ISSN 1077-260X
- IEEE, P802.3ba 40 Gb/s and 100 Gb/s Ethernet Task Force. <http://www.ieee802.org/3/ba/>
- Jäger, D. (2003). Microwave Optical Interaction Devices, In: *Microwave Photonics*, Vilcot, A.; Cabon, B. & Chazelas, J. (Ed.), 82-91, Kluwer Academic Press, ISBN 1-4020-7362-3, Boston
- Koyama, F. (2006). Recent advances of VCSEL photonics. *Journal of Lightwave Technology*, Vol. 24, No. 12, (December 2006) 4502-4513, ISSN 0733-8724

- Kshetrimayum, R. S. (2009). An Introduction to UWB Communication Systems. *Potentials, IEEE*, Vol. 28, Issue 2, (March-April 2009) 9-13, ISSN 0278-6648
- Malyshev, S. & A. Chizh, A. (2004). State of the art high-speed photodetectors for microwave photonics applications, *Microwaves, Radar and Wireless Communications, MIKON-2004 15 International Conference on*, Vol. 3, issue 17-19, 765-775, May 2004, ISBN 83-906662-7-8, Warsaw
- Mathieu, H. (1998). *Physique des semiconducteurs et des composants electroniques*. Masson, ISBN 2-225-83151-3, Paris
- Pepeljugoski, P.; Golovich, S.E.; Ritger, A. John; Kolesar, P. & Risteski, A. (2003). Modeling and simulation of next-generation multimode fiber links. *Journal of Lightwave Technology*, Vol. 21, No. 5, (May 2003) 1242-1255, ISSN 0733-8724
- Ran, M; Ben Ezra, Y. & Lembrikov B.I. (2009). Ultra-wideband Radio-over-optical-fibre Technologies, *In Short-Range Wireless Communications*, Kraemer, R. & Katz, M. D. (Eds.), 271-327, Wiley, ISBN 978-0-470-69995-9 (H/B), Chichester, England
- Rao, N.N.(2000). *Elements of Engineering Electromagnetics*, Prentice Hall, ISBN 0-13-013201-2, London
- Seeds, A. J. (2002). Microwave Photonics, *IEEE Trans. Microwave Theory, Tech., MTT-50*, 3, 877-887, ISSN 0018-9480
- Shieh, W.; Bao, H. & Tang, Y. (2008). Coherent optical OFDM: theory and design. *Optics Express*, Vol.16, No. 2, (January 2008) 841-859, ISSN 1094-4087
- Winzer, J. P. & Essiambre, R.-J. (2006). Advanced Optical Modulation Formats, *Proceedings of the IEEE*, Vol.94, No. 5 (May 2006) 952-985, ISSN 0018-9219
- Winzer, J. P. & Essiambre, R.-J. (2006). Advanced Modulation Formats for High-Capacity Optical Transport Networks, *IEEE Journal of Lightwave Technology*, Vol. 24, No.12 (December 2006). 4711-4728, ISSN 0733-8724
- Yang, L. & Giannakis, G.B. (2004). Ultra-Wideband Communications. *IEEE Signal Processing Magazine*, Vol. 21, No. 6; (November 2004) 26-54, ISSN 1053-5888

Nonlinear Impairment Compensation using Backpropagation

Ezra Ip¹ and Joseph M. Kahn²

¹*NEC Labs America, Princeton, NJ, USA*

²*Stanford University, Stanford, CA, USA*

1. Introduction

The ultimate information capacity of fiber is limited by the Kerr nonlinearity, wherein the refractive index of the waveguide changes in proportion to the signal intensity. Nonlinearity makes it impossible to achieve an arbitrarily high capacity by increasing the launched power, as nonlinear distortion ultimately grows faster than the signal-to-noise ratio (SNR). At low launched power, system performance is limited by additive white Gaussian noise (AWGN), so the capacity increases with power. At high power, however, nonlinear effects dominate. For a given channel, there exists an optimum launched power and ultimate capacity that are dependent on the system design parameters. The capacity of fiber has been studied in (Mitra & Stark, 2001) and (Essiambre et al., 2008).

Recently, coherent optical receivers have begun to approach technological maturity. In a coherent receiver, the optical signal is downconverted to the electronic domain, preserving all relevant information on the optical electric fields in the two polarizations. The baseband equivalent electrical signals can be sampled and processed by a digital signal processor (DSP), enabling software algorithms to compensate channel impairments (Ip, et al. 2008).

Various methods of compensating nonlinearity have been proposed. It was shown in (Ho & Kahn, 2004) that in zero-dispersion fiber, interaction between nonlinearity and noise, known as nonlinear phase noise (NLPN), causes the received constellation to be spiral-shaped. A receiver can partially compensate NLPN by either de-rotating the received signal by a phase proportional to the received power, or by using modified decision boundaries. Improvement in system performance by 0.5 to 1 dB has been observed in submarine systems with low local dispersion and near-perfect dispersion compensation per span (Charlet et al., 2006).

Nonlinear phase rotation has also been used in orthogonal frequency-division multiplexing (OFDM) systems, where it is called self-phase modulation compensation (SPMC). In (Lowery, 2007a), transmitter-side SPMC was proposed, while (Lowery, 2007b) showed that further performance improvement can be obtained by splitting the SPMC between the transmitter and receiver. An investigation of the performance dependence on the dispersion map was carried out in (Liu & Tkach, 2009).

Signal propagation is ultimately governed by a nonlinear Schrödinger equation (NLSE). We shall see later that the efficacy of a nonlinear compensation algorithm depends on how

accurately it estimates the optical signal amplitude at each point in the fiber. In the aforementioned algorithms, the signal amplitude at the receiver and/or transmitter is assumed to be an accurate estimator of the signal profile in the fiber, and nonlinear compensation is applied using the received and/or transmitted signal(s). For zero-dispersion fiber, in which signal amplitude changes are small, arising only from noise, this is a good assumption, so performance improvement has been observed in submarine systems. In systems where local dispersion exceeds a symbol period, however, nonlinear phase rotation fails (Ip & Kahn, 2008), as interaction between intersymbol interference (ISI) and nonlinearity gives rise to “intra-channel” nonlinear effects, which have been studied in (Essiambre et al, 1999). As a first-order approximation, it has been assumed that the nonlinear phase distortion at a given symbol depends not only on the instantaneous amplitude, but on the amplitude profile of the received signal spanning a time interval equal to the fiber’s impulse response duration. An intra-channel four-wave mixing (IFWM) compensation scheme was studied in (Lau et al., 2008), and can lead to a small improvement in performance.

The ultimate nonlinear compensation method is backpropagation, which inverts the NLSE. In this framework, receiver-based optical dispersion compensation or electronic linear equalization can be seen as special cases of backpropagation where the receiver inverts only chromatic dispersion (CD). Similarly, mid-span phase conjugation is an example of backpropagation where the second half of the transmission link inverts the impairments of the first half (Chowdhury & Essiambre, 2004). Electronic backpropagation was first studied in (Roberts et al., 2006) as a transmitter-side compensation method, since in the absence of coherent detection, manipulation of the field is only possible at the modulator. With coherent detection, however, recovery of the received electric field enables receiver-side backpropagation, which was first studied in (Mateo et al, 2008). Receiver-side backpropagation has the advantage that it can ultimately be adaptive without the need for a feedback channel.

In this work, we review the principles of backpropagation and present recent results. Since backpropagation requires solving the NLSE, we begin by reviewing techniques for finding its numerical solutions. This is an area which has been well studied in simulation of optical networks. We will review split-step methods, emphasizing the length scales of different fiber effects, the computational costs of different algorithms, the step size requirements, and their dependence on system parameters. Backpropagation will then be introduced, firstly for single-polarization transmission for a single wavelength channel. In later sections, we will generalize backpropagation for wavelength-division-multiplexed (WDM) systems and for dual-polarization transmission. Simulation results will be presented.

2. Signal Propagation

2.1 Nonlinear Schrödinger Equation (NLSE)

Propagation in optical fiber is affected by a combination of linear and nonlinear phenomena. At low symbol rates and short transmission distances, where pulse spreading due to polarization-mode dispersion (PMD) is confined well within a symbol period, we can model signal propagation by a scalar nonlinear Schrödinger equation (NLSE) (Agrawal, 2001):

$$\frac{\partial E}{\partial z} = (\hat{D} + \hat{N})E \quad (1)$$

$$\hat{D} = -\frac{1}{2}\alpha - j\frac{\beta_2}{2!}\frac{\partial^2}{\partial t^2} + \frac{\beta_3}{3!}\frac{\partial^3}{\partial t^3} \tag{2}$$

$$\hat{N} = j\gamma|E|^2 \tag{3}$$

where E is the signal electric field, \hat{D} and \hat{N} are the linear and nonlinear operators, and α , β_2 , β_3 and γ are the fiber's attenuation, group velocity dispersion, dispersion slope, and nonlinear coefficients, respectively. In (1)–(3), we have specified the electric field in a moving co-ordinate system that propagates at the group velocity of the fiber, so the $\partial/\partial t$ term has been neglected.

It has been shown that the NLSE is an accurate model for a wide variety of optical phenomena, including single-wavelength and dense wavelength-division-multiplexed (DWDM) systems, solitons, and ultra-short pulses down to a few optical cycles in duration. Only in very special conditions (e.g., solitons) does the NLSE yield analytical solutions. In general, the NLSE must be solved numerically. Various solution methods have been developed, including finite-difference methods and split-step methods (SSMs). The latter are generally preferred because of the computational advantage of the fast Fourier transform and related transforms.

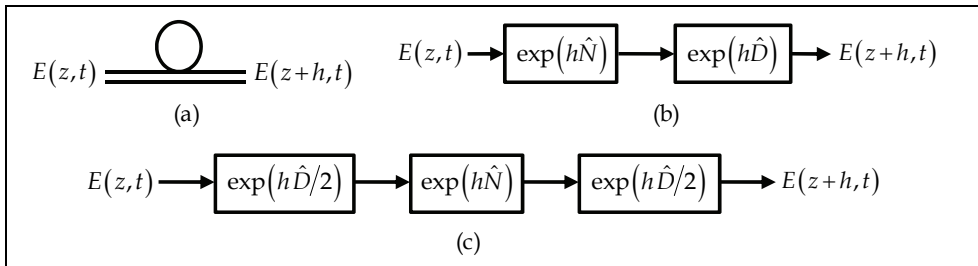


Fig. 1. (a) Propagation through a fiber section of length h modeled using the (b) asymmetric split-step method, and (c) symmetric split-step method.

In the split-step method, the fiber is divided into sections, where for each section we perform the integration:

$$E(z+h, t) = \exp\left(h\left(\hat{D} + \hat{N}\right)\right)E(z, t). \tag{4}$$

Although the linear and nonlinear operators can each be evaluated exactly when they appear in isolation, this is not the case in (4). Two popular approximations to (4) are the asymmetric split-step method (A-SSM) approximation (Fig. 1a):

$$E(z+h, t) \approx e^{h\hat{D}}e^{h\hat{N}}E(z, t), \tag{5}$$

and the symmetric split-step method (S-SSM) approximation (Fig. 1b), where the linear operator is split into two parts to be evaluated on either side of the nonlinear operator:

$$E(z+h, t) \approx e^{h\hat{D}/2}e^{h\hat{N}}e^{h\hat{D}/2}E(z, t). \tag{6}$$

The accuracy of the two approximations can be compared using the Baker-Hausdorff formula (Weiss & Maradudin, 1962):

$$\exp(\hat{a})\exp(\hat{b}) = \exp\left(\hat{a} + \hat{b} + \frac{1}{2}[\hat{a}, \hat{b}] + \frac{1}{12}[\hat{a} - \hat{b}, [\hat{a}, \hat{b}]] + \dots\right), \quad (7)$$

where $[\hat{a}, \hat{b}] = \hat{a}\hat{b} - \hat{b}\hat{a}$ is the commutator. It can be shown that the A-SSM and S-SSM lead to:

$$e^{h\hat{D}}e^{h\hat{N}} = \exp\left(h(\hat{D} + \hat{N}) + \frac{1}{2}h^2[\hat{D}, \hat{N}] + \dots\right). \quad (8)$$

$$e^{h\hat{D}/2}e^{h\hat{N}}e^{h\hat{D}/2} = \exp\left(h(\hat{D} + \hat{N}) + \frac{1}{6}h^3\left[\hat{N} + \frac{\hat{D}}{2}, \left[\hat{N}, \frac{\hat{D}}{2}\right]\right] + \dots\right). \quad (9)$$

In (8) and (9), all other terms inside the exponential apart from $h(\hat{D} + \hat{N})$ are error terms.

When high accuracy is required, the S-SSM has superior performance because the error is third order in h , whereas the error in the A-SSM is only second order in h . Split-step methods with accuracy higher than third order have been studied in (Muslu & Erbay, 2005), but have higher complexity. In backpropagation, high accuracy is generally not required because the signal is already corrupted by noise. Depending on the SNR and the power penalty requirement, a global relative accuracy of $\sim 10^{-3}$ is typically sufficient. Thus, computational cost, and the ability to parallelize and pipeline the algorithm are more pertinent considerations for real-time implementations. The S-SSM is considered here because it is possible to combine the linear half-step operators between adjacent sections so there is no difference between the complexities of S-SSM and the A-SSM (Fig. 3c).

To propagate a signal using (5) or (6), we can evaluate the linear operator as a multiplication by an all-pass filter in the frequency domain:

$$\begin{aligned} \mathcal{F}\left\{\exp(h\hat{D})E(z,t)\right\} &= \exp\left(h\mathcal{F}\left\{\hat{D}\right\}\right)\mathcal{F}\left\{E(z,t)\right\} \\ &= \exp\left(\left(-\frac{\alpha}{2} + j\frac{\beta_2}{2!}\omega^2 + j\frac{\beta_3}{3!}\omega^3\right)h\right)E(z,\omega) \end{aligned} \quad (10)$$

where $E(z,\omega)$ is the Fourier transform of the time-domain signal $E(z,t)$. This is known as the split-step Fourier method (SSFM).

The nonlinear operator, on the other hand, is most easily evaluated as a phase rotation in time:

$$\exp(h\hat{N})E(z,t) = \exp\left(j\gamma h|E(z,t)|^2\right)E(z,t). \quad (11)$$

In contrast with the linear operator, the nonlinear operator depends on signal amplitude. One way to improve the accuracy of the SSM is to use the trapezoidal rule for the integral of \hat{N} . For the S-SSM, we have (Agrawal, 2001):

$$\begin{aligned} E(z+h,t) &= \exp\left(\frac{h}{2}\hat{D}\right)\exp\left(\int_z^{z+h}\hat{N}(z')dz'\right)\exp\left(\frac{h}{2}\hat{D}\right)E(z,t) \\ &\approx \exp\left(\frac{h}{2}\hat{D}\right)\exp\left(h\frac{\hat{N}(z+h)+\hat{N}(z)}{2}\right)\exp\left(\frac{h}{2}\hat{D}\right)E(z,t). \end{aligned} \quad (12)$$

Since $\hat{N}(z+h) = j\gamma |E(z+h,t)|^2$ depends on the output, (12) is solved iteratively using the numerical procedure in Fig. 2. We initially assume that $\hat{N}(z+h) \approx \hat{N}(z)$. Using (12), we compute an updated estimate of the output, $E_{new}(z+h,t)$, which enables a new estimate for $\hat{N}(z+h)$. We then apply (12) again, and so forth, until convergence or until a preset number of iterations is reached. This method is known as the iterative, symmetric SSFM (IS-SSFM). Since iteration is time-consuming, a faster, but less accurate non-iterative method can also be used. These are:

$$E(z+h,t) \approx \exp(h\hat{D}) \exp(h\hat{N}(z)) E(z,t), \text{ and} \quad (13)$$

$$E(z+h,t) \approx \exp\left(\frac{h}{2}\hat{D}\right) \exp(h\hat{N}(z+h/2)) \exp\left(\frac{h}{2}\hat{D}\right) E(z,t) \quad (14)$$

for the A-SSM and S-SSM, respectively. Note that for non-iterative case (NA-SSM), the order of the operators is based on the heuristic that nonlinear effects occur at high power, which is typically found at the beginning of a fiber section unless backward Raman pumping is used, so for large step sizes, the nonlinear operator should be applied first.¹

The SSFM algorithm is thus summarized in Fig. 3. The linear and nonlinear operators are successively evaluated in the frequency- and time-domains, with fast Fourier transforms (FFT) and inverse fast Fourier transforms (IFFT) used to switch between the domains. The complexity of the algorithm is dominated by the Fourier transforms, since the evaluation of an N -point FFT or IFFT requires $O(N \log N)$ operations, whereas the filtering and phase rotation operations in (10) and (11) are only $O(N)$.

¹ In backpropagation, we would apply the linear operator first.

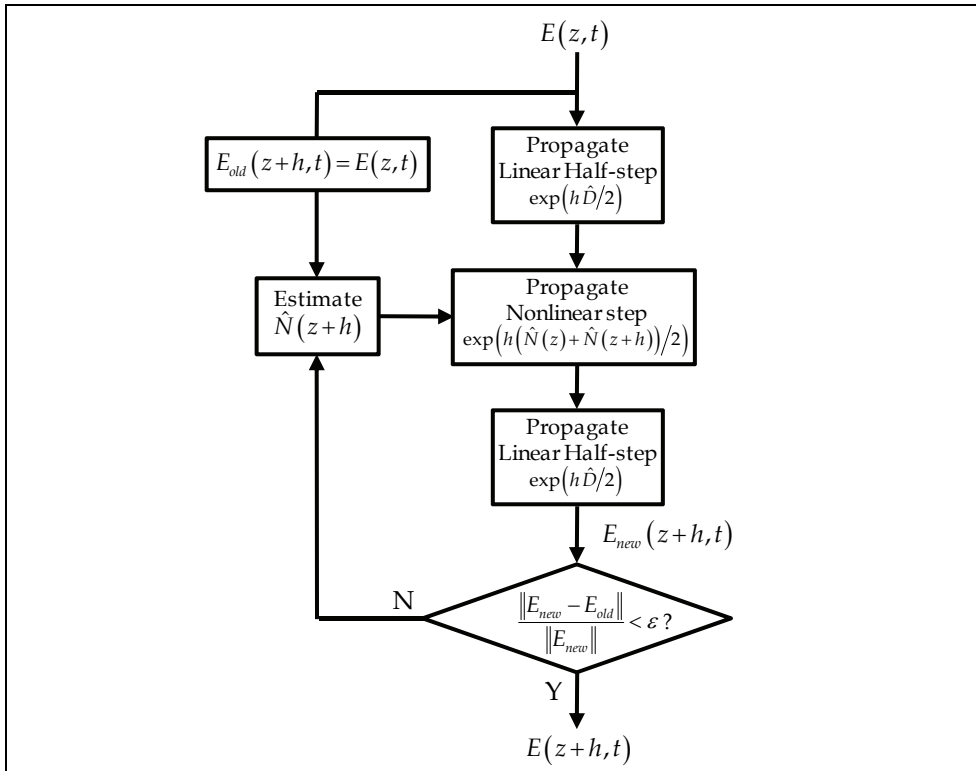


Fig. 2. Iterative, symmetric split-step method evaluation.

In offline simulations, it is possible to take the FFT/IFFT of the entire signal. This approach has high computational cost due to a large N , and cannot work in real-time systems. As (10) is a linear filtering operation, well-known methods can be used to design a digital filter that approximates $H(\omega) = \exp\left(\left(-\frac{\alpha}{2} + j\frac{\beta_2}{2!}\omega^2 + j\frac{\beta_3}{3!}\omega^3\right)h\right)$ over the frequency range of interest, $|\omega| \leq 2\pi/T$, where T is the sampling period. If a finite-impulse response (FIR) filter is employed, the required filter length for a target accuracy will be proportional to the impulse duration of $\sim 2\pi|\beta_2|/T^2$ samples. It is also possible to use an infinite-impulse response (IIR) filter to reduce the tap requirement (Plura et al., 2001). However, IIR filters are not desirable for real-time implementation because the delay of digital multipliers is typically much longer than a symbol period. Hence, an IIR filter output can only respond to input samples after this multiple-symbol delay has elapsed. Since FIR filters have no feedback, they are not constrained by delay. Moreover, FIR filters can be parallelized and efficiently implemented in the frequency-domain (Oppenheim & Schaffer), and are therefore more suitable for real-time implementation. Other methods of evaluating the linear operator, such as using wavelets have studied in (Kremp & Freude, 2005; Goldfarb & Li, 2009), and may lead to further computational savings compared to the standard SSFM.

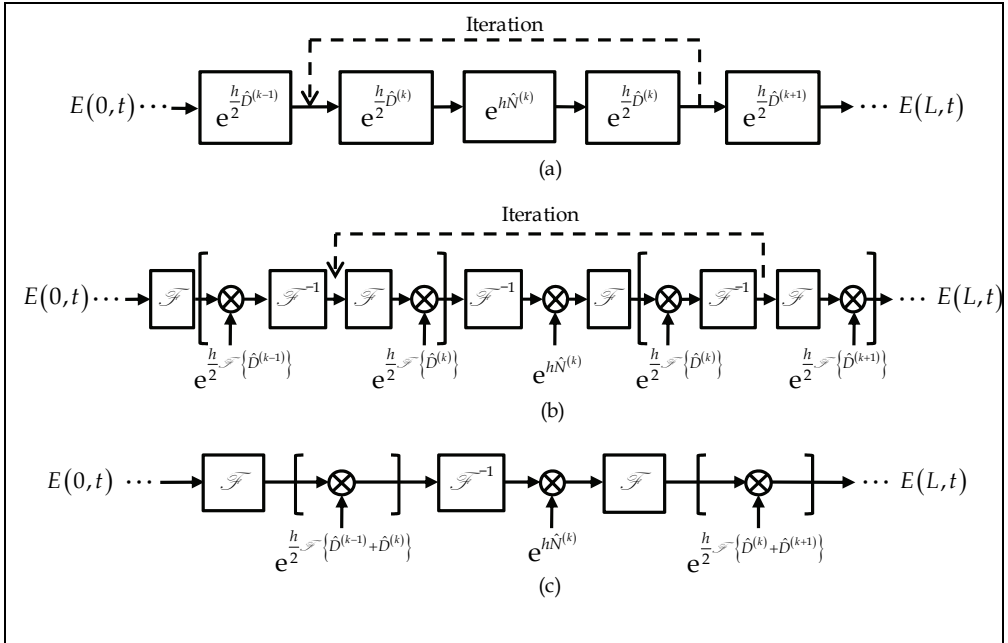


Fig. 3. (a) S-SSM with optional iterative procedure for solving each section. (b) S-SSF with optional iterative procedure for solving each section. (c) If non-iterative method is used, adjacent linear operators can be combined so the total complexity is the same as the A-SSM.

2.2 Step Size Selection

The SSFM can be made increasingly accurate by reducing the step size h . For a given numerical accuracy, the step size requirement was studied in (Sinkin et al., 2003) and (Zhang & Hayee, 2008). Traditionally, the step size was selected based on the characteristic lengths of the system, which are the distances over which each impairment induces one radian of phase distortion. For CD and nonlinearity, these are:

$$l_{\text{CD}} \sim 2/\beta_2 \omega_{\text{max}}^2, \text{ and} \quad (15)$$

$$l_{\text{NL}} \sim 1/\gamma P_{\text{tx}}, \quad (16)$$

where ω_{max} is the highest frequency component of the signal and P_{tx} is the launched power.² We can bound the maximum distortion of each step by setting:

$$h = \min(\Phi_{\text{CD}} l_{\text{CD}}, \Phi_{\text{NL}} l_{\text{NL}}). \quad (17)$$

The choice of Φ_{CD} and Φ_{NL} depends on the accuracy required. Since CD is usually the larger impairment, (Sinkin et al., 2003) found that setting h based on CD walkoff length

² Strictly speaking, no signal is bounded in frequency. For single-carrier signals, we can define $\omega_{\text{max}} = 2\pi R_s$ where R_s is the symbol rate. For OFDM, we define $\omega_{\text{max}} = 2\pi(N_u + 1)\Delta f_s$, where N_u is the number of used subcarriers and Δf_s is the subcarrier frequency spacing.

gives good numerical performance for both single- and multi-channel systems over the accuracy range of interest.

Another approach is to bound the error of each step directly. (Sinkin et al., 2003) proposed a “local error method” approach, where the step size is varied throughout a fiber to ensure that the relative local error $\delta = \|E_t - E_{SSM}\|/\|E_t\|$ between the numerical SSM solution and the true NLSE solution is constant for every step. Relative local error is related to the closeness with which the A-SSM and S-SSM in (5) and (6) approximate the integral in (4). According to (8) and (9), the error in the exponential involves the commutator of \hat{D} and \hat{N} . (Rieznik et al., 2005) used quantum mechanics to derive results, while (Zhang & Hayee, 2008) used a related approach that considered the change in pulse width when the ordering of operators is swapped. Both analyses produced the same result that to keep relative local error constant, the step sizes of the A-SSM and S-SSM should be:

$$h^2(z) = \Delta\zeta / [\gamma P(z) |\beta_2| \omega_{\max}^2], \text{ and} \quad (18)$$

$$h^3(z) = \Delta\xi / [\gamma P(z) (|\beta_2| \omega_{\max}^2)^2]. \quad (19)$$

In comparison with (17), the dispersion and nonlinear parameters have a multiplicative contribution in h . This is intuitively satisfying, since the NLSE can be solved analytically in the limit when either dispersion or nonlinearity is zero, allowing the use of an arbitrarily large step size. Secondly, the step size requirement varies with z because power is decreasing with distance.

Ultimately, signal propagation involves evaluating many steps of the SSM. The parameter of interest is not the error of each step, but the global relative error between the numerical solution and the true NLSE solution over the entire propagation path. In WDM transmission over multiple spans of fiber, (Zhang & Hayee, 2008) showed that global error grows linearly with the number of spans. To keep global error constant, $\Delta\zeta/h$ or $\Delta\xi/h$ should be kept constant. For the A-SSM, h should therefore vary as $1/|\beta_2|$, $1/\omega_{\max}^2$ and $1/P(z)$ with respect to the dispersion strength, signal bandwidth, and signal power; while for the S-SSM, h should vary as $1/|\beta_2|$, $1/\omega_{\max}^2$ and $1/\sqrt{P(z)}$. These rules provide useful guidelines on the change in the complexity of backpropagation as system parameters are varied. For example, a WDM signal with N_{ch} channels has roughly N_{ch} times the bandwidth and N_{ch} the power of a single channel, so using the S-SSM, complexity increases as $N_{ch}^{5/2}$. Whereas a typical step size for simulating a single wavelength channel is tens of kilometers, the requirement for a 16-channel WDM signal is reduced to less than 100 meters.

Finally, although local error methods may be computationally efficient, a variable step size may not be desirable because it will require different filter coefficients and FFT sizes for each linear operator of the different sections. Practical implementation may dictate using a constant step size for each fiber type in the channel, in which case, (18) or (19) may still be used, but a single h is computed for each fiber replacing $P(z)$ with the maximum power P_{\max} .

3. System Model

We use the generalized transmission model shown in Fig. 4. At the transmitter, a digital signal processor (DSP) converts input symbols into four digital signals corresponding to the I and Q components of the two transmitted polarizations. These are converted to analog by arbitrary waveform generators represented by digital-to-analog converters (D/A), driving a pair of Mach-Zehnder (MZ) modulators that perform upconversion onto an optical carrier. The channel is comprised of a concatenation of single-mode fiber (SMF) spans, with inline amplification and dispersion-compensation fiber (DCF) after each span. At the receiver, the optical signal is mixed with a local oscillator (LO) laser through a network of optical hybrids and photodetectors (PD), yielding electronic signals corresponding to the I and Q components of the two received polarizations. These are synchronously sampled and digitized by analog-to-digital (A/D) converters at a rate of $1/T = (M/K)(1/T_s)$, where T_s is the symbol period and M/K is a rational oversampling rate, and then processed by a DSP.

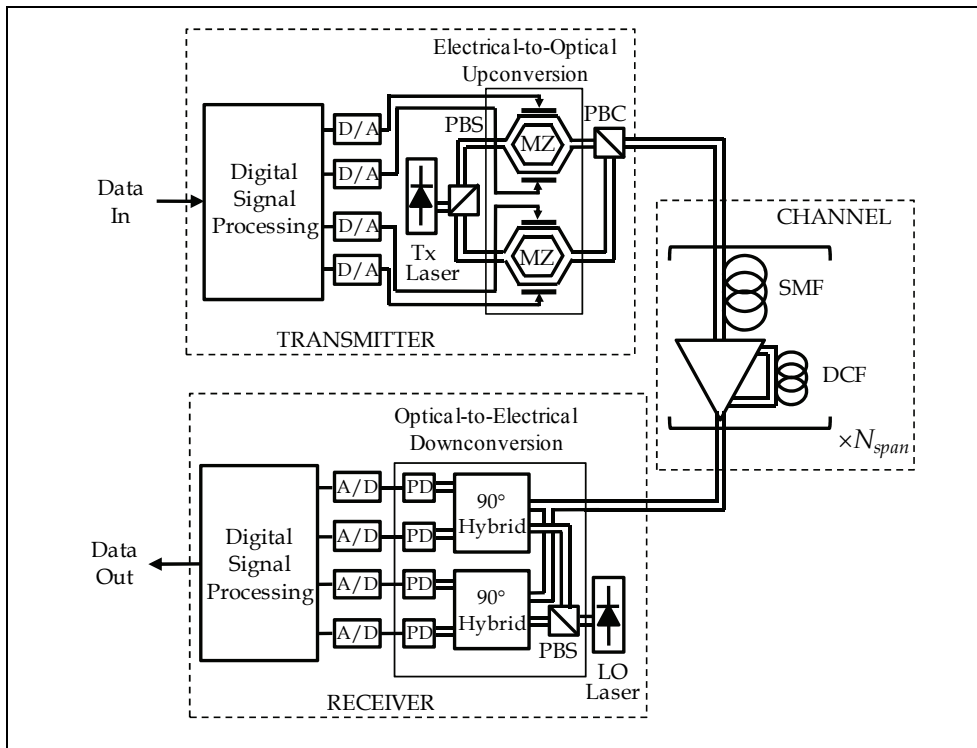


Fig. 4. Coherent system with digital signal processing at the receiver and/or transmitter.

A defining feature of the system shown is that baseband signals equivalent to the transmitted (and received) optical fields are available at the transmitter (and receiver). This enables an arbitrary waveform be transmitted over the channel, and enables arbitrary manipulation of the received waveform for recovery of the transmitted symbols. For

example, the transmitter DSP can implement any signal pre-distortion algorithms, including CD pre-compensation, nonlinear phase noise pre-compensation or transmitter-side backpropagation. Similarly, the receiver DSP can implement any algorithm to combat signal distortion by the channel, including linear equalization, nonlinear phase noise post-compensation, receiver-side backpropagation, carrier recovery and clock recovery. We note that Fig. 4 is a canonical model for any modulation format. In OFDM, for example, the DSP algorithm at the transmitter and receiver include FFT and IFFT operations to convert between frequency-domain symbols and time-domain signals. For single-polarization transmission, the unneeded MZ modulator and D/As can be removed; while for single-carrier transmission, pulse shaping can be performed digitally by the DSP, or a pair of MZ modulators for pulse carving can be inserted before or after the data modulators.

4. Backpropagation

The NLSE is an invertible equation. In the absence of noise, the transmitted signal can be exactly recovered by “backpropagating” the received signal through the inverse NLSE given by:

$$\frac{\partial E}{\partial z} = (-\hat{D} - \hat{N})E. \quad (20)$$

This operation is equivalent to passing the received signal through a fictitious fiber having opposite-signed parameters (Fig. 5a). It is also possible to perform backpropagation at the transmitter side by pre-distorting the signal to invert the channel, and then transmitting the pre-distorted waveform (Fig. 5b). In the absence of noise, both schemes are equivalent. We shall focus on receiver-side backpropagation.

Backpropagation operates directly on the complex-valued field $E(z,t)$. Hence, the technique is universal, as the transmitted signal can have any modulation format or pulse shape, including multicarrier transmission using OFDM. Moreover, as backpropagation simply involves finding a numerical solution to the NLSE, the methods and step size settings developed in Section 2 are applicable.

Some differences between optical system simulation and impairment compensation should be noted. In the former, knowing the input to a fiber enables the output to be computed to arbitrary precision; whereas in backpropagation, noise prevents exact recovery of the transmitted signal. It has been demonstrated that in the presence of noise, a modified backpropagation equation is effective in compensating nonlinearity:

$$E_{BP}(z,t) = \exp(-h(\hat{D} + \xi\hat{N}))E_{BP}(z+h,t), \quad (21)$$

where $0 \leq \xi \leq 1$ is the fraction of the nonlinearity compensated. For every set of system parameters, there exists an optimum ξ that minimizes the mean square error (MSE) between the transmitted signal $E(0,t)$ and the backpropagation solution $E_{BP}(0,t)$. In zero-dispersion fiber, for example, where backpropagation is equivalent to nonlinear phase rotation, it was shown that $\xi = 0.5$ is optimal (Ho & Kahn, 2004).

The existence of an optimum ξ can be appreciated by considering that in a typical fiber, the magnitude of the dispersion operator is much greater than the nonlinear operator. Thus,

nonlinearity can be viewed as a perturbation to a mostly dispersive channel. The optimum phase to de-rotate at each backpropagation step depends on the accuracy of $E_{BP}(z,t)$ as an estimate of $E(z,t)$. The more accurately the receiver estimates $E(z,t)$, the closer we can set ξ to one, since we are confident that the nonlinear phase rotation will lead to an an output closer to the original signal. Conversely, if $E(z,t)$ is not known accurately, error in amplitude will be converted to random phase rotations by the nonlinear operator $h\xi\hat{N}$, yielding an output that is even further away from the desired signal in Euclidean distance. Hence, the optimum ξ depends on the received SNR as well as any uncompensated distortions that are present during backpropagation. In particular, simulation results in Section 4.1 will show that system performance depends on the dispersion map, owing to interaction between signal and noise. Thus, the optimum ξ is also dependent on the dispersion map and other system parameters, and needs to be individually optimized for each application.

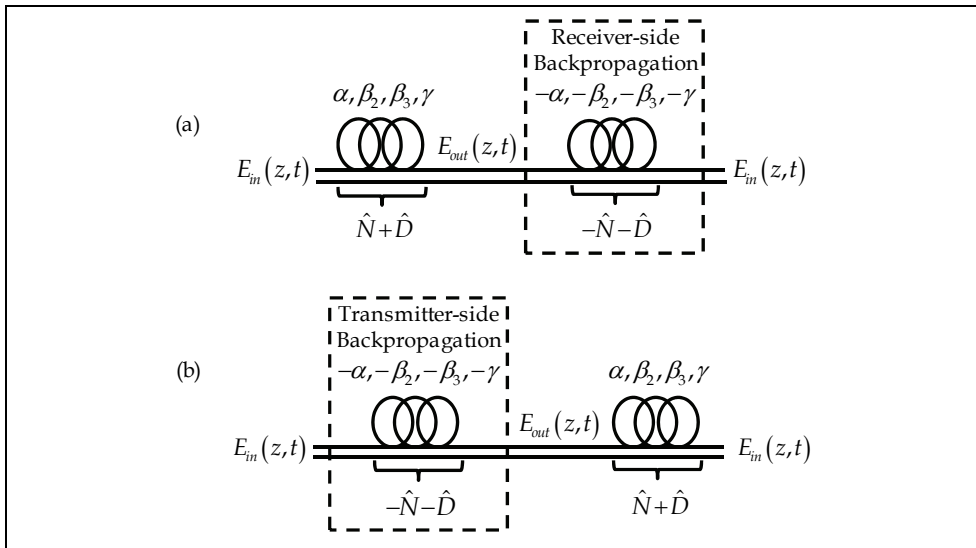


Fig. 5. (a) Transmitter-side and (b) receiver-side backpropagation.

4.1 Single Channel Results

The performance improvement enabled by backpropagation can be seen in Fig. 6, where 21.4 Gb/s RZ-QPSK was transmitted over 25x80-km spans of SMF, with loss fully compensated after each span, and 10% residual dispersion compensation per span (Fig. 6a). The fiber and EDFA parameters are shown in Table 1, and the system dispersion map is shown in Fig. 6c. At intermediate points along the fiber, the accumulated dispersion (quantified in terms of group delay difference per unit wavelength) is much larger than a symbol interval, so the amplitude profile of the propagated signal differs significantly from that of either the transmitted or received signal. Interaction between dispersion and

nonlinearity leads to strong IFWM, and the nonlinear phase de-rotation method (NLPN + Lin. Eq.) offers no performance gain over linear equalization alone (Fig. 6d). Fig. 7 shows the constellations obtained at the output of each method at a launched power of 0 dBm. Rather than spiral-shaped, circular clusters are observed in Fig. 7a, so nonlinear phase de-rotation is not effective. In contrast, even a crude backpropagation approximation: NA-SSFM with a step size equal to the length of a span (Fig. 6b), improves performance at high power (Fig. 6d).

	SMF	DCF		EDFA #1	EDFA #2
Attenuation (α)	0.2 dB/km	0.6 dB/km	Gain	G	G
Dispersion (β_2)	17 ps/nm	-80 ps/nm	Noise Figure	5 dB	5 dB
Nonlinear parameter (γ)	0.0013 m ⁻¹ W ⁻¹	0.0053 m ⁻¹ W ⁻¹			
Length (L)	80 km	0% RDPS: 17 km 10% RDPS: 15.3 km 100% RDPS: 0 km			

Table 1. Fiber and EDFA simulation parameters.

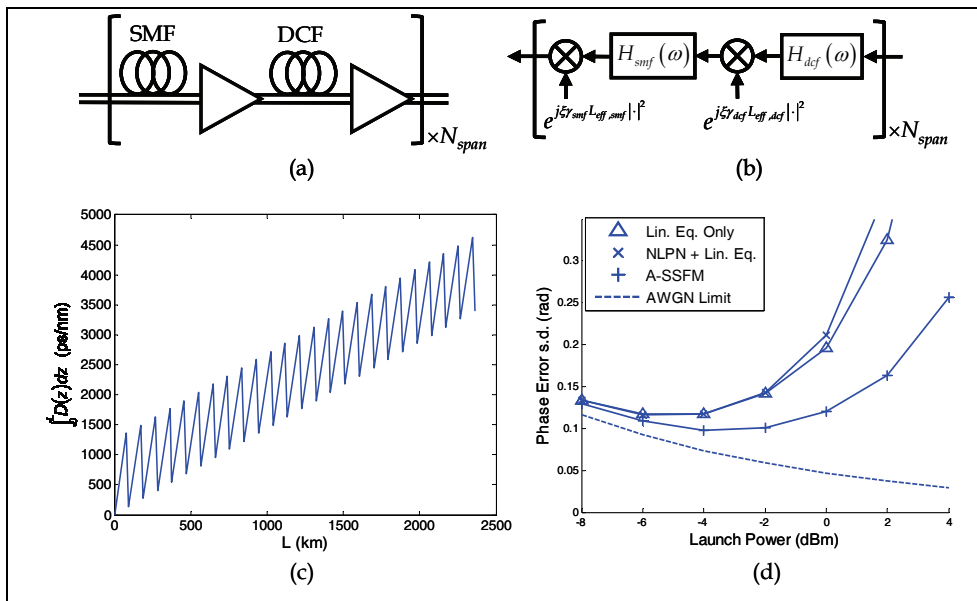


Fig. 6. (a) Long-haul transmission over multiple identical spans of fiber with amplification and dispersion compensation, (b) backpropagation model using A-SSFM with step size equal to a span length, (c) dispersion map, (d) system performance using different channel compensation algorithms for 21.4 Gb/s RZ QPSK over 25×80-km SMF with 10% RDPS.

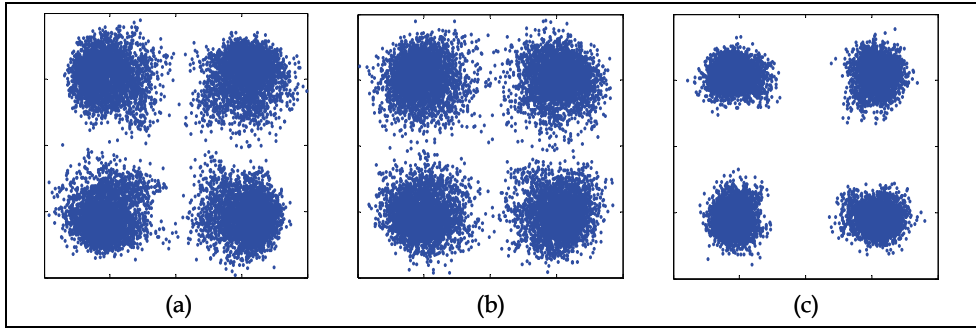


Fig. 7. Constellation diagrams obtained using (a) linear equalization only, (b) nonlinear phase noise compensation + linear equalization, and (c) backpropagation using A-SSFM with step size equal to a span length.

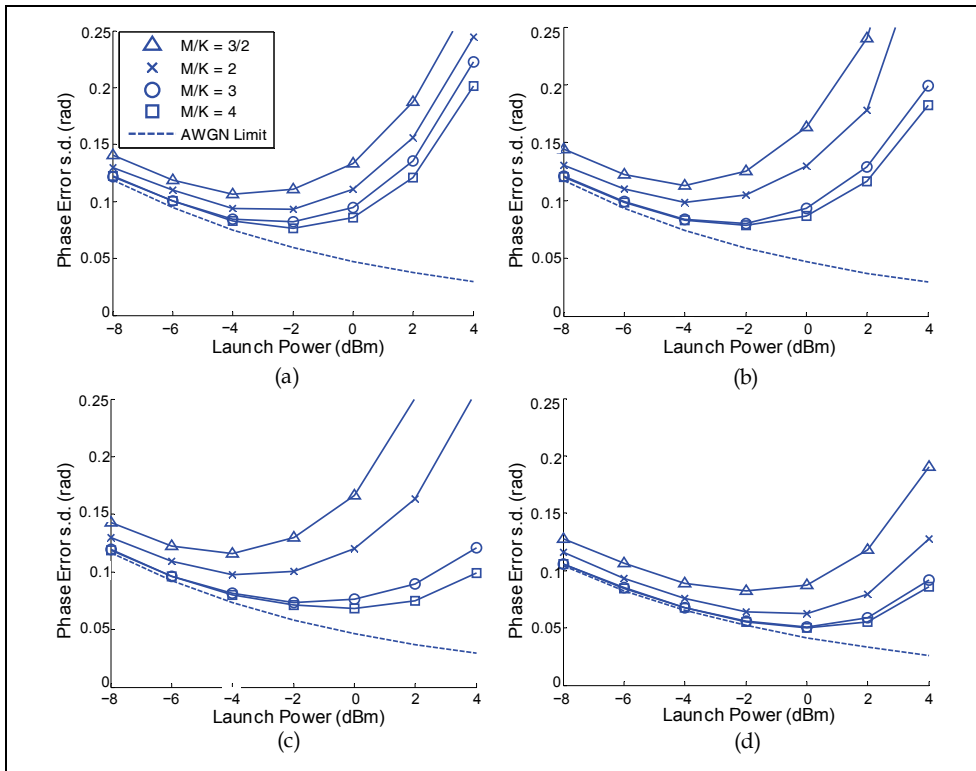


Fig. 8. System performance for 21.4 Gb/s RZ QPSK over 25×80-km SMF with values of different residual dispersion per span (a) 0%, (b) 5%, (c) 10%, and (d) 100%.

System performance is strongly dependent on the dispersion map. In Fig. 8, RZ-QPSK at 21.4 Gb/s was again transmitted over 25×80-km spans of SMF with loss fully compensated after each span, but the residual dispersion per span (RDPS) was varied. In addition,

different sampling rates were used for each map. It is observed that performance improves with (i) increased CD undercompensation, and (ii) increased oversampling. The first result can be explained because DCF incurs loss and nonlinearity. In coherent systems, CD can be compensated by a digital linear equalizer without undesired effects, so DCF is unnecessary and should be removed. This reduces the amplification requirement and thus optical amplifier noise. In addition, dispersion facilitates walkoff between the signal and out-of-band noise, reducing their nonlinear interactions. Increasing oversampling also improves performance because digital backpropagation becomes a better approximation to ideal analog backpropagation. As the nonlinear term in the NLSE is third order in the electric field, there is a performance gain when backpropagation is performed at an oversampling ratio of at least 3.

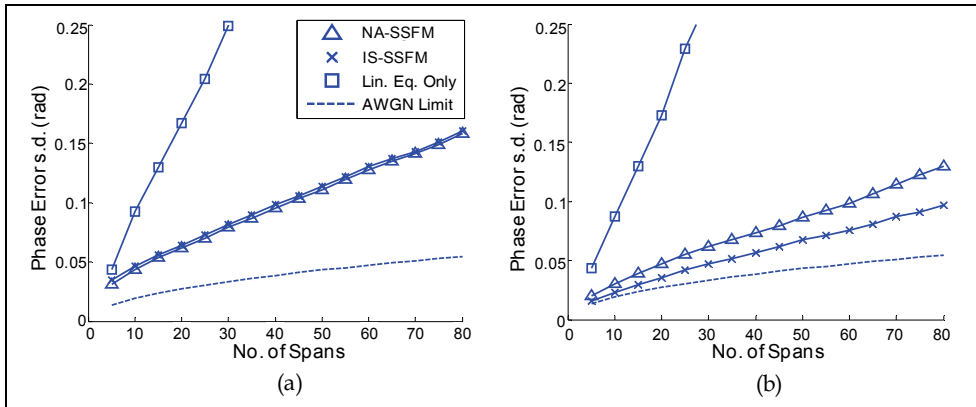


Fig. 9. System performance for 21.4 Gb/s RZ QPSK 100% RDPS versus number of 80-km spans at (a) 2x and (b) 3x oversampling.

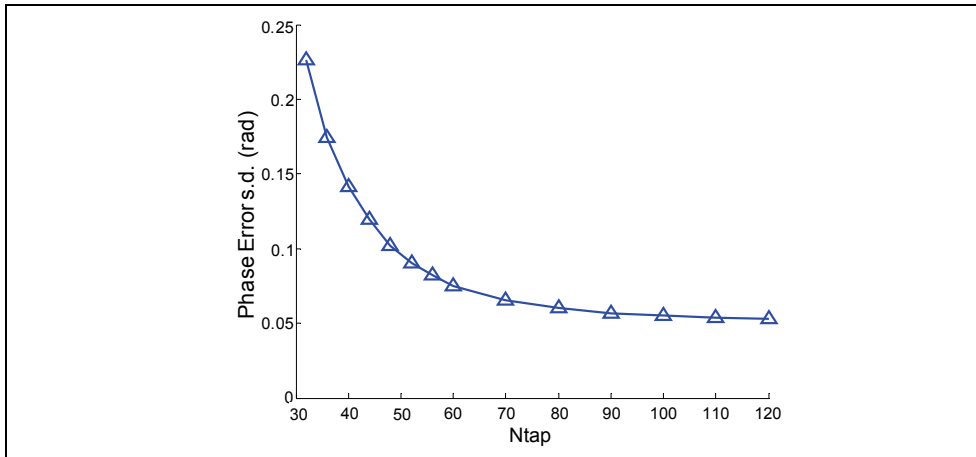


Fig. 10. Performance versus number of taps used to emulate linear operator for 21.4 Gb/s RZ QPSK over 25x80-km SMF with 100% RDPS.

With DCF removed, Fig. 9 shows the increase in transmission distance enabled by backpropagation. For a target bit-error ratio (BER) of 10^{-3} , the phase error standard deviation should be less than 0.23 radians. Whereas linear equalization achieves a system reach of 2,000 km (25×80 -km spans), backpropagation extends this to over 6,400 km (80×80 -km spans). At $2 \times$ oversampling, backpropagation using the IS-SSFM with 20 steps per span gives the same performance as the crude NA-SSFM method with span-length step size. This is because at a low oversampling rates, the backpropagated signal is not very accurate, and numerical errors due to insufficient sampling rate are the dominant effect. At $3 \times$ oversampling, IS-SSFM offers somewhat better performance, but has much higher computational cost.

To estimate the complexity of backpropagation, Fig. 10 shows the filter length required to emulate the linear operator in NA-SSFM for the system considered in Fig. 9, when h is equal to one span at $3 \times$ oversampling. Approximately 70 taps are required. The most efficient realization of an FIR filter this length is frequency-domain implementation (Oppenheim &

Schafer), whose complexity is $\min_{B: N_h + B - 1 = 2^V} \left(\frac{4}{B} (N_h + B - 1) (\log_2 (N_h + B - 1) + 1) \right)$ real

multiplications per sample, where B is the block size, and N_h is the filter length. The nonlinear operator further requires 7 real multiplications per sample.

Table 2 compares the complexity of backpropagation with linear equalization, where the filter length requirement is $2\pi |\beta_2| N_{span} L_{span} R_s^2 (M/K) = 47$ taps at $3/2 \times$ oversampling. The complexities of direct implementation of both methods are also shown. It is observed that backpropagation is two orders of magnitude more computationally expensive than linear equalization. We also note that the length of the linear operator, at 70 taps, is much larger than expected from $2\pi |\beta_2| L_{span} R_s^2 (M/K)$ (Ip, et al. 2008). This is due to amplitude ringing in the frequency domain when an FIR filter is designed using the windowing method. Since backpropagation requires multiple iterations of the linear filter, amplitude distortion due to ringing accumulates (Goldfarb & Li, 2009).

	Linear Equalization	Backpropagation
Direct Implementation	188	21515
Frequency domain implementation	44	3992

Table 2. System complexity in real multiplications per symbol for linear equalization and backpropagation for 21.4 Gb/s RZ QPSK over 25×80 -km SMF with 100% RDPS

5. Multichannel Backpropagation

In DWDM transmission, the ability to overcome interchannel nonlinear impairments depends on the system design. Consider the two systems shown in Fig. 11. In point-to-point transmission, cross-phase modulation (XPM) and four-wave mixing (FWM) are deterministic effects. Hence, they can be effectively compensated by backpropagation. In a mesh network, however, signals of different wavelengths can be dynamically routed by reconfigurable add/drop multiplexers (ROADMs). Signals received in adjacent channels may not be the same signals that were transmitted in adjacent channels. Two sources of

error can arise when backpropagation is performed. Firstly, the receiver has no knowledge of the channels that were dropped, so nonlinear effects involving their fields cannot be compensated. Secondly, nonlinear effects arising from channels added at a intermediate nodes do not extend all the way back to the transmitter, hence when the received signal is fully backpropagated, spurious nonlinear effects will result. In the worst case, channels are either added or dropped just prior to the receiver³. Both uncompensated and spurious nonlinear effects can severely degrade system performance, especially if the channels added or dropped are near neighbors of the desired channel. Hence, backpropagation may not always be effective in mitigating nonlinear effects in mesh networks. In such systems, cross-channel nonlinearity may still be reduced using dispersion-unmanaged transmission, exploiting walkoff to suppress interchannel nonlinearity. The receiver can then perform single-channel backpropagation to mitigate SPM.

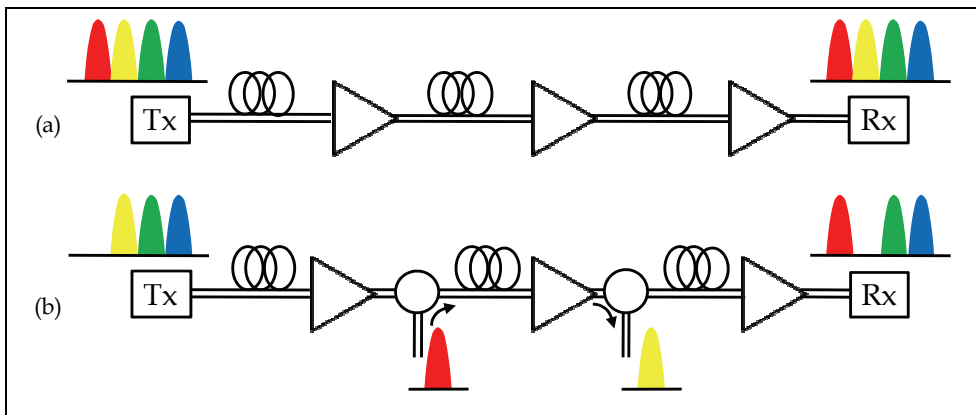


Fig. 11. Wavelength-division-multiplexed (WDM) transmission. (a) Point-to-point link, backpropagation can effectively mitigate interchannel nonlinearity, (b) Mesh network, backpropagation has limited benefit.

For point-to-point links, multichannel backpropagation can be used to mitigate interchannel nonlinearity. This was studied in (Mateo et al., 2008). Since the bandwidth of a DWDM signal is typically much greater than that of a single photoreceiver, we can need to use a structure like that shown in Fig 12a, where a bank of local oscillator lasers are tuned to the frequencies of the channels, translating the signal around each LO frequency to baseband. Provided the frequencies and phases of the local oscillators are synchronized, possibly using mode-locked lasers, the full electric field of the WDM signal can be reconstructed via the coherent sum:

$$E(z,t) = \sum_m E_m(z,t) \exp(-jm\Delta\omega t), \quad (22)$$

where $\Delta\omega$ is the channel spacing. Recovery of $E(z,t)$ enables the receiver to perform a “total-field” backpropagation using the procedure discussed in Section 2. The step size

³ Conversely, for transmit-side backpropagation, the worst-case scenario involves channels added or dropped near the transmitter.

equations derived previously can also be re-used by substituting ω_{\max} to be the bandwidth of the WDM signal, and P_{tx} to be the total transmitted power.

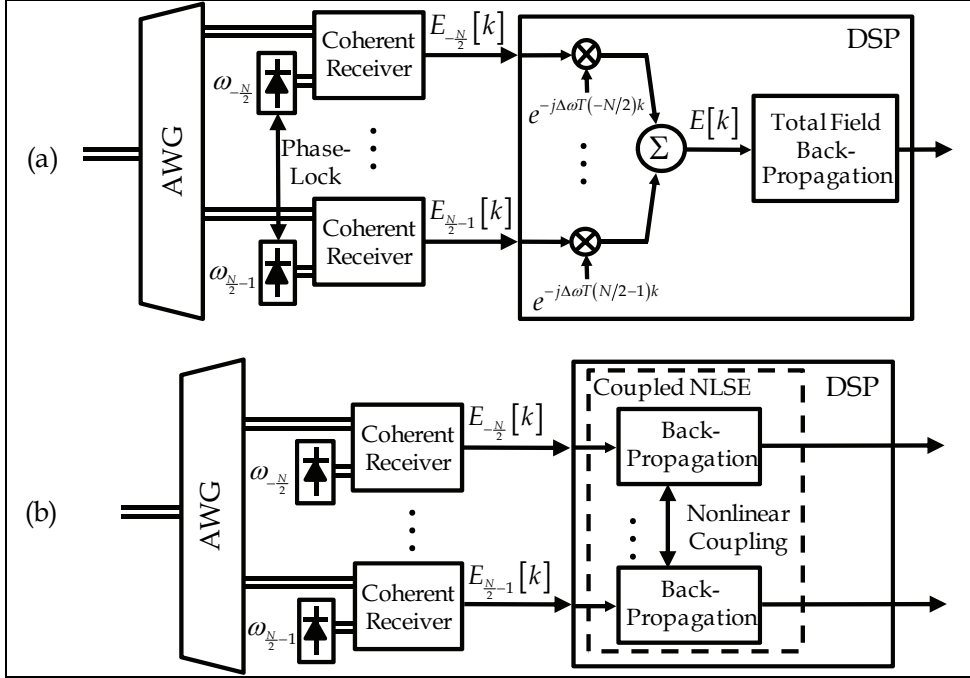


Fig. 12. Multichannel backpropagation using (a) total-field NLSE, (b) coupled NLSE.

In most installed fibers, CD results in low FWM efficiency. If (22) is substituted into the NLSE in (3), and the FWM terms are neglected, the total-field NLSE reduces to a set of coupled equations each describing the evolution of an individual WDM channel through the channel (Leibrich & Rosenkranz, 2003):

$$\frac{\partial E_i}{\partial z} = (\hat{D}_i + \hat{N}_i) E_i, \quad (23)$$

$$\hat{D}_i = -\frac{1}{2}\alpha - \beta_{1,i} \frac{\partial}{\partial t} - j \frac{\beta_{2,i}}{2!} \frac{\partial^2}{\partial t^2} + \frac{\beta_{3,i}}{3!} \frac{\partial^3}{\partial t^3}, \quad (24)$$

$$\hat{N}_i = j\gamma \left(|E_i|^2 + 2 \sum_{j \neq i} |E_j|^2 \right). \quad (25)$$

We observe that different DWDM channels have different group velocities, dispersions, and dispersion slopes, whose values are given by the Taylor Series expansion $\beta_{m,i} = \sum_s \beta_{m+s} (i\Delta\omega)^s / s!$, where $\beta_k \triangleq \beta_{0,k}$ denotes the values defined at the center wavelength.

In addition, the nonlinear operator for channel- i in (25) has contributions from the fields of the other channels. But since this interaction only depends on the amplitude $|E_j|^2$ and is

therefore phase-insensitive, synchronization of the local oscillators is not required. The coupled NLSE may therefore be more practical to implement than the total-field NLSE. The receiver structure for the coupled NLSE is shown in Fig. 12b.

6. Dual-polarization Systems

6.1 Signal Propagation

In real fibers, birefringence causes PMD. Since it is impractical – if not impossible – to estimate the Jones matrix of each increment in the fiber, the performance of backpropagation will be degraded. PMD may ultimately limit the signal bandwidth over which backpropagation can be performed. Additionally, polarization-multiplexed transmission enables the doubling of capacity keeping the same receiver sensitivity in SNR per bit. To study signal propagation in two polarizations, we use the vector NLSE:

$$\frac{\partial \mathbf{E}}{\partial z} = (\hat{\mathbf{D}} + \hat{\mathbf{N}}) \mathbf{E}, \tag{26}$$

$$\hat{\mathbf{D}} = -\frac{1}{2} \boldsymbol{\alpha} - \boldsymbol{\beta}_1 \frac{\partial}{\partial t} - j \frac{1}{2!} \boldsymbol{\beta}_2 \frac{\partial^2}{\partial t^2} + \frac{1}{3!} \boldsymbol{\beta}_3 \frac{\partial^3}{\partial t^3}, \tag{27}$$

$$\hat{\mathbf{N}} = j\gamma \left[|\mathbf{E}|^2 \mathbf{I} - \frac{1}{3} (\mathbf{E}^H \boldsymbol{\sigma}_3 \mathbf{E}) \boldsymbol{\sigma}_3 \right]. \tag{28}$$

In these equations, $\mathbf{E} = [E_x \ E_y]^T$ is the Jones vector of the electric field, and $\boldsymbol{\alpha}$, $\boldsymbol{\beta}_1$, $\boldsymbol{\beta}_2$ and $\boldsymbol{\beta}_3$ are the loss, group velocity, CD and dispersion slope parameters. The 2x2 matrix representation of the parameters allows the most general polarization dependence. For example, setting $\boldsymbol{\alpha}$ to have unequal eigenvalues enables polarization-dependent loss (PDL) to be modeled. In comparison with (3), the nonlinear operator has an extra term that arises as a result of the cross-polarization nonlinearity. The matrix $\boldsymbol{\sigma}_3$ is a Pauli spin matrix expressed in the standard notation of (Gordon & Kogelnik, 2000):

$$\boldsymbol{\sigma}_1 = \begin{bmatrix} 1 & 0 \\ 0 & -1 \end{bmatrix}, \boldsymbol{\sigma}_2 = \begin{bmatrix} 0 & 1 \\ 1 & 0 \end{bmatrix} \text{ and } \boldsymbol{\sigma}_3 = \begin{bmatrix} 0 & -j \\ j & 0 \end{bmatrix}. \tag{29}$$

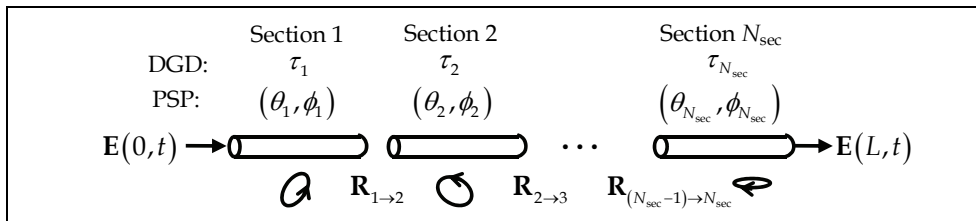


Fig. 13. Model of a fiber with polarization-mode dispersion.

In most fibers, the polarization dependence of $\boldsymbol{\alpha}$, $\boldsymbol{\beta}_2$ and $\boldsymbol{\beta}_3$ is negligible, so they may be replaced by scalars. To model arbitrary PMD of all orders, a fiber is typically divided into short sections, each possessing only first-order PMD, and the principal states of polarization

(PSP) are randomly rotated between adjacent sections (Fig. 13). Thus, for the k -th fiber section, β_1 can be expressed as:

$$\beta_1(z) = \mathbf{R}(\theta_k, \phi_k) \left(\frac{\delta}{2} \sigma_1 \right) \mathbf{R}^H(\theta_k, \phi_k), \quad (30)$$

where,

$$\mathbf{R}(\theta_k, \phi_k) = \begin{bmatrix} \cos \theta_k \cos \phi_k - j \sin \theta_k \sin \phi_k & \sin \theta_k \cos \phi_k + j \cos \theta_k \sin \phi_k \\ \sin \theta_k \cos \phi_k + j \cos \theta_k \sin \phi_k & \cos \theta_k \cos \phi_k + j \sin \theta_k \sin \phi_k \end{bmatrix} \quad (31)$$

is a generalized polarization rotation matrix whose columns are the Jones vectors of the PSPs. The first column denotes the slow axis and is a unit vector on the Poincaré sphere with azimuth and ellipticity angles of $2\theta_k$ and $2\phi_k$, respectively. δ_k is the differential group delay (DGD) of the section, and is a Maxwellian-distributed variable with mean $\bar{\tau}_{pmd} \sqrt{h}$, where $\bar{\tau}_{pmd}$ is the mean PMD of the fiber and h is the section length.

In order to model PMD accurately, the section length should be less than the PMD characteristic length given by:

$$l_{PMD} \sim (T_s / \bar{\tau}_{PMD})^2. \quad (32)$$

Typically, this number is large compared to the characteristic length of CD. Hence in practical fibers, the step sizes derived in Section 2.2 are sufficiently fine for accurate modeling of PMD.

The dual-polarization NLSE can be solved using the split-step methods introduced in Section 2 with the linear and nonlinear operators applied successively in the frequency- and time-domains. Note that for clarity, we have expressed (26) to (28) in Jones co-ordinates. For implementation, the nonlinear operator of the vector NLSE has a slightly simpler form when the electric field is specified in circular polarization co-ordinates.

6.2 Backpropagation

Like the scalar NLSE, the vector NLSE is invertible. In the absence of noise, knowledge of the fiber parameters enables backpropagation to exactly invert the channel. We define the backpropagation equation as:

$$\mathbf{E}(z, t) = \exp\left(-h\left(\hat{\mathbf{D}} + \xi \hat{\mathbf{N}}\right)\right) \mathbf{E}(z+h, t), \quad (33)$$

where $\hat{\mathbf{D}}$ and $\hat{\mathbf{N}}$ are given in (27) and (28), and $0 \leq \xi \leq 1$ is a parameter to be optimized. We note that reversing the sign of the PMD term $-\beta_1^{(k)} = \mathbf{R}(\theta_k, \phi_k) \left(-\frac{\delta}{2} \sigma_1 \right) \mathbf{R}^H(\theta_k, \phi_k)$ has the intuitive meaning of rotating the signal into the fiber PSPs and then undoing the section's DGD. The difference between the scalar and vector NLSE is that PMD makes the linear operator $h\hat{\mathbf{D}}(z)$ dependent on z even if a constant step size is used. Fig. 14 shows dual-polarization backpropagation. The order of the linear operators applied should be in reverse order to forward propagation.

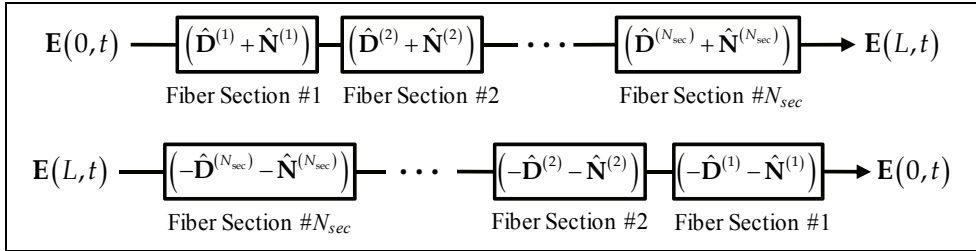


Fig. 14. Dual-polarization backpropagation.

If the Jones vector for each fiber section not be known at the receiver, the best estimate of the linear operator is:

$$\hat{\mathbf{D}}^{no\ pm d} = -\frac{1}{2}\boldsymbol{\alpha} - j\frac{1}{2!}\boldsymbol{\beta}_2\frac{\partial^2}{\partial t^2} + \frac{1}{3!}\boldsymbol{\beta}_3\frac{\partial^3}{\partial t^3}. \tag{34}$$

The receiver shown in Fig. 15 can be used, where a linear equalizer follows backpropagation. In the absence of nonlinearity, backpropagation inverts the fiber CD, so PMD is mitigated by the linear equalizer. At realistic transmission distances and symbol rates, PMD has only short duration, so we expect the signal amplitude profile will not be significantly distorted by PMD. Hence, backpropagation with the linear operator in (34) can still compensate most of the interactions between CD and nonlinearity. The linear equalizer compensates PMD and any residual linear effects not already compensated by backpropagation. This receiver structure is general. If backpropagation includes PMD, the linear equalizer is reduced to a fixed downsampler.

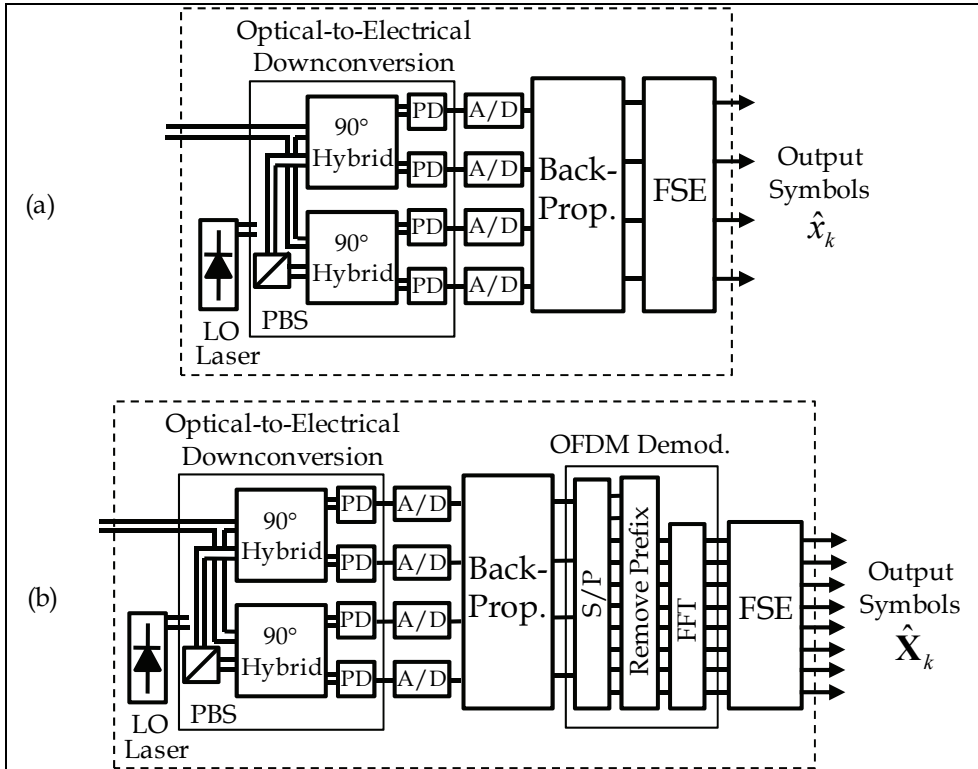


Fig. 15. Backpropagation receiver with output linear equalizer to mitigate residual linear distortion for (a) single-carrier, (b) OFDM.

6.3 Results

The performances of single-carrier and OFDM at 107 Gb/s over 25×80-km SMF are compared for different dispersion maps in Fig. 16. The fiber and EDFA parameters are shown in Table 3. Gain is fully compensated after each span, but unlike Section 4, the individual gains of the two EDFAs G_1 and G_2 are optimized for best performance. For single-carrier, we assume polarization-multiplexed QPSK (PM-QPSK) with 50% RZ pulse shaping, corresponding to 4 bits encoded per symbol. For OFDM, the FFT-size (N_c), number of used subcarriers (N_u) and prefix length (N_{pre}) are shown for different dispersion maps in Table 4, and PM-QPSK was transmitted on all the used subcarriers. The metric of comparison is the phase error standard deviation, which in the absence of nonlinearity, satisfies $\sigma_\epsilon = \sqrt{1/2\gamma_s}$, where γ_s is the SNR per symbol. For OFDM, all the subcarriers were found to have similar σ_ϵ , so the average σ_ϵ across all the subcarriers is shown. In each plot shown in Fig. 16, linear equalization is compared to different backpropagation methods. IS-SSFM denotes using the iterative, symmetric SSFM for solving the inverse NLSE, with the same step size equal to that used in simulating forward propagation. NA-SSFM denotes

using the crude non-iterative, asymmetric SSFM with a step size equal to one span. For each method, comparison is made with the receiver including PMD ($\hat{\mathbf{D}}$ given by (27)) and excluding PMD ($\hat{\mathbf{D}}$ given by (34)) during backpropagation.

	SMF	DCF		EDFA #1	EDFA #2
Attenuation (α)	0.2 dB/km	0.5 dB/km	Gain	G_1	G_2
Dispersion (β_2)	17 ps/nm	-85 ps/nm	Noise Figure	4 dB	4 dB
Dispersion Slope (β_3)	0.09 ps/nm ² /km	-0.3 ps/nm ² /km			
Nonlinear parameter (γ)	0.0013 m ⁻¹ W ⁻¹	0.0053 m ⁻¹ W ⁻¹			
Mean PMD ($\bar{\tau}_{pmd}$)	0.1 ps/ $\sqrt{\text{km}}$	0.1 ps/ $\sqrt{\text{km}}$			
Length (L)	80 km	0% RDPS: 16 km 10% RDPS: 14.4 km 100% RDPS: 0 km			

Table 3. Fiber and EDFA simulation parameters.

	N_{pre}	N_u	N_c
0% RDPS	4	13	16
10% RDPS	43	213	256
100% RDPS	391	1706	2048

Table 4. OFDM parameters used for different dispersion maps.

The results show that at 0% RDPS using linear equalization only, single-carrier outperforms OFDM, because the FWM between subcarriers makes OFDM susceptible to nonlinearity. At 100% RDPS using backpropagation, the performances of single-carrier and OFDM become similar, because dispersion causes both signals to become approximately Gaussian-distributed regardless of the signal profile at transmission. It is observed that using the more accurate IS-SSFM to solve the inverse NLSE despite the receiver not knowing the channel PMD gives better performance than the receiver knowing the PMD but using the less accurate NA-SSFM. As expected, IS-SSFM (including PMD) delivers the best performance, reducing phase error standard deviation by 1 to 3 dB compared to linear equalization only.

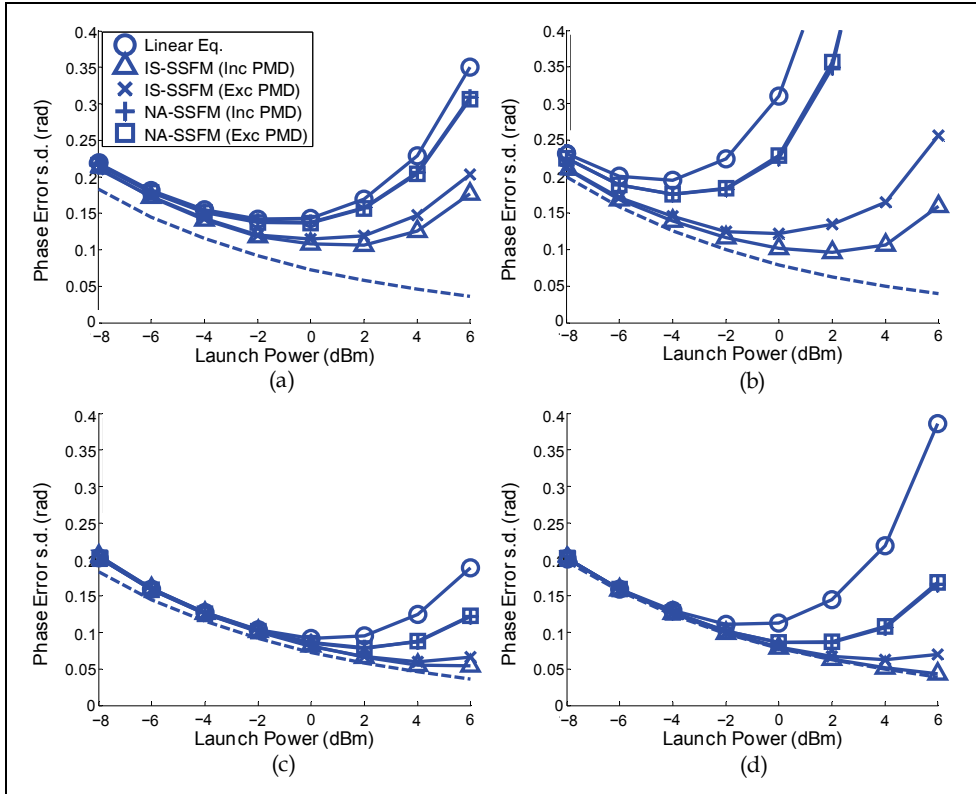


Fig. 16. System performance for polarization-multiplexed 107-Gb/s transmission through 25x80-km SMF for (a) single-carrier at 0% RDPS, (b) OFDM at 0% RDPS, (c) single-carrier at 100% RDPS, and (d) OFDM at 100% RDPS.

7. Further Discussion

The ability of backpropagation to undo nonlinear effects depends on how accurately it can estimate the signal amplitude profile at every point in the fiber. Noise, PMD, and other distortions not estimated by the receiver, but which change the signal intensity profile, thus degrading performance. Since these effects accumulate with distance, the further a signal is backpropagated, the higher the relative error. In receiver-side backpropagation, the signal intensity profile is known accurately at the receiver, but becomes progressively less accurate as it is traced back to the transmitter. We may therefore expect a small improvement in performance using the setup in Fig. 17, where backpropagation is split evenly between the transmitter and receiver: transmit-side backpropagation inverts the first half of the channel, while receive-side backpropagation inverts the second half. To account for the change in relative error with distance, the parameter ξ should also vary with distance; a larger ξ is used for the spans closer to the transmitter (and receiver), while a smaller ξ is used for spans further away, where the estimated signal intensity is less reliable.

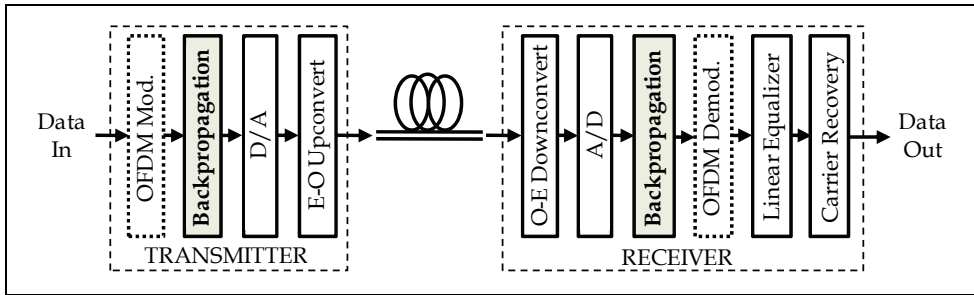


Fig. 17. Backpropagation at transmitter and receiver.

Since backpropagation reduces the effects of nonlinearity, the nonlinear regime of the channel is pushed towards higher launched power (Fig. 18). This has the impact of increasing the optimum launched power and the ultimate achievable capacity. With backpropagation, deterministic nonlinearities do not decrease capacity as they can be mitigated. Furthermore, dispersion-unmanaged transmission causes walkoff between signal and out-of-band noise, reducing their nonlinear interaction. The ultimate limit to capacity therefore arises as a result of nonlinear interaction between signal and in-band noise.

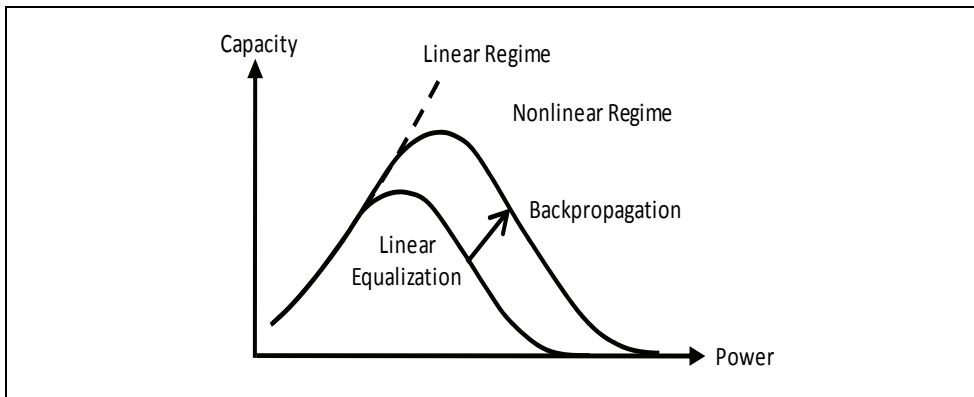


Fig. 18. Effect of backpropagation on capacity.

8. Conclusion

Backpropagation is a universal method for jointly compensating linear and nonlinear impairments in an arbitrary channel. The method works independently of the modulation format, and requires finding a numerical solution to the inverse nonlinear Schrödinger equation, which is obtained by reversing the order of the fibers in the link and the signs of the parameters of each fiber. The performance of backpropagation depends on how accurately it estimates the signal amplitude profile at every point in the fiber. Noise, PMD, and other effects not taken into account by the receiver can degrade performance. The best system performance is obtained using dispersion-unmanaged transmission because walkoff reduces nonlinear interaction between signal and out-of-band noise. Interaction between

signal and in-band noise ultimately limits capacity. Using backpropagation in conjunction with dispersion-unmanaged transmission extends the linear regime of the fiber, enabling higher usable launched power and higher capacity.

9. References

- Agrawal, G. P. (2001). *Nonlinear Fiber Optics 3rd Edition*, Academic Press, ISBN 0120451433, San Diego, CA, U.S.A.
- Charlet, G.; Maaref, N.; Renaudier, J.; Mardoyan, H.; Tran, P. & Bigo, S. (2006). Transmission of 40 Gb/s QPSK with coherent detection over ultra-long distance improved by nonlinearity mitigation, *Proceedings of the European Conference on Optical Communication (ECOC 2006)*, Paper Th4.3.4, Cannes, France, September 2006.
- Chowdhury, A & Essiambre, R.-J. (2004). Optical phase conjugation and pseudolinear transmission, *Optics Letters*, Vol. 29, No. 10, (May 2004) pp. 1105–1107, ISSN 1539-4794.
- Essiambre, R.-J.; Mikkelsen, B. & Raybon, G. (1999). Intra-channel cross-phase modulation and four-wave mixing in high-speed TDM, *Electronic Letters*, Vol. 35, No. 18, (September 1999) pp. 1576–1578, ISSN 0013-5194.
- Essiambre, R.-J.; Winzer, P. J.; Qang, X. Q.; Lee, W.; White, C. A. & Burrows, E. C. (2006). Electronic predistortion and fiber nonlinearity, *IEEE Photonic Technology Letters*. Vol. 18, No. 17, (September 2006) pp. 1804–1806, ISSN 1041-1135.
- Essiambre, R.-J.; Foschini, G. J.; Winzer, P. J.; Kramer, G. & Burrows, E. C. (2008). The capacity of fiber-optic communication systems, *Proceedings of Optical Fiber Communication Conference (OFC 2008)*, Paper OTuE17, San Diego, CA, U.S.A., March 2008.
- Goldfarb, G. & Li, G. (2009). Efficient backward-propagation using wavelet-based filtering for fiber backward-propagation, *Optics Express*, Vol. 17, No. 11, (May 2009) pp. 8815–8821, ISSN 1094-4087.
- Gordon, J. P. & Kogelnik, H. (2000). PMD fundamentals: Polarization mode dispersion in optical fibers, *Proceedings of the National Academy of Science*. Vol. 97, No. 9, (April 2000) pp. 4541–4550, ISSN 0027-8424.
- Ho, K.-P. & Kahn, J. M. (2004). Electronic compensation technique to mitigate nonlinear phase noise. *Journal of Lightwave Technology*, Vol. 22, No. 3, (March 2004) pp. 779–783, ISSN 0733-8724.
- Ip, E.; Lau, A. P. T.; Barros, D. J., & Kahn, J. M. (2008). Coherent detection in optical fiber systems. *Optics Express*, Vol. 16, No. 2, (January 2008), pp. 753–791, ISSN 1094-4087.
- Ip, E. & Kahn, J. M. (2008). Compensation of dispersion and nonlinear effects using digital backpropagation, *Journal of Lightwave Technology*, Vol. 26, No. 20, (October 2008) pp. 3416–3425, ISSN 0733-8724.
- Jaworski, M. (2008). Step-size distribution strategies in SSFM simulation of DWDM links, *Proceedings of International Conference on Transparent Optical Networks (ICTON-MW'08)*, Paper Fr2A.1, Marrakech, Morocco, December 2008.
- Kremp, T. & Freude, W. (2008). Fast split-step wavelet collocation method for WDM system parameter optimization, *Journal of Lightwave Technology*, Vol. 23, No. 3, (March 2005) pp. 1491–1502, ISSN 0733-8724.

- Lau, A. P. T.; Rabbani, S. & Kahn, J. M. (2008). On the statistics of intrachannel four-wave mixing in phase-modulated optical communication systems, *Journal of Lightwave Technology*, Vol. 26, No. 14, (July 2008) pp. 2128–2135, ISSN 0733-8724.
- Leibrich, J. & Rosenkranz, W. (2003). Efficient numerical simulation of multichannel WDM transmission systems limited by XPM. *IEEE Photonics Technology Letters*. Vol. 15, No. 3, (March 2003) pp. 395–397, ISSN 1041-1135.
- Li, X.; Chen, X.; Goldfarb, G.; Mateo, E.; Kim, I.; Yaman, F. & Li, G. (2008). Electronic post-compensation of WDM transmission impairments using coherent detection and digital signal processing, *Optics Express*, Vol. 16, No. 2, (January 2008) pp. 881–888, ISSN 1094-4087.
- Liu, X. & Tkach, R. W. (2009). Joint SPM compensation for inline-dispersion-compensated 112-Gb/2 PDM-OFDM transmission, *Proceedings of Optical Fiber Communication Conference (OFC 2009)*, Paper OTuO5, San Diego, CA, U.S.A., March 2009.
- Lowery, A. (2007a). Fiber nonlinearity mitigation in optical links that use OFDM for dispersion compensation, *Photonics Technology Letters*, Vol. 19, No. 19, (October 2007) pp. 1556–1558, ISSN 1041-1135.
- Lowery, A. (2007b). Fiber nonlinearity pre- and post-compensation for long-haul optical links using OFDM, *Optics Express*, Vol. 15, No. 20, (September 2007) pp. 12965–12970, ISSN 1094-4087.
- Mateo, E.; Zhu, L. & Li, G. (2008). Impact of XPM and FWM on the digital implementation of impairment compensation for WDM transmission using backward propagation, *Optics Express*. Vol. 16, No. 20, (September 2008), pp. 16124–16137, ISSN 1094-4087.
- Mitra, P. P. & Stark, J. B. (2001). Nonlinear limits to the information capacity of optical fiber communications. *Nature*, Vol. 411, No. 6841, (June 2001) pp. 1027–1030, ISSN 0028-0836.
- Muslu, G. M. & Erbay, H. A. (2005). Higher-order split-step Fourier schemes for the generalized nonlinear Schrödinger equation, *Mathematics and Computers in Simulation*, Vol. 67, No. 6 (January 2005) pp. 581–595, ISSN 0378-4754.
- Oppenheim, A. V. & Schaffer, R. W. *Discrete-time signal processing*, Prentice-Hall, ISBN 013216292X, Upper Saddle River, NJ, U.S.A.
- Plura, M.; Kissing, J., Gunkel, M.; Lenge, J.; Elbers, J.-P.; Glingener, C.; Schulz, D. & Voges, E. (2001). Improved split-step method for efficient fiber simulations, *Electronic Letters*, Vol. 37, No. 5, (March 2001) pp. 286–287, ISSN 0013-5194.
- Rieznik, A. A.; Tolisano, T.; Callegari, F. A.; Grosz, D. F. & Fragnito, H. L. (2005). Uncertainty relation for the optimization of optical-fiber transmission systems simulations, *Optics Express*, Vol. 13, No. 10, (May 2005) pp. 3822–3834, ISSN 1094-4087.
- Roberts, K.; Li, C.; Strawczynski, L.; O'Sullivan, M. & Hardcastle, I. (2006). Electronic precompensation of optical nonlinearity, *Photonic Technology Letters*, Vol. 18, No. 2, (January 2006) pp. 403–405, ISSN 1041-1135.
- Sinkin, O. V.; Holzlöhner, R.; Zweck, J. & Menyuk, C. (2003). Optimization of the split-step Fourier method in modelling optical-fiber communication systems, *Journal of Lightwave Technology*, Vol. 21, No. 1, (January 2003) pp. 61–68, ISSN 0733-8724.
- Weiss, G. H. & Maradudin, A. A. (1962). The Baker-Hausdorff formula and a problem in crystal physics, *Journal of Mathematical Physics*, Vol. 3, No. 4, (July 1962) pp. 771–777, ISSN 0022-2488.

Zhang, Q. & Hayee, M. I. (2008). Symmetrized split-step Fourier scheme to control global simulation accuracy in fiber-optic communication systems, *Journal of Lightwave Technology*, Vol. 26, No. 2, (January 2008) pp. 302–316, ISSN 0733-8724.

Fiber Optical Parametric Amplifier as Optical Signal Processor

Shunsuke Ono

*Department of Electrical Engineering, Nara National College of Technology
Japan*

1. Introduction

In this chapter, using numerical simulation and experimental results, the optical signal processing characteristics of Fiber-based Optical Parametric Amplifier (FOPA) using novel highly non-linear fibers (HNLFs) including Photonic Crystal Fibers (PCFs) will be described. In the last decade, to overcome the limitation of the electrical signal processing to the ultra high bit-rate optical data streams, ultrafast all-optical signal processing techniques including OTDM (Optical Time Division Multiplex), transparent wavelength conversion and all-optical sampling have been studied and proposed for over 160 Gb/s optical data streams. For those ultrafast optical processing techniques, highly-nonlinear glass fiber-based optical signal processors have been promising due to its ultrafast response time of the nonlinear effects in glass fibers and low loss characteristic to the light signals.

FOPA exploiting four-wave mixing (FWM) occurs in HNLFs has been one of those highly-nonlinear glass fiber-based all optical signal processors for ultrafast On-Off Keyed (OOK) optical signals such as Return-to-Zero (RZ) and Non-Return-to-Zero (NRZ). In recent years, with the emergences of novel glass fiber-based HNLFs with periodical microstructures including PCFs, which shows high nonlinearity using newly proposed germanium oxide silica glasses and novel heavy-metal oxide glasses, FWM-based FOPA has shortened its fiber device length drastically from tens of kilometers to tens of meters and improved its ultrafast optical signal processing characteristics remarkably. Also, with increasing application of the phase shift keyed (PSK) optical signals such as Differential Phase Shift Keying (DPSK) and Differential Quadrature Phase Shift Keying (DQPSK) in the feasibility studies of 40 Gb/s-based optical communication systems, FWM-based FOPA has attracted much more attention again to its ultrafast optical phase controllability on time scale of a few femtoseconds. In Section 2 of this chapter, we will overview the development of the highly nonlinear glass fibers and the highly-nonlinear glass fiber-based optical signal processors including FWM-based- FOPAs. Numerical model of the signal processing characteristics of FWM-based FOPA will be introduced and overview the signal processing characteristics of FWM-based FOPA with the numerically simulated parametric gain characteristics of FWM-based FOPA In Section 4, we will introduce our experimental results of the parametric gain enhancement and the ultrafast signal processing experiments using highly-nonlinear silica glass-based FOPAs with over 160 Gb/s ultrafast optical signal data streams. Practical

applications of FOPA for optical signals are discussed and we will summarize results and suggest directions of FOPA as an ultra fast optical signal processing device in Section 5.

2. Optical Signal Processors based on Novel Glass-Based HNLFs

2.1 Fiber-Based Ultrafast Optical Signal Processors

To overcome the limitation of the electrical signal processing to the ultra high bit-rate data streams, ultrafast all-optical signal processing techniques including the Optical Time Domain Multiplexing (OTDM), the transparent wavelength conversion and all-optical samplings have been eagerly studied and proposed in last decades (Westlund et al., 2002; Hedekvist et al., 1997; J. Li et al., 2001; Ho et al., 2001).

In particular, fiber-based optical signal processors exploiting the nonlinear optical effects in the glass fibers such as Self Phase Modulation (SPM), Cross Phase Modulation (XPM) and Four-Wave Mixing (FWM) and Stimulated Raman Scattering (SRS) have been promising to realize the ultrafast all optical processing devices (Optical Add/Drop Multiplexer (OADM), Demultiplexer (DEMUX), Wavelength Converter (WC), Fiber Optical Parametric Amplifier (FOPA) etc.) due to its ultrafast response time and low loss characteristic.

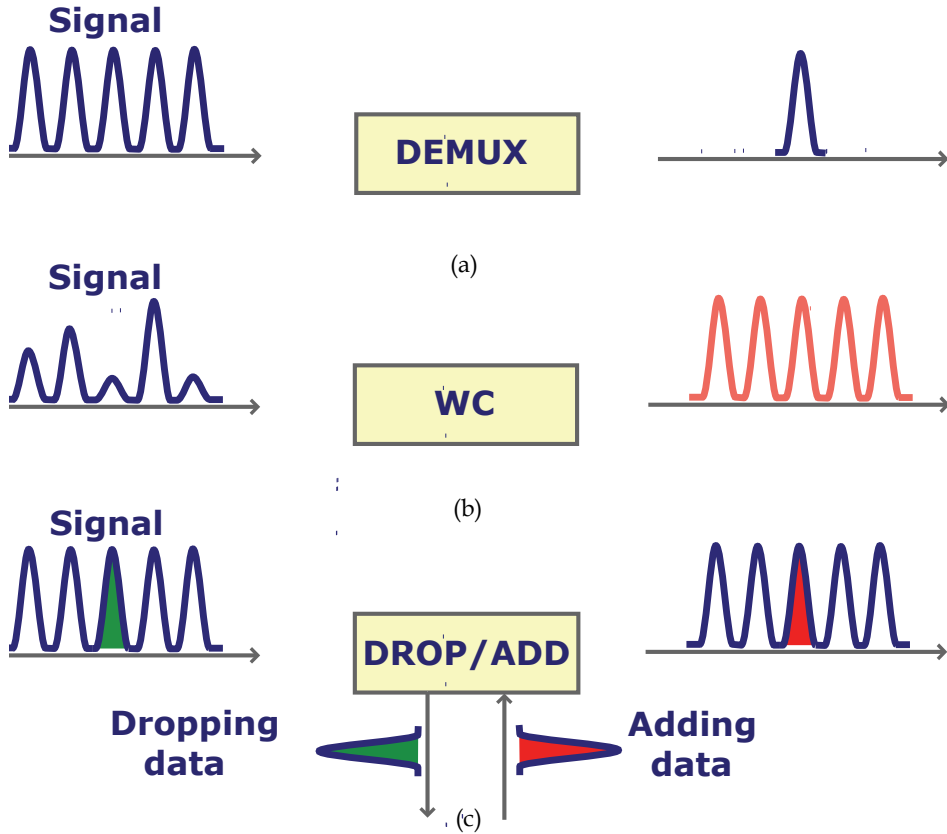


Fig. 1. Schematic diagrams of all optical ultrafast signal processors: (a) Optical DEMUX, (b) WC, and (c) OADM.

Figure 1 shows the schematic diagrams of all optical ultrafast signal processors: Optical DEMUX, WC and OADM. In particular, WC shows three active optical processings including wavelength conversion, re-amplification and re-shaping of distorted optical signals. The optical processing with re-amplification and re-shaping is usually called as optical “2R”.

Generally, the nonlinear optical effects in glasses are known to occur on time scale of femto seconds (fs) which can realize the optical signal processing devices that have ultrafast response times. However, fiber-based optical signal processors have been also less realistic devices compared to other electrical signal processing devices because of their long fiber lengths. Because the fiber-based optical signal processors have been basically proposed using the silica-based glass fibers such as Dispersion Shifted Fibers (DSFs) without high nonlinearities to process the ultrafast optical signals, the fiber lengths of the silica-based nonlinear fiber devices have become very long in excess of a few hundred meters to achieve enough nonlinearities to process optical signals (Yang et al., 1997).

In general, we can obtain larger nonlinear effects in glass fibers as the fiber lengths get longer. Therefore, in order to obtain high nonlinearities, long device lengths have been required for fiber-based optical signal processors. However, such long fiber lengths have led to the relative time delay among optical signals caused by the chromatic dispersions of the fibers. As in recent commercially deployed wavelength division multiplexing (WDM) optical telecommunication systems, equally frequency-spaced many optical signal channels have been used to enhance the transmission capacities of optical transmission systems. When the fiber lengths of the fiber-based optical signal processors become longer, the chromatic dispersions of these fiber devices give rise to the relative time delay among the optical signals in WDM transmission systems, which makes it difficult to process the ultrafast optical signals allocated in wide wavelength region simultaneously. Thus, in order to work as ultrafast optical signal processors, undesirable long device lengths have been required for fiber-based optical devices to obtain enough high nonlinearities.

2.2 Developments of Highly-Nonlinear Fibers based on Novel Glasses

In last decade, due to the development of the synthetic techniques of the novel glass materials, nonlinear characteristics of glass materials have been improved drastically and made it realize to emerge various highly-nonlinear fibers (HNLFs).

In addition, owing to the establishment of the design techniques for the spatial strong photon localization in the periodically microstructured materials and fibers based on novel highly-nonlinear glasses, Photonic Crystal Fibers (PCFs) (Birks et al., 1997), have realized extremely high nonlinearities in considerably shorter fiber lengths than those of fibers with simple core-cladding structures. The emergences of these HNLFs and PCFs fabricated by novel highly-nonlinear glass materials have given different kinds of applications for ultrafast all optical processing devices. Among these optical signal processing applications in large capacity communication networks, wavelength conversion plays a major role in providing wavelength flexibility. Therefore, in particular, WC based on FWM have been mainly proposed as a possible application for newly proposed HNLFs and PCFs in order to evaluate the optical signal processing characteristics of these HNLFs and PCFs.

On the basis of the glass fiber compositions of HNLFs and PCFs, two types of highly-nonlinear fibers have been proposed. One is the type of the glass fibers fabricated by conventional silica-based glasses and the other is the type of the glass fibers fabricated by non-silica-based glasses.

Table 1 shows the typical fiber parameters of various newly proposed silica-based and non-silica-based highly-nonlinear fibers. In particular, heavy metal oxide glass-based highly-nonlinear fibers are introduced as non-silica-based highly-nonlinear fibers.

As shown in Table 1, owing to the silica-based glass composition, silica-based highly-nonlinear fiber shows very low loss α to be 0.0005 dB/m (Onishi et al., 1997). This low loss characteristic of silica-based highly-nonlinear fiber means good compatibilities to the silica-based fibers used as transmission fibers in telecommunication systems, which leads to the low loss characteristics of silica-based highly-nonlinear fiber devices. In addition, nonlinear coefficient γ of silica-based HNLF has been reported to be $\sim 20 \text{ W}^{-1}\text{km}^{-1}$ (Onishi et al., 1997). Silica-based HNLF realizes the high refractive index contrast between the core and clad refractive indices using germanium-doped and fluoride-doped silica glasses as the materials for the core and clad. Silica-based PCF enhances nonlinearity due to its periodical special

microstructure and achieves over three times higher nonlinear coefficient than that of the silica-based HNLf with simple core-cladding structure (Onishi et al., 1997).

Owing to the enhanced nonlinearities of silica-based HNLfs, the fiber lengths of optical signal processors using silica-based HNLfs have become much shorter than those of ones based on conventional DSFs. Also, with effectively shortening the required fiber length from kilometers to tens of meters, good optical signal processing characteristics have been evaluated for silica-based PCF using WC characteristic (Lee et al., 2003). Nevertheless, optical signal processing devices using silica-based HNLfs and PCFs still have tens of meters long fiber lengths. These rather long device lengths are much likely to bring the relative time delay among ultrafast optical signals over 160 Gb/s.

Glass composition	Structure	n^2 ($\times 10^{-20} \text{m}^2/\text{W}$)	γ ($\text{W}^{-1} \text{km}^{-1}$)	$D@1.5 \mu \text{m}$ (ps/nm/km)	$\alpha @1.5 \mu \text{m}$ (dB/m)
Germanium-doped silica	Step index	~5	~20	-	0.0005
Silica	PCF	2.8	70	-30	0.19
SF57	PCF	41	640	~50	2.6
Chalcogenide	Step index	400	-	-	6.6@1.3 μm
Bismuth oxide	Step index	-	1100	-260	0.8
Bismuth oxide	PCF	-	580	-9.9	1.9

Table 1. Fiber parameters of silica glass-based and non-silica glass-based highly-nonlinear fibers.

As shown in Table 1, nonlinear coefficients of the heavy metal oxide glass-based HNLfs and PCFs become nearly over ten times larger than those of silica-based HNLfs and PCFs. These enhancements of nonlinearities of heavy metal oxide glass-based HNLfs and PCFs are due to the high refractive indices of heavy metal oxide glasses. Owing to the extremely high nonlinearities of heavy metal oxide glasses, heavy metal oxide glass-based HNLfs have shortened fiber device lengths successfully from tens of meters to a few meters. In addition, using bismuth oxide glass-based HNLf, less than 1 meter-long fiber-based WC has been proposed (Lee et al., 2005). However, bismuth oxide glass-based HNLf inevitably has large material dispersion similar with other non-silica-based HNLfs fabricated by heavy metal oxide glasses, which limits the working bandwidth of WC. In general, heavy metal oxide glass-based HNLfs have been found to have extremely high nonlinearities but at the same time suffer from large group velocity dispersions (GVD), large fiber losses and large splice losses between heavy metal oxide glass-based HNLfs and conventional silica-based

fibers. In order to obtain broadband wavelength conversion characteristics using FWM, the glass fiber used as WC should have high nonlinearity, low dispersion and low loss characteristics (Inoue et al., 1992).

Thus, in order to realize practical optical signal processing devices such as OADM, WC, DEMUX and FOPA, high nonlinearity, low dispersion, low fiber loss, low coupling loss with conventional silica-based fiber are the required fiber characteristics for silica-glass based and heavy metal oxide glass-based highly nonlinear fibers. However, at the moment, we have not obtained the highly nonlinear fiber that can satisfy all required these fiber characteristics simultaneously.

3. Optical Parametric Amplification using Four-Wave Mixing

FWM has been as a main nonlinear effect to realize all optical signal processors. The optical signal processing characteristics of newly proposed HNLFs have been examined initially with the FWM efficiencies of WC using newly proposed HNLFs. Therefore, in this Section, we will introduce the precise theory of FWM and derive the coupling propagation equations of a signal, an idler and a pump light waves to establish numerical simulation model for FWM. In addition, we will overview the signal processing characteristics of FWM-based FOPA with the numerically simulated propagation characteristics of the signal along highly-nonlinear glass fibers.

3.1 Theory of Optical Parametric Amplification based on Four-Wave Mixing

As cited in Section 1 and Section 2, FWM is one of the well-known nonlinear effects occur in glass fibers similar with SPM and XPM. SPM and XPM mainly affect the phase of the pulsed optical signals due to the additional nonlinear phase shifts and cause the spectral broadening of pulsed signals, whereas FWM gives rise to the energy exchange among optical signals. Figure 2 shows the schematic diagram of FWM in the frequency domain. As shown in Figure 2, when a signal light wave and two pump light waves are input into a nonlinear glass fiber, an additional new light wave that has higher frequency than those of the two pump light waves is generated. The additional new light wave is usually called as an "idler" light.

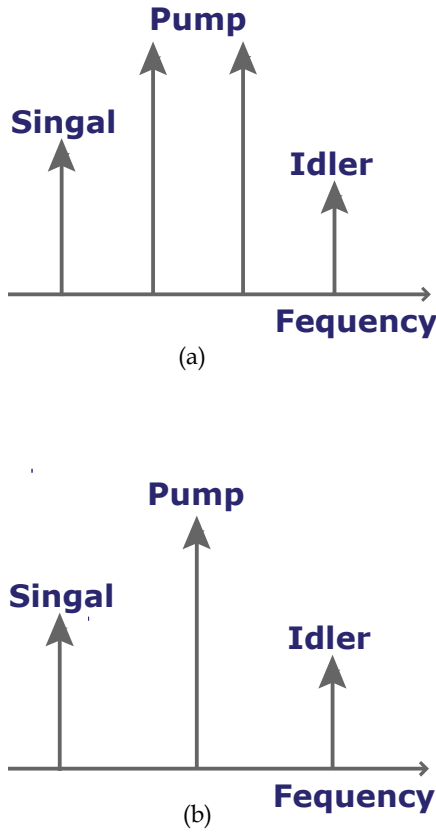


Fig. 2. Schematic diagrams of FWMs with (a) two pump lights and (b) one pump light in the frequency domain.

When the frequencies of two pump light waves are different, the relationship among the frequencies of the signal, the two pump and the idler light waves is given by,

$$\omega_i = \omega_{p1} + \omega_{p2} - \omega_s, \tag{1}$$

where ω_s , ω_{p1} , ω_{p2} and ω_i are the frequencies of the signal, pumps and idler, respectively. As can be seen from Eq. (1), the energies of the signal and two pump lights are transferred to that of the idler. Therefore, FWM is usually thought to be the energy transfer phenomenon caused by the nonlinear effects in glass fibers.

When the frequencies of two pump lights are identical ($\omega_{p1} = \omega_{p2} = \omega_p$), the energies of two pump lights are equally transferred to those of the signal and the idler.

Therefore, Eq. (1) becomes as follows:

$$2\omega_p = \omega_s + \omega_i. \tag{2}$$

This case where ω_{pump1} and ω_{pump2} coincide is called as “Degenerated” Four-Wave Mixing (DFWM). In this degenerated case, the frequencies of the three waves are symmetrically

positioned relatively to each other in the frequency domain. Optical parametric amplification can be viewed from a quantum mechanical picture. Here, the degenerated parametric amplification case is manifested as the conversion of two pump photons at frequency ω_{pump} to a signal and an idler photon at frequencies ω_{signal} and ω_{idler} . The conversion needs to satisfy the energy conservation relation as in Eq. (2). From the quantum-mechanical point of view, in the degenerated case, the photon momentum conservation relation is also needed to be satisfied as follows:

$$\Delta\beta = \beta(\omega_s) + \beta(\omega_i) - 2\beta(\omega_p) = 0, \quad (3)$$

where $\beta(\omega_s)$, $\beta(\omega_i)$ and $\beta(\omega_p)$ are the wave number in vacuum, respectively and $\Delta\beta$ is the mismatch among these wave numbers. For the rest of this chapter, we will focus on the degenerated case including one pump at ω_p , one signal at ω_s and one idler light wave at ω_i . From the electromagnetic point of view, Eq. (3) is also called as "linear phase matching" condition because the wave numbers of the three light waves are directly linked to the phases of those light waves. Therefore, Eq. (3) can be considered to be the relative phase shift among the three light waves. The propagation equations of these three light waves in a transmission media are given by the following three nonlinear couple-mode equations (Agrawal., 1995):

$$\frac{dA_p}{dz} = \frac{1}{2}\alpha A_p + i\gamma \left\{ [|A_p|^2 + 2(|A_s|^2 + |A_i|^2)]A_p + 2A_s A_i A_p^* \exp(i\Delta\beta z) \right\}, \quad (4)$$

$$\frac{dA_s}{dz} = \frac{1}{2}\alpha A_s + i\gamma \left\{ [|A_s|^2 + 2(|A_i|^2 + |A_p|^2)]A_s + A_i^* A_p^2 \exp(-i\Delta\beta z) \right\}, \quad (5)$$

$$\frac{dA_i}{dz} = \frac{1}{2}\alpha A_i + i\gamma \left\{ [|A_i|^2 + 2(|A_s|^2 + |A_p|^2)]A_i + A_s^* A_p^2 \exp(-i\Delta\beta z) \right\}. \quad (6)$$

where A_s , A_i and A_p are the complex field amplitude of the signal, the idler and pump light waves, respectively. z is the longitudinal coordinate along the fiber as the transmission media. α is the loss of the glass fiber for these three light waves. $\gamma = 2\pi n_2 / A_{\text{eff}}$ is the nonlinear coefficient of the fiber where n_2 is the nonlinear parameter and A_{eff} is the effective modal area of the fiber. In Eq. (4), Eq. (5) and Eq. (6), the first two terms are responsible for the nonlinear phase shift caused by SPM and XPM, respectively. The last terms of these couple-mode equations contribute to the energy transfer among the signal, the idler and the pump light waves.

Furthermore, to obtain further understanding to the propagation characteristics of the three light waves in the fiber, Eq. (4), Eq. (5) and Eq. (6) are rewritten by using $A_j = P_j^{1/2} \exp(i\phi_j)$ ($j=s, i, p$) where P_j ($j=s, i, p$) is the power of the three light waves and ϕ_j ($j=s, i, p$) is the phases of the these light waves, respectively. Thus, we can obtain practical propagating equations to describe the propagation characteristics of the signal, the idler and the pump lights as follows:

$$\frac{dP_p}{dz} = \alpha P_p - 4\gamma[(P_s P_i P_p^2)^{1/2} \sin\theta], \quad (7)$$

$$\frac{dP_s}{dz} = \alpha P_s + 2\gamma[(P_s P_i P_p^2)^{1/2} \sin \theta], \quad (8)$$

$$\frac{dP_i}{dz} = \alpha P_i + 2\gamma[(P_s P_i P_p^2)^{1/2} \sin \theta], \quad (9)$$

$$\frac{d\theta}{dz} = \Delta\beta + \gamma(2P_p - P_s - P_i) + \gamma[(P_p^2 P_i / P_s)^{1/2} + (P_p^2 P_s / P_i)^{1/2} - 4(P_s P_i)^{1/2}] \cos \theta. \quad (10)$$

Here, Eq. 10 describes the propagation characteristics of the relative phase among three light waves. The first term of Eq. 10 is the contribution from the linear phase shift that does not depend on the powers of three light waves. The second and third term of Eq. 10 show the contributions from the nonlinear phase shifts caused by the nonlinearity of the glass fiber.

To simulate the frequency dependence of the optical amplification characteristics based on FWM, we will expand the linear phase shift $\Delta\beta$ in Taylor series to the fourth order around the zero-dispersion frequency ω_0 . Thus, we can obtain the frequency-dependent linear phase shift $\Delta\beta$ given by,

$$\Delta\beta = \left\{ \beta_3(\omega_p - \omega_0) + \frac{\beta_4}{2}[(\omega_p - \omega_0)^2 + \frac{1}{6}(\omega_p - \omega_s)^2] \right\} (\omega_p - \omega_s)^2. \quad (11)$$

Here, β_3 and β_4 is the third and fourth order dispersions defined at ω_0 . Also, β_2 (the second order dispersion of $\beta(\omega)$) becomes zero because $\beta_2(\omega_0) = 0$. Usually, β_2 and β_3 are called as “dispersion” and “dispersion slope” of the fiber, respectively. In addition, when the pump frequency ω_p is chosen to become $\omega_p = \omega_0$, the frequency dependent part of $\Delta\beta$ is fully dominated by the fourth-order dispersion β_4 . Therefore, the gain bandwidth of FOPA is strongly limited by the fourth-order dispersion β_4 (Marhic et al., 1996). To realize the broad band optical signal wavelength converter using FOPA based on FWM, the value of β_4 has been improved in silica-based highly nonlinear glass fibers (Hirano et al., 2005). Higher order dispersions become an important limiting factor as the optical signal operating bandwidth $\Delta\lambda = |\lambda_p - \lambda_s|$ exceeds 100 nm.

3.2 Numerical Analysis on Gain Characteristics of FWM-based FOPA

Next, using the simulation model based on the reduced propagation equations (7), (8), (9) & (10), we will overview the signal processing characteristics of FWM-based FOPA with the numerically simulated parametric gain characteristics of FWM-based FOPA. In this numerical simulation, we used further reduced Eq. (12) and Eq. (13) obtained by neglecting β_4 and by assuming that FOPA are operated in a phase-matching condition that the relative phase remains near $\pi/2$ in Eq. (10) and Eq. (11). Eq. (12) and Eq. (13) are given by,;

$$\kappa = \Delta\beta + 2\gamma(P_p - P_s - P_i), \quad (12)$$

$$\Delta\beta = -\frac{2\pi\lambda_0^3}{\lambda_p^3 \lambda_s^2} \frac{dD_c}{d\lambda} (\lambda_p - \lambda_s)^2 (\lambda_p - \lambda_0), \quad (13)$$

where κ and $\Delta\beta$ show the linear and total phase mismatch parameters, respectively. γ is the nonlinear coefficient of HNLF. P_j ($j=s, p, i$) and λ_j ($j=s, p, i$) show the powers and wavelengths of signal, pump and idler, respectively. $dD/d\lambda_c$ is the dispersion slope at the

zero dispersion wavelength of HNLF. It is known that the parametric gain of FWM-based FOPA shows the maximum value when FWM-based FOPA is operated in the total phase-matching condition $\kappa = 0$ is satisfied.

As shown in Eq. (12), the total phase mismatch consists of the linear phase mismatch part $\Delta\beta$ and the nonlinear phase mismatch part $2\gamma(P_p - P_s - P_i)$. The linear phase mismatch part $\Delta\beta$ does not depend on the powers of signal, pump and idler. Therefore, $\Delta\beta$ becomes the constant phase mismatch factor for FOPA. On the other hand, the nonlinear phase mismatch part $2\gamma(P_p - P_s - P_i)$ apparently depends on the powers of signal, pump and idler.

Therefore, when the powers of signal, pump and idler are varied in FWM-based FOPA, parametric gain characteristics of FWM-based FOPA are affected sensitively by the total phase mismatching due to the variation of these powers.

Firstly, we will overview this parametric gain variation of FWM-based FOPA induced by the input power with the gain characteristics of FWM-based FOPA with different pump powers shown in Figure 3.

Table 2 shows the fiber parameters of silica-based HNLF used in this analysis on the parametric gain characteristics of FWM-based FOPA. In this numerical simulation, the parametric gain media of FOPA is assumed to be a germanium-doped silica-based HNLF with nonlinear coefficient $25 \text{ W}^{-1}\text{Km}^{-1}$ and 150 m of the fiber length. Then, the pump wavelength is set to be 1562 nm longer than zero dispersion wavelength of the fiber 1555.5 nm. The input signal power into HNLF is -30 dBm. As shown in Figure 3, the parametric gain of FOPA becomes to show two symmetrical peaks about the pump wavelength as the higher pump power input into HNLF. At the wavelengths where the parametric gain shows its peaks, total phase-matching condition $\kappa = 0$ is fully satisfied. Whereas the parametric gain shows peaked gain shape with high pump power ($P_p = 30 \text{ dBm}$), almost flat parametric gain shape is obtained with low pump power ($P_p = 20 \text{ dBm}$). This pump power dependence of the parametric gain characteristics shows that the difference in the parametric gain evolution rates is induced by the power-dependent nonlinear phase mismatch part $2\gamma(P_p - P_s - P_i)$. Generally, it is known that the parametric gain characteristics are exponentially proportional to the applied pump power in the wavelength region where the perfect phase-matching condition $\kappa = 0$ is satisfied. Also, the parametric gain characteristics are quadratically proportional to the applied pump power in the wavelength region where the linear phase-matching condition $\Delta\beta = 0$ is satisfied. Figure 4 shows the simulated parametric gain evolutions of a signal and an idler along the silica-based HNLF with two different wavelengths. One is 1540 nm where the total phase-matching condition $\kappa = 0$ is found to be almost satisfied show in Figure 3. The other is 1560.5 nm near the pump wavelength 1562 nm where the linear phase-matching condition $\Delta\beta = 0$ is satisfied.

As shown in Figure 4, the difference between parametric gains at 1540 nm and 1560.5 nm becomes larger as the signal propagation distance gets longer. This implies that the fiber length should be shortened to obtain the flat parametric gain shape of FOPA. On the other hand, long fiber length is required to obtain large parametric gain of FOPA. Thus, it is difficult to realize large and flat gain characteristics of FOPA simultaneously. So far, in order to achieve large and flat gain characteristics of FOPA, the gain enhancement schemes of FOPA with broad gain characteristics have been proposed. Therefore, in Section 4, in order to realize the FOPA with large and flat gain characteristics, we will propose a novel parametric gain enhancement scheme of FOPA with flat gain characteristics.

Simulation parameters of HNLF	
Glass composition	Germanium SiO ₂
Fiber length [m]	150
Nonlinear coefficient [W ⁻¹ km ⁻¹]	25
Zero dispersion wavelength [nm]	1555.5
Dispersion Slope [ps/nm/km ²]	0.03
Fiber loss [dB/km]	0.5

Table 2. Fiber parameters of silica-based HNLF.

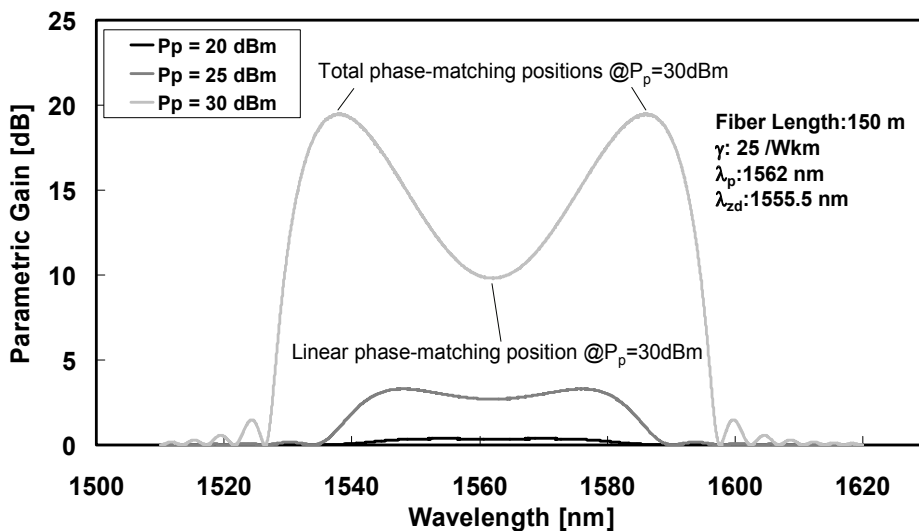


Fig. 3. Simulated parametric gain characteristics of silica glass-based FOPA with various pump powers ($P_p = 10$ dBm , 20 dBm and 30 dBm).

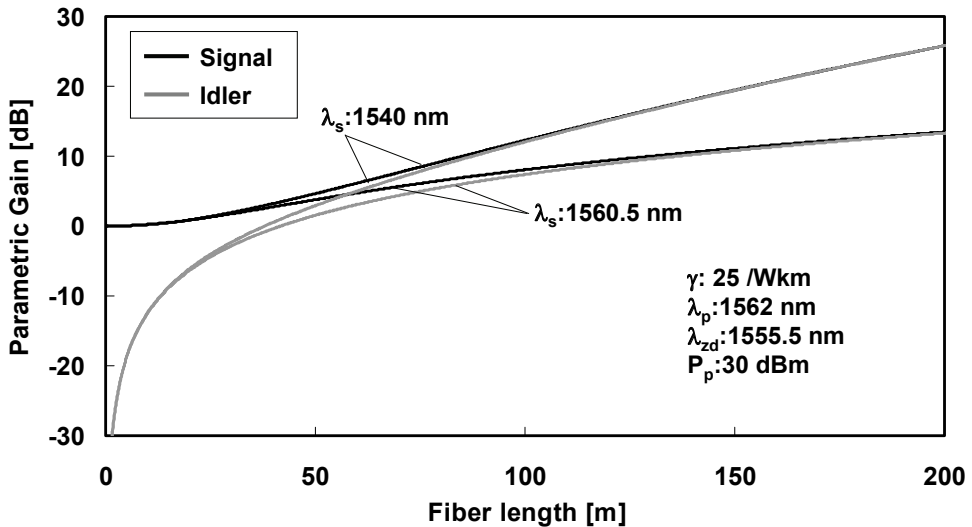


Fig. 4. Fiber propagation characteristics of the parametric gains of signals and idlers with different wavelengths ($\lambda_s = 1540$ nm and 1560.5 nm).

4. Application of FOPA to Ultrafast Optical Signal Processing Device

In this Section, we will introduce our experimental results of the ultrafast signal processing experiments using single-pumped FOPAs as an broadband ultrafast optical DEMUX with large parametric gain characteristics for over 160 Gb/s optical signal data streams. On the basis of our proposed design schemes for FOPA, we performed evaluations on the parametric gain characteristics of the single-pumped cascaded silica-glass-based HNLFs with different dispersions and dispersion slopes.

As results of this evaluation, it was shown that over 20 dB parametric gains can be achieved in ~ 50 nm bandwidth in C-band wavelength region. Apparent improvement in the parametric gain characteristics was observed in the wavelength region near the pump wavelength. Furthermore, to verify the capability of our proposed FOPA as an ultrafast optical signal processor, we performed transparent 160 Gb/s - 10 Gb/s DEMUX experiments using 160 Gb/s On-Off keyed (OOK) data using the parametric gain-enhanced FOPA by our proposed design scheme. As a result, no error penalty occurred for 160 Gb/s ultrafast data streams in the transparent 160 Gb/s - 10 Gb/s DEMUX experiment.

4.1 Broadband FOPA Design Scheme with Perfect Phase-matching Condition

So far, FOPA and Nonlinear Loop Mirror (NOLM) have been proposed as all optical fiber-based DEMUX. In principle, the optical gating action controlled by optical clock pulses is required for optical DEMUX. Figure 5 shows the comparison of the optical DEMUX characteristics of NOLM-based DEMUX and FOPA-based DEMUX.

As shown in Figure 5, NOLM-based DEMUX cannot amplify the input signal and can bring the interference between incoming and counter propagate pulse. For ultrafast optical fast

signals, this interference between incoming and counter propagate pulse can deteriorate the optical data streams in NOLM-based DEMUX. On the other hand, FOPA based DEMUX can amplify the incoming data signal with parametric gain. Also, there is no interference of data pulses in FOPA-based DEMUX. Therefore, in this work, we used FOPA as optical DEMUX for ultrafast optical signal processing. The results of transparent 160 Gb/s - 10 Gb/s DEMUX experiments using FOPA-based ultrafast DEMUX are will be shown in Section 4.

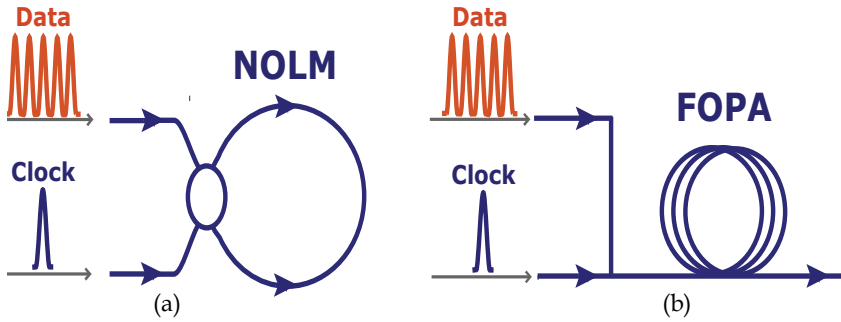


Fig. 5. Schematic diagrams of the principles of the optical gating operations in (a) NOLM and (b) FOPA.

In order to realize the broadband ultrafast optical DEMUX using FOPA, large FOPA gain characteristics in a wide wavelength region should be realized. So far, in order to achieve large and broad gain characteristics of FOPA, the gain enhancement schemes of FOPA with broad gain characteristics have been proposed using many cascaded HNLFs with dual pump scheme. However, using many HNLFs and dual pump scheme is not suitable way to realize the practical FOPA for optical signal processors because of the complicated HNLF's configuration and the use of two pump lasers, which leads to the increase of splice losses between HNLFs and the less cost effectiveness. Particularly, in order to realize an optical DEMUX using FOPA, the optical gating of the optical DEMUX should be controlled by single pump light source as an optical clock pulse because it is extremely difficult to adjust and control the relative timing among ultrafast optical signals over 160 Gb/s and multi-pump light pulses. In order to realize a practical FOPA with large and broad parametric gain characteristics using single pump light source, simpler design scheme of FOPA are required. Therefore, we propose a simple and practical design scheme to achieve large and broad parametric gain characteristics of FOPA exploiting the perfect phase-matching condition of FWM.

Figure 6 shows the optical parametric gain characteristics of FOPA achieved in the perfect-matched and linear phase-matching conditions. When the perfect phase-matching condition $\kappa = \Delta\beta + 2\gamma(P_p - P_s - P_i) = 0$ is achieved, the parametric gain shows the exponential characteristics in terms of the pump power as shown in Section 3. In addition, if the linear phase-matching condition $\Delta\beta = 0$ is only satisfied, the parametric gain characteristics becomes quadratic one. In our design scheme, we particularly tried to improve the gain characteristics in the wavelength region near the pump wavelength because the gain depletion occurs significantly in that wavelength region.

Figure 7 shows the schematic design concept of the switching gain band width enhancement using quasi-cascaded two HNLFs with different dispersions and dispersion slopes. The term “quasi” is used because there is not much difference between the optical parameters of these two HNLFs. In this two HNLFs configuration scheme, the zero dispersion wavelength of 1st HNLF is set to become slightly shorter than the pump wavelength, which makes the wavelength of the parametric gain peak relatively far from the pump wavelength. Also, the zero dispersion wavelength of 2nd HNLF is set to become shorter than that of the 1st HNLF in order to make the wavelength of the gain peak of 2nd HNLF longer. In addition, the dispersion slope of the 2nd HNLF is set to be relatively steeper than that of 1st HNLF to make the maximum gain peak of the 2nd HNLF shift toward the pump wavelength in the shorter wavelength. With this design scheme, the improvement of the parametric gain characteristics particularly in the wavelength region near the pump wavelength can be expected.

4.2 Experimental Setup

4.2.1 Evaluations of Optical Parametric Gain Characteristics of FOPA

Figure 8 shows the experimental configuration for the parametric gain characteristic evaluation. The proposed design scheme for HNLFs to achieve high and broadened parametric switching gains was tested using a quasi-cascaded HNLF consists of two HNLFs.

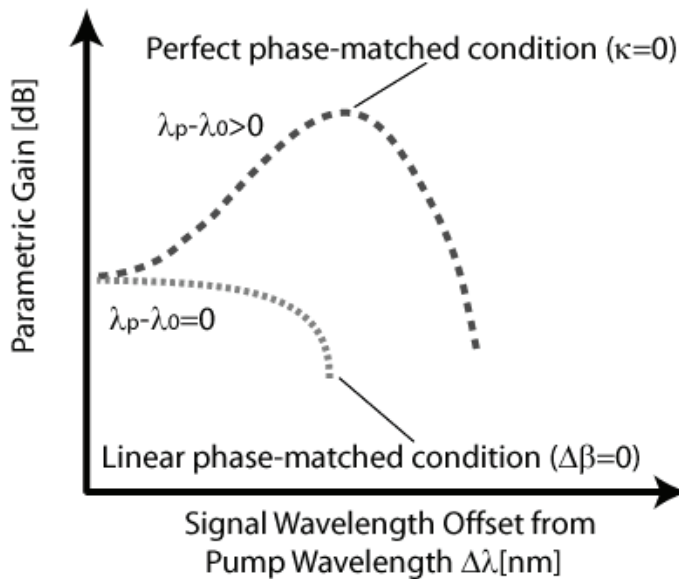


Fig. 6. Schematic diagrams of the optical parametric gain characteristics of FOPA achieved in the perfect-matched ($\kappa = 0$) and the linear phase-matching conditions ($\Delta\beta = 0$).

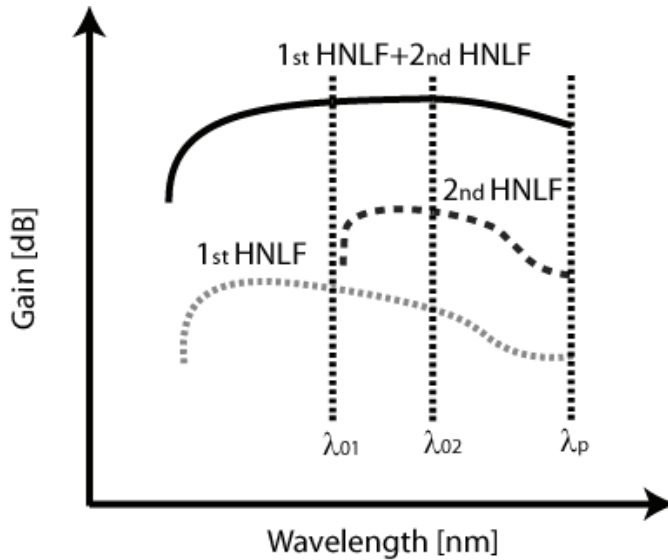


Fig. 7. Schematic diagram of the design concept for the parametric gain bandwidth enhancement using the quasi-cascaded two HNLFs with different dispersions and dispersion slopes.

Two HNLFs have the zero dispersion slopes and the zero dispersion wavelengths (λ_{01} , $dD/d\lambda_{01} = (1570 \text{ nm}, 0.03 \text{ ps/nm}^2/\text{km})$ and (λ_{02} , $dD/d\lambda_{02} = (1555 \text{ nm}, 0.035 \text{ ps/nm}^2/\text{km})$), respectively. The nonlinear coefficients γ of the HNLFs are $\sim 21 \text{ W}^{-1}\text{km}^{-1}$. A modelocked Fiber laser (MLFL) as a signal source generated a 10 GHz optical pulse train at wavelengths in the wavelength region from 1520 nm to 1550 nm. A tunable laser source was used as pump source, which was modulated by an Electro-Absorbitive (EA) modulator and a LiNbO₃ intensity modulator (LN, 10 Gb/s, PRBS: 2²³-1) to realize the wide pulse width with the repetition rate 311MHz and a high peak power at the fiber input. Maximum pump peak power was about 43 dBm. A signal was input to the quasi-cascaded HNLFs together with a pump pulse that had ~ 45 degree-aligned polarization to that of the signal pulse. The wavelength of the pump pulse was 1570.5 nm to have almost the same wavelength of the 1st HNLf. The pulse widths (FWHM) of the signal and control pulses were 1.6 ps and 25 ps, respectively.

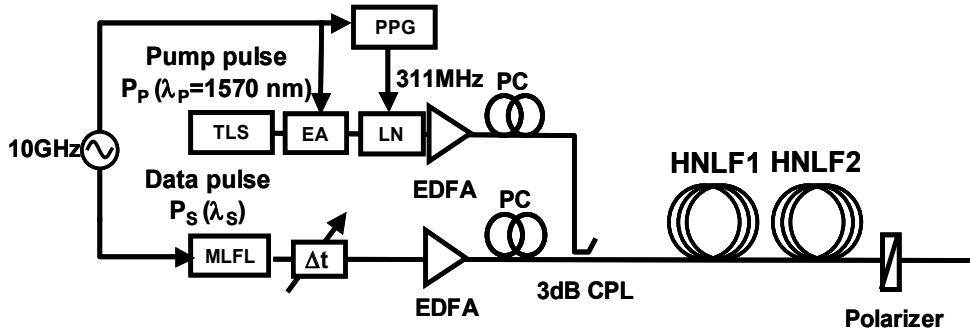


Fig. 8. Schematic diagram of the experimental setup for the evaluation on the parametric gain characteristic of proposed quasi-cascaded HNLFs.

4.2.2 160 Gb/s -10 Gb/s DEXUM Experiment using Quasi-Cascaded HNLFs

Furthermore, we evaluated the signal processing characteristics of the perfect phase-matching FOPA using ultrafast pulse trains. 160 Gb/s - 10 Gb/s OTDM DEMUX experiment was performed using another modelocked fiber laser, which generates 1.6 ps light pulse with the pulse repetition rate 10 GHz at the wavelength $\lambda_s = \sim 1540$ nm where the parametric gain characteristics improved by our proposed FOPA design scheme. This 10 Gb/s pulse was optically time-division multiplexed to generate a single polarized 160 Gb/s data pulse train. Using this pulse train as a signal, we performed 160 Gb/s - 10 Gb/s OTDM DEMUX experiments to verify the capability of the proposed FOPA as an ultrafast optical signal processor.

4.3 Results

4.3.1 Parametric Gain Characteristic of Quasi-Cascaded HNLFs

Figure 9 shows the parametric signal gain characteristics of 1st, 2nd and 1st + 2nd HNLFs. As shown in Figure 9, parametric signal gain characteristics of 1st and 2nd HNLF show the parametric gain peaks at the wavelengths ~ 1520 nm and ~ 1550 nm where phase-matching conditions $\kappa = 0$ in 1st and 2nd HNLF are satisfied. Parametric signal gain characteristic of quasi-cascaded HNLFs (1st + 2nd HNLFs) is also shown in Figure 8. As shown in Figure 8, with our proposed design concept for FOPA, parametric signal gain characteristic of cascaded HNLFs becomes flat shape compared to those of 1st and 2nd HNLF. As results of this evaluation, it was shown that over ~ 20 dB parametric gains can be achieved in ~ 50 nm bandwidth (from 1510 nm to 1560 nm) in C-band wavelength region. In particular, improvement in the parametric gain characteristics was observed in the wavelength region near the pump wavelength 1570 nm.

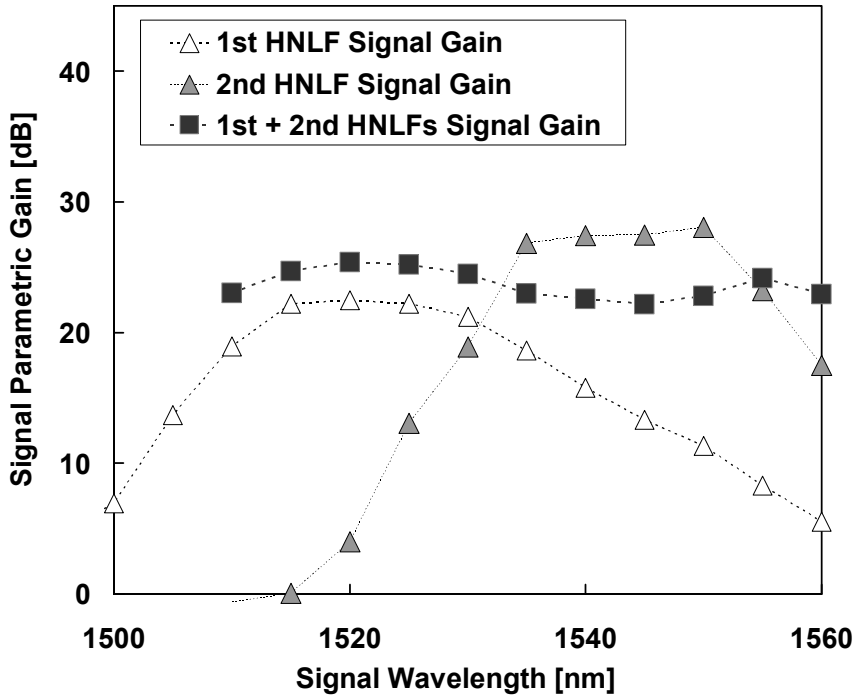


Fig. 9. Parametric gain characteristics of 1st HNLf, 2nd HNLf and 1st + 2nd HNLfs.

4.3.2 High Speed Switching Characteristics in 160 Gb/s – 10 Gb/s DEMUX

Figure 10 shows the measured bit error rates (BERs) obtained by 160 Gb/s - 10 Gb/s OTDM DEMUX experiments. The eye-patterns in the BER measurements of 10 Gb/s reference and 160 Gb/s - 10 Gb/s OTDM DEMUX are also shown (inset (a) and inset (b)). As shown in Figure 10, error free operations were demonstrated successfully without wavelength conversion for the OTDM DEMUXs of 160 Gb/s pulse trains. No penalty was occurred in the 160 Gb/s - 10 Gb/s transparent OTDM experiment compared to the 10 Gb/s reference BER curve. Therefore, No degradations of demuxed 10 Gb/s signal pulses occur after optical signal processing using our proposed FOPA-based optical demultiplexer. Also, compared to the input 160 Gb/s pulse trains, DEMUXed 10 Gb/s signal pulses show over 20 dB pulse gain induced by a perfect phase-matching. As results of 160 Gb/s - 10 Gb/s OTDM DEMUX experiments, our proposed FOPA is considered to be work as optical DEMUX with large parametric gain for up to 160 Gb/s ultrafast optical data streams.

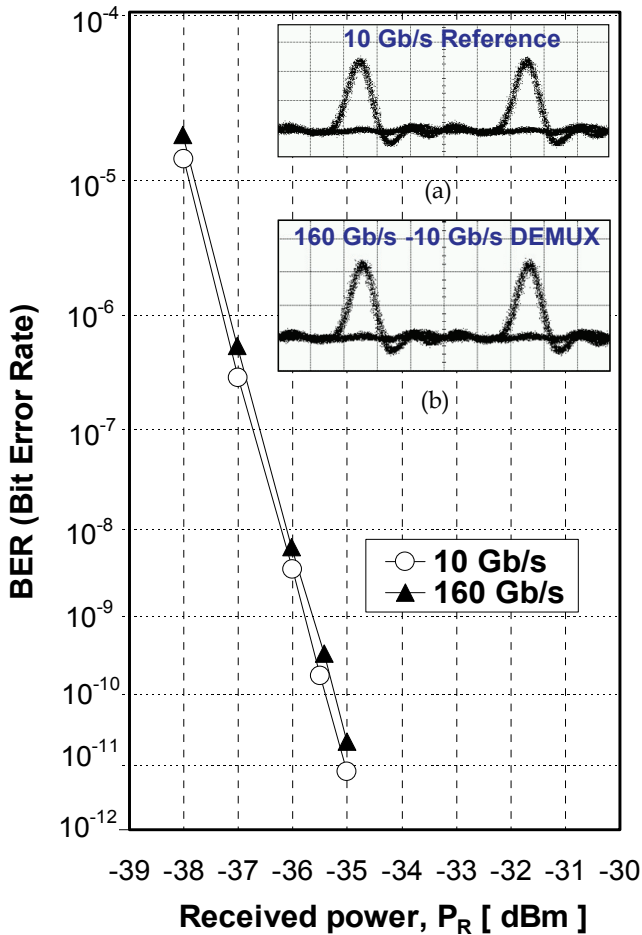


Fig. 10. Bit error rates (BERs) obtained by 160 Gb/s - 10 Gb/s OTDM DEMUX experiments. The eye-patterns in the BER measurements of 10 Gb/s reference (inset (a)) and 160 Gb/s - 10 Gb/s OTDM DEMUX (inset (b)) are also shown.

5. Conclusion

In this chapter, we overviewed the developments of highly-nonlinear glass materials and the optical signal processing functions of highly-nonlinear glass-based FOPA. The parametric gain characteristics of highly-nonlinear glass based FOPA in phase-matching conditions were introduced using numerical simulations based on FWM coupling equations. Using the parametric gain characteristics of FOPA in perfect phase-matching condition, in order to realize a practical glass-fiber based FOPA, we proposed the simple and practical design scheme to achieve the broad and large parametric gain characteristics of FOPA using silica glass-based HNLF and single pump. As a result, with proposed FOPA design scheme,

over 20 dB parametric gain was achieved in 50 nm band width in the C-band wavelength region. In particular, apparent improvement in the parametric gain characteristics was observed in the wavelength region near the pump wavelength. Furthermore, we performed 160 Gb/s - 10 Gb/s OTDM DEMUX experiments at the wavelength where the parametric gain characteristics improved. In the ultrafast DEMUX experiments, we verified that no error penalty occurred for 160 Gb/s pulse trains. This result shows that our design scheme for FOPA using the perfect phase-matching condition of FWM is effective for the transparent DEMUX of the ultra high bit-rate pulses over 160 Gb/s.

6. References

- Agrawal, G. P. (1995). *Nonlinear Fiber Optics*, 2nd edition, Academic press, San Diego, CA, USA.
- Aso, O.; Arai, S.; Yagi, T.; Tadakuma, M.; Suzuki, Y. & Namiki, S. (2000). Broadband four-wave mixing generation in short optical fibers, *Electron. Lett.* Vol. 36, pp. 709 - 711.
- Asobe, M.; Kanamori, T. & Kubodera, K. (1993). Applications of highly nonlinear chalcogenide glass fibers in ultrafast all-optical switches, *IEEE Journal of Quantum Electronics*. Vol. 29, pp. 2325-2333.
- Birks, T.A.; Knight, J.C. & St. J. Russell, P. (1997) Endlessly single-mode photonic crystal fiber, *Optics Letters*, Vol. 22, No 13, pp. 961-963.
- Chow, K. K.; Kikuchi, K.; Nagashima, T.; Hasegawa, T.; Ohara, S. & Sugimoto, N. (2007). Four-wave mixing based widely tunable wavelength conversion using 1-m dispersion-shifted bismuth-oxide photonic crystal fiber, *Optics Express* Vol. 15, pp. 15418-15423.
- Hedekvist, P. O.; Karlsson, M. & Andrekson, P. A. (1997). Fiber four-wave mixing demultiplexing with inherent parametric amplification, *J. Lightwave Technol.*, vol.15, pp. 2051 - 2058.
- Hirano, M.; Nakanishi, T.; Okuno, T. & Onishi, M. (2005). Broadband Wavelength Conversion over 193-nm by HNL-DSF Improving Higher-order Dispersion Performance, *ECOC 2005 Proceedings*, Vol. 6, pp. 43-44.
- Ho, M. C.; Uesaka, K.; Marhic, M. E.; Akasaka, Y. & Kazovsky, L. G. (2001). 200-nm-bandwidth fiber optical amplifier combining parametric and raman gain, *Journal of Lightwave Technology*, vol.19, pp. 977 - 981.
- Inoue, K. & Toba, H. (1992). Wavelength conversion experiment using fiber four-wave mixing, *IEEE Photonics Technology Letters*, Vol. 4, pp. 69-72.
- Lee, J. H.; Belardi, W.; Furusawa, K.; Petropoulos, P.; Yusoff, Z.; Monro, T.M.; & Richardson, D.J. (2003). Four-wave mixing based 10 Gbit/s tunable wavelength conversion using a holey fiber with a high SBS threshold, *IEEE Photonics Technology Letters*, Vol.15, pp. 440-442.
- Lee, J. H.; Nagashima, T.; Hasegawa, T.; Ohara, S.; Sugimoto, N. & Kikuchi, K. (2005). Four-wave-mixing-based wavelength conversion of 40-Gb/s nonreturn-to-zero signal using 40-cm bismuth oxide nonlinear optical fiber, *IEEE Photonics Technology Letters*, Vol.17, no.7, pp. 1474-1476.
- Li, J.; Hansryd, J.; Hedekvist, P. O.; Andrekson, P. A. & Knudsen, S. N. (2001). 300Gbit/s eye-diagram measurement by optical sampling using fiber and Exhibit, *Optical Fiber Communication Conference*, March 17-22, Anaheim, CA.

- Marhic, M. E.; Kagi, N.; Chiang, T.-K. & Kazovsky, L. G. (1996). Broadband fiber optical parametric amplifiers, *Optics Express*, Vol. 21, pp. 573-575.
- Onishi, M.; Okuno, M.; Kashiwada, T.; Ishikawa, T. ; Akaska, S. & Nishimura, N. (1997). Integrated Optics and Optical Fiber Communications, 11th International Conference on, and 23rd European Conference on Optical Communications, Vol. 2, pp. 115 - 118.
- Petropoulos, P.; Ebendorff-Heidepriem, Heike.; Finazzi, V.; Moore, R.; Frampton, K.; Richardson, D. & Monro, T. (2003). Highly nonlinear and anomalously dispersive lead silicate glass holey fibers, *Optics Express* Vol.11, pp. 3568-3573.
- Yang, F. S.; Ho, M. C.; Marhic, M. E. & Kazovsky, L. G. (1997). Demonstration of two-pump fiber optical parametric amplification, *Lasers and Electro-Optics Society Annual Meeting 1997, LEOS '97 10th Annual Meeting*. Vol. 1.
- Westlund, M.; Hansryd, J.; Andrekson, P. A. & Knudsen, S. N. (2002). Trans-parent wavelength conversion in fiber with 24nm pump tuning range, *Electron. Lett.*, vol.38, pp. 85 - 86.

Fibre Based Schemes for Ultrafast Subsystems: Nonlinear Optical Loop Mirrors Traditional Design and Novel Applications

Antonella Bogoni¹, Francesco Fresi², Paolo Ghelfi¹, Emma Lazzeri²,
Luca Poti¹ and Mirco Scaffardi¹

¹*Consorzio Nazionale Interuniversitario per le Telecomunicazioni (CNIT), Pisa*

²*Scuola Superiore Sant'Anna, Pisa*

¹*Italy*

²*Italy*

1. Nonlinear Optical Loop Mirrors: an introduction

All-optical technology is nowadays one of the most promising alternatives to electronics in various applications, ranging over a wide variety of fields such as information transmission and signal processing due to its ultrafast performances and electromagnetic interference immunity.

In this scenario, fibre-based devices are interesting because of the ultrafast response of the Kerr effects that leads to fast dynamics.

In this Chapter an exhaustive analysis of the structure of a Nonlinear Optical Loop Mirror (NOLM) is given together with the theoretical description of the phenomena behind NOLM behaviour putting emphasis on the Cross Phase Modulation (XPM) and Self Phase Modulation (SPM) effects. The theoretical description is followed by a simple and straightforward matrix model of a NOLM that allows an effortless design of multiple NOLM structures by interleaving the basic element describing the mirror. The Mickey NOLM is investigated as an example of multiple NOLM structures design and shows the potential of the model.

The Chapter also introduces novel applications by means of theoretical design and experimental results. In this section, all-optical logic gates based on NOLMs are illustrated together with the scheme of an optical decision element that allows the improvement of the receiver performances in an optical Return to Zero (RZ) transmission system and with the three stage regeneration and demultiplexing for 160-Gb/s Transmission Systems based on nonlinear optical loop mirrors.

1.1 Structure

Nonlinear Optical Loop Mirrors are powerful nonlinear interferometric devices often used in all-optical processing because of their ultra-fast time response due to the Kerr effect in fibre, and could therefore represent the answer to the mentioned issues. NOLMs are based

on the Sagnac interferometer structure where the phase shift of the counterpropagating signals are unbalanced to made them interfering in a way that is suitable for the desired processing aim.

The loop is simply composed by an optical fibre coupler where the two output arms are connected to form a ring as shown in Fig. 1(a). Nonlinear elements such as Highly Nonlinear optical Fibre (HNLF) can be inserted in the loop to perform the phase shift unbalancing.

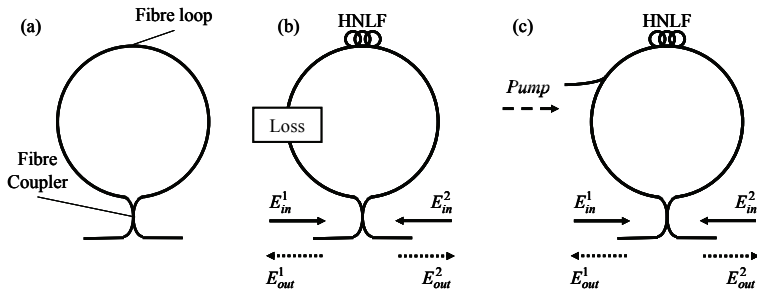


Fig. 1. (a) Main Structure of a Sagnac Interferometer; (b) HNLF-based NOLM exploiting SPM effect; (c) HNLF-based NOLM exploiting XPM effect.

1.2 XPM and SPM

When dealing with HNLF as nonlinear element inside the loop, two main nonlinear effects can be exploited to unbalance the phase-shifts of the counter-propagating signals interfering in the loop: Self Phase Modulation and Cross Phase Modulation.

In the former case, the fibre itself acts as nonlinear medium and a lumped loss is utilized to unbalance the two counter-propagating signal components as depicted in Fig. 1(b); since the amount of SPM (and consequently of nonlinear phase shift) experienced by a signal depends on its optical power, the presence of the lumped loss affects the system dynamic response.

In the latter case, a pump signal is introduced in the loop and circulates in only one direction as shown in Fig. 1(c); the phase shift induced in the co-propagating part of the input field depends on the instantaneous pump power, while the other portion of the input signal (counter-propagating with respect to the pump) experiences a phase shift that is determined by the pump average power.

2. NOLM Simple and Straightforward Model

Modular models based on basic building blocks are easy to handle when dealing with analytical description of complex physical phenomena. Assembling basic blocks allows building composite structure in a simple way and releases the model for further complications. In the model described here, each basic block is associated with a physical device and it is therefore straightforward to use.

Fig. 2(a)Left shows the structure of a Cross Phase Modulation based Polarization Maintaining NOLM (PM-NOLM) in the case of clockwise propagating pump. This interferometer was chosen to be the principal basic block of our model because of its flexibility given by the chance to use a pump signal to opportunely drive the device,

although Self Phase Modulation based NOLM could be preferred in some application where a control signal is not required. The loop comprises a Highly Non-Linear Fibre (HNLF) of length L_{HNLF} [Km], non-linear coefficient γ [$W^{-1}Km^{-1}$], negligible chromatic dispersion and dispersion slope, and two couplers, the former used to introduce the power of a pump signal at a wavelength λ_p (dashed arrows) into the loop, the latter to complete the NOLM structure as well as to allow the insertion of input fields and drop of output ones. The couplers have splitting ratios ρ_p and ρ respectively.

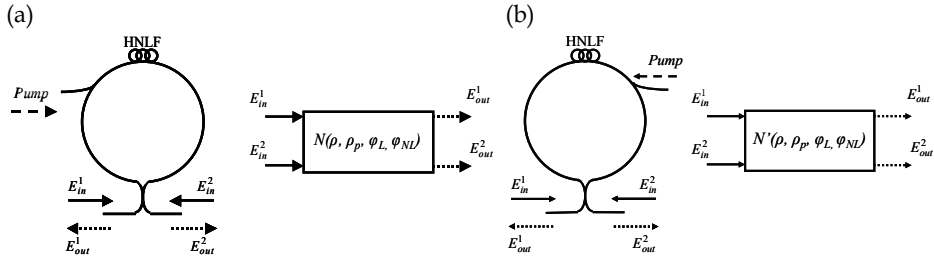


Fig. 2. (a) XPM based PM NOLM structure (Left) and its representation as a quadripole (Right) in the case of a clockwise propagating pump; (b) XPM based PM NOLM structure (Left) and its representation as a quadripole (Right) in the case of a counterclockwise propagating pump.

In a PM-NOLM all the components are polarization maintaining. Although this aspect can affect the system performances (non-PM fibres require the use of a polarization controller in the loop that adds a degree of freedom in the optimization process (Scaffardi et al., 2004), we choose to use a PM configuration in order to simplify the model that thus considers all fields as polarized along one of the fibre birefringence axes.

In our approach we describe each NOLM as a single basic quadripole defined through its dimensionless 2x2 matrix N . This way, each NOLM that composes the multiple structure is completely characterized and can be simply taken into account in the overall transfer function computing.

The block accepts an input vector \overline{E}_{in} (solid arrows) and returns an output vector \overline{E}_{out} (dotted arrows) that can be found as:

$$\overline{E}_{out} = \begin{bmatrix} E_{out}^1 \\ E_{out}^2 \end{bmatrix} = N \overline{E}_{in} = N \begin{bmatrix} E_{in}^1 \\ E_{in}^2 \end{bmatrix} \quad (1)$$

with:

$$N = \begin{bmatrix} n_{1,1} & n_{1,2} \\ n_{2,1} & n_{2,2} \end{bmatrix} \quad (2)$$

where:

$$n_{1,1} = \sqrt{\rho_p} e^{j\varphi_L} \sqrt{\rho(1-\rho)} (1 + e^{j\varphi_{NL}}) e^{j\frac{\pi}{2}} \quad (3)$$

$$n_{1,2} = \sqrt{\rho_p} e^{j\varphi_L} (\rho - (1-\rho) e^{j\varphi_{NL}}) \quad (4)$$

$$n_{2,1} = \sqrt{\rho_p} e^{j\varphi_L} (\rho e^{j\varphi_{NL}} - (1-\rho)) \quad (5)$$

$$n_{2,2} = \sqrt{\rho_p} e^{j\varphi_L} \sqrt{\rho(1-\rho)} (1 + e^{j\varphi_{NL}}) e^{j\frac{\pi}{2}} \tag{6}$$

Equations (1)-(6) state that the PM-NOLM processes the input fields introducing two different phase shifts: a linear one, φ_L , which is referable to the delay caused by the loop length L_{loop} , $\varphi_L = \beta L_{loop}$ (where β is the propagation constant of the field into the optical fibre) and a nonlinear one, φ_{NL} , that is due to the XPM effect induced by the pump power in the highly non linear fibre as stated in the following equation:

$$\varphi_{NL} = 2\gamma(1-\rho_p)L_{HNLf}P_p \tag{7}$$

where P_p is the instantaneous pump power and the coupler loss has been taken into account All the elements $n_{ij}(\varphi_{NL})$, $i,j=1,2$ are periodic functions of period 2π .

The model assumes the input signals to be continuous waves at a certain wavelength $\lambda_{in} \neq \lambda_p$ and, for the sake of simplicity, it neglects nonlinearities due to counter-propagating signals. This last simplification can be done considering the pump average power low enough, as in the case of a pulsed train with an appropriate duty cycle (Bogoni et al., 2004 a). Due to the low value for D and S, walk-off effect is also neglected.

The model validity domain can be estimated by considering following standard fibre parameters: $L_{HNLf} = 0.5$ Km, $\gamma = 10$ W⁻¹Km⁻¹, $D < 0.1$ ps·nm⁻¹km⁻¹, and $S < 0.01$ ps²·nm⁻¹km⁻¹. Accumulated chromatic dispersion $D_{tot} < 0.05$ ps·nm⁻¹ gives 175 fs pulse broadening for a 1 ps, 3.5 nm Gaussian pulse width or, similarly, a walk-off of about 1 ps when spectral displacement between interacting signal is 20 nm.

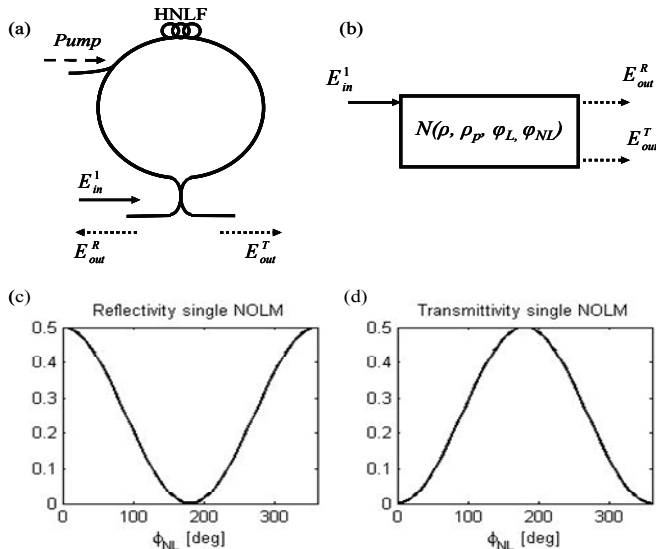


Fig. 3. XPM based PM NOLM structure (a), its representation as a quadripole (b). Reflectivity (c) and Transmittivity (d) functions in the case of a clockwise propagating pump with a single input Field.

On the other hand, phase shift due to SPM effect is limited to $\gamma L_{HNL} P_{in}$ and can be considered negligible if lower than 10° thus giving an upper bound for input signal power of about 15 dBm.

Fig. 2(b) shows a XPM based PM NOLM structure and its representation as a quadripole in the case of counter-clockwise propagating pump. Assuming the same references for the input and output fields as in Fig. 2(a), it is possible to demonstrate that the dimensionless matrix that describes the NOLM corresponds to the transpose of N , i.e. N^T .

The model introduced above can be used to describe a single NOLM as Fig. 3 shows. The results suppose the structure to be fed with a single input field ($E_{in}^2=0$) represented by a continuous wave at $\lambda_{in}=1550$ nm. Fig. 3 shows both the Reflectivity and the Transmittivity as functions of the nonlinear phase shift induced by the pump power as stated in (7).

3. Multiple Structure Design

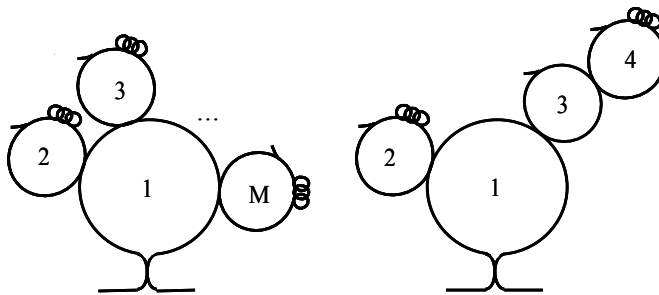


Fig. 4. Example of multiple NOLM device schemes. Left - A principal NOLM structure is connected to $M-1$ single NOLMs. Right - NOLM no. 1 is united to two separated NOLMs (no. 2 and no.3), while NOLM no.4 is attached only to NOLM no.3.

Once the modular model is verified for single and cascaded NOLMs, more complex structures can be considered in order to investigate for new schemes where a simple parameters tuning can lead to considerable changes in the output functions. Single NOLM response in terms of Transmittivity and Reflectivity have a sinusoidal shape, whilst numerical (Nayar et al., 1991) and experimental (Nayar et al., 1993) investigations have shown that cascading several NOLMs leads to a sharpening of the overall switching characteristics that results in steeper switching edges and flatter peaks. Single or cascaded NOLMs structures are therefore used to perform diverse all-optical processing tasks such as wavelength conversion (Sakamoto et al., 2001) and to build important network devices like soliton switches (Pattison et al., 1995). However, to the best of our knowledge, no work has been done to describe analytically or experimentally the performance of multiple and interleaved NOLM configurations such as the ones shown in Fig. 4.

3.1 Interleaving the basic element

Multiple and interleaved NOLM configurations can be composed by interconnecting the basic block defined in this Section with other elements such as fibre spans and couplers; for this purpose these elements can be described with matrices as reported in equations (8) and

(9), where C models the behaviour of a coupler with splitting ratio ρ and D represents the phase shift induced by a fibre span of length L_F .

$$C = \begin{bmatrix} \sqrt{\rho} & \sqrt{1-\rho} e^{j\frac{\pi}{2}} \\ \sqrt{1-\rho} e^{j\frac{\pi}{2}} & \sqrt{\rho} \end{bmatrix} \tag{8}$$

$$D = [e^{j\theta}], \theta = \beta L_F. \tag{9}$$

The corresponding blocks are depicted in Fig. 5 that shows the structure, block diagram and results of a two XPM based PM NOLMs cascade fed with a single input field ($E_{in}^2=0$) represented by a continuous wave at $\lambda_{in}=1550$ nm. In this case, Transmittivity and Reflectivity were studied as functions of the normalized pump powers defined as:

$$P_p^k \Gamma = \varphi_{NL}^k \tag{10}$$

where:

$$\Gamma = 2\gamma(1 - \rho_p^k) \tag{11}$$

By introducing a linear dependence between the normalized pump powers, different Reflectivity and Transmittivity curves can be extracted from the bi-dimensional plots as shown in Fig. 6(c). In order to give an accurate performance comparison with the corresponding single NOLM characteristics the curves are plotted as functions of the normalized total pump power:

$$P_{tot} \Gamma = (P_p^1 + P_p^2) \Gamma = P_p^2 (m + 1) \Gamma = \varphi_{NL}^2 (m + 1) \tag{12}$$

The linear dependence $P_p^2 = P_p^1 m$ is shown by the black superimposed line on the bi-dimensional plots. All curves are compared with the corresponding single NOLM T or R functions (dashed curves) that have sinusoidal shapes. Simulations were run using following parameters: $\varphi_L^1=0^\circ, \varphi_L^2=0^\circ, \theta=0^\circ, m=1$.

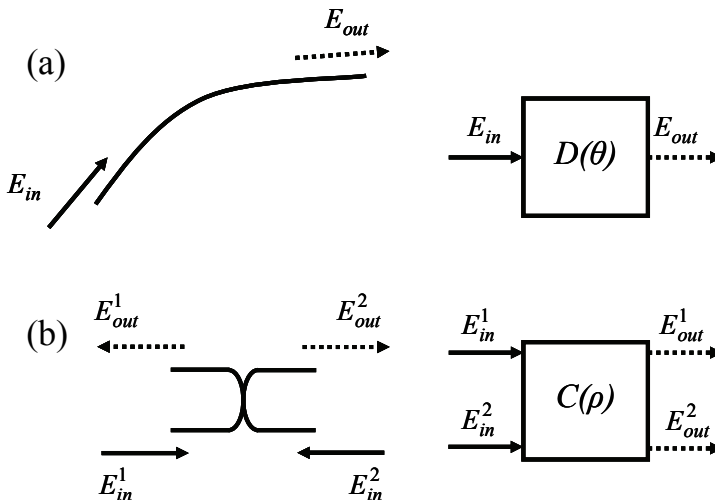


Fig. 5. (a) - Fibre span (left) and block representation (right); (b) - Coupler (left) and block representation (right).

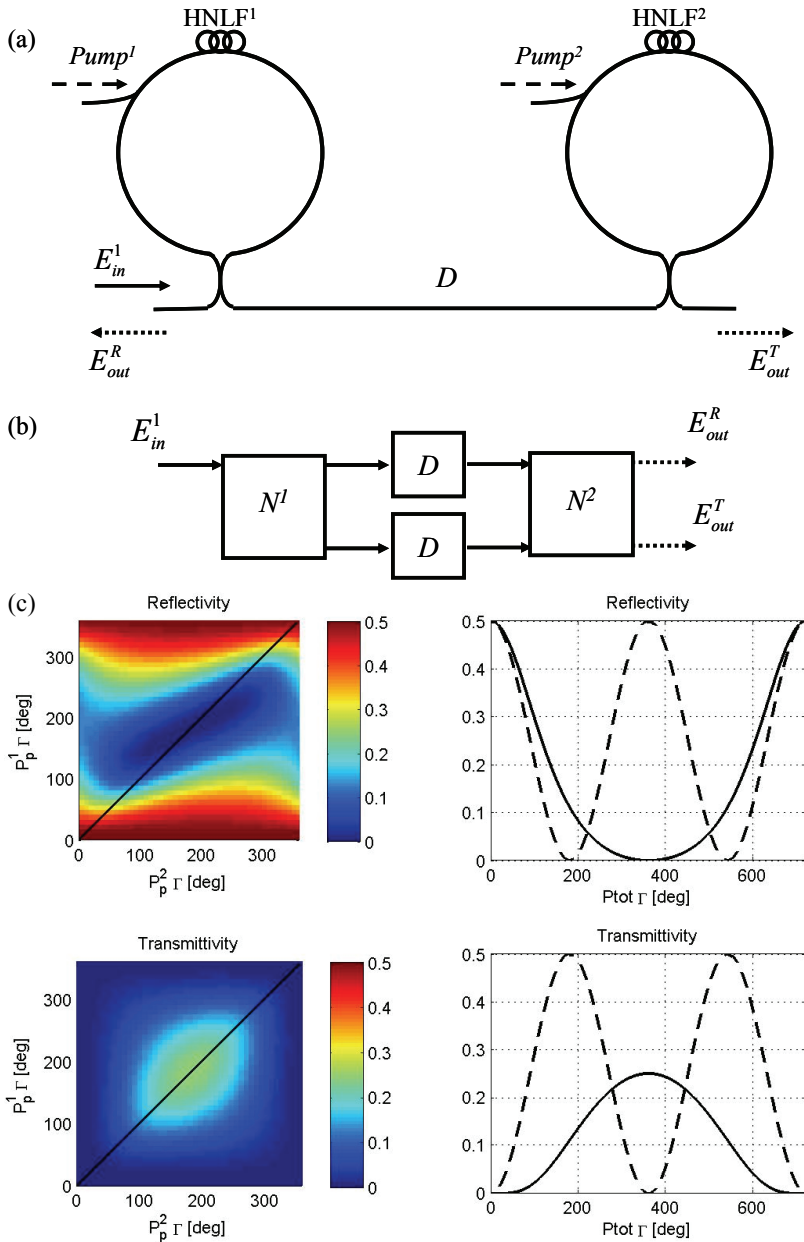


Fig. 6. Cascade of two XPM based PM NOLMs structure (a), block diagram (b) and simulation results (c) in the case of a clockwise propagating pumps with a single input Field.

3.2 Mickey NOLM

A particular configuration, which we will address to as Mickey NOLM, was designed to test the model described in section II. The structure of Mickey NOLM is shown in Fig. 7. Considering the NOLM versions related to clockwise and counter-clockwise propagating pumps, we can imagine to have four diverse configurations corresponding to the possible XPM-based PM NOLMs combinations. Ignoring the redundant configurations due to the possible input and output ports switch, we end up with only three versions of the Mickey NOLM that are shown in Fig. 7.

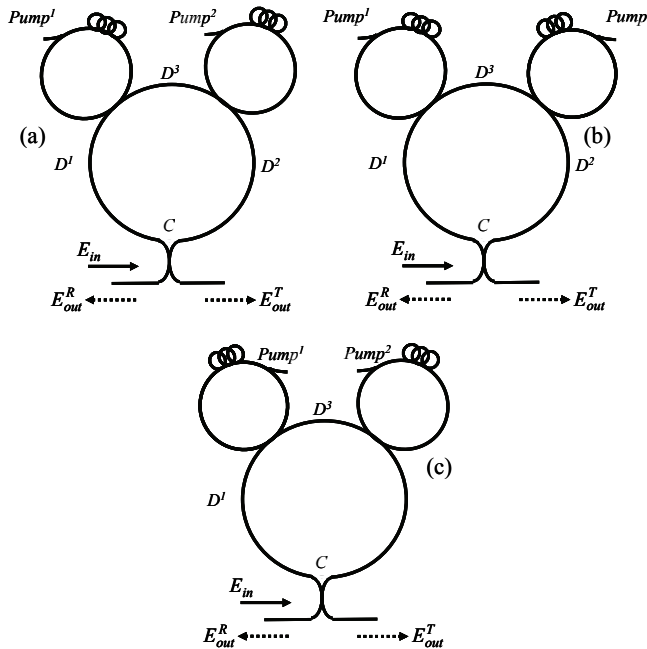


Fig. 7. Mickey NOLM possible structures; the three versions differ from each other in the pumps propagating directions; (a) - the XPM-based PM NOLMs both present clockwise propagating pumps; (b) - the XPM-based PM NOLM on the left side of the device present clockwise propagating pump while the one on the right makes use of counter-clockwise propagating pump; (c) - the XPM-based PM NOLM on the right side of the device present clockwise propagating pump while the one on the left makes use of counter-clockwise propagating pump.

To compose the Mickey NOLM, two XPM-based PM NOLM are connected with three fibre spans of certain lengths L_F^m ($m=1,2,3$) and one coupler ($C(\rho)$ as in equation (8)). One input field is fed into the structure (solid arrow in Fig. 7) to produce two outputs: the transmitted and the reflected fields (dotted arrows in Fig. 7). Our interest is focused on Reflectivity (R) and Transmittivity (T) as functions of the nonlinear phase shifts $\varphi_{NL}^1, \varphi_{NL}^2$ that can be easily

ascribed to the pump powers (P_p^1, P_p^2) by linear conversion as established in equation (7); to compute R and T, we first need to outline the Mickey NOLM block diagram by means of the basic elements shown in Figures Fig. 2Fig. 5. The resulting diagram is shown in Fig. 8(a) where N k ($k = 1, 2, \dots$) indicate the XPM-based PM NOLMs, $D^m = [e^{j\theta^m}]$, $\theta^m = \beta L_F^m$ indicate the three different fibre spans, and C is the coupler as described in (8).

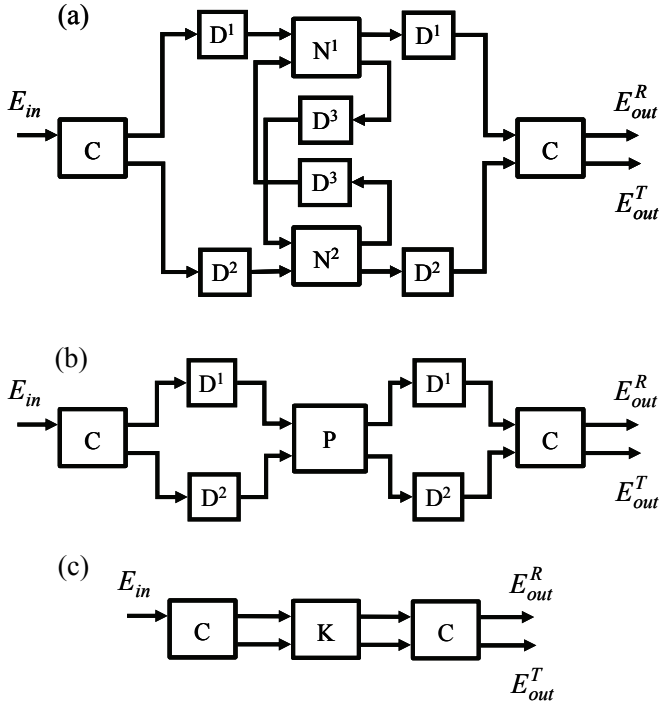


Fig. 8. Mickey NOLM block diagram.

Linear phase shifts introduced in the structure depend on the particular fibre span or loop lengths, and are considered as parameters in the following equations that define the Transmittivity (T) and the Reflectivity (R):

$$T(\varphi_{NL}^1, \varphi_{NL}^2; \varphi_L^1, \varphi_L^2, \theta^1, \theta^2, \theta^3) = \frac{P_{out}^T}{P_{in}} = \frac{|E_{out}^T|^2}{|E_{in}|^2}, \tag{13}$$

$$R(\varphi_{NL}^1, \varphi_{NL}^2; \varphi_L^1, \varphi_L^2, \theta^1, \theta^2, \theta^3) = \frac{P_{out}^R}{P_{in}} = \frac{|E_{out}^R|^2}{|E_{in}|^2}.$$

To find the complete R and T expressions, the block diagram in Fig. 8(a) can be simplified as shown in Fig. 8(b), where block P substitutes N^1, N^2 and D^3 , and is defined by the following 2x2 matrix:

$$P = \begin{bmatrix} p_{1,1} & p_{1,2} \\ p_{2,1} & p_{2,2} \end{bmatrix} \quad (14)$$

where:

$$p_{1,1} = \left(n_{1,1}^1 + \frac{n_{1,2}^1 n_{1,1}^2 n_{2,1}^1 e^{j2\theta^3}}{1 - n_{1,1}^2 n_{2,2}^1 e^{j2\theta^3}} \right) \quad (15)$$

$$p_{1,2} = \left(\frac{n_{1,2}^1 n_{1,2}^2 e^{j\theta^3}}{1 - n_{1,1}^2 n_{2,2}^1 e^{j2\theta^3}} \right) \quad (16)$$

$$p_{2,1} = \left(\frac{n_{2,1}^1 n_{2,1}^2 e^{j\theta^3}}{1 - n_{1,1}^2 n_{2,2}^1 e^{j2\theta^3}} \right) \quad (17)$$

$$p_{2,2} = \left(n_{2,2}^2 + \frac{n_{2,1}^2 n_{2,2}^1 n_{1,2}^2 e^{j2\theta^3}}{1 - n_{1,1}^2 n_{2,2}^1 e^{j2\theta^3}} \right) \quad (18)$$

Furthermore, block K in Fig. 8(c) replaces P, D^1 and D^2 blocks, and it is characterized by the matrix defined in ():

$$K = \begin{bmatrix} k_{1,1} & k_{1,2} \\ k_{2,1} & k_{2,2} \end{bmatrix} \quad (19)$$

where:

$$k_{1,1} = e^{j2\theta^1} p_{1,1} \quad (20)$$

$$k_{1,2} = e^{j(\theta^1 + \theta^2)} p_{1,2} \quad (21)$$

$$k_{2,1} = e^{j(\theta^1 + \theta^2)} p_{2,1} \quad (22)$$

$$k_{2,2} = e^{j2\theta^2} p_{2,2} \quad (23)$$

Finally, the expressions of T and R can be obtained by matrix computing:

$$\overline{E}_{out} = \begin{bmatrix} E_{out}^R \\ E_{out}^T \end{bmatrix} = C K C \begin{bmatrix} E_{in} \\ 0 \end{bmatrix} \quad (24)$$

The null value in the input vector, states that only one input field has been considered.

By substituting expressions (1)-(6), (8)-(9), (14)-(24) in (13) we find that the Transmittivity and Reflectivity functions depend on the phase difference $\Delta\theta = \theta^1 - \theta^2$ and not on the single linear phase shifts, thus resulting in a dependence of T and R on the relative length of paths D^1 and D^2 and not on the specific lengths of the fibre spans:

$$\begin{aligned} T &= T(\varphi_{NL}^1, \varphi_{NL}^2; \varphi_L^1, \varphi_L^2, \Delta\theta, \theta^3); \\ R &= R(\varphi_{NL}^1, \varphi_{NL}^2; \varphi_L^1, \varphi_L^2, \Delta\theta, \theta^3). \end{aligned} \quad (25)$$

As a result of $n_{ij}^k(\varphi_{NL}^k)$, $i, j, k=1,2$ periodicity, T and R are periodic functions of φ_{NL}^1 and φ_{NL}^2 of period 2π .

By a proper linear phase shifts tuning, different Transmittivity and Reflectivity functions can be obtained. To opportunely tune the linear phase shifts, optical delay lines can be used. In order to reduce the number of tunable parameters in our simulations, we fixed all the couplers splitting ratios equal to 0.5 and we considered the HNLF to be of equal length L_{HNLF} and to have the same nonlinear coefficient γ . We show here a set of results obtained for different configurations and parameters values.

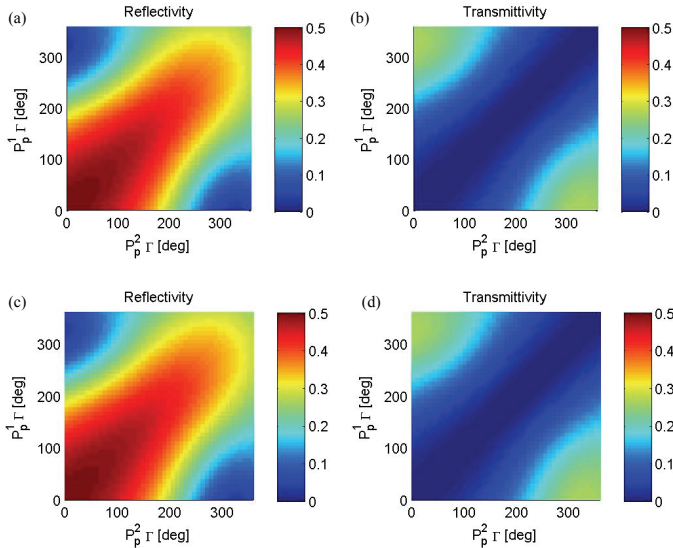


Fig. 9. All figures are obtained with: $\varphi_{L^1}=0^\circ$, $\varphi_{L^2}=20^\circ$, $\theta^3=10^\circ$, $\Delta\theta=280^\circ$ applied to Fig. 7(a) structure; (a) - Reflectivity for $\theta^1=280^\circ$ and $\theta^2=0^\circ$; (b) - Transmittivity for $\theta^1=280^\circ$ and $\theta^2=0^\circ$; (c) - Reflectivity for $\theta^1=0^\circ$ and $\theta^2=80^\circ$; (d) - Transmittivity for $\theta^1=0^\circ$ and $\theta^2=80^\circ$. Mickey NOLM block diagram.

All results suppose the input field E_{in} to be a continuous wave at $\lambda_{in}=1550$ nm.

The property stated in equation (25) can be confirmed graphically as in Fig. 9, where the transfer functions (R and T) are shown for two different sets of linear phase shifts: while φ_{L^1} , φ_{L^2} , θ^3 and $\Delta\theta$ are kept constant, the values of θ^1 and θ^2 are varied, but the overall Transmittivity and Reflectivity functions do not differ.

Fig. 10-Fig. 12 show the Transmittivity and Reflectivity bi-dimensional plots and the corresponding curves obtained by introducing a linear dependence between the pump powers.

A scheme with a steep soft limiting function, like the one reported in Fig. 10, can be used as an efficient in-line data regenerator of the pump signals. Fig. 10 shows a T -curve that can be exploited as logical port: the port input signals $S_1(t)$ and $S_2(t)$ are combined to form the pump signals that are exactly the same for the two XPM-based NOLM blocks. Fig. 11(c) shows the truth table of the corresponding NOR logic gate. In this case the single port can be physically realized by means of a 3dB coupler that adds $S_1(t)$ and $S_2(t)$ and then splits the signal obtained in order to produce two identical pump signals.

Steeper curves can be obtained by tuning the set of parameters as in Fig. 12; this aspect is quite important because steeper curves mean that lower power is needed to cover the whole switching characteristic

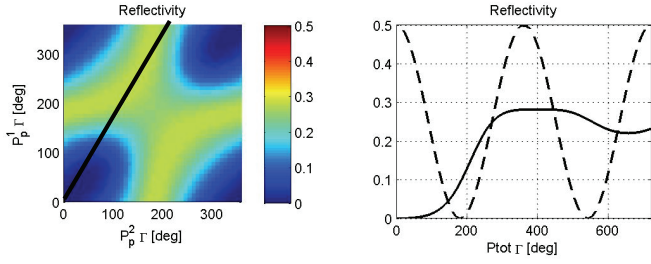
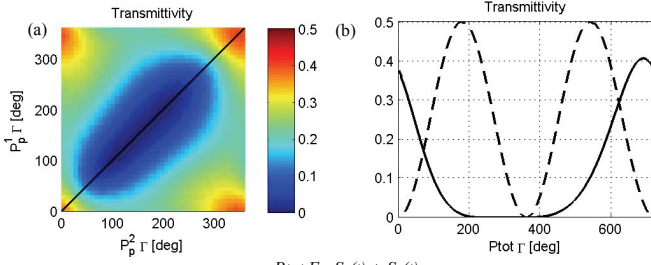


Fig. 10. Parameters used in the simulation: $\varphi^1_L=0^\circ$, $\varphi^2_L=20^\circ$, $\theta^3=170^\circ$, $\Delta\theta=10^\circ$, $m=1.71$ applied to Fig. 7(a) structure; results are compared to the Reflectivity of a single XPM-based NOLM (dashed curve); Left - Reflectivity bi-dimensional plot as function of normalized pump powers; Right - R-curve (solid curve) obtained by introducing a linear dependence between the pump powers that can be exploited in in-line pulse train regeneration .



(c) $P_{tot} \Gamma = S_1(t) + S_2(t)$

$S_1(t)$	$S_2(t)$	Out (NOR)
0	0	1
0	1	0
1	0	0
1	1	0

Fig. 11. Parameters used in the simulation: $\varphi^1_L=0^\circ$, $\varphi^2_L=20^\circ$, $\theta^3=170^\circ$, $\Delta\theta=70^\circ$, $m=1.00$ applied to Fig. 7(c) structure; results are compared to the Transmittivity of a single XPM-based NOLM (dashed curve); (a) - Transmittivity bi-dimensional plot as function of normalized pump powers; (a) - T-curve obtained by introducing a linear dependence between the pump powers that can be exploited for building a NOR logic gate as truth table explains (c).

Fig. 13 shows a different use of the bi-dimensional plot: here the pump powers are utilized as binary input signal for a NOR logical gate.

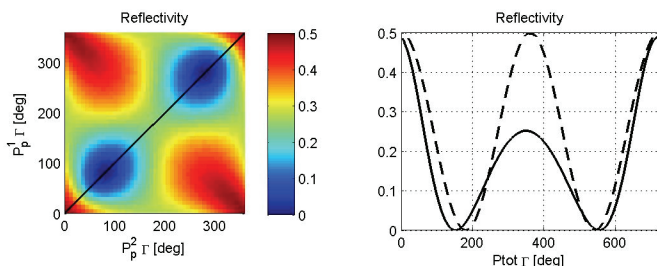


Fig. 12. Parameters used in the simulation: $\varphi^1_L=0^\circ$, $\varphi^2_L=20^\circ$, $\theta^3=170^\circ$, $\Delta\theta=0^\circ$, $m=0.99$; results are compared to the Reflectivity of a single XPM-based NOLM (dashed curve); Left – Reflectivity bi-dimensional plot as function of normalized pump powers; Right – R -curve obtained by introducing a linear dependence between the pump powers that shows fast dynamics

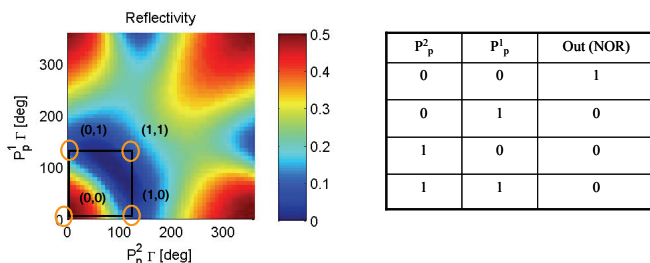


Fig. 13. Parameters used in the simulation: $\varphi^1_L=0^\circ$, $\varphi^2_L=190^\circ$, $\theta^3=130^\circ$, $\Delta\theta=0^\circ$ applied to Fig. 7(c) structure; Reflectivity bi-dimensional plot as function of normalized pump powers (Left) exploited for building a NOR logic gate as truth table explains (Right); in this case the pump signals are used as input signal of the logical port.

4. Novel Experimental Applications

4.1 Logic Gates

All-optical digital logic gates are indispensable in the ultra-fast all-optical signal processing. In literature examples of all-optical logic gates have been presented, exploiting nonlinear effects in semiconductor devices (Stubkjaer 2000; Ibrahim et al., 2003; Webb et al., 2003; Hall & Rauschenbach, 1998), optical fibre (Olsson & Andrekson, 1998; Ahn et al., 1997; Chbat et al., 1992), or waveguides (Collecutt & Drummond, 2000). Self Phase Modulation and Cross Phase Modulation in Dispersion Shifted Fibre (DSF) can be used in Nonlinear Optical Loop Mirror to obtain AND/OR/XOR, and NOR/XNOR functions respectively. These same structures have been presented in (Olsson & Andrekson, 1998; Ahn et al., 1997) to obtain reconfigurable logic gates with advantages in term of flexibility and low complexity.

With reference to the NOLM behaviour (Bogoni et al., 2004 a; Agrawal, 1994), if the NOLM is built with non-Polarization-Maintaining (non-PM) fibre, a polarization controller into the loop can change the NOLM characteristic (power of the signal inducing the phase shift in DSF versus the output power), adding a constant shift of the phase difference between the counterpropagating signals at the output of the loop. This shift allows changing the pump

power levels that produce constructive or destructive interference at the output. This property due to the interaction between the linear transformation operated by the polarization controller and the nonlinear effect in the DSF (Bogoni et al., 2004 a), can be exploited in order to obtain different logic functions with the same scheme.

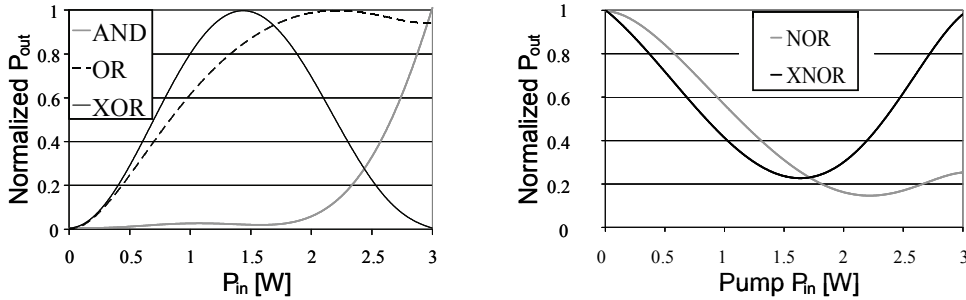


Fig. 14. Nonlinear characteristics of a SPM-based (top) and XPM-based (bottom) NOLM scheme.

Fig. 14 shows the different nonlinear characteristics that can be obtained with the SPM-based (left) and a XPM-based (right) NOLM reported in Fig. 15, by opportunely adjusting the polarization controller into the loop. If we consider the signal inducing the phase shift in the DSF, (abscissa in the plot) as the sum of two digital signals A and B, both with the low level equal to 0 W and the high level at 1.5 W, the characteristics in the figure represent the logic function AND, OR, XOR (left) and XNOR, NOR (right) of the signals A and B. Note that the non-PM fibre implementation in the case of XPM-based NOLM allows the realization of inverting functions (Bogoni et al., 2004 a). The optimization of the polarization controller state can be experimentally made. In Fig. 14 it is also possible to evaluate the on-off contrast ratio for each considered logic gate: in the best cases (AND, XOR, OR) the ratio is more than 20 dB, while in the worst case (XNOR) it is higher than 6.5 dB due to the pedestal of the output signal. Anyway, the contrast ratio can be further improved by adding a SPM-based NOLM in cascade, acting as pedestal suppressor (Bogoni et al., 2004 b).

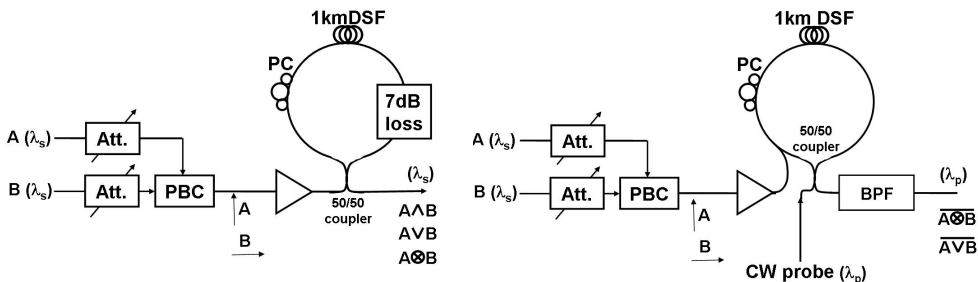


Fig. 15. Experimental set-up for AND/OR/XOR (left) and XNOR/NOR (right) gates.

Fig. 15 shows the experimental set-up of the all-optical logic gates. The signals A and B are combined at the same wavelength, in order to avoid four wave mixing in the DSF and walk-

off impairments, and with orthogonal polarization in order to eliminate instability due to phase interference.

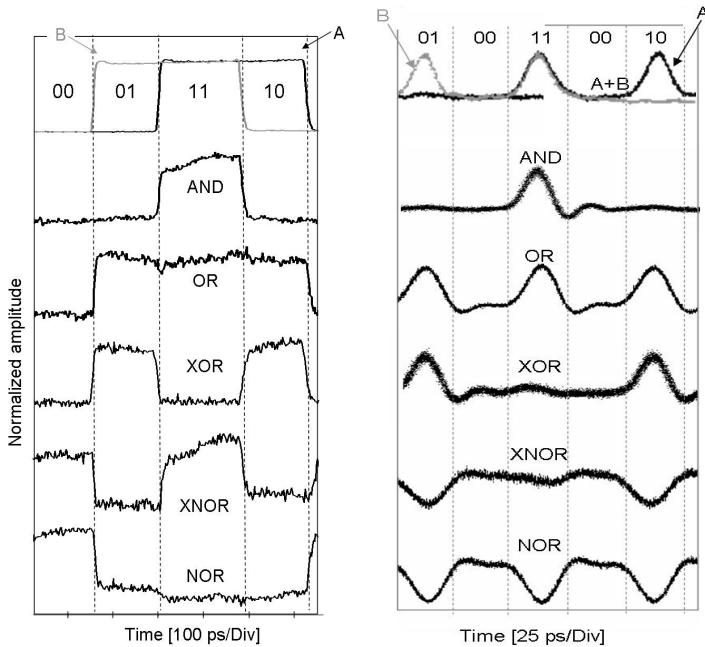


Fig. 16. Signal A and B at the input of the all-optical logic gates (top) and corresponding output of AND, OR, XOR, XNOR, and NOR (bottom) for NRZ (left) and RZ (right) signals; RZ Results obtained by means of 4ps wide pulses.

Fig. 16 shows the normalized time behaviour of the signals A and B at the input of the implemented all-optical logic gates (top) and the normalized outputs (bottom), considering 10 GHz Non Return to Zero (NRZ) (left) and 40GHz RZ (right) signals. In a NOLM the counter-propagating light experiences SPM/XPM due to nonlinear interaction between counter-propagating signals, depending on the mean power of the light responsible for the effect (Chbat et al., 1992). If the duty-cycle d of the signal inducing SPM or XPM is low (low-bit rate ultra-short pulsed signal), this effect can be neglected, since the mean power is much smaller than the peak power. But when the duty-cycle gets higher these effects rapidly increase and they can strongly affect the NOLM performance. The use of a NRZ modulation format (high d value ≈ 0.5) allows verifying the effectiveness of a non-PM loop implementation, compensating for undesirable counter-propagating effects (Chbat et al., 1992). The AND, XOR, and OR logic gates present also regenerative properties. In fact an improvement of 3 dB of the output signal on-off contrast ratio has been measured with respect to the 17 dB on-off contrast ratio of the input signals. This improvement is due to the capability of the SPM-based NOLM to act as pedestal suppressor (Bogoni et al., 2004 b).

Note that here the input signals have been intentionally generated with a not negligible zero level in order to obtain a on-off contrast ratio of 17 dB.

Finally, considering an input Q-factor of 5 for both A and B signals, an increase in the output Q-factor between 1 and 2 has been measured for all the logic gates but the XNOR, which, on the other hand, has shown a decrease of 1. This Q-factor decrease due to the pedestal of the output signal can be avoided inserting a pedestal suppressor stage. Note that the Q-factor in this case directly gives the scheme performances without strong relationship with any system bit error rate (BER).

4.2 Optical Decision Element

The development of new generation optical networks is gathering increasing interest towards Return to Zero data formats, since they will be used in both systems exploiting Optical Time Division Multiplexing (OTDM) and Wavelength Division Multiplexing (WDM) (Rhode et al., 2004; Murakami et al., 1998). Optical RZ signals present a bandwidth B exceeding the bit rate R of the single channel, and the bandwidth of the optimum RZ receiver should be proportional to B (Winzer et al., 2001), rather than to R as for NRZ data formats. Therefore, since future increases in RZ system capacity would require pulsed signals with increasing bandwidths, the optimum conventional RZ receivers will consequently need expensive very fast electronic and optoelectronic components to match the input signal characteristics, even in the case of relatively low bit rates as for demultiplexed OTDM channels. In this scenario an attractive alternative to conventional optimum receivers, which performs an electrical decision, could be the use of an additional all-optical ultra-fast decision element just before the conventional band-limited receiver, as shown in Fig. 17. This way, a first decision is carried out in the optical domain without any bandwidth limitation, improving the quality of the signal to be received. The very large bandwidth of all-optical nonlinear phenomena, together with the possibility to develop bit rate transparent, integrable and low-cost optical schemes, make this solution competitive with the conventional optimum receiver.

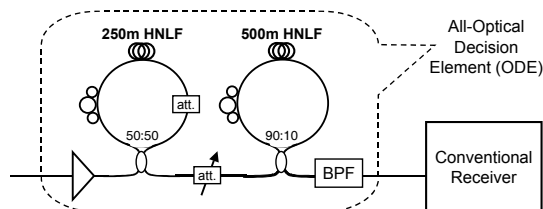


Fig. 17. Scheme of the proposed receiver. The HNLF has a nonlinear coefficient $\gamma = 10W^{-1}km^{-1}$ and $\lambda_0 = 1553nm$. Attenuation in the first NOLM: 2.5dB.

A decision element can be obtained in the optical domain exploiting the nonlinear characteristic of NOLM structures (Bogoni et al., 2004 b), which allow faster operations compared to other schemes, based for example on semiconductor devices. Moreover the possibility to use short spans of new highly nonlinear fibres allows increasing the stability and efficiency of the interferometric scheme. Fig. 17 shows the implemented ODE, constituted by an Erbium Doped Fibre Amplifier (EDFA) followed by two cascaded

NOLMs. The first one exploits a 3dB coupler and 250m of Highly Non-Linear Fibre (Bogoni et al., 2004 b). The second NOLM comprises a 10/90 coupler and 500m of HNLF (Meissner et al., 2003). Finally an optical filter eliminates the out-of-band Amplified Spontaneous Emission (ASE) noise. Note that this configuration allows using just one EDFA at the input of the first NOLM, since the power required by the second fibre loop is available at the output of the first NOLM without further amplification.

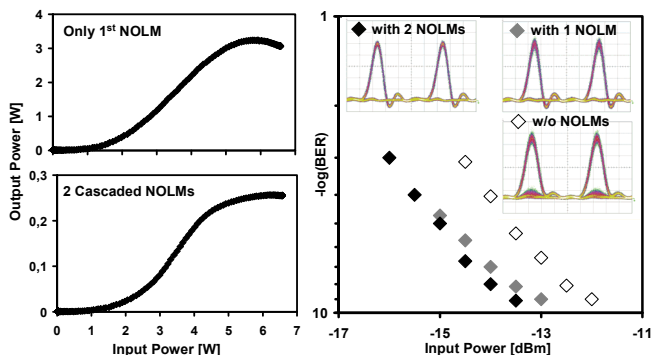


Fig. 18. Left: nonlinear characteristic of the ODE made with 1 and 2 NOLMs. Right: BER measured for 0.3nm bandwidth input signal, with OSNR=15dB. Insets: eye-diagrams at the receiver (20ps/div).

In Fig. 18(left) the nonlinear characteristics of the first NOLM alone and of the two cascaded fibre loops are shown. The contribution of the second NOLM on the total characteristic is evident, making it very similar to the ideal step function. Moreover, in order to evaluate the advance in using two cascaded NOLMs, the all-optical schemes based on one or on two fibre loops can be compared in terms of BER using the set-up described in the following. Fig. 18(right) shows the BER curve measured at the input of the ODE, at the output of the first NOLM, and at the output of the second one. It can be noted that, in the considered case, the use of the additional ODE improves the performance of the conventional receiver of 1dB and 1.5dB at BER=10⁻⁹, using respectively one single NOLM and two cascaded NOLMs. The improvement in the signal quality passing through the two stages of the ODE is also evident from the eye-diagrams in the insets of Fig. 18.

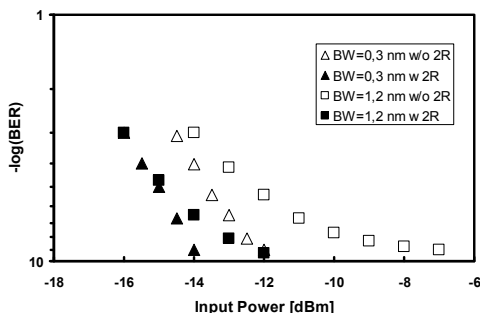


Fig. 19. BER measured with OSNR=15dB, for different signal bandwidths.

To evaluate the benefits of using an additional ODE before a band-limited conventional receiver, a 10Gbps RZ system including a conventional 10GHz NRZ receiver can be used.

Fig. 19 and Fig. 20 show Bit Error Rate measurements obtained with the experimental set-up depicted in Fig. 17 using an RZ signal generated by a fibre mode-locked laser at 1551nm producing 4ps-wide optical pulses at 10GHz. The pulses have been then modulated with a $2^{31}-1$ pseudo-random bit sequence. This signal has been coupled with the noise emitted by an ASE source. Adjusting the noise level, different Optical Signal to Noise Ratios (OSNRs) have been realized. An optical filter then has been exploited to reshape the optical signal and to suppress out-of-band noise. Two different filters have been used, with a bandwidth of 0.3nm and 1.2nm, generating final pulse widths of about 15ps and 5ps respectively. At the receiver input a variable optical attenuator has permitted to change the input power maintaining the OSNR unvaried.

The performance improvement due to the use of the NOLM based ODE can be evaluated by changing the signal bandwidth, in order to study the impact of different levels of mismatching between the bandwidths of the conventional receiver and the RZ signal. Fig. 19 reports the BER curves measured with and without the additional ODE, for 0.3nm and 1.2nm pulse bandwidth, and a fixed OSNR=15dB (@ 0.1nm resolution bandwidth). It is clear that the use of the ODE improves the performance of the receiver. Interpolations of the linear region of the BER curves allow to measure a negative power penalty at BER= 10^{-9} of 1.5dB and 2dB for 0.3nm and 1.2nm signal bandwidth, respectively. This result confirms that the performance improvement due to the use of the additional ODE increases with the mismatching between signal and conventional receiver bandwidth. Moreover, in the case of 1.2nm signal bandwidth, the conventional receiver reaches a floor in the BER curve, while using the proposed scheme this floor is not evident considering BER up to 10^{-10} .

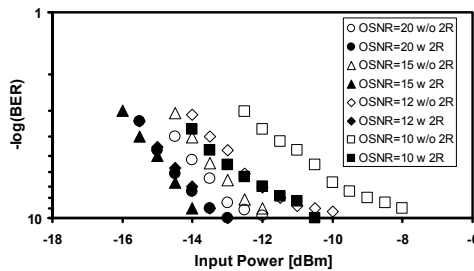


Fig. 20. BER measured with 0.3nm signal bandwidth, for different OSNRs.

The behaviour of the proposed receiver can also be investigated for different OSNRs of the input signal. Experimental results are shown in Fig. 20 where the BER curves with and without the additional ODE are reported for OSNR=10, 12, 15 and 20dB, using 0.3nm signal bandwidth. In each considered case the presence of the ODE improves the performance of the conventional receiver, with negative power penalties at BER= 10^{-9} from 1.5dB (OSNR 20dB) to 2dB (OSNR 10dB), increasing for decreasing OSNR. It is important to notice that in the cases of OSNR=12, 15, and 20dB, the BER curves obtained using the additional ODE are compressed into 0.5dB. This is due to the characteristic of the scheme (Fig. 18), which can decide the signal correctly if the input noise is confined into its flat regions. As the noise

exceeds these regions, the ODE can't decide correctly and the BER increases, as it is in the case of OSNR=10dB.

4.3 3R Regeneration

The development of high bit rate optical transmission systems is facing strong limitations due to the impairments caused by fibre nonlinearities, chromatic and polarization mode dispersion. Therefore an in-line regeneration of the optical signal is necessary in order to increase the maximum transmission distance. For system bit rates higher than 40 Gbit/s the regeneration must be done in the optical domain, since the bandwidth of the electronic devices does not allow an optoelectronic conversion. Up to now, experimental results of all-optical regeneration have been presented for signal bit rates up to 40 Gbit/s.

By splitting the regeneration process in three different steps based on the use of Nonlinear Optical Loop Mirrors, it is possible to perform the regeneration of a 160 Gbit/s OTDM signal.

An all-optical pulse regenerator is a functional block that receives a noisy and distorted signal and transmits an undistorted and noise-free signal. One of the possible methods to realize a signal regeneration is to transfer the information from the incoming data signal to a locally generated pulsed clock, whose characteristics in terms of pulse width, pulse shape and stability are suitable for the transmission. During this process the noise of the incoming data signal must be eliminated.

Because of the strong limitations due to low efficiency, long response time or high noise of the different regeneration techniques, it is very difficult to regenerate a 160 Gbit/s signal in a single step. Therefore a possible way to realize the regeneration at very high bit rate is to split the process in different steps. This can be done using a pedestal suppressor to eliminate the noise on the zero level, an inverting data transfer block to move the data to a synchronized clock, so that the noise on the one level is transferred to the zero level; and then another zero noise suppressor to eliminate this residual noise (Fig. 21). The advantage of this technique is that it requires well-known subsystems: two pedestal suppressors and a wavelength converter.

The functions of data transfer and zero noise suppression could both be realized exploiting nonlinear phenomena in semiconductor devices as the electro-absorption modulator or the semiconductor optical amplifier (Awad et al., 2000; Gavioli & Bayvel, 2000). Due to their limited recovery time and to the low efficiency of their fast dynamics, it is preferable to use nonlinear effects in optical fibres.

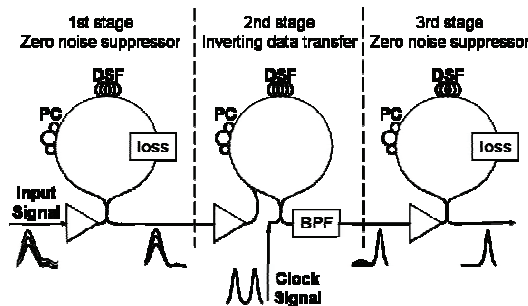


Fig. 21. Scheme of the working principle of the NOLM-based 3-stage regenerator.

To realize the zero noise suppressors two NOLMs based on Self Phase Modulation in a Dispersion Shifted fibre can be used (Pelusi et al., 1999). The data transfer block is realized using a third NOLM exploiting Cross Phase Modulation in a DS fibre (Kaewplung & Thipchatchawanwong, 2002). The input signal of the data transfer block is a pulsed clock, while the data stream is used as control signal inducing the phase shift. The data transfer block works in inverted logic thanks to an appropriate adjustment of the polarization of the two counterpropagating parts of the clock in the NOLM. The complete scheme of 3-stage NOLM-based regenerator is shown in Fig. 21.

Fig. 22 to Fig. 24 show experimental results obtained using two synchronized harmonic mode locked fibre lasers at 10 GHz, at 1557 nm and 1550 nm respectively. The signal pulses were modulated in a PRBS-driven Mach-Zehnder modulator and then distorted, so that the pulses to be regenerated were noisy and about 16 ps wide. The second pulsed laser was compressed with a higher order soliton compressor, and the pedestal was suppressed in a NOLM (Pelusi et al., 1999) obtaining a pulse width of 2 ps. Since it is not possible to visualize a 160 Gbit/s signal on the oscilloscope due to its limited bandwidth, the results shown are obtained at 10 Gbit/s using clock pulse width suitable for a 160 Gbit/s signal.

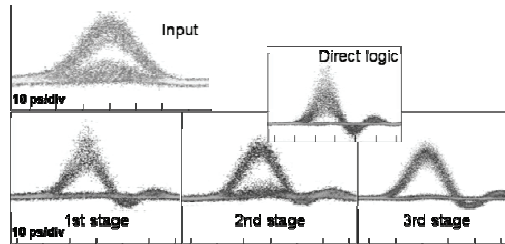


Fig. 22. Eye diagrams at the regenerator input and after each regenerator stage. Inset: 2nd stage output eye diagram working in direct logic.

The improvement of the signal along the regenerator is shown in Fig. 22. In the first stage, the noise on the low level of the data signal is well suppressed using 1 km of dispersion shifted fibre and a mean input power of 20 dBm. In order to induce the same non linear effects, a 160 Gbit/s data signal should have a mean power lower than 27 dBm. The fibre length is a trade-off between high power requirements using a short fibre, and instability and pulse broadening using a long fibre. In the second stage the mean optical power of the data signal inducing the phase shift is 19.4 dBm. The DS fibre is about 1 km long since this fibre length, working with a 160 Gbit/s signal, is the best trade-off between cross-talk due to the walk-off, instability and pulse broadening on one hand, and high power requirements on the other. The data transfer block transfers the information to the clock signal with a logic inversion, so that the high level of the eye diagram is clean, while the zero level is still noisy. In the third stage, even this noise contribution is cancelled and the signal is regenerated, using 1 km of DS fibre and 15 dBm mean power (27 dBm at 160 Gbit/s). In the inset of Fig. 22 the output of the data transfer block working in direct logic is reported: in this case the input noise is transferred to the clock and amplified, and can not be reduced afterwards. The logic inversion instead moves the noise to the zero level allowing its reduction using the zero noise suppressor.

Measuring the Q-factor of the eye diagrams, the bit error rate of the signal before and after the regeneration can be evaluated. In Fig. 23 the results in four different cases are reported, demonstrating the improvement in the quality of the signal. For each case, the input and output eye diagrams are reported in the insets. Best results show a BER improvement from $7 \cdot 10^{-4}$ to $9 \cdot 10^{-9}$. The performance of the regenerator depends on the input conditions: high noise on the zero level, on the one level or on both. In any case the regenerator ensured a BER improvement of a factor higher than 10^3 .

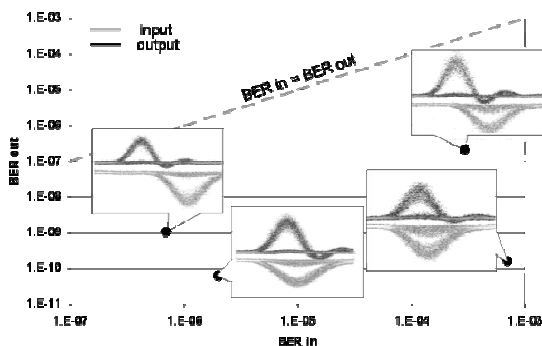


Fig. 23. BER improvement in four different cases. The insets show the eye diagrams for each considered case. Gray dots: regenerator input (inverting photodiode). Black dots: regenerator output.

To analyse the behaviour of the scheme in presence of cross-talk the signals can be multiplexed with 25 ps delay, as in a 40 Gbit/s system, so that the oscilloscope could still resolve the two pulses. Fig. 24 shows that the regenerator can transfer the information with a significant improvement of the eye diagram and a complete suppression of the cross-talk. A BER improvement of a factor 10^6 is performed.

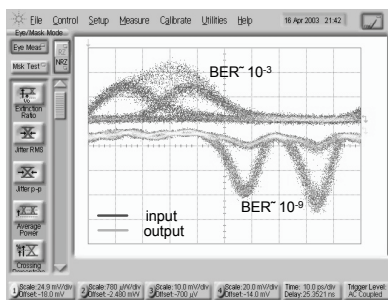


Fig. 24. Eye diagram and BER value for 40 Gbit/s transmitted pulses (black dots) and regenerated 2 ps pulses (gray dots).

5. References

- Agrawal, G. P. (1994). *Nonlinear Fibre Optics*, Accademic Press, 0-12-045142-5, San Diego, California, USA
- Ahn, K. H.; Cao, X. D.; Liang, Y.; Barnett, B. C.; Chaikammerd, S. & Islam, M. N. (1997). Cascadability and functionality of all-optical low-birefringent nonlinear optical loop mirror: experimental demonstration. *Journal of the Optical Society of America B-Optical Physics*, Vol. 14, No. 5, (May 1997) pp. 1228, 0740-3224.
- Awad, E. S.; Cho, P. S.; Richardson, C.; Moulton, N.; Goldhar, J. (2000). Optical 3R regeneration with all-optical timing extraction and simultaneous wavelength conversion using a single electro-absorption modulator, *Proceedings of ECOC2002*, (2002), 6.3.2 Vol 3, 87-90974-65-4, Copenhagen, Denmark, 8-12 September 2002
- Bogoni, A.; Scaffardi, M.; Ghelfi, P. & L. Poti (2004). Nonlinear Optical Loop Mirrors: investigation solution and experimental validation for undesirable counterpropagating effects in all-optical signal processing. *IEEE Selected Topics in Quantum Electronics*, Vol. 10, No. 5, (Sept./Oct. 2004) pp. 1115-1123, 1077-260X
- Bogoni, A.; Ghelfi, P.; Scaffardi, M. & Poti, L. (2004). All-Optical Regeneration and Demultiplexing for 160 Gb/s Transmission Systems Using a NOLM-Based Three-Stage Scheme. *IEEE Selected Topics in Quantum Electronics*, Vol. 10, No. 1, (Jan./Feb. 2004) pp. 192-196, 1077-260X
- Chbat, M. W.; Hong, B.; Islam, M. N.; Soccolich, C. E. & Prucnal, P. R. (1992). Ultrafast soliton-trapping AND gate. *IEEE Journal of Lightwave Technology*, Vol.10, No. 12, (Dec. 1992) pp. 2011-2016, 0733-8724
- Collecutt, G.R. & Drummond, P.D. (2000). Digital response in an all optical AND gate using parametric ($\chi^{(2)}$) solitons, *Proceedings of CLEO2000*, pp. 194, 1-55752-634-6, San Francisco, California, USA 7-12 May 2000
- Gavioli, G. & Bayvel, P. (2002). Novel, high stability 3R all-optical regenerator based on polarization switching in a semiconductor optical amplifier *Proceedings of ECOC2002*, 7.3.2 Vol 3, 87-90974-65-4, Copenhagen, Denmark, 8-12 September 2002
- Hall, K. L. & Rauschenbach, K. A. (1998). 100-Gbitsbitwise logic. *Optics Letters*, Vol. 23, No. 16, (Aug. 1998) pp.1271-1273, 0146-9592
- Ibrahim, T. A.; Grover, R.; Kuo, L. C.; Kanakaraju, S.; Calhoun, L. C. & Ho, P. T. (2003). All-optical AND/NAND logic gates using semiconductor microresonators, *IEEE Photonics Technology Letters*, Vol. 15, No. 10, (Oct. 2003) pp. 1422-1424, 1041-1135
- Kaewplung, P. & Thipchatchawanwong, P. (2002). Performance improvement of 40Gbit/s optical soliton transmission system by employing all-optically regenerative repeater using nonlinear optical loop mirror. *Proceedings of APCCAS '02*, pp. 215-218 Vol. 2, 0-7803-7690-0, Denpasar, Bali, Indonesia, October 2002.
- Meissner, M.; Rosch, M.; Schmauss, B. & Leuchs, G. (2003). 12 dB of noise reduction by a NOLM-based 2-R regenerator, *IEEE Photonics Technology Letters*, Vol. 15, No. 9, (Sept. 2003) pp. 1297-1299, 1041-1135
- Murakami, M.; Matsuda, T. & Imai, T. (1998). Quarter terabit (25x10Gb/s) over 9288 km WDM transmission experiment using nonlinear supported RZ pulse in higher order fibre dispersion managed line, *Proceedings of ECOC1998*, pp. 77-81 Vol.3, 84-89900-1 7-5, Madrid, Spain, 20-24 September 1998.

- Nayar, B. K.; Blow, K. J. & Doran, N. J. (1991). All-optical switching in nonlinear fibre loop mirror devices. *Optical Computing and Processing* Vol. 1, No. 1, (Jan.-March 1991) pp. 81-89, 0954-2264
- Nayar, B. K.; Finlayson, N. & Doran, N. J. (1993). Concatenated All-optical Loop Mirror Switches. *Journal of Modern Optics*, Vol. 40, No. 12, (1993) pp. 2327-2332, 1362-3044
- Olsson, B. E. & Andrekson, P.A. (1998). Polarization-independent all-optical AND-gate using randomly birefringent fibre in a nonlinear optical loop mirror. *Proceedings of OFC98*, pp. 375-376, 1-55752-528-5, San Jose, California, USA 22-27 February 1998
- Pattison, D.A.; Forsyiaik, W.; Kean, P. N.; Bennion, I. & Doran, N. J. (1995). Soliton switching using cascaded nonlinear-optical loop mirrors. *Optics Letters*, Vol. 20, No. 1, (January 1995) pp.19-21, 0146-9592
- Pelusi, M. D.; Matsui, Y. & Suzuki, A. (1999). Pedestal suppression from compressed femtosecond pulses using a nonlinear fibre loop mirror, *IEEE Journal of Quantum Electronics*, Vol. 35, No. 6, (June 1999) pp. 867-874, 0018-9197
- Rohde, H.; Lehmann, C. & Schairer, W. (2004). Towards a meshed ultra high speed TDM optical network: concept, OADM architecture and proof of principle, *Proceedings OFC2004*, TuH6, 1-55752-772-5, Los Angeles, California, USA, 23-25 February 2004.
- Sakamoto, T.; Futami, F.; Kikuchi, K.; Takeda, S.; Sugaya, Y. & Watanabe, S. (2001). All-optical wavelength conversion of 500-fs pulse trains by using a nonlinear-optical loop mirror composed of a highly nonlinear DSF. *IEEE Photonics Technology Letters*, Vol. 13, No. 5, (May 2001) pp. 502-504, 1041-1135
- Scaffardi, M.; Ghelfi, P.; Bogoni, A. & Potì, L. (2004). Investigation and solution for undesirable counter-propagating effects in nonlinear optical loop mirrors. *Proceedings of CLEO 2004*, Vol. 2, pp. 2-3, 1-55752-777-6, San Francisco, California, USA 17-19 May 2004
- Stubkjaer, K. E. (2000). Semiconductor optical amplifier-based all-optical gates for high-speed optical processing. *IEEE Selected Topics in Quantum Electronics*, Vol. 6, No. 6, (Nov./Dec. 2000) pp. 1428-1435, 1077-260X
- Webb, R. P.; Manning, R. J.; Maxwell, G. D. & Poustie, A. J. (2003). 40 Gbit/s all-optical XOR gate based on hybrid-integrated Mach-Zehnder interferometer. *IEE Electronics Letters*, Vol. 39, No. 1, (Jan. 2003) pp.79-81, 0013-5194
- Winzer, P. J.; Pfennigbauer, M.; Strasser, M. M. & Leeb, W.R. (2001). Optimum filter bandwidths for optically preamplified NRZ receivers, *IEEE Journal of Lightwave Technology*, Vol. 19, No. 9, (Sept. 2001) pp. 1263-1273, 0733-8724

Digitally Fast Programmable Optical Signal Processing Devices

Xinwan LI, Zehua HONG, Shuguang LI and Jianping CHEN
Shanghai Jiao Tong University
P.R.China

1. Introduction

Optical delay, buffering, filtering, and switching are very important devices in both of optical communications and optical sensing areas. In order to decrease the cost of optical signal transferring/switching for digital data or analogue sensing signal, easy way is to increase the bandwidth utilities of optical communication/sensing systems to support mountains of users, like computers, sensor nodes in one network. However, the dynamic abilities of the above devices are becoming a big challenge, and which are also the bottleneck in available technologies. This chapter presents a comprehensive review and overview on the cutting-edge frontier science and engineering of fast digital optical signal processing application. It discusses on the theory, design, fabrications of several typical examples of digital optical signal processor (DOSP) devices, which is in the form of semiconductor optical amplifier (SOA) and optical fibre delay lines (OFDL). The issues include the fast programmable optical fibre true delays, the fast programmable optical fibre buffer, the digital optical wavelength selective switches, etc.

2. Programmable optical fibre true delay (Li, 2007)

In last several years, the programmable optical fibre true delay has shown its powerful application abilities in microwave photonics and other areas. One typical example is the application of optical fibre delay lines as a notch filter replacing the traditional radio frequency (RF) signal processing to carry out the unwanted signals from the targets in the moving target identification ground radar system. In this section, we will introduce a kind of feed-forward optical fibre delay lines.

2.1 Brief review of optical fibre delay lines (OFDLs)

Programmable optical fibre delay lines (OFDLs) have many applications, such as antenna beam forming in phase array radar system(Seeds, 2006) and microwave signal processing(Capmany, 2005; Wilner, 1976), due to various advantages in comparison with the traditional electrical methods. It can provide true delay of microwave signal, very high product of time-bandwidth, immunization to electromagnetic interference (EMI) and

the possibility of spatial and wavelength parallelism by using WDM techniques. So far, two types of optical fibre delay lines have been proposed as buffers for optical packet communication networks: re-circulating type and traveling-wave type(Chang, 2006). Re-circulating buffers are compact and require fewer components to implement. However, the fibre loop length is fixed and hence it is not suitable for applications in phase array radar system and microwave signal processing. Traveling-wave buffer has the potential for the above applications, which will be introduced in the following section. It can be cascaded to provide desired delay using, e.g., 2×2 optical switches or broadcast-and-select configuration (Chang, 2006). Of course, high-speed (≤ 1 ns) and low-loss (≤ 1 dB) optical switches are required(Seeds, 2005; Seeds2002).

Two typical high speed devices, i.e. LiNbO₃ switch(Murphy, 1996) and semiconductor optical amplifier (SOA) ON-OFF gate, can be considered. For LiNbO₃ 2×2 switch, the large insertion loss, polarization dependence and crosstalk need to be addressed before they can be used in phase array radar system and microwave signal processing. SOA ON-OFF gate has nanosecond switching speed, large on-off extinction ratio and wide optical bandwidth. It seems more suitable for traveling-wave type of fibre delay lines(Yeo, 2004).

In this section, we proposed a novel 3^n feed-forward OFDL using SOAs as switching components. Theoretical analysis and experimental verification are presented. Important issues, such as the attenuation(Moslehi, 1992), polarization, delay precision, and etc., are addressed in detail(Capmany, 2006; Ho-Quoc, 1996).

2.2 Design of k^n feed-forward optical fibre true delay line

Traditionally, the programmable traveling-wave fibre delay line is implemented by using $1 \times N$ optical switch, or equally by using $1 \times N$ coupler plus on-off gate (e.g. SOA) in each arm, as shown in Fig. 1(a)(Blumenthal, 1994). In this configuration, the maximum number of possible delays, y , is equal to the amount of SOAs, x . It is apparently not suitable to be scaled for large delays. The delay performance can be enhanced by configuring it in an alternative way with 2×2 switches(or 2×2 couplers plus ON-OFF SOA gates) and same number of SOAs as shown in Fig. 1(b). In this configuration, the total number of delays can be expressed as follows:

$$y = 2^{x/2} \quad (1)$$

where the number of SOAs, x , is supposed to be even. We define such structure as 2^n structure, where, $n=x/2$, is the number of stages.

Similarly, we can use x SOAs to build k^J structure as shown in Fig. 1(c), where k is the dimension of each stage and J is the number of stages($J=x/k$ is an integer). It can be derived the total number of delays, y , is given by:

$$y = k^{x/k} \quad (2)$$

Equation (2) can be rewritten as:

$$\frac{\log(y)}{x} = \frac{\log(k)}{k} \quad (3)$$

Equation (3) shows that for the same x , there is an optimal k that gives maximum y . We use $L(k)$ to express the right side of Equation(3):

$$L(k) = \frac{\log(k)}{k} \tag{4}$$

The peak value of $L(k)$ can be obtained mathematically by differential operation on $L(k)$ as follows:

$$\frac{dL(k)}{dk} = 0 \tag{5}$$

So, the k can be obtained by solving Equations (4) and (5):

$$k = e = 2.718 \tag{6}$$

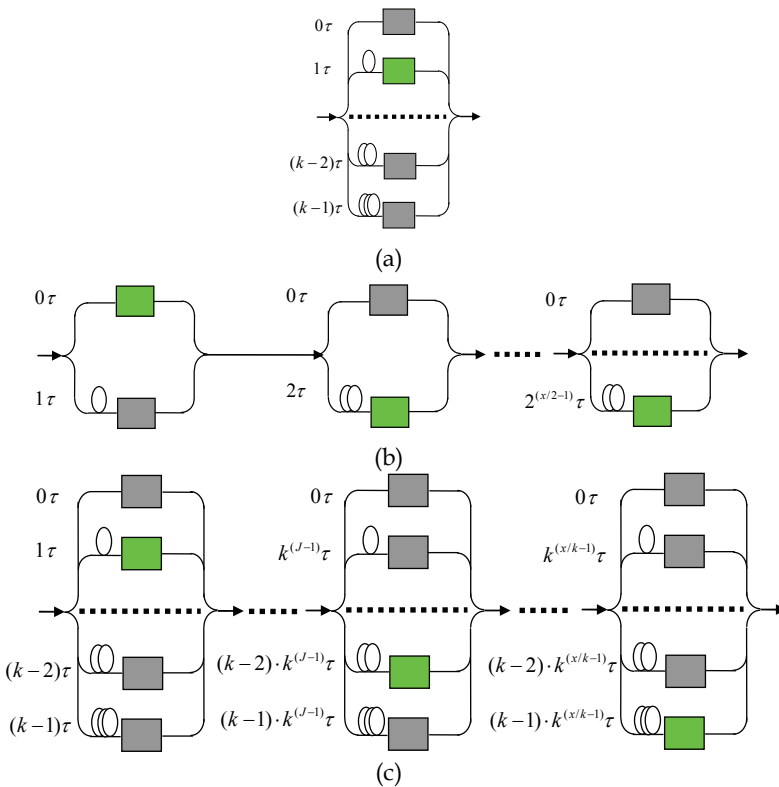


Fig. 1. The architectures of traveling-wave fibre delay lines ($y=x$ for (a), $y=2^{x/2}$ for (b), and $y=k^{x/k}$ for (c), where y is the maximum number of possible delays, and x is the number of SOAs)

However, as shown in Fig. 1, the physics meaning of k is the number of delay lines in each stage, so, k should be integer. Fig. 2 shows the relationship between $L(k)$ and k . It can be easily found that the optimal value k is 3. It can also be proved that 4^n structure is exactly the same as 2^n structure:

$$y(x) = k^{x/k} \xrightarrow{k=4} y(x) = 4^{x/4} = (2^2)^{x/4} = 2^{2 \cdot x/4} = 2^{x/2} \rightarrow k = 2 \tag{7}$$

When the number of SOAs used is small, the difference between the maximum numbers of delays available for $k=2$ and $k=3$, respectively, are also small. However, as more SOAs are used, the difference becomes significant, as shown in Fig. 3. From the figure, we can see that fast tunable true delay line with large number of delays can be obtained by employing 3^n structure and certain number of SOAs. Fig. 4 shows the structure of 3^n delay lines, and Table 1 shows the delays of two stages from 0τ to 8τ respectively.

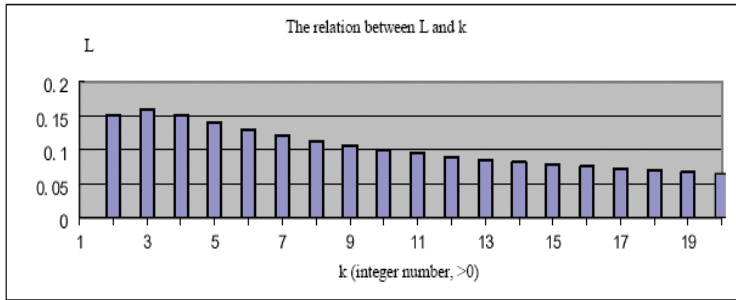


Fig. 2. $L(k)$ as a function of k

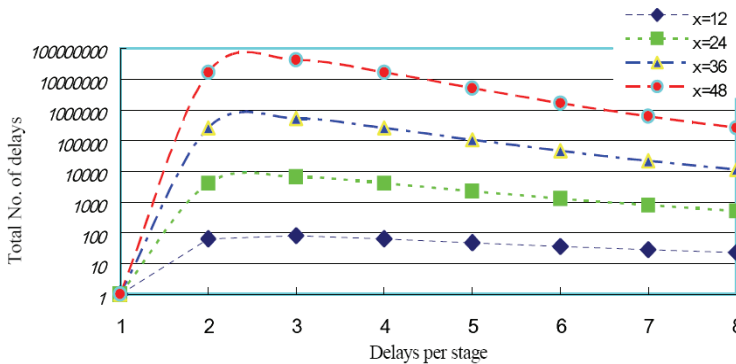


Fig. 3. Dependence of total delay number on the delay units per stage (x : the number of SOAs)

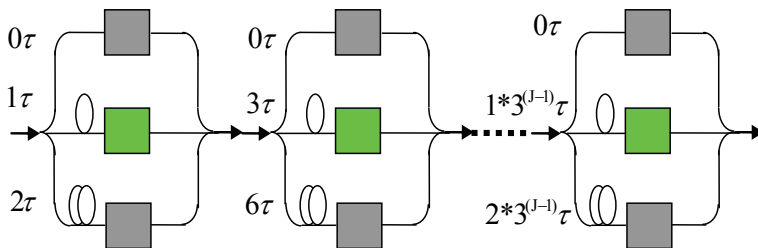


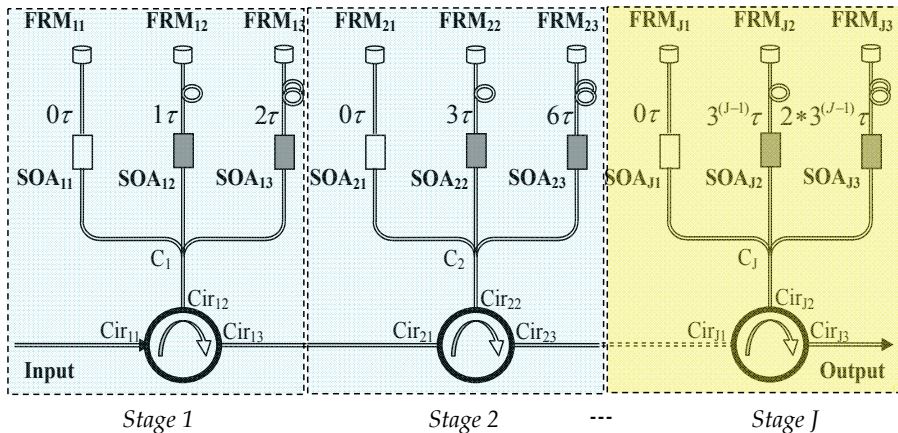
Fig. 4. The structure of 3^n delay lines

Total delay	Stage 1 ($0\tau, 1\tau, 2\tau$)	Stage 2 ($0\tau, 3\tau, 6\tau$)
0	0	0
1τ	1τ	0
2τ	2τ	0
3τ	0	3τ
4τ	1τ	3τ
5τ	2τ	3τ
6τ	0	6τ
7τ	1τ	6τ
8τ	2τ	6τ

Table 1. Delays of two stages from 0τ to 8τ in series

2.3 Implementation and performance measurement

According to the above analysis, 3^n feed-forward optical fibre true delay line based on SOAs can provide large amount of delays with fast tunability and easier scalability. For practical applications, problems such as insertion loss and polarization dependence should be considered. The former can be overcome by SOA itself for it provides gain in addition to ON-OFF gating. In fact, this is also one of advantages of employing SOAs. For the factors of the polarization dependence in optical fibre and in SOAs, we use Farady rotation mirrors (FRMs) to alleviate it. The SOAs we used are bi-directional SOA without inside optical isolators at input and output. Due to the low backward reflection of the SOA and the polarization rotation by FRM, no oscillation can be observed. Fig. 5 shows the structure for practical implementation and we built a two-stage (the first two stages in the experiment in hand) feed-forward optical fibre true delay line for experimental verification. For each stage, the light is fed from the input port of the optical circulator. It experiences delay whose amount is determined by turning on one of the SOAs and is then forwarded to the next stage via the output port.

Fig. 5. A practical structure of 3^n feed-forward optical fibre true delay line

The main insertion loss is caused by 1×3 coupler. The light beam passes the coupler twice and experience about 12 dB loss (excluding the coupler's excess loss). By taking the losses resulted from the FRM and the circulator into consideration, the total loss of each stage is around 13 dB. It should be noted that the beam also passes SOA twice. Usually, an SOA can provide with 5-8 dB gain for small optical signals, e.g. -10dBm, under moderate drive current (~ 80 mA). Therefore, by careful design of the drive current of each SOA, it is possible to obtain a delay stage with no insertion loss. This feature is particularly important for practical applications. It enables the proposed structure to be cascaded without limitation on the stage number.

The resolution is another key issue to be addressed. The delay introduced by a light path distance of 0.15mm, or fibre length of 0.103mm (group refractive index of 1.46 is supposed), is about 0.5 ps. It corresponds to a phase control precision of about 1.8° in X-band ($\lambda \sim 3$ cm). In order to reach the above precision level, we used hydrogen flame to precisely adjust the fibre length, with the help of the high precision reflectometer (HP8504)(Shi, 2006). This equipment is used to precisely measure the lightpath difference between the measured arm and reference arm of Michelson interferometer. The measurement span (equivalent distance in air) is up to 400mm with resolution of $20 \mu\text{m}$. Fig. 6 show the delay length measurements scheme using high precision reflectometer (HP8504).

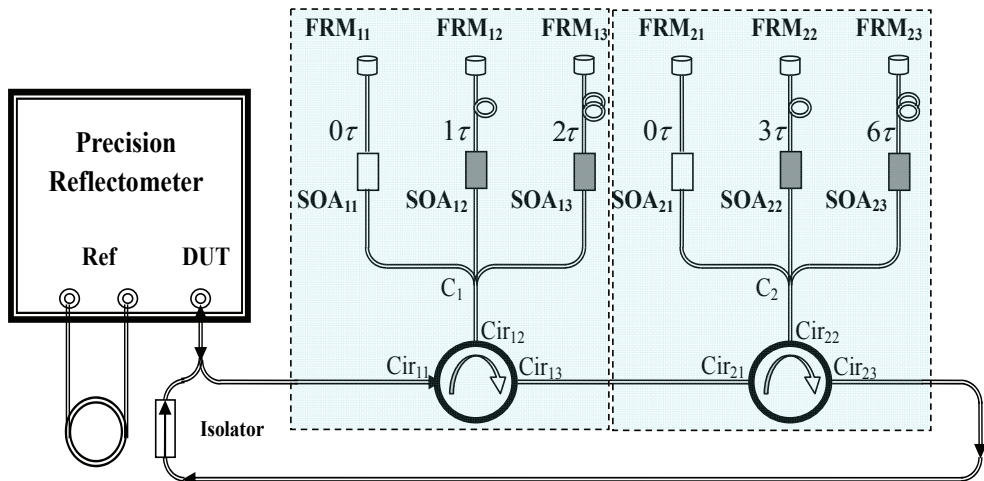


Fig. 6. The delay length measurements scheme

Fig. 7 shows the result when we set all six SOAs ON. It can be clearly seen that there are 9 peaks, which represent the all possible delays to be obtained, and each delay can be programmably switched by setting of the relative one SOA per stage. The measured relative light path distances in three arms of the first stage are 20.756mm, 20.914mm, 21.056mm, respectively. The correspondent fibre lengths are 14.216 mm, 14.325mm, 14.422mm, respectively. These data indicate that τ as shown in Fig. 7 is 0.5 ps and the precision is kept within 0.03ps. One may note that there are insertion losses in stages 2 and

3. This is because of the limited drive current of the circuit we used, resulting in small SOA gain incapable to compensate the inherent insertion loss mentioned above.

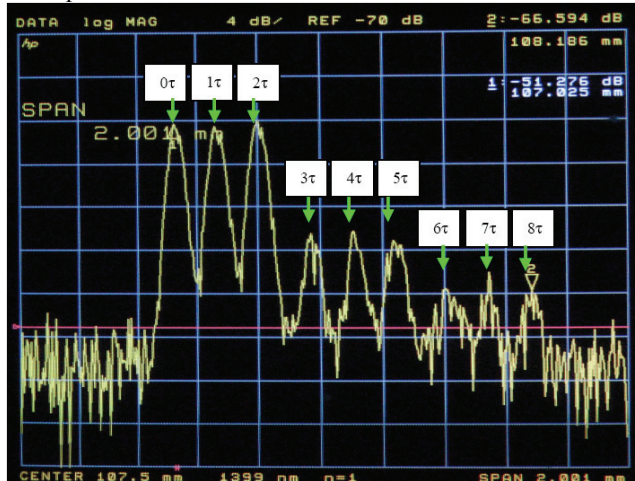


Fig. 7. Measured result of relative fibre lengths
 x-axis: light path difference(0.2 mm/div), y-axis: relative intensity of the output(dB)

Fig. 8 and Fig. 9 show the measurement schemes and results of tuning speed respectively. The rise time is 18.6 ns and the fall time is 39.4 ns. Such speed can enhance the scanning performance of microwave significantly. The scanning frequency may be improved from tens of kHz up to 10 MHz. The drive circuit for the SOAs was implemented with conventional electronic devices at hand. There is large potential to improve the tuning speed, especially the switching-off performance. One may note that there is extra delay in switching-off process, which is mainly resulted in from the large junction capacitance in the device.

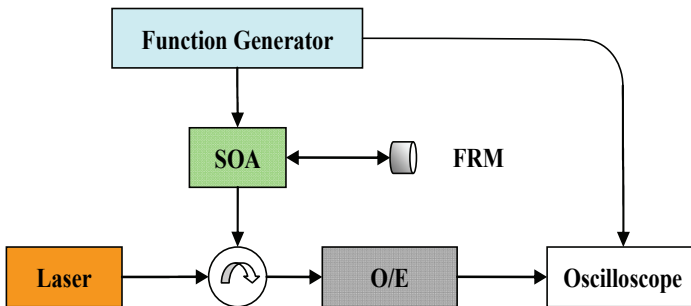


Fig. 8. The measurement scheme of tuning speed

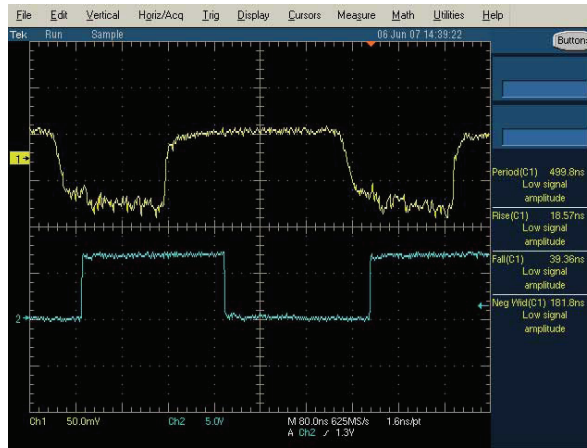


Fig. 9. Photograph of tuning speed measurement (lower trace: drive pulse, upper trace: optical output)

We also measured the polarization dependence loss (PDL) using polarization controller. The measured result is 0.18 dB. In comparison with the PDL of SOA ($\sim 0.3\text{dB}$), there is improvement that is mainly due to the employment of FRM. Fig. 10 shows the experiment scheme of measuring the polarization dependence loss (PDL).

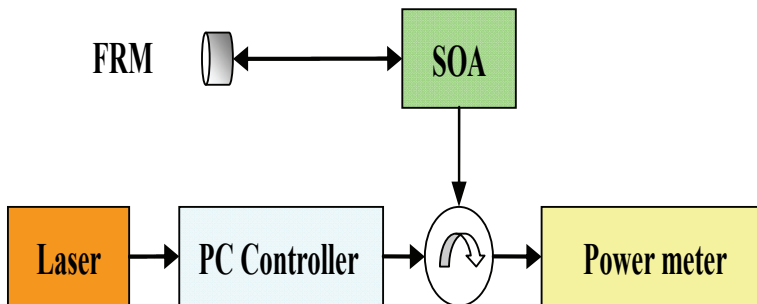


Fig. 10. The experiment scheme of measuring the polarization dependence loss

The relatively low noise figure of the SOA may bring a certain limitation to the proposed structure for some applications, especially for those requiring high transmission SNR. This indicates that for expansion purpose, noise performance should be taken into consideration, which is a topic worthy of intensive study and, however, beyond the scope of the paper. The following Table.2 exhibits the description of five specifications. From the Table. 2, we can see that the insertion loss and polarization dependent loss are very low, and the switch speed of ON/OFF is very fast, meanwhile we can use small number of SOAs to obtain large number of delays in series.

Specification		Description
Insertion loss		<1dB
Switch speed	Rise time	18.6ns
	Fall time	39.4ns
Polarization dependent loss		0.18dB
Delay efficiency		Small SOAs to obtain large delays
Delay precision		1ps, error <10%

Table 2. Specification of 3rd feed-forward optical fibre delay lines

3. Fast programmable travelling-wave buffer (Li, 2008)

The novel structure mentioned in the second section can be applied for a fast programmable traveling-wave buffer with a re-circulating one. The round trip time of the loop can be controlled as wanted.

3.1 Brief Introduction of traveling-wave buffer

As well known, the fast programmable optical buffering is quite an important technique to provide dynamic delay for photonic packets in an optical switching node. So far, two types of optical fibre delay lines have been proposed as buffers for optical communication networks: the re-circulating and traveling-wave structures (Chang, 2006) as addressed in the second sections of this chapter. Re-circulating buffers are compact and require fewer components to implement. However, the fibre loop length is fixed and hence the delay can only be the multiple of the round trip length of fibre loop. Traveling-wave buffers have the potential to avoid the above limitation. It can be cascaded to provide desired delay using, e.g., 2×2 optical switches or broadcast-and-select configuration (Blumenthal, 1994; Murphy, 1996). However, large delay requires tremendous fibre length, which results in bulky structure. In this section, we present a novel structure, which combines a fast programmable traveling-wave buffer with a re-circulating one. The round trip time of the loop can be controlled as wanted. Such structure is applicable to optical packet switching, especial to optical burst switching, and also to other fields such as microwave photonics. In order to obtain high systematic performance, fast (e.g., ≤1ns) and low-loss (e.g., ≤1dB) optical switches are required (Blumenthal, 1994).

3.2 The principle and implementation

The proposed structure is shown in Fig.11. The optical fibre loop is interconnected via a 2×2 optical switch to the input and output. In order to support high speed switching, LiNbO₃ switch (Murphy, 1996) can be used. In the loop, there are M in-fibre optical circulators, each of which connects a stage of delay lines via a 1×3 coupler. In each stage, the amount of delay is selected by one of the gated semiconductor optical amplifiers (SOAs) on three delay units (e.g. 0τ , 1τ and 2τ) with a Faraday rotation mirror (FRMs, marked as M in Fig.11) at each end. Each stage can be regarded as a programmable traveling-wave delay line. It has been found that the total number of delays for the J stages of delay lines can be expressed as Equation (2) (Li, 2007). The relation among x , y and k is shown in Fig.12. For the same

amount of total delays, the minimum number of SOAs needed can be found in the case of $k=3$. Hence, each stage containing three delay lines is the optimal structure. With the proposed J-stage traveling-wave fibre delay line embedded in a re-circulating loop, the total number of delays per loop, N , can be expressed as:

$$N = 3^{x/3} \tag{8}$$

And the maximum delay per loop is

$$\tau_{total} = \tau_R + \tau \times 3^{x/3} \tag{9}$$

where, τ_R is the reference delay induced in the loop excluding the traveling-wave delay lines. The number of SOAs, x , is supposed to be the multiples of 3.

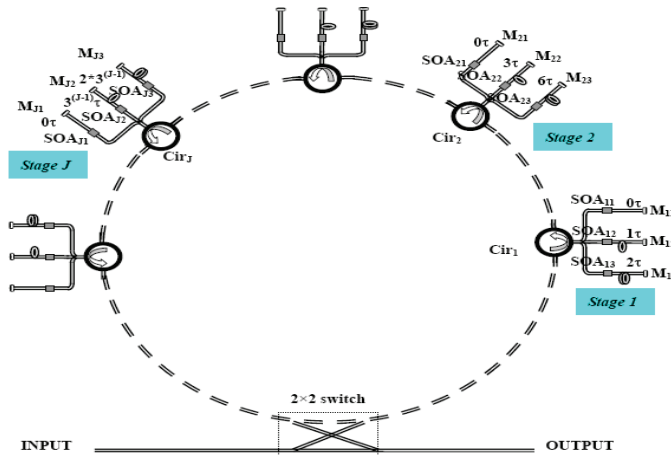


Fig. 11. The layout of re-circulating structure embedded with traveling-wave delay

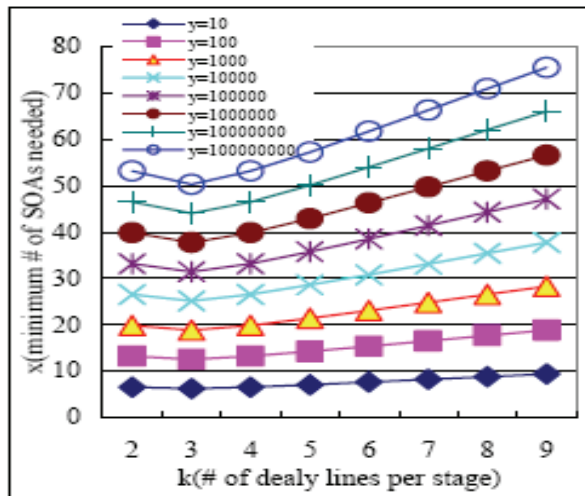


Fig. 12. The relation among the x , y , and k

Next, we will analyze some properties of this buffer structure, such as the insertion loss, polarization dependent loss, the resolution of the fibre delay lines, and the tuning speed.

SOAs are used here to compensate the insertion loss mainly induced by couplers(excluding the coupler's excess loss). Because of the potential gain of SOA, it is possible to obtain a delay stage with no insertion loss. We use FRM here decrease the polarization dependent loss(PDL) for the polarization's elimination of FRM.

Several experiments have been carried out. The first is the length measurement with high precision reflectometer (HP8504)(Shi, 2006)of different buffer route. This scheme includes two stages of the buffer unit with six arms, and the results are the same as the second section, for we used the same basic fibre delay lines structure. The measured relative light path distances in three arms of the first stage are 20.756mm, 20.914mm, 21.056mm, respectively. The correspondent fibre lengths are 14.216 mm, 14.325mm, 14.422mm, respectively. These data indicate that τ as marked in Fig. 7(same delay lines used for these two applications: feed-forward OFDLs in section 2 and programmable optical buffer in this section) is 0.5 ps and the precision is kept within 0.03ps.The loop length was measured as 532 ps excluding the traveling-wave delay induced in each stage, which can be multiplied by re-circulating. The second experiment is about the tuning speed. The rise time is 17.7 ns and the fall time is 31.3 ns. The drive circuit for the SOAs was implemented with conventional electronic devices at hand. There is large potential to improve the tuning speed. Also the gain of SOAs was not optimized due to the limited drive ability of the circuit (one may note there are relatively large insertion loss, which can be overcome via the careful increase of the drive current). For this structure, we also measured the polarization dependence loss (PDL) using polarization controller with the result of 0.18 dB. Compared with the PDL of SOA (~0.3dB), there is improvement due to the employment of FRM.

4. Digitally tunable optical filter based on DWDM thin film filters and semiconductor optical amplifiers (Li, 2005)

Tunable optical filters have important application in fibre optic communications and other optical fields. Tuning ability is usually achieved by introducing extra phase shift via the electro optic, thermo optic, acoustic optic or piezoelectric effect, etc. The most commonly component for phase shift is interferometric structure(Sadot,1998) such as Fabry-Perot (FP), Mach-Zehnder (MZ) and Michelson interferometer. Those device based on interferometric structure have the similar defect – instability in operating wavelength, so the electronics should be adapted to stabilize the central wavelength.

Other kinds of tunable optical filters, digitally tunable optical filters (DIOFs)(Ishida, 1997), which can get over the problem of instability, have received widely attentions. One of DIOF structure based on arrayed waveguide grating (AWG) has been reported (Glance,1996; Zirngibl, 1994; Glance, 1994). Compared with the interferometric structure consisting of FP, MZ or Michelson interferometer, the AWG offers the advantages of low losses, high port counts, and mass productivity. However, AWG usually suffers the problem of temperature dependence, so the DIOF based on AWG may require precision thermal control. Another DIOF based on DWDM thin film filters (TTFs) and semiconductor optical amplifier (SOA) show the very stable characteristic in temperature performance. Furthermore it requires less SOAs to achieve the same wavelength tuning range in comparison with the reported structure(Zirngibl, 1994; Glance, 1994). Next, this structure will be introduced in detail.

4.1 The configuration of this digitally tunable filter

Fig. 13 shows the experimental configuration of the proposed DTOF. It consists of eight DWDM TTFs, six SOAs, one 1×2 splitter and one 4×1 combiner. Each of the TTFs is used as 1×2 or 2×2 wavelength selection element, as depicted in Fig. 14, depending on the position in the structure. For the 1×2 structure, we used a dual fibre collimator as one pair of input/output fibre ports and a single fibre collimator as the second output port. All the wavelengths from the input fibre will be reflected to the dual fibre collimator output, except for the wavelength which is equal to the center wavelength, λ_i , of the TTF (thin film filter). This wavelength will pass through the filter and arrive at the second output. In the 2×2 structure, we used another single fibre collimator as the second input. The work principle of the 2×2 structure is the same as the 1×2 one. Because the TTF only allows one wavelength to pass through, the wavelengths of the two input ports are arbitrary, i.e., independent of each other. In the DTOF of the proposed, TTFs of $\lambda_2, \lambda_4, \lambda_6, \lambda_8$ are set as 2×2 wavelength selection element, TTFs (thin film filters) of λ_3, λ_5 , are set as 1×2 wavelength selection element, and TTFs of λ_1, λ_7 function as optical filters. The eight TTFs are connected in the order as shown in Fig. 13.

The input light to the DTOF is divided into two portions via the splitter and is firstly "selected" by SOA₁₁ or SOA₁₂. For example, when SOA₁₁ is turned on (SOA₁₂ is off), all the wavelengths will arrive at the thin film filter with center wavelength of λ_2 and only one wavelength, namely λ_2 , will pass through the filter, all the other wavelengths will be reflected and arrive at the subsequent TTFs (thin film filters). SOA_{2i} (i=1, 2, 3, 4) performs the second "selection" of wavelengths. In the above case, λ_2 will arrive at the output through the 4×1 combiner if SOA₂₁ is on. The control table is listed in Table 3. In the table, "1" means that the SOA is turned "ON" and "0" means that the SOA is turned "off". It can be seen that this structure allows the center wavelength to be arbitrarily selected among the eight TTF wavelengths. For example, the DTOF is set at λ_1 with SOA₁₂ and SOA₂₁ "ON". The routing path for λ_1 is as follows: Input (multiple wavelengths) → SOA₁₂ (ON) → λ_4 (Reflection) → λ_5 (Reflection) → λ_8 (Reflection) → λ_1 (Transmission) → λ_2 (Reflection) → SOA₂₁ (ON) → Output.

The above configuration can be expanded to larger size. The expansion will not bring additional insertion loss for every wavelength undergoes transmission or reflection at most five times (four reflections and one transmission), independent of the filter size (i.e., the number of wavelengths). Of course the TTFs should be rearranged, i.e. configured as 1×2 or 2×2 structures according to the scale.

The number of SOAs to be used, which is important for cost consideration, is determined as follows. Suppose the number of wavelengths to be digitally tuned is N, where $N=2^n$. The numbers of SOAs at the output side and the input are:

$$N_{\text{output}}=2^{n-1} \quad (10)$$

and,

$$N_{\text{input}}=2^{n-2} \quad (11)$$

respectively. The total number of SOAs is:

$$N_{\text{total}}=N_{\text{input}}+N_{\text{output}}=2^{n-2}+2^{n-1}=3 \cdot 2^{n-2} \quad (12)$$

In comparison with the structure reported in Ref(Glance,1996). and Ref(Zirngibl, 1994)., the proposed structure can save up 25% of SOAs for the same wavelength tuning range. The center wavelengths of the proposed DTOF are well in consistency with the ITU-T suggested

ones. Furthermore it does not have the thermal stability problem as the arrayed waveguide grating does (Hibino, 2002).

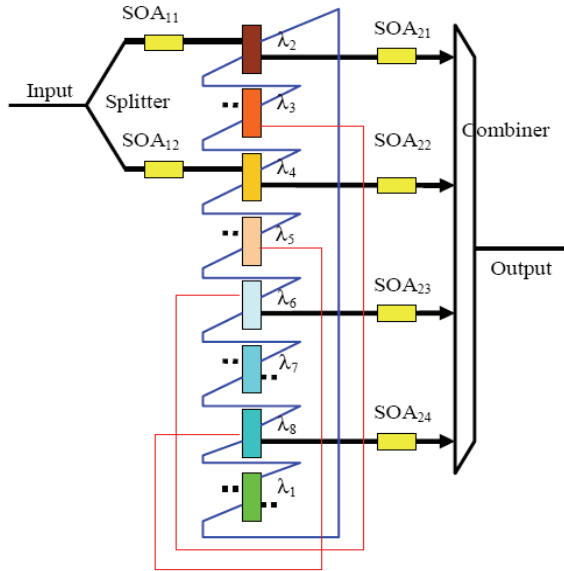
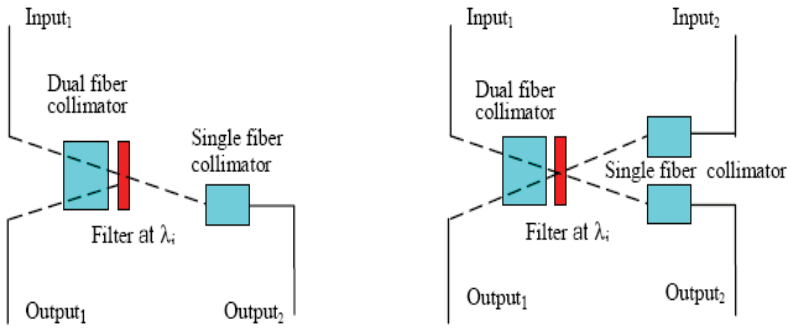


Fig. 13. The configuration of eight-channel digitally tunable optical filter



(a) 1x2 wavelength selection element

(b) 2x2 wavelength selection element

Fig. 14. The structures of 1x2 and 2x2 wavelength selection elements

SOA ₁₁	SOA ₁₂	SOA ₂₁	SOA ₂₂	SOA ₂₃	SOA ₂₄	Selected wavelength at output
0	1	1	0	0	0	λ_1
1	0	1	0	0	0	λ_2
1	0	0	1	0	0	λ_3

0	1	0	1	0	0	λ_4
0	1	0	0	1	0	λ_5
1	0	0	0	1	0	λ_6
1	0	0	0	0	1	λ_7
0	1	0	0	0	1	λ_8

Table 3. The control table of the proposed DTOF (control states of SOAs: "1" stands for ON; "0" for OFF)

4.2 The performance of this digitally tunable filter

Fig. 15 is the transmission spectrum of the proposed DTOF. Its performance is list in Table 4 and 5. The eight wavelengths range from 1552.54nm to 1558.14nm. Table 4 lists the insertion loss for each wavelength channel. The maximum difference of the insertion loss among all eight wavelength channels is 3.76dB. The drive current of each SOA was set at 80mA for the "ON" state. The insertion loss difference can be compensated by optimizing the SOA drive current. In Table 5, the polarization dependent loss is less than 0.4dB and the isolation is better than 40 dB. The relatively large polarization dependent loss is partially induced by SOA. Another contribution may arise from the angled incidence on TTF (thin film filters) for its 1×2 and 2×2 application, which may decrease via careful design. The tuning speed was tested. It can be seen that the rise time and fall time of the optical response are 8.82 ns and 15.49 ns, respectively, and the delay time between the control signal and the optical response 31.07 ns. As is known, SOA has faster response than the measured results. This relatively larger rise/fall time and delay are mainly due to the poor response of the driving system which uses components at hand.

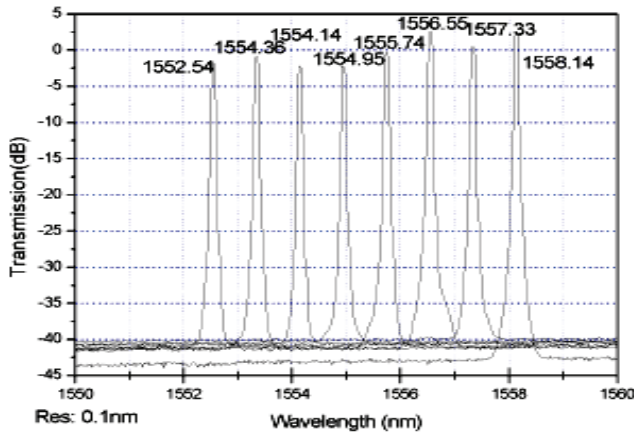


Fig. 15. The measured transmission spectrum of the proposed DTOF

Specification	Unit	Value	Notes
Polarization dependent loss	dB	< 0.4	Induced by SOA and the angled incidence on TTF
Isolation	dB	>40	
Tuning speed	Raise time	ns	The poor response of driving system lead to this relatively larger
	Fall time	ns	

				rise/fall time
Insertion loss		dB	In table 3	

Table 4. Specifications of the proposed DTOF

Wavelength (nm)	1552.54	1553.36	1554.14	1554.95
Insertion loss (dB)	5.94	5.56	6.67	6.9
Wavelength (nm)	1555.74	1556.55	1557.33	1558.14
Insertion loss (dB)	5.2	2.21	4.08	2.14

Table 5. The insertion loss for each wavelength channel

5. Digital wavelength selective optical switch

Digital wavelength selective optical switches (DWSS) have played an important role in wavelength-division-multiplexing (WDM) networking, and inspired widely research interest. Digital wavelength selective optical switch is a kind of optical switch which can make certain wavelengths from multiwavelength pass through or not according to the requirement of user(Li,2005). Several methods for optical switch have reported (Wang, 2006; Baxter, 2006; Goebuchi, 2006; Kishikawa, 2005). Optical switch based on those reported structure is polarization dependent, so strictly polarization control is necessary. In recently, we designed a new structure of wavelength selective optical switch based on Michelson interferometer, Faraday Rotation Mirror and Semiconductor Optical Amplifier.

5.1 The operating principle

Fig. 16 is the schematic for proposed digital wavelength selective optical switch. As shown in Fig. 16, it is divided into three sections: section I is a $1 \times N$ coupler; section II is constituted serials of fibre delay line, it's a key part, we can select the wavelengths we want by assembling different fibre delay line. In theory, C_N^2 wavelengths can be selected, if there are N fibre delay fibres; section III is the control part of this digital wavelength selective optical switch, according to the requirement two of the SOAs are turn on, then a set of wavelengths are selected and others turn off immediately.

Under normal operating state, only two SOAs would be turned on. So in fact, the proposed structure is a Michelson interferometer. And the transfer can be written as:

$$E_{out} = T_C \cdot T_D \cdot T_S \cdot T_{FM} \cdot T_S \cdot T_D \cdot T_C \cdot E_{in} \quad (13)$$

Where, E_{in} and E_{out} are the electric field complex amplitude of input and output light respectively; T_C , T_D , T_S and T_{FM} are the transfer matrixes of coupler, fibre delay lines, SOAs and Faraday rotation mirrors respectively. For simplifying the question, we assume the coupler is a 3dB direction coupler, and then those matrixes can be described as:

$$T_C = \begin{bmatrix} \sqrt{\alpha} & j\sqrt{1-\alpha^2} \\ j\sqrt{1-\alpha^2} & \sqrt{\alpha} \end{bmatrix} \quad (14)$$

Where, α is the splitting ratio of coupler.

$$T_D = \begin{bmatrix} \exp(-j\beta l_1) & 0 \\ 0 & \exp(-j\beta l_2) \end{bmatrix} \tag{15}$$

β is the propagation constant of light, l_1 and l_2 are the length of Michelson interference arms. Matrixes S and FM are identity matrixes.

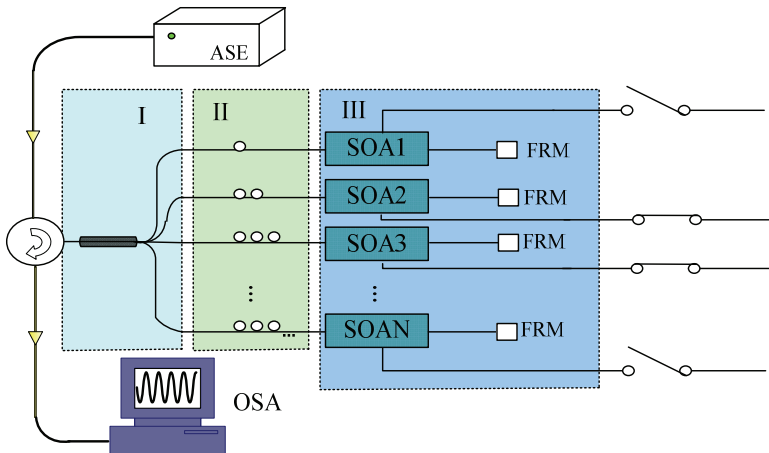


Fig. 16. Schematic of experimentally digitally wavelength selective optical switch. SOA_N ($N=1, 2, 3 \dots$) is the Semiconductor Optical Amplifiers in the N^{th} interference arm; FRM is Faraday rotation mirror. ASE is a light source of Amplified Spontaneous Emission. OSA is an Optical spectrum analyzer.

It can be seen, from above expressions, the length difference between interference arms determine the selective wavelength. So the fibre delay lines play an important role in this device. Another important component of the device is Faraday rotation mirror, which consist of a 45° Faraday rotator and an ordinary mirror. It can automatically compensate for any polarization dependent effect. As a result, the wavelength selective optical switch is a polarization independent device.

5.2 Relation between the number of choice wavelength and insertion loss

With the increasing number of fibre delay line, as we know, the number of choice wavelength increase following the rule C_N^2 . However, the insertion loss of this wavelength selective optical switch also increases.

According to the definition of insertion loss for optical switch, if the gain of SOAs is set at 0, the expression of insertion loss can be written theoretically as:

$$IL = -10 \log_{10} \left(\frac{2}{N^2} \right) \text{ (dB)} \tag{16}$$

Where, IL is the insertion loss; N is the number of SOA.

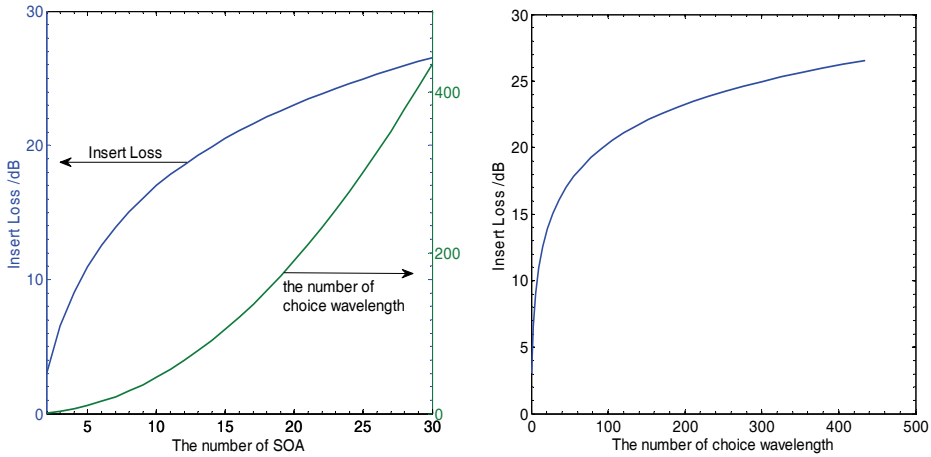


Fig. 17. Relation among N , number of choice wavelength and insertion loss

Fig. 17 shows the relation among N , number of choice wavelength and insertion loss. From it, we can see with the increase in the number of choice wavelength, the insertion loss also increase. So, the compromise between the number of choice wavelength and the insertion loss should be adapted in the design of this structure. Fig. 17 (left) shows the insertion loss is increasing with the number of SOA at exponential function and the number of choice wavelength at square function. Fig. 17 (right) shows the relationship between insertion loss and the number of choice wavelength, it indicates that the insertion loss began to increase rapidly, then slowly increased until stabilized with the number of choice wavelength. However in this structure, the insertion loss can be compensated by optimizing the SOA gain.

5.3 Performance measurement

Fig. 18 shows the transmission spectrum of our proposed digital wavelength selective optical switch. The operating wavelength is set at 1550.5 nm. While the difference between Michelson interferometer arms (ΔL) is 0.172 mm, the working state is "ON" as shown in Fig. 18 (a), otherwise the working state is "OFF" as shown in Fig. 18 (b).

Fig. 19 is the result of insertion loss for proposed DWSS (SOA1 and SOA2 gain > 0). As can be seen about four wavelengths are selective from the range of 1530 ~ 1560nm and the insertion loss of selective wavelengths are about -6 ~ -2dBm.

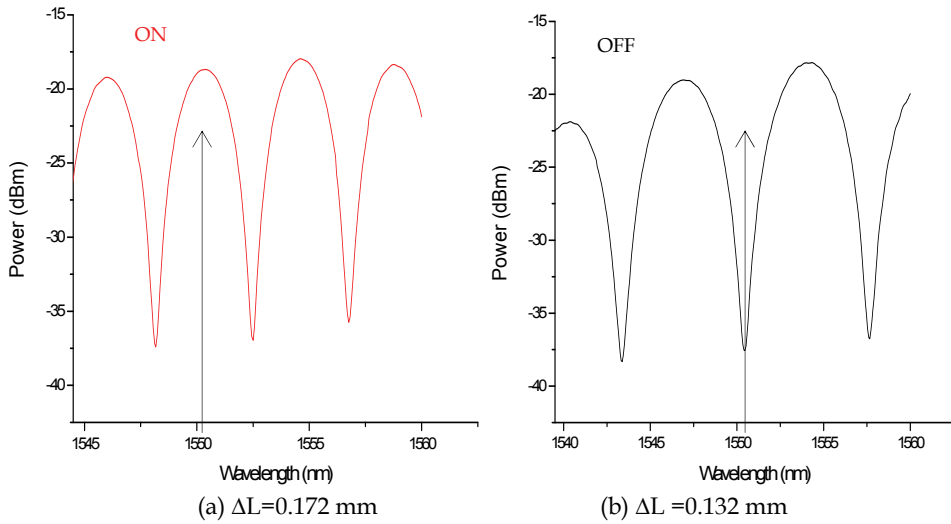


Fig. 18. The transmission spectrum of proposed DWSS.
 (ΔL : the difference between Michelson interferometer arms)

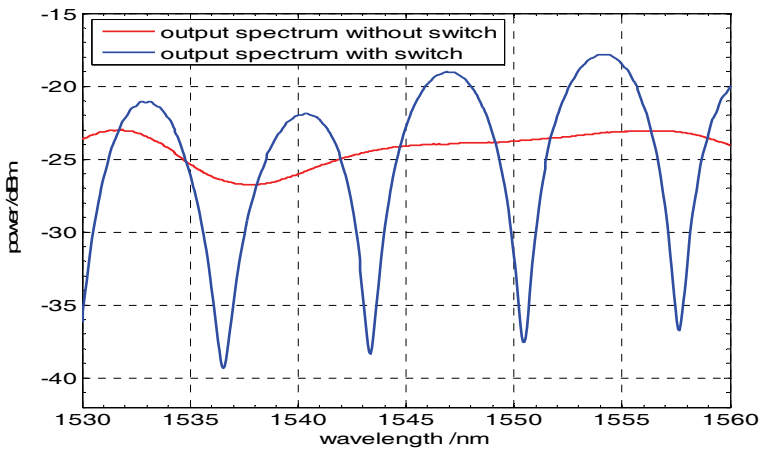


Fig. 19. Insertion loss of the proposed DWSS.
 (The red line is output spectrum without switch and blue line with switch, the difference between two lines is the insertion loss of operating wavelength)

The response speed of proposed DWSS was test and the result is shown in Fig. 20. The red trace is control signal to drive SOAs, and the green trace is the response curve of the DWSS in time domain. It can be seen that rise time of the response curve is 65.05 ns. As is known, the response speed of SOA can achieve a few hundred picoseconds. So the relatively larger rise time is mainly owing to the poor response speed of the signal generator which generates the control signal in our measurement.



Fig. 20. Response speed of proposed DWSS

6. Micro/nano-photonics integration for VLSI photonics

The demand for higher communication speeds and greater capacity has grown exponentially. Especially, as the world entered the 21st century, it is experiencing an explosive increase which is driven by popular, bandwidth-hungry video applications (Nilsson, 2009).

Increase of communication capacity can be achieved by utilizing several resources including dense wavelength division multiplexing (DWDM), optical time division multiplexing (OTDM) and space division multiplexing techniques and so on. However, those techniques may encounter many technical bottlenecks, if the 40Gbit/s or 100Gbit/s transponders are launched largely. At present, it is a challenge for traditional discrete-component-based optical systems to drive down space and power per bit because the complex modulation techniques required for higher fibre capacity require a large number of optical and electronic components. To solve this question, micro & nano photonic integration was proposed recently due to photonic integration device have many crucial advantages comparing with discrete optical components (Nilsson, 2009), such as enabling rapid capacity addition in optical networks, reducing overall size and power consumption and improving reliability and so on.

Many progress of micro & nano photonic integration has been reported (Corzine, 2008; Ticknor, 2000; Park, 2000). In March 23, 2009, Infinera has demonstrated photonic integrated circuits delivering 400 Gigabits/second (Gb/s) of optical capacity in a single pair of chips using complex modulation formats. It will enable Infinera's next generation optics to deliver up to 80% power savings over competitor 40 Gb/s wavelength optics based on conventional discrete optical components (Bob Blair, 2009).

On the other hand, photonic device based on micro/nano fibre has attracted widely attention owing to its characteristics of ultra-low-loss, compact structure and easily coupled with optic-fibre (Tong, 2003; Brambilla, 2004; Yu, 2008). So the integrated photonics based on micro/nano fibre will provide a new way for very large-scale integration (VLSI) photonics. At present, our most efforts focus on the design and fabrication of photonics device based on micro/nano optic-fibre. Fig. 21 shows an architecture of the photonics integrated chip

based on micro/nano fibre (nf-PIC). In this chip most of function of an optical switching node can be realized. Next, we will simply introduce mainly micro/nano photonic device in this chip.

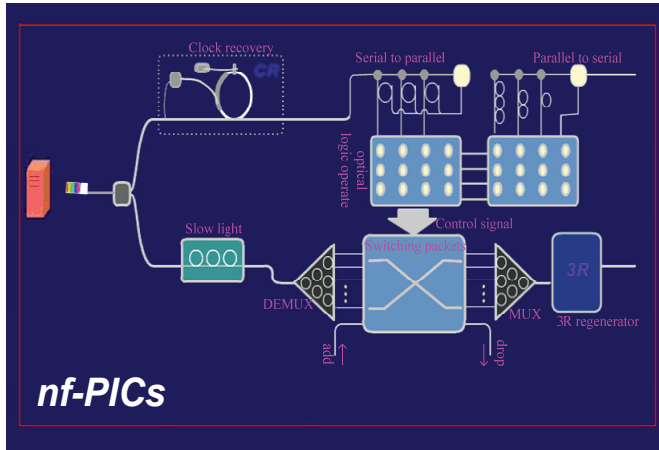


Fig. 21. Architecture of photonic integrated chip for optical switching node based on micro/nano fibre device (nf-PIC)

6.1 Micro/nano fibre taper

Fig. 21 doesn't show the details of each device, but it plays an important role in photonic integrated chip. Optical signal transport in different devices may have different modes, so a mode adapter is necessary to convert one mode to another. Otherwise, the excess loss will be very large in high-density photonic integrated chip due to the mode mismatch. So, to minimize the excess loss in micro/nano photonic integrated chip, a kind of optimized low loss micro/nano fibre taper is an important device. This micro/nano fibre taper can meet the desire of low loss and compact structure in photonic integrated chip.

6.2 Clock recovery

Clock recovery is a key element for a communication system. In the proposed photonic integrated chip, mode-locked lasers based on micro ring resonator will be adapted to achieve the function of clock recovery.

Fig. 22 shows the operation principle of clock recovery based on fibre microring resonator. While an optical pulse signal with cycle T passes through the nonlinear optical modulator, a period-phased modulation is appeared in the laser due to cross-phase modulation effect, and the output clock signal is synchronized with the input signal.

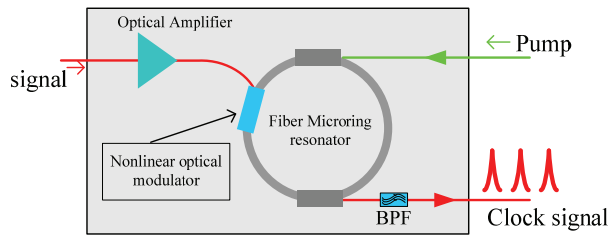


Fig. 22. Schematic of clock recovery. BPF: band-pass filter

6.3 Optical logic gate.

So far, almost the entire commercial logical device, its logic function is completed in electrical domain. As the development of higher speed and greater capacity communication, logic operation based on electronic component will don't encounter the demand owing to the bottleneck speed of electronic calculating. All-optical logic operation is one of choice to break the bottleneck speed of electronic component.

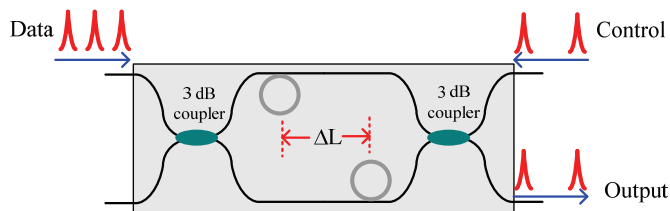


Fig. 23. AND logic gate based on microring and Mach-Zehnder interferometer

Fig. 23 addresses a kind of optical AND logic gate based on microring and Mach-Zehnder interferometer. On the one hand, if the control is "0", the output will be "0" owing to the symmetrical arms of Mach-Zehnder interferometer; on the other hand, if the control and data are "1" simultaneously, the symmetrical structure will be break, then the output will be "1". Table 6 shows the truth table of this logic gate.

Control	Data	Output
0	0	0
0	1	0
1	0	0
1	1	1

Table 6. The truth table

6.4 Slow light

Slow light is a promising solution for memory, buffering and time domain processing of optical signal. There are many procedures to control velocity of light, one of is arrays of microrings resonator. Arrays of microring based on Micro/nano fibre have good prospects for generating slow light because they are compact, low loss and higher nonlinear effect, and can offer wide-bandwidth propagation.

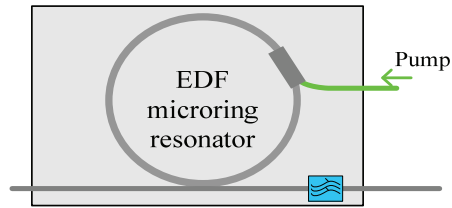


Fig. 24. Delay time tunable device for slow light

According to Kramers-Kronig relationship, as long as there are Gain or transparency window, the slow light phenomenon will appear. So the resonator, such as microring, fibre grating and Fabry-perot, can generate slow light in its transparency window.

Microring shown in Fig. 24 can realize the function of delay time tunable because the ring was fabricated by Doped-Erbium Fibre, so the loss can be tunable of the ring, and the loss of microring resonator is one of a factor which can influence the delay time. As a result, we can tune the delay time by change the gain of EDF.

6.5 MUX/DEMUX

MUX/DEMUX is used frequently in optical communication system. Many techniques are adapted to fabricate MUX/DEMUX, such as optical lens, interferometric filter, holographic grating, fibre grating, waveguide grating, Mach-Zehnder interferometer and array waveguide grating and so on. But those structures are not easy to be integrated on chip. Arrays of fibre microrings due to the characteristic of high-Q, high finesse and compact structure and the convenience integrated on chip will be adapted on our proposed photonic integrated chip.

Fig. 25 shows a wavelength demultiplexer, it can also serve as wavelength multiplexer. The structure of microring resonator determines the wavelength which can set up resonance in microring, so multi-wavelength signal can be demultiplied by arrays of microring resonator.

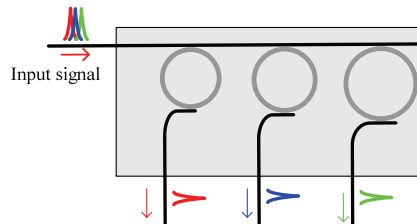


Fig. 25. Schematic of wavelength demultiplexer.(It also can be served as wavelength multiplexer.)

6.6 Optical switching

It is the core component in our proposed photonic integrated chip. The switching packets of this chip is achieved finally just by the optical switching. With the characteristics of microring, integrated arrays of fibre microring can also finish the optical switching with excellent performance.

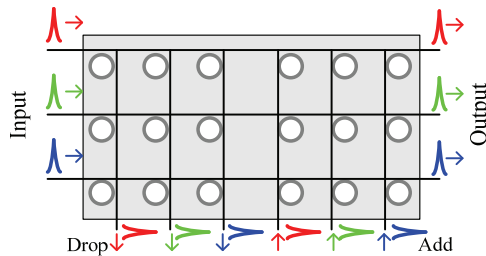


Fig. 26. Reconfigurable optical add-drop multiplexing

Fig. 26 shows a structure of reconfigurable optical add-drop multiplexing (ROADM) based on arrays of fibre microring resonator. Demultiplexed wavelength signals are input into ROADM, some of them pass through the ROADM, others dropped from drop port while the corresponding microrings are turned on by control signal. At the same principle, the wavelength can also be added in add port.

7. Conclusion

This chapter includes six sections. Except for the section of introduction, we will give brief conclusion the left five sections as follows:

In the second section, we introduced a new kind of 3rd feed-forward optical fibre delay lines. Theoretical analysis shows that it can provide large delays and is easy to be expanded. Experimental demonstration to implement such delay lines using SOAs and Farady rotation mirrors is presented. Delay step as small as 0.5 ps with precision of about 0.03 ps was realized. Measured results verify the feasibility of the proposed method. Its excellent expandability, low insertion loss, low polarization dependence loss and high tuning speed are suitable for application in phase array radar system and microwave signal processing.

Based on the structure above, we introduced a new kind of buffering structure by embedding 3rd feed-forward optical fibre delay lines into a re-circulating loop in the third section. Measurements have been carried out and the results have shown the fine property.

In the fourth section, a novel structure of eight-channel digitally tunable optical fibre based on thin film filters and semiconductor optical amplifiers has been demonstrated. The tuning speed is up to 8.82ns, the total insertion loss is between 2.14dB and 6.76dB. The isolation is over 40dB. The number of SOAs used in the proposed configuration is $3 \times 2^{(\log_2 N)-2}$ where N is the number of tuned wavelengths. This means that the structure can save up 25% SOAs in comparison with the conventional digitally tunable optical filters. It can be expanded to large size with no additional insertion loss. Its wavelengths are well agreed with the defined ones by ITU-T and its temperature performance is stable. This kind of filter has potential application in wavelength selective switching based optical networks.

In the fifth section, a novel structure of digitally wavelength selective optical switch based on Michelson interferometer and semiconductor optical amplifiers has been demonstrated. The response speed is up to 65.05ns, the insertion loss is between -6 dB and -2 dB. In this structure, Faraday rotation mirrors are adapted, which can automatically compensate for any polarization dependent effect. As a result, the wavelength selective optical switch is a polarization independent device.

Many techniques for photonic integration have been reported. In the sixth section, we proposed another way based on micro/nano fibre device for VSLI photonics. Micro/nano-photonics integration is exhibiting its superiority in almost all of aspects of optical information process and communication technology. We hope the Micro/nano-photonics integration will achieve great success in 21st century like what the microelectronics had gain in 20th century.

8. Acknowledgement

This work was supported partially by National Science Foundation of China (NSFC) (ID60877012), 863 Project (ID2006AA01Z242 and 2007AA01Z275), Dawn Program for Excellent Scholars by the Shanghai Municipal Education Commission, the Key Disciplinary Development Program of Shanghai (T0102), HangTian Innovation Foundation and National Key Lab special Projects(GKZD030004). The authors are with the State Key Laboratory on Advanced Optical Communication Systems and Networks, Shanghai Jiao Tong University, Shanghai, China (e-mail: lixinwan@sjtu.edu.cn)

9. References

- A. J. Seeds, K. J. Williams. (2006). Microwave photonics, *Journal of Lightwave Technology*, Vol 24, No.12,pp .4628-4641
- J. Capmany, B. Ortega, D. Pastor, S. Sales, (2005). Discrete-time optical processing of microwave signals, *Journal of Lightwave Technology*, Vol. 23, No.2, pp .702-723
- K. Wilner and A. P. Van Den Heuvel. (1976). Fibre-optic delay lines for microwave signal processing, *Proc.IEEE*, Vol 64, No.5, pp.805-807
- G. K. Chang, J. J Yu, Y. K. Yeo, A. Chowdhury, Z. S. Jia. (2006). Enabling technologies for next-generation optical packet-switching networks, *Proceedings of the IEEE*, Vol 94, No.5, pp .892-910
- A. J. Seeds. (2002). Microwave photonics, *IEEE Transactions on Microwave Theory and Techniques* . Vol 50, No.3, pp .877-887
- E. J. Murphy, T. O. Murphy, A. F. Ambrose, R. W. Irvin, B. H. Lee, P. Peng, G. W. Richards, A.Yorinks. (1996). 16×16 strictly nonblocking guided-wave optical switching system, *Journal of Lightwave Technology* ,Vol 14, No.3, pp .352- 358
- Y.K. Yeo, J. J. Yu, G. K. Chang. (2004). A dynamically reconfigurable folded-path time delay buffer for opticalpacket switching, *IEEE Photonics Technology Letters*, Vol 16, No.11, pp .2559 - 2561
- B. Moslehi. (1992). Fibre-optic filters employing optical amplifiers to provide design flexibility, *Electronics Letters* , Vol. 28, No.3, pp .226-228
- J. Capmany, B.Ortega, D. Pastor. (2006). A tutorial on microwave photonic filters, *Journal of Lightwave Technology* ,Vol 24, No.1,pp.201-229

- A. Ho-Quoc, S. Tedjini, A. Hilt. (1996). Optical polarization effect in discrete time fiber-optic structures for microwave signal processing, *IEEE MTT-S International Microwave Symposium Digest*, Vol. 2, pp.907-910
- D.J. Blumenthal, P. R. Prucnal, J. R. Sauer. (1994). Photonic packet switches: architectures and experimental implementations, *Proceedings of the IEEE*, Vol. 82, No.11, pp. 1650-1667
- C.H. Shi, J.P. Chen, G.L. Wu, X.W.Li. (2006). Stable dynamic detection scheme for magnetostrictive fiber-optic interferometric sensors, *Optics Express*. Vol.14, No.12. pp .5098-5102, <http://www.opticsinfobase.org/abstract.cfm?URI=oe-14-12-5098>
- X.W. Li, L.M. Peng, S.B. Wang, Y.-C. Kim, J.P. Chen. (2007). A novel kind of programmable 3ⁿ feed-forward optical fiber true delay line based on SOA, *Optics Express*, Vol.15, No.25, pp .16760-16766, <http://www.opticsinfobase.org/oe/abstract.cfm?URI=oe-15-25-16760>
- Xinwan Li, Limei Peng, Jianping Chen, Songbo Wang, Guiling Wu, Jialin Lu, Young-Chon Kim. (2008) A novel fast programmable optical buffer with variable delays, *OFC/NFOEC 2008*, paper JThA41
- Xinwan Li, Jianping Chen, Guiling Wu, Ailun Ye. (2005), Digitally tunable optical filter based on DWDM thin film filters and semiconductor optical amplifiers, *Optics Express*, Vol. 13, No. 4, pp. 1346-1350
- D.Sadot. (1998). Tunable optical filters for dense WDM networks. *IEEE Commun. Magn*, Vol.36, No.12. pp .50-55
- O.Ishida. (1997). Digitally tunable optical filters using arrayed-waveguide grating (AWG) multiplexers and optical switches. *Journal of Lightwave Technology*, Vol.15, No.2. pp. 321-327
- B.Glance. (1996). Wavelength-tunable add/drop optical filter. *IEEE Photonics Technology Letters*, Vol.8, No.2. pp. 245-247
- M.Zirngibl. (1994). Digitally tunable channel dropping filter/equalizer based on waveguide grating router and optical amplifier integration. *IEEE Photonics Technology Letters*, Vol.6, No.4, pp. 513-515.
- B.Glance. (1994). Applications of the integrated waveguide grating router. *Journal of Lightwave Technology*, Vol.12, No.6. pp. 957-962
- Yoshinori Hibino. (2002). Recent advances in high-density and large-scale AWG Multi/demultiplexers with higher index-contrast silica-based PLCs. *IEEE J. Sel. Top. Quantum Electron*, Vol.8, No.6, pp. 1090-1101
- Li X.W., Chen J. P., Wu G.L, Wang H., Ye A. L, (2005), An experimental study of an optical burst switching network based on wavelength-selective optical switches, *IEEE Communications Magazine*, Vol. 43, No.5, pp. S3-S10
- Fan Wang, Jianyi Yang. & Limei Chen. (2006). Optical switch based on multimode interference coupler. *IEEE Photonics Technology Letters*, Vol. 18, No. 2, pp .421-423
- Glenn Baxter, Steven Frisken. & Dmitri Abakoumov. (2006). Highly programmable wavelength selective switch based on liquid crystal on silicon switching elements, *Proceedings of OFC/NFOEC 2006*, OTuF2, Anaheim, California, USA, 2006, California.
- Yuta Goebuchi, Tomoyuki Kato. & Yasuo Kokubun. (2006). Fast and stable wavelength-selective switch using double-series coupled dielectric microring resonator. *IEEE Photonics Technology Letters*, Vol. 18, No. 3, pp . 538-540

- Hiroki Kishikawa. & Nobuo Goto. (2005). Proposal of all-optical wavelength-selective switching using waveguide-type Raman amplifiers and 3-dB couplers. *Journal of Lightwave Technology*, Vol. 23, No. 4, pp .1631-1636
- Alan C. Nilsson, Geoffrey S. Bennett. & David F. Welch. (2009). Advanced photonic integration and the revolution in optical networks, *Proc. of SPIE*, Vol. 7221, pp. 722102-1-722102-5
- S. Corzine ; P. Evans. & M. Kato. (2008). Photonic integrated circuits for phase modulation formats, *Proceedings of IEEE Lasers and Electro-Optics Society. LEOS 2008. 21st Annual Meeting of the*, pp.334-335
- Ticknor, A., Lipscomb, G.F. (2009). Passive PICs are key elements in 40- and 100-Gbps systems, *Lightwave*, Vol.26, No.3, pp. 7-12
- Park, S.-G. & Spiekman. (2000). Chirp consequences of all-optical RZ to NRZ conversion using cross-phase modulation in an active semiconductor photonic integrated circuit, *IEEE Photonics Technology Letters*, Vol.12, No.3, pp. 233-235
- Bob Blair, Jeff Ferry, (2009), Infinera's 400 Gb/s PIC sets new record for integration, release at website <http://www.infinera.com/j7/servlet/NewsItem?newsItemID=150>
- Limin Tong, Rafael R. and Gattass. (2003). Subwavelength-diameter silica wires for low-loss optical wave guiding, *Nature*, Vol. 426 pp.816-819
- Gilberto Brambilla, Vittoria Finazzi. & David J. Richardson. (2004). Ultra-low-loss optical fiber nanotapers, *Optics Express*, Vol.12, No.10, pp. 18-23
- Wu Yu, Zeng Xu. and Hou Changlun. (2008). A tunable all-fiber filter based on microfiber loop resonator, *Applied Physics Letters*, Vol.92, No.19, pp. 11-12.

All Glass Micro-structured Optical Fibres

Liang Dong
IMRA America Inc.
USA

1. Introduction

Micro-structured fibres with air holes have been studied widely in the last decade for a large variety of applications (Russell, 2006). The first notable one is the ability to engineer anomalous dispersions below $1.3\mu\text{m}$ (Ranka 2000). Material dispersion of silica is normal when wavelength falls below $1.3\mu\text{m}$. Substantial anomalous waveguide dispersion is required for a total anomalous dispersion at these short wavelengths. This is made possible by the strong refractive index contrast between glass and air holes in micro-structured fibres with air holes. Octave-spanning super-continuum generation in these micro-structured fibres at wavelengths where femtosecond lasers are readily available leads quickly to the development of f_{ceo} -stabilised frequency combs and a new convenient timing standard at optical frequencies (Jones 2000).

A second major application of micro-structured fibres with air holes is the possibility of making a pump cladding with air holes in a double clad fibres used in high power lasers to convert a low brightness large pump beam into a much smaller diffraction-limited output beam guided in a rare-earth-doped single mode core in the middle of the pump guide (Limpert 2004, 2005, 2006). The high refractive index contrast between glass and air is especially beneficial for the guiding of pump power in a relatively small pump guide for efficient pump absorption. Optical fibres with large heat-dissipating surface placed very close to an active core have proven in the recent years to be very effective in producing high average powers in excess of multi-kilowatts while mitigating thermal effects commonly found in solid state lasers (Gapontsev 2009). Commercial realm of high power fibre lasers has been rapidly expanding in recent years.

It is worth noting that, in the two applications mentioned above, air holes do not need to be placed periodically, and consequently I have referred to the fibres as micro-structured fibres instead of photonic crystal fibres, where a periodicity is implied. Indeed, in both cases, non-periodical cladding is proven to be highly sufficient (Dong 2008, Fu 2008, Limpert 2004, 2005, 2006). In the third important application, periodic cladding is critical (Robert 2005). This is the case of hollow-core photonic crystal fibres, where optical mode is guided in a larger air hole in the centre of the fibre. The largely air-guidance leads to low nonlinearity for high peak power delivery and strong interaction between the guided mode and gas in the core for gas spectroscopy. The high refractive index contrast and periodic cladding are both essential in these fibres.

Fibre lasers have been very successful in producing high average powers and are, however, limited in their ability to generate high peak powers. This is due the small core found in most conventional single mode fibres. The tight confinement in combination with long effective length allows nonlinear effects to accumulate, ultimately limiting fibre laser's ability for high peak power generations. Self-phase modulation (SPM) originates from nonlinear Kerr effect, where different temporal part of an optical pulse propagates at different group velocity, and can lead to new frequency generation at the leading and trailing edges of an optical pulse. It can eventually lead to significant spectral broadening for sub-ps pulses. Stimulated Raman scattering (SRS) originates from the interaction of optical power with optical phonons and can lead to significant power transfer to longer wavelengths for high peak power pulses. Stimulated Brillouin scattering (SBS) originates from the interaction of optical power with acoustic phonons and can lead to significant power transfer to the backward-propagating and slightly frequency-downshifted optical powers in spectrally narrow fibre lasers.

There is, therefore, an urgent need for large core fibres that supports single spatial mode operation to further extent peak powers of fibre lasers. These high peak power lasers of femtosecond, picoseconds and nanosecond durations are especially useful for micro-machining in material processing, biological and medical applications. Conventionally, single mode operation is ensured when normalized frequency $V=2\pi\rho NA/\lambda$ is below 2.405, where ρ is core radius, NA is numerical aperture, and λ is wavelength. A lower NA is clearly desirable for large core size. It is, however, limited by two issues. The first one is that a lower NA leads to a reduction in guidance and consequently higher bend loss. The second issue is the control accuracy of refractive index during fibre preform fabrication. It is generally accepted that the minimum NA=0.06 is a good compromise of all factors involved. This leads to a maximum core diameter of $\sim 13\mu\text{m}$ at $1\mu\text{m}$ and $\sim 20\mu\text{m}$ at $1.55\mu\text{m}$. It has been pointed out that single mode operation in multimode fibres can be achieved, assuming one is careful in launching only the fundamental mode (Fermann 1998). In practice coiling is also used to create additional propagation loss for the higher order modes (Koplow 2000). This extends core diameters to $\sim 30\mu\text{m}$ at $1\mu\text{m}$ for effective single mode operation. Further increase of core diameter leads to much increased difficulties in launching only fundamental mode and in creating differential mode loss by coiling to due the much higher mode density in much larger core fibres which leads to a high degree of mode coupling.

2D micro-structuring of cladding can lead to new designs which are not possible in conventional optical fibres with essentially 1D design in radial direction. Leakage channel fibres described in this chapter are one of the new designs made possible by 2D micro-structuring of cladding for much improved differential mode loss controls (Dong 2007, 2008, 2009). Micro-structuring also allows much lower NAs to be implemented for strictly single mode fibres with large cores. Two examples are given in this chapter, i.e. endless single mode fibres (Dong 2008) and stress-induced waveguides (Fu 2009). These two types of fibre have very limited ability to be coiled. It is very useful, however, in applications where a short straight fibre is usually sufficient, e.g. in short fibre amplifiers with highly doped cores which are demonstrated recently (Suzuki 2009) and generations of SPM-broadened spectra for compression in ultra short pulse generations. A very important point to note is that high refractive index contrast is not necessary for these large core fibre designs, where a low refractive index contrast is sufficient and advantageous for further limiting higher order

mode propagations. This leads to all glass micro-structured fibres with much improved ease of fabrication and use comparing to micro-structured fibres with air holes.

Despite the fact that air is a readily available ingredient there are a number of drawbacks related to the use of air holes in fibres. The first one is the difficulty in precisely controlling the dimension of air holes in fibre fabrication, an intrinsic problem of a holey structure due to the air hole's tendency to collapse during fibre drawing. This is usually countered by a precise control of pressurization of the air holes, a process dependent on drawing conditions such as furnace temperature, feed rate, and drawing speed. When small air holes are desirable as in endless single-mode PCFs (Birks 1997), high pressure is required to maintain air hole dimensions due to the significantly increased tendency for the air holes to collapse by surface tension in this regime. This can make air hole dimensions to become highly sensitive to drawing conditions. This delicate balance of pressurization and collapse can lead to issues of controllability and repeatability in PCF fabrication. The air holes in a PCF can also disturb smooth fracture wave propagation during fibre cleaving, leading to a poor cleaved surface due to the appearance of deep fractures behind the air holes, a problem often aggravated by large air holes and high cleaving tensions. In addition, air holes are often thermally sealed at fibre ends to minimize environmental contaminations, and mode distortion can occur due to asymmetrical stress over the fibre cross section and along the fibre from the collapsing or splicing process. This is especially true for large-mode-area fibres, which are much more susceptible to small perturbation.

2. All Glass Endlessly Single Mode Fibres

The first endless single-mode photonic crystal fibre (PCF) was demonstrated in 1996 (Knight 1996). It is the first application, followed by many others, where unique features of PCFs are demonstrated. In the case of an endless single-mode PCF, the dispersive nature of a photonic crystal cladding is used to make a fibre that supports single-mode operation over its entire range of guidance. The fibre possesses a short wavelength cut-off, due to diminishing guidance as a result of light's increasing ability to avoid air holes, and a long-wavelength cut-off, due to the vanishing ability of the fibre to confine the localized mode at an increasing wavelength as in any conventional fibres. One major application of the endless single-mode PCF has been in making fibres with a large effective mode area, a topic under intense study for power scaling in optical fibre lasers limited by nonlinear effects (Limpert 2004, 2005).

The first analysis of an endless single-mode PCF was performed using a method approximating a hexagonal unit cell with a circular one and assuming $\rho \approx \Lambda$ (Birks 1997), where Λ being centre-to-centre hole separation or pitch. This allows effective V value to be evaluated and gives an endless single mode regime for designs with relative hole size $d/\Lambda < 0.16$, where d being hole diameter. A number of theoretical studies subsequently refined the single mode and multimode boundary of the PCFs and allow these PCFs to be easily designed. Using a multipole mode solver, Kuhlmeiy et al could accurately simulate confinement loss of modes in a PCF (Kuhlmeiy 2002). They showed that the confinement loss of the 2nd order mode displays two distinctive regimes over wavelength. The two regimes both have near linear dependence on normalized wavelength when plotted on a logarithmic scale. The 2nd order mode is well confined to the core in the short wavelength regime and is no longer localized in the long wavelength regime, indicating a loss of core guidance. The

peak in the second order derivative of the 2nd order mode confinement loss is used in to pinpoint the exact transitional point where the 2nd order mode is no longer guided in the core. This gives an endless single-mode regime for PCFs with $d/\Lambda < 0.406$. This method also gets around the arbitrariness of defining $\rho = \Lambda$ (Birks 1997). Furthermore, Kuhlmeij et al in a separate paper also point out that fundamental mode does not have the same clear cut-off (Kuhlmeij 2002), a point analogous to that of a fundamental mode in conventional step index fibres, which is always guided and just gets weaker in guidance at smaller V values. It is also worth noting that Nielsen et al puts endless single mode regime to be at $d/\Lambda < 0.43$, using a more geometrical argument involving transverse mode dimension (Nielsen 2003).

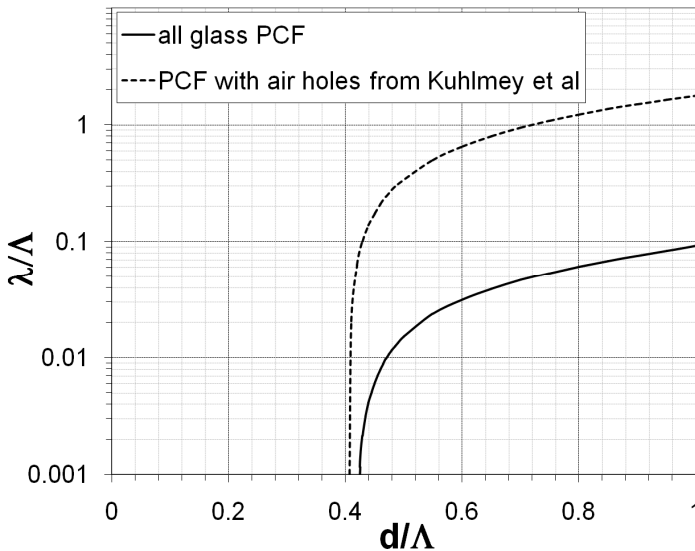


Fig. 1. Single mode and multimode boundary of PCFs, where all glass PCFs have a refractive index difference of 1.2×10^{-3} between the background and cladding features.

The multipole method can be used to evaluate confinement loss of the 2nd order mode in all glass PCFs with refractive index difference between that of the low index glass rods n_r and the background glass n_b , $\Delta n = n_b - n_r = 1.2 \times 10^{-3}$ (Dong 2008). This low refractive index contrast is chosen because the fluorine-doped silica glass is commercially available and especially suitable for large core operation. This refractive index contrast is also used throughout this chapter. The single mode and multimode boundary, i.e. 2nd order mode cut-off, is summarized in fig. 1 as a solid line for the all glass PCFs, along with the corresponding dashed-line curve for PCFs with air holes (Kuhlmeij 2002). Single mode regime is to the top-left of each curve while multimode regime is to the bottom-right of each curve. Endless single-mode regime is characterized by being single mode for the entire wavelength range. This requires $d/\Lambda < 0.42$ for the all glass PCFs, which is only slightly different from $d/\Lambda < 0.406$ for PCFs with air holes. This is remarkable, considering the refractive index contrast has changed by over two orders of magnitude in these two cases. This is, however, an indication that the dispersive behaviour of the photonic crystal cladding responsible for

the endless single-mode regime is much more sensitive to the normalized geometry and much less to refractive index contrast at the short wavelength limit. It can also be seen from fig. 1 that the all glass PCFs also have a significantly increased regime of single mode operation for $d/\Lambda > 0.42$, reducing required normalized wavelength λ/Λ by over an order of magnitude. This is due to a significant reduction of the effective refractive index difference between the silica core and the composite cladding in the all glass PCFs, leading to a lower effective V value at the same d/Λ . In general, the all glass PCF is expected to be more bending sensitive due to the reduced effective refractive index difference. They, however, allows well over an order of magnitude larger core diameters for single mode operation.

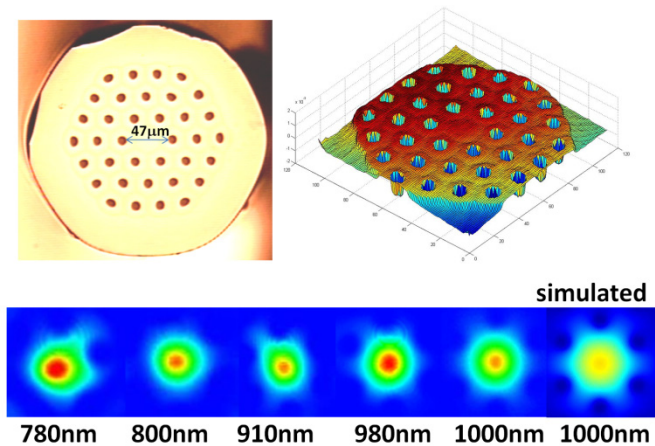


Fig. 2. Fabricated PCF cross section ($2\rho=47\mu\text{m}$, $d/\Lambda=0.36$, $\Lambda=28.7\mu\text{m}$, $d=10.3\mu\text{m}$), measured 2D refractive index, measured modes at various wavelengths and simulated mode at $1\mu\text{m}$.

An all glass PCF is fabricated with $d/\Lambda=0.36$ and $\Lambda=28.7\mu\text{m}$ using silica background and fluorine-doped silica rods in the cladding, using the standard stack-and-draw technique. The cross section of the all glass PCF is shown in fig. 2 along with a 2D refractive index scan of the fibre. Birks et al have also pointed out that, at long wavelength cut-off, PCF behaves like a standard fibre and, at short wavelength cut-off, the critical bending radius of a PCF approximately scales as $R_c \propto \rho^3/\lambda^2$ (Birks 1997), a result directly comes from the constant V value of PCFs over a wide range of wavelengths. The fabricated all glass PCF has normalized wavelength $\lambda/\Lambda \approx 0.035$ at $\lambda=1\mu\text{m}$. This certainly put the fabricated PCF in the short wavelength regime and its critical bend radius would scale with cube of core radius to be at least three orders of magnitudes larger than that of the PCF reported by Birks et al (Birks 1997) to be estimated at several meters. To characterize mode properties at different wavelengths, light from a broad band supercontinuum source is filtered by a 10nm band-pass filter and is then focused down to a size matched to the MFD of the fibre mode to launch it into a straight 20cm length of the fabricated all glass PCF. Clear single mode operation at $1.05\mu\text{m}$ is observed with no sign of any guided higher order mode in the core even for such short length of fibre. The band-pass filter is then changed to a second band-pass filter centred at a different wavelength. The launch optics is re-adjusted to match the mode size at the new wavelength. Mode at the new wavelength is then measured. Measured

output mode patterns are shown in fig. 2 along with the simulated mode at 1000nm. Loss of fundamental mode guidance is observed at below 800nm. This would give us a maximum $2\rho/\lambda$ of ~ 60 . The simulation gives an effective mode area of $2147\mu\text{m}^2$ at $1\mu\text{m}$ wavelength. The loss of the fabricated fibre is estimated to be less than 0.1dB/m at $\sim 1\mu\text{m}$ when kept straight, dominated by material losses.

3. Stress-induced Waveguides

In all glass micro-structured fibres with fluorine-doped silica glass features, the cladding features have a slightly larger coefficient of thermal expansion than that of the surrounding silica glass. It would contract more than the surrounding silica during cooling after exiting the furnace on the fibre drawing tower. This contraction is, however, constrained by the surrounding silica glass and will consequently put the surrounding silica glass under compression and the adjacent fluorine-doped glass under tension. This stress causes a refractive index rise in the silica glass next to each fluorine-doped rod and a corresponding refractive index reduction in the adjacent fluorine-doped glass. Frozen-in drawing tension can also contribute towards this refractive index change. It is worth noting that the refractive index change from a mismatch of coefficients of thermal expansion cannot be eliminated by thermal annealing, while the index change from the frozen-in drawing tension can be annealed above glass transition temperature. This stress-induced refractive index change is very small. Its effect is negligible in the all glass endless PCF with core diameter of $\sim 50\mu\text{m}$ or lower described in the last section. It is, however, a convenient and controllable way to produce very small refractive index contrast, and can be used to make strictly single mode waveguide with $V < 2.405$ with very large core diameters.

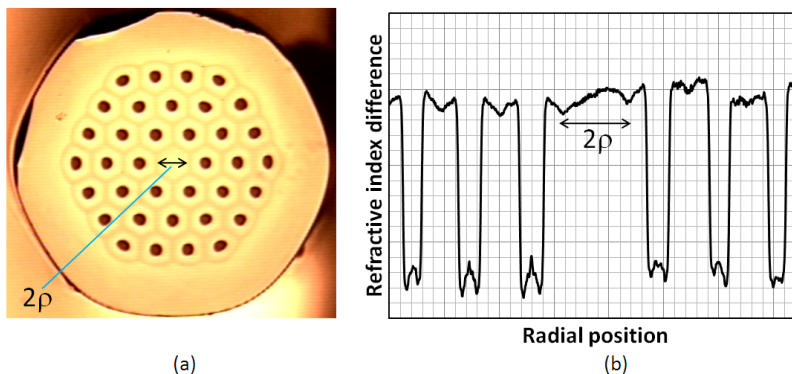


Fig. 3. (a) Fibre cross section and (b) refractive index scan through the centre of the fibre.

The cross sections of all the fabricated fibres are identical and an example is shown in fig. 3a, along with its refractive index profile in fig. 3b. The fibres are made with a hexagonal array of slightly fluorine-doped silica rods in a silica background. A single fluorine-doped rod is missing in the centre. This fibre is very similar to the fibre used in the all glass endless single-mode PCF described in the last section, but has a much larger core. A rod diameter d to a centre-to-centre spacing Λ ratio, $d/\Lambda=0.36$ is used. A hexagonal low index trench,

shown as dark line in the fibre cross section in fig. 3a, develops half way between the low index rods. This effectively forms an index guiding core in the centre of the fibre with a near parabolic refractive index profile and a core diameter 2ρ (see fig. 3b). The refractive index scan in fig. 3b is right through the centre of the fibre and the centres of six low index rods. The six low index rods can be clearly seen, along with the refractive index rise in the silica glass adjacent to each low index rod due to the compressive stress as well as the corresponding refractive index reduction in the fluorine-doped silica glass adjacent to the silica glass due to the tensile stress. The low index trench between the low index rods (dark hexagonal line in fig. 3a) can also be seen clearly in the refractive index profile in fig. 3b. Clearly visible is also the parabolic core with a diameter of 2ρ .

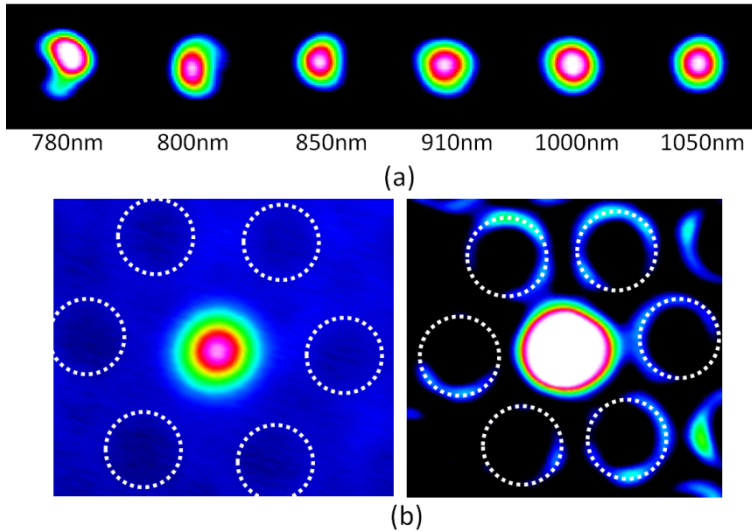


Fig. 4. (a) Measured modes at various wavelengths in the fibre with $2\rho=82\mu\text{m}$ by a broad band supercontinuum source and a band-pass filter, (b) captured mode image in the fibre when fibre end is illuminated and captured mode image when launched power is increased to saturate the mode on the CCD. White dotted circles mark the location of the inner six low index rods.

Of the several fibres fabricated, the first one has $\Lambda=90\mu\text{m}$, $2\rho=82\mu\text{m}$, and a fibre diameter of $835\mu\text{m}$. The second fibre has $\Lambda=142\mu\text{m}$, $2\rho=130\mu\text{m}$, and a fibre diameter of 1.32mm . Since we are not able to measure refractive index of large fibres, two smaller fibres with $\Lambda=18\mu\text{m}$ and $31\mu\text{m}$ are also drawn for refractive index measurements. Both sets of measurements show a parabolic index profile of the core and a refractive index difference between the centre of the core and the low index trench ΔN of $\sim 6 \times 10^{-5}$, largely independent of pitch Λ . Our waveguide mode analysis with a parabolic index profile of $\Delta N=6 \times 10^{-5}$ and $2\rho=82\mu\text{m}$ gives a LP₁₁ mode cut-off wavelength at 960nm for the first fibre. This makes the first fibre a strictly single mode fibre at $1\mu\text{m}$. The same analysis also gives a MFD of $\sim 68\mu\text{m}$ and an effective mode area of $\sim 3600\mu\text{m}^2$ at $1\mu\text{m}$, setting a record for effective mode area of a single mode fibre at $1\mu\text{m}$. Similar analysis with $2\rho=130\mu\text{m}$ gives a LP₁₁ mode cut-off wavelength of $1.5\mu\text{m}$ for

the second fibre. This would make the second fibre few-moded at $1\mu\text{m}$, but single mode at $1.55\mu\text{m}$. The same analysis also gives the second fibre a MFD of $\sim 80\mu\text{m}$ and effective mode area of $\sim 5000\mu\text{m}^2$ at $1\mu\text{m}$ and a MFD of $\sim 108\mu\text{m}$ and an effective mode area of $\sim 9100\mu\text{m}^2$ at $1.55\mu\text{m}$.

The mode at various wavelengths is further characterized with a broad band supercontinuum source and a band-pass filter. Stable single-mode operation is easily seen above 850nm (see Fig 4(a)). At shorter wavelengths, evidence of higher order mode is observed. Strictly single-mode operation at $\sim 1\mu\text{m}$ is also tested when the output mode is continuously monitored while the launch positioning stage is moved away from the optimal position and then back. An ytterbium ASE source is used for this test. No higher order mode is observed while adjusting the launch position up to the point where the fundamental mode is entirely turned off at the fibre output. Total transmission with reference to the power just before the fibre input end is measured to be 91.4% at $\sim 1\mu\text{m}$. This includes reflection losses at the two fibre ends, indicating extremely high launch efficiency and low transmission loss of less than 0.05dB/m at $\sim 1\mu\text{m}$. To confirm that the mode is guided in the high index region in the centre of the fibre, not by PCF guidance, the fibre output end is illuminated by additional white light source while the output mode is monitored at $\sim 1\mu\text{m}$. It can be clearly seen that the mode only occupies the centre part of the PCF core and does not extend to the low index rods (see the captured image shown on in Fig. 4(a)). White circles mark the location of the inner six low index rods. A further test is done by monitoring the output mode while increasing the launched power until the centre part of the mode is saturated (see Fig. 4(b)). This way, faint structures away from the mode can be observed. The weak light in the high index ring around each low index rods can be clearly seen (the location of the inner six low index rods is marked by white circles). Also visible is that the output mode is confined within the low index trench around the parabolic refractive index core. It is clearly evident from the two tests shown in fig. 4 that the mode is guided by the local high index core in the centre of the fibre.

Robust single-mode propagation is also easily observed in the second fibre at $\sim 1\mu\text{m}$ using a similar experimental set-up, an ytterbium ASE source and $\sim 1\text{m}$ straight fibre. The second mode can be seen in this second fibre at $\sim 1\mu\text{m}$ when launch is optimized to excite it. No higher order mode than the second mode is observed. Both the fundamental and second mode are clearly seen being guided by the parabolic index core in the centre of the fibre.

4. All Glass Leakage Channel Fibres

4.1 Introduction

Leakage channel fibres (LCFs) differ from conventional optical fibres by breaking up the continuity of the core and cladding boundary. This broken boundary at the core and cladding interface in a LCF effectively ensures that internal reflection cannot be satisfied everywhere, unlike in a conventional optical fibre, and, consequently, makes the waveguide leaky for all modes. This unique property of LCFs enables them to be precisely engineered to have high confinement loss for all higher order modes and low confinement loss for the fundamental mode, significantly extending the fundamental mode effective area comparing

to that of a conventional single mode optical fibre. We essentially exploited the increased ability of higher order modes to leak through small gaps in the core and cladding boundary while maintaining good fundamental mode confinement, a concept elegantly explained recently by Russell (Russell 2006).

4.2 Differential Mode Loss in LCFs

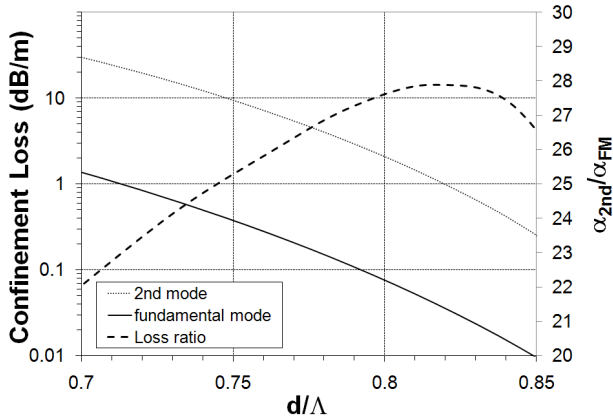


Fig. 5. Effect of d/Λ on confinement loss and the loss ratio between the 2nd mode and fundamental mode for a LCF with $2\rho=50\mu\text{m}$.

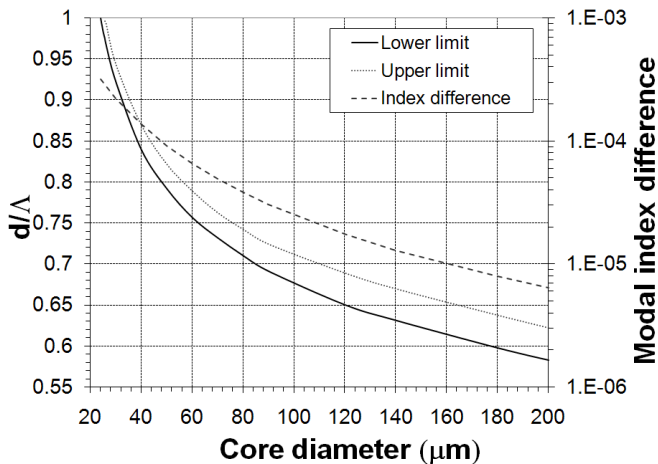


Fig. 6. Effect of core diameters on upper limit, $\alpha_{2nd}=1\text{dB/m}$, and lower limits, $\alpha_{FM}=0.1\text{dB/m}$, of LCF designs and the modal index difference of the fundamental and 2nd order modes near the lower limit in LCFs with $\Delta n=1.2\times 10^{-3}$.

The effect of normalized hole diameter d/Λ is studied in fig. 5 for confinement losses and the ratio of the 2nd mode loss to the fundamental mode loss. The confinement loss for both

the fundamental and 2nd modes increases towards small d/Λ with the loss ratio changed very little over the entire range of d/Λ , from 22 to 28. This almost constant nature of the loss ratio against d/Λ makes it a good measure of design quality when studying LCFs. Once a design is optimized for the maximum loss ratio, differential loss between modes, a more meaningful measure of higher order mode suppression in a fibre amplifier, can be obtained after d/Λ is determined to give an acceptable fundamental mode loss. The loss ratio of all glass LCFs is very similar to a LCF with air holes (Dong 2007). Slightly larger d/Λ is, however, required for achieving a similar confinement loss.

Using an example design criteria which requires the fundamental mode loss, $\alpha_{FM} < 0.1 \text{ dB/m}$, and the 2nd order mode loss, $\alpha_{2nd} > 1 \text{ dB/m}$, the design space at various core diameters is studied in fig. 6. It is interesting to see that the design space rapidly disappears below $2\rho < 30 \mu\text{m}$ and totally vanishes at $2\rho \sim 24 \mu\text{m}$, limited by $d/\Lambda < 1$. Design space widens at large core diameters and smaller d/Λ is required for large core diameters. It is, nevertheless, easy to see from fig. 6 that designs for very large core diameters are possible. Maximum achievable core diameter will ultimately be limited by intermodal coupling due to the vanishing modal index difference. Core diameters of over $200 \mu\text{m}$ may indeed be possible with appropriate choice of fibre diameters.

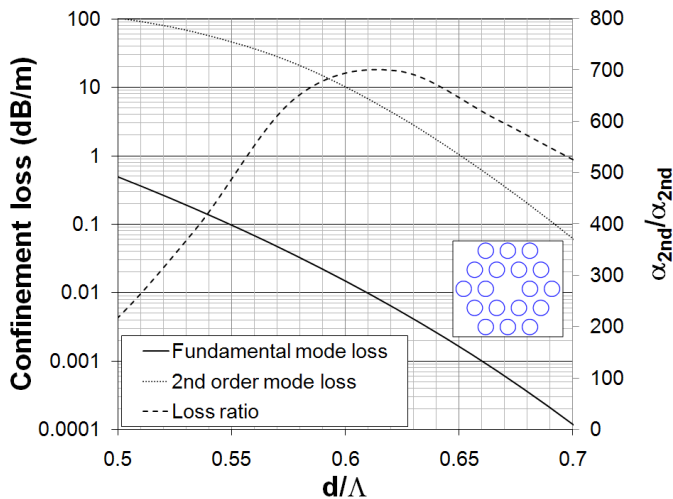


Fig. 7. Effect of d/Λ on confinement loss and the loss ratio between the 2nd mode and fundamental mode for a LCF with two layers of features and $2\rho = 50 \mu\text{m}$.

LCFs with two layers of features can be used to further improve the differential confinement loss between the fundamental and 2nd order mode at the expense of bending performance. Acceptable fundamental mode loss at smaller feature sizes can be realized in LCFs with two layers of features due to the improved fundamental mode confinement, while leakage of higher order modes is substantially increased by a reduction of feature size despite the additional layer of features. Higher differential loss between modes can therefore be realized. Since bending loss of the fundamental mode is very strongly dependent on feature size, a reduction of feature size increases bend loss of the fundamental mode in LCFs. A LCF

with two layers of features is studied in fig. 7. Both the fundamental mode and 2nd order mode loss shows the characteristic increase at small d/Λ , while the loss ratio α_{2nd}/α_{FM} is increased by over an order of magnitude comparing to the designs in fig. 5. At $d/\Lambda \approx 0.548$, the fundamental mode loss $\alpha_{FM} \approx 0.1 \text{ dB/m}$, while the 2nd order mode loss $\alpha_{2nd} \approx 48 \text{ dB/m}$, a loss ratio α_{2nd}/α_{FM} of ~ 480 . A very high loss ratio α_{2nd}/α_{FM} of ~ 700 is possible at $d/\Lambda = 0.62$. In LCFs with two layers of features, the loss ratio α_{2nd}/α_{FM} can change significantly over a small range of d/Λ and will no longer serves as a useful parameter as that in the LCFs with a single layer of features.

4.3 Bend Loss of LCFs

LCFs with hexagonal features as illustrated in fig. 8 are also studied for bending effects. Circular features have also been studied and the conclusion in this section is found to be largely independent of feature shapes. The fundamental, 2nd and 3rd modes in a LCF at bend radius $R=20 \text{ cm}$ for both AA and BB bends are shown in fig. 8. This LCF has $2\rho=50 \mu\text{m}$, and $d/\Lambda=0.75$. Generally, modes moves away from the bend centres and can be severely distorted from the straight case. The 2nd mode loss versus the fundamental loss for various bend radii and both AA and BB bends is summarized in fig. 9. For the AA bends, the loss ratio α_{2nd}/α_{FM} converges to a line defined by $\alpha_{2nd}/\alpha_{FM} \approx 8$ at small bend radius regardless d/Λ values. For the BB bends, the 2nd mode loss can be much lower than that of the corresponding AA bend at small bend radius. Bend orientation needs to be carefully managed if it is required to operate at very small bend radii. It is, therefore, preferable not to operate at very small bend radii.

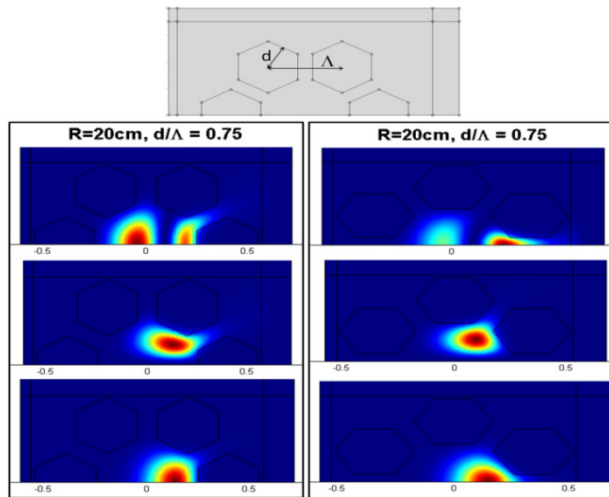


Fig. 8. Illustration of the simulated LCF with hexagonal features and the fundamental mode (bottom), the 2nd mode (middle) and the 3rd mode (top) for $2\rho=50 \mu\text{m}$, $d/\Lambda=0.75$ and bend radius $R=20 \text{ cm}$ for both AA (left) and BB (right) bend planes. The structure for the AA plane simulation is shown in the top figure. For the BB bend plane simulation, the fibre is rotated by 90 degree and the top half is chosen for the simulation.

Critical bend radius for $\alpha_{FM} = 1\text{dB/m}$ and 2dB/m for LCFs with of six circular features, $2\rho=50\mu\text{m}$, and $d/\Lambda=0.9$, is plotted in fig. 10. The critical radius changes slowly at small core diameters, but increases faster at large core diameters. Coil diameters of less than 0.5m can be realized for core diameters as large as $100\mu\text{m}$.

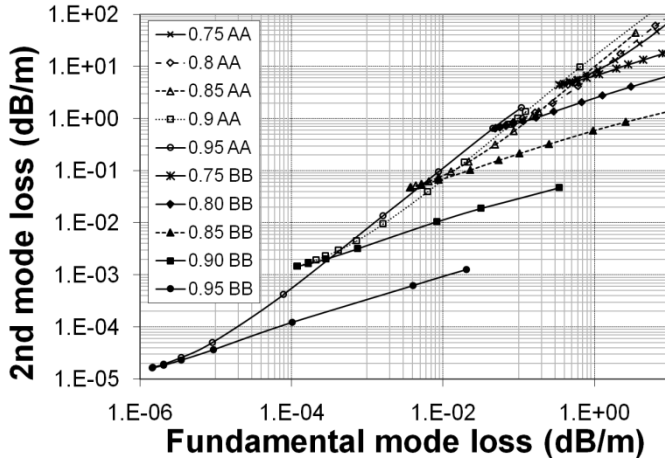


Fig. 9. The 2nd order mode bend loss versus the fundamental mode loss for AA and BB bend planes is plotted for LCFs with six hexagonal features, $2\rho=50\mu\text{m}$, and $d/\Lambda=0.75, 0.8, 0.85, 0.9$ and 0.95 .

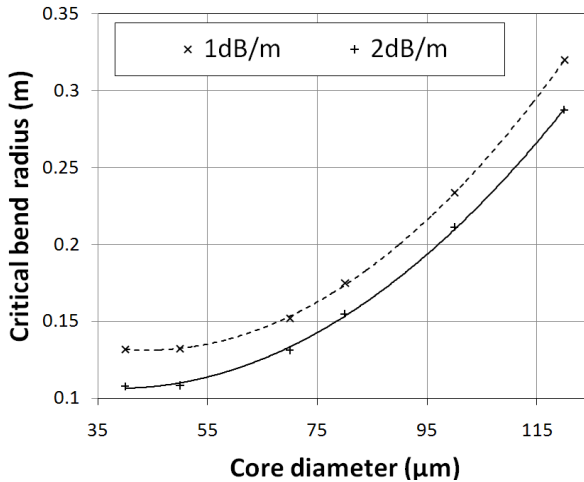


Fig. 10. Critical bend radius for $\alpha_{FM} = 1\text{dB/m}$ and 2dB/m for LCFs with six circular features, $\Delta n=1.2 \times 10^{-3}$, $2\rho=50\mu\text{m}$, and $d/\Lambda=0.9$.

4.4 Resonantly Enhanced LCFs

The analysis so far is performed considering a waveguide formed by six or eighteen features in an infinite background glass. In reality, there is a finite fibre diameter and additional coatings on the optical fibre. There are typically two types of coatings used. A high index polymer coating is typically employed for standard optical fibres and a low index coating is used to form a double clad fibre which supports a multimode pump within the low index coating. In case of LCFs, there is a strong optical coupling between the core formed by the six low index features and the second cladding region beyond the six low index features. A deeper understanding of LCFs requires a study of the overall fibre with coating included. For high average output powers, a high power multimode pump is usually deployed in combination with a double clad fibre. An example of a double clad fibre is a LCF with low index polymer coating where a multimode pump is guided within the low index coating while a single spatial mode laser beam is guided in the core doped with active ions. Many modes are guided in a double clad LCF when considering the overall fibre. Fig. 11 tracks a number of lower order modes for a LCF with $2\rho=50\mu\text{m}$, $d/\Lambda=0.7$, and $n_{\text{coating}}=1.37$, while varying fibre outer diameter. The refractive index of the background silica glass is simulated by an empirical formula at $\lambda=1.05\mu\text{m}$ (Ghatak 1998).

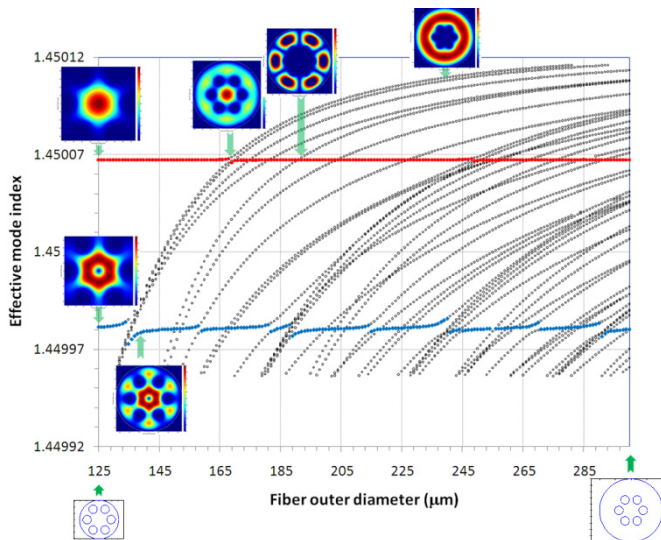


Fig. 11. Effective index of modes in a double clad LCF with $2\rho=50\mu\text{m}$, $d/\Lambda=0.7$ and $n_{\text{coating}}=1.37$ at $\lambda=1.05\mu\text{m}$.

The Fundamental core mode is represented by red dots (top horizontal line) and the second core mode by blue dots (bottom horizontal line) respectively in fig. 11. All the other modes are represented by black circles. The first point to note is that the fundamental core mode is no longer the fundamental mode (the mode with largest effective index) of the fibre at larger fibre diameters, which is a mode with most of its power in the second cladding region beyond the six low index features. In other words, the fundamental core mode is just another higher order mode of the fibre, which happens to resemble a Gaussian beam in the

core. The second point to note is that there are strong anti-crossings, where strongly interacting modes take on each other's features, e.g., a fundamental core mode at $\sim 170\mu\text{m}$ or a second core mode at $\sim 135\mu\text{m}$ (see insets in fig. 11 for modes), and weak anti-crossings, e.g. fundamental core mode at $\sim 195\mu\text{m}$ (see inset for mode), where the concerned modes share very little common features in practice (coupling is forbidden by symmetry). A third point to note is that there are many more strong anti-crossings for the second core mode. Strong anti-crossing is interesting, because the mode can have a larger part of its power in the cladding where there is no gain and, more importantly, the increased reliance on the glass and coating boundary for its guidance makes it more vulnerable to power leakage to coating and higher order modes through macro and micro bending as well as perturbation-induced coupling at the glass and coating interface. If a fibre diameter is chosen such that the second core mode is at a strong anti-crossing, further higher order mode suppression and much improved single mode operation in the core can be achieved.

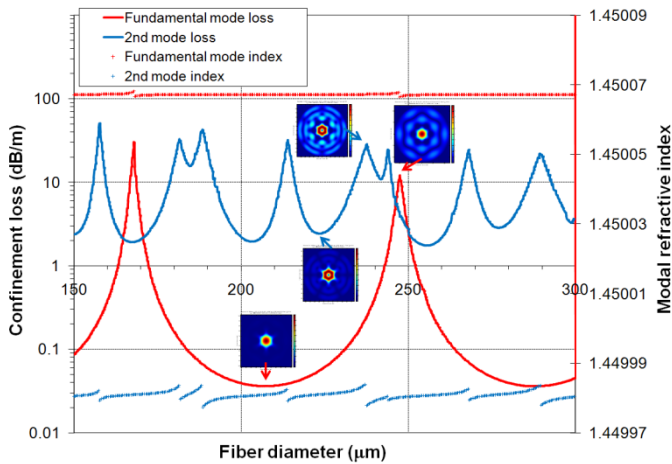


Fig. 12. Confinement loss and modal index of fundamental and 2nd order mode in a LCF with $2p=50\mu\text{m}$, $d/\Lambda=0.7$ and $n_{\text{coating}}=1.54$ at $\lambda=1.05\mu\text{m}$.

In a double clad LCF with low index coating, all guided modes are theoretically lossless, i.e. there is total internal reflection for the large number of guided modes at the glass and coating boundary. Though all modes are guided in this case, the modes which derives significant part of its guidance from glass and coating interface and less of their guidance from the inner cladding features are much more susceptible to macro and micro bending due their much large spatial presence and to glass and coating interface imperfections. This will effectively remove power away from these modes and reduce their effective propagation distance in the core, effectively rendering them lossy. Robust single mode operation in the core in this case implies that adequate core guidance is only possible for the fundamental core mode. In case where the core is doped with active ions, only the fundamental core mode will be strongly amplified.

While all guided modes are lossless in a LCF with low index coating, all modes are leaky in a LCF with high index coating and modes which rely strongly on glass and coating interface

and less on the inner cladding features for its guidance will leak out quickly. Confinement loss, in this case, provides a good measure of how much a mode is guided by the inner cladding features, and, consequently, of mode discrimination in propagation. The significant part of the respective mode features remain unchanged when the higher index coating is replaced by a lower one, and, consequently, the analysis for the case of high index coating also provides a good measurements in terms of mode robustness for the case of low index coating in a double clad fibre. The confinement losses of the same LCF with a high index coating of $n_{\text{coating}}=1.54$ and $\lambda=1.05\mu\text{m}$ is shown in fig. 12. Modes higher than 2nd mode, in general, have much higher loss and do not need to be considered in practice (Dong 2007). The peaks in the confinement loss are from strong anti-crossings. They remain at the same locations as those in fig. 11 with low index coating. It can be clearly seen that a significant increase of mode discrimination can be achieved by operating at a strong second core mode anti-crossing.

4.5 Experiments

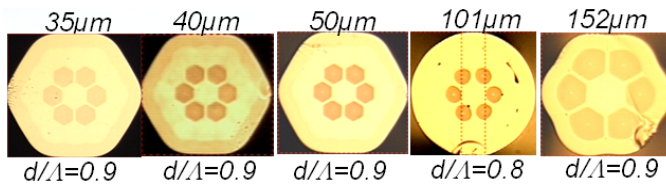


Fig. 13. Some examples of fabricated all Glass LCFs.

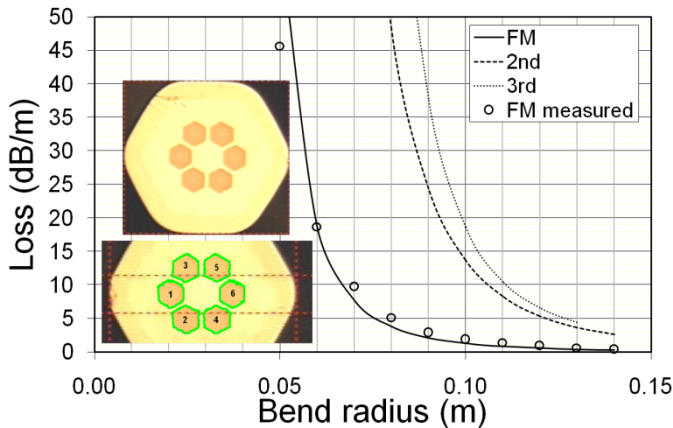


Fig. 14. Measured and simulated bend loss in a LCF with $2\rho=50\mu\text{m}$ and $d/\Lambda\approx 0.9$.

A wide range of all glass LCFs are fabricated from core diameters from $35\mu\text{m}$ to well over $100\mu\text{m}$. All fibres are made with silica glass as the background glass and slightly fluorine-doped silica glass as the features. LCFs with both circular and hexagonal features are fabricated and tested. The condition for the fabrication of LCFs with hexagonal features also creates LCFs with rounded hexagonal outline (see fig. 13). Such a shape is known to be preferred for the pump mode mixing in a double clad fibre where pump propagates in a

much large cladding guide. A LCF with $2\rho=30\mu\text{m}$ and $d/\Lambda=0.9$ is also fabricated and tested. The fundamental mode in this fibre is found to be not well confined with much of its power in the cladding. This is not too surprising, considering that it has been anticipated from fig. 6 that design space for LCFs with core diameter below $30\mu\text{m}$ rapidly vanishes. All other fabricated fibres in fig. 13 are easy to achieve fundamental mode propagation with a varying degree of bend loss performance. In general, bend loss increases rapidly with a core diameter increase.

A fabricated LCF with hexagonal features, $2\rho=50\mu\text{m}$ and $d/\Lambda=0.9$ (see insets in fig. 14) is first have it bend loss measured without any deliberate effort to identify bend orientations. This LCF is also simulated by FEM using the extracted feature contours from the measured cross section photo of the fibre (see bottom inset in fig. 14). All fibre parameters used in the simulation are directly from the measured cross section, which define the locations and sizes of each feature. The simulated fundamental mode bend losses along AA and BB bend planes are found to be reasonably close for this fibre over this range of bend radius. The bend loss of AA bend plane is plotted and is found to fit very well with the measured data, providing a reasonable level of confidence in the FEM simulation.

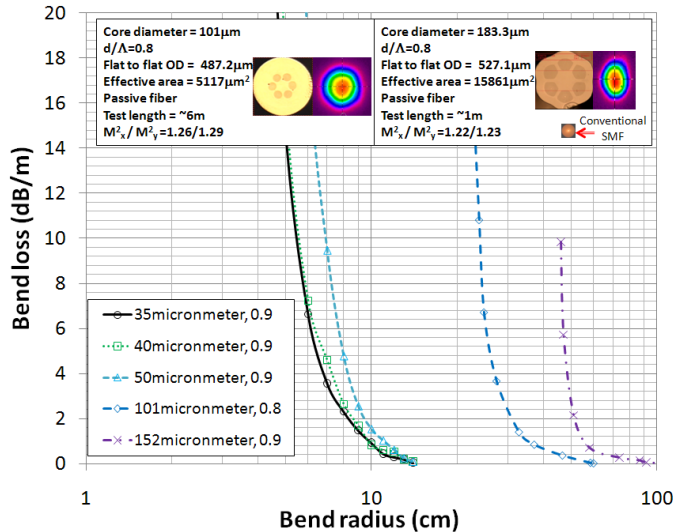


Fig. 15. Cross section, measured mode and fibre details are given for the LCF with $101\mu\text{m}$ core, left inset, and the LCF with $183.3\mu\text{m}$ core, right inset. Both fibres have coating index of 1.54. Measured bend loss for LCFs with various core diameters.

The LCF, shown on the top left inset in fig. 15, has $2\rho=101\mu\text{m}$, $d/\Lambda=0.9$ and a coating with $n_{\text{coating}}=1.54$. The effective mode area of the LCF is calculated to be $5117\mu\text{m}^2$. A length of the LCF $\sim 6\text{m}$ long is loosely coiled in a 1m coil and the Measured M^2 with an ASE source and Spiricon M^2 -200 is $M^2_x=1.26$ and $M^2_y=1.29$. M^2 is commonly used for beam quality measurement. A M^2 value of 1 corresponds to a perfect Gaussian beam profile, with all practical beams having an M^2 value >1 . The LCF, shown on the top right inset, has $2\rho=183.3\mu\text{m}$, $d/\Lambda=0.8$ and a coating with $n_{\text{coating}}=1.54$. A conventional single mode optical

fibre of the same scale is also shown for comparison. The effective mode area of this LCF is calculated to be $15861\mu\text{m}^2$, a record effective mode area and over two orders of magnitude improvement over conventional single mode optical fibre. The Measured M^2 of a 1m straight fibre with an ASE source is $M^2_x=1.22$ and $M^2_y=1.23$. Measured mode pattern at the output of the fibres are also shown in fig. 15. Mode, in general, is more sensitive to external stress on the fibre at very large core diameters, leading to the distortion on the mode pattern.

Fig. 15 also summarizes bend loss measurements in fibre LCFs with core diameters of $35\mu\text{m}$, $40\mu\text{m}$, $50\mu\text{m}$, $101\mu\text{m}$ and $152\mu\text{m}$ respectively. The fibre is first laid in prefabricated circular grooves with various diameters. Transmission at each coil diameters is then measured after the output mode pattern is confirmed. Absolute transmission of the fibres is measured by a separate cut-back measurement. The absolute transmission is then used to re-calibrate the relative bend loss measurement. The ability of LCFs to be bent diminishes very quickly as the core diameter increases. This effect is fundamentally related to the fact that the ability of guided modes to navigate a bend is related to how rapidly a mode can change its spatial pattern without breaking up while propagating, i.e. maintain adiabatic transition. As the mode gets larger, this ability to change diminishes very quickly.

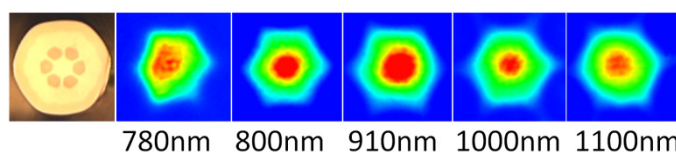


Fig. 16. The cross section and measured modes for a LCF with $\Delta n=1.2 \times 10^{-3}$, $2\rho=52.7\mu\text{m}$, $d/\Lambda=0.8$, flat-to-flat dimension= $254.2\mu\text{m}$, effective mode area= $1548\mu\text{m}^2$ at $1.05\mu\text{m}$, pump absorption= 11dB/m at 976nm , pump NA= 0.45 . Measured M^2 at 1064nm is $1.17/1.18$.

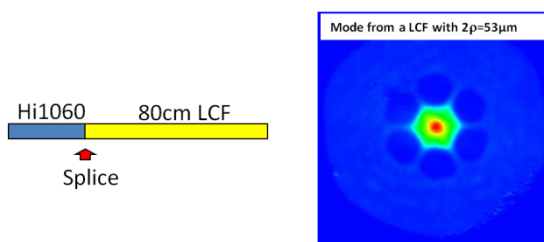


Fig. 17. Measured mode of the Hi1060-spliced and ytterbium-doped LCF.

Ytterbium-doped all glass LCFs is also fabricated by incorporating ytterbium-doped glass with refractive index closely matched to that of the silica glass. An example of such a fibre is shown in fig. 16. This LCF is coated with a low index polymer, which guides pump with a pump NA of 0.45 . This LCF has pump absorption of 11dB/m at the peak of ytterbium absorption at $\sim 976\text{nm}$. This LCF also has $2\rho=52.7\mu\text{m}$ and $d/\Lambda=0.8$. This gives simulated effective area of $1548\mu\text{m}^2$ at $1.05\mu\text{m}$. This LCF has a rounded hexagonal shape and a flat-to-flat dimension of $254.2\mu\text{m}$.

The mode from a 20cm piece of this LCF is measured using a broad band super-continuum source followed by a band-pass filter. Captured mode at various wavelengths is shown in fig. 16. It can be seen that fundamental mode operation is achieved in such a short length of fibre for wavelength as low as 800nm. This LCF is found to robustly guide the fundamental mode at $\sim 1\mu\text{m}$. The output mode pattern is essentially independent of launch conditions. This test also shows that mode quality is not compromised by the incorporation of the ytterbium-doped glass in the core. It is further demonstrated that this LCF can be directly spliced to Hi1060. The splice loss is measured at $1.3\mu\text{m}$ away from the ytterbium absorption to be $\sim 1.5\text{dB}$. This is much lower than the expected $\sim 10\text{dB}$ from modal overlap, indicating a significant level of mode-matching at the splice. No compromise of mode quality is observed when light is launched via Hi1060 at $\sim 1\mu\text{m}$, demonstrating potential for all-fibre devices with much improved stability and reliability (see fig. 17).

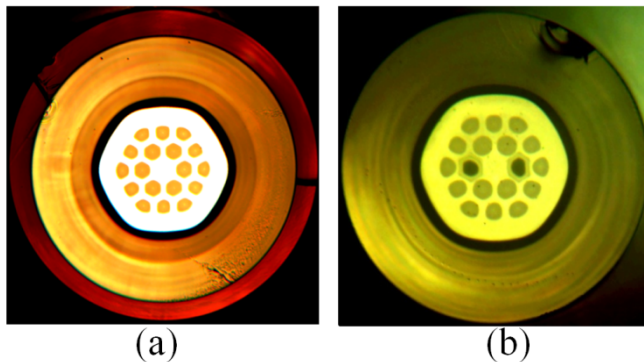


Fig. 18. (a) An all glass active LCF and (b) an all glass PM active LCF with highly fluorine-doped pump cladding.

Additionally, active double clad all glass leakage channel fibres can be fabricated with highly fluorine-doped silica as pump cladding (see fig. 18). The new all glass leakage channel fibres have no polymer in the pump path and have independent control of fibre outer diameters and pump cladding dimension, and, therefore, enables designs with smaller pump guide for higher pump absorption and, at the same time, with large fibre diameters to minimize micro and macro bending effects, a much desired features for large core fibres where intermodal coupling could an issue due to much increased mode density. Stress rods can also be added for PM LCFs (see fig. 18).

5. Conclusion

All glass micro-structured fibres enables access to many new 2D designs beyond conventional optical fibres while maintaining the ease of fabrication and use akin to that of conventional optical fibres. This new technology has proven to be especially useful for single mode operations in fibre with core diameters much beyond conventional optical fibres. These fibres are starting to find significant applications for power scaling in fibre lasers, potentially enabling fibre lasers to be able to compete with solid state laser in offering

pulsed laser systems of high peak powers for material processing and biomedical applications.

6. References

- Birks, T.A.; Knight, J.C. & Russell, P.St.J. (1997), Endless single-mode photonic crystal fibre *Optical Letters*, vol. 22, 961-963.
- Brooks, C.D. & Di Teodoro, F. (2006), Multi-megawatt peak-power, single-transverse-mode operation of a 100 μm core diameter, Yb-doped rod-like photonic crystal fibre amplifier, *Applied Physics Letters*, vol. 89, 111119-111121.
- Dong, L.; Peng X. & Li, J. (2007), Leakage channel optical fibres with large effective area, *Journal of the Optical Society of America B*, vol. 24, 1689-1697.
- Dong, L.; Li, J.; McKay, H.A.; Marcinkevicius, A.; Thomas, B.T.; Moore, M.; Fu L. & Fermann, M.E. (2008), Robust and practical optical fibres for single mode operation with core diameters up to 170 μm , *Conference on Lasers and Electro-optics*, post-deadline paper CPDB6, San Jose, CA, May.
- Dong, L.; McKay, H.A. & Fu, L. (2008), All glass endless single mode photonics crystal fibres, *Optics Letters*, vol. 33, 2440-2442.
- Dong, L.; Thomas, B.K. & Fu, L. (2008), High nonlinear silica suspended core fibres, *Optical Express*, vol. 16, 16423-16430.
- Dong, L. (2008), Approximate treatment of nonlinear waveguide equation in the regime of nonlinear self-focus, *Journal of Lightwave Technology*, vol. 26, 3476-3485.
- Dong, L.; Wu, T.; McKay, H.A.; Fu, L.; Li, J. & Winful, H. (2009), All Glass Large Core Leakage Channel Fibres,, *Journal of Selected Topics in Quantum Electronics*, vol. 14, 47-53.
- Feng, X.; Monro, T.M.; Petropoulos, P.; Finazzi, V. & Hewark, D. (2003), Solid micro-structured optical fibre, *Optics Express*, vol. 11, 2225-2230.
- Farrow, R.L.; Kliner, D.A.V.; Hadley, G.R. & Smith, A.V. (2006), Peak-power limits on fibre amplifiers imposed by self-focusing, *Optics Letters*, vol. 31, pp.3423-3425.
- Fermann, M.E. (1998), Single-mode excitation of multimode fibres with ultra short pulses, *Optics Letters*, vol. 23, 52-54.
- Fibich, G. & Gaeta, A.L. (2000), Critical power for self-focusing in bulk media and in hollow waveguides, *Optics Letters*, vol. 25, 335-337.
- Fini, J.M. (2005), Design of solid and microstructure fibres for suppression of higher order modes,, *Optics Express*, vol. 13, 3477-3490.
- Fini, J.M. (2006), Bend-resistant design of conventional and micro-structured fibres with very large mode area, *Optics Express*, vol. 14, 69-81.
- Fu, L.B.; Thomas, B.K. & Dong, L. (2008), Efficient supercontinuum generations in silica suspended core fibres, *Optics Express*, vol. 16, 19629-19642.
- Fu, L.B.; McKay, H.A. & Dong L. (2009), Extremely large effective mode areas single-mode fibres by index guiding, *Optical Express*, submitted. vol. 17, 11782-11793.
- Galvanauskas, A.; Cheng, M.Y.; Hou K.C. & Liao, K.H. (2007), High peak power pulse amplification in large core Yb-doped fibre amplifiers, *IEEE Journal of Selected Topics in Quantum Electronics*, vol. 13, 559-566.
- Gapontsev, V.P. (2009), Recent progress on high power CW fibre lasers, *SPIE Photonics West*, paper 7195-07, San Jose.

- Ghatak A. & Thyagarajan, K. (1998), Introduction to Fiber Optics, *Cambridge University Press*.
- Jones, D. J.; Diddams, S.A.; Ranka, J.K.; Stentz, A.J.; Windeler, R.S.; Hall, J.L. & Cundiff, S.T. (2000), Carrier envelope phase control of femtosecond mode-locked lasers and direct optical frequency synthesis, *Science*, vol. 288, 635-639.
- Knight, J.C.; Birks, T.A.; Russell, P.St.J. & Atkin D.M. (1996), All-silica single-mode optical fibre with photonic crystal cladding, *Optical Letters*, vol. 21, 1547-1549.
- Knight, J.C.; Birks, T.A.; Cregan, R.F.; Russell, P.St.J. & de Sandro, J.P. (1998), Large mode area photonic crystal fibre, *Electronic Letters*, vol. 34, 1347-1348.
- Koplow, J.P.; Kliner, D.A.V. & Goldberg, L. (2000), Single-mode operation of a coiled multimode fibre amplifier, *Optics Letters*, vol. 25, 442-444.
- Kuhlmey, B.T.; McPhedran, R.C. & Martin de Sterke, C. (2002), Modal cutoff in microstructured optical fibres, *Optics Letters*, vol. 27, 1684-1686.
- Kuhlmey, B.T.; McPhedran, R.C.; Martin de Sterke, C.; Robinson, P.A.; Renversez, G. & Maystre, D. (2002), Microstructured optical fibers: where's the edge?, *Optical Express*, vol. 10, 1285-1290.
- Limpert, J.; Liem, A.; Reich, M.; Schreiber, T.; Nolte, S.; Zellmer, H.; Tünnermann, A.; Broeng, J.; Petersson, A. & Jakobsen, C. (2004), Low-nonlinearity single-transverse-mode ytterbium-doped photonic crystal fibre amplifier, *Optics Express*, vol. 12, 1313-1319.
- Limpert, J.; Deguil-Robin, N.; Manek-Hönninger, I.; Salin, F.; Röser, F.; Liem, A.; Schreiber, T.; Nolte, S.; Zellmer, H.; Tünnermann, A.; Broeng, J.; Petersson, A. & Jakobsen, C. (2005), High-power rod-type photonic crystal fibre laser, *Optics Express*, vol. 13, 1055-1058 (2005).
- Limpert, J.; Schmidt, O.; Rothhardt, J.; Röser, F.; Schreiber, T. & Tünnermann, A. (2006), Extended single-mode photonic crystal fibre, *Optics Express*, vol. 14, 2715-2719.
- Nielsen, M.D. and Mortensen, N.A. (2003), Photonic crystal fibre design based on the V-parameter, *Optics Express*, vol. 11, 2762-2768.
- Ramachandran, S.; Nicholson, J.W.; Ghalimi, S.; Yan, M.F.; Wisk, P.; Monberg, E. & Dimarcello, F.V. (2006), Light propagation with ultra large modal areas in optical fibres, *Optics Letters*, vol. 31, 1797-1799.
- Ranka, J.K.; Windeler, R.S. & Stentz, A.J. (2000), Visible continuum generation in air-silica micro-structured optical fibres with anomalous dispersion at 800nm, *Optics Letters*, vol. 25, 25-27.
- Röser, F.; Eidam, T.; Rothhardt, J.; Schmidt, O.; Schimpf, D.N.; Limpert, J. & Tünnermann, A. (2007), Millijoule pulse energy high repetition rate femtosecond fibre chirped-pulse amplification system, *Optics Letters*, vol. 32, 3495-3497.
- Robert, P.J.; County, F.; Sabert, H.; Mangan, B.J.; Williams, D.P.; Farr, L.; Mason, M.W.; Tomlinson, A.; Birks, T.A.; Knight J.C. & Russell, P.St.J. (2005), Ultimate low loss of hollow-core photonic crystal fibres, *Optical Express*, vol. 13, 236-244
- Russell, P.St.J. (2006), Photonic crystal fibres, *Journal of Lightwave Technology*, vol. 24, 4729-4749.
- Suzuki, S.; McKay H.A.; Peng, X.; Fu, L. & Dong L. (2009), Efficient ytterbium-doped silica fibres with record high doping levels, *Optical express*, submitted. vol. 17, 9924-9932.
- Tsuchida, Y.; Saitoh, K. & Koshihara, M. (2007), Design of single-mode holey fibres with large-mode-area and low bending losses: the significance of the ring-core region, *Optics Express*, vol. 15, 1794-1803.

- White, T. P.; Kuhlmeier, B. T.; McPhedran, R. C.; Maystre, D.; Renversez, G.; Martijn de Sterke, C. & Botten, L. C. (2002), Multipole method for microstructured optical fibres. I. Formulation, *Journal of Optical Society of America B*, vol. 19, 2322-2330.
- Wu, T.; Dong, L. & Winful, H. (2008), Bend performance of leakage channel fibres, *Optics Express*, vol. 16, 4278-4285.

